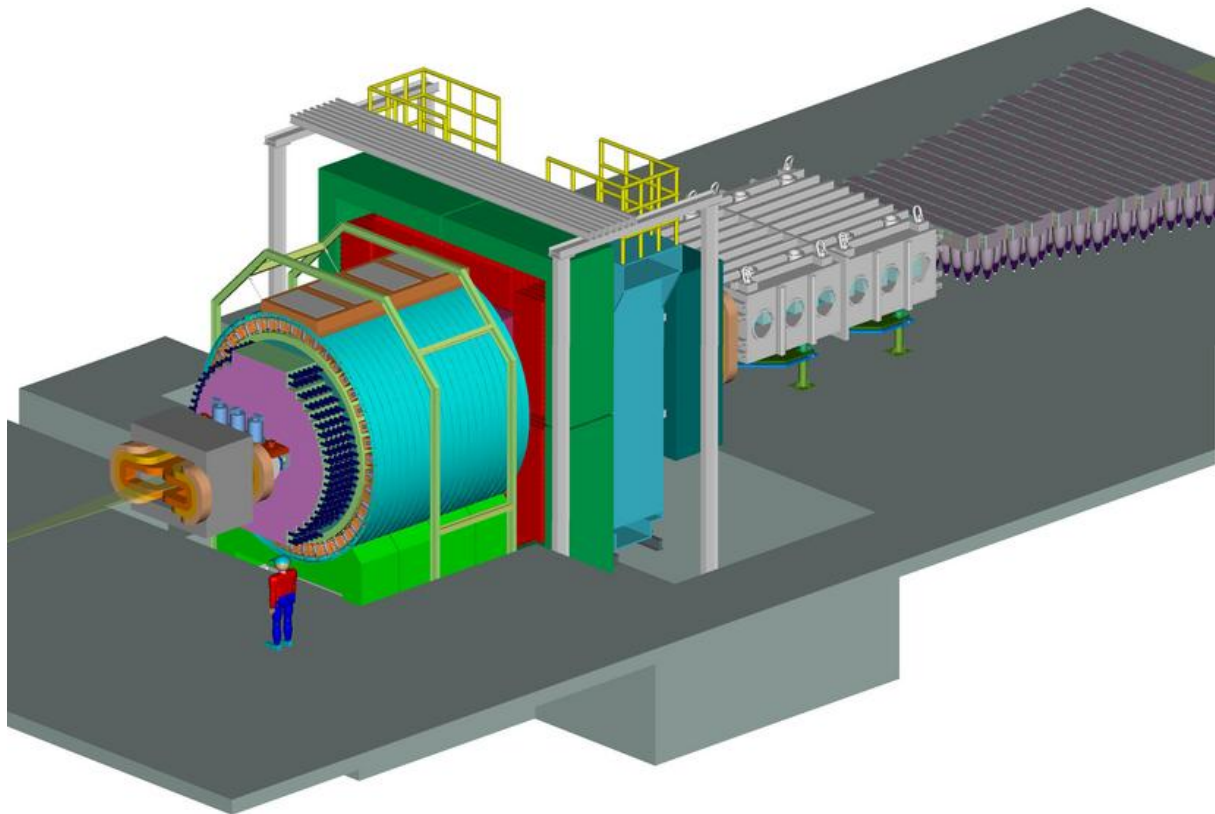


KOPIO Project

# Conceptual Design Report

April, 2005



## KOPIO Collaborators

### Arizona State University

J.R. Comfort, J. Figgins

### University of British Columbia, Canada

D. Bryman, M. Hasinoff, J. Ives

### Brookhaven National Laboratory

D. Beavis, I.-H. Chiang, A. Etkin, J.W. Glenn, A. Hanson, D. Jaffe, S. Kettell, D. Lazarus, K. Li,  
L. Littenberg, G. Redlinger, C. Scarlett, M. Sivertz, R. Strand

### University of Cincinnati

K. Kinoshita

### IHEP, Protvino, Russia

G. Britvich, V. Burtovoy, S. Chernichenko, L. Landsberg, A. Lednev, V. Obraztsov, R. Rogalev,  
V. Semenov, M. Shapkin, I. Shein, A. Soldatov, N. Tyurin, V. Vassil'chenko, D. Vavilov, A. Yanovich

### INR, Moscow, Russia

A. Ivashkin, D. Ishuk, M. Khabibullin, A. Khotjanzev, Y. Kudenko, A. Levchenko, O. Mineev,  
A. Vasiljev, N. Yeshov

### KEK, Japan

M. Kobayashi

### Kyoto University of Education, Japan

R. Takashima

### Kyoto University, Japan

H. Morii, Y. Nakajima, T. Nomura, N. Sasao, T. Sumida, N. Taniguchi, H. Yokoyama

### University of Montreal, Canada

J.-P. Martin

### University of New Mexico

B. Bassalleck, N. Bruner, D.E. Fields, J. Lowe, T.L. Thomas

### INFN, University of Perugia, Italy

E. Imbergamo, A. Nappi, M. Valdata, M. Viti

### Stony Brook University

N. Cartiglia, I. Christidi, M. Marx, P. Rumerio, R.D. Schamberger

### TRIUMF, Vancouver, Canada

P. Amaudruz, M. Barnes, J. Doornbos, P. Gumplinger, R. Henderson, N. Khan, J. Mildemberger, A.  
Miller, A. Mitra, T. Numao, R. Poutissou, F. Retiere, A. Sher, G. Wait

### Tsinghua University, Beijing, China

S. Chen

### University of Virginia

E. Frlez, D. Pocanic

### Virginia Polytechnic Institute and State University

M. Blecher, N. Graham, A. Hatzikoutelis

**Yale University** G. Atoyan, S.K. Dhawan, V. Issakov, A. Poblaguev, M.E. Zeller

**University of Zurich, Switzerland** P. Robmann, P. Truöl, A. van der Schaaf, S. Scheu

# Contents

<b>1</b>	<b>Introduction</b>	<b>1</b>
<b>2</b>	<b><math>K_L^0 \rightarrow \pi^0 \nu \bar{\nu}</math> — Theoretical Motivation</b>	<b>4</b>
2.1	Standard Model . . . . .	4
2.2	Beyond the Standard Model . . . . .	7
2.3	Theoretical Summary . . . . .	10
<b>3</b>	<b>Overview of the <math>K_L^0 \rightarrow \pi^0 \nu \bar{\nu}</math> Measurement Technique</b>	<b>12</b>
<b>4</b>	<b>AGS Modifications</b>	<b>17</b>
4.1	Motivations . . . . .	17
4.1.1	Microbunch Width . . . . .	17
4.1.2	Microbunch Separation . . . . .	17
4.1.3	Interbunch Extinction . . . . .	18
4.2	General Requirements . . . . .	18
4.3	Primary Beam Parameters for KOPIO . . . . .	19
4.4	Intensity Upgrades . . . . .	19
4.4.1	Booster Modifications . . . . .	19
4.4.2	AGS Modifications . . . . .	20
4.5	Switchyard Modifications . . . . .	20
4.6	KOPIO-Specific Microbunching Modifications . . . . .	21
4.6.1	Extraction RF Cavities: 25 MHz and 100 MHz . . . . .	21
4.6.2	Injection Systems Kicker Magnets . . . . .	23
<b>5</b>	<b>Neutral Beam</b>	<b>25</b>
5.1	Primary Proton Beam . . . . .	25
5.2	The KOPIO Neutral Beam . . . . .	27
5.2.1	The Spoiler . . . . .	29
5.2.2	Sweeping Magnets . . . . .	30
5.2.3	Collimators . . . . .	31
<b>6a</b>	<b>Preradiator</b>	<b>33</b>
6a.1	Performance Requirements . . . . .	33
6a.2	Design Concept . . . . .	33
6a.3	Performance Simulations and Measurements . . . . .	34
6a.4	The PR Detectors . . . . .	35
6a.4.1	Drift Chamber . . . . .	35
6a.4.2	Scintillators . . . . .	37
6a.4.3	External Photon Veto . . . . .	41
6a.4.4	Module Construction . . . . .	41
6a.4.5	Module Support and Installation . . . . .	42
6a.5	Electronics . . . . .	46
6a.5.1	Anode Electronics . . . . .	47
6a.5.2	Cathode Electronics . . . . .	48
6a.5.3	Scintillator Electronics . . . . .	50
6a.5.4	Control and Cooling . . . . .	51



<b>6b Calorimeter</b>	<b>54</b>
6b.1 KOPIO Shashlyk Module. . . . .	55
6b.1.1 Simulation of the Shashlyk Calorimeter . . . . .	55
6b.1.2 Methods to Improve Energy Resolution . . . . .	58
6b.2 Design of the Calorimeter Module . . . . .	58
6b.2.1 Improvement of the module geometry . . . . .	59
6b.2.2 WLS fibers . . . . .	61
6b.2.3 Scintillator . . . . .	61
6b.2.4 Photodetector . . . . .	63
6b.3 Experimental Study of Prototype Modules . . . . .	67
6b.3.1 Energy Resolution . . . . .	69
6b.3.2 Time Resolution . . . . .	70
6b.3.3 Photon Detection Inefficiency . . . . .	71
6b.3.4 Long-term APD Stability . . . . .	72
6b.4 Mass Production of the Shashlyk modules . . . . .	72
6b.5 Calorimeter Mounting . . . . .	73
6b.6 Calorimeter Cooling System . . . . .	73
6b.7 Calorimeter HV System . . . . .	74
6b.8 Calorimeter Front-End Electronics . . . . .	74
6b.9 Calibration and Monitoring of Calorimeter . . . . .	75
6b.9.1 Pre-calibration System . . . . .	75
6b.9.2 Monitoring System . . . . .	75
6b.10 Summary . . . . .	76
<b>6c KOPIO Photon Veto System</b>	<b>78</b>
6c.1 Barrel Veto Detector . . . . .	79
6c.1.1 Barrel Shashlyk Concept . . . . .	79
6c.1.2 Optimization of BV Shashlyk Modules . . . . .	79
6c.2 Log Veto Detectors . . . . .	85
6c.2.1 Log Sandwich Design Issues . . . . .	85
6c.3 Tests of Log Sandwich Modules . . . . .	87
6c.3.1 Design of the Tested Modules . . . . .	87
6c.3.2 Evaluation of Log Veto Performance . . . . .	91
6c.3.3 Conceptional Design for the Photon Veto Log Detectors . . . . .	93
6c.4 Readout and Electronics . . . . .	94
<b>6d Charged Particle Veto</b>	<b>98</b>
6d.1 Purpose . . . . .	98
6d.2 Requirements . . . . .	98
6d.3 Description of the System to be Built . . . . .	99
6d.4 Fundamental Limitations to the Detection Efficiency of Charged Particles . . . . .	99
6d.5 Detector R&D . . . . .	102
6d.6 Detector Concepts . . . . .	104
6d.6.1 Barrel CPV . . . . .	105
6d.6.2 Downstream CPV . . . . .	107
6d.6.3 Front-end Electronics . . . . .	108

<b>6e</b>	<b>Beam Catcher</b>	<b>109</b>
6e.1	Overview . . . . .	109
6e.2	Aerogel Catcher . . . . .	110
6e.2.1	Conceptual Design . . . . .	110
6e.2.2	Base Design of the Aerogel Catcher . . . . .	110
6e.2.3	Experimental Study of Prototypes . . . . .	112
6e.3	Guard Counter . . . . .	114
6e.4	Expected Performance . . . . .	117
6e.4.1	Efficiency for Photons . . . . .	117
6e.4.2	Response to Neutrons . . . . .	119
6e.4.3	Response to Neutral Kaons . . . . .	121
6e.4.4	Responses to Beam Photons . . . . .	123
6e.5	Summary . . . . .	123
<b>6f</b>	<b>Photon Detection Inefficiency</b>	<b>124</b>
6f.1	Overview . . . . .	124
6f.2	Sources of photon detection inefficiency . . . . .	124
6f.2.1	Sampling fluctuations . . . . .	124
6f.2.2	Punch-through . . . . .	126
6f.2.3	Photonuclear Interactions . . . . .	126
6f.3	E949 Measurements of Photon Detection Inefficiency . . . . .	126
6f.4	FLUKA Simulation of E949 Photon Veto . . . . .	128
6f.5	Estimation of KOPIO Photon Detection Inefficiency . . . . .	128
6f.6	Future Work . . . . .	131
<b>7</b>	<b>The Vacuum</b>	<b>132</b>
<b>8</b>	<b>Photodetector Electronics</b>	<b>135</b>
8.1	Photosensor Mounted Systems . . . . .	135
8.1.1	HV System . . . . .	135
8.1.2	LV System . . . . .	136
8.1.3	Preamplifier . . . . .	136
8.2	Calibration and Monitoring System . . . . .	136
8.2.1	Pre-calibration System . . . . .	137
8.2.2	Monitoring System . . . . .	138
8.3	Readout System . . . . .	139
8.3.1	Wave Form Digitizers (WFD) . . . . .	140
8.3.2	Crate Data Collectors . . . . .	141
<b>9</b>	<b>Trigger</b>	<b>144</b>
9.1	Introduction and Requirements . . . . .	144
9.2	Trigger Simulations . . . . .	145
9.2.1	Simulation programs . . . . .	145
9.2.2	Trigger conditions . . . . .	146
9.2.3	Efficiencies and rates . . . . .	148
9.3	Trigger Architecture Overview . . . . .	149
9.4	L1 Trigger . . . . .	150
9.4.1	Trigger outputs of the photodetector digitizers (WFD) . . . . .	151
9.4.2	Collector Boards . . . . .	152
9.4.3	Logic Modules . . . . .	153
9.5	Trigger Supervisor . . . . .	155

9.6	Clock System . . . . .	156
<b>10</b>	<b>Data Acquisition and High-Level Trigger</b>	<b>157</b>
10.1	Overview . . . . .	157
10.2	Event Builder . . . . .	158
10.3	Level 3 Trigger . . . . .	159
10.3.1	Requirements . . . . .	159
10.3.2	Initial Look at Algorithms . . . . .	159
10.4	Level 2 . . . . .	160
10.5	Online Software . . . . .	161
10.6	Open Issues and Near-term R&D . . . . .	161
<b>11</b>	<b>Offline Computing</b>	<b>163</b>
11.1	Overview . . . . .	163
11.2	Offline Compute Farm . . . . .	163
11.3	Offline Software . . . . .	164
11.3.1	Software Framework and Components . . . . .	164
11.3.2	Simulations . . . . .	165
11.3.3	Event Reconstruction . . . . .	165
<b>12</b>	<b>Conventional Systems and Integration</b>	<b>167</b>
12.1	Installation and Integration . . . . .	167
12.2	Conventional Utilities . . . . .	167
12.3	Protection and Safety . . . . .	167
<b>13</b>	<b>Signal and Background Estimates</b>	<b>175</b>
13.1	Tools . . . . .	175
13.2	Flux Assumptions . . . . .	175
13.3	Veto Inefficiency and Resolution . . . . .	176
13.3.1	Photon Veto Inefficiency . . . . .	177
13.3.2	Charged Particle Veto Inefficiency . . . . .	178
13.3.3	Detector Resolutions . . . . .	179
13.4	Detection Methods . . . . .	180
13.5	Background Mechanisms . . . . .	180
13.6	Backgrounds due to $K_L^0$ Decays . . . . .	180
13.6.1	$K_L^0 \rightarrow \pi^0 \pi^0$ Background . . . . .	181
13.6.2	$K_L^0 \rightarrow \pi^0 \pi^+ \pi^-$ Background . . . . .	186
13.6.3	$K_L^0 \rightarrow \pi^\pm e^\mp \nu \gamma$ Background . . . . .	186
13.6.4	$K_L^0 \rightarrow \pi^0 \pi^\pm e^\mp \nu$ Background . . . . .	186
13.6.5	$K_L^0 \rightarrow \gamma \gamma$ , $K_L^0 \rightarrow \pi^0 \pi^0 \pi^0$ , and $K_L^0 \rightarrow \pi^0 \gamma \gamma$ Backgrounds . . . . .	188
13.7	Candidate Event Selection . . . . .	188
13.8	Other Potential Backgrounds . . . . .	202
13.8.1	Background from $\Lambda \rightarrow \pi^0 n$ . . . . .	202
13.8.2	Background from $K_S^0$ Decays . . . . .	202
13.8.3	Background from Charged Kaons in the Beam . . . . .	202
13.8.4	Background from $K_L^0 \rightarrow K^\pm e^\mp \nu$ . . . . .	203
13.8.5	Background from $\pi^\pm \rightarrow \pi^0 e^\pm \nu$ . . . . .	203
13.8.6	Background from Neutrons . . . . .	205
13.8.7	Background from Antineutrons . . . . .	206
13.9	Signal Losses . . . . .	206
13.10	Summary of Signal and Backgrounds . . . . .	210

13.11	Parameter variations . . . . .	210
<b>14</b>	<b>Additional Physics Goals</b>	<b>216</b>
14.1	Introduction . . . . .	216
14.2	$K_L^0 \rightarrow \pi^0 X$ and $K_L^0 \rightarrow \pi^0 \pi^0 X$ . . . . .	216
14.3	Radiative Decays: $K_L^0 \rightarrow \gamma\gamma$ , $K_L^0 \rightarrow \gamma\gamma^*$ , $K_L^0 \rightarrow \gamma^*\gamma^*$ , $K_L^0 \rightarrow \gamma\gamma\gamma$ . . . . .	217
14.4	$K_L^0 \rightarrow \pi^0\gamma\gamma$ and $K_L^0 \rightarrow \pi^0\pi^0\gamma$ . . . . .	218
14.5	$K_L^0$ beta decay, $K_L^0$ Lifetime, and Tagged $\pi^0$ Decays . . . . .	219
<b>15</b>	<b>Operations Plan</b>	<b>221</b>
<b>16</b>	<b>Summary</b>	<b>222</b>

## List of Figures

1.1	Five- $\sigma$ upper and lower exclusion limits versus the fractional running time for the KOPIO experiment. The models listed start to be constrained at the levels indicated by the horizontal lines. . . . .	3
2.1	The leading electroweak diagrams inducing $K_L^0 \rightarrow \pi^0 \nu \bar{\nu}$ . . . . .	4
2.2	The unitarity triangle. . . . .	5
2.3	Expected relative error on $\mathcal{B}(K_L^0 \rightarrow \pi^0 \nu \bar{\nu})$ versus the fraction of the full KOPIO run, assuming the central Standard Model branching ratio. . . . .	6
2.4	Upper plot: standard UT fit compared to the band resulting from the central experimental value of $\mathcal{B}(K^+ \rightarrow \pi^+ \nu \bar{\nu})$ . Lower plot: UT from 10% measurements of charged and neutral $K \rightarrow \pi \nu \bar{\nu}$ at currently predicted values. Also lines corresponding to different values of these branching ratios (from Ref.[4]). . . . .	7
3.1	Elements of the KOPIO concept: a pulsed primary beam produces low-energy kaons whose time-of-flight reveals their momentum when the $\pi^0$ from $K_L^0 \rightarrow \pi^0 \nu \bar{\nu}$ decay is reconstructed. . . . .	13
3.2	Plan and elevation views of the KOPIO detector. . . . .	14
3.3	Two events simulated by GEANT3: (a) both photons from the $\pi^0 \rightarrow \gamma \gamma$ decay converted in the Preradiator, (b) one photon converted in the Preradiator and the second photon was detected in the Barrel Veto calorimeter. . . . .	16
3.4	Reconstructed $\pi^0$ kinetic energy squared $T_{\pi^{*2}}$ vs. the log of the apparent missing energy $\ln(E_{\text{miss}})$ for signal (left) and background (right). Whereas the signal events show an approximately constant distribution over the allowed phase space, backgrounds are concentrated in a low $T_{\pi^{*2}}$ region populated by $K_L^0 \rightarrow \pi^- \pi^+ \pi^0$ decays and a high $T_{\pi^{*2}}$ region populated by $K_L^0 \rightarrow \pi^0 \pi^0$ decays. . . . .	16
4.1	Kaon momentum distribution in MeV/c for KOPIO. . . . .	17
4.2	Kinematic rejection of the reconstructed pion in $K_L^0 \rightarrow \pi^0 \pi^0$ decays. (a) shows the reconstructed pion momentum in the kaon rest frame versus the energy difference between the two photons. (b) shows the same reconstructed pions when the kaon is produced 10 nanoseconds earlier than the microbunch time. This timing shift causes the background events to fall in the middle of the signal region, making kinematic rejection impossible. The colors are contours in event density, running from most dense (black) to least dense (yellow). . . . .	18
4.3	Measured and simulated microbunch time distributions for a 93-MHz RF cavity operating at 22 kV. . . . .	22
4.4	Log plot of the time structure of microbunches extracted from the AGS. The horizontal axis is the event time (in nanoseconds) of the arrival of an antiproton at the detector telescope, relative to an RF pulse. A possible interbunch event can be seen at the far right-hand side of the plot. The 225-ns spacing of the three visible microbunches is characteristic of the 4.5-MHz RF cavity. . . . .	23
5.1	Current AGS switchyard. . . . .	25
5.2	AGS switchyard for RSVP. . . . .	26
5.3	Beam transport envelope . . . . .	27
5.4	Floor layout of the KOPIO detector. . . . .	28
5.5	Photon energy distributions accepted in the neutral channel for spoiler thicknesses of 0 cm (blue), 5 cm (red), and 7 cm (green). . . . .	29
5.6	$K_L^0$ momentum distribution at the entrance to the decay tank. . . . .	30
5.7	Vertical position of charged kaons at $z = 1000$ cm (left) and $z = 1400$ cm (right). . . . .	31
5.8	The collimators in elevation view (left) and plan view (right). The lines indicate the determination of the vertical (left) and horizontal (right) downstream collimation surfaces. . . . .	32
5.9	Neutron intensities for four collimator aspect ratios that provide the same acceptance. . . . .	32

6a.1	Simulated photon angular resolution from smeared GEANT tracks at incident photon energies of 350, 250 and 150 MeV. The vertical axis is the estimated resolution in photon angle projected on one plane in milliradians, and the horizontal axis is the photon angle of incidence in radians. . . . .	35
6a.2	Angular resolution measurements with tagged photon beams at normal incidence to a radiator stack with all wire planes parallel to each other. The plots at the top row are for angles projected in one coordinate plane by using only anode information, and those on the bottom in the orthogonal coordinate by using only cathode information. The plots in the first column are for $E_\gamma = 150$ MeV, and the second for $E_\gamma = 250$ MeV. . . . .	36
6a.3	Left panel: The KOPIO Preradiator consisting of four quadrants surrounding the wide kaon beam line. The support legs (hangers) are shown below (above) the assembly. Right panel: One of the eight mechanically independent PR Modules that make up each quadrant. (One of the large L-shaped support plates is removed for visibility.) The large flat area is the scintillator/drift-chamber sandwich. It is surrounded by the Shashlyk modules of the EPV system, which are in turn surrounded by the six electronic crates for the chamber readout. . . . .	37
6a.4	Details of the design of the PR cathode-strip drift chambers. The upper (lower) panel shows the inner corner proximal to (outer corner distal from) the beam axis. The inner corner includes the WLS fibers from the scintillator layer just behind the chamber, between which are the numerous ground contacts for interconnecting the ground planes of all the chambers in a module. . . . .	38
6a.5	Drift cell isochrones separated by 2 ns of drift time in an Ar/ethane (50/50) gas mixture. . . . .	39
6a.6	The upper panel shows the arrangement of drift chambers surrounding a cathode-strip drift chamber that was used to obtain the results shown in the lower panel, which is the tracking residual of a single cathode-strip plane as a function of incident angle, using cosmic-ray muon tracks defined by four anode planes on either side. The function fitted to the angular dependence of the widths of the Gaussian shapes describing the residual distributions is $\sigma^2 = \sigma_0^2 + (\sigma_\theta \tan \theta)^2$ , where $\sigma_0 = 220 \pm 10 \mu\text{m}$ and $\sigma_\theta = 573 \pm 4 \mu\text{m}$ . . . . .	40
6a.7	A prototype drift chamber with 2-m-long cathode strips. . . . .	41
6a.8	An example of a polystyrene scintillator plank that was extruded with six 1.4 mm diameter holes for WLS fibers. . . . .	42
6a.9	Conceptual design of a lower-quadrant PR module mounted on its support system. The scintillator/detector stack fits between the reinforcing webs of the vacuum vessel shown at the top right. The array of EPV Shashlyk modules surround the detector stack, and WLS fiber bundles pass over the Shashlyk modules from the stack to PMTs behind those modules. Cooling air-flow paths are shown through the six chamber readout crates mounted along the outer two edges of the support frame. . . . .	43
6a.10	Elevation view of the conceptual design for the installation of the PR modules in the KOPIO Experiment. Removal or installation of the entire lower-right 8-module quadrant as a unit is shown, while the lower left shows the same operation for a single module, which must be slightly lowered for this movement to clear cables, etc. . . . .	44
6a.11	Plan views of the conceptual design for the installation of the PR modules in the KOPIO Experiment. The upper (lower) panels show sectional views through the upper (lower) quadrants, while removal of a single module (quadrant) is shown on the left (right). The support frame from which the upper quadrants hang is itself supported on the four pillars shown in rectangular outline most visibly in the lower panel, two outside of the downstream end of the Barrel Veto, and two downstream of the Calorimeter location. . . . .	45
6a.12	Plan view of the conceptual design of the PR installation in the context of the rest of the KOPIO subsystems in the experimental hall. . . . .	46
6a.13	The pit needed in the floor of the experimental hall for installation and servicing of the lower PR quadrants. . . . .	47

6a.14	Wire chamber readout scheme. . . . .	48
6a.15	A readout crate for the PR chambers, containing four 96-channel TDC cards for the anode wires, four 96-channel ADC cards for the cathode strips, and one collector card. . . . .	49
6a.16	Functional diagram of the anode readout card. . . . .	50
6a.17	Tested prototypes of readout cards for the anode wires (left) and cathode strips (right). . . .	51
6a.18	Functional diagram of the cathode readout card. . . . .	52
6a.19	The Slow Control data path. The Chamber Collector card hosts the slow control processor for the eight readout cards in that crate. . . . .	52
6a.20	The prototype electronics crate that was used for cooling tests. . . . .	53
6b.1	A sketch view of the KOPIO Photon Calorimeter. . . . .	54
6b.2	The light collection efficiency of scintillation light from a scintillator plate for green light in WLS fibers versus the thickness of scintillator plate. The circles are for experimental data with optical contact between fibers and scintillator, the stars are for experimental data without optical contact, and the curves show the optical model simulation. . . . .	56
6b.3	Relative light output for different diameter KURARAY Y11 fibers compared to a 1.0-mm-diameter fiber. The solid line is an optical model calculation. . . . .	56
6b.4	Calorimeter response and energy resolution as a function of lead and scintillator plate thicknesses and number of layers. It is assumed that the calorimeter consists of 6000 layers of 0.35-mm lead and 1.5-mm of scintillator unless otherwise noted in histograms. . . . .	57
6b.5	The simulation of the light response function of the Shashlyk module at the entrance of the photodetector for a 250 MeV photon. The simulated signal in a Wave Form Digitizer if APD/Amplifier/Cable time-response function is taken into account is shown by dashed line. . . . .	57
6b.6	A Shashlyk module assembly is shown in the left picture. The module design is shown in the right picture. . . . .	58
6b.7	The dependence of the light collection efficiency on the $x$ -coordinate of the point-like light source. Solid lines are the simulations for the specified reflection efficiencies $\varepsilon_R$ of the wrapping material. . . . .	60
6b.8	The effective attenuation of the light in the fibers of Shashlyk module. Experimental data (marks) are fit by the exponential dependence $\exp(-x/L)$ (solid lines), where $x$ is the distance to the PMT and $L$ is the effective attenuation length. Measurements were made with a muon beam. . . . .	60
6b.9	The parametric dependence of the light collection efficiency on the effective attenuation length due to the reflection efficiency. The solid line is the result of a calculation based on the model of Ref.[6]. The experimental results are taken from Table 6b.3. For each scintillator, the calculated reflection efficiency is displayed. . . . .	62
6b.10	Comparison of a light-yield spread for the scintillator tiles used in 1998 (bottom) and 2003 (top) Shashlyk modules prototypes. . . . .	62
6b.11	The closed circles and solid line are the measured emission spectra of the BASF143E-based scintillator. The dashed line is the absorption spectrum of KURARAY Y11(200)MS WLS fibers. . . . .	62
6b.12	A quantum efficiency of the various APDs and 9903B PMT versus the light wavelength. An emission spectrum of the Kuraray Y11200MS WLS fiber (a solid green line) is shown in the same picture. . . . .	65
6b.13	The APD excess noise factor versus the APD gain for various pre-selected APDs. . . . .	65
6b.14	The APD dark current densities as a functions of the APD gains for the various pre-selected APDs. KOPIO data. . . . .	66
6b.15	Equivalent Noise Charge (ENC) versus the input capacitance for some fast Charge Sensitive Amplifiers. Integration time was 100 ns in all measurements. . . . .	66
6b.16	Equivalent energy noise of an APD/amplifier chain versus the APD gain for various environment temperature. . . . .	66

6b.17	PMT-9903B (left) and APD-630-70-74-510 (right) responses to the short light pulse. The duration of the light pulse is about 3 ns. The intensity of the light pulse is about 40,000 photons which corresponds to the 700-MeV photon signal. . . . .	67
6b.18	View of an APD unit. . . . .	68
6b.19	The functional scheme of an APD charge sensitive amplifier. . . . .	68
6b.20	A typical response of the nonet of Shashlyk modules to 340-MeV photons. . . . .	69
6b.21	Comparison of the experimental (marks) and simulated (lines) energy spectra in the Shashlyk nonet with the APD+WFD readout. . . . .	69
6b.22	Energy resolution of a prototype of the Shashlyk Calorimeter for KOPIO. . . . .	70
6b.23	The energy resolution of nonets of modules versus energy of the electron,photon beam for configurations described in the figure. The lines show the results of simulation. . . . .	70
6b.24	The typical distribution of photon energy in the nonet of the Shashlyk modules during timing measurements. Here, 340-MeV photons hit the nonet at a boundary between central (#5) and left (#4) modules. . . . .	71
6b.25	Experimental evaluation of the time resolution of a Shashlyk module. Solid line is a calculation for a $90 \text{ ps}/\sqrt{E \text{ (GeV)}}$ time resolution in both modules. . . . .	71
6b.26	Results of a Monte Carlo calculation of the time resolution of the Shashlyk module for photon, electron, and Minimum Ionizing Particles (MIP). The solid line corresponds to a $(90 \text{ ps})/\sqrt{E \text{ (GeV)}}$ time resolution, which has been obtained in a similar Monte Carlo simulation of the test beam measurements. . . . .	71
6b.27	The dependence of the photon detection inefficiency on the incident angle. . . . .	72
6b.28	Illustration of the long-term stability and gain dependence on the rate for the APD readout of the Calorimeter prototypes. The beam intensity was 300 kHz. . . . .	72
6b.29	Calorimeter structure in closed and opened positions. . . . .	73
6b.30	A sketch of the cooling unit. . . . .	74
6c.1	Positions of the photon veto detectors along the beam. The Magnet Photon Veto is mounted inside the D4 sweeping magnet, which is placed behind the Calorimeter. . . . .	78
6c.2	Cylindrical Barrel Veto assembled from 840 Shashlyk modules. Shashlyk rings of 2.5-m inner diameter are shifted in the azimuthal plane relative to neighboring rings so as to close the gaps in polar angles between modules. . . . .	80
6c.3	Prototype Shashlyk module for the photon Barrel Veto. . . . .	81
6c.4	“Pass-through” and sampling inefficiencies vs. the lead-layer thickness at fixed module radiation length, and with 1.5-mm-thick scintillator tiles. Photons of 20 MeV are incident at an angle of $30^\circ$ with respect to the normal to the surface. . . . .	82
6c.5	“Pass-through” inefficiencies vs. the energy of normally incident photons for different radiation lengths. . . . .	83
6c.6	Total photon inefficiency (without photonuclear interactions) in the BV with a realistic kaon beam model and parameters as described in the text. The detection threshold is 0.5 MeV. The solid line is the inefficiency expected for the KOPIO detectors in Sec. 6f. . . . .	84
6c.7	Integral photon detection inefficiency in the BV versus the size of the empty gaps between the Shashlyk modules. . . . .	85
6c.8	Schematic view of a veto sandwich module. . . . .	86
6c.9	Light yield along the sandwich modules. The outermost points were taken at a distance of 25 cm from the module edges. The attenuation curves were fitted with the function $A = A_s \cdot \exp(-\frac{x}{L_s}) + A_L \cdot \exp(-\frac{x}{L_L})$ . . . . .	89
6c.10	The light yield of the first sandwich module over a period of years. The errors are determined by systematics. . . . .	90
6c.11	Light yield for each end of the second module versus its sag (left plot); rate of module bowing (right plot). . . . .	90



6c.12	Time resolutions obtained at the centers of sandwich modules. The combination $(\text{TDC}_{\text{left}} - \text{TDC}_{\text{right}})/2$ was used to make the timing spectra for the modules. The half-sum of these spectra produced a time resolution of 235 ps. The TDC scale is 50 ps/ch. . . . .	91
6c.13	Time resolution (rms) vs. light output. TDC1 and TDC2 are the ends of the first module, TDC3 and TDC4 are the ends of the second module. . . . .	92
6c.14	Time resolution (rms) measured at the center of the first module over several years. The points fluctuate around 300 ps within the time-fitting error. . . . .	92
6c.15	A view of the Upstream Veto wall made of 132 modules. Central modules are cut the for beam entrance. . . . .	94
6c.16	Location and segmentation of the Downstream Veto. Simulated volumes are shown. . . . .	95
6c.17	D4 magnet region, where the Magnet Photon Veto is located. . . . .	96
6c.18	Waveform of a typical signal from a Shashlyk module recorded with a 5 GHz oscilloscope (black). Red color marks a signal reconstructed at 250 MHz sampling rate. . . . .	97
6c.19	$\chi^2$ versus the sampling rate. $\chi^2$ was calculated as a fit of the reference signal with a signal waveform reconstructed at a smaller sampling rate. Reference signal was recorded at 5 GHz. Waveform was reconstructed by two algorithms, linear and spline fits. . . . .	97
6d.1	. . . . .	100
6d.2	Scale drawing of the setup used to measure the response of a plastic scintillator to $\pi^\pm$ , $\mu^\pm$ and $e^\pm$ . Beam enters from the left. Counters 1-3 and wire chambers WC1-2 are used to identify an incoming beam particle and measure its trajectory. The dimensions indicate detector thicknesses in the beam direction. . . . .	101
6d.3	Response of plastic scintillator counter 4 to 290-MeV/c $\pi^\pm$ for (i) all events with trajectories pointing at counter 4, (ii) the subset of (i) that are contained in the pedestal peak of the NaI(Tl) crystal, and (iii) the subset of (ii) contained in the pedestal peak of the second plastic scintillator, counter 5. Because the histograms are plotted on top of each other, the visible areas indicate the differences between two event samples, so orange corresponds to events of type (i) and not (ii), <i>i.e.</i> particles producing signals in the NaI(Tl) crystal. The insets give expanded views of the pedestal regions $50 < \text{ADC} < 100$ . . . . .	101
6d.4	Pion detection inefficiencies caused by interactions in the 80-mg/cm <sup>2</sup> dead material between the scintillator and the preceding wire chamber (WC2), and by a 200-keV detection threshold. These results do not include an additional factor of two in rejection capability by the photon calorimeter behind the scintillator. . . . .	102
6d.5	Two full-scale prototype modules: a) readout with WLS fibers in a returning mode; b) cross section through fiber detector; c) direct readout with three photomultipliers. . . . .	103
6d.6	Pion detection inefficiencies for CPV+PV versus momentum. The PSI results are normalized to a 50-keV detection threshold and 1-mg/cm <sup>2</sup> dead layer, corresponding to a coated scintillator. . . . .	104
6d.7	. . . . .	105
6d.8	Position dependence of the light yield observed with three photomultipliers coupled directly to the scintillator, which has a thickness of 6.4 mm (see also Table 6d.1). . . . .	106
6d.9	Position dependence of the leading-edge timing from the three photomultipliers, and their sum. Colors correspond to 1-ns intervals. . . . .	106
6d.10	Vertical cross section through the Downstream CPV. . . . .	107
6e.1	Energy distributions of photons in (left) and near (right) the neutral beam for $K_{\pi_2\text{even}}$ (red) and $K_{\pi_2\text{odd}}$ (blue) type events. Actually, the left (right) figure shows the energy spectrum of photons that hit the aerogel (guard) counter, described in the text. The vertical axis indicates the expected number of backgrounds after our standard cuts. . . . .	109
6e.2	The design of the catcher module. . . . .	110

6e.3	The design of the catcher configuration. . . . .	111
6e.4	Side views of optical design candidates that were studied. . . . .	112
6e.5	Sketch of the second prototype. . . . .	113
6e.6	The experimental setup of the beam test for the second prototype. . . . .	113
6e.7	The measured number of photoelectrons of the second prototype as a function of $1/\beta^2$ . . . . .	114
6e.8	The measured efficiency for protons with the second prototype as a function of momentum. The efficiency here is the coincidence of two layers, as described in the text. The lines guide the eye. . . . .	114
6e.9	The measured efficiency for protons with the second prototype as a function of momentum. In the left (right) figure, the threshold was set to be 1 p.e. (2 p.e.). The lines guide the eye. . . . .	115
6e.10	The profile of the neutrons at the face of the Catcher. Left (right) figure shows the horizontal (vertical) profile of the neutron beam. The vertical axis indicates the estimated number of neutrons in a microbunch. Note that these are the plots for wider (100 mrad in horizontal) aperture and thus the current horizontal beam profile (90 mrad) would be 10% narrower than in the figure. . . . .	115
6e.11	The schematic view of the concept of the guard counter. The left figure shows the mechanism to detect photons, while the right one indicates how the sensitivity to neutron-induced slow particles can be reduced. . . . .	116
6e.12	The schematic drawing of the guard counter. The upper (lower) figure shows the front (side) view of the counter. Each layer consists of 48 modules as in the left figure, and three modules are placed in sequence. . . . .	116
6e.13	Efficiencies for photons as a function of incident energy. Each figure shows the efficiency of the aerogel catcher (left) and the guard counter (right). In the right figure, there are two lines indicating the efficiencies of the guard counter alone and the combined efficiency with the aerogel catcher. . . . .	118
6e.14	Efficiencies for photons as a function of the incident $X$ (left) and $Y$ (right) positions. The vertical (horizontal) position was fixed to be at the center in the left (right) figure. . . . .	118
6e.15	Hit probabilities for neutrons as a function of kinetic energy. Each figure shows the hit probability of the aerogel catcher (left) and the guard counter (right). The hit condition in each figure is same as the one described in previous section. Note that only the effects of secondary particles from interactions between the core beam and the aerogel catcher were considered in the right plot, because they are the main contributor to the count rate of the guard counter. . . . .	119
6e.16	Estimated singles counting rate due to neutrons as a function of kinetic energy. Each figure shows the rate of the aerogel catcher (left) and the guard counter (right). As in Fig. 6e.15, only the effects of secondary particles from interactions between the core beam and the aerogel catcher were considered in the right plot. . . . .	120
6e.17	Estimated false veto probability due to neutrons. The upper line with square dots indicates the expected number of neutrons in a microbunch. Multiplying the coincidence hit probability shown in Fig. 6e.15, the false veto activity in a microbunch as a function of neutron kinetic energy could be obtained, shown as the lower line with closed circles. In the plots of the guard counter, only the effects of secondary particles from beam interactions were considered. . . . .	120
6e.18	Hit probabilities for $K_L$ as a function of momentum. Each figure shows the hit probability of the aerogel catcher (left) and the guard counter (right). The hit conditions in these figures are described in the section of "Efficiency for Photons". . . . .	121
6e.19	Estimated s counting rate due to neutral kaons as a function of kinetic energy. Each figure shows the rate for the aerogel catcher (left) and the guard counter (right). . . . .	122

6e.20	Estimated false veto probability due to neutral kaons. Multiplying the hit probability shown in Fig. 6e.18 with the false veto probability, the false veto activity in a microbunch as a function of $K_L$ momentum was obtained, as the lower line with closed circles. . . . .	122
6f.1	The energy resolution ( $\sigma/\sqrt{E}$ ) and visible fraction versus the thickness of a scintillator layer in the case of 0.5- and 1-mm lead. The resolution is determined from pure sampling and leakage fluctuations. The number of layers is 180 for 0.5-mm Pb, and 100 for 1-mm Pb. . . . .	125
6f.2	Total electromagnetic cross-section in lead vs. photon energy. Blue circles show the cross section of photonuclear absorption in Pb as measured in Ref.[4]. . . . .	127
6f.3	Total photonuclear cross-sections for lead and carbon versus the photon energy, and a compilation of experimental data. . . . .	127
6f.4	E949 photon detection inefficiency as a function of photon energy for normal incidence. Thresholds are for visible energy. . . . .	128
6f.5	Dots: photon detection inefficiency as a function of photon energy, measured in E949 with 1-MeV (visible) threshold for normal incidence. Triangles: FLUKA simulation of E949. The horizontal error bars for the FLUKA points should be ignored. . . . .	129
6f.6	Left: Expected photon detection inefficiency in KOPIO, broken down by source, for a 1 MeV visible energy threshold and normally incident photons. Also shown is the photon detection inefficiency measured in E949. Right: the same plot on an expanded photon energy scale. . .	130
6f.7	Left: Expected photon detection inefficiency in KOPIO as a function of photon energy and angle of incidence, for a 1-MeV visible energy threshold. Right: the same plot on an expanded photon energy scale. . . . .	130
7.1	Vacuum system design. . . . .	133
7.2	Layout of the decay tank. . . . .	134
7.3	Conceptual design of the downstream tank. . . . .	134
8.1	Schematic diagram of one HV channel, with 12-V input power and 0–5-V control voltage from a VME based DAC. . . . .	136
8.2	Schematic diagram of a clipping preamplifier. . . . .	137
8.3	Overview of the LED Monitoring System. This system is triggerable (Start) with feedback control from a PIN Diode, which is also readout into the standard DAQ system with a WFD. . . . .	139
8.4	Overview of the FEE/Trig/DAQ and their interconnections. This diagram shows a generic layout of one of the WFD VME crates. The Crate Data Collection module is labeled SBC and is connected via Infiniband links (IB) to the WFDs and to the DAQ. The crate data collector also hosts the Clock Receivers, which broadcast the clock and trigger information to each WFD. Data is transferred synchronously to the trigger from each WFD via custom serial links. . . . .	140
8.5	Schematic diagram of WFD board. . . . .	142
9.6	Data-flow model. . . . .	144
9.7	Trigger functional scheme. Thick lines represent serial links carrying data used for trigger formation (red lines) or monitoring (blue lines). The clock system encodes the trigger decision received by the trigger supervisor over the clock signal (thin black lines) sent to the front end electronics. . . . .	149
9.8	Format of the data packet for zero-suppressed multiplexed L1 communications. . . . .	151
9.9	Principle of the L1 asynchronous communication protocol. Data are zero-suppressed and multiplexed in output, demultiplexed and resynchronized in input. . . . .	151
9.10	Channel combinations for the trigger outputs of the Calorimeter digitizers. . . . .	152
9.11	Collector modules and their connections with Preradiator and Calorimeter digitizers. The figure shows the components needed to process signals from one of the quadrants ( <i>A</i> , color code blue). For quadrant <i>C</i> only the components processed together with quadrant <i>A</i> are shown. . . . .	154
9.12	Use of the logic modules to produce the trigger conditions of Table 9.5. . . . .	155

10.1	Block diagram of the DAQ system. Red: Infiniband (or other multi-gigabit links). Blue: Gigabit ethernet . . . . .	157
10.2	Distance at Level 3 (in units of Moliere radii) between the “signal” photons and the extra photons in the Preradiator/Calorimeter. . . . .	160
11.1	Dataflow of GLEAM, the top-level GLAST package. . . . .	164
12.1	The pit for the KOPIO detector. . . . .	169
12.2	The pit with the D3 magnet . . . . .	169
12.3	The Upstream Photon Veto assembly. . . . .	170
12.4	The Barrel Photon Veto assembly. . . . .	170
12.5	The Preradiator and Calorimeter components. . . . .	171
12.6	The Preradiator and Calorimeter joined together. . . . .	171
12.7	The KOPIO assembly through the Barrel Veto. . . . .	172
12.8	The KOPIO assembly through the Preradiator/Calorimeter. . . . .	172
12.9	The downstream tank assembly. . . . .	173
12.10	The downstream tank components joined together. . . . .	173
12.11	The assembled KOPIO detector. . . . .	174
13.1	The relative KOPIO sensitivity as a function of spill length. The optimum spill length is 4.90 seconds; however, spill lengths from $\sim 3.5$ to $\sim 7$ seconds would entail a loss of only $\sim 5\%$ in sensitivity. . . . .	176
13.2	The dashed line represents the parameterized photon veto efficiency for the beam Catcher. The points are taken from simulation and the solid line is drawn to guide the eye. “Threshold = 4pe, 2pe” refers to the photon identification procedure described in Sec. 6e. . . . .	177
13.3	The charged pion veto inefficiency as a function of the pion momentum. The charged pion inefficiencies are taken from fits to PSI measurements (Sec. 6d) and extrapolated for a dead material thickness of $6.7 \text{ mg/cm}^2$ and a 50-keV energy threshold. Component 1(2) corresponds to the effect of dead material (threshold). The “NaI veto” in the legend corresponds to measurements made with a NaI detector behind the CPV to take into account the effect of the PV in KOPIO. . . . .	178
13.4	The charged lepton veto inefficiencies as a function of momentum. The momentum-dependence of the positron inefficiency is an approximation to annihilation cross-section. The discontinuity in the curves corresponds to the assumption that the inefficiency is reduced by up to $\times 0.01$ due to detection by PV behind all CPV elements for kinetic energy above 10 MeV. . . . .	179
13.5	The reconstructed kinetic energy distributions of the $\pi^0$ in the $K_L^0$ rest frame for signal and backgrounds. The dashed (dotted) lines in the histograms show the spectrum for “even” and “odd” combinations. . . . .	182
13.6	The reconstructed two photon mass spectrum for signal and backgrounds. The dashed (dotted) lines in the histograms show the spectrum for “even” and “odd” combinations. . . . .	183
13.7	The $T_{\pi^0}^{*2}$ vs $\ln(E_{\text{miss}}(\text{MeV}))$ distributions for signal and backgrounds. . . . .	184
13.8	The $T_{\pi^0}^{*2}$ vs $\ln(E_{\text{miss}}(\text{MeV}))$ distribution for $K_{\pi 2}$ background (top,left), Kcp3 background (top,right) and signal (bottom) weighted by the photon veto inefficiency. . . . .	185
13.9	The $\Delta$ vs. $M_\nu^2$ distributions of Ke3g, Kcp3, and Ke4 before setup cuts. The vertical dashed line shows the setup cut that suppresses background with slow tracks and/or decay-in-flight. . . . .	187
13.10	Cartoon showing the mechanism for $K_L^0 \rightarrow \pi^- e^+ \nu \gamma$ background. The positron annihilates before detection in the CPV that lines the vacuum vessel and produces $\gamma_0$ and $\gamma_1$ . The neutral pion candidate is formed from the radiative photon $\gamma_2$ and one of the annihilations photons $\gamma_1$ whilst $\gamma_0$ is undetected. The negative pion from $K_L^0$ decay must also escape detection for this decay to form a background. . . . .	188
13.11	The $\Delta$ (ns) vs $z(K, \text{recon}) - z(K, \text{true})$ (cm) after setup cuts on $\chi^2$ , DOCA and $z(K)$ (Table 13.3). An additional cut $ M_{\gamma\gamma} - M(\pi^0)  < 20 \text{ MeV}$ has also been applied. . . . .	190

13.12	Left columns: $T^{*2}$ vs $\ln(E_{\text{miss}})$ and Right columns: $M(\gamma, \gamma) - M(\pi^0)$ for the $2\gamma$ PR detection method for signal and backgrounds after tight cuts. These distributions are weighted such that total number of entries in each distribution is the total number of expected events. .	191
13.13	Left columns: $T^{*2}$ vs $\ln(E_{\text{miss}})$ and Right columns: $M(\gamma, \gamma) - M(\pi^0)$ for the $2\gamma$ PR detection method for signal and backgrounds after loose cuts. These distributions are weighted such that total number of entries in each distribution is the total number of expected events. .	192
13.14	For the $2\gamma$ PR detection method, the total in-bunch background and the components of the in-bunch background by $K_L^0$ decay mode vs. the expected number of signal events as the likelihood cut severity is decreased. . . . .	196
13.15	For the $2\gamma$ PR detection method, the relative rate of the total wrap-around background to the total in-bunch background and the relative rate of the components of the wrap-around background by the $K_L^0$ decay mode vs. the expected number of signal events as the likelihood cut severity is decreased. . . . .	196
13.16	For the $2\gamma$ PR detection method, absolute rate (upper) and rate relative to in-bunch (lower) background of the interbunch background <i>before applying the interbunch extinction rate</i> and the rates of the significant components of the interbunch background as a function of the time from the central time of the “in-bunch” bunch for the loosest of the likelihood cuts for the $2\gamma$ PR detection method. The $K_{\pi 2}$ background dominates the interbunch rate. For negative times, the reconstructed kaon momentum is less than the actual kaon momentum so that the reconstructed $T_{\pi^0}^*$ is less than the true $T_{\pi^0}^*$ and moves the $K_{\pi 2}$ -even peak into the low background region. . . . .	197
13.17	The upper distribution shows the probability of of beam $K_L^0$ per 16.4 ps determined from the interbunch rate measurements of Section 5 where we assume that the interbunch background is constant between the bunches The lower distribution shows the calculated total background rate as function of the time from the central time of the “in-bunch” bunch for the loosest of the likelihood cuts for the $2\gamma$ PR detection method using the rates shown in Fig. 13.16. The $\pm 1$ -ns region is classified as the “in-bunch” background and is removed from this calculation. The total background rate from the wrap-around mechanism is 6.5 events for these cuts. The interbunch background makes a negligible contribution to the total background rate. . . . .	198
13.18	Top: The total background and the components as a function of the signal yield for the $2\gamma$ PR detection method. The “standard” background is the in-bunch background. The lower figure shows the signal over the total background as a function of the signal yield. . . . .	199
13.19	The signal-to-background ratio (S/B) as a function of signal for all detection methods (black line) and for each of the three detection methods. The $2\gamma$ PR method is shown in red, the $1\gamma$ PR/CAL method is shown in green and the $1\gamma$ PR/BV method is shown in blue. . . . .	200
13.20	Left: Events per channel where events are sorted into channels by b/s until a channel contains ten background events. The upper curve shows the total number of events expected in each channel. Right: The integrated number of events as a function of the total background to total signal ratio in each channel. The “statistical error” (right scale) shown is the square root of the integrated number of events divided by the total signal yield at each channel. This would be the relative uncertainty on a $K_L^0 \rightarrow \pi^0 \nu \bar{\nu}$ branching fraction measurement if there were no uncertainty in the background yield and if the full power of the likelihood method were not employed. . . . .	201
13.21	The energy spectrum of the $e^\pm$ from pion beta decay for pions from Ke3. The upper (lower) plot shows the distributions with no (fiducial) cuts. . . . .	204
13.22	The energy spectrum of the $e^\pm$ from pion beta decay for pions from Km3. The upper (lower) plot shows the distributions with no (fiducial) cuts. . . . .	204

13.23	Neutron carbon-12 cross-sections for neutron energies from 200 to 3000 MeV from the ENDF compilation[4]. The dark blue line is the total cross-section, the turquoise line is the cross-section into one or more neutral pions. . . . .	206
13.24	Upper: The reconstructed $z(K)$ distribution for $nN \rightarrow \pi^0 X$ production at (0,4,950) cm fitted with a double Gaussian. P2 and P5(P3 and P6) are the fitted means(sigmias). (For this study, the decay region extended from 950 to 1350 cm.) The other plots from top to bottom and left to right show the distributions of $\chi^2$ vs $M_{\gamma\gamma} - M_{\pi^0}$ in MeV for increasingly harder cuts on $z(K)$ . The box in these plots corresponds to $\chi^2 < 15$ and $ M_{\gamma\gamma} - M_{\pi^0}  < 20$ MeV. These plots correspond to the $2\gamma$ PR detection mode and used an early, more pessimistic model of the PR. . . . .	207
13.25	Comparison of the reconstructed kaon decay time vs reconstructed kaon momentum for signal(open boxes) and neutron halo(red shaded boxes) events from the upstream end of the decay region. Only basic reconstruction cuts are applied and are listed in the figure. The lower plot has the current nominal cut on $z(K)$ ; the upper plot has a looser $z(K)$ cut to increase statistics. Each reconstructed event is weighted by the production weight (decay probability) for neutrons (kaons). . . . .	208
13.26	Variation of the three FOMs as the BV radius is changed. The FOM variation is approximately $\pm 12\%$ as the BV radius is changed by $\pm 10\%$ , as expected qualitatively because the area of the PR increases as the radius increases. . . . .	211
13.27	Variation of the three FOMs as the global PV thickness in radiation lengths is changed. There is little improvement in the FOM with a thicker PV. . . . .	212
13.28	Variation of the three FOMs as a function of the energy resolution. The FOMs for S/B=8 has changes by $\approx 20\%$ as the energy resolution changes by 20%. The signal yield for S/B=2 is less sensitive to the energy resolution. . . . .	212
13.29	Variation as a function of the PR angular resolution. As for the energy resolution, the high purity signal yield has the most dramatic dependence on the angular resolution of the PR. . .	213
13.30	Variation of the three FOMs as a function of the position resolution. . . . .	213
13.31	Variation of the three FOMs as the PV inefficiency is globally degraded. Globally increasing the PV inefficiency by a factor of 1.5 decreases the signal yield by factors of 0.35 (S/B=8) to 0.54 (S/B=2). Roughly speaking, an increase of the inefficiency by a factor of 1.5 should increase the $K_{\pi^2}$ background by $1.5^2 = 2.25$ . . . . .	214
13.32	Left: Variation of the three FOMs as the thickness in radiation lengths of each layer of the PR is changed. The dimensions of the PR are fixed so the total thickness of the PR in radiation lengths changes in proportion to the change in thickness of each layer. Center: The S/B vs S for the sum of all detection methods. Right: The S/B vs S for the $2\gamma$ PR detection method only. In general, increasing the thickness per layer increases the conversion probability but decreases the resolution due to the increase in multiple scattering. . . . .	214
13.33	Variation of the three FOMs as the time resolution is changed. The signal yield is only slightly degraded if the time resolution worsens. . . . .	215

## List of Tables

6b.1	Evolution of the energy resolution of Shashlyk modules. . . . .	55
6b.2	Parameters of the $3\%/\sqrt{E}$ (GeV) KOPIO prototype module. . . . .	59
6b.3	Scintillators tested for the KOPIO Shashlyk module. The “light yield” is the amount of light produced in the scintillator without respect to the light collection efficiency, while “MIP light yield” is the detected light signal per minimum ionization particle passing through the scintillator tile. The “effective attenuation length” was measured for thin, 1.5-mm scintillator tile. . . . .	63
6b.4	Some experimental and catalog parameters of the green-extendeds PMT-9903B and three pre-selected large-area APDs. Data for a well-known small-area APD, produced by Hamamatsu Corporation, are shown for comparison. . . . .	64
6c.1	Parameters of extruded polystyrene counters with 4.3-m-long WLS fiber readout. Fibers were fast Bicron BCF92 or BCF99-29 types. The counter made of BC404 scintillator is also shown for comparison. . . . .	87
6c.2	The expected veto performance. . . . .	93
6c.3	Specification for Electron Tubes 9903B photomultipliers. . . . .	95
6d.1	Photoelectron (p.e.) yields of various light collection schemes. Scintillator: BC-412 by BICRON; photomultipliers: Burle 83062E ( $\varnothing 22$ mm). . . . .	103
6e.1	The base parameters of the aerogel catcher. . . . .	113
6e.2	The base parameters of the guard counter. . . . .	117
6e.3	The summary of the resultant parameters. . . . .	123
8.1	Light intensity parameters of some commercial LED lamps. . . . .	138
8.2	Channel count for photosensor based front-end electronics. The number of channels from the PMT/APD is listed along with the number of WFD boards and Crate Data Collector boards. . . . .	143
9.3	Conditions defining the sample of $\pi^0\nu\bar{\nu}$ events for which efficiency is quoted . . . . .	146
9.4	Veto counters used for the trigger. . . . .	147
9.5	Signal loss and rejection. Each line gives the effect of the individual conditions for microbunches satisfying all other conditions. The last two lines give the global results obtained applying all conditions (“Low rate” option) or all conditions except the ones marked with a * in the Rate column (“High rate” option). . . . .	148
10.1	Rejection and acceptance of the Level 3 cuts. Note that the offline photon vetoes were not applied as part of the setup cuts in this study; such cuts lower the apparent acceptance of the L1 trigger. . . . .	160
13.1	The assumed detector resolutions ( $\sigma$ of a Gaussian) used for estimates of signal and background yields by the FastMC simulation. All energies are in GeV. PR/(CAL&EPV) corresponds to the primary detection method where both photons convert in the PR and the energy is accumulated in the PR, CAL and EPV (Sections 6a and 6b). CAL corresponds to the detection method that requires a single photon conversion in the PR and the other photon conversion in the CAL (Sec. 6b). BV corresponds to the detection method that requires a single photon conversion in the PR and the other photon conversion in the BV (Sec. 6c.2). Detection methods are described in Sec. 13.4. . . . .	179
13.2	The name, final state, branching fraction[1] and branching fraction relative to signal for $K_L^0$ decay modes assuming the standard model rate for signal. . . . .	181

13.3	Description of the “setup” cuts. DOCA is the distance of closest approach of the two candidate $\gamma$ , $z(K_L^0)$ is the reconstructed $z$ of a $K_L^0$ candidate, $z_1$ is 75cm (100cm) from the upstream end of the decay volume for the $2\gamma$ PR (1 $\gamma$ PR) detection method, and $z_2$ is 50cm (100cm) from the downstream end of the decay volume for the $2\gamma$ PR (1 $\gamma$ PR) detection method. $DK12 \equiv \sqrt{(\text{DOCA1} + \text{DOCA2} - 5.)^2 + (z_1(K_L^0) - z_2(K_L^0))^2}$ where $\text{DOCA}i$ is the distance of closest approach of the $i^{\text{th}}$ measured photon to $\vec{X}_2(K_L^0)$ , the fitted $K_L^0$ vertex from the fit 2, and $z_i(K_L^0)$ is the reconstructed $z_{K_L^0}$ from the $i^{\text{th}}$ fit. Fit 1(2) fits the two photons to a common vertex without (with) a $\pi^0$ mass constraint. The performance of these cuts on signal and backgrounds is shown in Table 13.4. . . . .	189
13.4	The total number of decays in the decay volume and candidates for the $2\gamma$ PR detection method for each decay mode surviving the listed cut. Only in-bunch candidates are considered; that is, “wrap-around” backgrounds are not included. The cuts are applied sequentially from top to bottom. There can be more than one candidate per generated decay due to combinations of the available photons. $\mathcal{A}(\text{Geom})$ is the geometric acceptance, $\mathcal{P}(\text{decay})$ is the $K_L^0$ decay probability, $\mathcal{P}(\text{conv.})$ is the two photon conversion probability in the PR, and $\bar{\epsilon}$ is the veto inefficiency. The results between the double horizontal lines show the suppression due to the setup cuts. The “likelihood” cuts at the bottom of the table are cuts of increasing severity resulting from the optimization procedure. . . . .	193
13.5	The total number of decays in the decay volume and candidates for the 1 $\gamma$ PR/BV detection method for each decay mode surviving the listed cut. Only in-bunch candidates are considered; that is, “wrap-around” backgrounds are not included. The cuts are applied sequentially from top to bottom. There can be more than one candidate per generated decay due to combinations of the available photons. $\mathcal{A}(\text{Geom})$ is the geometric acceptance, $\mathcal{P}(\text{decay})$ is the $K_L^0$ decay probability, $\mathcal{P}(\text{conv.})$ is the photon conversion probability in the PR, and $\bar{\epsilon}$ is the veto inefficiency. The results between the double horizontal lines show the suppression due to the setup cuts. The “likelihood” cuts at the bottom of the table are cuts of increasing severity resulting from the optimization procedure. . . . .	194
13.6	The total number of decays in the decay volume and candidates for the 1 $\gamma$ PR/CAL detection method for each decay mode surviving the listed cut. Only in-bunch candidates are considered; that is, “wrap-around” backgrounds are not included. The cuts are applied sequentially from top to bottom. There can be more than one candidate per generated decay due to combinations of the available photons. $\mathcal{A}(\text{Geom})$ is the geometric acceptance, $\mathcal{P}(\text{decay})$ is the $K_L^0$ decay probability, $\mathcal{P}(\text{conv.})$ is the photon conversion probability in the PR, and $\bar{\epsilon}$ is the veto inefficiency. The results between the double horizontal lines show the suppression due to the setup cuts. The “likelihood” cuts at the bottom of the table are cuts of increasing severity resulting from the optimization procedure. . . . .	195
13.7	FastMC estimate of $K_L^0 \rightarrow \pi^\pm \ell^\mp \nu$ , $\pi^\pm \rightarrow \pi^0 e^\pm \nu$ background. In the table $\mathcal{B}(K) = \mathcal{B}(K_L^0 \rightarrow \pi^\pm \ell^\mp \nu)$ , $\mathcal{B}(\pi) = \mathcal{B}(\pi^\pm \rightarrow \pi^0 e^\pm \nu)$ , and $\mathcal{B}(s) = \mathcal{B}(K_L^0 \rightarrow \pi^0 \nu \bar{\nu})$ . The upper portion of the table gives the number of surviving candidates after the listed cuts. The lower portion of the table has the background rate relative to the signal after successive cuts. . . .	203
13.8	Parameter variations. Parameters in bold list the baseline assumptions. A variation of the resolution by $\pm 20\%$ indicates that the resolutions used to smear the appropriate quantities are modified as $\sigma(\text{new}) = \pm 1.20 \times \sigma(\text{baseline})$ . “50% worse” PV inefficiency means that the inefficiency is globally increased by a factor of 1.50, or $\bar{\epsilon}(\text{new}) = 1.50 \times \bar{\epsilon}$ . . . . .	211
14.1	Current status of radiative decay branching ratios of the $K_L^0$ and the experiments that defined them. . . . .	218



# 1 Introduction

CP violation is one of the most important outstanding issues in elementary particle physics. It has profound implications for the relationship among the quarks (and now, perhaps, the leptons), and for the origin of matter in the universe. Since its discovery in 1964, CP violation has been studied by using  $K$  decays and, more recently, from  $B$  decays. With the advent of the Standard Model (SM), the primary question has revolved around establishing whether or not the observed CP violation is due to the complex phase in the Cabibbo-Kobayashi-Masakawa (CKM) quark-mixing matrix, *i.e.* direct CP violation. Evidence supporting this picture was obtained in measurements of  $K \rightarrow \pi\pi$  decays ( $\epsilon'/\epsilon$ ) at CERN and Fermilab, although without a precise theoretical interpretation for the underlying parameters. CP-violating phenomena have also been vigorously pursued in the  $B$  sector and have provided consistency with the SM picture, most notably through measurements of the CP asymmetry in  $B^0 \rightarrow J/\psi K_S^0$  decays. An array of major thrusts are underway to study CP violation in  $B$  decays including BaBar at SLAC's PEP-II, and BELLE at KEKB. In addition, the CDF and D0 facilities at Fermilab have vigorous programs for studying  $B$  physics and CP violation. In the future, LHCb at CERN will provide measurements with very high statistics.

It is generally accepted that the Standard Model does not offer a complete picture for many important observations, and therefore physics beyond that contained in the SM likely exists. For instance, it is apparent that known sources of CP violation fall short, by many orders of magnitude, to explain the baryon asymmetry of the universe. Thus, one important strategy is to use precise expectations for CP-violating phenomena as a basis to search for and to discover new physics. Among many possible measurements relating to CP violation, four “golden” processes stand out as theoretically unambiguous and will allow such comparisons with theory to be made. Two of the processes are the quarry of the current  $B$  experiments mentioned above, asymmetries in  $B^0 \rightarrow J/\psi K_S^0$  decays and the ratio of  $B_s$  to  $B_d$  mixing; the two others are the branching ratios of the charged and neutral  $K \rightarrow \pi\nu\bar{\nu}$  decays. Many other approaches involving rare  $B$  decays are also under intense study.

Among  $K$  and  $B$  decays, the rare decays  $K^+ \rightarrow \pi^+\nu\bar{\nu}$  and  $K_L^0 \rightarrow \pi^0\nu\bar{\nu}$  are special because their branching ratios can be computed to an exceptionally high degree of precision that is not matched by any other  $K$  or  $B$  meson decay. While the theoretical uncertainties in predictions of the branching ratios of prominent decays such as  $B \rightarrow X_s\gamma$ ,  $B \rightarrow X_s\mu^+\mu^-$ , and  $B_s \rightarrow \mu^+\mu^-$  amount typically to  $\pm 10\%$  or larger, the corresponding uncertainties in  $K_L^0 \rightarrow \pi^0\nu\bar{\nu}$  amount to 1–2%. In the absence of new physics, the single most incisive measurement in the study of direct CP violation in the context of the SM is the measurement of the branching ratio for  $K_L^0 \rightarrow \pi^0\nu\bar{\nu}$  ( $\mathcal{B}(K_L^0 \rightarrow \pi^0\nu\bar{\nu})$ ). In the SM,  $\mathcal{B}(K_L^0 \rightarrow \pi^0\nu\bar{\nu})$  is unique because it directly measures the area of the CKM unitarity triangles, *i.e.* the physical parameter that characterizes all CP violation phenomena or, alternatively, the height of the triangle. Measurements of both  $\mathcal{B}(K_L^0 \rightarrow \pi^0\nu\bar{\nu})$  and  $\mathcal{B}(K^+ \rightarrow \pi^+\nu\bar{\nu})$  would allow the triangle to be reconstructed unambiguously from  $K$ -decay information alone. In addition, the ratio of these two branching ratios can be compared with  $\sin 2\beta$  (see Sec. 2) obtained from the  $B^0 \rightarrow J/\psi K_S^0$  decay. This test has the smallest known uncertainty for CP violation. Thus, the KOPIO measurement of  $\mathcal{B}(K_L^0 \rightarrow \pi^0\nu\bar{\nu})$  will add a vital new dimension to the world-wide effort to elucidate the nature of CP violation.

The  $K_L^0 \rightarrow \pi^0\nu\bar{\nu}$  decay mode is also unique in that it is completely dominated by direct CP violation[1] in the context of the Standard Model and is governed entirely by short-distance physics involving the top quark. Theoretical uncertainties are extremely small because hadronic effects can be extracted from the well-measured decay  $K^+ \rightarrow \pi^0 e^+ \nu$ . Unlike the case of many other processes, this situation remains intact even in the presence of many non-SM models[2]. Thus, the measurement of  $\mathcal{B}(K_L^0 \rightarrow \pi^0\nu\bar{\nu})$  will provide a standard against which all other CP-violating observables can be compared, and even small deviations from expectations will unambiguously signal the presence of new physics. By using current estimates for SM parameters,  $\mathcal{B}(K_L^0 \rightarrow \pi^0\nu\bar{\nu})$  is expected to lie in the range  $(3.0 \pm 0.6) \times 10^{-11}$ [3].

The experimental aspects of measuring  $\mathcal{B}(K_L^0 \rightarrow \pi^0\nu\bar{\nu})$  are quite challenging. The mode is a three-body decay where only a  $\pi^0$  is observed. There are competing decays which also yield  $\pi^0$ s, but whose branching ratios are millions of times larger. Observing a decay mode with a branching ratio on the order of  $3 \times 10^{-11}$  requires a prodigious number of kaons in order to achieve the desired sensitivity. Because the measurement

is so demanding, a detection technique must be adopted that provides maximum possible redundancy for this kinematically unconstrained decay, that has an optimum system for insuring that the observed  $\pi^0$  is the only observable particle emanating from the  $K_L^0$  decay, and that has multiple handles for identifying possible small backgrounds that might simulate the signal. It is with these issues in mind that the KOPIO experiment has been designed.

KOPIO employs a low-energy, time-structured  $K_L^0$  beam to allow determination of the incident kaon momentum. The intense beam required, with its special characteristics, exploits the very high intensity proton beam of BNL's Alternating Gradient Synchrotron (AGS). The AGS now serves as the injector for BNL's Relativistic Heavy Ion Collider (RHIC) but is available for the KOPIO experiment in a non-interfering way. Utilizing low momentum also permits a detection system for the  $\pi^0$  decay photons that yields a fully constrained reconstruction of the  $\pi^0$  mass, energy, and momentum. The system for vetoing extra particles is also well understood. These features, similar to those employed successfully in the BNL E787/E949[4] measurements of  $K^+ \rightarrow \pi^+ \nu \bar{\nu}$ , provide the necessary redundancy and checks.

The goal of KOPIO is to explore the range of branching ratios, for decays that have experimental signatures similar to  $K_L^0 \rightarrow \pi^0 \nu \bar{\nu}$ , down to the level of the SM prediction so as to uncover new physics processes if they are present. In the absence of a clear non-SM result, KOPIO will obtain a sensitivity equivalent to 10% or better on the  $K_L^0 \rightarrow \pi^0 \nu \bar{\nu}$  branching ratio at the SM level. This sensitivity would yield a statistical uncertainty in the measurement of the area of the CKM unitarity triangle of about 5%. While the search for deviations from the SM prediction or precise measurement of the  $K_L^0 \rightarrow \pi^0 \nu \bar{\nu}$  decay process is clearly the focus of KOPIO, other radiative-type  $K$  decays of significant interest for studies of low-energy QCD and numerous searches for non-SM processes will also be accessed simultaneously.

As sensitivity increases during the running of the KOPIO experiment, the absence of a positive signal allows successively smaller non-SM branching ratios to be eliminated. When KOPIO reaches the sensitivity goal stated above, an exclusion limit of five standard deviations ( $\sigma$ ) would require a fluctuation from the SM branching ratio to be  $\mathcal{B}(K_L^0 \rightarrow \pi^0 \nu \bar{\nu})_{\text{SM}} \cdot (1 \pm 0.50)$ . Thus, a measurement of the  $K_L^0 \rightarrow \pi^0 \nu \bar{\nu}$  branching ratio at the level of the SM would exclude non-SM models that have predictions outside of the range from 0.50 to 1.50 times that value. A plot of this exclusion as a function of the fraction of the running time anticipated for KOPIO is given in Fig. 1.1 for several non-SM approaches discussed below. Because the background rejection capability must be sufficient for the ultimate sensitivity, background levels during the early part of the running period will be negligible, and progress in ruling out (or discovering!) branching ratios well above the SM level will be swift and will be nearly linear in running time. To bound the branching ratio from below takes considerably more running time.

## References

1. M.K. Gaillard and B.W. Lee, Phys. Rev. D **10**, 897 (1974); J. Ellis, M.K. Gaillard and D.V. Nanopoulos, Nucl. Phys. **B109**, 213 (1976); L. Littenberg, Phys. Rev. D **39**, 3322 (1989).
2. A. J. Buras, F. Schwab and S. Uhlig, preprint arXiv:hep-ph/0405132.
3. G. Buchalla and A.J. Buras, Nucl. Phys. **B548**, 309 (1999).
4. S. Adler *et al.* [E787 Collaboration], Phys. Rev. Lett. **84**, 3768 (2000).

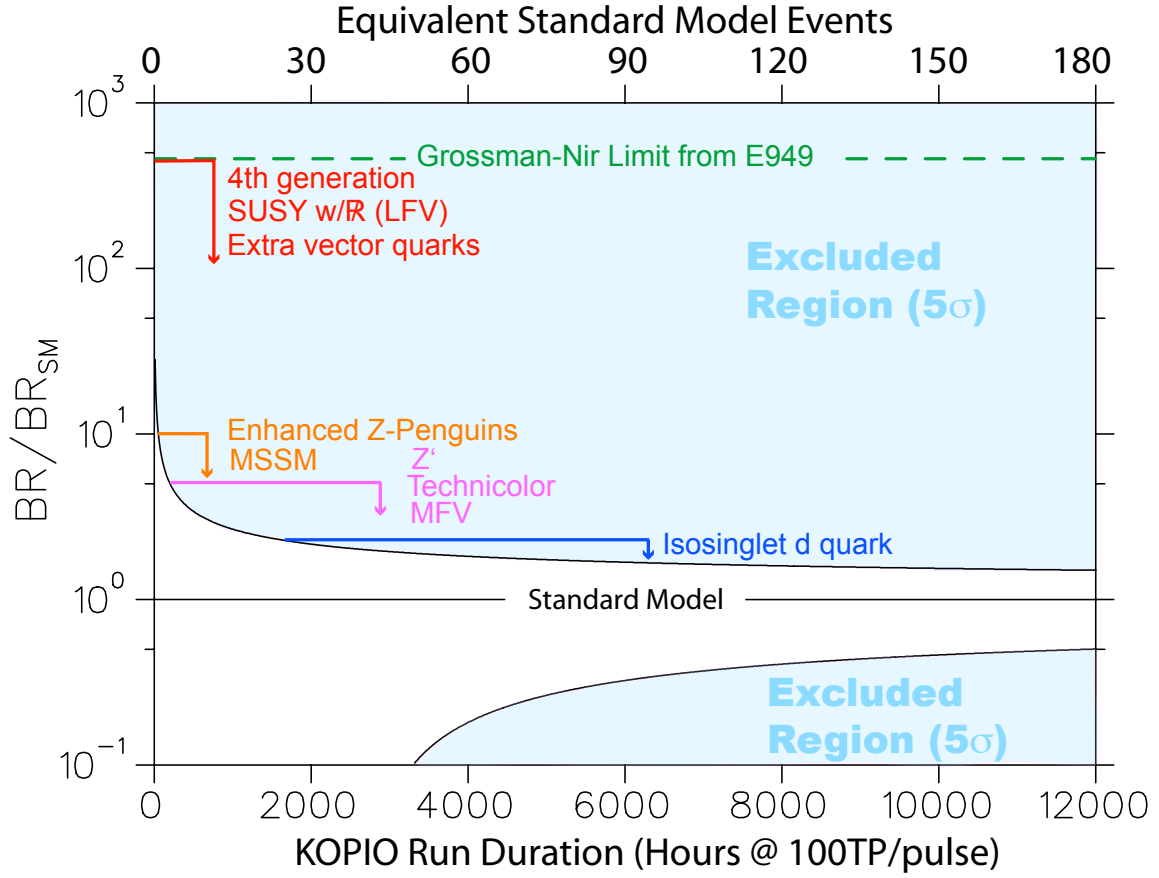


Fig. 1.1. Five- $\sigma$  upper and lower exclusion limits versus the fractional running time for the KOPIO experiment. The models listed start to be constrained at the levels indicated by the horizontal lines.

## 2 $K_L^0 \rightarrow \pi^0 \nu \bar{\nu}$ — Theoretical Motivation

### 2.1 Standard Model

Understanding the phenomenology of quark mixing and CP violation is currently one of the central goals of particle physics. Examining the CKM ansatz of the Standard Model (SM) through precise determinations of its basic parameters, and comparison between these determination in different systems, is crucial. To assure a clear interpretation of experimental results, the ideal observable must not only be sensitive to fundamental parameters, but must also be calculable with little theoretical ambiguity.

The rare decay  $K_L^0 \rightarrow \pi^0 \nu \bar{\nu}$  is unique among potential SM observable processes. It is dominated by direct CP violation[1] and is entirely governed by short-distance physics involving the top quark (for general reviews see[2,3,4]). Long distance effects have been shown to be negligible[5]. Theoretical uncertainties are extremely small because the hadronic matrix element can be extracted from the well-measured decay  $K^+ \rightarrow \pi^0 e^+ \nu$ , where small isospin-breaking effects have been calculated[6]. Because the dominant uncertainty due to renormalization scale dependence has been practically eliminated by including next-to-leading-order (NLO) QCD corrections, the remaining theoretical uncertainty for the branching ratio  $\mathcal{B}(K_L^0 \rightarrow \pi^0 \nu \bar{\nu})$  is reduced to  $\sim 2\%$ .

The  $K_L^0 \rightarrow \pi^0 \nu \bar{\nu}$  decay is a flavor-changing neutral current (FCNC) process that is induced through loop effects in the Standard Model. The leading electroweak diagrams are shown in Fig. 2.1. The expression

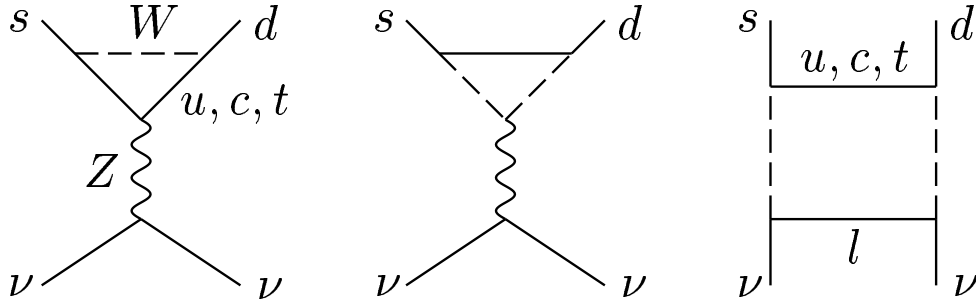


Fig. 2.1. The leading electroweak diagrams inducing  $K_L^0 \rightarrow \pi^0 \nu \bar{\nu}$ .

for the  $K_L^0 \rightarrow \pi^0 \nu \bar{\nu}$  branching ratio can be written as

$$\mathcal{B}(K_L^0 \rightarrow \pi^0 \nu \bar{\nu}) = r_{IB} \frac{\mathcal{B}(K^+ \rightarrow \pi^0 e^+ \nu)}{|V_{us}|^2} \frac{\tau(K_L^0)}{\tau(K^+)} \frac{3\alpha^2}{2\pi^2 \sin^4 \Theta_W} [Im(V_{ts}^* V_{td}) X(x_t)]^2 \quad (1)$$

where

$$X(x) \equiv \eta_X \cdot \frac{x}{8} \left[ \frac{x+2}{x-1} + \frac{3x-6}{(x-1)^2} \ln x \right], \quad \eta_X = 0.995, \quad (2)$$

and  $x_t \equiv m_t^2/M_W^2$ . Here the appropriate top quark mass to be used is the running  $\overline{\text{MS}}$  mass,  $m_t \equiv \overline{m}_t(m_t)$ , which is related by  $\overline{m}_t(m_t) = m_t^* (1 - 4/3 \cdot \alpha_s(m_t)/\pi)$  to the pole mass  $m_t^*$  measured in collider experiments. With this choice of mass definition, the QCD correction factor is given by  $\eta_X = 0.995$  and is essentially independent of  $m_t$ [7,8,9]. Recent measurements of  $m_t^*$  lead to  $X(x_t) = 1.529 \pm 0.042$ [4]. The coefficient  $r_{IB} = 0.944$  summarizes the leading isospin-breaking corrections in relating  $\mathcal{B}(K_L^0 \rightarrow \pi^0 \nu \bar{\nu})$  to  $\mathcal{B}(K^+ \rightarrow \pi^0 e^+ \nu)$ [6].

The  $K_L^0 \rightarrow \pi^0 \nu \bar{\nu}$  decay is driven by direct CP violation due to the CP properties of  $K_L$ ,  $\pi^0$ , and the relevant short-distance hadronic transition current. Because  $K_L^0$  is predominantly a coherent, CP-odd superposition of  $K^0$  and  $\bar{K}^0$ , only the imaginary part of  $V_{ts}^* V_{td}$  survives in the amplitude. Since the value of the sine of the Cabibbo angle is well known ( $|V_{us}| = \lambda = 0.224$ ), this quantity is equivalent to the Jarlskog invariant  $\mathcal{J} \equiv -Im(V_{ts}^* V_{td} V_{us}^* V_{ud}) = -\lambda(1 - \frac{\lambda^2}{2}) Im(V_{ts}^* V_{td})$ . In turn,  $\mathcal{J}$  is equal to twice the

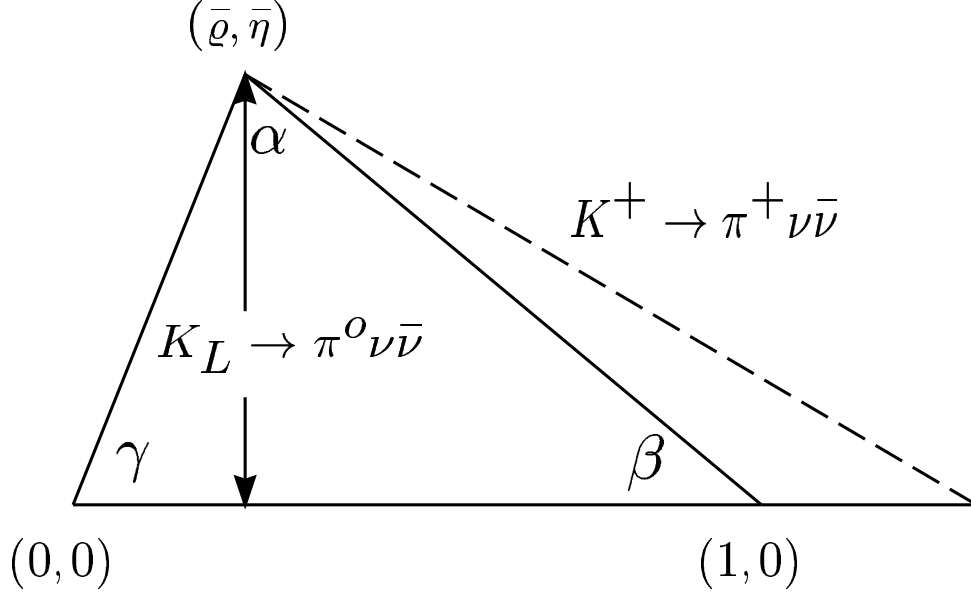


Fig. 2.2. The unitarity triangle.

area of any of the six possible unitarity triangles[10]. A comparison of the area of any unitarity triangle (UT) obtained indirectly through studies of the  $B$  system or otherwise with the same quantity obtained directly from  $K_L^0 \rightarrow \pi^0 \nu \bar{\nu}$  is then a critical test of the SM explanation of CP violation.

To facilitate the SM prediction of  $\mathcal{B}(K_L^0 \rightarrow \pi^0 \nu \bar{\nu})$  and exhibit its relation to other measurements, we employ the Wolfenstein parameterization  $(\lambda, A, \bar{\varrho}, \bar{\eta})$  of the CKM matrix, which allows a display of unitarity in a transparent way. In this representation, Eq. 1 can be recast as

$$\mathcal{B}(K_L^0 \rightarrow \pi^0 \nu \bar{\nu}) = (2.12 \pm 0.03) \cdot 10^{-10} \eta^2 A^4 X^2(x_t). \quad (3)$$

Inserting the current estimates for SM parameters into Eq. 3, the branching ratio for  $K_L^0 \rightarrow \pi^0 \nu \bar{\nu}$  is expected to lie in the range  $(3.0 \pm 0.6) \cdot 10^{-11}$ [4]. The unitarity relation

$$1 + \frac{V_{td}V_{tb}^*}{V_{cd}V_{cb}^*} = -\frac{V_{ud}V_{ub}^*}{V_{cd}V_{cb}^*} \equiv \bar{\varrho} + i\bar{\eta} \quad (4)$$

determines the most commonly discussed triangle in the  $(\bar{\varrho}, \bar{\eta})$  plane. Here  $\bar{\varrho} = \varrho(1 - \lambda^2/2)$  and  $\bar{\eta} = \eta(1 - \lambda^2/2)$ . This unitarity triangle is illustrated in Fig. 2.2. A clean measure of its height is provided by the  $K_L^0 \rightarrow \pi^0 \nu \bar{\nu}$  branching ratio. We note that, with all other parameters being known, Eq. 3 implies that the relative error on  $\eta$  is half that of  $\mathcal{B}(K_L^0 \rightarrow \pi^0 \nu \bar{\nu})$ . Thus, for example, a 10% measurement of  $\mathcal{B}(K_L^0 \rightarrow \pi^0 \nu \bar{\nu})$  can in principle determine  $\eta$  to 5%.

To construct the complete unitarity triangle in the  $K$  system, the charged mode  $K^+ \rightarrow \pi^+ \nu \bar{\nu}$ , which is closely related to  $K_L^0 \rightarrow \pi^0 \nu \bar{\nu}$ , is also needed. However,  $K^+ \rightarrow \pi^+ \nu \bar{\nu}$  is not CP violating and receives a non-negligible charm contribution leading to a somewhat higher theoretical uncertainty. This uncertainty is currently about 10% in the branching ratio[11], but NNLO calculations currently underway are expected to reduce it to  $\sim 3\%$ [4]. Measurement of  $\mathcal{B}(K^+ \rightarrow \pi^+ \nu \bar{\nu})$  allows the extraction of  $|V_{td}|$  with the least theoretical uncertainty. The observation of  $K^+ \rightarrow \pi^+ \nu \bar{\nu}$  was first reported by BNL AGS E787 in 1997[12]. A second event was reported in 2001[13] and a third event was observed by the successor experiment E949[14]. The combined branching ratio  $\mathcal{B}(K^+ \rightarrow \pi^+ \nu \bar{\nu}) = 1.47_{-0.89}^{+1.30} \times 10^{-10}$  is twice as high as the central SM prediction (although statistically consistent with it). Analysis of additional data is ongoing. Together with

$\mathcal{B}(K_L^0 \rightarrow \pi^0 \nu \bar{\nu})$ , the unitarity triangle is completely determined in that  $Im\lambda_t$  and  $Re\lambda_t$  (where  $\lambda_t = V_{td}V_{ts}^*$ ) can both be obtained. With the addition of  $|V_{cb}|$ , one can also extract  $\bar{\eta}$  and  $\bar{\rho}$  as shown in Fig. 2.2. Only a few other possible SM observables (e.g.  $x_s/x_d$ ,  $B \rightarrow l^+l^-$ , or certain CP asymmetries in  $B$  decays) provide similar opportunities for unambiguously revealing SM effects. Fig. 2.3 shows the expected fractional measuring error on  $\mathcal{B}(K_L^0 \rightarrow \pi^0 \nu \bar{\nu})$  as a function of the KOPIO run. A 10% measurement is expected after

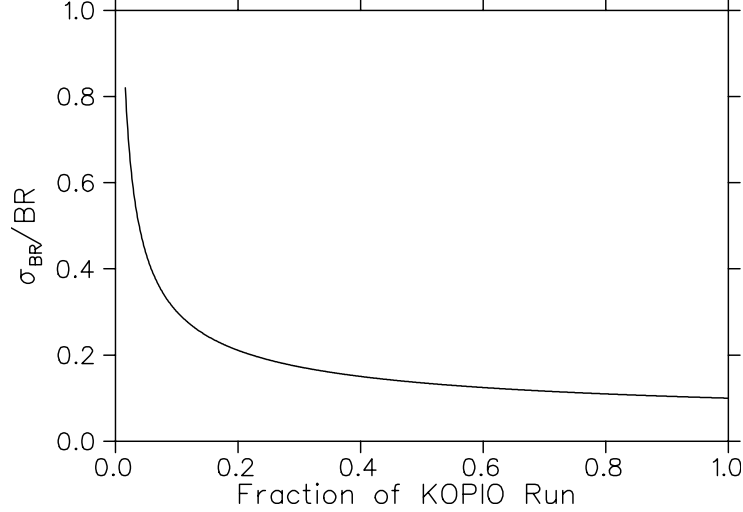


Fig. 2.3. Expected relative error on  $\mathcal{B}(K_L^0 \rightarrow \pi^0 \nu \bar{\nu})$  versus the fraction of the full KOPIO run, assuming the central Standard Model branching ratio.

the full run. A similar precision on  $\mathcal{B}(K^+ \rightarrow \pi^+ \nu \bar{\nu})$  is the goal of the NA48/3 initiative at CERN[15]. The impact of such 10% measurements of  $\mathcal{B}(K^+ \rightarrow \pi^+ \nu \bar{\nu})$  and  $\mathcal{B}(K_L^0 \rightarrow \pi^0 \nu \bar{\nu})$  on determinations of the unitarity triangle is shown in Fig. 2.4.

The pure  $B$ -system alternative to  $K \rightarrow \pi \nu \bar{\nu}$  for obtaining  $\bar{\rho}$  and  $\bar{\eta}$  (Fig. 2.2) involves the measurement of CP-violating, time-dependent asymmetries in  $B$  decays to obtain  $\beta$  and  $\alpha$ . Studies of  $B^0$  or  $\bar{B}^0 \rightarrow J/\psi K_S^0$  and related decays have produced  $\sin 2\beta = 0.739 \pm 0.048$ [16]. Measurement of  $\sin 2\alpha$  is potentially complicated by uncertainties due to Penguin contributions[17]. However, such contributions in  $B \rightarrow \rho\rho$  decays turn out to be substantially smaller than in  $B \rightarrow \rho\pi$  and  $B \rightarrow \pi\pi$ [18]. Aided by the fact that  $B \rightarrow \rho\rho$  is almost entirely longitudinally polarized and thus is in a nearly pure CP-even state,  $B \rightarrow \rho\rho$  analysis yields a measurement of  $\alpha = (94 \pm 12 \pm 13)^\circ$  by using the solution for  $\alpha$  in agreement with a global CKM fit[16]. To infer values of  $\bar{\rho}$  and  $\bar{\eta}$  from these measurements involves discrete ambiguities that can be resolved by measuring the sign of  $\cos 2\beta$  in  $B \rightarrow J/\psi K\pi$  decays[19] and by including additional information (e.g. on the size of  $|V_{ub}|$ ). Theoretical uncertainties associated with this extraction are not fully understood, but they are probably comparable to those of the alternative that uses the measurement of  $x_s/x_d$  in conjunction with  $\sin 2\beta$  from  $B \rightarrow J/\psi K_S^0$ . The CKM analysis for  $K \rightarrow \pi \nu \bar{\nu}$  is less complicated than either of these approaches. It could turn out to be a considerable advantage in the unitarity triangle determination.

Alternatively, results from the CP violation experiments in  $B$  physics and a  $K_L^0 \rightarrow \pi^0 \nu \bar{\nu}$  measurement could also be combined for high precision determinations of the CKM matrix. One could complete a CKM matrix determination that is essentially free of hadronic uncertainties[20]. The method could become particularly interesting when CP asymmetries in  $B$  decays are measured with improved precision at the LHC. Such a precise determination of the independent CKM parameters, in which  $K_L^0 \rightarrow \pi^0 \nu \bar{\nu}$  plays a crucial role, would provide an ideal basis for comparison with other observables sensitive to mixing angles, such as  $K^+ \rightarrow \pi^+ \nu \bar{\nu}$ ,  $B \rightarrow \pi l \nu$ ,  $x_s/x_d$ , or  $V_{cb}$  from  $b \rightarrow c$  transitions. Any additional, independent determination of CKM parameters would then constitute a test of the Standard Model. Any significant deviation would point to new physics.

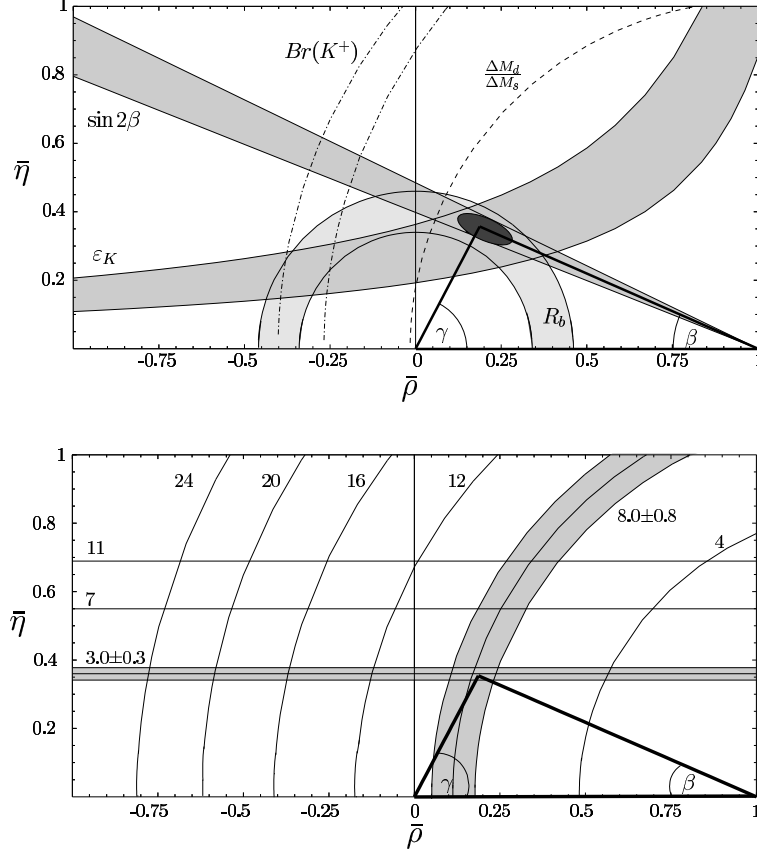


Fig. 2.4. Upper plot: standard UT fit compared to the band resulting from the central experimental value of  $B(K^+ \rightarrow \pi^+ \nu \bar{\nu})$ . Lower plot: UT from 10% measurements of charged and neutral  $K \rightarrow \pi \nu \bar{\nu}$  at currently predicted values. Also lines corresponding to different values of these branching ratios (from Ref.[4]).

Additional strategies for combining and comparing information from the rare  $K$  and the  $B$  sector are described in Refs.[3,21,22,23,24]. Finally, it should be emphasized that it is very desirable that such fundamental quantities as  $\varrho$  and  $\eta$  be measured redundantly via methods that do not share the same systematic errors.

## 2.2 Beyond the Standard Model

Extensions of the Standard Model can in principle modify the physics discussed above in many ways. Extended models usually introduce a variety of new degrees of freedom and *a priori* unknown parameters, and it is therefore difficult to obtain definite predictions. However, one can make a few general remarks relevant for  $K_L^0 \rightarrow \pi^0 \nu \bar{\nu}$  and the comparison with information from the  $B$  system. For reviews of CP violation in  $B$  physics beyond the SM see Refs.[25,26,27].

A clean SM test is provided by comparing  $\eta$  from  $K_L^0 \rightarrow \pi^0 \nu \bar{\nu}$  with that triangulated from measurements of  $\sin 2\beta$  and  $x_d/x_s$ . Similarly, if  $B(K^+ \rightarrow \pi^+ \nu \bar{\nu})$  is measured, a very clean test is to compare the value of  $\sin 2\beta$  obtained from the two kaon decays with that determined from the CP asymmetry in  $B \rightarrow J/\psi K_S^0$ [28]. Other incisive tests involve comparisons of the Jarlskog invariant obtained from  $B(K_L^0 \rightarrow \pi^0 \nu \bar{\nu})$  with indirect determinations of the same quantity from the  $B$  system. Any discrepancy would clearly indicate new physics. The more theoretically precise the observables under discussion are, the smaller the deviation that could be detected.



The branching ratio  $\mathcal{B}(K_L^0 \rightarrow \pi^0 \nu \bar{\nu})$  is unlikely to be greater than about  $1.4 \times 10^{-9}$  on the basis of an argument by Grossman and Nir[29]. They set a “model-independent” limit on this quantity in terms of  $\mathcal{B}(K^+ \rightarrow \pi^+ \nu \bar{\nu})$  (measured by E787 and E949). This argument depends on the isospin symmetry relation  $A(K^0 \rightarrow \pi^0 \nu \bar{\nu})/A(K^+ \rightarrow \pi^+ \nu \bar{\nu}) = 1/\sqrt{2}$  and some rather general assumptions about the relative phase between the  $K - \bar{K}$  mixing amplitude and the  $s \rightarrow d \nu \bar{\nu}$  decay amplitude. They obtain  $\mathcal{B}(K_L^0 \rightarrow \pi^0 \nu \bar{\nu}) < \frac{1}{r_{is}} \frac{\tau_{K_L^0}}{\tau_{K^+}} \mathcal{B}(K^+ \rightarrow \pi^+ \nu \bar{\nu})$ , where  $r_{is}$  is an isospin and phase-space correction factor equal to 0.954[6]. The 90% confidence level (CL) upper limit derived from the E949 result is  $\mathcal{B}(K^+ \rightarrow \pi^+ \nu \bar{\nu}) < 3.22 \times 10^{-10}$ [14], which yields the above-mentioned  $\mathcal{B}(K_L^0 \rightarrow \pi^0 \nu \bar{\nu}) < 1.4 \times 10^{-9}$ . There is window of opportunity of a factor of roughly 400 between the current direct limit  $\mathcal{B}(K_L^0 \rightarrow \pi^0 \nu \bar{\nu}) < 5.9 \cdot 10^{-7}$  at the 90% CL[30] and the Grossman-Nir bound. Any result in this range would be extremely striking and would require a reassessment of not only the Standard Model, but of virtually all the current candidates for augmenting or replacing it.

Andrzej Buras and his collaborators have explored the possible consequences for  $\mathcal{B}(K_L^0 \rightarrow \pi^0 \nu \bar{\nu})$  in a generic class of models characterized by minimal flavor violation (MFV)[31]. These are models in which there are no new sources of flavor or CP-violation. As far as  $K \rightarrow \pi \nu \bar{\nu}$  is concerned, these models replace  $X(x_t)$  with another (real) function. There can also be similar changes in other processes, such as  $\bar{B} - B$  and  $\epsilon'/\epsilon$ . Specific examples of MFV models for which calculations are available include two Higgs-doublet models[32,33] (these now seem to give rather small effects[34]), models with universal extra dimensions[35] which can give about a 15% enhancement of the branching ratio, and minimal SUSY in which the CKM matrix remains the sole source of CP-violation. The implications of the MSSM with minimal flavor and CP violation have been studied by a number of authors[36,37,38,39], culminating in the work of Buras and collaborators[40]. After a careful accounting for all extant phenomenological constraints, the latter authors conclude that the new effects on rare  $K$  decays (mainly from charged Higgs and charginos) are quite small, but that our current estimates of the CKM parameters could be substantially “polluted” by supersymmetric effects in  $B_d^0 - \bar{B}_d^0$  mixing. As a result, the prediction for  $\mathcal{B}(K_L^0 \rightarrow \pi^0 \nu \bar{\nu})$  can be significantly affected. There is a strong tendency for it to be suppressed, and the predicted range is between 0.41 and 1.03 times that of the SM. Since there are seven input parameters even in this simplified version of SUSY, it is not possible to reverse the arguments of Ref.[40] and exhibit the constraints imposed by particular values of  $\mathcal{B}(K_L^0 \rightarrow \pi^0 \nu \bar{\nu})$ . However, it is clear that these branching ratios will be more powerful than those of most of the other phenomenological inputs, because the latter are afflicted by problematic hadronic matrix elements and other plagues to which  $K_L^0 \rightarrow \pi^0 \nu \bar{\nu}$  is not subject. Clearly if  $\mathcal{B}(K_L^0 \rightarrow \pi^0 \nu \bar{\nu})$  is significantly higher than current expectations, more complicated supersymmetric extensions of the Standard Model will be required. Once the MFV assumption is relaxed, as will be discussed below, large supersymmetric enhancements of  $\mathcal{B}(K_L^0 \rightarrow \pi^0 \nu \bar{\nu})$  are possible, even in the MSSM.

It should be noted that, in general, MFV models can give large effects. In these models, there is a close relation between  $\mathcal{B}(K_L^0 \rightarrow \pi^0 \nu \bar{\nu})$  and  $\mathcal{B}(K^+ \rightarrow \pi^+ \nu \bar{\nu})$ , given a value for the mixing-induced CP asymmetry,  $a_{\psi K_S}$ . For any value of  $\mathcal{B}(K^+ \rightarrow \pi^+ \nu \bar{\nu})$ , there are two possible values for  $\mathcal{B}(K_L^0 \rightarrow \pi^0 \nu \bar{\nu})$ . For example, for  $a_{\psi K_S} = 0.74$  and  $\mathcal{B}(K^+ \rightarrow \pi^+ \nu \bar{\nu}) = 1.5 \cdot 10^{-10}$ , which are near the current measured values for these quantities,  $\mathcal{B}(K_L^0 \rightarrow \pi^0 \nu \bar{\nu})$  can equal  $7.5 \cdot 10^{-11}$  or  $16.6 \cdot 10^{-11}$  (both values being far outside the SM range).

The E787 and E949 results for  $K^+ \rightarrow \pi^+ \nu \bar{\nu}$  and the confirmation of a large value for  $\epsilon'/\epsilon$ [41,42] have focused much attention on the possible contributions of flavor-changing  $Z$ -penguin diagrams in generic low-energy supersymmetric extensions of the Standard Model[43,44,45,46,47,48]. Such diagrams can interfere with the weak penguins of the Standard Model, and either raise or reduce the predicted  $\mathcal{B}(K_L^0 \rightarrow \pi^0 \nu \bar{\nu})$  by substantial amounts. When only the mass insertion approximation is considered,  $\mathcal{B}(K_L^0 \rightarrow \pi^0 \nu \bar{\nu})$  can be enhanced by up to a factor of four, or even a full order of magnitude in some cases[47].

Once measured, of course,  $\mathcal{B}(K_L^0 \rightarrow \pi^0 \nu \bar{\nu})$  would constrain such models much more effectively than  $\epsilon'/\epsilon$ . Reversing the constraint would throw light on the confusion surrounding the latter quantity. This type of model has recently been invoked in connection with the anomalous behavior observed in  $B \rightarrow \pi K$ [49,50]. In this scenario  $\mathcal{B}(K_L^0 \rightarrow \pi^0 \nu \bar{\nu})$  can vary from less than one tenth of the SM level to more than ten times it.



Another type of proposed model that enhances  $Z^0$  penguins has been advanced by Chanowitz[51] to explain the apparent anomalies in  $A_{LR}$  and the  $b$ -quark front-back, left-right polarization asymmetry. This type of resolution of the SLC anomaly could be ruled out by a value for  $\mathcal{B}(K_L^0 \rightarrow \pi^0 \nu \bar{\nu})$  in the Standard Model range.

Recently Buras and collaborators considered the case of the MSSM in full generality (but with  $R$ -parity conserved)[52]. Very large effects are possible, with  $\mathcal{B}(K_L^0 \rightarrow \pi^0 \nu \bar{\nu})$  being nearly as large as the Grossman-Nir limit. It is even easier to get large enhancements if the MSSM is given up. Models with broken  $R$ -parity are closely related to models with Lepton Flavor Violation[53] and can generate large CP-conserving contributions to  $K_L^0 \rightarrow \pi^0 \nu \bar{\nu}$  and a total rate as large as the Grossman-Nir bound.

Hattori et al.[55] have studied the effects of a possible fourth generation of fermions on the branching ratios for rare decays. They claim that very large values, nearly as high as the Grossman-Nir bound, are allowed by the current phenomenology, including the measured values of or limits on  $\Delta m_K$ ,  $\epsilon$ ,  $x_d$ ,  $x_s$ ,  $\Delta m_D$ ,  $\mathcal{B}(K^+ \rightarrow \pi^+ \nu \bar{\nu})$ , and  $\mathcal{B}(K_L^0 \rightarrow \mu^+ \mu^-)$ . They do not explore all of the possible parameter space, but make various plausible ansatzes for the mixing patterns. The facts that (1) the range of prediction of  $\mathcal{B}(K_L^0 \rightarrow \pi^0 \nu \bar{\nu})$  is so large ( $0.5 - 220 \times 10^{-11}$ ) and (2) that the prediction based on the input parameters is so clean, suggest that a measurement of  $\mathcal{B}(K_L^0 \rightarrow \pi^0 \nu \bar{\nu})$  would be very powerful in limiting the possible values for the couplings. More recently, Yanir[56] confirmed that values as large as the Grossman-Nir bound are possible.

Xaio and collaborators[57,58] studied the possible contribution to rare  $K$  decays from two varieties of a technicolor model. They obtain very large ranges of prediction for  $\mathcal{B}(K_L^0 \rightarrow \pi^0 \nu \bar{\nu})$  (in one case right up to the Grossman-Nir limit). However, the charged and neutral varieties of  $K \rightarrow \pi \nu \bar{\nu}$  are strongly correlated, so that when the above-mentioned upper limit on  $\mathcal{B}(K^+ \rightarrow \pi^+ \nu \bar{\nu})$  is imposed,  $\mathcal{B}(K_L^0 \rightarrow \pi^0 \nu \bar{\nu})$  is limited to about  $30 \times 10^{-11}$  in walking technicolor models and  $8 \times 10^{-11}$  in topcolor-assisted models.

Kiyo et al.[59] attempted to extend the idea of the seesaw model for neutrino masses to quarks. They claim that it is possible in this sort of model to have a scalar contribution that enhances  $\mathcal{B}(K_L^0 \rightarrow \pi^0 \nu \bar{\nu})$  by up to 30%. This model is nearly unique in predicting a distortion of the normally vector-like  $\pi^0$  momentum spectrum in  $K_L^0 \rightarrow \pi^0 \nu \bar{\nu}$ .

He and Valencia[60] studied  $K \rightarrow \pi \nu \bar{\nu}$  in a L-R symmetric model with a heavy  $Z'$ . Consistent with phenomenological constraints,  $\mathcal{B}(K_L^0 \rightarrow \pi^0 \nu \bar{\nu})$  can be as large as  $1.4 \cdot 10^{-10}$ .

Chang and Ng find that  $\mathcal{B}(K_L^0 \rightarrow \pi^0 \nu \bar{\nu})$  can be enhanced by  $\sim 50\%$  in a 5D (*i.e.* one extra dimension) split fermion scenario[61].

Grossman and Nir[29] demonstrated that it is possible to construct a phenomenologically allowed model that can yield  $\mathcal{B}(K_L^0 \rightarrow \pi^0 \nu \bar{\nu})$  in the neighborhood of their bound. Their model contains extra quarks in vector-like representations of the Standard Model gauge group  $d_4(3, 1)_{-1/3} + \bar{d}_4(\bar{3}, 1)_{+1/3}$ . These quarks arise in GUTs with an  $E_6$  gauge group. Mixing such objects with the standard quarks and leptons would give rise to tree level FCNC currents in  $Z^0$  interactions, and these could be CP-violating. This model allows  $\mathcal{B}(K_L^0 \rightarrow \pi^0 \nu \bar{\nu})$  to be as large as their limit without seriously upsetting the flavor-diagonal  $Z^0$  couplings or conflicting with the current measurements of  $\mathcal{B}(K^+ \rightarrow \pi^+ \nu \bar{\nu})$  and  $\mathcal{B}(K_L^0 \rightarrow \mu^+ \mu^-)$ . In this model,  $\mathcal{B}(K_L^0 \rightarrow \pi^0 \nu \bar{\nu})$  directly measures the imaginary part of the new coupling  $U_{ds}$  through  $\frac{\Gamma(K_L^0 \rightarrow \pi^0 \nu \bar{\nu})}{\Gamma(K^+ \rightarrow \pi^0 e^+ \nu)} = r_{is}^0 \frac{1}{4} \frac{|Im U_{ds}|^2}{|V_{us}|^2}$ , where  $r_{is}^0 = 0.944$  is an isospin-breaking correction. For a measured  $\mathcal{B}(K_L^0 \rightarrow \pi^0 \nu \bar{\nu})$  in the Standard Model range,  $|Im U_{ds}|$  would be limited to about  $3 \times 10^{-5}$  (it could otherwise be  $\mathcal{O}(1)$ ).

Figure 1.1 (see Sec. 1) shows the  $5\sigma$  exclusion range given by the KOPIO experiment at each point of its run. The region between the solid lines is the region that can be excluded. After the entire run, for example, the SM can be excluded at the  $5\sigma$  level or better if the branching ratio is larger than  $1.5\times$  or less than  $0.5\times$  the central value of the SM prediction. (We assume that by the time the experiment is finished, this prediction is very precise).

An indication of the power of KOPIO to probe new physics is that the experiment is sensitive to a factor of almost 500 below the Grossman-Nir bound, of which only about 1% is allowed by the Standard Model. Figure 1.1 shows that this territory is stocked with many accessible candidates. It's notable that the progress

is extremely fast at the beginning of the run.

### 2.3 Theoretical Summary

As a consequence of unprecedented theoretical precision and anticipated experimental accessibility, a measurement of  $K_L^0 \rightarrow \pi^0 \nu \bar{\nu}$  can unambiguously test the SM origin of CP violation, directly measure the area of the unitarity triangle, and ultimately yield the most accurate determination of the CKM CP-violating phase  $\eta$ . This rare decay mode therefore provides a unique opportunity for making significant progress in our understanding of flavor-dynamics and CP violation. It is competitive with and complementary to future measurements in the  $B$  meson system. If new physics is manifesting itself in  $K^+ \rightarrow \pi^+ \nu \bar{\nu}$  or  $\epsilon'/\epsilon$ , it is virtually certain to show up in an unambiguous way in a measurement of  $K_L^0 \rightarrow \pi^0 \nu \bar{\nu}$  at the sensitivity of the SM-predicted level. The absence of  $K_L^0 \rightarrow \pi^0 \nu \bar{\nu}$  within the branching ratio range of about  $(3 \pm 1.5) \times 10^{-11}$ , or a conflict with other CKM determinations, would certainly indicate new physics.

### References

1. M.K. Gaillard and B.W. Lee, Phys. Rev. D **10**, 897 (1974); J. Ellis, M.K. Gaillard and D.V. Nanopoulos, Nucl. Phys. **B109**, 213 (1976); L. Littenberg, Phys. Rev. D **39**, 3322 (1989).
2. A.R. Barker and S.H. Kettell, Ann. Rev. Nucl. Part. Sci. **50**, 249 (2000); L. Littenberg and G. Valencia, Ann. Rev. Nucl. Part. Sci. **43**, 729 (1993); B. Winstein and L. Wolfenstein, Rev. Mod. Phys. **65**, 1113 (1993); J.L. Ritchie and S.G. Wojcicki, Rev. Mod. Phys. **65**, 1149 (1993); G. Buchalla, A.J. Buras and M.E. Lautenbacher, Rev. Mod. Phys. **68**, 1125 (1996).
3. A.J. Buras and R. Fleischer, in *Heavy Flavours II*, Eds. A.J. Buras and M. Linder, 65-238 (World Scientific, 1997).
4. A. J. Buras, F. Schwab and S. Uhlig, preprint arXiv:hep-ph/0405132.
5. D. Rein and L.M. Sehgal, Phys. Rev. D **39**, 3325 (1989); G. Buchalla and G. Isidori, Phys. Lett. **B440**, 170 (1998).
6. W.J. Marciano and Z. Parsa, Phys. Rev. D **53**, R1 (1996).
7. G. Buchalla and A.J. Buras, Nucl. Phys. **B400**, 225 (1993).
8. M. Misiak and J. Urban, Phys. Lett. **B451**, 161 (1999).
9. G. Buchalla and A.J. Buras, Nucl. Phys. **B548**, 309 (1999).
10. C. Jarlskog and R. Stora, Phys. Lett. **B208**, 268 (1988).
11. G. Buchalla and A.J. Buras, Nucl. Phys. **B412**, 106 (1994).
12. S. Adler *et al.*, Phys. Rev. Lett. **79**, 2204 (1997).
13. S. Adler *et al.* [E787 Collaboration], Phys. Rev. Lett. **88**, 041803 (2002).
14. V. V. Anisimovsky *et al.* [E949 Collaboration], Phys. Rev. Lett. **93**, 031801 (2004).
15. D. Munday *et al.*, CERN-SPSC-2004-029.
16. J. Charles *et al.* [CKMfitter Group], preprint arXiv:hep-ph/0406184.
17. M. Gronau, Phys. Lett. **B300**, 163 (1993).
18. B. Aubert *et al.* [BABAR Collaboration], preprint arXiv:hep-ex/0412067.
19. B. Aubert *et al.* [BABAR Collaboration], preprint arXiv:hep-ex/0411016.
20. A.J. Buras, Phys. Lett. **B333**, 476 (1994).
21. A. J. Buras, P. Gambino, M. Gorbahn, S. Jager and L. Silvestrini, Phys. Lett. **B500**, 161 (2001).
22. Y. Zhou and Y. Wu, Mod. Phys. Lett. A **15**, 185 (2000).
23. G. D'Ambrosio, G. F. Giudice, G. Isidori and A. Strumia, Nucl. Phys. **B645**, 155 (2002).
24. S. Bergmann and G. Perez, JHEP **0008**, 034 (2000).
25. C. Dib, D. London and Y. Nir, Int. J. Mod. Phys. **A6**, 1253 (1991).
26. Y. Grossman, Y. Nir, and R. Rattazzi, in *Heavy Flavours II*, Eds. A.J. Buras and M. Lindner, pp. 755-794 (World Scientific Publishing Co., Singapore, 1997).
27. A. Masiero and O. Vives, Ann. Rev. Nucl. Part. Sci. **51**, 161 (2001).
28. G. Buchalla and A. J. Buras, Phys. Lett. **B333**, 221 (1994).
29. Y. Grossman and Y. Nir, Phys. Lett. **B398**, 163 (1997).
30. A. Alavi-Harati *et al.*, Phys. Rev. D **61**, 072006 (2000).
31. A. J. Buras and R. Fleischer, Phys. Rev. D **64**, 115010 (2001).
32. G. Bélanger, C.G. Geng and P. Turcotte, Phys. Rev. D **46**, 2950 (1992).

33. C.E. Carlson, G.D. Dorata and M. Sher, Phys. Rev. D **54**, 4393 (1996).
34. G. Belanger, P. Turcotte and C. Q. Geng, Phys. Rev. D **48**, 5419 (1993).
35. A. J. Buras, M. Spranger and A. Weiler, Nucl. Phys. **B660**, 225 (2003).
36. S. Bertolini and A. Masiero, Phys. Lett. **B174**, 343 (1986).
37. I. I. Y. Bigi and F. Gabbiani, Nucl. Phys. **B367**, 3 (1991).
38. G. Couture and H. Konig, Z. Phys. C **69**, 167 (1995).
39. T. Goto, Y. Okada and Y. Shimizu, Phys. Rev. D **58**, 094006 (1998).
40. A. J. Buras, P. Gambino, M. Gorbahn, S. Jager and L. Silvestrini, Nucl. Phys. **B592**, 55 (2001).
41. A. Alavi-Harati *et al.* [KTeV Collaboration], Phys. Rev. Lett. **83**, 22 (1999).
42. J. R. Batley *et al.* [NA48 Collaboration], Phys. Lett. **B544**, 97 (2002).
43. Y. Nir and M. Worah, Phys. Lett. **B423**, 319 (1998).
44. A.J. Buras, A. Romanino, and L.Silvestrini, Nucl. Phys. **B520**, 3 (1998).
45. G. Colangelo and G. Isidori, JHEP **09**, 009 (1998).
46. A.J. Buras and L.Silvestrini, Nucl. Phys. **B546**, 299 (1999).
47. A.J. Buras, G. Colangelo, G. Isidori, A. Romanino and L. Silvestrini, Nucl. Phys. **B566**, 3 (2000).
48. S. Bosch, A.J. Buras, M. Gorbahn, S. Jager, M. Jamin, M.E. Lautenbacher, and L. Silvestrini, Nucl. Phys. **B565**, 3 (2000).
49. A. J. Buras, R. Fleischer, S. Recksiegel and F. Schwab, Nucl. Phys. **B697**, 133 (2004).
50. A. J. Buras, R. Fleischer, S. Recksiegel and F. Schwab, Phys. Rev. Lett. **92**, 101804 (2004).
51. M.S. Chanowitz, preprint hep-ph/9905478(v2) (1999).
52. A. J. Buras, T. Ewerth, S. Jager and J. Rosiek, preprint arXiv:hep-ph/0408142.
53. Y. Grossman, G. Isidori and H. Murayama, Phys. Lett. **B588**, 74 (2004).
54. R. Fleischer, G. Isidori and J. Matias, JHEP **0305**, 053 (2003).
55. T. Hattori, T. Hasuike, and S. Wakaizumi, Phys. Rev. D **60**, 113008 (1999).
56. T. Yanir, JHEP **0206**, 044 (2002).
57. Z. Xiao, C. Li and K. Chao, Eur. Phys. J. **C10**, 51 (1999).
58. Z. Xiao, L. Lu, H. Guo, and G. Lu, Eur. Phys. J. **C7**, 487 (1999).
59. Y. Kiyo, T. Morozumi, P. Parada, M.N. Rebelo, and M. Tanimoto, Prog. Theor. Phys. **101**, 671 (1999).
60. X. G. He and G. Valencia, Phys. Rev. D **70**, 053003 (2004).
61. W. F. Chang and J. N. Ng, JHEP **0212**, 077 (2002).

### 3 Overview of the $K_L^0 \rightarrow \pi^0 \nu \bar{\nu}$ Measurement Technique

Along with the challenge of obtaining sufficient detection sensitivity, one of the main issues in measuring an ultra-rare process is the control of systematic uncertainties in estimating levels of backgrounds. In general, Monte Carlo calculations are of limited value in assessing problems associated with very rare physics processes that can simulate the signal. The only reliable recourse is to use data to systematically study the backgrounds. This method is feasible when there is enough experimental information for each event so that the signal can be securely grasped, the backgrounds confidently rejected, and the background levels independently measured in spite of limited statistics. Only with reliable background determinations can observation of an extremely small signal be firmly established. The KOPIO experiment has been designed with this approach in mind.

The experimental signature for the  $K_L^0 \rightarrow \pi^0 \nu \bar{\nu}$  decay mode consists of exactly two photons with the invariant mass of a  $\pi^0$ , and nothing else. The primary experimental challenge arises from the 34% probability that a  $K_L^0$  will emit at least one  $\pi^0$ , while the expected decay probability for  $K_L^0 \rightarrow \pi^0 \nu \bar{\nu}$  is ten orders of magnitude smaller. Compounding the difficulty, interactions between neutrons and kaons in the neutral beam with residual gas in the decay volume can also result in emission of single  $\pi^0$ s, as can the decays of hyperons which might occur in the decay region, *e.g.*  $\Lambda \rightarrow \pi^0 n$ . The current experimental limit for  $\mathcal{B}(K_L^0 \rightarrow \pi^0 \nu \bar{\nu})$  of  $< 5.9 \times 10^{-7}$  [1] comes from a Fermilab experiment that employed the Dalitz decay  $\pi^0 \rightarrow e^+ e^- \gamma$ . Further improvement in sensitivity may be achieved by the KEK E391 experiment. Thus, for KOPIO, an experimental improvement in sensitivity by six orders of magnitude beyond the current limit is required to obtain a robust signal for  $K_L^0 \rightarrow \pi^0 \nu \bar{\nu}$  at the Standard Model level of  $\mathcal{B}(K_L^0 \rightarrow \pi^0 \nu \bar{\nu}) = 3 \times 10^{-11}$ .

For any experiment seeking to measure  $K_L^0 \rightarrow \pi^0 \nu \bar{\nu}$ , the most important means of eliminating unwanted events is to determine that nothing other than one  $\pi^0$  was emitted in the decay, *i.e.* to veto any extra particles. The most difficult mode to suppress is  $K_L^0 \rightarrow \pi^0 \pi^0$  ( $K_{\pi 2}$ ). Because the efficiency of photon detection is limited by physical processes such as photonuclear effects as well as by construction and geometrical considerations, additional handles are needed to suppress all backgrounds.

One such handle is provided by measurement of the  $K_L^0$  momentum via time-of-flight (TOF). From knowledge of the decaying  $K_L^0$  momentum, the  $\pi^0$  can be transformed to the  $K_L^0$  center-of-mass frame and kinematic constraints can be imposed on an event-by-event basis. This technique facilitates rejection of bogus kaon decays and suppression of all other potential backgrounds, including otherwise extremely problematic ones such as hyperon decays and beam neutron and photon interactions.

For KOPIO, copious low-energy kaons will be produced at the AGS in an appropriately time-structured beam. The suppression of background is achieved by using a combination of hermetic high-sensitivity photon vetoing and full reconstruction of photons through measurements of position, angle, and energy. Events originating in the two-body decay  $K_L^0 \rightarrow \pi^0 \pi^0$  identify themselves when reconstructed in the  $K_L^0$  center-of-mass system. Furthermore, those events with missing low-energy photons, the most difficult to detect, can be identified and eliminated. With the two independent criteria based on precise kinematic measurements and demonstrated photon veto levels, not only is there enough experimental information so that  $K_L^0 \rightarrow \pi^0 \pi^0$  and other backgrounds can be suppressed to the required level, but the background levels can also be measured directly from data.

The beam and detectors for KOPIO employ well known technologies. Important aspects of the system are based on measurement techniques proven in earlier AGS experiments performed by KOPIO collaborators, and new aspects have been studied in beam measurements and with prototypes and simulations. Figure 3.1 shows a simplified representation of the beam and detector concept and Fig. 3.2 gives a schematic layout of the entire apparatus. The 25.5-GeV primary proton beam is presented to the kaon production target in 200-ps-wide pulses at a rate of 25 MHz. A neutral beam with a 360- $\mu$ sr solid angle is extracted at 42.5° to produce a “soft”  $K_L$  spectrum peaked at 0.65 GeV/c; kaons with momenta above 0.4 GeV/c are used. The vertical acceptance of the beam (4 mrad) is kept much smaller than the horizontal acceptance (90 mrad) so that effective collimation can be obtained to severely limit beam halos and to obtain another constraint on the decay vertex position. Downstream of the final beam collimator is a 4-m-long decay region which is surrounded by the main detector. The beam region is evacuated to a level of  $10^{-7}$  Torr to suppress neutron-

induced  $\pi^0$  production. The decay region is surrounded by a thin-walled vacuum tank which encloses layers of plastic scintillators used to veto charged particles\*. Outside the vacuum is an efficient lead/scintillator photon veto detector (“Barrel Veto”) which also serves as a detector for some signal photons as described below. In order to simplify triggering and offline analysis, only events with the signature of a single kaon decay that produces two photons within the period between microbunches are accepted.

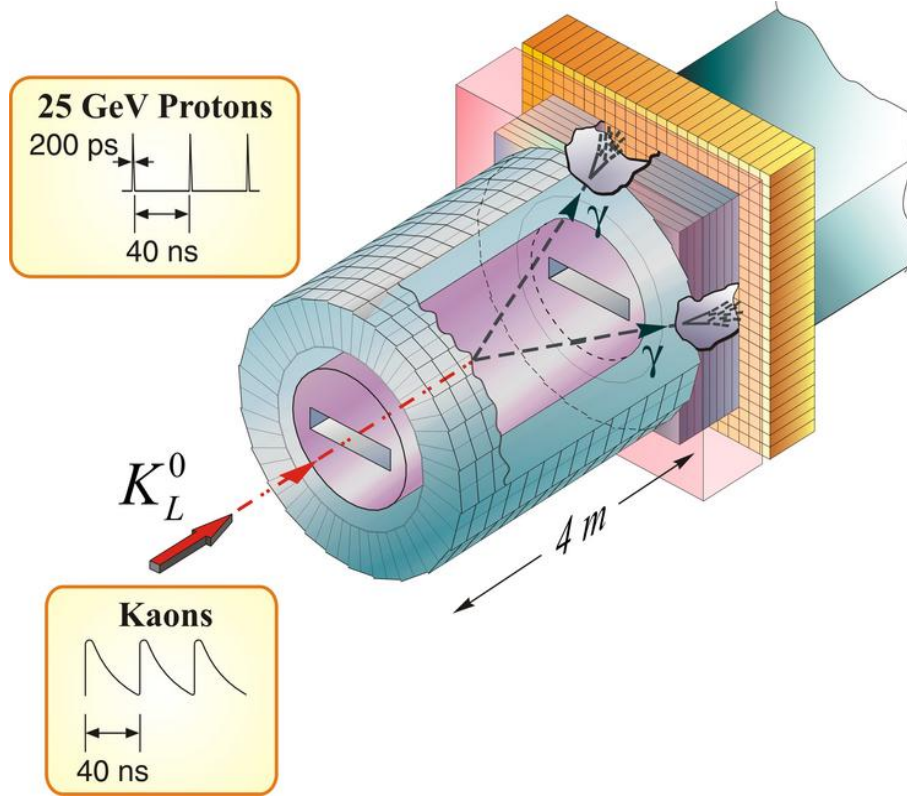


Fig. 3.1. Elements of the KOPIO concept: a pulsed primary beam produces low-energy kaons whose time-of-flight reveals their momentum when the  $\pi^0$  from  $K_L^0 \rightarrow \pi^0 \nu \bar{\nu}$  decay is reconstructed.

Photons from  $K_L^0 \rightarrow \pi^0 \nu \bar{\nu}$  decay are observed in a two-stage “pointing Calorimeter”. It is comprised of a 2.7-radiation-length ( $X_0$ ) fine-grained Preradiator (PR) calorimeter followed by a 19- $X_0$  electromagnetic calorimeter. The PR obtains the energies, times, positions and angles of the interacting photons from  $\pi^0$  decay by determining the initial trajectories of the first  $e^+e^-$  pairs. The PR includes 64 layers of dual-coordinate drift chambers sandwiched between plastic scintillators. The thickness of a chamber-scintillator pair is 0.04  $X_0$ . The PR measures the photon positions and directions accurately in order to allow reconstruction of the  $K_L$  decay vertex. In addition, because it is constructed of mostly active plastic scintillator detectors, the Preradiator contributes principally to the achievement of excellent energy resolution.

The Calorimeter is located behind the Preradiator and consists of “Shashlyk” modules, roughly 11 cm by 11 cm in cross section. A Shashlyk Calorimeter module is comprised of a stack of square tiles with alternating layers of lead and plastic scintillator read out by penetrating Wavelength Shifting (WLS) fibers. The Preradiator-Calorimeter combination is expected to have an energy resolution of  $\sigma_E/E \simeq 2.7\%/\sqrt{E} [\text{GeV}]$ . Shashlyk is a well established technique that has been used effectively in BNL experiment E865 and is currently the main element in the PHENIX calorimeter at RHIC.

\*The charged particle veto scintillators will be located in a vacuum region that is separated from the  $10^{-7}$  Torr beam vacuum region by a thin membrane.

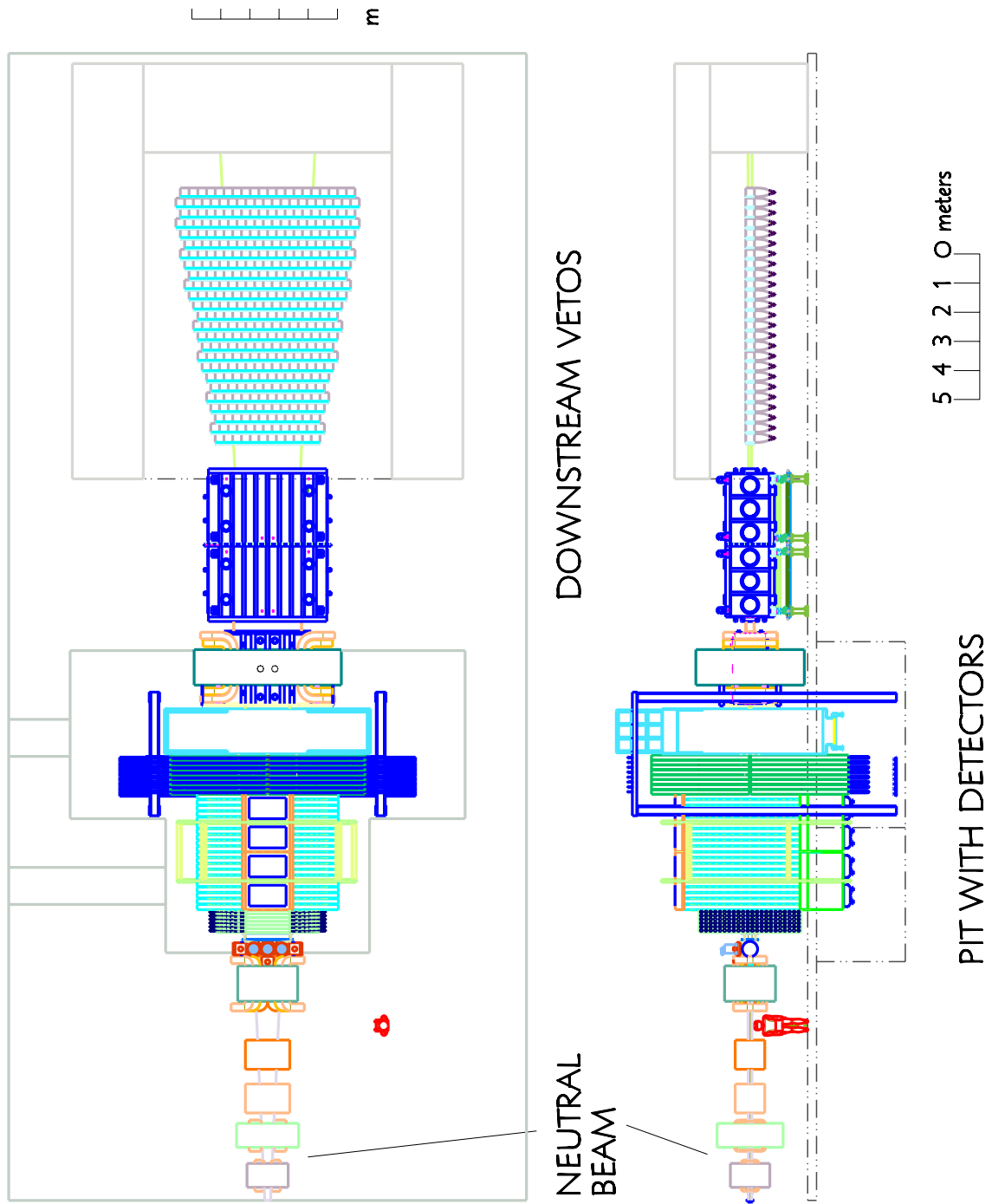


Fig. 3.2. Plan and elevation views of the KOPIO detector.



Suppression of most backgrounds is provided by a hermetic, high-efficiency, charged-particle and photon detector system surrounding the decay volume. A Charged Particle Veto system of scintillators is located inside the vacuum chamber (Sec. 6d). Photon veto systems include a decay-volume Barrel Veto detector, an Upstream Wall, and several systems downstream of the main decay volume (Sec. 6c). The Barrel Veto Shashlyk detectors provide about 18  $X_0$  for photon conversion and detection. The detection efficiency for photons has been extensively studied with a similar system in BNL experiment E787/E949.

The downstream section of the veto system is needed to reject events where photons or charged particles leave the decay volume through the beam hole. It consists of a sweeping magnet with a horizontal field, scintillators to detect charged particles deflected out of the beam, and photon veto modules. A special group of counters – collectively, the “Catcher” – vetos photons that leave the decay volume but remain in the beam envelope. This system takes advantage of the low-energy KOPIO environment to provide the requisite veto efficiency while being insensitive to neutrons and  $K_L^0$ s in the beam. The Catcher uses Čerenkov radiators read out with phototubes.

The KOPIO system described above will identify the  $K_L^0 \rightarrow \pi^0 \nu \bar{\nu}$  decay signal and effectively reject backgrounds by using kinematic measurements involving  $\pi^0$  reconstruction in the  $K_L^0$  center of mass system. The  $K_L^0 \rightarrow \pi^0 \nu \bar{\nu}$  signal events will be selected with two main topologies: events in which both photons from a  $\pi^0$  decay convert in the Preradiator, and those in which one photon converts in the Preradiator and one is detected the Barrel Veto detector. Figure 3.3 illustrates these event topologies. By tagging the  $K_L$  momentum as well as determining the energy and direction of at least one photon, one can reconstruct the kinematics in 2-body  $K_{\pi 2}$  decays.

As discussed above, the primary weapons for removing backgrounds are the highly efficient photon calorimeters and charged-particle detectors surrounding the fiducial decay region. Remaining backgrounds can be separated from the  $K_L^0 \rightarrow \pi^0 \nu \bar{\nu}$  signal events by virtue of their different phase-space distributions. The separation is based primarily on the following three quantities:

- $T_\pi^*$ , the  $\pi^0$  kinetic energy in the kaon center-of-mass system. For  $K_{\pi 2}$ -even events where the two observed photons come from the same  $\pi^0$ ,  $T_\pi^* = m_K c^2 / 2 - m_\pi c^2 \approx 110$  MeV; for  $K_L^0 \rightarrow \pi^- \pi^+ \pi^0$ ,  $T_\pi^* < 54$  MeV.
- $E_{\text{miss}}$ , the missing energy in the laboratory system. Because the detection efficiencies for photons and charged particles increase with energy, the background rejection by the veto counters improves at larger values of  $E_{\text{miss}}$ .
- $m_{2\gamma}$ , the  $2\gamma$  invariant mass which allows the efficient suppression of  $K_{\pi 2}$ -odd events where the two observed photons come from different  $\pi^0$ s.

Figure 3.4 shows simulated distributions of  $T_\pi^{*2}$  vs.  $\ln(E_{\text{miss}})$  for both signal and total background after suppression of events with signals in the veto systems.

Data analysis will make use of a likelihood method to calculate the probability for each event to be due either to signal or background based on the quantities discussed above. For the full data set, at the level predicted by the SM, the uncertainty on  $\mathcal{B}(K_L^0 \rightarrow \pi^0 \nu \bar{\nu})$  would be  $\sigma_{\mathcal{B}}/\mathcal{B} < 10\%$  as discussed in Sec. 13.

## References

1. A. Alavi-Harati *et al.*, Phys. Rev. D **61**, 072006 (2000).

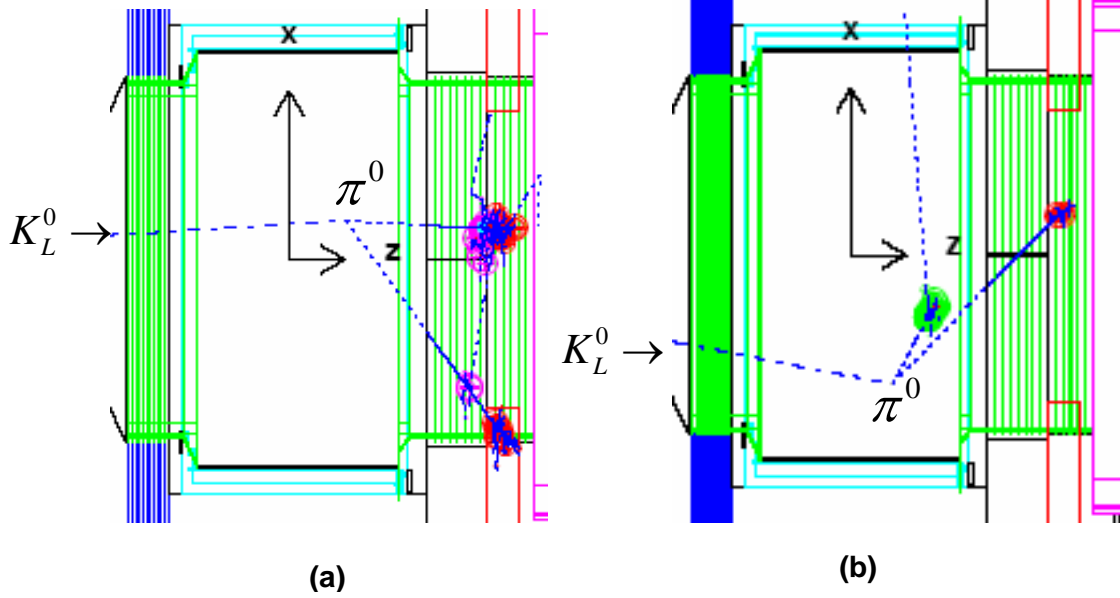


Fig. 3.3. Two events simulated by GEANT3:  
 (a) both photons from the  $\pi^0 \rightarrow \gamma\gamma$  decay converted in the Preradiator,  
 (b) one photon converted in the Preradiator and the second photon was detected in the Barrel Veto calorimeter.

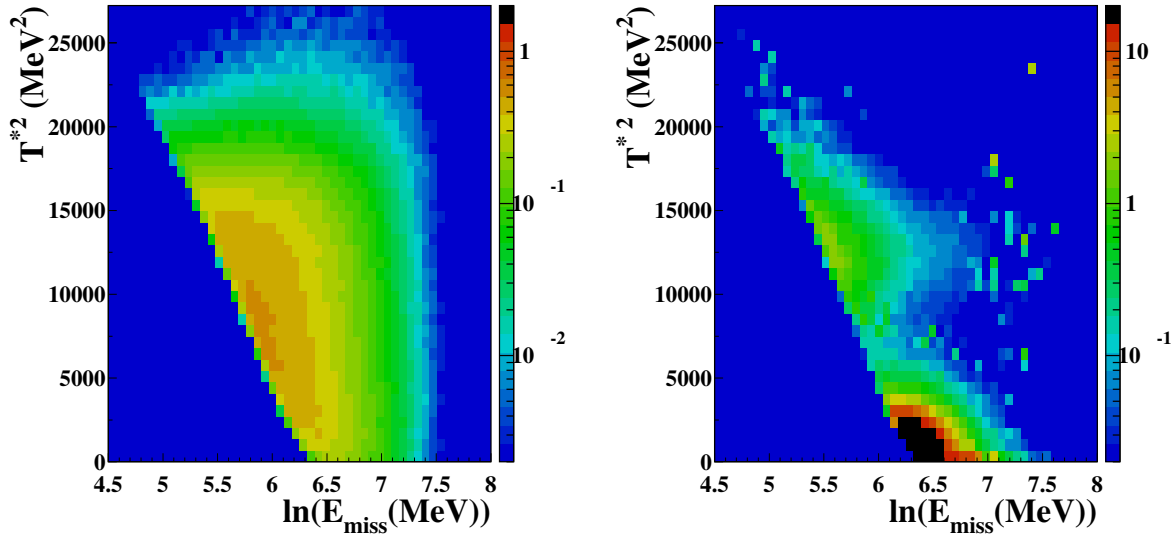


Fig. 3.4. Reconstructed  $\pi^0$  kinetic energy squared  $T_{\pi^*}^2$  vs. the log of the apparent missing energy  $\ln(E_{\text{miss}})$  for signal (left) and background (right). Whereas the signal events show an approximately constant distribution over the allowed phase space, backgrounds are concentrated in a low  $T_{\pi^*}^2$  region populated by  $K_L^0 \rightarrow \pi^-\pi^+\pi^0$  decays and a high  $T_{\pi^*}^2$  region populated by  $K_L^0 \rightarrow \pi^0\pi^0$  decays.



## 4 AGS Modifications

Although the modifications required for running the AGS for KOPIO are detailed in a separate document covering the changes for all of RSVP[1], those items that are specific to KOPIO or primarily benefit KOPIO will be described here. For a complete description of the AGS Mods, refer to the AGS TDR.

### 4.1 Motivations

#### 4.1.1 Microbunch Width

The KOPIO experiment requires that the AGS produce high intensity extracted proton beams with a time structure characterized by very short pulses called microbunches cleanly separated from each other by an interval of 40 ns. The microbunches are needed so that a measurement of the kaon velocity can be made via time-of-flight. The flight time is determined from the moment the primary proton beam strikes the KOPIO target and the measured time when a photon from  $\pi^0$  decay is observed in the Preradiator and Calorimeter. The time spread of the proton microbunch interacting in the target should not dominate the timing resolution. Contributions to the timing resolution come from the Preradiator and Calorimeter which have measured time resolutions on the order of  $(90 \text{ ps})/\sqrt{E}$  for photons of energy  $E$  in GeV. Additional contributions to the time resolution come from the uncertainty in the location of the production point in the target which adds on the order of 100 ps to the time resolution as a function of the kaon momentum. Based on simulation studies of time resolution on the kaon velocity, the microbunch width was selected to be 200 ps RMS.

#### 4.1.2 Microbunch Separation

The KOPIO technique of using a microbunched proton beam to measure the kaon velocity relies on the assumption that the microbunch in which the kaon originated is known. The proton beam produces a kaon momentum spectrum shown in Fig. 4.1. The KOPIO detector has good acceptance for kaons with momentum  $p > 400 \text{ MeV}/c$ . The spread in time-of-flight for this momentum distribution amounts to about 30 ns at the

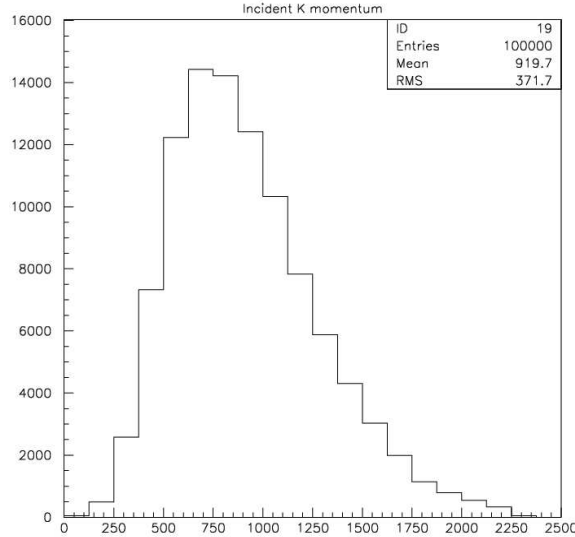


Fig. 4.1. Kaon momentum distribution in  $\text{MeV}/c$  for KOPIO.

front face of the Preradiator. Kaons with lower momenta can straggle in even later. A time separation of 40 ns between microbunches was selected to optimize the signal rate and minimize backgrounds produced by misidentifying the microbunch that was the source of the kaon.

### 4.1.3 Interbunch Extinction

In addition to the effects of stragglers, KOPIO is sensitive to kaons produced in the time interval between the microbunches. Although KOPIO uses Photon Vetoes and Charged Particle Vetoes to identify background events, part of the rejection comes from the kinematical cuts on the two-body decay  $K_L^0 \rightarrow \pi^0 \pi^0$ . In this decay, the  $\pi^0$  is monoenergetic in the kaon rest frame. After observing the two photons from a  $\pi^0$  and using them to measure the kaon velocity by time-of-flight, we can transform to the kaon rest frame and determine whether the momentum of the  $\pi^0$  is consistent with the two-body decay mode or not. This powerful technique affords KOPIO an additional kinematical rejection power of  $\sim 100$  for the  $\pi^0 \pi^0$  mode, dependent on the kaon momentum. If the kaon is not produced at the microbunch time, but comes from the interbunch time, then the time-of-flight will be confounded, giving an incorrect velocity for the kaon. This mismatch, in turn, will cause the pion momentum in the kaon rest frame also to be incorrect, diluting the power of the kinematical rejection. Figure 4.2 shows the pion momentum distribution in the kaon rest frame as a function of the energy difference between the two photons. The narrow band near 200 MeV is displaced to lower momenta when the wrong production time is assumed. This shift causes the background events to fall in the middle of the signal region, completely defeating the kinematical rejection.

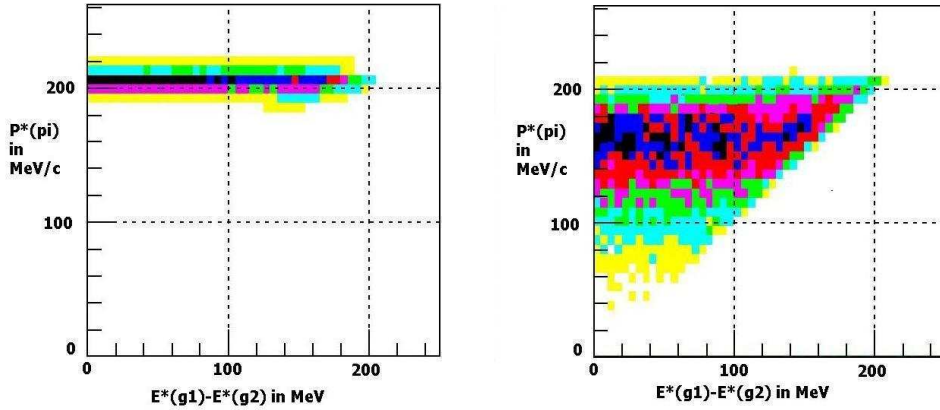


Fig. 4.2. Kinematic rejection of the reconstructed pion in  $K_L^0 \rightarrow \pi^0 \pi^0$  decays. (a) shows the reconstructed pion momentum in the kaon rest frame versus the energy difference between the two photons. (b) shows the same reconstructed pions when the kaon is produced 10 nanoseconds earlier than the microbunch time. This timing shift causes the background events to fall in the middle of the signal region, making kinematic rejection impossible. The colors are contours in event density, running from most dense (black) to least dense (yellow).

Simulations of the kinematical rejection power required to bring the background under control determined that the ratio of the number of protons between the microbunches to the number within the microbunch should be less than  $10^{-3}$ . This ratio defines the interbunch extinction requirement for KOPIO.

## 4.2 General Requirements

The AGS modifications can be divided up into four basic categories. First and foremost are modifications to the Booster and AGS that will insure that RSVP operations do not compromise RHIC operations. Second, there are modifications that are required to ensure compliance with laboratory environmental protection guidelines. Third, there are modifications necessary to enable the accelerators to be brought back to normal high intensity operation. Finally, there are modifications that are required to meet RSVP experimental specifications. A description will be given for each of the modifications planned. The modifications required for microbunching will be motivated by the effects on signal and background in the KOPIO experiment.

### 4.3 Primary Beam Parameters for KOPIO

The primary proton beam for KOPIO will have a momentum of 25.5 GeV/c. The beam will be extracted from the AGS in the slow-extraction mode, with a spill length of 4.88 seconds and a repetition period of 7.18 seconds. The remaining 2.3 seconds are required for injection and acceleration of the beam in the AGS. During the 4.88-second spill, a total of  $10^{14}$  protons will be delivered to the KOPIO target. The extracted beam will have a microbunched time structure with 40 ns between microbunches and a microbunch width of 200 ps RMS. The KOPIO experiment also specifies that the interbunch extinction, or the ratio of protons between the microbunches to the protons in the microbunches, be less than  $10^{-3}$ .

### 4.4 Intensity Upgrades

The beam intensity is limited by a number of different factors. Each stage in the acceleration process from the Linac to the experiment has associated beam losses. In each area, the details of the given process dictates the loss mechanisms. For example, during Booster injection beam has to be captured inside the RF momentum and phase acceptance, which is called an RF bucket, and there is an intrinsic RF capture beam loss during this process. At high intensity, forces due to space charge cause additional beam losses. Significant time can be spent in adjusting parameters to minimize these losses during operations for high intensity. As a result, there exist fundamental limits on achievable beam intensities due to the amount of initial beam available from the ion source as well as on the transmission efficiencies at the various stages of the accelerators. The modifications in both the Booster and AGS for intensity are focused entirely on improving transmission efficiencies in the various stages of the accelerators.

Another limitation on the beam intensity is the acceptable rate of the beam losses during a given operation period. The accelerators have to be maintainable by people, and so the amount of activation produced by the accelerators is managed administratively to keep the workers' occupational dose to as low as reasonably achievable. The most significant modification to the AGS for RSVP running is the addition of Shield Caps to prevent contamination of the groundwater with tritium levels above 5% of the Drinking Water Standard. Although there are coverings over several areas above the Booster and AGS complexes, the newly revised standard requires that the ground above the entire AGS ring and Booster be sealed to prevent penetration of the soil by rainwater that might then leach radioactivity in the form of tritium into the sole-source aquifer. This task can only be accomplished during periods when the AGS is not operating. Since Shield Caps have already been installed over parts of the AGS and Booster, this project is well understood. More detailed description of the Booster and AGS modification can be found in the Booster/AGS TDR.

#### 4.4.1 Booster Modifications

Prior beam losses during injection have activated two Booster main dipole magnets enough to damage the insulation and cause the magnets to short to ground. In one case, the C7 magnet had to be replaced. The replacement was modified to allow the magnet to survive longer, but recent observations of this magnet show that the insulation is becoming radiation damaged again. One of the modifications for the Booster would be to fix this magnet before beginning high intensity operations. Another magnet activated during injection is the C5 main dipole, which is a special magnet, due to a hole that was put in the side of the magnet to allow beam to be injected into the Booster. The stripping foil, to convert the  $H^-$  beam from the Linac to  $H^+$ , is located immediately after this magnet. The C5 magnet failed in the fall of 2003 and had to be repaired. One of the modifications to the Booster will be to add collimation to the transfer line between the Linac and Booster, so that beam losses on these magnets can be reduced during injection. Another modification to these magnets will be the addition of carbon blocks in the areas of beam losses to absorb and diffuse lost particles before they interact in the magnet coils and damage the insulation.

A number of components in the Booster have become radiation damaged from previous high intensity operation periods. Damage to cables and to the pulse forming network (PFN) components of the extraction kicker have been identified as requiring repair or replacement prior to beginning the next high intensity operation. The PFN will be redesigned and new components purchased, to reduce the radiation burden.

Cables and cable trays in the Booster will be replaced and repaired to eliminate damaged items and to reduce the risk of fire or electrical hazards. (Note, the trays are not radiation damaged, but physical damage to cable trays has been observed and needs to be repaired.)

Only a single spare magnet exists for the Booster extraction septum magnet, known as the F6 septum. This magnet is very difficult to replace and, out of 5 replacements that have been carried out in the past, 3 resulted in the spare unit becoming shorted and requiring immediate repair. This work increased the occupational dose to workers and extended the repair periods. A second spare magnet will be built prior to high intensity operation.

The C3 inflector, used to inject heavy ions into the Booster, was damaged during previous running at high intensity. Although the C3 inflector has been repaired, a new protection system is required to ensure that RSVP running will not lead to the same type of damage in the future. The RF cavities need to be upgraded with a fast RF feedback system. One set of RF cavities has already had feedback systems installed, but the modifications were only sufficient for low intensity heavy ion operation for RHIC. These improvements provide better beam stability and will improve the RF capture process during injection.

Upgrading the instrumentation for Booster-to-AGS (BtA) transfers will allow for faster switchovers from RHIC Heavy Ion running to RSVP proton running. Upgrading the Controls System with new VME interfaces, database engineering and software will also improve the reliability of running.

#### **4.4.2 AGS Modifications**

Complementary to the Booster intensity upgrades, the AGS requires that the injection kicker at A5 be upgraded with the addition of new kicker magnets, Pulse Forming Networks (PFNs), power supplies, and capacitor banks. This new injection system will enable the AGS to accept higher intensity beam with lower radiation losses, and more reliable operation. The intensity upgrade also requires that the F5 and F10 thin magnetic septa and their power supplies be replaced, as well as the H20 electrostatic septum which needs to be redesigned in order to operate for MECO.

The existing AGS long-loss monitoring system, which is used to monitor losses for administrative management, is aging and operating on obsolete controls. In addition, the system is not adequate for the intensity levels specified by the RSVP experiments. This system will be repaired and upgraded for RSVP operation.

There are a number of magnet coils in the AGS ring that have been damaged over the years, and C-AD has identified a set of magnets that have received the highest beam losses and need to have their coils replaced before any high intensity running begins. Specifically, the sextupoles have had 12 sets of coils replaced already and require the replacement of 16 more coils. The coils of seven AGS main magnets in the extraction region will also be replaced prior to RSVP operation.

Some of the existing instrumentation in the AGS has exceeded its useful life, and needs to be upgraded. The instruments include the gas leak servo for the Ionization Profile Monitor, many of the motion controls for flags and beam instrumentation, and cameras for those flags. Like the Booster, maintenance of the cable trays and cables is necessary to ensure reliable and safe operation of the AGS. New controls would benefit from new VME interfaces, software, and database engineering to make the operation trouble-free.

#### **4.5 Switchyard Modifications**

The modifications planned for the Switchyard are motivated primarily to reduce beam losses and occupational dose to C-AD workers. In addition to the reliability and ease of operation that the simplifications in the overall design afford, the modifications will ensure higher beam quality and availability. The new design removes three electrostatic beam splitters, removes the two thin Lambertson magnets, the thick Lambertsons, skew quads, tilted dipoles, ramped dipoles, beam servo dipoles, and all servo-SWICs in the beam lines. This simplification is made possible because RSVP will not make use of split-beam operation. The only extracted beams that will be used will be for KOPIO or MECO, and those experiments will never be run at the same time. New zero dispersion tunes have been developed for both experiments that promise

to make for much more stable beam conditions, and much simpler set-up and operation. This more robust switchyard design promises lower activation, easier tuning, and lower maintenance and running costs with reduced demands on the power grid. Simplified vacuum interfaces with fewer flanges mean that the vacuum system operations will also be more reliable. One by-product of this design is that the existing D-line will be decommissioned. This change has the added benefit of freeing up shielding, transport magnets, and floor space for other uses, such as the RSVP experiments. New elements in the Switchyard include a new beam plug after the first four quadrupoles CQ1-4, allowing work in experimental areas when there is beam in the AGS. Shielding changes will be required where the beam penetrates the shielding wall in order to allow access to the switchyard and beam lines during running of the AGS. This new shielding will need to incorporate a new collimator.

## 4.6 KOPIO-Specific Microbunching Modifications

### 4.6.1 Extraction RF Cavities: 25 MHz and 100 MHz

The microbunching technique proposed for KOPIO[2] is useful for slow extraction schemes such as that used at the AGS. It proceeds according to the following steps. First, protons are injected into the AGS in 6 buckets, and accelerated to the operating momentum of 25.5 GeV/c by using the 4.5-MHz RF accelerating cavities. Then the phase of the RF cavities is flipped, causing the protons in the 6 buckets to debunch, effectively spreading the protons around the AGS in a continuous band. This debunching establishes the DC coasting beam that will be extracted, uniform in phase, with a fractional momentum distribution defined by a mean of  $p_0$  and a dispersion of  $dp/p_0$ . A beam dynamics simulation called SLEX-Long1D[3] that is used to evaluate this microbunch extraction process makes use of coordinates relative to a reference frame co-rotating with the equilibrium orbit. The simulation does not make use of beam transport elements, but instead calculates an orbit-by-orbit transfer function based on a symplectic Hamiltonian. The beam dynamics for the  $i^{th}$  particle depends on the vertical and horizontal coordinates,  $x_i$ ,  $x'_i$ ,  $y_i$ , and  $y'_i$  as well as the orbital coordinates  $s_i$  and  $s'_i$  where the “prime” denotes the derivative with respect to the equilibrium orbit parameter  $s$ . This is a  $2 + 2$  dimensional simulation, tracking horizontal (transverse) and longitudinal motion only, with no vertical components in the model. There is no explicit coupling in the Hamiltonian between the transverse and longitudinal motion; only that provided by chromatic dependence of the beam tune  $\nu$ .

Once the coasting beam is established, the extraction RF cavities are brought on at a frequency that is far from any betatron resonance. KOPIO plans to make use of a 25-MHz cavity and a 100-MHz harmonic cavity. The voltage on both cavities is increased slowly so that the beam response is adiabatic. When the cavities are at operating voltage, typically 150 kV for KOPIO, the frequency is reduced, thus bringing the beam closer and closer to the  $8\frac{2}{3}$  resonance. Those beam particles that are far from resonance will receive RF kicks that sometimes increase their energy and sometimes decrease their energy, giving no net effect. Only a narrow momentum band of beam particles will be within the resonance condition. The RF potential gives them a net increase in energy each time they pass through the RF cavities. The resonance condition, created by a set of sextupoles in the AGS, causes progressively larger transverse oscillations producing a large amplitude horizontal deviation from the equilibrium orbit. This horizontal excursion takes the particle across the aperture of the extraction septum which bends the particle out of the circulating beam orbit and towards the extraction beam line.

The narrowness of the regions in phase space that overlap the extraction resonance determines the shortness of the extracted microbunches in the time domain. The overlap region can be made narrower by increasing the depth of the RF buckets by increasing the voltage on the RF cavities. But the microbunch width depends only on the square root of the cavity voltage, making large gains hard to achieve in this manner. Adding a 100-MHz harmonic cavity to the 25-MHz cavity allows for tighter time structure without the difficulty of operating the cavities at prohibitively high voltages. The effect of the higher harmonic cavity is to steepen the phase dependence of the RF buckets, like trying to create a square wave by adding higher harmonics to a sine wave. Because only the particles at the nodes of the RF buckets receive transverse

displacements, there is no mechanism for extracting particles at times between the microbunches. This extraction technique offers very tight time distributions with no contribution from particles extracted between the microbunches.

Studies with test beams were conducted in 2002 and 2004 to measure the microbunch width and interbunch extinction performance of the AGS based on this extraction technique. In 2002, a simple photon telescope observing a thin target in the extracted proton beam was used to look for prompt photons, taken to reproduce the microbunch time structure of the proton beam. By using a single 93-MHz RF cavity operating at 22 kV, a microbunch width of 240 ps was observed. This result is in good agreement with the expected microbunch width and the simulation result of 218 ps. Figure 4.3 shows the data and simulation results for the test-beam case.

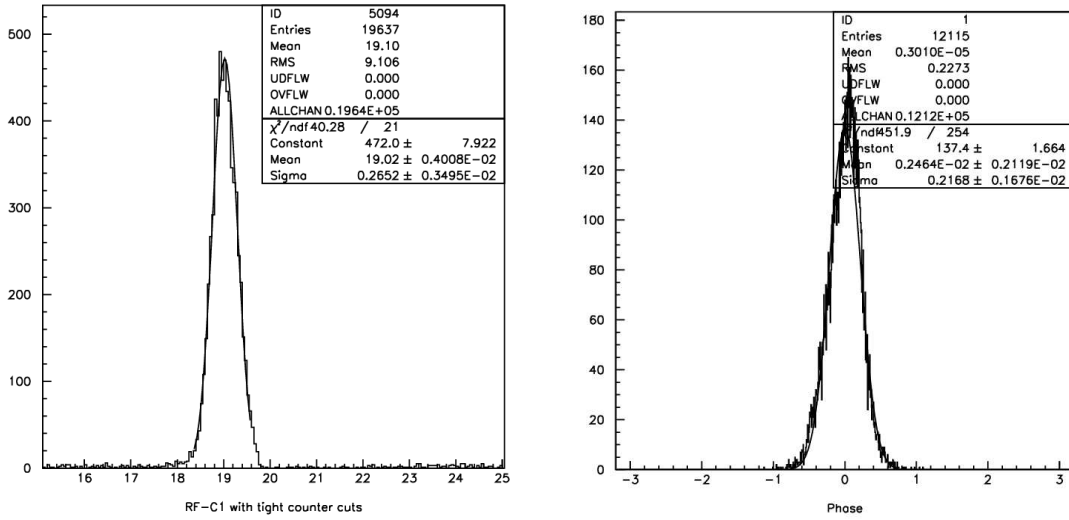


Fig. 4.3. Measured and simulated microbunch time distributions for a 93-MHz RF cavity operating at 22 kV.

A separate test-beam study in 2004 was required for the precision measurement of the interbunch extinction that KOPIO demands. A doubly separated momentum-analyzed beam of 1.4 GeV/c antiprotons was used to look at the time distribution of protons extracted from the AGS with a 4.5-MHz RF cavity. The antiprotons provided a very clean signature to reject backgrounds and accidentals that could make it difficult to obtain a good result at the level of 1 part in  $10^6$ . A scintillator telescope followed by a lead/scintillator calorimeter was used to identify the antiprotons produced when the primary proton beam struck a thick platinum target. The secondary beam line had a narrow momentum acceptance of  $\sim 2\%$ , ensuring that the antiproton timing would reproduce the microbunch time structure of the primary beam. Many machine configurations were studied in order to understand all the factors that contribute to good microbunch timing and interbunch extinction. A broad range of operating conditions that would allow excellent interbunch extinction were established. An example of the results achieved is shown in Fig. 4.4. Only one interbunch event was observed in this run for an extinction value of  $8 \times 10^{-6}$ . Numerous runs produced results similar to this example, demonstrating that the AGS can operate in a mode that delivers good microbunch width and excellent interbunch extinction. These two results for the microbunch width and interbunch extinction provide confidence that the AGS extraction technique planned for KOPIO will be able to deliver the primary proton beam required for the success of the KOPIO experiment.

The design and fabrication of the 25-MHz cavity will be performed at TRIUMF. The work is funded by a grant from the Canada Foundation for Innovation. The TRIUMF facility has an experienced team of RF experts who have successfully built RF cavities of this type. The design will be based on the 28-MHz cavities that are currently in use at the RHIC facility at BNL. These cavities are designed to operate at

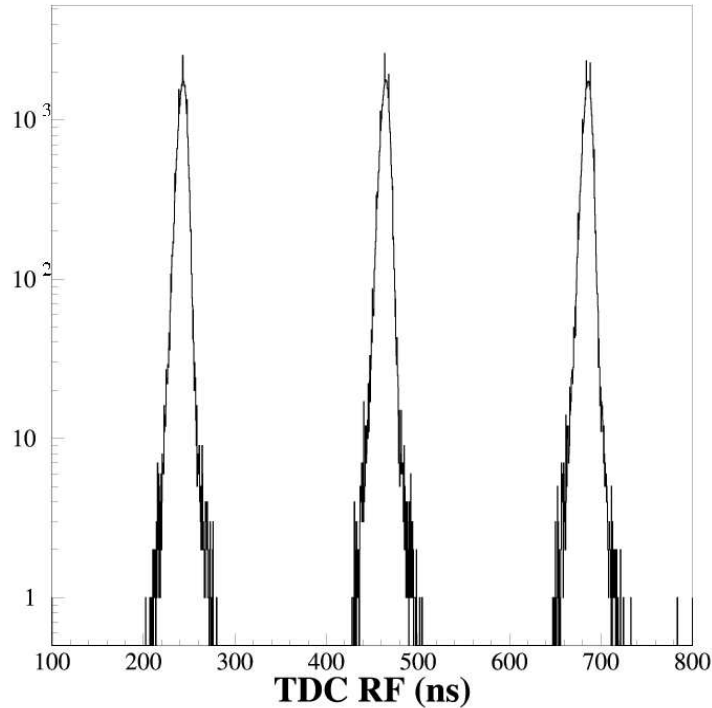


Fig. 4.4. Log plot of the time structure of microbunches extracted from the AGS. The horizontal axis is the event time (in nanoseconds) of the arrival of an antiproton at the detector telescope, relative to an RF pulse. A possible interbunch event can be seen at the far right-hand side of the plot. The 225-ns spacing of the three visible microbunches is characteristic of the 4.5-MHz RF cavity.

voltages up to 300 kV. The installation and commissioning of the 25-MHz cavity is the responsibility of the BNL group. It is anticipated that construction funds will be available by late 2005. With a construction schedule started by October 2005, the cavity should be completed in  $\sim 36$  months, allowing installation in late 2009. Testing and commissioning are anticipated to take place after the end of RHIC running in early summer 2010. Fabrication and installation of the 100-MHz cavity will continue immediately after personnel are made available by the completion of the 25-MHz work. The testing and commissioning of this cavity will be accomplished at BNL as soon as the operating schedule permits.

#### 4.6.2 Injection Systems Kicker Magnets

KOPIO has requested that the AGS deliver a primary proton beam of intensity  $10^{14}$  protons per pulse. This value represents a 30% increase in total beam delivered over the record  $0.73 \times 10^{14}$  protons per pulse that E949 observed. The spill structure for KOPIO is slower, spreading the beam out over 4-5 seconds rather than the 2.2 seconds for E949, making the instantaneous beam intensity quite comparable to earlier running experience. The largest increase in performance is in the transfer of beam from the Booster to the AGS. Currently the kicker magnets responsible for the transfer are operating beyond their capabilities, causing losses in both the Booster and the AGS. Mismatched apertures reduce the efficiency of transfer due to the inability of the kicker magnets to give the beam a large enough kick to get into a stable orbit in the AGS. Upgrading the kicker magnets that are used to kick the beam out of the Booster, and kick the beam back into the AGS, would allow higher beam currents to be maintained with lower beam losses. Because the AGS is to be operated in a mode where it is very nearly limited by radiation losses, improving the beam transfer is a crucial step for increasing the beam intensity.

Many components play a role for increased beam intensity. Some are already listed above. Those that are specific to KOPIO, and are being developed in concert with the TRIUMF group, include the A10 kicker magnets, PFNs, and power supplies in the AGS. TRIUMF is responsible for providing the new high voltage portion including the Transmission Line kicker magnet and vacuum enclosure, HVPS, Thyratrons and switch assembly, optically isolated thyatron grid drive circuits, PFL cables, HV transmission cables, terminating resistors, cooling, vacuum tank, and fast anti-parallel (“clipper”) diodes with grading capacitors. The TRIUMF group is using designs based on the KAON Factory. BNL will be responsible for controls and timing, as well as a new A10 building. BNL will also provide new cable runs to A10 as short as possible to minimize any tail on the field pulse. With the modifications detailed in the AGS TDC, the AGS is expected to be capable of running reliably at the level of  $10^{14}$  protons per pulse as demanded by the KOPIO experiment.

### References

1. C-AD CDR, Phil Pile, and RSVP-AGS-04-001, Kevin Brown.
2. J.W. Glenn *et al.*, Microbunching the AGS slow external beam, *Proc. of the 1997 Particle Accelerator Conf.*, Vancouver B.C. Canada, May 1997, IEEE Press, p. 967.
3. S. Koscielniak, TRIUMF Design Note 01-25 (2001), <http://www.triumf.ca/people/koscielniak/tridn-2001-25.pdf>.



## 5.1 Primary Proton Beam

The AGS slowly extracted beam (SEB) exits F10 and enters a series of four quadrupole magnets, CQ1-CQ4, that are used to match the extracted beam to the transport acceptance. The current transport system, often referred to as the switchyard, was designed to deliver the proton beam to four primary beam lines simultaneously. The best way to meet the needs of KOPIO, MECO, and other future high-intensity experiments is to redesign the transport to provide only one primary beam at a time.

The new beam optics has been designed to provide stable beam to the KOPIO target. The beam is nearly achromatic, and therefore active servos and ramps on various transport magnets are unnecessary. A profile of the 99% beam envelope for the beam transport to KOPIO is shown in Fig. 5.3. The vertical and horizontal





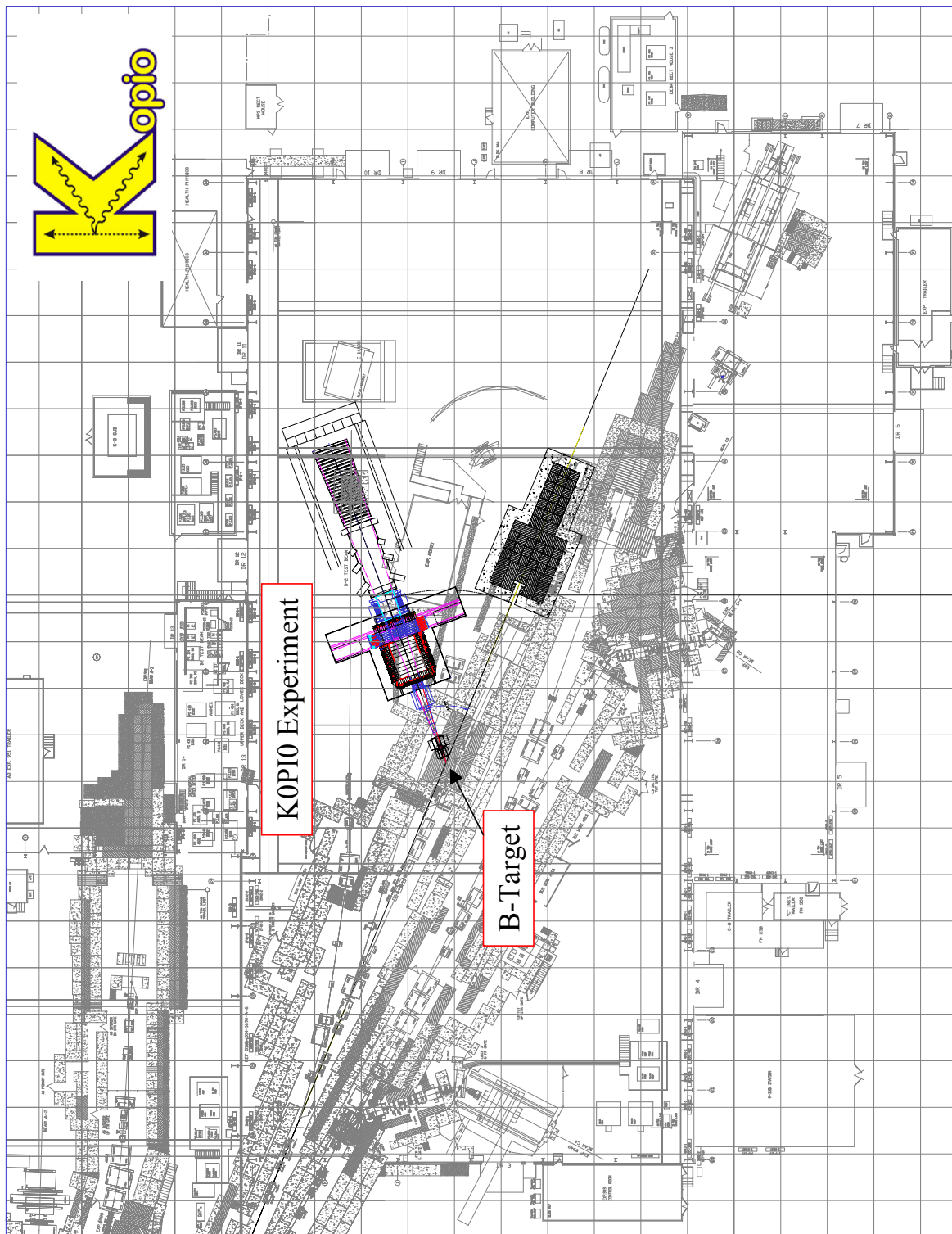


Fig. 5.4. Floor layout of the KOPIO detector.

The neutral beam accepts particles at a production angle of  $42.5^\circ$ . The choice of this production angle is a compromise between particle rates and the energy spectra of the particles. A solid-angle acceptance of  $400 \mu\text{sr}$  produces sufficient beam rate for the experiment. The angular acceptance of the neutral channel has been chosen to be 90 mr horizontally by 4 mr vertically. The small vertical acceptance is important for maintaining the neutron halo to acceptable levels, and the corresponding small vertical neutral beam size in the decay tank is used to help remove backgrounds. A large acceptance in the horizontal direction is helpful to provide acceptance for particles produced over the entire length of the 106-mm-long target.

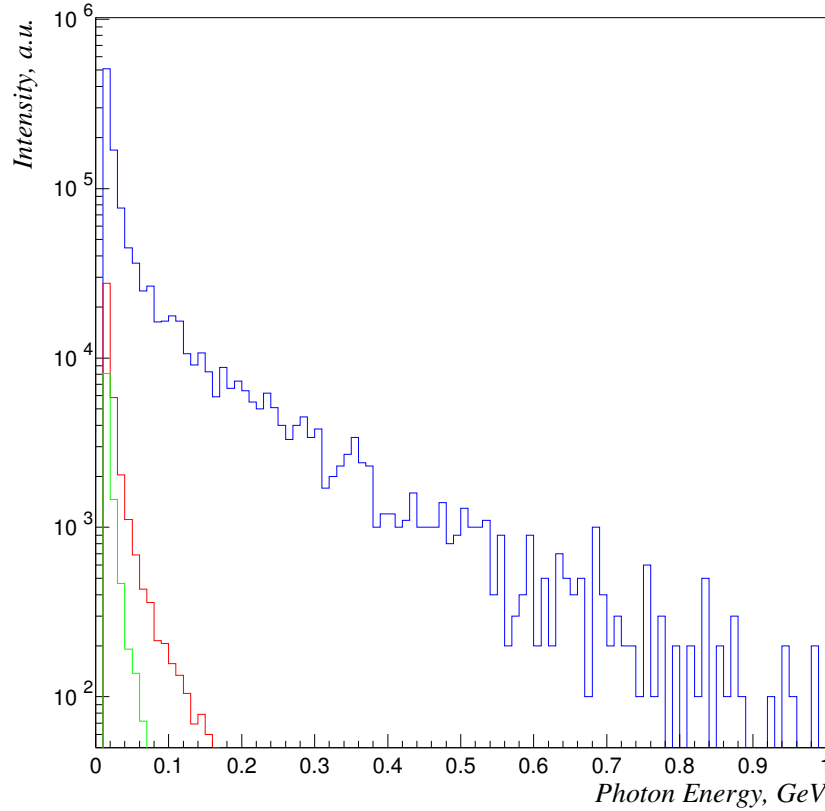


Fig. 5.5. Photon energy distributions accepted in the neutral channel for spoiler thicknesses of 0 cm (blue), 5 cm (red), and 7 cm (green).

### 5.2.1 The Spoiler

The first component of the neutral channel is a lead spoiler. The lead spoiler reduces the photon flux into the neutral channel. Large photon fluxes from the target reduce the effectiveness of the Catcher, as will be discussed in Sec. 6e. Monte Carlo studies have been conducted to examine the photon rate as a function of spoiler thickness. Figure 5.5 displays the energy distribution of the photons accepted into the neutral channel for spoiler thicknesses of 0, 5, and 7 cm. The 5-cm-thick lead spoiler reduces the number of photons by a factor of 30. A 7-cm spoiler can reduce the photon flux by a factor of 100 and the integrated photon energy by a factor of 1,000 when compared to the case with no spoiler present. Sufficient reduction in the photon flux at the Catcher is provided by a spoiler 7-cm thick.

The spoiler affects the acceptance of neutral hadrons into the region of the experiment. Increasing the spoiler thickness decreases both the  $K_L^0$  and neutron flux in the beam. Figure 5.6 displays the  $K_L^0$  momentum distribution at the entrance to the decay tank for several spoiler thicknesses. An increase in spoiler thickness from 5 cm to 7 cm causes a 15% decrease in the  $K_L^0$  flux and a similar decrease for the neutron flux. In



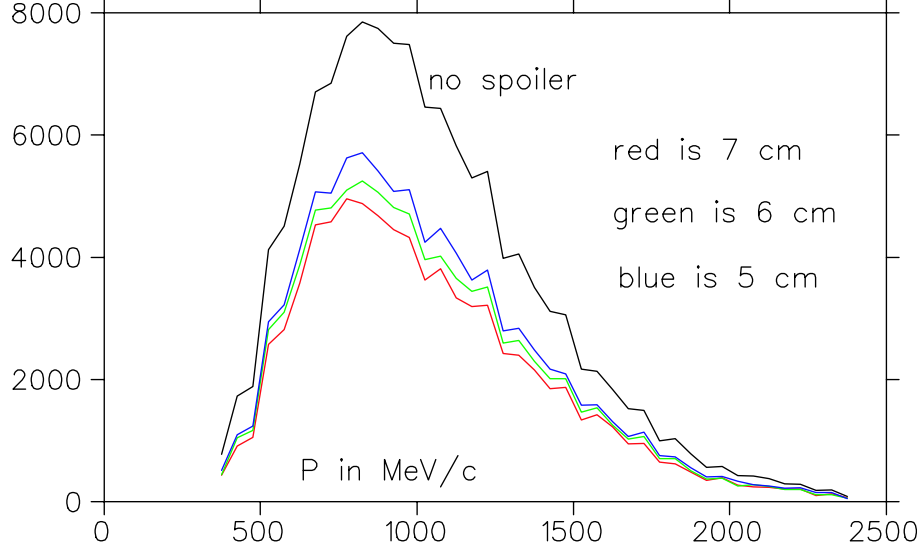


Fig. 5.6.  $K_L^0$  momentum distribution at the entrance to the decay tank.

addition, the neutron halo increases with the spoiler thickness. Increasing the spoiler thickness from 5 cm of lead to 7 cm causes the neutron halo ( $P > 750$  MeV/c and outside the core of the neutral beam) to increase by 50% to  $1.7 \times 10^{-5}$  of the neutron beam. The effects of the spoiler thickness on the  $K_L^0$  flux, neutron halo, and photons in the Catcher were considered in selecting 7 cm as the initial spoiler thickness. The spoiler will be designed such that it can be changed after the initial beam tests, and its thickness optimized based on actual data within the experiment.

### 5.2.2 Sweeping Magnets

The neutral channel has four sweeping magnets. All magnets bend charged particles in the vertical plane to quickly remove them from the acceptance of the experiment. The first two magnets D1 and D2 are immediately downstream of the spoiler and remove all charged particles produced in the target and the spoiler. These magnets have an integral  $B \cdot dl$  of 3.37 T-m. All charged particles will be removed by the aperture early in the collimator system. The D1 magnet has been designed with mineral-insulated coils to withstand the harsh radiation environment. Two magnets were chosen instead of one magnet due to considerations of the close proximity to the target, the need for mineral-insulated coils for D1, and the wide aperture in the horizontal plane.

The third sweeping magnet D3 is placed near the end of the neutral beam collimator system. The magnet has an integral field of nearly 2 T-m. Charged kaons can be created along the collimator system and have the potential to decay within the decay tank. The flux of charged kaons into the decay tank is a few times  $10^{-7}$  of the  $K_L^0$  flux. The D3 magnet sweeps the charged kaons out of the vertical region where the  $K_L^0$  decays occur, providing the experiment with another means to remove this background. Figure 5.7 shows the vertical position of charged kaons at two locations within the decay tank,  $z = 1000$  cm and  $z = 1400$  cm, after they have been vertically displaced by D3.

The final sweeping magnet D4 is located downstream of the decay tank. The Catcher is not efficient for charged hadrons that may be created from decays within the decay tank. The D4 sweeping magnet will pitch charged particles, which are in the neutral beam line, out of the vertical plane and into downstream veto counters. The magnet is designed to use an existing magnet 48D48, which has the gap opened to 300 cm and has booster coils added. The integral field on the axis of the magnet is 0.52 T-m, and this bending power is more than sufficient to bend charged particles from decays into the veto counters.

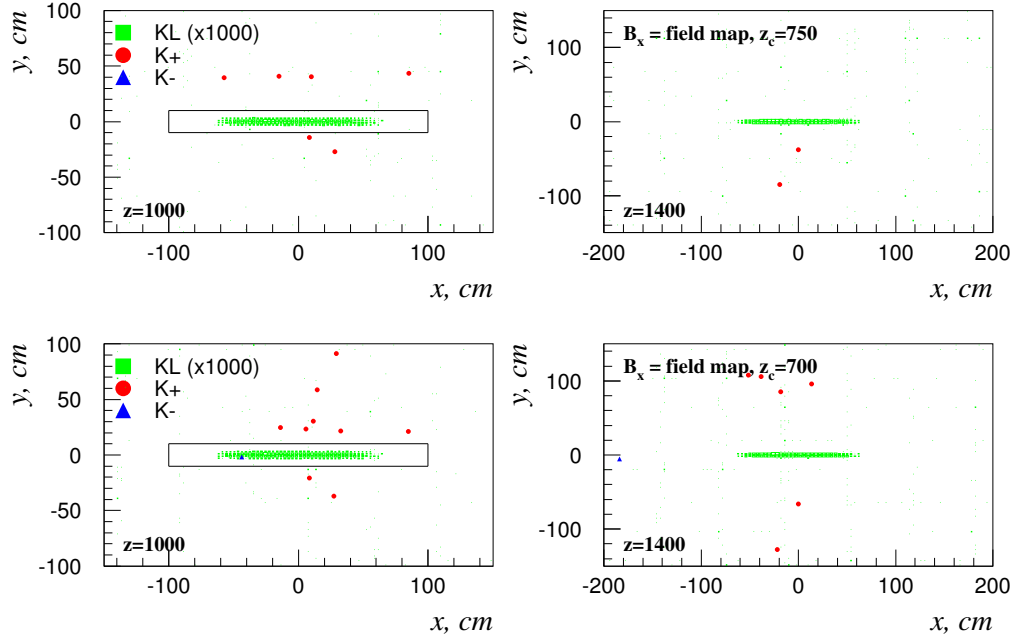


Fig. 5.7. Vertical position of charged kaons at  $z = 1000$  cm (left) and  $z = 1400$  cm (right).

### 5.2.3 Collimators

The collimator system defines the beam acceptance of the experiment and must prevent large transverse tails to the neutral beam. Neutrons with  $P > 750$  MeV/ $c$  can interact in materials and create neutral pions, which could generate a false signal for the experiment. Extensive Monte Carlo studies of the collimator system have been conducted with particular attention given to halo neutrons ( $P > 750$  MeV/ $c$  and outside the core of the beam). The collimator system is a sequence of five collimators. The first two collimators C0 and C1 define the initial acceptance for the neutral beam. The following three collimators, C2-C4, have apertures that increase faster than the initial acceptance established by C0 and C1. Increasing the angle of the collimator faces as one approaches the experimental area prevents these surfaces from being illuminated by interactions occurring near the surface of the upstream collimators. Figure 5.8 (left) illustrates the collimators in elevation view. The lines indicate how the downstream surfaces of vertical collimation are determined. The plan view with lines indicating how the horizontal collimator surfaces are determined is displayed in Figure 5.8 (right). This scheme of increasing the angle of collimation is an important aspect of the collimator design and achieving a small neutron halo.

Other important considerations of the collimator design are the aspect ratio of the collimator aperture and the collimator composition. Figure 5.9 displays the neutron intensity for neutrons with  $P > 750$  MeV/ $c$  as a function of  $y$  for four collimator aspect ratios providing the same acceptance. The curves labeled 1, 2, 3, and 4 represent calculations for vertical acceptances of 5.2, 6.4, 7.6, and 4 mr, respectively. It is clear that the halo is smallest for the smallest vertical acceptance. The sensitivity of the halo to collimator material has also been studied. The collimators will be constructed from a non-magnetic material with hadronic interaction properties similar to iron such as a stainless-steel box filled with lead. The innermost surface will be lined with a few millimeters of heavy metal. The Monte Carlo studies showed that a thin liner of heavy metal is sufficient for most of the collimators without causing an increase in the neutron halo. The C4 collimator will require 1-2 cm of heavy metal to achieve the best possible results. The neutron halo resulting from the collimator system is a few times  $10^{-5}$  of the total neutron beam.

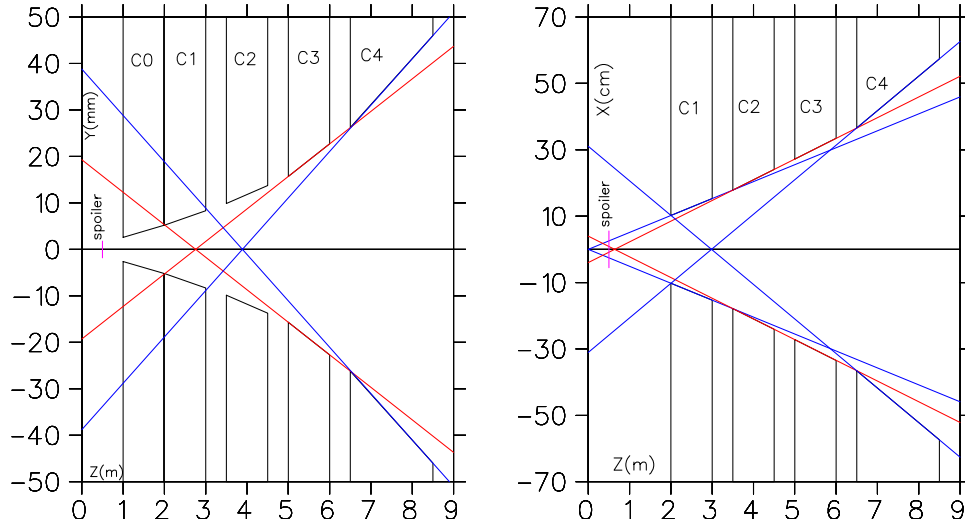


Fig. 5.8. The collimators in elevation view (left) and plan view (right). The lines indicate the determination of the vertical (left) and horizontal (right) downstream collimation surfaces.

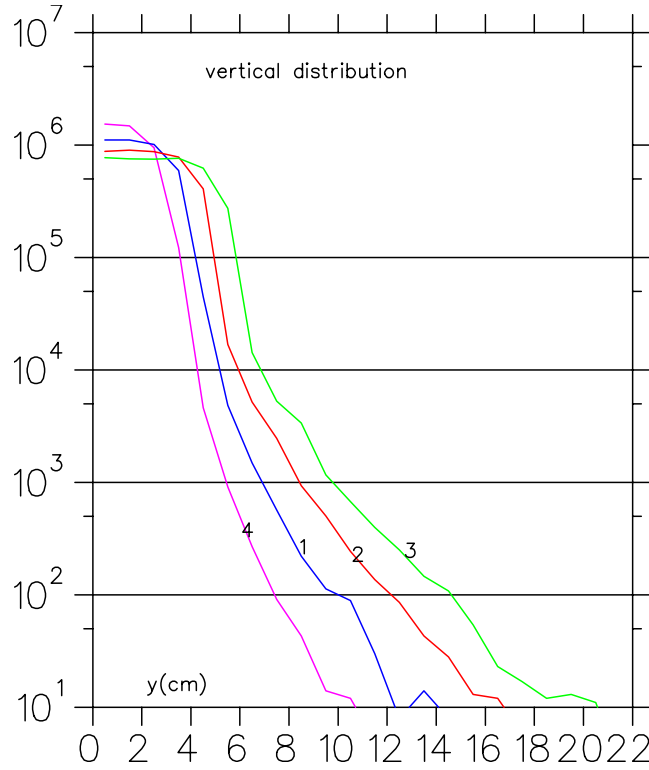


Fig. 5.9. Neutron intensities for four collimator aspect ratios that provide the same acceptance.

The performance of the neutral beam channel depends on a careful integration of all of its components. A conceptual design of the target, spoiler, sweeping magnets, and collimators has been made. Detailed simulations have shown that the neutral beam produced will meet the requirements of the experiment. It is expected additional refinements will occur as the final design is achieved.



## 6a Preradiator

Measurements of the energies and directions of photons from  $\pi^0$  decay by the KOPIO Preradiator (PR) and Calorimeter, along with momentum tagging of the parent  $K_L$  by time-of-flight (TOF), provide positive identification of the signal and powerful kinematic constraints for suppressing backgrounds. Among the most effective constraints are the invariant mass  $m_{\gamma\gamma}$  of the two photons and the  $\pi^0$  center-of-mass energy  $E_{\pi^0}^*$ . The reconstructed  $\pi^0$  decay vertex from photon tracking defines the flight path for the  $K_L$  TOF measurement, and also helps to reject accidentals and particles produced outside the fiducial decay volume (e.g. near the surface of a detector) by the beam halo. The PR also serves as part of the hermetic photon veto system by detecting extra photons.

### 6a.1 Performance Requirements

The requirements of the PR include a photon angular resolution of approximately 25 mrad at 250 MeV, a photon conversion efficiency of about 80%, a precision in shower position at the initial pair conversion point of 0.5 cm, and a resolution in the deposited energy better than  $2.7\%/\sqrt{E \text{ (GeV)}}$ . The latter requirement arises because a substantial fraction of the photon energy is typically deposited in the PR. The PR total thickness along the beam direction needs to be as short as possible to limit the transverse shower size in order to better resolve any additional photons from background decay modes that may be present. For the measurement of the  $K_L$  velocity, the time resolution of the PR is required to be approximately  $(100 \text{ ps})/\sqrt{E \text{ (GeV)}}$  (comparable to the beam-bunch width). The physical segmentation of the prompt trigger signals from the PR must be fine enough to allow the first-level trigger to estimate the number of converted photons. Finally, the photon detection inefficiency of the combination of the PR and surrounding Shashlyk modules is required to be less than  $10^{-4}$ . One implication is that the active areas of the detectors must approach as closely as possible to the vacuum vessel, with a minimum of additional dead material in the detector frames. Another is that multiple photons interacting in the PR be resolvable so that the total number of photons in an event may be known with high reliability.

### 6a.2 Design Concept

The PR consists of a close-packed multi-layer sandwich of 8-mm-thick plastic scintillator sheets for energy and time measurements, alternating with single-plane, thin-gap, dual-coordinate drift chambers with cathode strips. Even in such low- $Z$  material, more than 90% of the primary interactions of a 200-MeV photon are via  $e^+e^-$  pair production, with the rest via Compton scattering. The angular separation of a symmetric  $e^+e^-$  pair is of order  $m_e/E_\gamma \simeq 5 \text{ mrad}$  at  $E_\gamma = 100 \text{ MeV}$ . Hence they need not be resolved in order to obtain adequate angular resolution for the photon. One coordinate of the  $e^+e^-$  tracks is given by the chamber drift time and the other by the centroid of the charge distribution induced on the cathode strips by the avalanche near a wire. Both the drift cells and cathode strips running perpendicular to the wires are on the same pitch  $p = 5.2578 \text{ mm}$  (which is also half of the optical fiber pitch of the scintillator readout), while the anode-cathode gap in the chambers is 2.54 mm. Measurements in both coordinates have a resolution of better than  $250 \mu\text{m}$  for tracks with normal incidence. The thickness of each scintillator-chamber layer is chosen to be about  $4\% X_0$  in 16.4 mm, which is close to the minimum value that is compatible with practical self-supporting detector designs for these large areas, while using the minimum amount of material at the two inner edges. Since the angular resolution is dominated by Multiple Coulomb Scattering (MCS), only the first few layers after a photon conversion to an  $e^+e^-$  pair contribute effectively to the measurement of the photon direction.

In order to achieve the required efficiency for  $\pi^0$  detection, the total radiation length of the PR is  $2.7 X_0$ , yielding a single-photon conversion efficiency of about 85% (while requiring a conversion before the last 3 layers), and providing a  $\pi^0$  detection efficiency more than 70%. The total thickness of 1.375 m is thin enough for acceptable transverse shower spreading.

Because the separation of an  $e^+e^-$  pair created in the PR is generally not large enough to generate resolvable pulses, the anode wires can provide tracking information for only the particle track nearest to the

wire in each cell. The expected photon angular resolution based on Monte Carlo (MC) calculations with only anode information is predicted to be 30–40 mrad, and does not depend on the photon angle of incidence. On the other hand, both tracks contribute to the distribution of induced charges on the strips, so that the charge centroid represents the average position along the wires of the  $e^+e^-$  pair. This measurement is capable of providing an angular resolution of 15–35 mrad[1] for normal incidence. However, the resolution from the cathode strips degrades at larger angles of incidence due to the stochastic distribution of ionization clusters along the track in the gas. To complement the functionality of anodes and cathode strips, the wire direction in the drift chambers is alternated between vertical and horizontal in successive layers in a module. This arrangement results in the best overall performance that is minimally dependent on the angle of incidence of the photons. It also helps to resolve the left-right ambiguity inherent in the information from drift times, by using the cathode-strip information from adjacent layers.

GEANT simulations indicate that a typical shower deposits of order 70% of its total energy in the PR, and the remainder in the Calorimeter. The energy deposited in the PR is measured with sufficient precision (discussed below) to allow the full energy measurement combining the PR and the Calorimeter to be better than  $2.7\%/\sqrt{E}$ . With the large fraction of active material (scintillator) in the PR, good light collection becomes the main determinant for good resolution in measurements of both energy and time. Readout of the scintillators from both ends of Wavelength Shifting (WLS) fibers embedded in a linear grid of straight holes running through the scintillator sheets results in the required photon yield for the specified resolution. The relative timing from the two ends provides position information in the direction along the fibers. The information from the PR scintillator is used for triggering, timing measurements, and photon vetoing. Alternate planes have fibers running horizontally or vertically, providing two-dimensional position information. Eighteen WLS fibers spaced on a 10.6-mm pitch ( $2p$ ) are combined into each readout channel. Hit clustering in the resulting spatial segmentation provides information to the trigger system about the number of converted photons in each event.

In order to detect photons emitted toward the region of the downstream end of the Barrel Veto photon detector and the outer edges of the PR, an "External Photon Veto" (EPV) system surrounds the outer edges of the PR detector to fill the gap between the Barrel Veto system and the Calorimeter. The EPV consists of the same type of Shashlyk modules as the Calorimeter.

### 6a.3 Performance Simulations and Measurements

Figure 6a.1 shows the photon angular resolution as determined by a GEANT simulation of  $e^+/e^-$  track generation in the PR, followed by photon reconstruction that includes smearing according to anticipated resolutions of both  $e^+e^-$  pair positions from the cathode strip measurements and the nearest-track positions from drift times. A spatial resolution of  $150\ \mu\text{m}$  position resolution was assumed for both measurements, degraded by non-normal incidence in the case of the cathode strips by  $500\ \mu\text{m/radian}$  added in quadrature. The angular resolutions obtained are dominated by MCS and vary from  $\sigma = 17\ \text{mrad}$  at  $E_\gamma = 350\ \text{MeV}$  to  $33\ \text{mrad}$  at  $E_\gamma = 150\ \text{MeV}$ . Increasing the position resolutions up to  $350\ \mu\text{m}$  (for normal incidence) changed the angular resolutions by only about 10%. For use in subsequent MC studies, the angular resolutions are generally characterized by two Gaussians. The values for  $\sigma$  quoted here refer to the narrow Gaussian component which accounts typically for 75% of the total number of events. The wider Gaussians obtained from the fits are typically  $2\sigma$  in width.

The concept of obtaining photon angles from tracking  $e^+e^-$  pairs in a radiator sandwich similar to the KOPIO design was confirmed in test beam measurements with 100–300-MeV tagged photon beams at the BNL National Synchrotron Light Source. The chambers had a cathode geometry similar to the KOPIO design, but the wires of all planes were oriented in the same direction and the drift cells had a larger 8-mm diameter and were hexagonal in shape. The distributions for normal incidence are shown in Fig. 6a.2. The angular resolutions agree with those from MC calculations: *e.g.* in the case of cathode strips,  $\sigma = 31\ \text{mrad}$  at 150 MeV (upper left), and 25 mrad at 250 MeV (upper right).

The above simulations and measurements of the performance of this design show that it will satisfy the performance requirements.

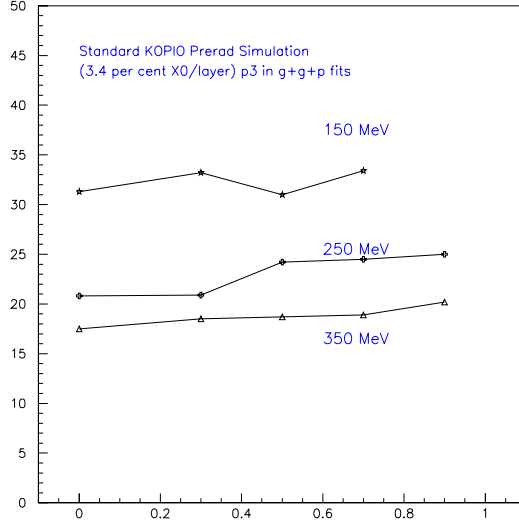


Fig. 6a.1. Simulated photon angular resolution from smeared GEANT tracks at incident photon energies of 350, 250 and 150 MeV. The vertical axis is the estimated resolution in photon angle projected on one plane in milliradians, and the horizontal axis is the photon angle of incidence in radians.

#### 6a.4 The PR Detectors

As shown in Fig. 6a.3, the PR system is divided into four quadrants surrounding the kaon beam line, each with an active area of  $1.5\text{ m} \times 1.5\text{ m}$ . Each quadrant consists of a sequence of eight identical modules, each of which in turn consists of nine scintillator planes alternating with eight drift chamber planes. The modules are mechanically independent and can be moved out individually for service access. Each module fits between the structural webs of the vacuum vessel in order to approach as close as possible to the kaon beam, to maximize both the signal acceptance and background veto capability. In order to provide photon veto coverage for the chamber frames, which is especially needed adjacent to the vacuum vessel, the scintillator sheets are slightly larger than the chambers.

##### 6a.4.1 Drift Chamber

The design of the thin-gap cathode-strip drift chambers is illustrated in Fig. 6a.4. They have an active area of  $1.5\text{ m} \times 1.5\text{ m}$ . The cell geometry of the drift chamber is very similar to that of the standard multi-wire proportional chamber except for the large ratio of wire pitch to gap between cathode planes, which exceeds unity. Each chamber has 288  $25\text{-}\mu\text{m}$ -diameter, gold-plated tungsten wires at positive high voltage, without field wires between the anode wires. The wire pitch is  $p = 5.2578\text{ mm}$ . Wires are held by crimp-pins in 1-mm-diameter holes that are precisely located within an accuracy of  $\pm 50\text{ }\mu\text{m}$ . Two parallel cathode planes, each consisting of a  $34\text{-}\mu\text{m}$ -thick ( $30\text{ mg/cm}^2$ ) copper foil laminated onto a 1.4-mm-thick epoxy/fiber-glass sheet, are located at  $\pm 2.54\text{ mm}$  from the anode wire plane. The molded, one-piece 5.08 mm thick epoxy/fiber-glass frame of the chamber is laminated to one of the two cathode planes, which thereby becomes designated the “base”. The base sheet has an additional copper layer on the outside face for mechanical stiffness and electromagnetic shielding. Wire-support combs are also carried by the “base”, positioned about every 50 cm of wire length. The other cathode plane is designated as a removeable “lid”, fastened by small screws that compress an O-ring in the frame. The single copper foil on the inside of the lid is cut into cathode strips on the same pitch  $p$  as the wires, oriented orthogonally to the wires.

A common drift chamber gas that is convenient from the point of view of safety is Argon/ethane (50/50) with 0.3% ethanol. The similarity of its density with that of air is an advantage in that it minimizes deflection

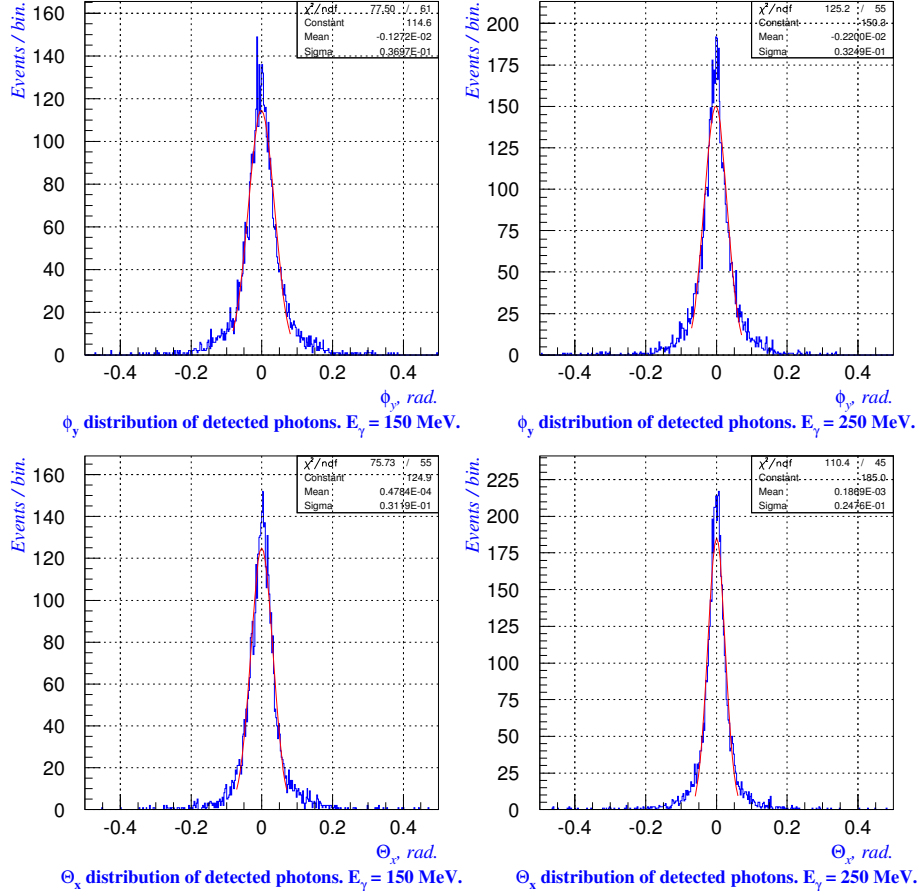


Fig. 6a.2. Angular resolution measurements with tagged photon beams at normal incidence to a radiator stack with all wire planes parallel to each other. The plots at the top row are for angles projected in one coordinate plane by using only anode information, and those on the bottom in the orthogonal coordinate by using only cathode information. The plots in the first column are for  $E_\gamma = 150$  MeV, and the second for  $E_\gamma = 250$  MeV.

of the chamber walls due to the difference in gravitational pressure gradients. The drift cell performance with this gas as simulated by the GARFIELD computer code is shown in Fig. 6a.5, where each isochrone represents 2 ns of drift time. The maximum drift time from the corner of the cell is predicted to be about 70 ns. The drift velocity for this gas is 5 cm/ $\mu$ s at a typical field in this cell. Hence its performance is adequate, although other gases are also being considered.

Five small eight-cell prototype chambers were constructed with various wire diameters (but no cathode strips) to test the performance of the drift cell. They were tested with an Ar/ethane (50/50) mixture, an Ar/isobutane (75/25) mixture, and a CF<sub>4</sub>/isobutane (80/20) mixture. A cell with a 25- $\mu$ m-diameter wire has a plateau of  $\geq 300$  V around 1600 V for the Ar/ethane mixture with a gas gain of  $10^4$ , and each 5- $\mu$ m increase in wire diameter corresponds to about a 100-V increase in high voltage. A larger wire diameter would reduce the significant signal attenuation along the 1.5-m wire length, but the resulting higher operating voltage increases the cost and size of the many high voltage decoupling components on the anode adapter cards that mate with the chamber. For the Ar/ethane mixture, the maximum drift time was found to be 80 ns, corresponding to the drift time from the corner of the cell. The cross talk between the adjacent wires was found to be around 2% of the original signal.

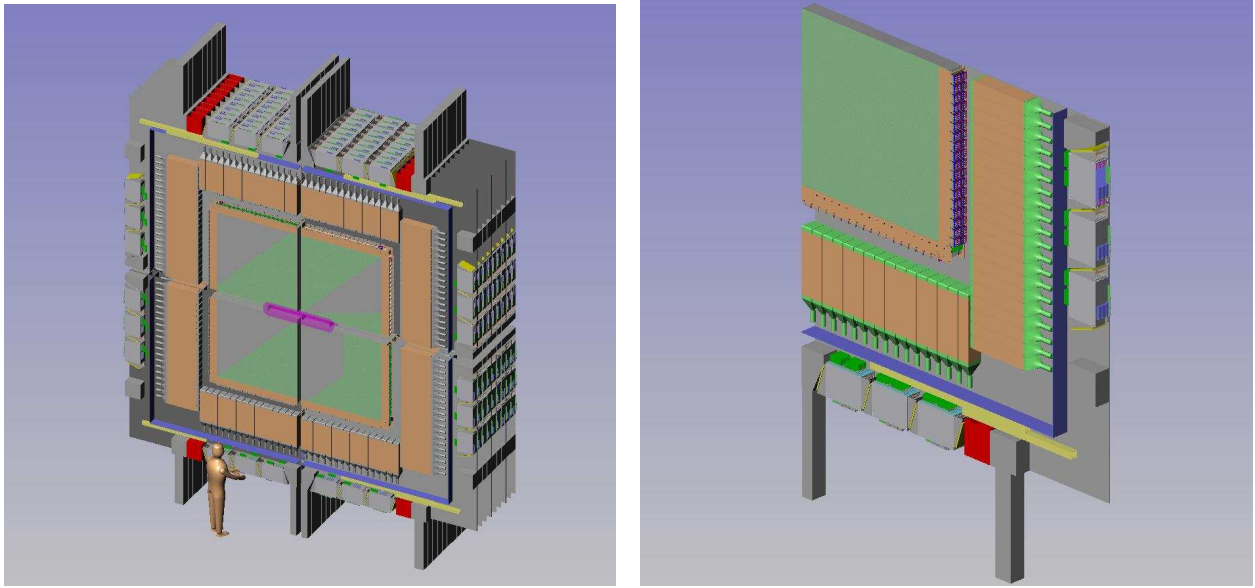


Fig. 6a.3. Left panel: The KOPIO Preradiator consisting of four quadrants surrounding the wide kaon beam line. The support legs (hangers) are shown below (above) the assembly. Right panel: One of the eight mechanically independent PR Modules that make up each quadrant. (One of the large L-shaped support plates is removed for visibility.) The large flat area is the scintillator/drift-chamber sandwich. It is surrounded by the Shashlyk modules of the EPV system, which are in turn surrounded by the six electronic crates for the chamber readout.

Two 30-cm $\times$ 30-cm prototype chambers with cathode strips were constructed. For testing, they were surrounded by existing drift chambers, four on either side, as shown in Fig. 6a.6 (upper). The spatial resolution from drift time was found to be about 200  $\mu$ m (limited by the alignment precision). The resolution from the cathode strips was studied as a function of the angle of incidence. As shown in Fig. 6a.6 (lower), the dependence agrees with expectations and the maximum value satisfies the design requirement. Two long narrow chambers were also constructed to study signal reflections and distortion, one with 2-m-long anode wires and one with 2-m-long cathode strips. These prototypes also allowed testing of front-end amplifiers with realistic input loads. One of these chambers is shown in Fig. 6a.7.

#### 6a.4.2 Scintillators

The sheets of 8-mm-thick scintillator cover a 1.674-m $\times$ 1.657-m area, extending slightly beyond the frames of the chamber to veto events with photons in that otherwise inactive region. Each plane is read out by 158 Bicron BCF-92MC (or KURARAY Y-11) WLS fibers with 1-mm diameter, spaced on a 10.6-mm pitch ( $2p$ ) on a linear grid. The fibers always run along the 1.657-m dimension of the sheet, which is smaller to allow space at the end for bending and bundling of the fibers. They are installed loosely in 1.4-mm-diameter holes in the center plane of the sheet. This choice of “dry” holes greatly facilitates assembly of the detector, as the scintillator sheets can be painted before the fibers are installed. The resulting loss of about 1/3 of the light collection efficiency due to the lack of intimate optical coupling with the scintillator is acceptable. The paint is diffusely reflective with high reflectance in the near UV/visible range, such as Avian-D from Avian Technologies.

The WLS fibers are coupled to the same type of PMT assembly as is described in Sec. 6c. The PMT has a bialkali photocathode that is enhanced in the green for best performance with these fibers. To reduce the number of readout channels and the influence of phototube noise in the photon energy measurements,

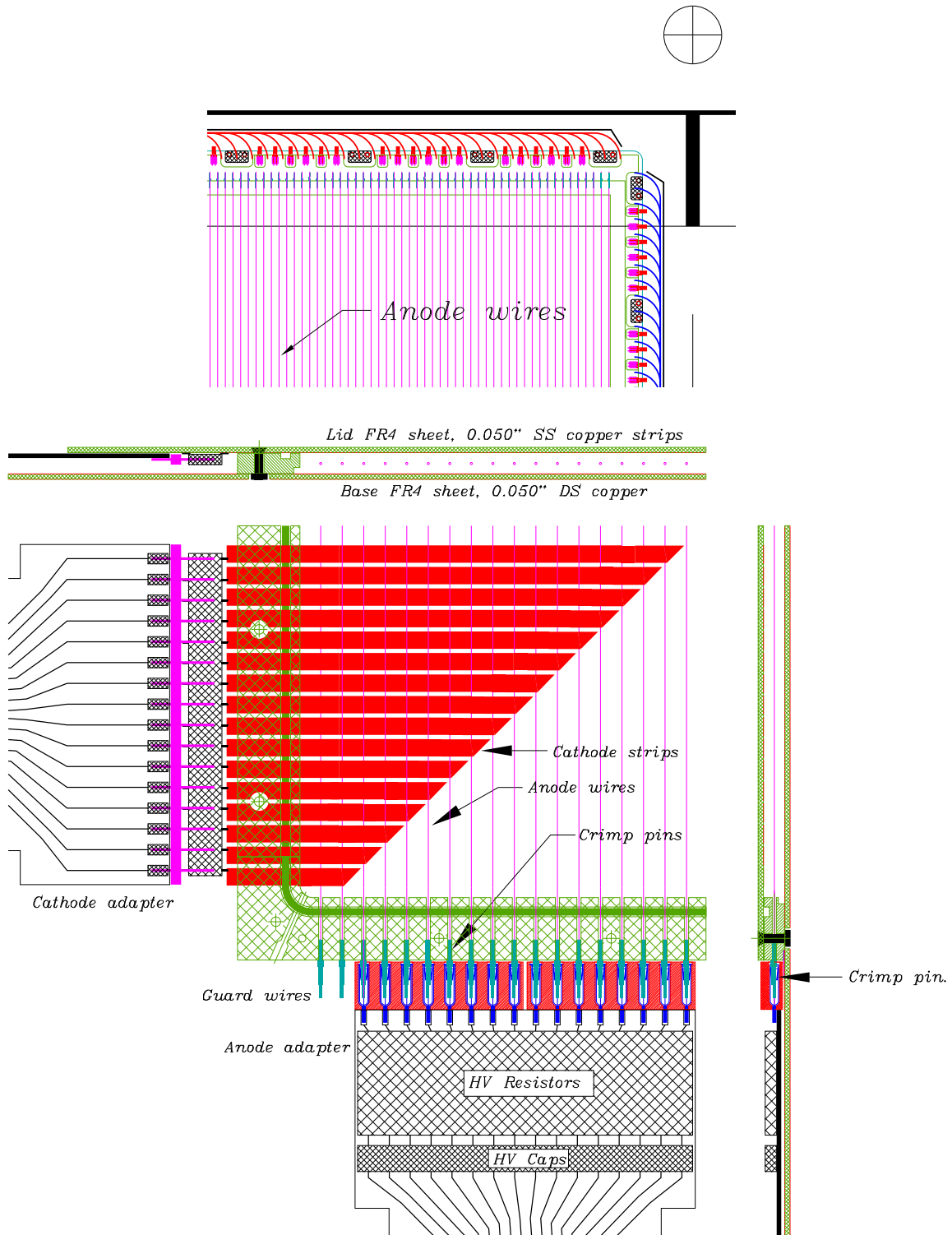


Fig. 6a.4. Details of the design of the PR cathode-strip drift chambers. The upper (lower) panel shows the inner corner proximal to (outer corner distal from) the beam axis. The inner corner includes the WLS fibers from the scintillator layer just behind the chamber, between which are the numerous ground contacts for interconnecting the ground planes of all the chambers in a module.



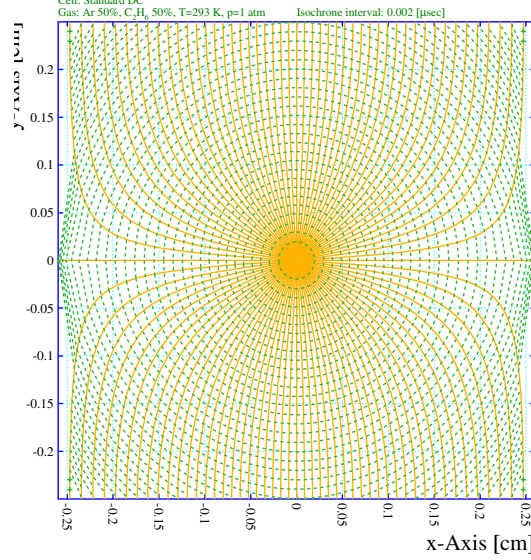


Fig. 6a.5. Drift cell isochrones separated by 2 ns of drift time in an Ar/ethane (50/50) gas mixture.

each phototube receives  $18 \times 5$  (4) fibers from five  $Y$  (four  $X$ ) planes at the same  $Y$  ( $X$ ) position in a module. This grouping results in  $9 \times 2$  (for two ends) readout channels for each  $X$  or  $Y$  edge, for a total of 1152 for the whole PR. In order to obtain the required energy resolution, the PMT gains must be calibrated and monitored to a precision better than 1%. The calibration can be achieved using background events that produce particles depositing known energies in the scintillators. An example is charged pions from  $Kcp2$  or  $Kcp3$  that stop in the PR and produce 4 MeV muons. The PMT gains will be continuously monitored by injecting light pulses into each PMT via an additional optical fiber included in its fiber cluster. The light pulser driving these monitor fibers will be stabilized by measurement of the pulser output by a separate monitor PMT that also views a scintillator counting particles of known energy from a radioactive source.

The scintillator sheets are assembled by gluing together 27 63.1-mm-wide (12p) planks, each formed by an extrusion process with six holes in the mid-plane. (Much of the initial width of the two outer planks is removed in the final machining step after gluing is complete.) The extruded scintillator is a formulation developed for the MINOS neutrino detector, and is composed of polystyrene with 1% PPO and 0.03% POPOP wavelength shifters. The extrusion shape required for KOPIO has been developed in collaboration with the CELCO company in Vancouver[2]. Scintillator planks that are 8-mm thick and 7-cm wide with six 1.4-mm-diameter extruded holes have been produced in lengths of typically 2 m with surfaces on both sides flat enough to obviate skimming on a mill. An example is shown in Fig. 6a.8. The edges of each scintillator plank are machined into a tongue-and-groove configuration for glueing together into sheets using a precise fixture. The depth and width of the mating surfaces are about 1/3 of the thickness of the scintillator.

The relative light yields and other characteristics of the scintillator material were measured in comparison to BC-408. The tests employed KURARAY Y-11 WLS fibers with 1-mm diameter, read out by PMTs with standard bi-alkali photocathodes. (These photocathodes have 25% lower quantum efficiency for the WLSF light than the green-enhanced ones that are intended for the PR scintillator readout.) Extruded scintillators were cut into 3-cm-long pieces (along the hole direction), polished and wrapped on all sides with aluminized mylar. Effects that might complicate the comparison, such as the presence of other holes and hole qualities (*e.g.* drilled in several diameters *vs.* extruded), were first confirmed to be within  $\pm 5\%$ . The uniformity of the light yield across a plank containing six fibers was tested to be within 1.4% (RMS). The ratio of the number of photoelectrons to that of BC-408 was found to be 0.60 for one 1-mm WLS fiber through a single plank, and 0.80 for a single fiber through a smaller  $1\text{-cm} \times 1\text{-cm}$  sample. The difference might be understood as a result of a shorter bulk attenuation length in the extruded polystyrene. However,

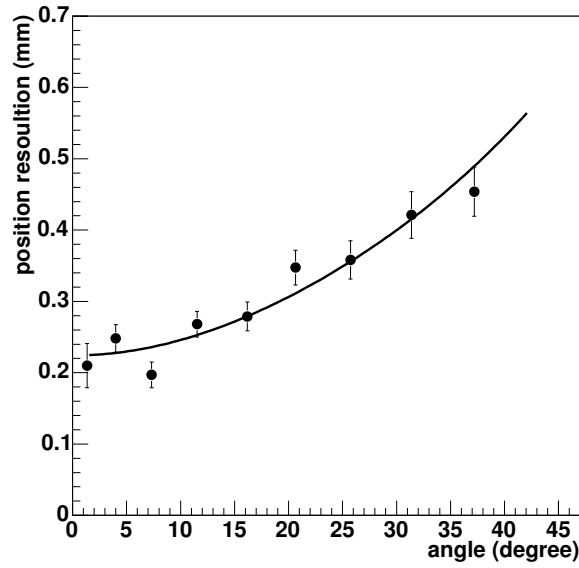
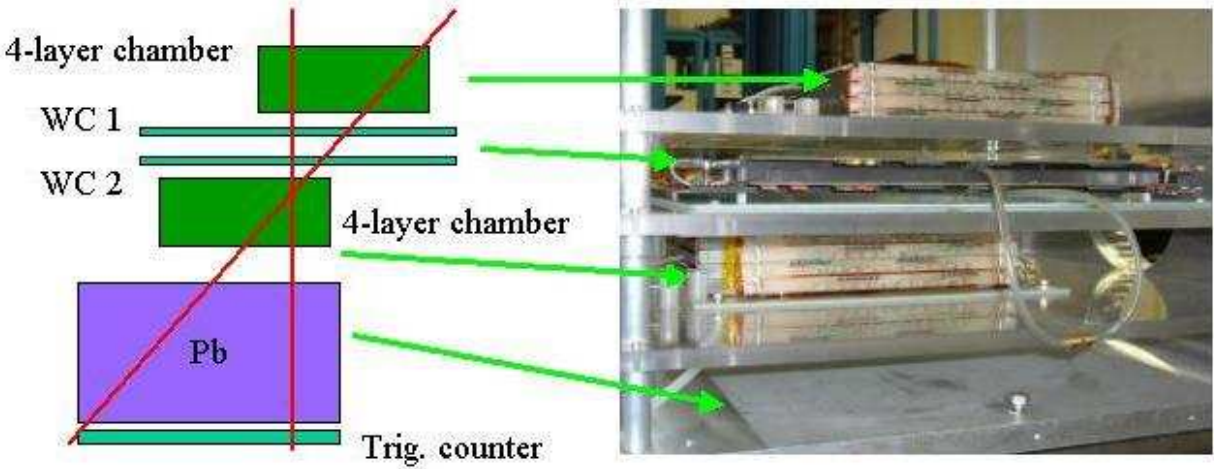


Fig. 6a.6. The upper panel shows the arrangement of drift chambers surrounding a cathode-strip drift chamber that was used to obtain the results shown in the lower panel, which is the tracking residual of a single cathode-strip plane as a function of incident angle, using cosmic-ray muon tracks defined by four anode planes on either side. The function fitted to the angular dependence of the widths of the Gaussian shapes describing the residual distributions is  $\sigma^2 = \sigma_0^2 + (\sigma_\theta \tan \theta)^2$ , where  $\sigma_0 = 220 \pm 10 \mu\text{m}$  and  $\sigma_\theta = 573 \pm 4 \mu\text{m}$ .

some of the additional photons that would be collected by having a longer attenuation length arrive too late in time to contribute to the time resolution. Based on studies with 3 planks glued together with all holes filled with fibers, the number of photoelectrons from each end of a fiber is estimated to be 7 p.e. per MeV deposited in the scintillator. With a green-enhanced photocathode, this becomes 9 p.e./MeV. After accounting for the sampling fraction of 0.5, this value implies that the purely statistical contribution to the energy resolution is about  $1.1\%/\sqrt{E \text{ (GeV)}}$ . (Other contributions may be expected to dominate.) Similarly, based on time resolution measurements with muons, the purely statistical contribution to the time resolution would be  $(90 \text{ ps})/\sqrt{E \text{ (GeV)}}$ .



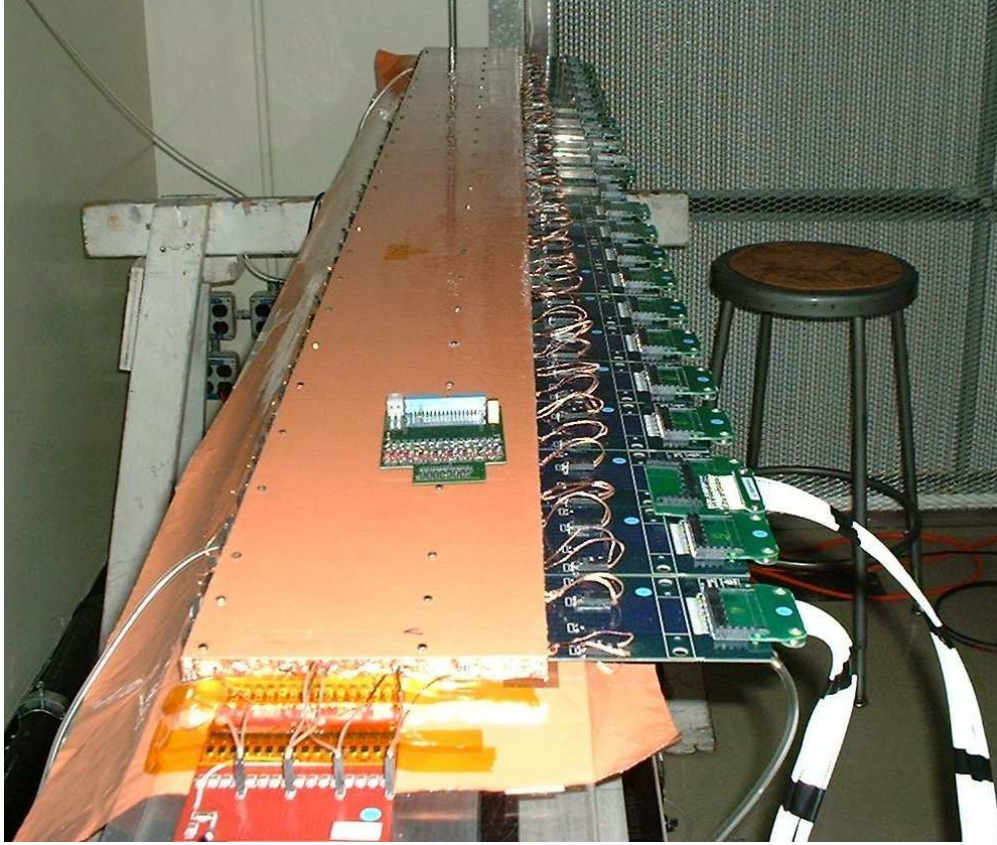


Fig. 6a.7. A prototype drift chamber with 2-m-long cathode strips.

#### 6a.4.3 External Photon Veto

The External Photon Veto system surrounds the edges of the PR and fills much of the gap between the Barrel Veto system and the Calorimeter. (A gap runs the full length of the EPV array of each module to carry cables from the chambers to the readout crates.) The EPV consists of the same type of Shashlyk modules as the Calorimeter. There are 1152 units of 11-cm $\times$ 11-cm $\times$ 75-cm long Shashlyk lead/scintillator sandwiches read out through WLS fibers. For construction details and performance, see Sec. 6b. The WLS fibers from these modules are coupled to the same type of PMT assemblies as are used for the Photon Veto system. For details, see Sec. 6c.

Even though the scintillator/chamber stack does not cover the small areas to the left and right of the kaon beam line, there are additional EPV modules covering this area. They are attached alternately to upper or lower modules so that they are vertically staggered.

#### 6a.4.4 Module Construction

The mechanical design of the PR is complicated by the large coefficient of thermal expansion of the polystyrene scintillator ( $7.8 \times 10^{-5} \Delta L/L/^\circ\text{C}$ ). In contrast, the support plates are of aluminum ( $2.7 \times 10^{-5} \Delta L/L/^\circ\text{C}$ ), and the wire chamber components are epoxy/fiber-glass ( $\sim 1 \times 10^{-5} \Delta L/L/^\circ\text{C}$ ). To avoid damage during shipment when the temperature range might be as large as  $\pm 20^\circ\text{C}$ , the mechanical assembly must allow for a relative length change of  $\pm 2$  mm over the 1.6-m length of the scintillators and wire-chambers. The tolerance is provided by clamping the scintillator sheets together independently from the chambers by using spacers along all four edges. The resulting polystyrene lattice provides the mechanical rigidity of each quadrant. In the spaces surrounded by the edge spacers, the chambers are lightly captured between

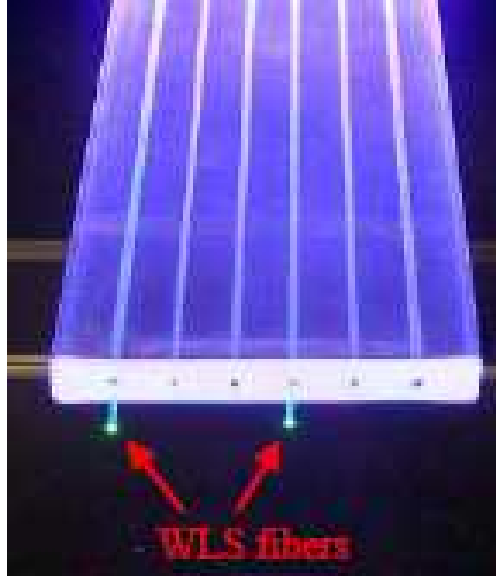


Fig. 6a.8. An example of a polystyrene scintillator plank that was extruded with six 1.4 mm diameter holes for WLS fibers.

the scintillator planes, and are locked to the scintillator lattice at only the central outer corner, remaining free elsewhere to slide via precise bolt slots parallel to each of the two outer edges. However, the structure is sensitive to internal thermal gradients that may arise from variations in the ambient air temperature in combination with the thermal time constant of the assembly, which is of order 10 hours for the surface layers. Such gradients can cause mechanical distortions that would change as the temperature varies, moving the wire chambers and smearing their tracking resolution. Hence it is necessary to provide an air temperature in the experimental hall that is stable to better than  $1^{\circ}\text{C}$ .

The conceptual design of an assembled module mounted on its support frame and combined with EPV modules and readout electronics crates is shown in Fig. 6a.9. The stack of 17 detectors in each module is 14.6 cm thick, including covers and fasteners. The cover on each face of each module for EM shielding is a 0.3 mm-thick sheet of epoxy/fiber-glass clad with copper on both sides. The modules are mounted on a pitch of 17.46 cm, which includes the thickness of the vacuum vessel fin with some clearance. The stack is supported at its two outer edges between two large L-shaped 6.35-mm-thick aluminum plates. The rigid structure created by this pair of interbridged plates also supports the Shashlyk modules of the EPV and the electronic readout crates for the PR chambers. There is a series of access holes in one of the plates to allow replacement of photomultiplier tubes. In total, each module is 16.83 cm thick including the two L-plates. When fully equipped with electronics boards (0.25 tons), each PR module weighs approximately 1.8 metric tons. With 32 modules, the total weight of the KOPIO PR is about 58 tons.

The light seal is made at the module level, as it is impractical to seal each individual scintillator sheet with its many fibers. The seal is made with a bag that closely fits the detector sandwich and is taped to the L-plates. On the two readout edges, a wall runs between the EPV modules (including their phototubes) and the PR readout crates (see Fig. 6a.15). The cables from the chambers and phototubes are potted in opaque silicone elastomer as they pass through holes in this wall. The L-plate acting as a lid will seal to this wall via a gasket.

#### 6a.4.5 Module Support and Installation

The conceptual design for the installation of the PR modules in the KOPIO Experiment is shown in Figs. 6a.10–6a.12. In order to minimize the vertical gap between the active areas of the modules and the horizontal gap between the modules and the vacuum vessel, there are no support structures in these gaps,

## Preradiator Module (+Vac.Vessel)

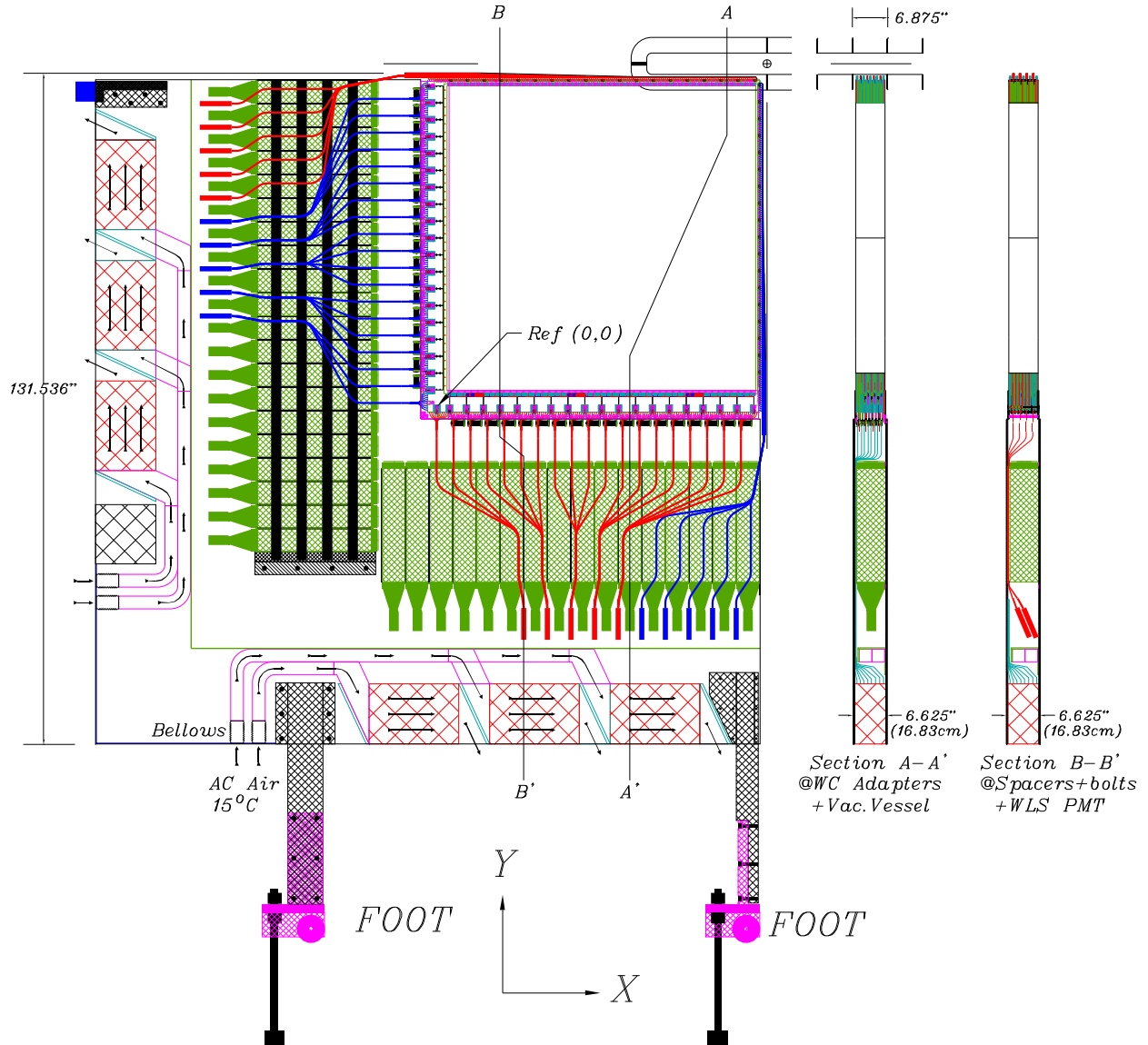


Fig. 6a.9. Conceptual design of a lower-quadrant PR module mounted on its support system. The scintillator/detector stack fits between the reinforcing webs of the vacuum vessel shown at the top right. The array of EPV Shashlyk modules surround the detector stack, and WLS fiber bundles pass over the Shashlyk modules from the stack to PMTs behind those modules. Cooling air-flow paths are shown through the six chamber readout crates mounted along the outer two edges of the support frame.

only chamber frames and space for bending WLS fibers. (Nevertheless, the vertical gap between the active areas of the wire chambers in left and right quadrants is 13.1 cm wide, and the corresponding gap between scintillators is 3.35 cm.) Each module in an upper quadrant of the PR hangs from two aluminum arms that extend down from trolleys on an overhead beam. All modules in a quadrant may be rolled collectively sideways on their trolleys away from the beam pipe. For access to a single one of these modules, it is raised slightly to clear the bridge stabilizing the others and rolled out of the 8-module stack. If it is to be replaced by a spare, it can then be lowered down onto a transport/support cradle. Installation would be the reverse procedure. The modules of the lower two quadrants run on rails in the bottom of a pit in the floor of the experimental hall, shown in Fig. 6a.13. The upper outer corner of the L-plate structure of each lower module is captured by a trolley rolling on a beam at the height of the kaon beam plane. The lower quadrants can also be rolled out collectively as units. For minor service, such as replacing phototubes, a single module can be lowered slightly and rolled sideways to allow access to the holes in an L-plate. (Readout cards in the electronic crates can be replaced *in situ*.)

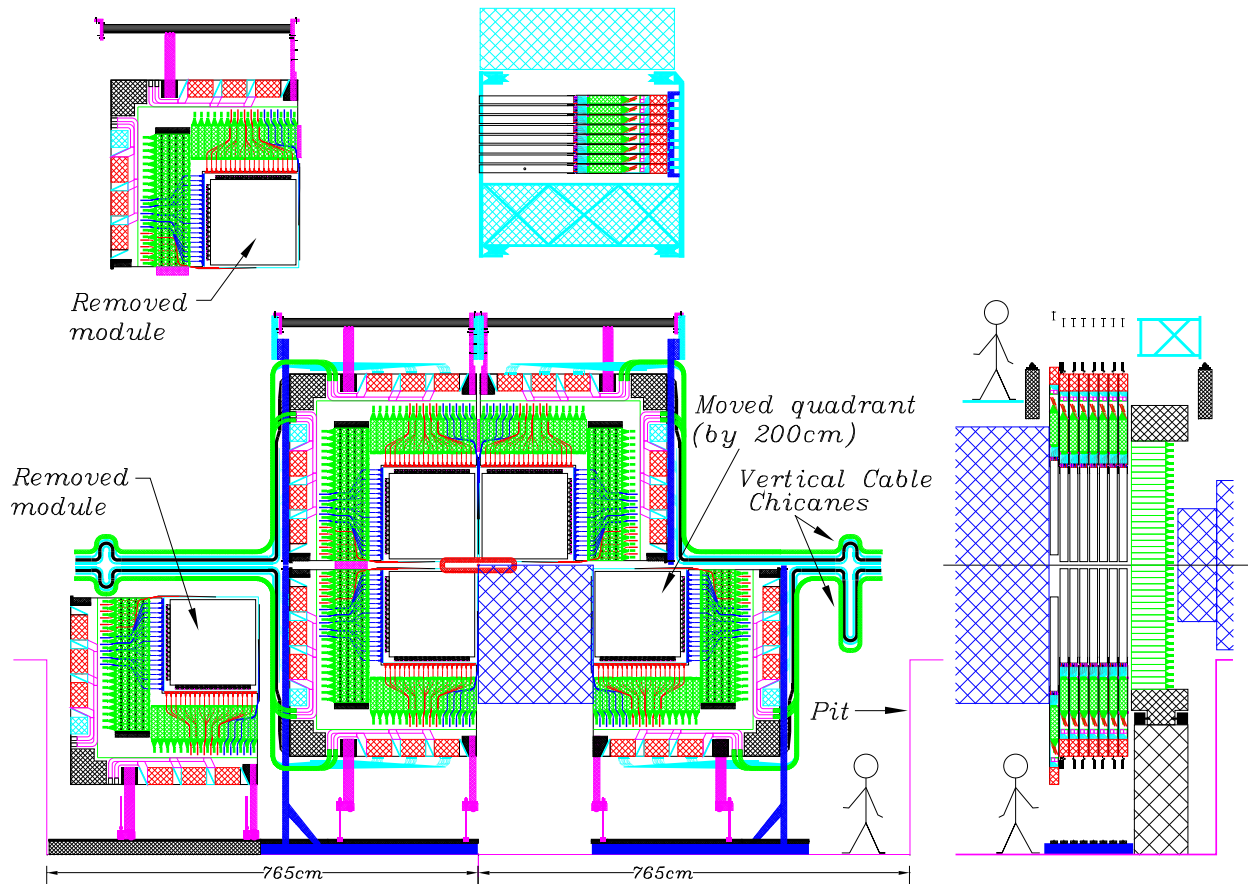


Fig. 6a.10. Elevation view of the conceptual design for the installation of the PR modules in the KOPIO Experiment. Removal or installation of the entire lower-right 8-module quadrant as a unit is shown, while the lower left shows the same operation for a single module, which must be slightly lowered for this movement to clear cables, etc.



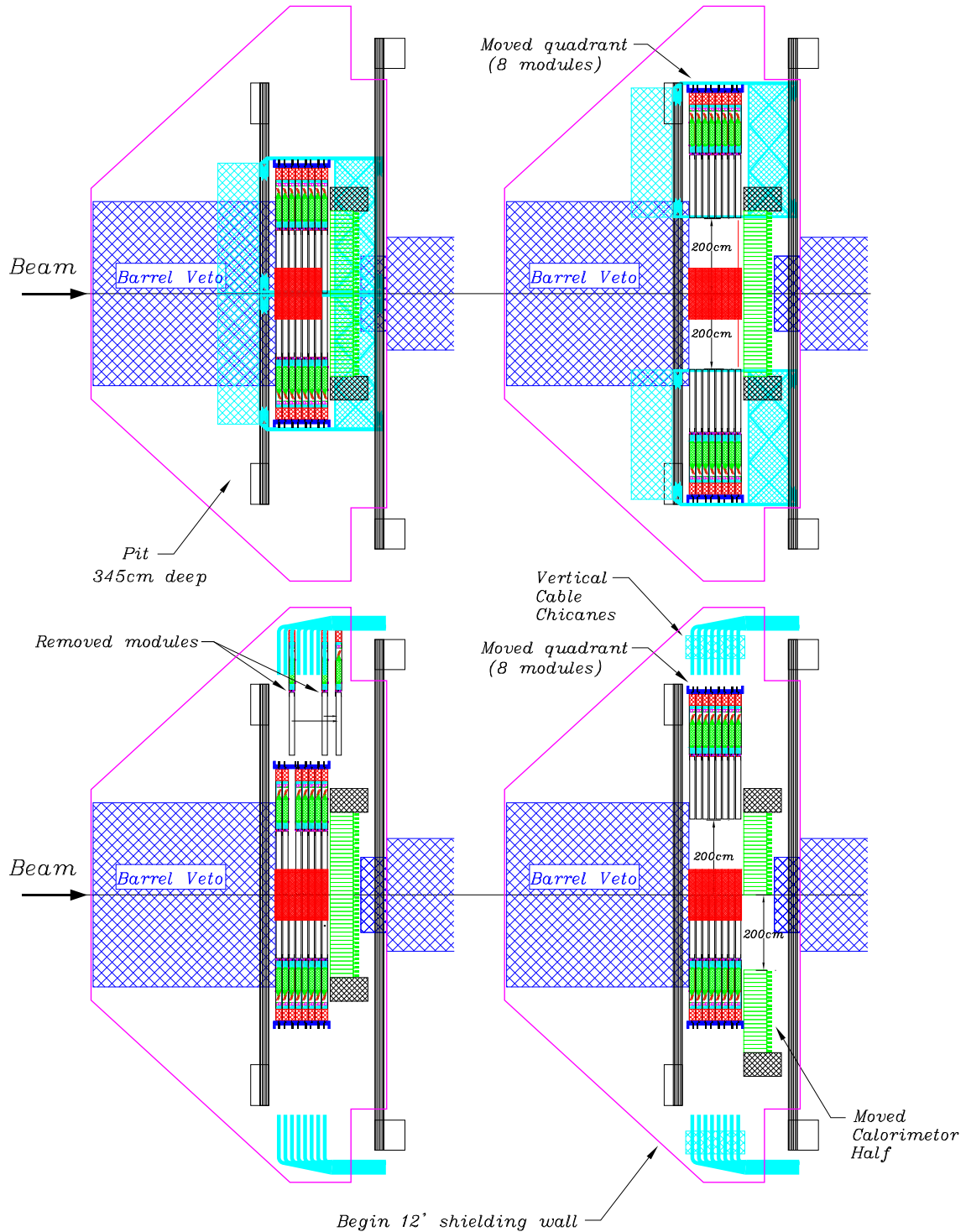


Fig. 6a.11. Plan views of the conceptual design for the installation of the PR modules in the KOPIO Experiment. The upper (lower) panels show sectional views through the upper (lower) quadrants, while removal of a single module (quadrant) is shown on the left (right). The support frame from which the upper quadrants hang is itself supported on the four pillars shown in rectangular outline most visibly in the lower panel, two outside of the downstream end of the Barrel Veto, and two downstream of the Calorimeter location.

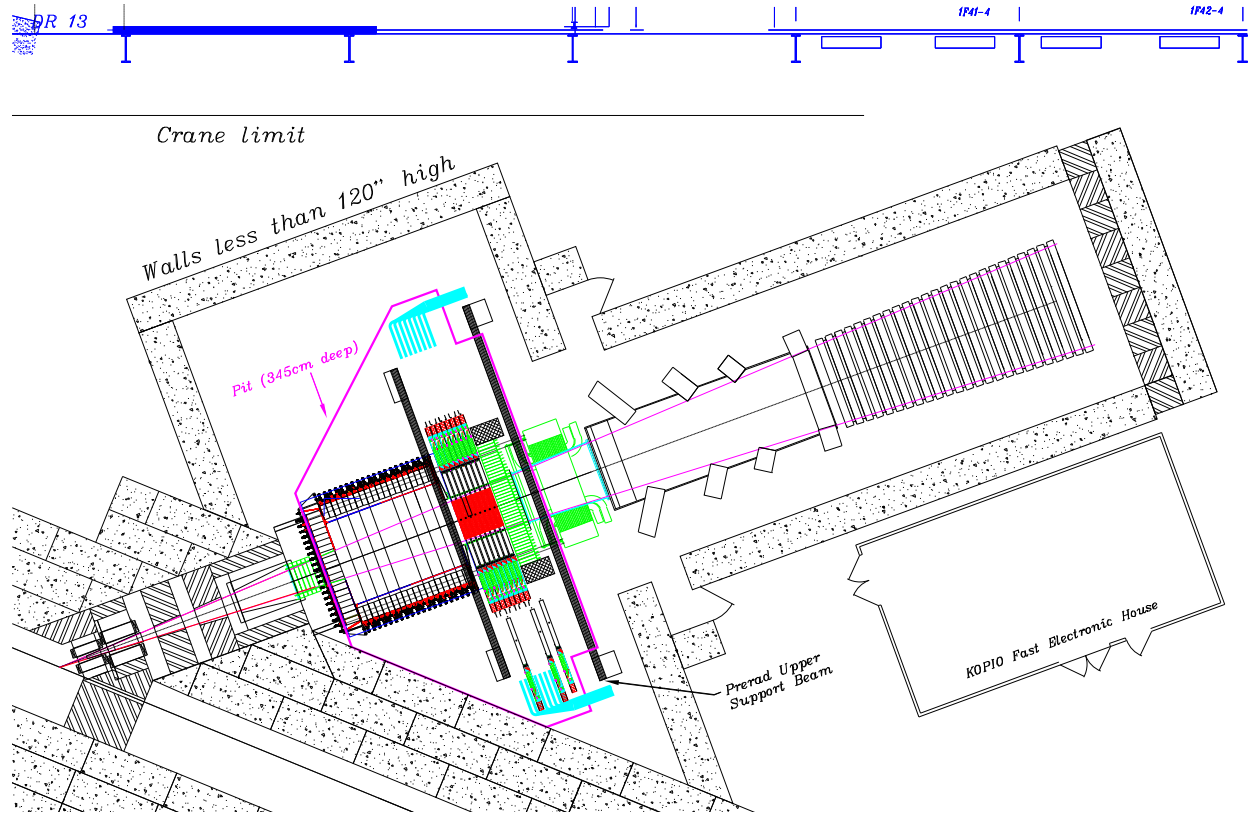


Fig. 6a.12. Plan view of the conceptual design of the PR installation in the context of the rest of the KOPIO subsystems in the experimental hall.

## 6a.5 Electronics

Features influencing the design of the PR chamber electronics include the following. The readout system must sense and digitize signals from the anode wires to yield drift times with a resolution of 3–4 ns. Charge signals (typically 5 fC) from cathode strips must be measured with a resolving time of about 100 ns in order to associate corresponding anode and cathode hits. Wire rates up to 40 kHz are expected for horizontal wires near the beam. The trigger (requiring two isolated photons in the PR and no activity in the charged particle detectors or photon veto detectors) will be based on scintillator signals and occurs at rates of 100 kHz or higher. The trigger latency is anticipated to be 10  $\mu$ s, during which all digitizer outputs (e.g. anode time stamps and ADC data from cathode strips) are pipelined. The crucial role played by the hermetic photon veto system requires that there be minimal dead material in front of the EPV modules. Also, the limited cooling access inside the light seal combined with the problem of thermal expansion of the polystyrene disallows the dissipation of a significant amount of power in preamplifiers mounted on the chambers. These restrictions impose constraints on the location of the chamber readout system. Therefore the chamber signals are transported 1.2 m to a location behind the EPV elements which surround the PR. Thus, reactive loading of the signals, already complicated by the 1.5-m-long wires and strips, becomes an important constraint on the front end electronics. Fortunately, front end ASICs suitable for KOPIO were developed recently for similar applications in large scale experiments at the LHC (CMS and ATLAS) and provide economical solutions.

There are approximately 75,000 readout channels for the anode wires and the same for the cathode strips. A schematic overview of the chamber readout system is presented in Fig. 6a.14. Mounted on each outer edge of the L-frame of each module are three 28-cm-deep 9U euro-crates, each accommodating four 96-channel anode boards, four 96-channel cathode boards, and one plane collector board. One such crate

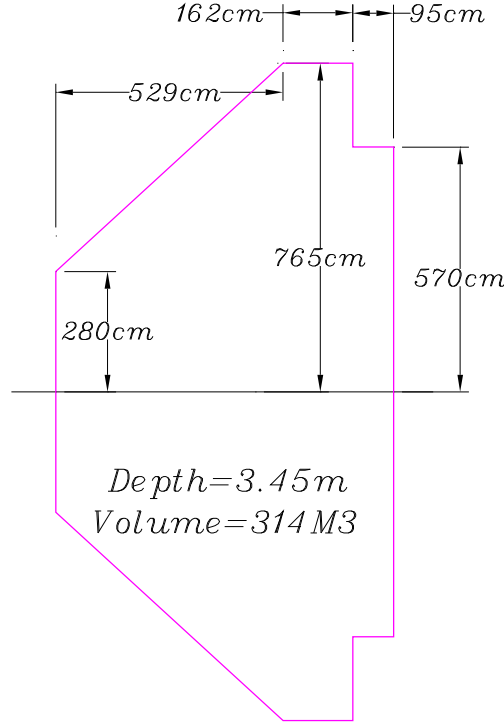


Fig. 6a.13. The pit needed in the floor of the experimental hall for installation and servicing of the lower PR quadrants.

is illustrated in Fig. 6a.15. These crates contain the first-stage readout for the chambers of a module. The anode and cathode signals are extracted from the edge of the chamber stack and brought to the crates through 1.2-m cables. Following pre-amplification and digitization, the data are collected, digitally processed and compacted on the same cards, and sent onwards to a plane collector board in the same crate. In turn, all six of the plane collectors on a module feed their data to a module collector board housed near the corner of the module, which retransmits the data to the DAQ system via an optical link. The Level-1 trigger information is received by the module card and distributed to the anode and cathode cards. The crates are fed by power supplies located in racks on the floor.

#### 6a.5.1 Anode Electronics

Chamber high voltage is fed through an anode cable card that mates with the chamber and has 16 100-k $\Omega$  registers for HV distribution to anode wires and 16 1000-pF decoupling capacitors. The 1.2-m-long connection between the front-end card and the preamplifier/readout system is made by 1-mm-diameter low-noise coaxial cable from GARG. The anode preamplifier is required to provide moderately fast timing ( $\sim 2$ -ns time resolution) with the input capacitance of about 80 pF (20 from the wire and 60 from the cable). The front end ASIC for the anode wires is an 8-channel Amplifier/Shaper/Discriminator called the ASD01A. It was developed by Yale and Boston University for the drift tubes of the ATLAS muon system[3]. Its input shaper has a peaking time of 15 ns, and its input RMS noise is 6000 electrons when loaded by 370  $\Omega$ . (It is not planned to terminate the 1.5-m-long wires in the PR chambers, so the load in this case is capacitive.)

A schematic diagram of the anode card is shown in Fig. 6a.16. Time digitization is accomplished with the Atlas Muon TDC (AMT-3) ASIC developed by KEK[3,4], also for the ATLAS muon drift tubes. This ASIC (now in its fourth revision) digitizes 24 individual LVDS inputs from the ASD01A discriminators, with an overall power consumption of 15 mW per channel. The anode readout card houses four AMT-3 chips for a total of 96 channels. The time measurement is based on interpolation by a phase-locked-loop

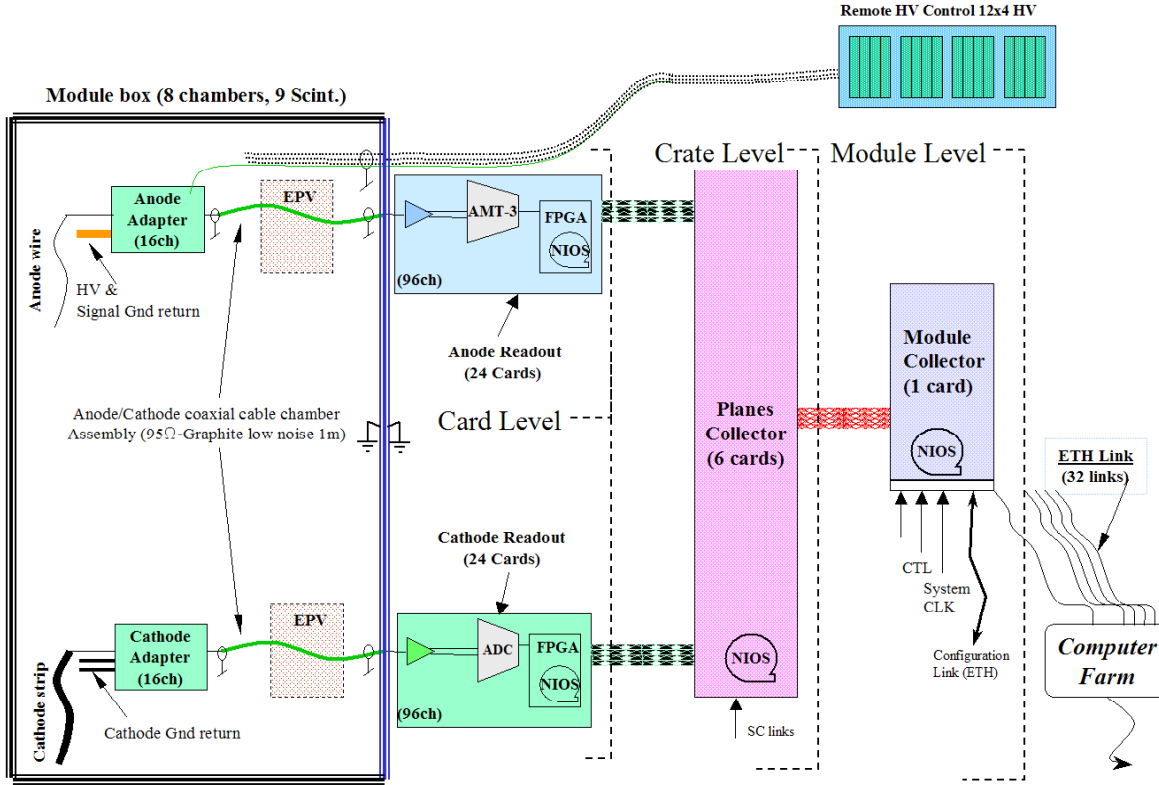


Fig. 6a.14. Wire chamber readout scheme.

time-memory cell with respect to a reference clock running at a fixed frequency between 10 and 70 MHz. The subdivision is a 32nd part of the reference clock making a resolution of 0.625 ns possible with a 50-MHz clock. There are two stages of buffering in the chip, the first stage for trigger latency and the second for queuing trigger-selected time stamps for output. The trigger latency can be as long as 51  $\mu$ s. The maximum rate that can be handled per channel is 0.5 MHz, which is larger than the expected wire rate of 40 KHz near the beam. All functions of the chip can be controlled externally through a JTAG port.

An Altera Cyclone Field Programmable Gate Array (FPGA) on the anode readout card accepts the data from all four TDC chips on serial LVDS links. It reformats and transmits the data to the collector card on another serial LVDS link.

A 96-channel prototype anode readout card has been made, partly populated with components, and tested successfully. It is shown in Fig. 6a.17a).

### 6a.5.2 Cathode Electronics

The same type of 1.2-m-long cables connect the cathode strips on the chamber to the 96-channel cathode cards. The cathode strip readout electronics is designed to collect the information necessary to reconstruct the charge centroid, in the possible presence of other charge clusters that are nearby in either space or time. Although centroid measurements require only relative measurements of the charges on adjacent strips in a hit cluster, timing jitter and pulse-shape variations can potentially affect the results. In order to accurately



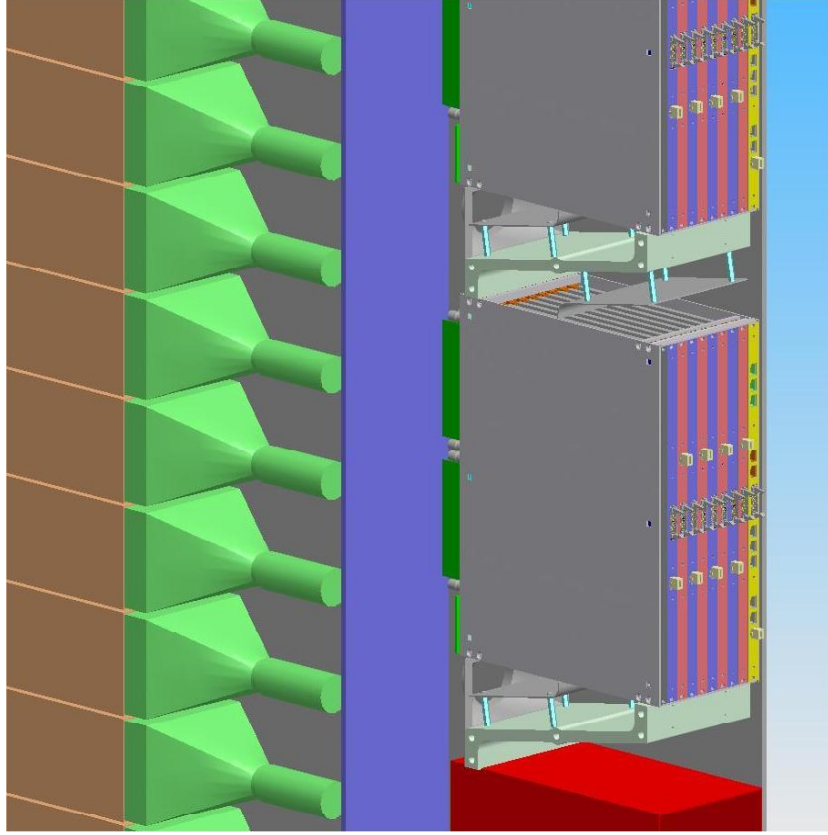


Fig. 6a.15. A readout crate for the PR chambers, containing four 96-channel TDC cards for the anode wires, four 96-channel ADC cards for the cathode strips, and one collector card.

measure the average position of the  $e^+e^-$  pair, whose signals may arrive at the electronics at different times due to the drift time, both contributions of induced charges on each strip need to be added without any bias. Continuously sampling the signals with “pipeline ADCs” allows optimal signal post-processing as well as the use of a low cost digital pipeline following the ADC to accommodate the trigger latency.

A schematic diagram of the cathode card is shown in Fig. 6a.18. The preamplifier/shaper is the 16-channel Buckeye ASIC designed for the cathode strip chambers in the CMS muon system[5]. It has a 100-ns shaping time to optimize the signal-to-noise ratio with the 200-pF input capacitance of a strip plus cable. Its other characteristics include an equivalent noise (RMS) of  $5000 e^- + 25e^-/\text{pF}$ , a 5-pole semi-Gaussian shaped wave form with tail cancellation, and a gain of 750 mV/pC.

The ADC will be an 8-channel 12-bit commercial pipeline ADC similar to the TI ADS5270, with a sampling rate of about 25 Msps. The ADC data streams are fed to dedicated programmable logic devices (PLDs) implemented as four FPGAs on the cathode card. They collect and process the sampled data in real time. The results of the algorithms combined with the time stamp and geographical information are then transferred to a local data collector residing in a separate PLD implemented as another FPGA on the same board, which will combine the multiple streams and forward the result to the plane collector card. These PLDs together with one on the Plane Collector Card process the ADC data in real time. Data less than the threshold will normally be suppressed in the FPGA, which is also used to correlate adjacent hits in space and time. Any strip that exceeds the threshold will cause the sample data for both itself and the adjacent strips to be forwarded, regardless of their charge. All sample data within the trigger time window that is from strips connected to channels near the “edges” of the cards will be forwarded for later consideration. There

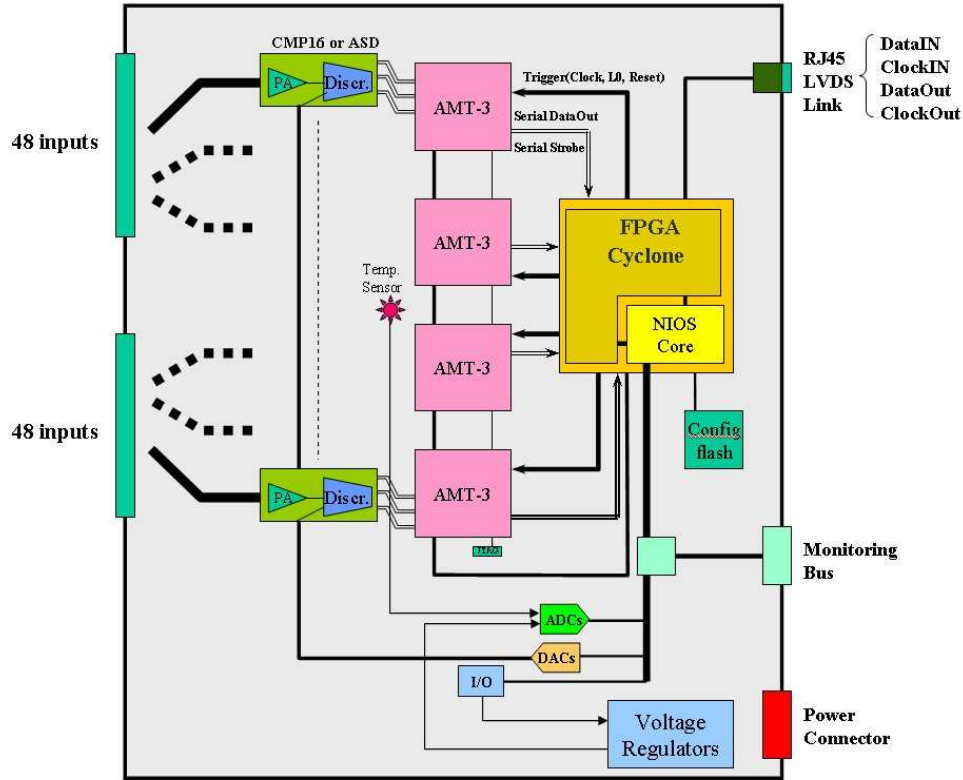


Fig. 6a.16. Functional diagram of the anode readout card.

is communication between the downstream neighboring FPGAs to form clusters involving these "edge" strips. The processing load is appropriately distributed among the PLDs. The main elements of the cathode processing are:

- Self-triggering (zero suppression);
- Input buffering;
- Charge measurement within the trigger time window;
- Evaluation of charge arrival time;
- Cluster charge reconstruction; and
- Data compaction

Of course the raw ADC data within the trigger time window can be transmitted instead of, or in addition to, the results of the above real-time cluster analysis, if the rates are low enough. This will be the operating mode at least during the early running.

A 48-channel half-size prototype cathode board with 20–65Msp/s ADCs and FPGAs has been built and successfully tested. It is shown in Fig. 6a.17b).

### 6a.5.3 Scintillator Electronics

There are 1152 phototubes for the PR scintillators and another 1152 for the EPV. The analog outputs from these phototubes are connected to the outside through patch panels at the perimeter of a module.

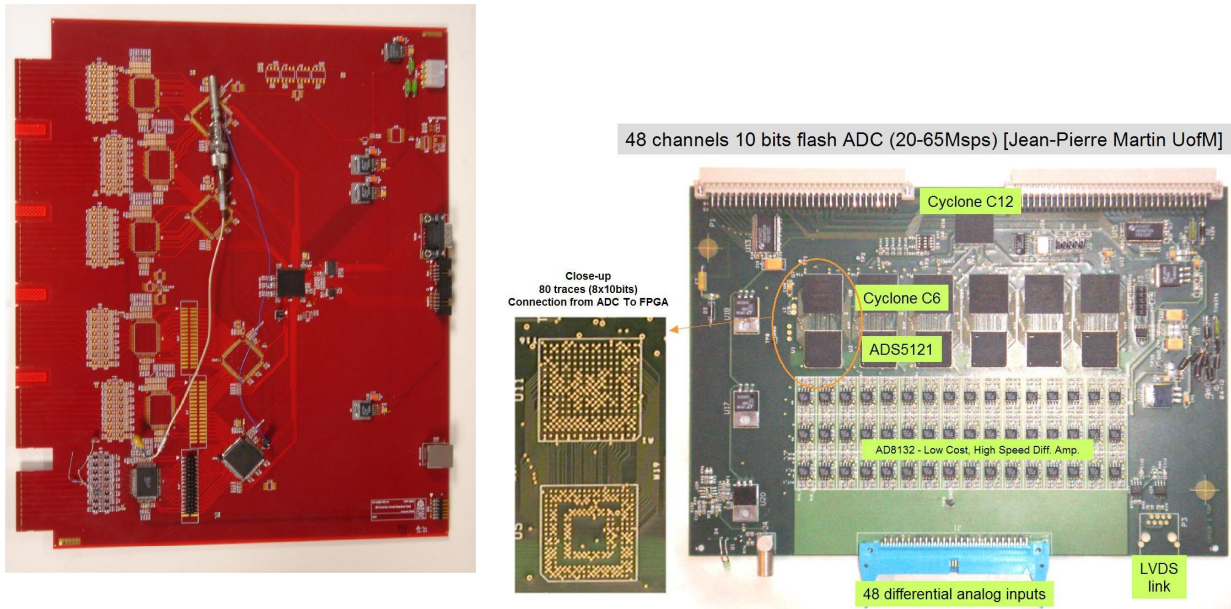


Fig. 6a.17. Tested prototypes of readout cards for the anode wires (left) and cathode strips (right).

In racks near the detector, electronics common to the other phototube readout systems such as that for the Calorimeter digitize the signals with flash ADCs and transfer data to the DAQ system. For details, see Sec. 8.

#### 6a.5.4 Control and Cooling

A Slow Control Processor (SCP) is mounted on each plane collector board to control, monitor and diagnose the anode and cathode boards, and to provide communication between the DAQ computers and the front-end read-out boards (see Fig. 6a.19). Threshold levels, amplifier gains, and pulse-shaping constants are loaded through the SCP. Data compaction and buffering FPGAs are also controlled by the SCP.

The expected power consumption in a crate is about 170 W, with 200 mW per channel for the cathode readout. Cooling of the electronics boards is provided by forced air circulation, as shown in Fig. 6a.20. In a study of the crate cooling, dummy resistors mounted on nine test boards in a prototype crate were powered and the temperatures at several locations on the boards were monitored. When no cooling was provided, the board surface temperature rose to 90°C at a power consumption of 200 W, but with an air-flow rate of 400 cfm the temperature was an acceptable 40°C. There is also nitrogen flow to the chamber perimeter inside the light seal to prevent HV sparking and to provide temperature stabilization for the detectors.

#### References

1. C. Albajar *et al.*, Nucl. Instr. Meth. **A364**, 473 (1995).
2. T. Numao *et al.*, KEK Proceedings 2004-4, p. 173.
3. Y. Arai *et al.*, IEEE Trans. Nucl. Sci. **51**, 2196 (2004).
4. Y. Arai, Nucl. Instr. Meth. **A453**, 365 (2000).
5. D. Acosta *et al.*, Nucl. Instrum. Meth. **A453**, 182 (2000).

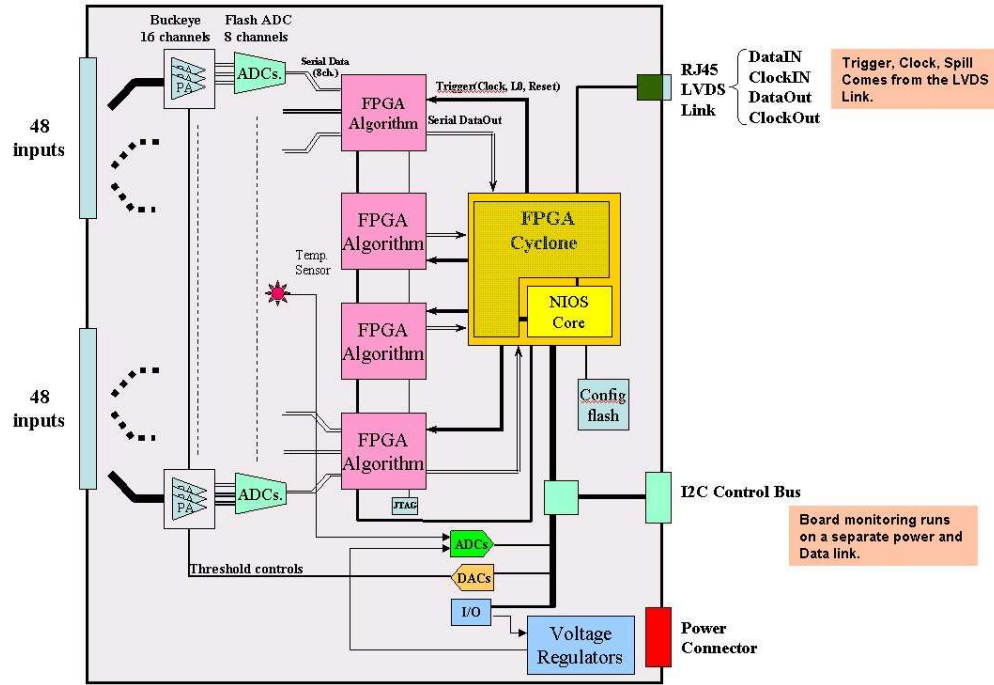


Fig. 6a.18. Functional diagram of the cathode readout card.

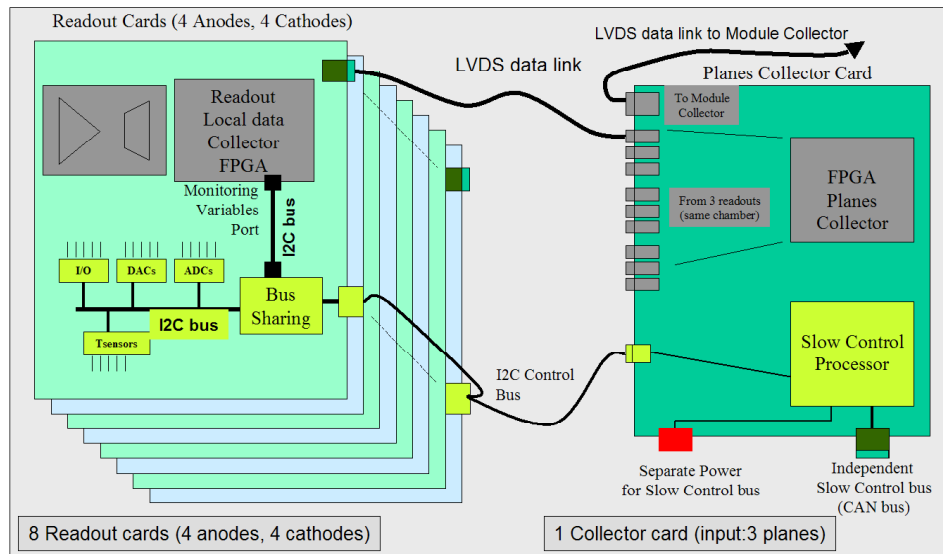


Fig. 6a.19. The Slow Control data path. The Chamber Collector card hosts the slow control processor for the eight readout cards in that crate.

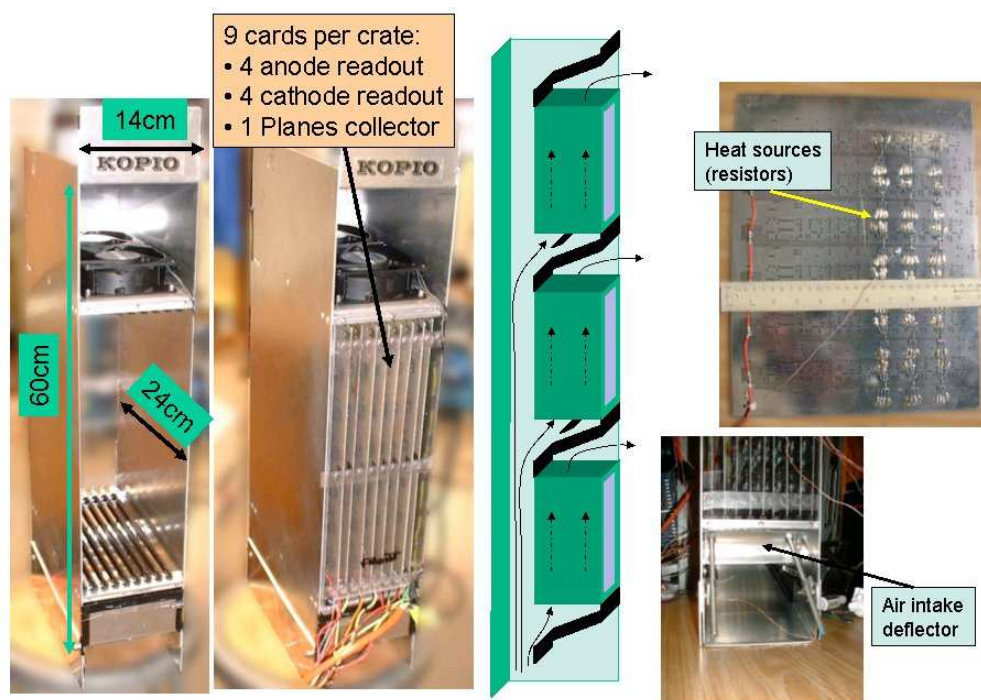


Fig. 6a.20. The prototype electronics crate that was used for cooling tests.



## 6b Calorimeter

A large, granulated Calorimeter is located behind the Preradiator and in front of a downstream sweeping magnet (D4). A sketch of the Calorimeter is shown in Fig. 6b.1.

Photons of interest from  $\pi^0$  decays first convert to  $e^+e^-$  pairs in the Preradiator. These electrons and positrons then traverse more than two radiation lengths of the Preradiator, on average, before entering the Calorimeter. Thus the photon energy measurements are made through a combination of the Preradiator and Calorimeter. With this arrangement, a modest energy resolution of about  $\sim 3\%/\sqrt{E \text{ (GeV)}}$ , sufficient for the KOPIO experiment, is obtained.

Because the Calorimeter does not see the primary photons, but rather secondary electrons and photons, the granularity of the Calorimeter need not be exceedingly high. In fact, because vetoing background must be done with high efficiency, a ‘coarse’ granularity reduces the total volume of cracks between the modules.

Taking into account the purpose of the Calorimeter in the experiment as well as the actual experimental environments, the following requirements were set for the Calorimeter.

- Energy resolution:  $\approx 3.0\%/\sqrt{E \text{ (GeV)}}$ .
- Time resolution:  $\approx 100 \text{ psec} / \sqrt{E \text{ (GeV)}}$ .
- Photon detection inefficiency:  $\leq 10^{-4}$ .
- Granularity:  $\sim 10 \text{ cm}$ .
- Radiation lengths: 19 (21.7 including the Preradiator).
- Size of the Calorimeter:  $4.4 \times 4.4 \text{ m}^2$ .
- Operation in a magnetic field of up to 500 Gauss.

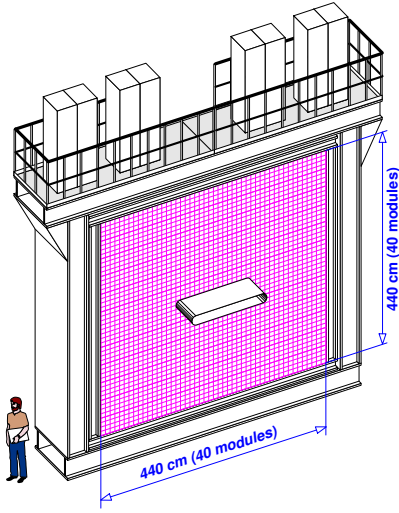


Fig. 6b.1. A sketch view of the KOPIO Photon Calorimeter.

The above considerations lead us to employ the Shashlyk technique for the Calorimeter. The performance level that can be achieved with such a technique is consistent with the needs of the experiment.

Shashlyk modules are lead-scintillator sandwiches read out by means of wavelength-shifting (WLS) fibers passing through holes in the scintillator and lead[1]. While we propose a module with significantly improved performance over previous manifestations, the technique is well proved, *e.g.* experiment E865 at Brookhaven[1,2], and has been adopted by others, *e.g.* the PHENIX RHIC detector[3], the HERA-B detector at DESY[4], and the LHCb detector at CERN[5].

Table 6b.1. Evolution of the energy resolution of Shashlyk modules.

Year of production	Number of layers	Lead thickness (mm)	Scintillator thickness (mm)	Energy resolution $\left(\times \sqrt{E} \text{ (GeV)}\right)$
1991 (E865)	60	1.4	4.0	8.0%
1996 (E923)	120	0.7	3.0	5.8%
1998 (E926)	240	0.35	1.5	4.0%
2003 (KOPIO)	300	0.275	1.5	3.0%

### 6b.1 KOPIO Shashlyk Module.

We have significant experience with the E865 calorimeter which was composed of 600 such modules and ran reliably in a higher rate environment than that expected in the KOPIO experiment. It is from that experience, and improvements which have been prototyped and simulated, that we gain confidence of being able to reach the design goals.

Through calculation and experimentation, we have improved the energy resolution of Shashlyk modules over the past few years. We note this progress in Table 6b.1.

#### 6b.1.1 Simulation of the Shashlyk Calorimeter

The energy resolution of a Shashlyk module depends on variety of factors including the following:

- sampling, *i.e.* the thicknesses of the lead and scintillator plates;
- longitudinal leakage, *i.e.* the fluctuation of energy leakage due to the finite length of the module;
- transverse leakage *i.e.* the fluctuation of energy leakage due to the limited number of modules used to reconstruct an electromagnetic shower;
- effects of the presence of holes, fibers, and wrapping materials;
- light attenuation in the fiber;
- the uniformity of light collection;
- photostatistics; and
- electronic noise in the photodetector readout chain.

To determine the dependence of the energy resolution on the mechanical and optical properties of a module, a simulation model of the module's response was developed[6]. This model is based on the GEANT3[7] description of electromagnetic showers and a special optical simulation of the light collection in the scintillator plates. To customize the model, we have used the results of test-beam measurements of a prototype Shashlyk calorimeter with an energy resolution of  $4\%/\sqrt{E} \text{ (GeV)}$ . These measurements were made by using 0.5–2.0 GeV/c positrons at the Brookhaven AGS. In addition, the simulation of the light collection efficiency was customized by using special optical measurements of the WLS fiber readout.

We used GEANT 3.21 to simulate the development of the electromagnetic showers in the module. It contains many tuning parameters which allow one to select between the speed and quality of the simulation. Cuts on the energy of the electrons and photons are crucial parameters for the correct simulation of the response of a Shashlyk module. To obtain an adequate simulation, we used low-energy cuts of 10 keV instead of the default 1 MeV. Also, delta-ray generation was enabled.

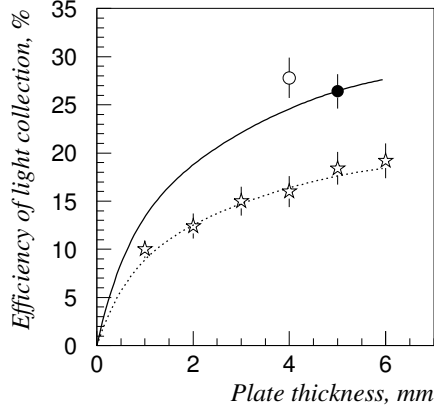


Fig. 6b.2. The light collection efficiency of scintillation light from a scintillator plate for green light in WLS fibers versus the thickness of scintillator plate. The circles are for experimental data with optical contact between fibers and scintillator, the stars are for experimental data without optical contact, and the curves show the optical model simulation.

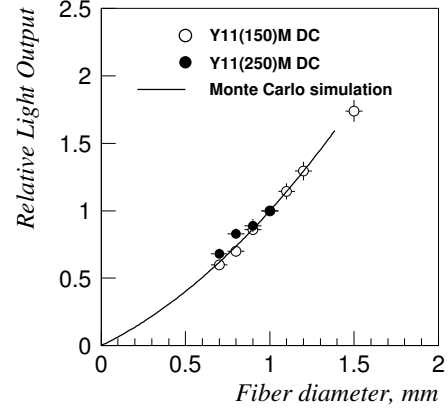


Fig. 6b.3. Relative light output for different diameter KURARAY Y11 fibers compared to a 1.0-mm-diameter fiber. The solid line is an optical model calculation.

To study the dependence of light collection on the optical parameters of scintillator plates, a special optical model was developed. Charged particles passing through a scintillator plate generate a number of randomly directed photons proportional to the energy deposited. Photons thus generated may be absorbed on, reflect from, or penetrate through the surfaces of the plate. Photons entering a fiber may be re-emitted or may exit the fiber, depending on the actual length of the photon track in the fiber. The model is customized by parameters such as the refractive indices of scintillator and fiber, the light attenuation length in scintillator, the probability of a photon re-emitting in a fiber, reflection efficiencies, and by geometry (size of the plate, hole diameter, fiber diameter). Examples of the optical model adjustments are shown in Figs. 6b.2 and 6b.3.

In spite of the simplicity of this model (*e.g.* it does not take into account the dependence of reflection probabilities on the incident angle and polarization of photons), it gives a reasonable description of light collection in the scintillator and allows one to compare different choices of the optics of the scintillator plates. Some examples of the dependence of the energy resolution on the module parameters are shown in Fig. 6b.4. More details may be found in Ref.[6].

To simulate the time response and time resolution of a Shashlyk module, a Monte Carlo model of the light signal in a module was later developed. An ionization produced by a charged particle in a scintillator tile survives several transformations before the corresponding light signal appears at the entrance of a photodetector. Ionization produced by an electromagnetic shower occur at different space points and different times, resulting in a time spread of the photoelectron emission in the photodetector. In addition, the actual emission delays depend randomly on the decay times in the scintillator and the WLS fibers, light collection time in the scintillator fiber, and the propagation of light in the WLS fiber. The following effects have been taken into account in the model:

- the space-time distribution of hits in the Shashlyk module scintillator;
- the decay time in scintillator;
- the light collection time in the scintillator tile;



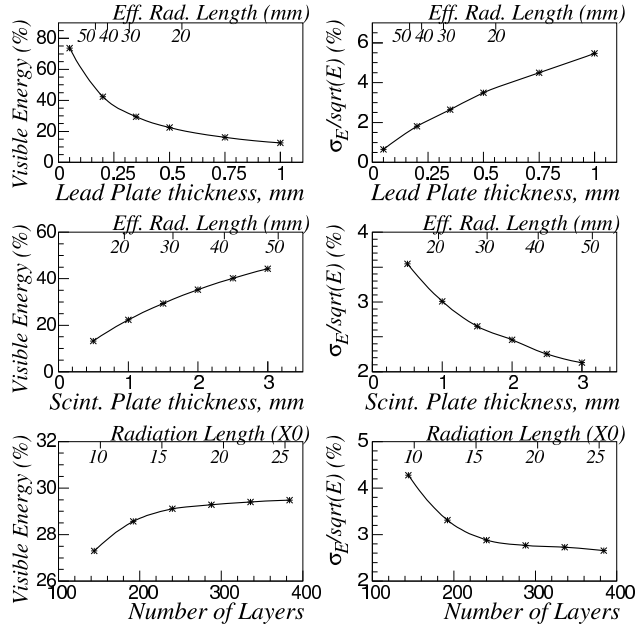


Fig. 6b.4. Calorimeter response and energy resolution as a function of lead and scintillator plate thicknesses and number of layers. It is assumed that the calorimeter consists of 6000 layers of 0.35-mm lead and 1.5-mm of scintillator unless otherwise noted in histograms.

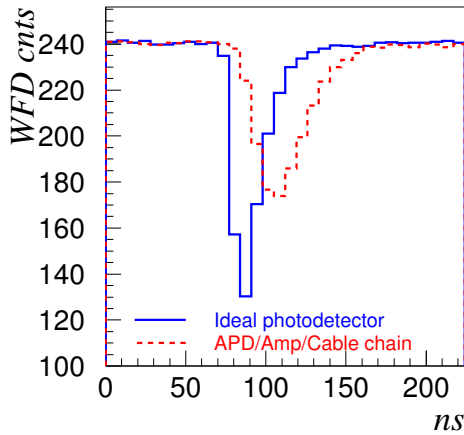


Fig. 6b.5. The simulation of the light response function of the Shashlyk module at the entrance of the photodetector for a 250 MeV photon. The simulated signal in a Wave Form Digitizer if APD/Amplifier/Cable time-response function is taken into account is shown by dashed line.

- the decay time in WLS fibers;
- the effective velocity of light propagation in WLS fibers;
- the light attenuation length in WLS fibers;
- bending loss in the WLS fiber loop; and
- the response function of the detector chain, including an Avalanche Photo Diode (APD) photodetector, preamplifier, cables, and waveform digitizer (WFD).

The simulated response of the Shashlyk module for the 250-MeV photons is shown in Fig. 6b.5. A shape of the simulated signal in a Wave Form Digitizer matches well an experimentally measured signal shown in Fig. 6b.20.

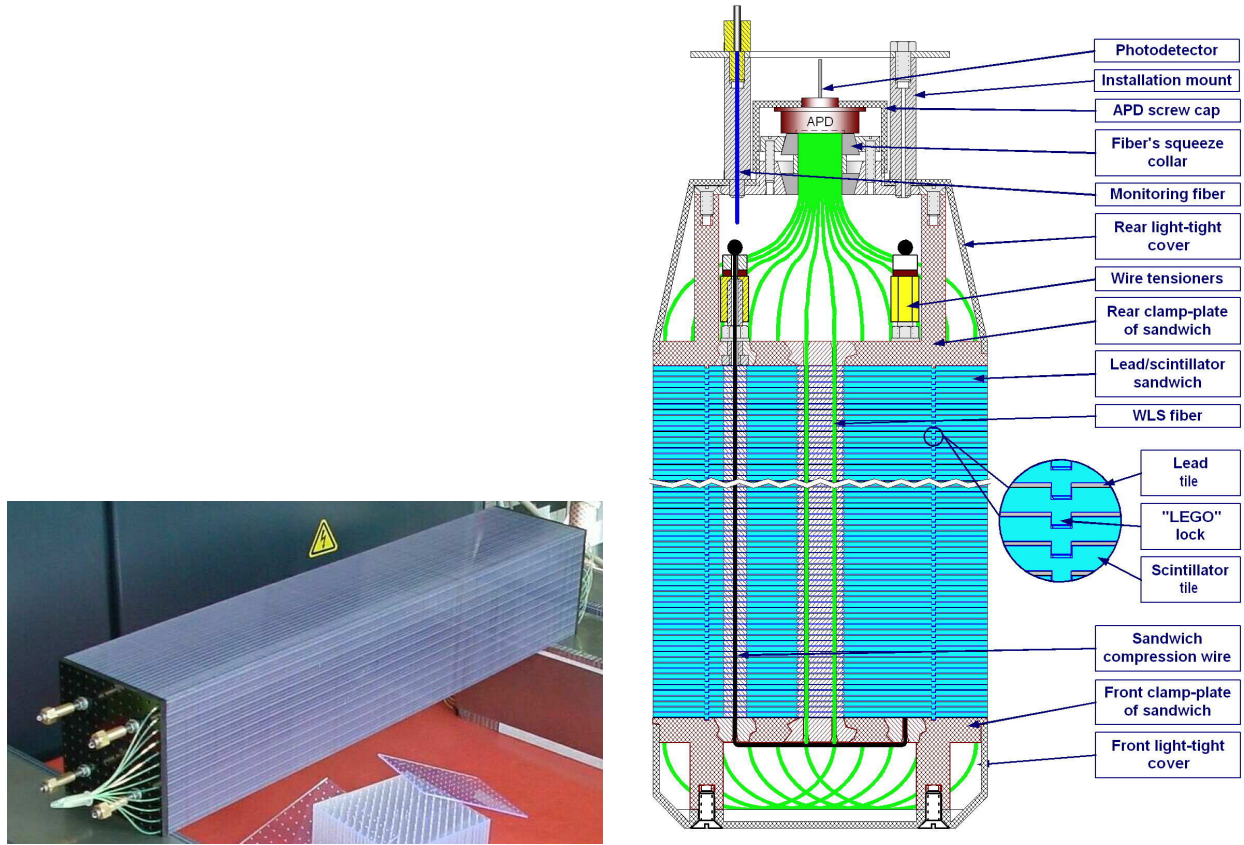


Fig. 6b.6. A Shashlyk module assembly is shown in the left picture. The module design is shown in the right picture.

### 6b.1.2 Methods to Improve Energy Resolution

While the 1998 Shashlyk module had excellent characteristics for that kind of detector, significant improvements had to be made so as to achieve the desired resolution of  $3\%/\sqrt{E} \text{ (GeV)}$ . To determine the means for improvement, we used the simulation model to analyze the main contributions to a module's energy resolution. The results of the analysis indicated (see details in Ref.[6]) that primary attention had to be given to improving the

- sampling,
- photostatistics, and
- light collection uniformity.

To achieve this goal, we revisited the mechanical construction of the module, and optimized the selections of the WLS fibers and photodetector. A new scintillator with improved optical and mechanical properties was specially developed for the KOPIO experiment at the IHEP scintillator facility (Protvino, Russia)[8]. The corresponding improvements to the module design have been implemented in the new KOPIO Calorimeter prototype modules (2003), with an energy resolution of about  $3\%/\sqrt{E} \text{ (GeV)}$ [9].

### 6b.2 Design of the Calorimeter Module

The design of the 2003 prototype module is shown in Fig. 6b.6. The module is a sandwich of alternating perforated stamped lead and injection-molded polystyrene-based scintillator plates. The cross sectional size

of a module is  $110 \times 110 \text{ mm}^2$ . There are 300 layers, each layer consisting of a 0.275-mm lead plate and 1.5-mm scintillator plate.\* The lateral size of a lead or scintillator plate is  $109.7 \times 109.7 \text{ mm}^2$ . Each plate has 144 holes equidistantly arranged in a  $12 \times 12$  matrix, the spacing between the holes being 9.3 mm. The diameter of the holes is 1.3 mm, both in the lead and the scintillator plates. Inserted into the holes are 72 WLS fibers, with each fiber looped at the front of the module so that both ends of a fiber are viewed by a photodetector. Such a loop (radius  $\sim 2.5 \text{ cm}$ ) may be approximated by a mirror with a reflection coefficient of about 95%[\[10\]](#). The fiber ends are collected in one bunch, squeezed, cut and polished, and connected to a photodetector though a small air gap. The complete stack of all plates is held in compression by four 1-mm stainless steel wires. The module is wrapped with 150- $\mu\text{m}$  TYVEK paper which has good light reflection efficiency of about 80%. The mechanical parameters of the module are summarized in Table [6b.2](#).

Table 6b.2. Parameters of the  $3\%/ \sqrt{E} \text{ (GeV)}$  KOPIO prototype module.

Lateral segmentation	$110 \times 110 \text{ mm}^2$
Scintillator thickness	1.5 mm
Spacing between scintillator tiles	0.350 mm
Lead absorber thickness	0.275 mm
Number of layers	300
WLS fibers per module	$72 \times 1.5 \text{ m} = 108 \text{ m}$
Fiber spacing	9.3 mm
Hole diameter (lead/scint.)	1.3 mm
Diameter of WLS fiber (Y11-200MS)	1.0 mm
Fiber bundle diameter	14.0 mm
External wrapping (TYVEK paper)	150 $\mu\text{m}$
Effective radiation length, $X_0$	34.9 mm
Effective Moliere radius, $R_M$	59.8 mm
Effective density	2.75 $\text{g/cm}^3$
Active depth	555 mm ( $15.9 X_0$ )
Total depth (without photodetector)	650 mm
Total weight	21 kg

### 6b.2.1 Improvement of the module geometry

The mechanical construction of the module was revisited to minimize the insensitive area, to increase the effective radiation density, and to improve the sampling ratio and transverse light collection uniformity.

An important innovation in the mechanical design of the module is the “LEGO” type locks for the scintillator tiles shown in Fig. [6b.6](#). These locks, four per tile, fix the position of the scintillators with the 350- $\mu\text{m}$  gaps, providing sufficient room for the 275- $\mu\text{m}$  lead tiles without optical contacts between lead and scintillator. The mechanical structure enables removal of 600 paper tiles, which were preventing optical contact between the scintillator and lead in the “standard” Shashlyk design, reducing the diameter of the

\*The module described here was produced in 2003. It has 16 radiation lengths in accordance with the original KOPIO Proposal. As currently designed, there will be 340 layers of 0.300 mm lead and 1.5 mm scintillator plates in KOPIO module, for a total of 19 radiation lengths.

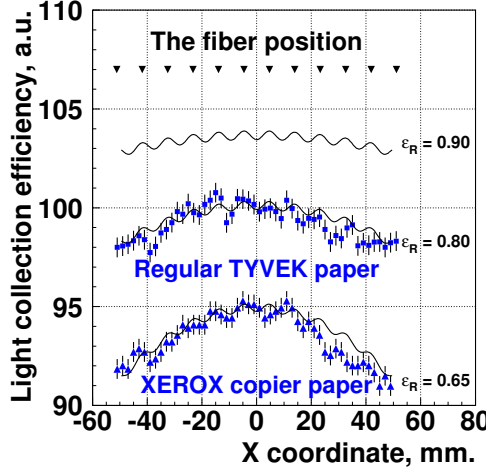


Fig. 6b.7. The dependence of the light collection efficiency on the  $x$ -coordinate of the point-like light source. Solid lines are the simulations for the specified reflection efficiencies  $\varepsilon_R$  of the wrapping material.

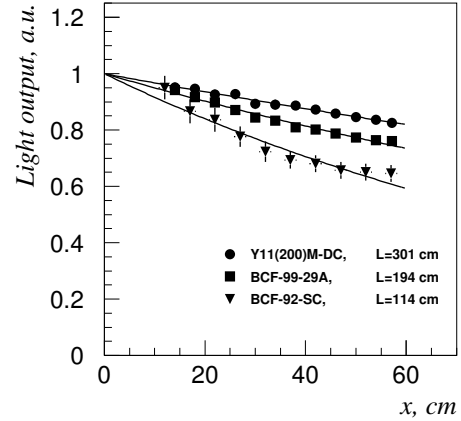


Fig. 6b.8. The effective attenuation of the light in the fibers of Shashlyk module. Experimental data (marks) are fit by the exponential dependence  $\exp(-x/L)$  (solid lines), where  $x$  is the distance to the PMT and  $L$  is the effective attenuation length. Measurements were made with a muon beam.

fiber holes to 1.3 mm, and removal of the compressing steel tapes at the sides of the module. Compared to the “standard” Shashlyk module, the holes/cracks and other insensitive areas were reduced from 2.5% to 1.6%, and the module’s mechanical properties such as dimensional tolerances and constructive stiffness were significantly improved. By removing the paper tiles, the effective radiation length could be reduced from 4.0 cm to 3.5 cm.

There is only a limited ability to improve the “pure” sampling contribution to the energy resolution of the Shashlyk module. Decreasing the thickness of the lead only will increase the length of the module, while the proportional decreasing of both the lead and scintillator thicknesses will reduce the light collection efficiency. Nevertheless, by removing the paper between the lead and scintillator tiles, both the sampling could be improved and the length of the module could be shortened. Compared to the design of the previous 1998 module[6], the sampling ratio was improved by a factor of 1.25.

The dominant source of non-uniformity of the light collection is the absorption of light at the edges of a scintillator tile. For improvement, the reflection efficiency on the edges of the scintillator tile is crucial. In the 2003 module, the WLS fiber density was effectively increased by “cutting the edges” of the scintillator tile. The transverse size of the tile, 10.97 cm, is smaller than the “uniform” size of 11.16 cm for 12 fibers with 0.93-cm spacing. In addition, the module was wrapped with TYVEK paper (reflection efficiency about 80%). As a result, the light collection efficiency at the edges of the scintillator tile is only 2.3% smaller than in the center of the tile for the point-like light source. In the case of a 250-MeV photon shower, the difference is only 0.5%, which is negligible compared to the energy resolution of about 6% for such photons.

The experimental results for the light collection uniformity for TYVEK and Xerox copier papers are presented in Fig. 6b.7. The measurements were made with a scintillator tile exposed to collimated  $^{90}\text{Sr}$  electrons. For comparison, the simulated light collection efficiencies are shown. One can see that a good consistency between the optical simulations and measurements. Further improvement may be achieved if Millipore paper with reflection efficiency of 90% will be used[11].

### 6b.2.2 WLS fibers

A main concern about the WLS fibers for the Shashlyk readout is the light attenuation length in a fiber. Because the longitudinal fluctuations of electromagnetic showers are about 3-4 cm (one radiation length), the effective attenuation length in fibers must be greater than 3–4 m to have this contribution to the energy resolution be much smaller than the sampling contribution. We have experimentally measured the light attenuation in three different fibers: (i) BCF-92-SC, (ii) BCF-99-29A, and (iii) KURARAY Y11(200)MS. Measurements were made by using muons that penetrated the modules transversely. The size of the beam spot was  $1 \times 1 \text{ cm}^2$ . Results of the measurements are presented in Fig. 6b.8. It should be noted that the measured values of effective attenuation lengths include the effects of the fiber loop and the short-distance component of light attenuation in the fibers, which have important roles in the light transmission over short distances. The effective attenuation length of 3.0 m in KURARAY Y11(200)MS fiber satisfies our requirements. In comparison with other fibers, this commercial fiber also provides the best reemission efficiency of blue scintillation light, and it has excellent mechanical properties – high tensile and bending strength – and high uniformity in cross-sectional dimensions. For example, its light reemission efficiency is a factor of 1.5 larger than that for any Bicron WLS fiber, and the diameter for any round fiber varies by no more than 2.0%.

### 6b.2.3 Scintillator

An important contribution for the improvement of the photostatistics over earlier designs of Shashlyk modules is the use of new scintillator tiles with an increased light collection efficiency. An optimization of the light yield of the scintillator tiles for the KOPIO Shashlyk modules has been developed and carried out at the IHEP scintillator facility (Protvino, Russia)[8]. In the previous Shashlyk calorimeters, scintillator based on PSM115 polystyrene was used. The new modules employ BASF143E-based scintillator. The test results for the several scintillators are shown in Table 6b.3.

Though there is no actual increase in the amount of light produced by a charge particle, the light collection efficiency in the scintillator tile has a gain by a factor of 1.6. Because the index of refraction for the polystyrene-based scintillator is 1.59, only light from total internal reflection at the large side of the scintillator tile can be captured by a WLS fiber. Potentially, the total internal reflection efficiency can be as large as 100%. However, this value is not reachable for realistic surfaces. Many reflections usually occur before light is captured and re-emitted by a WLS fiber. Both the effective attenuation length and the light collection efficiency in a scintillator tile depends on the light reflection efficiency. As shown in Fig. 6b.9, the parametric dependence of the light collection efficiency on the attenuation length, calculated from our optical model[6], is in a good agreement with the experimental results shown in Table 6b.3.

The new plastic base of the scintillator material and the new production technology of tiles yields 97% reflection efficiency from the scintillator surface, and strongly improves the reproduction quality (see Fig. 6b.10) of the tiles. The latter is crucial for good longitudinal light collection uniformity. Due to the fluctuation of the depth of the electromagnetic shower in the calorimeter module, good reproduction quality of the tiles is a mandatory condition for an appropriate performance of the  $3\%/\sqrt{E} \text{ (GeV)}$  module.

Fluors for the new scintillator composition, BASF143E polystyrene + 1.5%pTP + 0.04%POPOP were selected[12,13] to match well with the absorption spectrum of the Kuraray Y11(200)MS WLS fiber (Fig. 6b.11).

With selected BASF143E-based scintillator and KURARAY fibers, the effective light yield in the KOPIO Shashlyk module (at the entrance to the photodetector) becomes  $N_\gamma \sim 60$  photons per 1 MeV of the incident photon energy.

It was reported[12] that the radiation stability of BASF143E-based scintillator is a dose level 120 krad, and the recovery time is about 80 days. This limitation will not be a problem for the KOPIO Calorimeter. According to our estimates, the most active scintillator tiles will acquire only about 5 krad during 60 days of the KOPIO run. Also, a recent radiation stability test of the KOPIO Calorimeter scintillator showed a better result[14] than that quoted in Ref.[12]. This disagreement in BASF115E radiation stability measurements is being investigated further. The most likely reasons are changes in the technology of the scintillator production such as the effect of new special additives that speed up the recovery process.

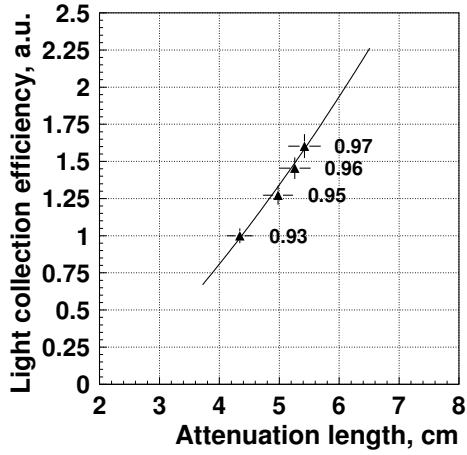


Fig. 6b.9. The parametric dependence of the light collection efficiency on the effective attenuation length due to the reflection efficiency. The solid line is the result of a calculation based on the model of Ref.[6]. The experimental results are taken from Table 6b.3. For each scintillator, the calculated reflection efficiency is displayed.

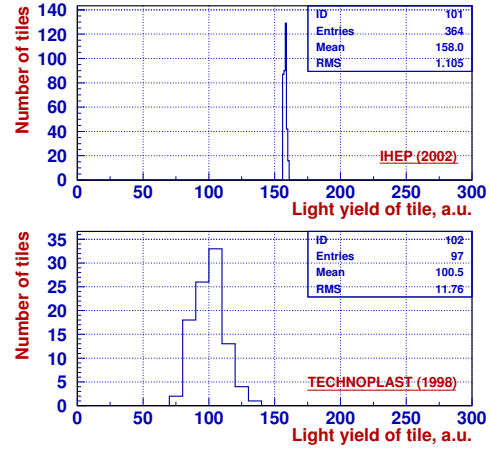


Fig. 6b.10. Comparison of a light-yield spread for the scintillator tiles used in 1998 (bottom) and 2003 (top) Shashlyk modules prototypes.

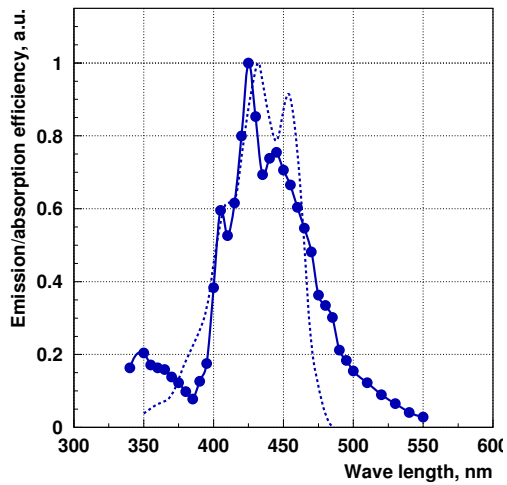


Fig. 6b.11. The closed circles and solid line are the measured emission spectra of the BASF143E-based scintillator. The dashed line is the absorption spectrum of KURARAY Y11(200)MS WLS fibers.



Table 6b.3. Scintillators tested for the KOPIO Shashlyk module. The “light yield” is the amount of light produced in the scintillator without respect to the light collection efficiency, while “MIP light yield” is the detected light signal per minimum ionization particle passing through the scintillator tile. The “effective attenuation length” was measured for thin, 1.5-mm scintillator tile.

Scintillator: Polystyrene+Fluor1+Fluor2 Manufacturer	Light yield (% of Anthracene)	Effective attenuation length in tile (cm)	MIP light yield ( p.e. per tile)
PSM115+1.5%pTP+0.04%POPOP TECHNOPLAST, 1998	$53 \pm 6$	$4.3 \pm 0.2$	$4.4 \pm 0.3$ 100%
BASF158K+1.5%pTP+0.04%POPOP IHEP, 2001	$56 \pm 6$	$5.0 \pm 0.2$	$5.6 \pm 0.3$ ( $127 \pm 10$ )%
BASF165H+1.5%pTP+0.04%POPOP IHEP, 2001	$56 \pm 6$	$5.3 \pm 0.3$	$6.4 \pm 0.3$ ( $145 \pm 10$ )%
BASF143E+1.5%pTP+0.04%POPOP IHEP, 2002	$54 \pm 6$	$5.4 \pm 0.2$	$7.1 \pm 0.3$ ( $161 \pm 10$ )%

#### 6b.2.4 Photodetector

The Avalanche Photo Diode (APD), a detector with high quantum efficiency, provides another important improvement of the photostatistics contribution to the energy resolution of the KOPIO Shashlyk module.

Our preliminary experimental studies of the fine-sampling Shashlyk modules[6] have shown that the performance of Shashlyk calorimeter modules with photomultiplier (PMT) readouts agrees with the simulations and nearly satisfies the requirements of the KOPIO experiment. However, these test measurements were made in an optimal environment for PMT readout: no magnetic fields, short measuring runs, and continuous and stable photon beams.

These conditions do not properly represent those that will be encountered in the KOPIO experimental environment. Our main concern is related to the leakage of the magnetic field from the downstream magnet of up to 500 Gauss. In addition, the quantum efficiency of PMTs, which is about 18% at 500 nm (the region of WLS-fiber response) for the best “standard” green-sensitive tubes, is relatively low.

This is why we searched for an alternative photodetector for the KOPIO Calorimeter. Recent progress in the development of new Avalanche Photo Diodes (APD) with large active areas (up to 200 mm<sup>2</sup>), low capacitance, low dark current, high gain (up to 1,000), and high quantum efficiency (up to 90%) allows us to consider these photodetectors as primary candidates for the KOPIO Calorimeter. Some characteristics of available large-area APDs are shown in Table 6b.4. For comparison, the parameters of the green-sensitive PMT-9903B and the well-known small-area Hamamatsu APD S8664-55 are also displayed.

Here, we briefly report the results of our study of the large area APDs.

*Operation in magnetic fields:* APDs can operate in a magnetic field of up to 80 kGs[15], far beyond the requirements of the KOPIO experiment.

Table 6b.4. Some experimental and catalog parameters of the green-extendeds PMT-9903B and three pre-selected large-area APDs. Data for a well-known small-area APD, produced by Hamamatsu Corporation, are shown for comparison.

<i>Item</i>	<i>PMT</i>	<i>APD</i>			
	9903B ( <i>Electron Tubes, Inc.</i> )	630-70-74-510 ( <i>Advanced Photonix, Inc.</i> )	S1315 ( <i>RMD Instruments, Inc.</i> )	C30703E ( <i>Perkin-Elmer, Inc.</i> )	S8664-55 ( <i>Hamamatsu Photonics, K.K.</i> )
Active area ( $S$ )	$\sim 600$ ( $\varnothing 30$ ) (mm <sup>2</sup> )	$\sim 200$ ( $\varnothing 16$ ) (mm <sup>2</sup> )	169 ( $13 \times 13$ ) (mm <sup>2</sup> )	100 ( $10 \times 10$ ) (mm <sup>2</sup> )	25 ( $5 \times 5$ ) (mm <sup>2</sup> )
Quantum eff. ( $Q$ ) at $\lambda = 550$ nm	19 (%)	94 (%)	66 (%)	76 (%)	81 (%)
Gain ( $M$ )	$\geq 10^5$	$\leq 1000$	$\leq 10000$	$\leq 200$	$\leq 200$
Specific capacitance ( $C$ )	$\sim 0.01$ (pF/mm <sup>2</sup> )	$\sim 0.65$ (pF/mm <sup>2</sup> )	$\sim 0.71$ (pF/mm <sup>2</sup> )	$\sim 1.0$ (pF/mm <sup>2</sup> )	$\sim 3.2$ (pF/mm <sup>2</sup> )
Series resistance ( $R_S$ )	—	$\sim 10$ (Ohm)	$\sim 40$ (Ohm)	$\sim 15$ (Ohm)	$\sim 5$ (Ohm)
Density of surface current ( $I_S/S$ )	$\leq 5$ (pA/mm <sup>2</sup> )	$\leq 300$ (pA/mm <sup>2</sup> )	$\leq 1700$ (pA/mm <sup>2</sup> )	$\leq 800$ (pA/mm <sup>2</sup> )	$\leq 100$ (pA/mm <sup>2</sup> )
Density of bulk current ( $I_B/S$ )	$\leq 0.1$ (pA/mm <sup>2</sup> )	$\leq 3$ (pA/mm <sup>2</sup> )	$\leq 4$ (pA/mm <sup>2</sup> )	$\leq 5$ (pA/mm <sup>2</sup> )	$\leq 6$ (pA/mm <sup>2</sup> )
Excess noise factor ( $F$ )	$\sim 1.5$ ( $M \sim 10^5$ )	$\sim 2.2$ ( $M \sim 100$ )	$\sim 2.1$ ( $M \sim 100$ )	$\sim 3.6$ ( $M \sim 100$ )	$\sim 2.7$ ( $M \sim 100$ )
$k$ -factor	—	$\sim 0.002$	$\sim 0.001$	$\sim 0.015$	$\sim 0.007$
Width (FWHM) of multiplication zone	—	$\sim 65$ ( $\mu$ m)	$\sim 75$ ( $\mu$ m)	$\sim 10$ ( $\mu$ m)	$\sim 12$ ( $\mu$ m)
Intensity of E-field inside of M-zone	—	$\sim 230$ (kV/cm)	$\sim 210$ (kV/cm)	$\sim 340$ (kV/cm)	$\sim 380$ (kV/cm)

*Size of the active area:* The fibers from the KOPIO Shashlyk module are collected to a 14 mm diameter bunch. This size is well matched to the Advanced Photonics Inc. APD 630-70-74-510 (API APD), which has diameter of 16 mm.

*Response uniformity of the active area:* This feature is important for the Shashlyk module because each fiber delivers light to only a small part of the total sensitive area. The response of the selected APD varies by less than 3% over the active area. Usually, PMTs exhibit poor spatial response uniformity ( $\geq 20\%$ ).

*Quantum efficiency of the sensitive area:* Photostatistics, directly dependent on the quantum efficiency ( $Q$ ) of the photodetector is an important contribution to the energy resolution of a calorimeter. For green light emitted by Kuraray fibers, the APDs have much higher quantum efficiencies than PMTs (see Fig. 6b.12). For example, the quantum efficiency of the API APD is 94%, a factor 5 higher than quantum efficiency of the 9903B PMT. It should be noted that the photostatistics contribution depends also on the fluctuations of the photodetector gain,  $(\sigma_E/E)_{\text{ph.stat.}}^2 = F/QN_\gamma$ , where  $F$  is the so-called excess noise factor and  $N_\gamma$  is the number of primary photons at the entrance of the photodetector. For an ideal photodetector,  $F = 1$ , for a high-linearity PMT  $F_{\text{PMT}}$  is usually between 1.3 and 1.6. For a high-gain APD, excess noise factor linearly depends on the gain  $M_{\text{APD}}$ ,  $F_{\text{APD}} \simeq 2 + kM_{\text{APD}}$  [16,17]. The experimentally measured behavior of  $F_{\text{APD}}$  versus  $M_{\text{APD}}$ , for some selected APDs, is shown in Fig. 6b.13. Taking into account both quantum



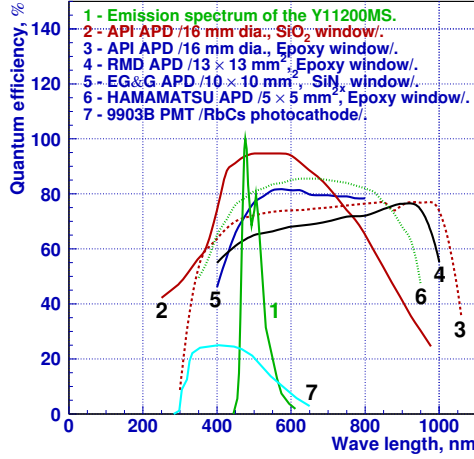


Fig. 6b.12. A quantum efficiency of the various APDs and 9903B PMT versus the light wavelength. An emission spectrum of the Kuraray Y11200MS WLS fiber (a solid green line) is shown in the same picture.

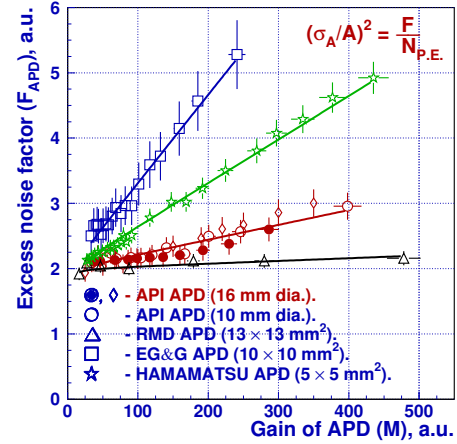


Fig. 6b.13. The APD excess noise factor versus the APD gain for various pre-selected APDs.

efficiency  $Q$  and excess noise factor  $F$ , we conclude that API APD has best “photostatistics quality”,  $Q/F \simeq 43\%$ , ( $M_{\text{APD}} \simeq 100$ ), about a factor 3.5 better than 9903B PMT.

*Electronic noise of the photodetector/amplifier chain:* The contribution of the electronic noise of the photodetector/amplifier chain to the energy resolution is usually referred to as the Equivalent Noise Charge (ENC) of a photodetector readout chain,  $\sigma_{\text{ENC}}$ . In the case of a Charge Sensitive Amplifier (CSA) with a simple  $CR$ - $RC$  shaper, the ENC can be estimated from:

$$\sigma_{\text{ENC}}^2 = \frac{I_S/M^2 + I_B F}{4q} \Delta t + \sigma_{\text{amp}}^2/M^2, \quad (5)$$

where  $q$  is the charge of an electron,  $\Delta t$  is the charge integrating time of the photodetector/amplifier chain and  $\sigma_{\text{amp}}$  is the ENC of the amplifier, Surface leakage current  $I_S$  and bulk current  $I_B$  are two independent components of the photodetector dark current  $I_d = I_S + I_B M$ . It is assumed that  $\Delta t$  is bigger than the signal pulse duration. For a PMT-readout without amplifier,  $\sigma_{\text{ENC}} \simeq 0$  due to a very small PMT dark current. The experimentally measured behavior of the APD dark current versus  $M_{\text{APD}}$  for some selected APDs is shown in Fig. 6b.14. For the API APD, the ENC contributions of the leakage current to the energy resolution may be estimated as  $\simeq 14$  electrons for  $\Delta t \approx 100$  ns and  $M_{\text{APD}} \geq 100$ . The value of the amplifier noise  $\sigma_{\text{amp}}$  is usually measured experimentally. The noise characteristics of some fast CSAs are shown in Fig. 6b.15. For the API APD, which has capacitance about 130 pF, and the  $2 \times \text{SK2394}$  CSA, the amplifier noise may be estimated as  $\sigma_{\text{amp}}/M_{\text{APD}} \simeq 18$  for  $M_{\text{APD}} \simeq 100$ . Assuming 60 photons at the entrance of photodetector per 1 MeV of the deposited energy, the total electronic noise contribution to the energy resolution of the KOPIO Shashlyk module is about 0.4 MeV for the API APD. This value is negligible for the energy range of the KOPIO experiment.

*Gain and noise dependence on the temperature:* The APD performance is very sensitive to the environmental temperature. Since,  $\frac{1}{M} \frac{dM}{dT} \simeq -4\%$ , thermostating and gain monitoring is an important condition of using APDs in the KOPIO experiment. For the API APD, noise dependence on temperature is shown in Fig. 6b.16. To reduce noise, a thermostable cooling system should be used.

*Gain dependence on High Voltage:* According to our experimental study of the API APD,  $\frac{1}{M} \frac{dM}{dV} \approx (2-3)\%$  depending on the environment temperature and gain. The dependence is similar to those of PMTs.

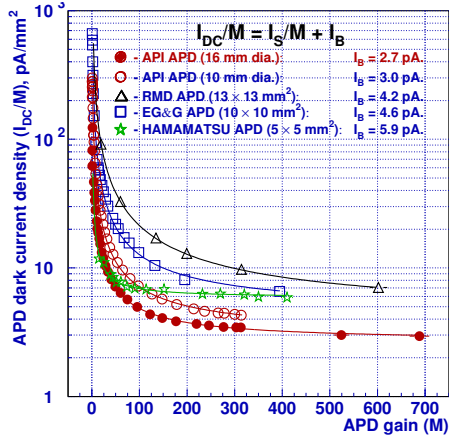


Fig. 6b.14. The APD dark current densities as a functions of the APD gains for the various pre-selected APDs. KOPIO data.

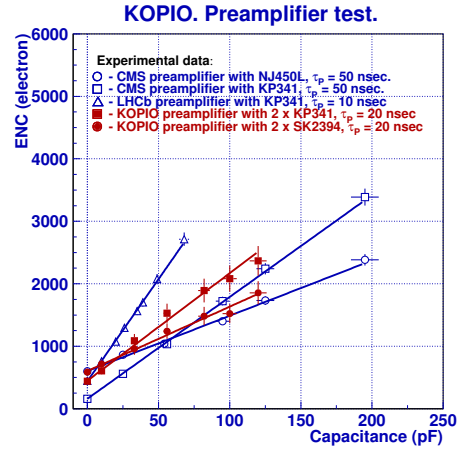


Fig. 6b.15. Equivalent Noise Charge (ENC) versus the input capacitance for some fast Charge Sensitive Amplifiers. Integration time was 100 ns in all measurements.

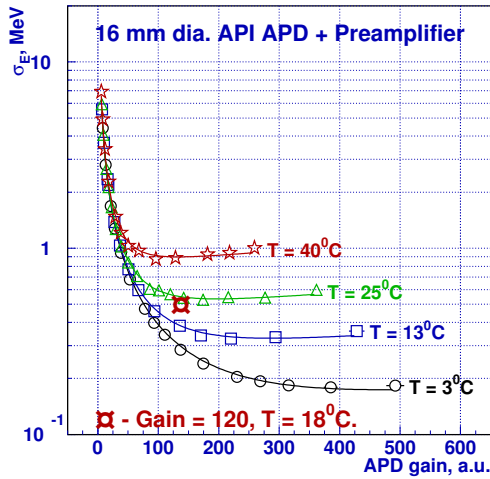


Fig. 6b.16. Equivalent energy noise of an APD/amplifier chain versus the APD gain for various environment temperature.

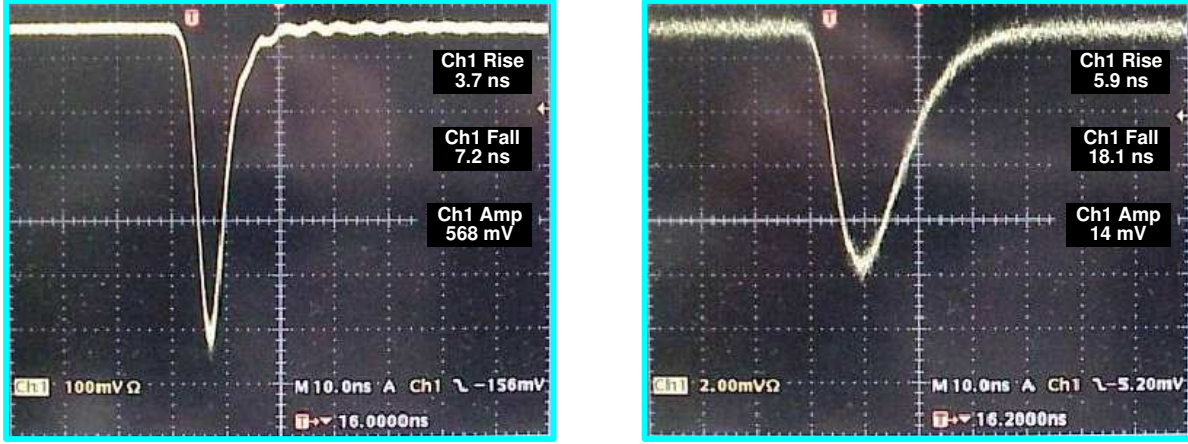


Fig. 6b.17. PMT-9903B (left) and APD-630-70-74-510 (right) responses to the short light pulse. The duration of the light pulse is about 3 ns. The intensity of the light pulse is about 40,000 photons which corresponds to the 700-MeV photon signal.

*Gain dependence on the rate:* Contrary to PMTs, there is almost no dependence of APD gain on rate. In our test measurements with API APD, we did not find any gain variations for the rates up to few MHz. However, APDs are used with preamplifiers. For slow preamplifiers, there may be rate dependence due to the pile-up.

*Time response of the API APD:* The time response of the API APD to a short-duration (3 ns) light pulse with an intensity corresponding to 700-MeV photon, is shown in Fig. 6b.17. One can see that a rise time of the APD response pulse (without any amplifier) is fast enough. Its value of 5.9 ns is comparable with 3.7 ns for the PMT-9903B response to the same light pulse. The fall time of the APD response pulse, 18.1 ns, is longer than that for the PMT response, 7.2 ns, due to higher APD capacitance. The difference between PMT and APD time response becomes less essential, if we take into account the Shashlyk module signal duration (see Fig. 6b.5).

To summarize, the Advanced Photonics Inc. APD 630-70-74-510 was chosen for the test beam measurements since it has the best properties for photoelectron statistics and for electronic noise. This commercial device has the highest quantum efficiency over a wide spectral range (see Fig. 6b.12), the lowest dark current and, especially, the lowest bulk dark current (see Fig. 6b.14) compared with other pre-selected APDs. Its excess noise factor is low enough,  $F$ -values are spread between 2.2 and 2.5 for the APD-gain range of 150–350 (see Fig. 6b.13).

These characteristics of the Advanced Photonics Inc. APD together with the improved light yield in the new Shashlyk module allow us to reduce the photostatistics contribution to the energy resolution of the calorimeter to the negligible level of  $0.7\%/\sqrt{E \text{ (GeV)}}$ , while the electronic noise contribution of  $\leq 0.4 \text{ MeV}$  is also negligible.

### 6b.3 Experimental Study of Prototype Modules

Test measurements of the prototype of a Shashlyk calorimeter with energy resolution of  $3\%/\sqrt{E \text{ (GeV)}}$  have been made with the photon beam from the Laser Electron Gamma Source (LEGS) facility[18] at Brookhaven National Laboratory.

The tagged photon beam had a mean intensity of  $\sim 3 \times 10^5 \text{ Hz}$ , a size of  $\sim 1.5 \text{ cm}$  at the detector position, and an angular spread of  $\sim 2 \text{ mrad}$ . The photon energy was tagged with an accuracy of  $\delta E_\gamma/E_\gamma \approx 1.5\%$ . The timing accuracy of the tagging spectrometer was  $\simeq 1 \text{ ns}$ . Several monochromatic photon energy lines in the range of 220–370 MeV were triggered in our measurements.

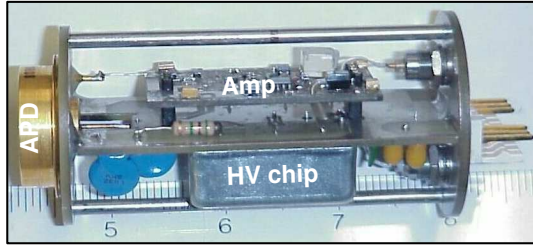


Fig. 6b.18. View of an APD unit.

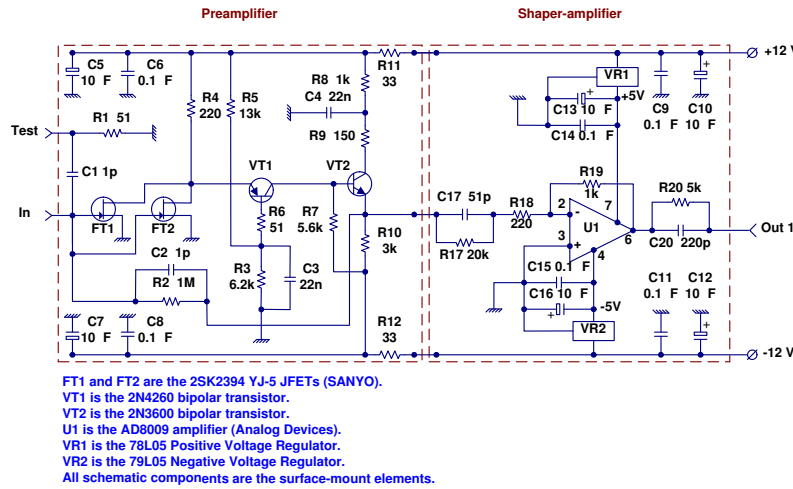


Fig. 6b.19. The functional scheme of an APD charge sensitive amplifier.

Two arrays of  $3 \times 3$  prototype modules with equal lead/scintillator structure were tested to compare response of the:

- conventional module's design (paper between lead and scintillator) with the new module's design (no paper between lead and scintillator);
- conventional PMT photodetection with the new APD photodetection; and
- conventional QDC digitizing of signals with the new Wave Form Digitizing (WFD) of signals.

The first array (prototype 1) contained 9 conventional modules with the 30-mm-diameter, green-extended PMT-9903B of *Electron Tube Inc.* The PMT signals were digitized with a conventional 12-bit *LeCroy* QDC. The second array (prototype 2) contained a nonet of new design modules equipped with the 16-mm-diameter APD 630-70-74510 of *Advanced Photonix Inc.* An instrumented APD-unit is shown in Fig. 6b.18, which includes the APD itself, the APD amplifier, and the APD HV bias.

For these test measurements, a fast low-noise CSA has been designed to optimize the signal-to-noise ratio and the double-pulse resolution. The overall linear chain of the amplifier is shown in Fig. 6b.19. It consists a charge-sensitive preamplifier and a shaper-amplifier. The charge-sensitive part of this scheme is designed as a cascode amplifier with two parallel-connected low-capacitance JFET transistors to improve the signal/noise ratio. The second stage of the amplifier provides a cancellation of the signal tail by a “pole-zero cancellation” network ( $\tau \simeq 18$  ns), and also provides an additional amplification of the signal. Two types of the low-capacitance input JFET transistors have been considered for this amplifier: the Russian 2P341A transistor and the Japanese SK2394/YJ5 transistor. Both transistors are characterized by a high transconductance ( $g_m > 20$  mA/V) for moderate drain current and low input capacitance ( $C_{JFET} < 10$  pF). The ENC of the designed amplifier for both versions of the input JFETs was measured for several detector

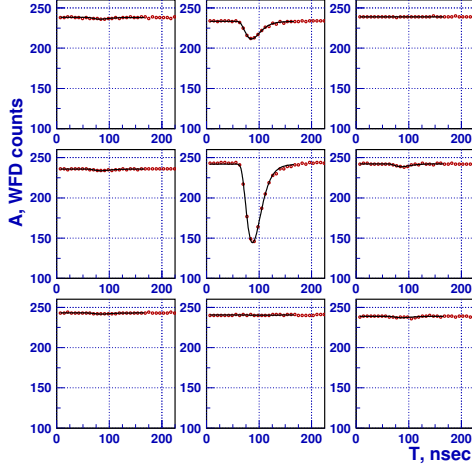


Fig. 6b.20. A typical response of the nonet of Shashlyk modules to 340-MeV photons.

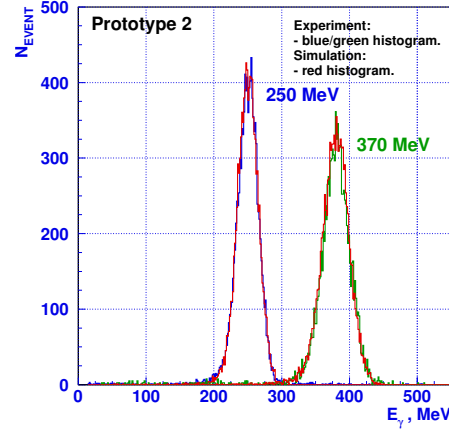


Fig. 6b.21. Comparison of the experimental (marks) and simulated (lines) energy spectra in the Shashlyk nonet with the APD+WFD readout.

capacitances up to 150 pF. Results are shown in Fig. 6b.15. We used the amplifier with two SK2394/YJ5 transistors (KOPIO -  $2 \times$  SK2394) in the test beam measurements.

To stabilize the APD's temperature at ( $18^\circ$  C during the test measurements, the prototype was placed in a thermostat. During the test period of 24 hours, the temperature variation did not exceed  $0.2^\circ$  C.

In the test measurements, two types of APD HV supplies were tested: a *BERTAN* 377P of NIM standard and a HV “built-in” unit (see Fig. 6b.18) with a new commercial compact LV-HV converter (C20), produced by *EMCO*. The stability of both bias systems was better than 0.1 V/hour, which provided an APD gain stability better than 0.3%. Both 8-bit 140-MHz WFDs, developed by Yale University, and conventional 12-bit LeCroy QDCs were used for digitizing the APD signals.

Both calorimeter prototypes were mounted on platforms that could be moved horizontally and vertically with respect to the beam line, so that each prototype module could be calibrated (with an accuracy  $\leq 1\%$ ) by using the 250-MeV photon beam that passed through the central region of the module at normal incidence. The PMT and APD gains were monitored continuously by using LED signals.

The pedestal response, the sum of electronic noise and pile-up for individual modules, was measured during the test runs by using a special gate signal that was shifted from the photon timing by up to  $1 \mu\text{s}$ . The contribution of this effective noise to the energy resolution was  $(0.5 \pm 0.1)$  MeV for the case of the “APD+QDC” readout. The total equivalent noise for the “APD+WFD” readout was  $(1.0 \pm 0.2)$  MeV. This value is twice as large as that for the first one due to a digitization uncertainty of the 8-bit WFD. The lowest equivalent noise,  $(0.2 \pm 0.1)$  MeV, was obtained with the PMT-9903B tubes.

The typical response of the nonet of the “APD+WFD”-instrumented modules to a 340-MeV photon hitting the nonet at the center of the central module, is shown in Fig. 6b.20. The measured signal distribution in the WFD was fit by a function  $Af(t - t_0) + P$ , where  $f(\tau)$  is an experimentally determined pulse shape function. The signal amplitude  $A$ , signal time  $t_0$ , and pedestal  $P$  were free parameters in the fit.

### 6b.3.1 Energy Resolution

The energy resolution was measured for both prototypes 1 and 2. The photon beam was directed to the center of the module nonets. Energy spectra of 250- and 370-MeV photons in the Shashlyk nonet with the APD+WFD readout are shown in Fig. 6b.21. Note the good agreement between Monte-Carlo and experimental distributions.



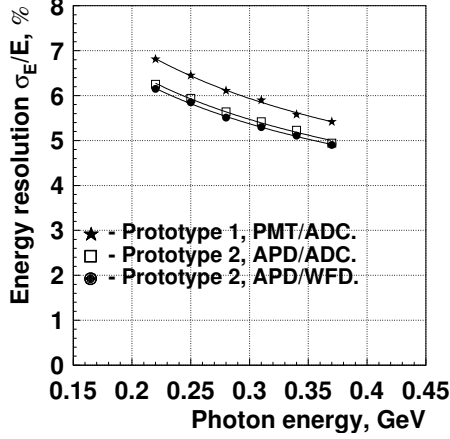


Fig. 6b.22. Energy resolution of a prototype of the Shashlyk Calorimeter for KOPIO.

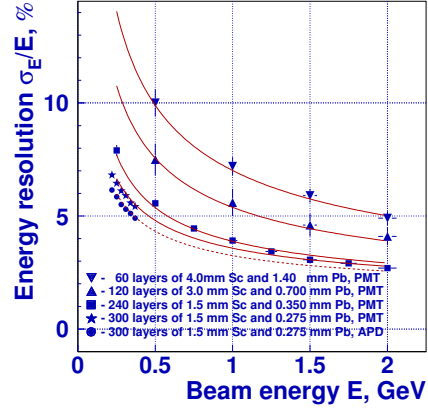


Fig. 6b.23. The energy resolution of nonets of modules versus energy of the electron/photon beam for configurations described in the figure. The lines show the results of simulation.

The energy-resolution results for various prototypes of calorimeters are displayed in Fig. 6b.22. The best result was achieved for the “APD+WFD” readout. A fit to these experimental data gives

$$\sigma_E/E = (1.96 \pm 0.1)\% \oplus (2.74 \pm 0.05)\%/\sqrt{E \text{ (GeV)}},$$

where  $\oplus$  means a quadratic summation. The relatively large constant term of 2% may be explained by the short,  $15.9\text{-}X_0$  radiation length of the module. However, this term is not essential for the KOPIO where a total of  $21.7$  radiation length will be used.

The model developed for the simulation of a Shashlyk module accurately predicts the energy resolution from the module parameters. A comparison of the predicted energy resolution with experimental results is shown in Fig. 6b.23.

### 6b.3.2 Time Resolution

To estimate the time resolution, we measured the time difference for the signals produced by the same shower in two neighbor modules. By using this measurement technique, the 340-MeV photon beam was directed between central module (#5) and left module (#4). The photon energy distributions in the nonet of the Shashlyk modules during the timing measurements, are shown in Fig. 6b.24.

Only events with the full photon energy ( $E_4 + E_5 = 320 \pm 20$  MeV) deposited in these two modules were selected for analysis. The dependence of the time difference dispersion on the energy deposited in one module is shown in Fig. 6b.25. The time difference resolution drops significantly if one of the two deposited energies is close to zero or, alternatively, if one of the energies is close to 340 MeV. Assuming that both modules have the same time resolution  $\sim 1/\sqrt{E}$ , we have obtained from Fig. 6b.25

$$\sigma_T = (90 \pm 10) \text{ psec}/\sqrt{E \text{ (GeV)}}.$$

In the Monte-Carlo simulation of these measurements, we have obtained

$$\sigma_{T4-T5}(E_4 = E_5) = 280 \text{ ps}$$

which is in a good agreement with the experimental value of 285 ps (see Fig. 6b.25).

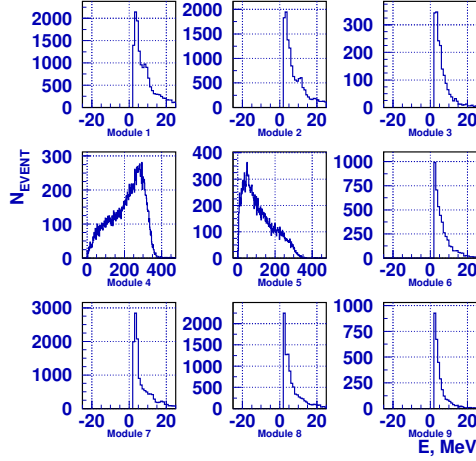


Fig. 6b.24. The typical distribution of photon energy in the nonet of the Shashlyk modules during timing measurements. Here, 340-MeV photons hit the nonet at a boundary between central (#5) and left (#4) modules.

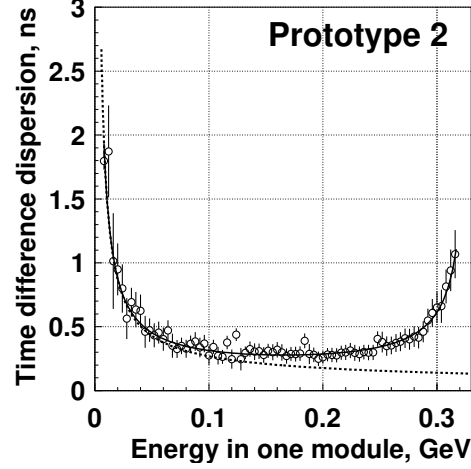


Fig. 6b.25. Experimental evaluation of the time resolution of a Shashlyk module. Solid line is a calculation for a  $90 \text{ ps}/\sqrt{E \text{ (GeV)}}$  time resolution in both modules.

The signals we compare to evaluate the time resolution are strongly correlated because they are produced by the same electromagnetic shower. This may result in a wrong value of the time resolution. For example, the contribution of the longitudinal fluctuation of the shower is suppressed in such measurement. To ensure that our test beam result does not underestimate the actual time resolution, we carried out the Monte Carlo calculation of the time resolution. One can conclude from Fig. 6b.26 that there is no evidence of underestimating the time resolution in our test beam measurement.

### 6b.3.3 Photon Detection Inefficiency

To estimate the photon detection inefficiency due to fiber holes, a prototype 1 nonet was located behind prototype 2 array. The absence of the signal in the front array, while the total photon energy was deposited in the second was interpreted as a penetration of the photon through the first prototype without interaction,

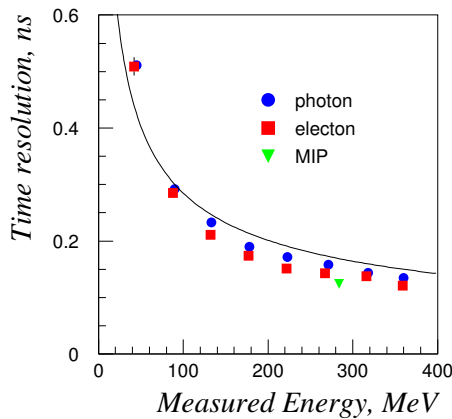


Fig. 6b.26. Results of a Monte Carlo calculation of the time resolution of the Shashlyk module for photon, electron, and Minimum Ionizing Particles (MIP). The solid line corresponds to a  $(90 \text{ ps})/\sqrt{E \text{ (GeV)}}$  time resolution, which has been obtained in a similar Monte Carlo simulation of the test beam measurements.



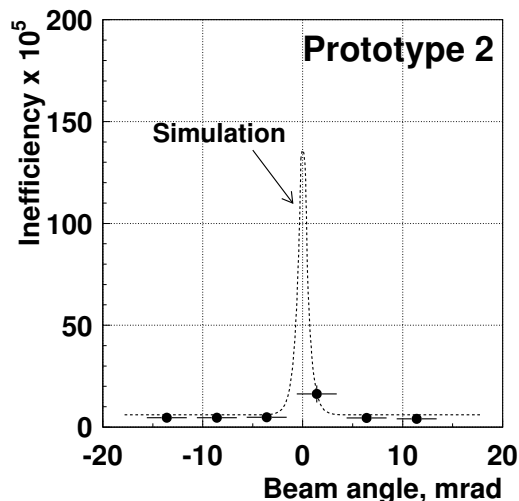


Fig. 6b.27. The dependence of the photon detection inefficiency on the incident angle.

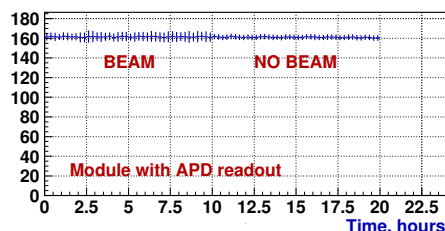


Fig. 6b.28. Illustration of the long-term stability and gain dependence on the rate for the APD readout of the Calorimeter prototypes. The beam intensity was 300 kHz.

*e.g.* through a fiber hole. 250 MeV photons were directed onto the face of the first array. The measured dependence of the photon detection inefficiency on the beam incident angle is compared with the simulation in Fig. 6b.27. The relatively coarse step in the measured angles does not allowed us to accurately compare experimental results with the simulation. However, our measurements clearly indicate that the effect of the WLS fiber holes is negligible if the incident angle is  $\geq 5$  mrad. For such angles, our experimental results agree well with the probability of photon interactions in about 8.25 cm of lead and 45 cm of scintillator.

#### 6b.3.4 Long-term APD Stability

The APD gains were monitored by using LED signals during a run time of 24 hours to test the long-term stability of the APD gain. Experimental data, illustrating the long-term stability of the APD readout of the calorimeter prototypes, are shown in Fig. 6b.28. No APD gain dependence on the photon beam intensity was observed after changing the photon beam rate from 0 kHz to 300 kHz. The variation of the APD gain did not exceed 1%.

#### 6b.4 Mass Production of the Shashlyk modules

Test beam study of the Shashlyk modules prototype showed that this module with APD+WFD readout satisfy the requirements of the KOPIO experiment. The only significant modification in module design will be an increase to 19 radiation lengths. This change may be accomplished with only a minor changes in the manufacturing technology, provided that new modules contain 340 layers of 300- $\mu\text{m}$  lead and 1.5-mm scintillator tiles. According to our experience, the energy and time resolution are expected to be the same as for the tested 15.9- $X_0$  prototypes. Some worsening of the energy resolution due to the new sampling ratio is compensating by the improvements due to the shorter effective radiation length and smaller longitudinal leakage of the shower.

We plan to produce all 1600 modules for the KOPIO calorimeter at IHEP[8], where prototypes were manufactured. Currently, all equipment is ready for mass production of the modules. It is expected that 6 APD-instrumented modules will be produced per day.

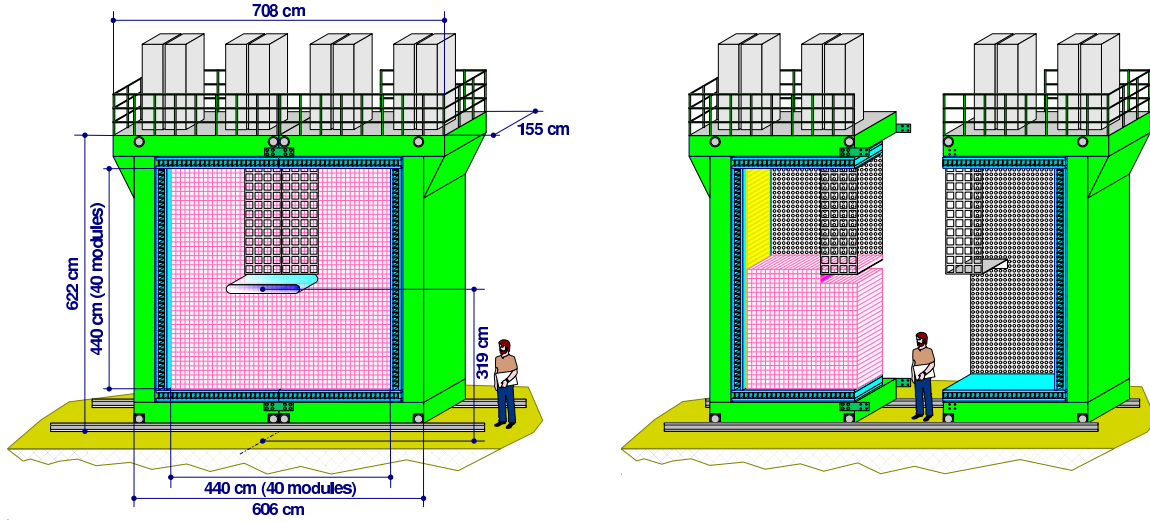


Fig. 6b.29. Calorimeter structure in closed and opened positions.

After the test beam measurements, when we successfully tested API APD, significant progress in the development of the large area APDs has been achieved by RMD Instruments Inc. and Hamamatsu Photonics. Thus the possibility of using other APDs, instead of the Advanced Photonics Inc. 630-70-74-510, is being considered. The technical characteristics as well as the cost will be taken into account.

### 6b.5 Calorimeter Mounting

The Calorimeter will be mounted in a support structure similar to that of the BNL E865[1] and HERA-B[4] calorimeters (Fig. 6b.29). Two requirements on the support structure beyond the simple necessity of structural strength and stability must be met. First, the rear of the Calorimeter must be accessible for maintenance of the photodetectors. This requirement means that the two halves of the Calorimeter must be movable horizontally to a point where the photodetectors are laterally displaced beyond the shield of the downstream sweeping magnet. Second, the modules directly over the beam pipe must be supported such that their weight is not on the pipe. The Calorimeter assembly will be mounted on wheels which roll on railroad tracks.

Two methods of holding the modules in place laterally are being considered. The first is to employ steel straps, about 100- $\mu$ m thick, affixed to the vertical columns of the support structure and running around the modules in half a row, from the edge to the center of the Calorimeter. This method is used in HERA-B and is thus known to be viable.

The second method of supporting the modules laterally is to support the modules with aluminum plates, front and back, each of which cover half the Calorimeter – from the edge to the center (see Fig. 6b.29). Because the thickness of the front aluminum plate can have fewer radiation lengths than a single lead plate in a module, this method of support does not compromise the performance of the Calorimeter.

Supporting the modules over the beam pipe can be accomplished with steel straps for the first method, and by the plates for the second method.

### 6b.6 Calorimeter Cooling System

To provide the required energy resolution of 6% for 250-MeV photons, the APD gain should be controlled with accuracy better than 0.5%. This corresponds to the temperature stability of  $\leq 0.1^\circ\text{C}$  for the API APD. However, if the APD gain is continuously monitored, a cooling system with  $\sim 0.5^\circ\text{C}$  thermo-stability can be used. The other purpose of the cooling system is to reduce the electronic noise. The APD temperature

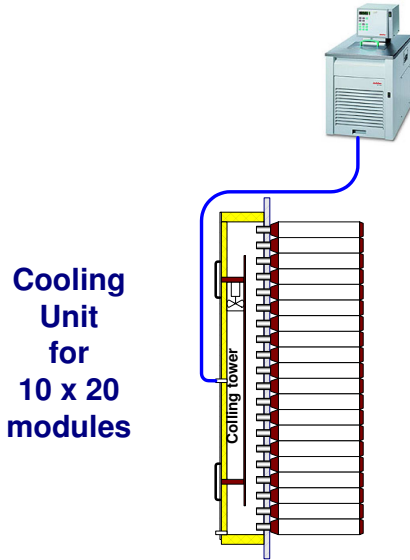


Fig. 6b.30. A sketch of the cooling unit.

of  $15^{\circ}\text{C}$  will allow us to keep the ENC below a 20 electron level, which corresponds to a 0.4 MeV in photon energy.

We plan to employ eight separate thermo-isolated cooling units (Fig. 6b.30) in the Calorimeter, one unit per 200 ( $10 \times 20$ ) channels. The unit operation is based on circulation of a liquid coolant through a heat exchanger, located inside the unit. The estimated total heat flow (mainly due to the air around the Calorimeter and readout electronics) is about 250 W per one unit. Each unit will be equipped with a commercial refrigerated bath circulator, JULABO FP50-HE produced by JD Instruments Inc, with a cooling capacity of 800 W at  $0^{\circ}\text{C}$ , pump capacity of 5 psi, and flow of 20 l/min. To prevent the accumulation of humidity inside the unit, a hermetic design of the unit and a chemical water-absorbing reagent will be employed.

A study by the MECO collaboration of a similar cooling system prototype showed a temperature stability of about  $0.1^{\circ}\text{C}$  during one month of monitoring[19].

### 6b.7 Calorimeter HV System

Because the new Calorimeter photodetector (APD) draws only its photocurrent with typical values much less than 0.1 mA, an economic way to build the Calorimeter HV system is to develop an active, compact, low-current individual HV-unit, mounted directly into each APD housing. This kind of HV system eliminates expensive and bulky HV cables and connectors, lowers the power consumption per individual power supply, and reduces the electrical HV hazard associated with traditional HV supplies.

We tested a new EMCO Corporation LV-HV converter, the C20 with analog control[20] (see Fig. 6b.18) Its performance was found to be satisfactory for the KOPIO calorimeter with APD readout. The technical characteristics of this converter are discussed in the “Photodetector Electronics” section of this report.

### 6b.8 Calorimeter Front-End Electronics

The front-end electronics (FEE) of the Calorimeter will process photodetector signals and provide energy, timing, and trigger information to the experiment’s data-acquisition and trigger systems. For the Calorimeter, the electronics will be designed to be capable of measuring energies with a digitization uncertainty of 0.2 MeV in a dynamic range of 0.5–1000 MeV and the time of arrival with respect to the beam microbunch clock with an uncertainty of less than 100 ps. Operation of the FEE has to be completely pipelined with no dead time. It will also be capable of forming and discriminating the total energy signals and the total number of hits in the Calorimeter. Taking into account the performance requirements for en-

ergy and timing resolutions of the calorimeter and other detectors with PMT or APD readout, our concern about effective and economic way for the energy and timing measurement and, also, our experience of the WFD-data processing, we have chosen a unified WFD design with a 250-MHz coding frequency and 10-bit dynamic range.

The design of the WFD board and the input chain for this board should satisfy the following conditions:

- Full duration times of pulses  $\leq 40$  ns to optimize the energy/time resolution (the signal-to-noise ratio) and the double-pulse resolution in order to avoid strong pile-up effects between consecutive microbunches;
- fast, 250-MHz, flash ADCs with a 10-bit dynamic range;
- an event storage in a 64-microbunch-deep pipeline buffer, providing a 10- $\mu$ s latency;
- transferring of raw data, selected by the L1-trigger, to Crate Data Collection boards at a rate of least 20 Mbytes/sec.

The proposed design of the Calorimeter front-end electronics is based on our beam test experience with the 8-bit 140-MHz WFD and on similar studies in the PHENIX[21] and LHCb[22,23] projects. Schematically, the Calorimeter FEE design is given in in Fig. 8.2 of the “Photodetector Electronics” section.

## 6b.9 Calibration and Monitoring of Calorimeter

To achieve the required energy resolution of the KOPIO Calorimeter,  $\sim 3.0\%/\sqrt{E}$ , an appropriate calibration and monitoring system must be developed.

The ultimate calibration will be done *in situ* by using  $\pi^0$  decays from backgrounds and specially triggered events acquired during the experiment. The advantage of such calibration is that it is carried out under the same conditions and with the same methods as those for the studied process. For example, the Calorimeter may be calibrated together with the Preradiator, by using photon showers distributed between both detectors. The drawback of such a process is that it requires a relatively long period of data accumulation to achieve a sufficient number of calibration events. Thus, two supplemental systems are required: one to pre-calibrate the Calorimeter with an accuracy of a few percent, and another to monitor its performance and restrict the variation of the photodetector gains to the order of 0.4%. We describe below our current ideas about such a system.

### 6b.9.1 Pre-calibration System

We will use cosmic-ray muons for pre-calibration, as we did in Experiment E865[2]. This pre-calibration is based on the assumption that the mean value of signals from cosmic-ray muons passing vertically through Shashlyk modules is approximately the same for all modules. In E865, we were able to pre-calibrate its 600 modules with an accuracy of 4% in one hour, even from a “cold start.” Cosmic-ray muon calibration also provided long term monitoring of the photodetector gains with an accuracy of 1–2%.

This technique simply requires a special trigger that recognizes cosmic muons vertically penetrating the entire Calorimeter. Such a trigger can be formed from a coincidence between the top and bottom horizontal layers of modules, gated between AGS pulses.

### 6b.9.2 Monitoring System

The monitoring system employs light flashers and must satisfy a number of specific requirements:

- high long-term and short-term temperature stability — better than 0.1%;
- short light pulse duration — less than 50 ns;
- small variation in the flash amplitude — less than 0.2%;

- a large number of photons in the light pulse – more than 10,000 photons/channel; and
- variable pulse repetition rate and intensity.

These requirements can be met with Light Emitting Diodes with a brightness of 5–10 Cd that have recently been developed (‘ultra bright LED lamps’). We plan to use the NSPB-500S to inject blue light into the scintillator.

The monitoring system is based on an electronic method of stabilization of the LED light output by means of an optical feedback provided by a PIN photodiode[24,25]. The PIN diode monitors the LED light output, and a feedback loop employs this signal to adjust the driving pulse amplitude of the LED. As shown in references[24] and[25], the PIN diode has a temperature coefficient  $\sim 4 \times 10^{-4}/^{\circ}\text{C}$ , with a long-term stability of better than  $10^{-4}$ . As a result, the monitoring system described in Ref.[24] shows a long-term stability of better than 0.1%.

A block diagram of the Calorimeter LED monitoring system is described in the “Photodetector Electronics” section of this report. From the analysis of existing monitoring systems and our preliminary test measurements of small prototypes, we conclude that the this type of monitoring system will have long-term and short-term stability that meets our 0.1% requirement. The monitoring system will also serve as a pre-calibration of the module readout chain at the 10% level.

## 6b.10 Summary

Modules for a KOPIO Shashlyk Calorimeter with energy resolution

$$\sigma_E/E = (1.96 \pm 0.1)\% \oplus (2.74 \pm 0.05)\%/\sqrt{E \text{ (GeV)}},$$

time resolution

$$\sigma_T = (90 \pm 10) \text{ psec}/\sqrt{E \text{ (GeV)}},$$

and a photon detection inefficiency due to Fiber holes of

$$\epsilon \leq 5 \times 10^{-5} \quad (\Theta_{\text{beam}} > 5 \text{ mrad})$$

have been constructed and experimentally tested. The characteristics experimentally determined for the Calorimeter prototype well meet the design goals of the experiment.

To optimize the Calorimeter module design, a Monte Carlo simulation model of the Shashlyk module response to incident particles, based on experimental data, was developed. It includes the effects of shower evolution, light collection in scintillator tiles and light transmission in WLS fibers, the response of the photodetector, and noise of the entire electronic chain. This model describes the experimental data very well.

The readout chain has been modeled on existing systems and fits well in the overall KOPIO readout scheme. The readout technique used for the Calorimeter will be used for other photodetector systems in the apparatus. Monitoring and calibration systems have also been designed based on existing technology. They will well meet the required precision and stability necessary to maintain the energy resolution of the Calorimeter,

The mechanical issues in mounting a large calorimeter have been addressed and solved in existing detectors. This fact also gives us confidence in our cost and manpower requirement estimates.

## References

1. G.S. Atoyan, *et al.*, Nucl. Instr. and Meth, **A320**, 144 (1992).
2. R. Appel *et al.*, Nucl. Instr. and Meth. A **479** 349 (2002).
3. L. Aphecetche, *et al.* [ The PHENIX Collaboration ] Nucl. Instr. and Meth. A **499**, 521 (2003).
4. G. Avoni *et al.* [The HERA-B ECAL Collaboration], Nucl. Instr. and Meth. A **461**, 332 (2001).

5. F. Muheim [For the LHCb Collaboration], Nucl. Instr. and Meth. A **462**, 233 (2001).
6. G.S. Atoian, *et al.*, Nucl. Instr. and Meth. A **531**, 467 (2004).
7. GEANT, Detector description and simulation tool, CERN Program Library, Long Writeup W5013 (1994).
8. <http://www1.ihep.su/ihep/ihepsc/index.html>.
9. G. Atoian *et al.*, *Test beam study of the KOPIO Shashlyk calorimeter prototype*, in Proceedings of the Eleventh International Conference on Calorimetry in Particle Physics, Perugia, Italy, 29 March – 2 April, 2004, Editors Claudia Cecchi, Patrizia Cenci, Pascuale Lubrano, and Monica Pepe, World Scientific, 2005, p.55.
10. Kuraray Co., LTD, *Scintillation materials. Plastic fibers*.
11. S.P. Stoll, PHENIX Note #245 (1996).
12. I.G. Britvich *et al.* Instr. Exp. Tech. **44**, 472 (2001).
13. I.G. Britvich *et al.* Instr. Exp. Tech. **45**, 644 (2002).
14. A. Soldatov, private communication.
15. J. Marler *et al.*, Nucl. Instr. and Meth. **449**, 311 (2000).
16. R.J. McIntyre, IEEE Trans. Electron Devices **ED-13**, 165 (1966).  
P.P. Webb, R.J. McIntyre, J. Conradi, RCA Review **27**, 164 (1966).  
R.J. McIntyre, IEEE Trans. Electron Devices **ED-19**, 703 (1972).
17. R.J. McIntyre, *A New Look at Impact Ionization-Part I: A Theory of Gain, Noise, Breakdown Probability, and Frequency Response*, IEEE TRANSACTIONS ON ELECTRON DEVICES, VOL. 46, NO. 8, 1623 (1999).  
P. Yuan *et al.*, *A New Look at Impact Ionization-Part II: Gain and Noise in Short Avalanche Photodiodes*, IEEE TRANSACTIONS ON ELECTRON DEVICES, VOL. 46, NO. 8, 1632 (1999).
18. D. H. Dowell *et al.*, Prog. Rep. BNL 37623 (1985), p. 29.
19. R. Dzhilkibaev, private communication.
20. <http://www.emcohighvoltage.com/>
21. A.L. Wintenberg *et al.*, PHENIX Project, internal paper, 2000.
22. The LHCb Technical Proposal. CERN/LHCC 98-4.
23. “*The Front-End Electronics for LHCb calorimeters*”, LHCb 2000-028.
24. W.L. Reiter *et al.*, Nucl. Instr. and Meth. **173**, 275 (1980).
25. A. Fyodorov *et al.*, Nucl. Instr. and Meth. **A413**, 352-356 (1998).

## 6c KOPIO Photon Veto System

The main concern in measuring  $K_L^0 \rightarrow \pi^0 \nu \bar{\nu}$  decays is rejection of background, most of which occurs when two photons from a  $K_L^0 \rightarrow \pi^0 \pi^0$  decay are missed. While kinematic reconstruction of the  $\pi^0$  gives a handle for suppressing such backgrounds, the primary background suppression technique involves obtaining the maximal efficiency for detecting any extra photons. KOPIO requires state-of-the-art photon veto detection efficiency *i.e.* better than 0.9999 per photon with energies above 150 MeV with minimal loss from random vetos. Because the momentum of the  $K_L^0$  in KOPIO is determined by time of flight, all elements of the photon veto system must have good time resolution of about 200 ps for photon energies of 100–200 MeV. The full solid angle around the 4-m-long kaon decay region must be covered.

Sandwich counters of lead and plastic scintillator will be used primarily for the KOPIO photon veto detectors. In addition to the PR/CAL system which covers the forward decay region, and the Catcher covering the direct downstream beam region, the Photon Veto (PV) system includes the Upstream Photon Veto wall (US), the Barrel Veto (BV), the Magnet Photon Veto (MPV), and the Downstream Photon Veto (DS). The PV systems will be described in this section.

The relative locations of the PV system in the setup are shown in Fig. 6c.1. The BV is assembled of Shashlyk modules. The other detectors are made of logs with readout at both ends. Because the BV is also used in some measurements of signal events as mentioned in Sec. 3, it features a high light output and fine sampling segmentation appropriate for energy measurements. The log design provides readout segmentation over its thickness. The light from the scintillators is read out through embedded Wavelength-Shifting fibers (WLS). A two-ended readout in the logs provides good timing as well as redundancy for failed channels. The WLS fibers in the logs are placed in grooves that run along the plastic scintillator slabs with a spacing of 10 mm. In the Shashlyk modules, the fibers pass through holes in the scintillator and lead plates. The large volume of plastic scintillator needed for coverage of a very large solid angle, and the extremely high detection efficiency required to reach the physics goals, makes the design of the veto system very challenging.

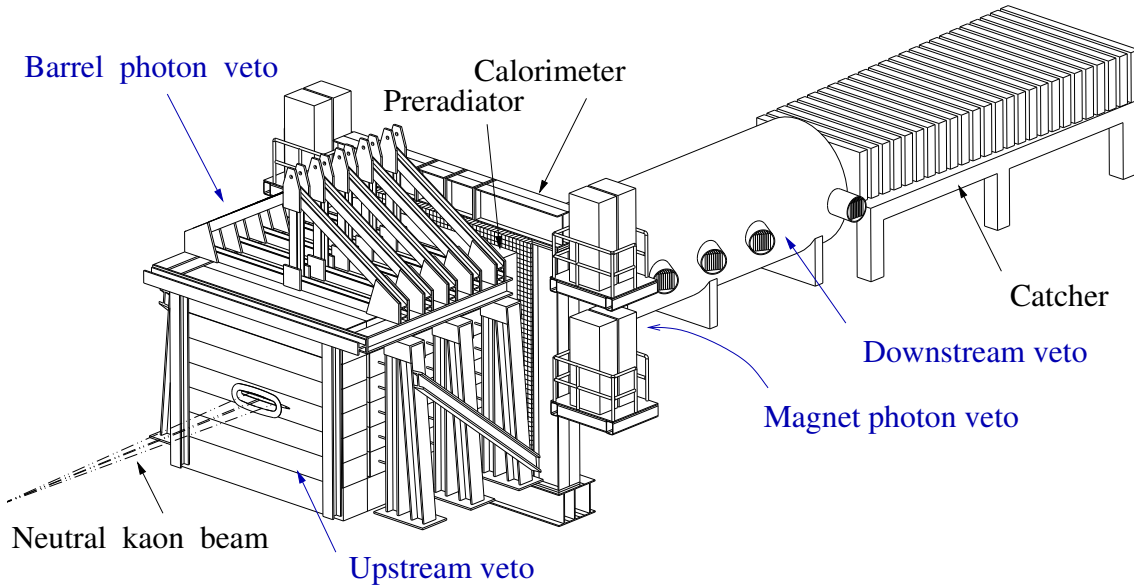


Fig. 6c.1. Positions of the photon veto detectors along the beam. The Magnet Photon Veto is mounted inside the D4 sweeping magnet, which is placed behind the Calorimeter.



## 6c.1 Barrel Veto Detector

### 6c.1.1 Barrel Shashlyk Concept

The Barrel Veto (BV) surrounds the kaon decay volume and the sides of the Preradiator as shown in Fig. 6c.1. It is the largest of the photon veto detectors with a total volume of about  $16 \text{ m}^3$  and 55-t weight. The initial design for the BV envisaged a detector assembled from logs. The current design is a cylindrically shaped BV assembled from 840 Shashlyk modules. This design is illustrated in Fig. 6c.2. The length of the BV is 4 m, and its inner diameter is 2.5 m.

The development of Shashlyk-type detectors in recent years has been impressive. Shashlyks can now provide timings that are about the same as for logs, yet with higher light output and better energy resolution. The fine-sampling structure of a Shashlyk produces good photon detection efficiency without an expensive increase in the number of applied WLS fibers, as would be required in logs. One of the possible problems, holes made in the Shashlyk medium to incorporate the readout fibers, was investigated with simulation tools. Due to the angular distribution of the incident photons, these holes in the BV modules contribute a negligible inefficiency compared with other sources. Furthermore, the cylindrical Shashlyk version of the BV appears to be preferable for the mechanical design of the support structures. Each of 20 rings has 42 Shashlyk modules shaped as truncated pyramids. Altogether, the rings cover a 4-m-long kaon decay volume. The modules are attached at their back ends to metal ring structures of 4-m outer diameter. Five rings form an independent section. The sections slide on rails in the downstream direction to open access inside the BV for service to the vacuum region and the charged-particle veto detectors. The method of supporting a Shashlyk module from an end was checked with the modules for the PHENIX calorimeter at the RHIC facility. A module attached to a wall was loaded at its free end with a similar module, and the deviation at the free end was measured to be about 0.1 mm. In a ring configuration, this type of deformation does not matter as the ring will be loaded with the modules in a horizontal plane. Then the ring is then lifted into the vertical position. Shashlyk ring assemblies are shifted in the azimuthal plane relative to their neighbors so as to close the gaps in polar angles between modules.

A few prototype modules for the Shashlyk BV were manufactured at the IHEP Scintillation Factory. An assembled module without WLS fibers is shown in Fig. 6c.3. Real modules for the BV will be roughly twice as large as those made on the base of existing technology for the KOPIO Calorimeter Shashlyks. A total of 240 Pb/Sci layers was assembled with two scintillator-molded plates per layer. A truncated pyramid shape was obtained by slicing the two sides of the whole module with a milling cutter.

Segmentation of the BV is defined by the following considerations. Cost restricts the number of modules. The module size is constrained by the background rate per readout channel and the algorithms for hit-pattern recognition. As a compromise, the cross-sectional size was chosen to be roughly  $20 \times 20 \text{ cm}^2$  at the front face.

### 6c.1.2 Optimization of BV Shashlyk Modules

The scintillator tile thickness was fixed to be 1.5 mm. The KOPIO Calorimeter Shashlyks made with such tiles produce about 32 photoelectrons (p.e.) per MeV of visible energy. Increasing the thickness would lead to a longer length of the module, and thus a wider spread of the electromagnetic shower. A larger detector volume deteriorates the timing and background conditions. Thinner scintillator tiles could change the light collection efficiency in the modules as well as reduce the sampling ratio between the active and passive media.

The thickness of a single lead layer and the radiation length of a module for photon detection efficiency were investigated. Figure 6c.4 shows the punch-through and sampling inefficiencies at different thicknesses of a single lead layer. The number of layers varies for a fixed radiation length. Simulations were done for 20-MeV photons, being the most difficult to detect. The incident angle of  $30^\circ$  with respect to the normal to the surface is a typical average angle with which the photons hit the BV. The detection threshold is 0.5 MeV. The optimum lead thickness for a fixed radiation length was taken to be the point where the punch-through inefficiency is close to the sampling one. For  $17 X_0$ , the optimum lead thickness is 0.55 mm.

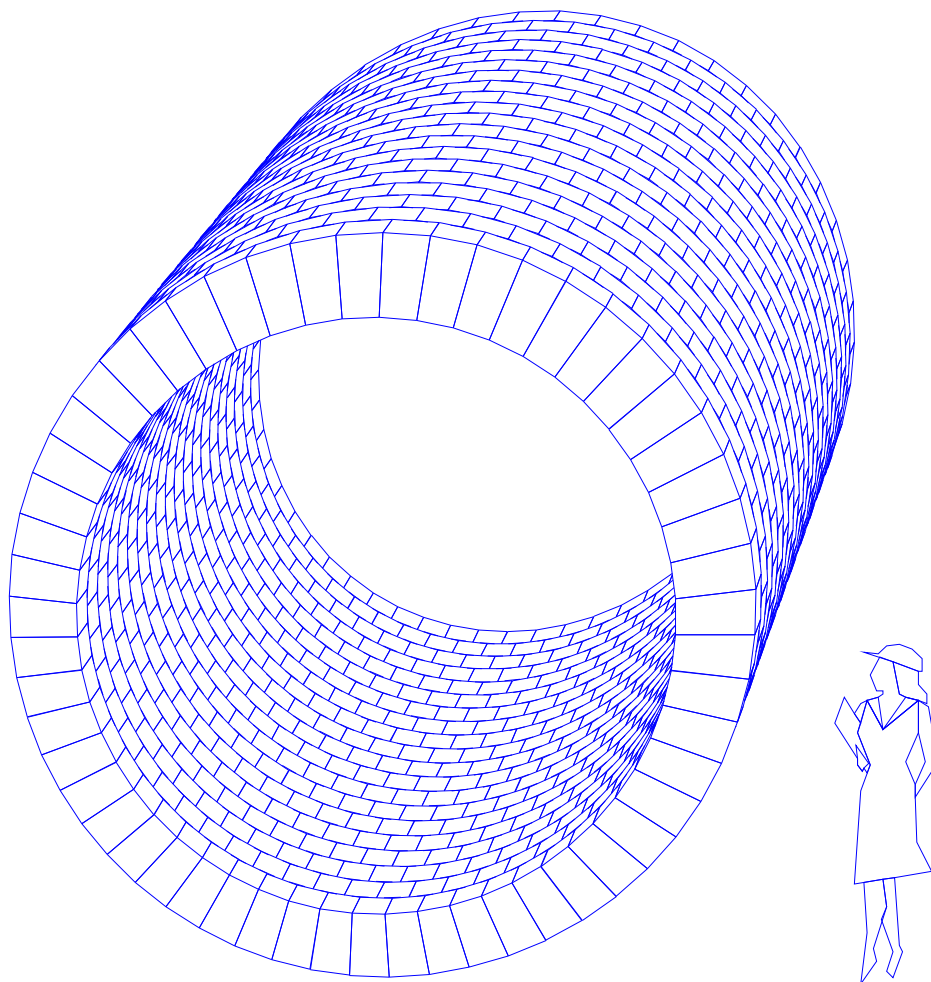


Fig. 6c.2. Cylindrical Barrel Veto assembled from 840 Shashlyk modules. Shashlyk rings of 2.5-m inner diameter are shifted in the azimuthal plane relative to neighboring rings so as to close the gaps in polar angles between modules.

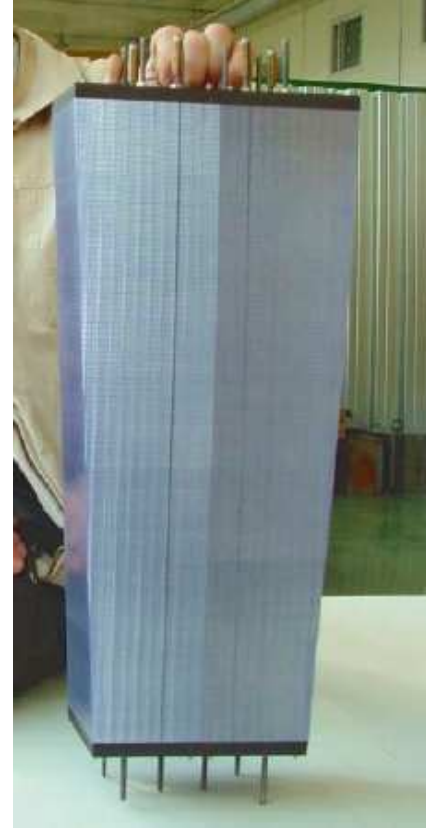
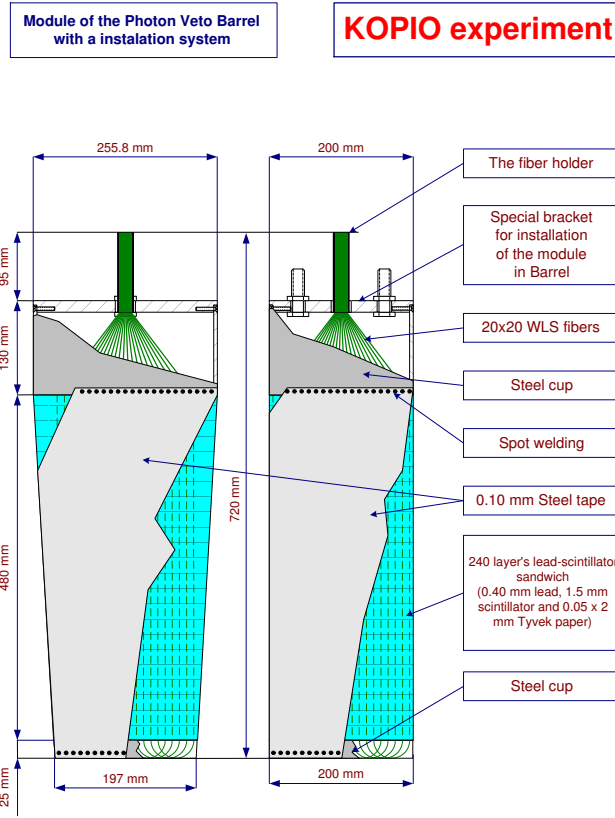


Fig. 6c.3. Prototype Shashlyk module for the photon Barrel Veto.

The thickness becomes 0.5 mm for  $19 X_0$ . As shown in Fig. 6c.4, there is almost no advantage in making the lead thinner than 0.4 mm so as to obtain a better sampling inefficiency, which is close to  $10^{-4}$  for 20-MeV photons. Increasing the number of radiation lengths from 17 to  $19 X_0$  reduces the punch-through inefficiency to the level of the sampling one. For 0.5-mm/1.5-mm Pb/Sci segmentation, the visible energy fraction is 22%. Photonuclear interactions and the desired energy resolution are the main reasons for reducing the lead thickness to 0.4 mm. The punch-through inefficiency versus energy is shown in Fig. 6c.5 for normally incident photons. Due to the angular distribution of photons, a  $17-X_0$  module corresponds to  $19-20 X_0$  of effective radiation length.

A BV assembled of Shashlyks was simulated with a realistic kaon beam model in order to obtain photon energy and angle distributions. The following Shashlyk parameters were applied: 0.5-mm/1.5-mm Pb/Sci layers, 190 layers ( $17 X_0$ ), 0.1-mm reflective wrapping, and a 0.25-mm empty gap between modules. The resulting inefficiencies shown in Fig. 6c.6 are almost an order of magnitude smaller than the inefficiency specified for KOPIO in Sec. 6f. Photonuclear interactions were not taken into account in this study. The visible energy threshold was 0.5 MeV, corresponding to about 15 p.e. The high light output of the Shashlyk modules enabled a reduction of the detection threshold, which is especially important for the photonuclear inefficiency. A fast Monte-Carlo study (see Sec. 13.1) of kaon decays shows that the photon veto inefficiency is insensitive to the BV module radiation length from  $17.2 X_0$  and deeper. So the radiation length of  $18 X_0$  was selected for the BV Shashlyk modules. The final BV module sampling structure is 240 layers of 0.4-mm lead and 1.5-mm scintillator. The spacing between the WLS fibers is about 9 mm as in the Calorimeter Shashlyk modules so that the total number of fibers thorough the module is about 460. Such spacing provides a high light yield as well as good light collection uniformity across the module.

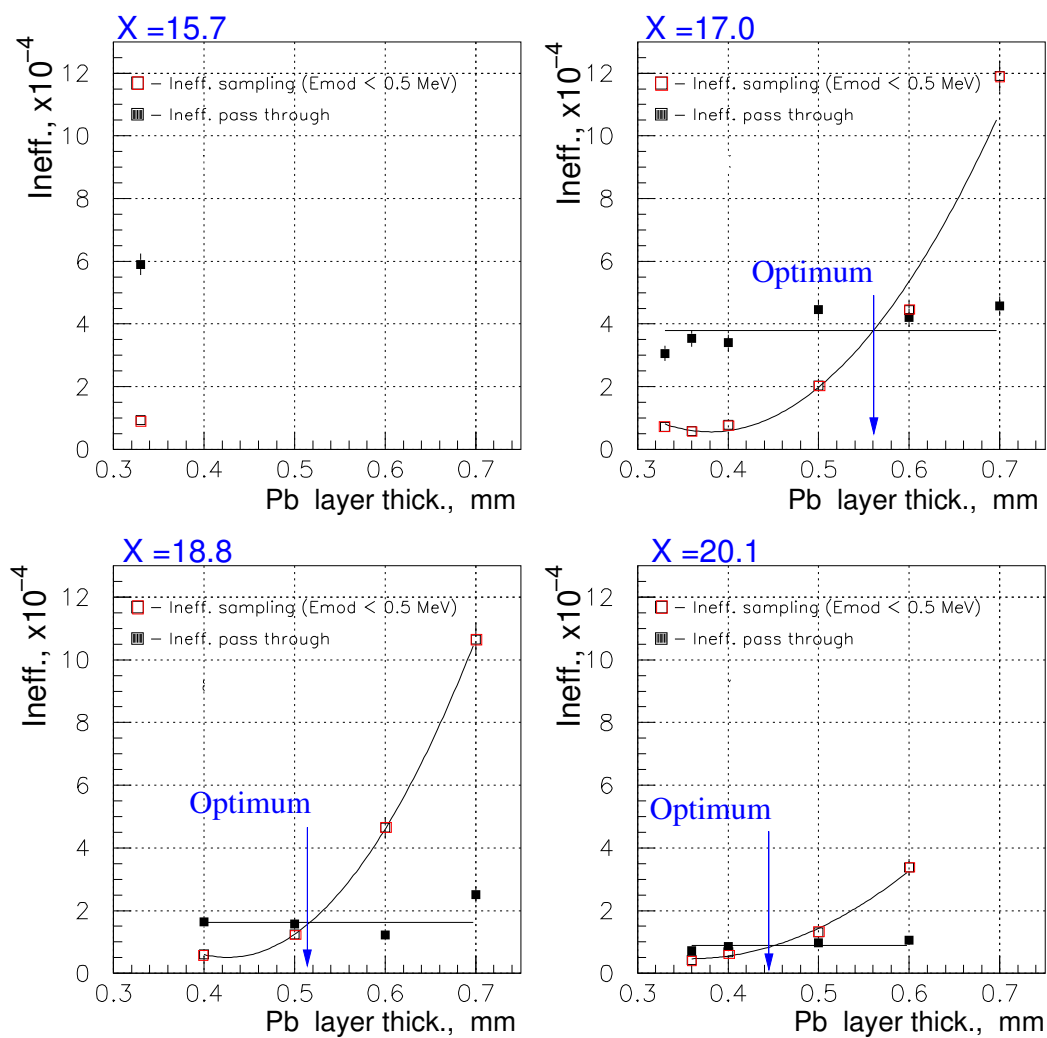


Fig. 6c.4. “Pass-through” and sampling inefficiencies vs. the lead-layer thickness at fixed module radiation length, and with 1.5-mm-thick scintillator tiles. Photons of 20 MeV are incident at an angle of  $30^\circ$  with respect to the normal to the surface.

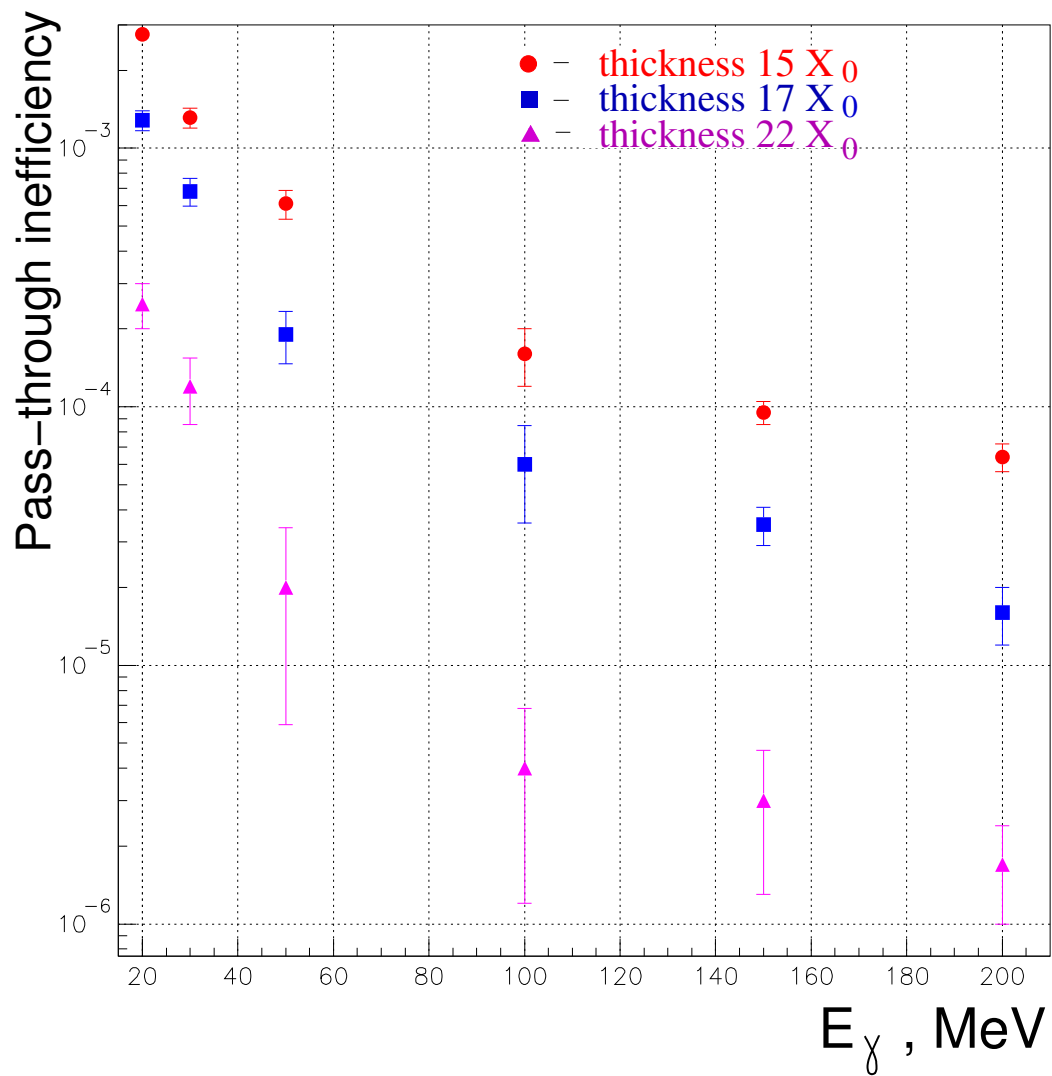


Fig. 6c.5. “Pass-through” inefficiencies vs. the energy of normally incident photons for different radiation lengths.

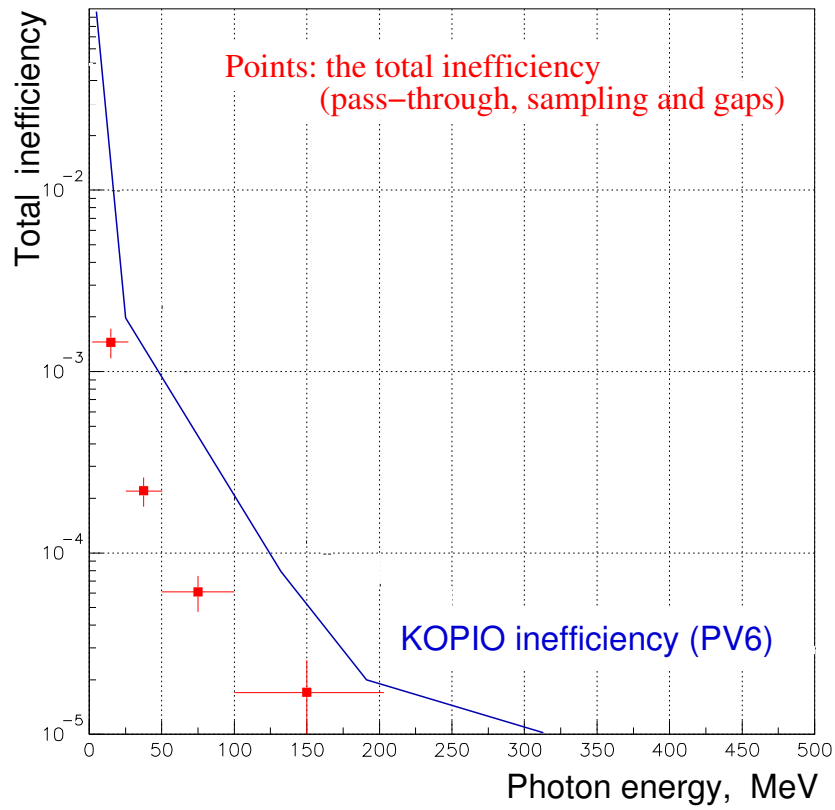


Fig. 6c.6. Total photon inefficiency (without photonuclear interactions) in the BV with a realistic kaon beam model and parameters as described in the text. The detection threshold is 0.5 MeV. The solid line is the inefficiency expected for the KOPIO detectors in Sec. 6f.

The effects of an increase in the gap between the modules in the BV configuration were also considered. The inefficiencies shown in Fig. 6c.7 show a weak dependence on the gap size, largely because the distribution of photon emission is mainly in a forward direction. Analytical estimates show a quadratic dependence of the projective losses on the gap width, which was confirmed by simulation results. The design target for the gap tolerance between the Shashlyk modules was set at 0.25 mm.

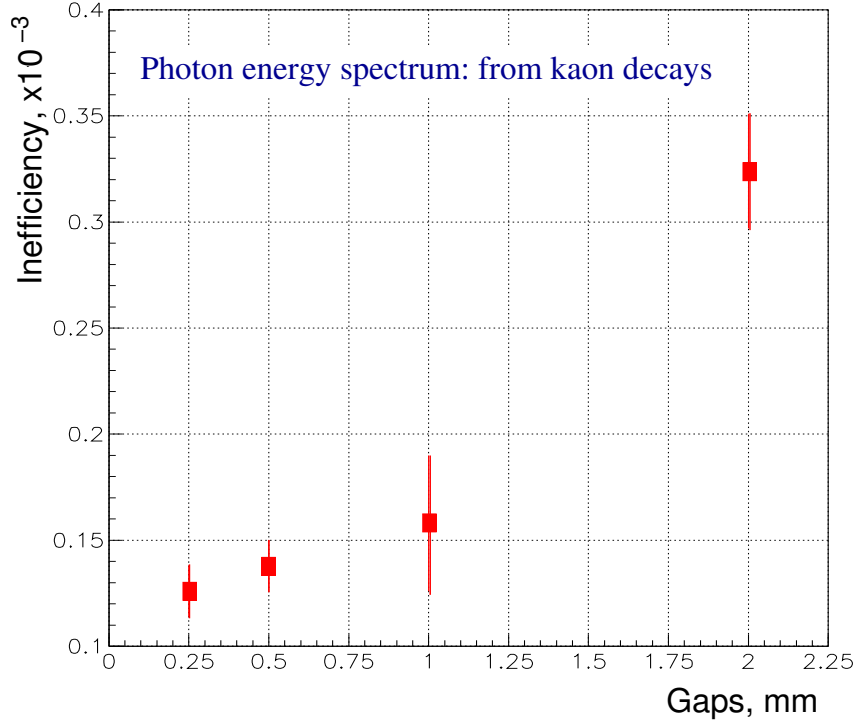


Fig. 6c.7. Integral photon detection inefficiency in the BV versus the size of the empty gaps between the Shashlyk modules.

## 6c.2 Log Veto Detectors

### 6c.2.1 Log Sandwich Design Issues

The log Photon Veto detectors in KOPIO will consist of many layers of long 7-mm plastic scintillator slabs interleaved with lead foil of 1-mm thickness. A schematic view of a sandwich element (module) is shown in Fig. 6c.8. A full log detector will be built with such modules. The WLS fiber readout technique provides uniform light collection over the area of the scintillator. The flexibility of the fibers eliminates the need for complicated systems of lightguides, which could pose serious problems for the veto coverage. A PMT views a bundle of about 200-300 WLS fibers at each end.

A lead thickness of 0.5–1.5 mm has been utilized in various experiments[3,4,5]. Test measurements at KAMI indicated that 0.5-mm-thick lead absorbers show no improvement over 1-mm-thick lead for detection efficiency, the most crucial parameter, although this experimental result conflicts the simulation results. We currently plan to use absorbers made of 1-mm lead foil so as to reach a high visible fraction of light with reasonable segmentation.



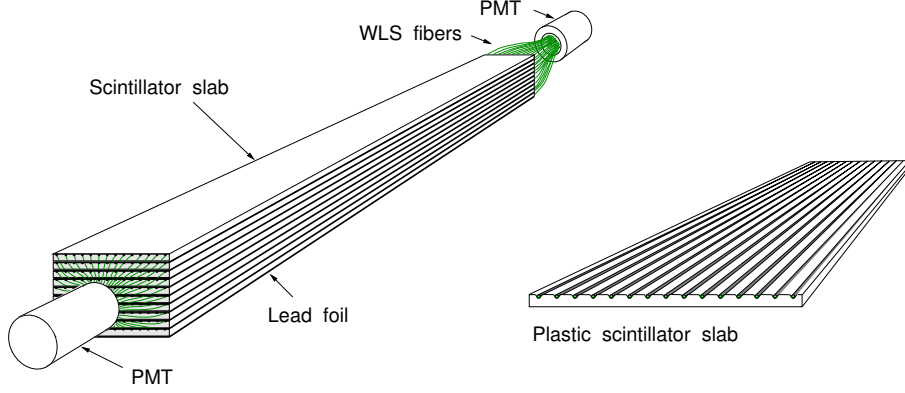


Fig. 6c.8. Schematic view of a veto sandwich module.

An approximate formula for the resolution of a typical Pb/Sci sampling calorimeter was published in Ref.[6]:

$$\sigma[\%] = \frac{14.5}{\sqrt{E_\gamma [GeV]}} \sqrt{\frac{t}{X_0}} \cdot \sqrt{1 + 0.57/n}, \quad (6)$$

where  $t$  is the thickness of the lead plates,  $X_0$  is the radiation length of lead, and  $n$  is the number of photoelectrons per minimum ionizing particle in a single scintillator sample (layer). Therefore, for  $n > 5$ , the photostatistics does not degrade the energy resolution, which is instead dominated by sampling fluctuations. However, it should be kept in mind that the detection efficiency could be very sensitive to  $n$ . It is interesting to note that  $\sigma$  does not depend on the scintillator thickness, a result of empirical approximations to data obtained from operating sampling calorimeters. Actually, thicker scintillators increase the visible fraction, which improves the energy resolution (see Fig. 6f.1). The formula is useful for roughly evaluating the real energy resolution of a sampling detector.

In applying 1 mm of lead foil, we expect (from the formula) to obtain a resolution no worse than  $\sigma = 6.1\%/\sqrt{E}$ , although the pure sampling fluctuations simulated by GEANT contribute only  $\sigma = 3.6\%$  for a structure of 1 mm of lead and 7 mm of scintillator. Log detectors in KOPIO will be used only for vetoing, so a calorimeter performance is not required of them. The energy resolution is taken as a parameter that affects the detection efficiency. In addition, good resolution can be used in the event reconstruction to avoid spurious vetoing.

While the light yield of a single active layer (a scintillator slab) does not in practice affect the energy resolution beyond some minimum photostatistics, the light output is very critical for detection of low-energy photons with the required efficiency. To increase the visible fraction of shower energy, the first layers of the veto detector can be made with thin lead foil of 0.5 mm.

Another important consideration for achieving a high light output is a requirement that the time resolution be better than  $(80 \text{ ps})/\sqrt{E_\gamma [GeV]}$ . Precise timing allow suppression of accidental hits and avoids extra vetos. Readout at both ends is required to obtain excellent time resolution. The WLS fiber readout gives better timing compared to a readout with lightguides for the same number of detected photoelectrons because there is much smaller photon path-length dispersion along a fiber than in a bulk scintillator.

The sampling segmentation of a sandwich, *i.e.* the thicknesses of the lead and scintillator, determines the main detector parameters such as sampling fluctuations, localization of an electromagnetic shower, energy resolution, timing, and inefficiency. The combination of the geometrical size and the number of layers in a single module also provides a segmentation. There are two main methods for increasing the light output per active layer: enhanced fiber readout and larger scintillator thickness. The latter one has cost advantages.

Moreover, the thicker active layer increases the visible part of deposited energy, thereby improving the energy resolution and efficiency.

Taking into account both the cost and the physics objectives, the proposed module structure is 16 layers of 7-mm-thick chemically etched scintillator and the same number of 1-mm-thick lead. The width of the layers depends on the location of modules, and the length is variable from 1 to 3.6 m.

### 6c.3 Tests of Log Sandwich Modules

#### 6c.3.1 Design of the Tested Modules

The extrusion technique of long grooved scintillators was developed at the Technoplast Factory, Vladimir, Russia. The results of tests of single extruded counters and a sandwich module prototype are reported in Ref.[7]. The main results are summarized in Table 6c.1. Although the attenuation length of extruded

Table 6c.1. Parameters of extruded polystyrene counters with 4.3-m-long WLS fiber readout. Fibers were fast Bicron BCF92 or BCF99-29 types. The counter made of BC404 scintillator is also shown for comparison.

Counter thickness mm	Spacing mm	Fiber type	Light yield p.e./MIP	$\sigma_t$ ns
7	19	multi-clad	11.2	
7	10	multi-clad	19.6	0.85
7	10	single-clad	14.4	0.87
7	7	multi-clad	26.2	0.71
7	7	single-clad	20.8	0.76
3	10	multi-clad	8.5	0.92
7 (BC404)	7	multi-clad	32	0.65

polystyrene scintillator for light is about 30 cm, the one with a WLS fiber readout produces 80% of the light yield of BC404 scintillator. Single-clad and multi-clad Bicron fibers provide nearly the same time resolution. Instead of using a wrapping material for a reflector, a novel technique was used: the scintillator was etched by a chemical agent that produces a micropore deposit over the plastic surface, following which a diffuse film is fixed in a settling tank. The thickness of the deposit (30-100  $\mu\text{m}$ ) depends on the etching time. An advantage of this approach over the commonly used white diffuse papers is an almost ideal contact of the reflector with the scintillator. Moreover, it provides the option of gluing a lead sheet to the reflector-covered plastic, which facilitates the assembly of a sandwich unit. A small sandwich assembly of five lead-plastic layers glued together with a high-viscosity polyurethane glue was tested. It was found that, after gluing, there was a reduction in the light output by about 6%, but then no subsequent degradation in the light yield was observed for two months.

Two straight modules have been manufactured at the Uniplast factory (Vladimir, Russia). Extruded scintillator slabs 7-mm thick and 1-mm lead plates were fixed together in a monolithic block by an elastic polyurethane glue. The glue does not soak into the micropore chemical reflector. The number of Pb/Sci layers in a single module is 15. The module width is 150 mm. Single-clad Bicron BCF-92 fibers of 1-mm diameter were attached with Bicron BC-600 optical glue into 1.5-mm-deep grooves which run along the slab with 7-mm spacing. The sandwich module is 4 m long. The WLS fibers which extend beyond the body of the module are 4.5 m long. FEU-115M phototubes with a green-sensitive photocathode view a bundle of 315 WLS fibers at each end through silicone cookies. The modules are wrapped in black light-isolation paper.

To manufacture the modules, single-clad fast Bicron fibers were collected from different sources. Different color tones of green were visually observed among the fibers. Test measurements also showed that the quality of the fibers was not uniform. However, these were the only fibers available.

### *Light output*

Two trigger counters selected cosmic minimum ionizing particles (MIPs) that passed through the sandwich modules that were placed one above another. The upper trigger counter was 15-mm wide and 80-mm long to localize the hit position. The four PMT signals from the modules were sent to analogue fan-outs where they were distributed to charge-sensitive ADCs and leading edge discriminators. Before measuring the module response, the single-photoelectron peak of each phototube was calibrated and these values were used to calculate the light yields. Previous experience with FEU-115M PMTs showed that the single-photoelectron peak can drift by  $\sim \pm 5\%$ . The accuracy of the light-yield measurements is determined mainly by this systematic error.

The light yield was scanned along the modules in steps of 30 cm. Results are shown in Fig. 6c.9. The first module yielded about 195 p.e./MIP at the center, corresponding to 9 p.e./MeV, and over 300 p.e./MIP near the ends. The second module yielded 160 p.e./MIP at the center. The smaller light yield is explained by the varying quality of available WLS fibers that resulted in a shorter attenuation length for the second module. The light-yield attenuation curves were fitted with a sum of two exponents. At distances greater than 1 m, the attenuation length of fast Bicron fibers was found to be 333 cm in the first module, and 280 cm in the second module.

The stability of the light output of the first module is shown in Fig. 6c.10. The reference point is the module center. During the first five months of testing, the trigger counters were moved along the module. Subsequently, the test bench was fixed to periodically read out the data. As can be seen in Fig. 6c.10, the light yield is stable over two years within a 5% systematic error.

The second module was subjected to a sagging test. During the test, both ends rested on supports and the sag was measured as a deviation of the module center from the straight horizontal level. Results are shown in Fig. 6c.11. The initial deviation was 2 cm. After two weeks, flexing of the module under its own weight led to fast uncontrolled bowing. However, the effect of the sag on the light yield is rather weak.

A single module was manufactured with multi-clad Kuraray Y11 WLS fibers of 1-mm diameter, which have a longer decay time. The light yield of this module was 500 p.e./MIP from both ends, or about 24 p.e./MeV. It is a factor of 2.5 larger than the light output for the straight sandwich modules, due to the new fibers. The long attenuation length was measured to be 4.3 m. Although Y11 fibers have a longer decay time than Bicron ones, the measured time resolution of  $\sigma_t = 320$  ps is close to the result (300 ps) for the straight modules. After eight months, the measured light yield at the center showed no change.

### *Timing*

A time-amplitude correction was applied to all signals from the sandwich modules. To suppress the timing spread caused by the trigger counters, the combination  $(\text{TDC}_{\text{left}} - \text{TDC}_{\text{right}})/2$  was used. The timing spectra obtained in this way at the module centers are shown in Fig. 6c.12. The time resolution is 300 ps for the first module, and slightly worse for the second module. Cosmic MIPs deposit 21 MeV in the scintillator of a single module. The combination  $(\text{TDC1}_{\text{left}} + \text{TDC2}_{\text{left}} - \text{TDC1}_{\text{right}} - \text{TDC2}_{\text{right}})/4$  produces a resolution of 235 ps.

The dependence of the resolution on the light output is shown in Fig. 6c.13. Only central values are shown because the error is determined by unspecified systematic factors. Fitting the points with the root-mean-square (rms) law yields  $\sigma_t[\text{ps}] = 4330/\sqrt{E[\text{p.e.}]} + 2.7$ , where  $E$  is the light yield in photoelectrons. Taking into account that the visible fraction for a module is 0.4, the time resolution for photons can be expressed as  $\sigma_t[\text{ps}] = 72\text{ps}/\sqrt{E_\gamma[\text{GeV}]} + 2.7$ . Figure 6c.14 shows the time resolution for the first module over two years.

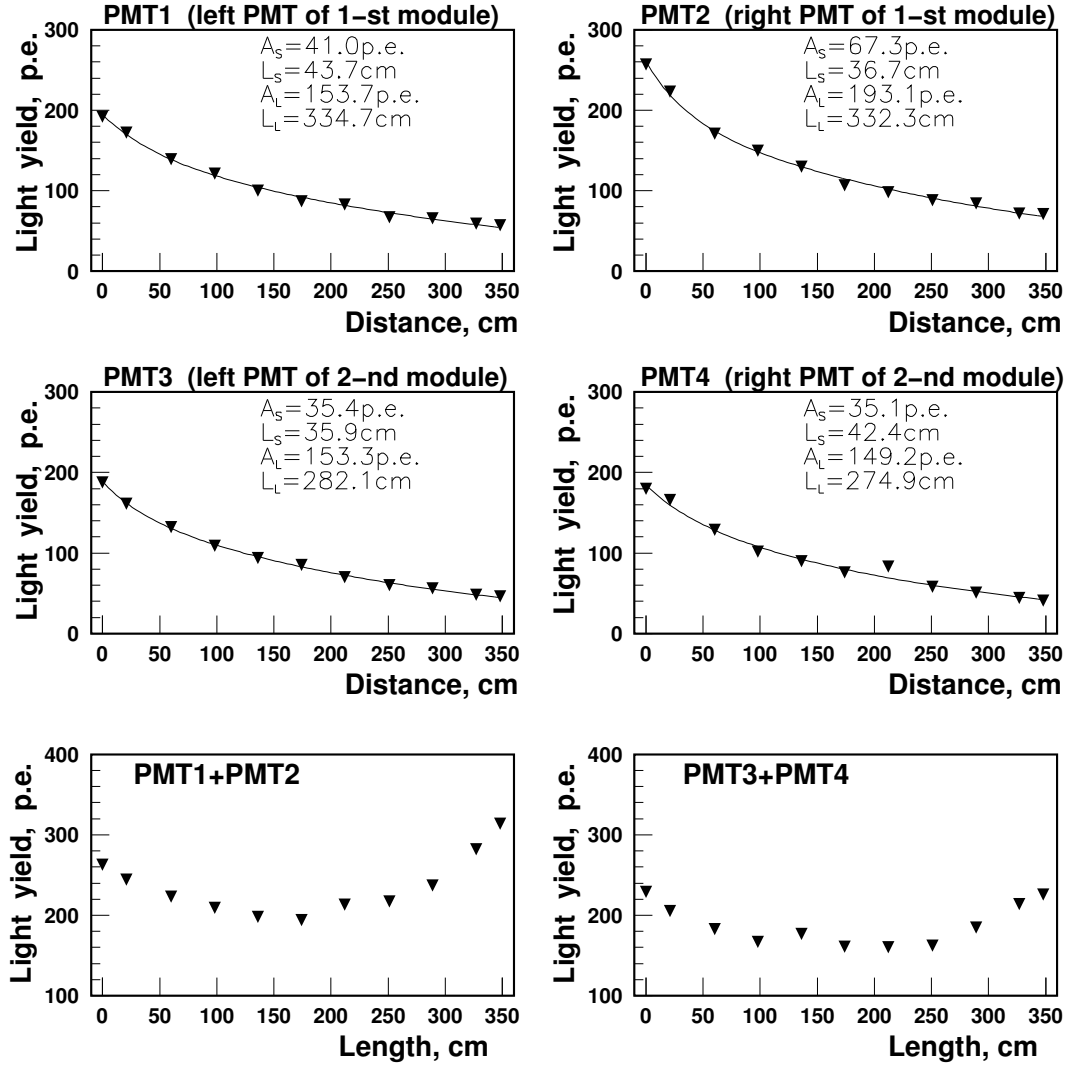


Fig. 6c.9. Light yield along the sandwich modules. The outermost points were taken at a distance of 25 cm from the module edges. The attenuation curves were fitted with the function  $A = A_s \cdot \exp(-\frac{x}{L_s}) + A_L \cdot \exp(-\frac{x}{L_L})$ .

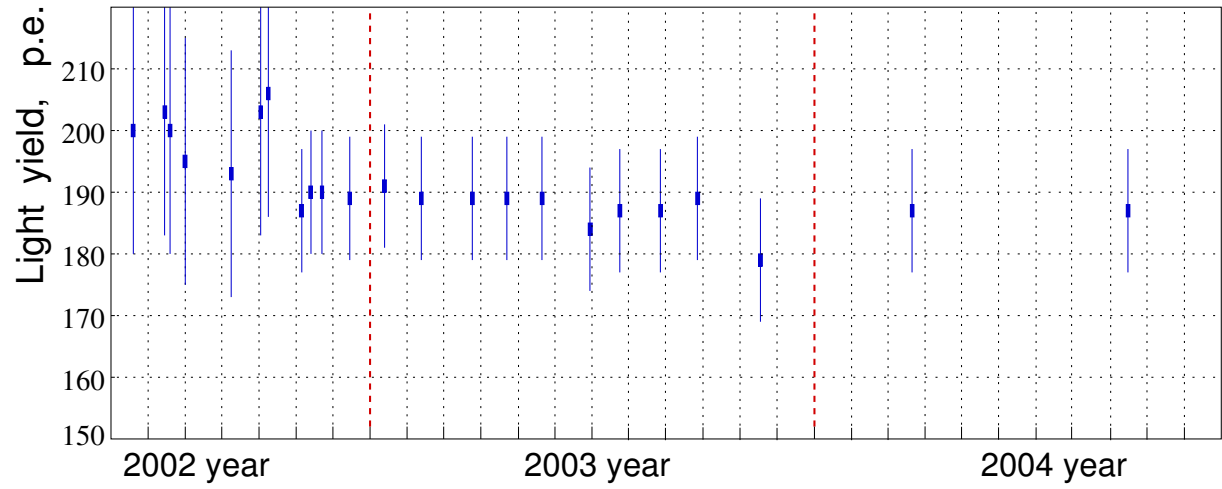


Fig. 6c.10. The light yield of the first sandwich module over a period of years. The errors are determined by systematics.

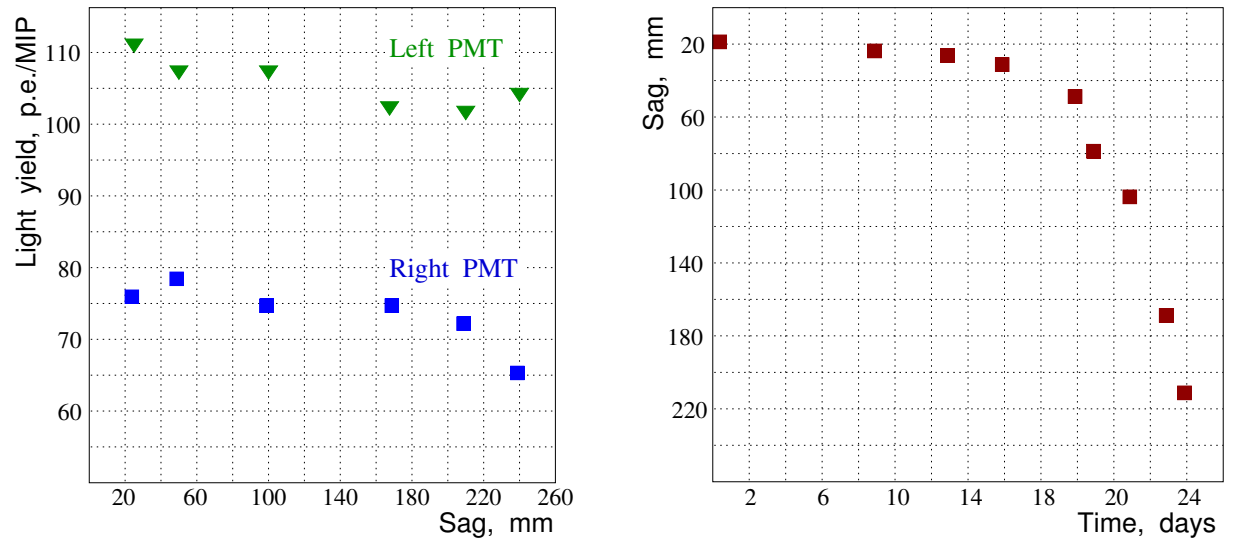


Fig. 6c.11. Light yield for each end of the second module versus its sag (left plot); rate of module bowing (right plot).

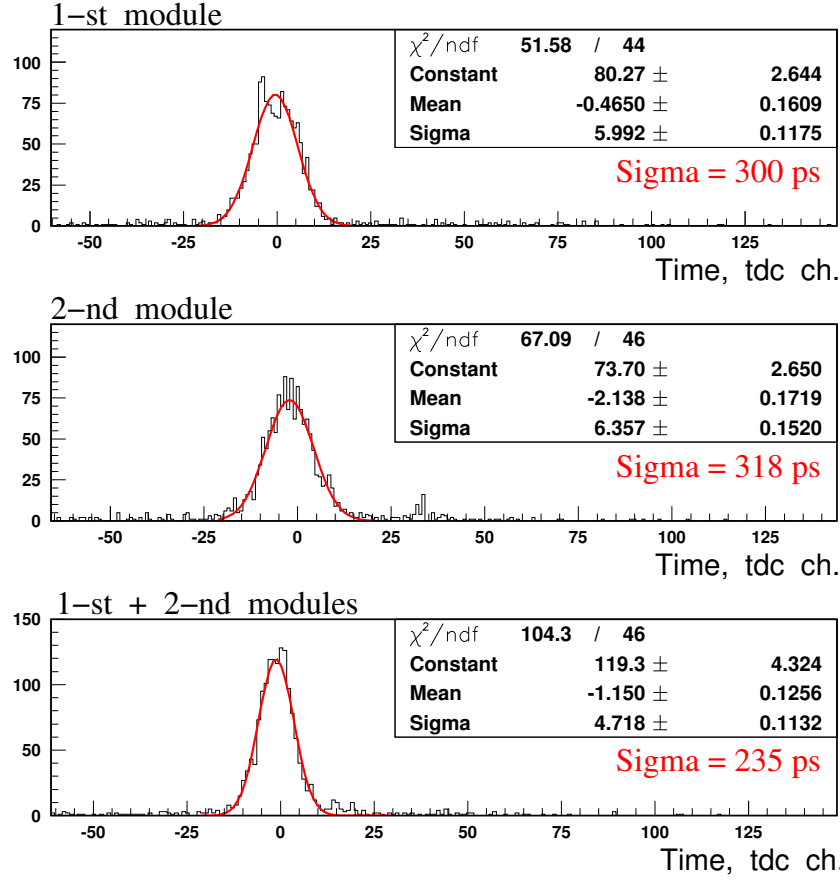


Fig. 6c.12. Time resolutions obtained at the centers of sandwich modules. The combination  $(\text{TDC}_{\text{left}} - \text{TDC}_{\text{right}})/2$  was used to make the timing spectra for the modules. The half-sum of these spectra produced a time resolution of 235 ps. The TDC scale is 50 ps/ch.

### 6c.3.2 Evaluation of Log Veto Performance

The expected performance of the sandwich detectors is summarized in Table 6c.2. The visible energy fraction for 1-mm lead and 7-mm scintillator is about 0.39. From test results with Kuraray WLS fibers, the photoyield was evaluated to be 10 p.e. per MeV of the energy deposited in both active (scintillator) and passive (lead) layers. This result means that up to 1000 p.e. for a typical 100-MeV photon can be collected.

The inefficiency was estimated with simulation tools and compared with the experimental results of similar sampling detectors. The result is below the KOPIO photon veto curve (see Fig. 6f.6) in the photon energy range for the US detector.

Extrapolating the parameters obtained for the prototype module, the time resolution of the Photon Veto detectors is estimated to be close to 200 ps (rms) for a 100-MeV photon. Direct extrapolation to higher energies gives  $72 \text{ ps}/\sqrt{E_\gamma [\text{GeV}]}$ . At 1 GeV, the time resolution includes not only a stochastic term, but also a systematic constant term that is difficult to estimate. However, in our energy range, the systematic constant term can be neglected. The KLOE calorimeter that was assembled by gluing 1-mm scintillation

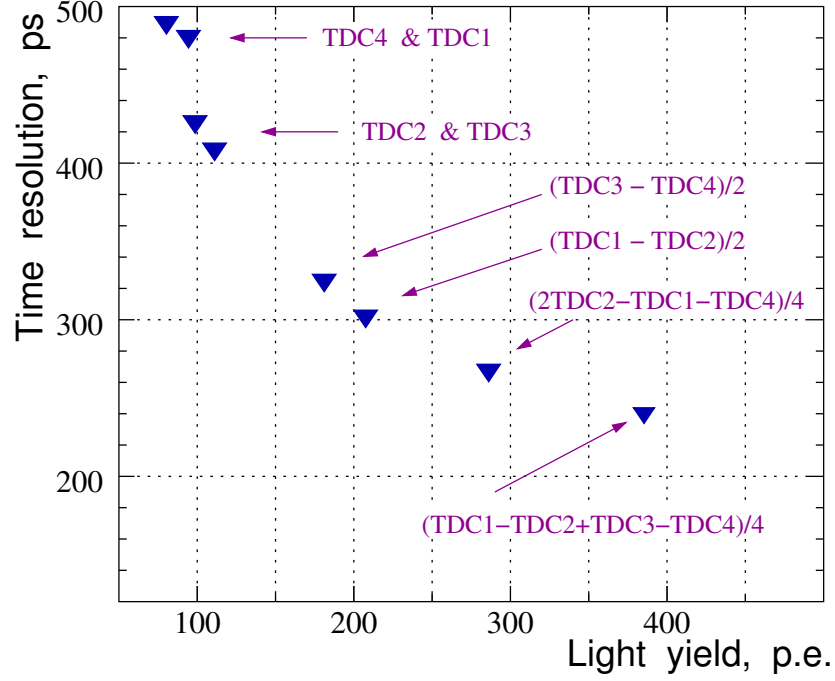


Fig. 6c.13. Time resolution (rms) vs. light output. TDC1 and TDC2 are the ends of the first module, TDC3 and TDC4 are the ends of the second module.

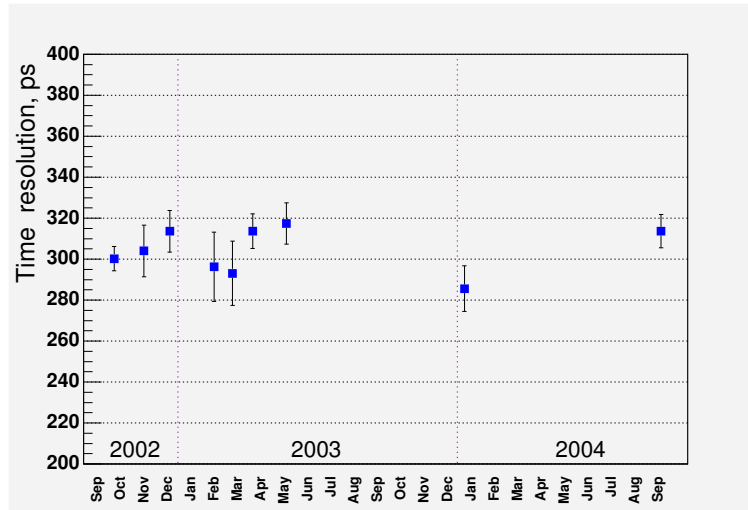


Fig. 6c.14. Time resolution (rms) measured at the center of the first module over several years. The points fluctuate around 300 ps within the time-fitting error.



Table 6c.2. The expected veto performance.

Parameter	Value	Note
Integral inefficiency	$< \times 10^{-4}$	Based on tests and E949 results
$\sigma_E/\sqrt{E}$ , %	3.6	Sampling fluctuations from GEANT
$\sigma_t/\sqrt{E}$ , ps	72	Stochastic term from prototype test
Position resolution, cm	3.5-4.3	Veto segmentation and timing

fibers of 4.3-m length between 0.5-mm lead foils reached a time resolution of  $72 \text{ ps}/\sqrt{E_\gamma}$  at the light output of 1660 p.e./GeV in a beam test[4]. Tests with cosmic rays of the KLOE modules produced even better resolution of  $58 \text{ ps}/\sqrt{E_\gamma}$ , which confirms our timing expectations for the KOPIO Veto Detectors.

Because the light propagation velocity in the fibers was measured to be 17 cm/ns, the accuracy of a localization of an electromagnetic shower could be about 3.4 cm (rms) for a 100-MeV photon. However, a spread of the electromagnetic shower degrades the spacial resolution along the fibers. The resolution in the other direction is defined by the width of the modules. For a 150-mm width,  $\sigma_x=4.3 \text{ cm}$ .

### 6c.3.3 Conceptional Design for the Photon Veto Log Detectors

The KOPIO setup has three Photon Veto log detectors. The largest one, the Upstream Veto wall (US), is located at the entrance of the neutral beam to the decay region. A group of 132 logs of different length are stacked in a wall as shown in Fig. 6c.15. This configuration was chosen so that the phototubes could be moved out of the residual magnetic field from the sweeping magnet that is located just before the US. The field around the beam entrance in the US varies from 800 to 1500 G, and drops to about 300 G in the place where the phototubes are located in the beam plane. The stray field for the phototubes located out of the beam plane is 30-50 G. The thickness of the wall is 6 modules or 96 sampling layers with 19  $X_0$  total radiation length. The height of the wall is 22 sandwich modules. The central modules are cut to form a hole for the beam, where a vacuum pipe will be inserted. US detector is separated in the middle. The upper part can be moved out with a crane, while the bottom part is firmly fixed.

The Downstream Vetos (DS) are required to eliminate background events where extra decay charged particles or gammas are emitted nearly in the beam direction  $Z$ . The Downstream Veto detector is located inside the vacuum pipe before the Catcher. This veto system detects photons as well as charged particles that are traveling along the beam at small angles. The basic design is similar to that of the US, but with different geometrical sizes. Simulated volumes for the Downstream Veto are shown in Fig. 6c.16. The DS detector is separated into six parts on each side, and in three parts above and below the beam. These parts can be built from 140 log modules readout from both ends for good timing.

Just downstream of the Calorimeter is the D4 sweeping magnet (see Fig. 6c.17) that provides a magnetic field directed in the  $X$  direction and so bends charged particles that are traveling in the  $Z$  direction vertically into the  $Y$  direction. A Magnet Photon Veto system consisting of alternating scintillator and lead sheets in a “poor” vacuum inside the sweeping magnet will detect these charged particles along with direct gamma rays that make small angles with the beam and which would not be seen by the Beam Catcher veto system. Sometimes charged particles convert to neutral pions or gamma rays before leaving energy in the scintillator. A backup system of Pb/Sci sheets will detect these photons.

The Magnet Photon Veto system consists of twenty modules above and below the beam, and twenty modules on each side of the beam. The modules are read out on each end through WLS fibers, much like

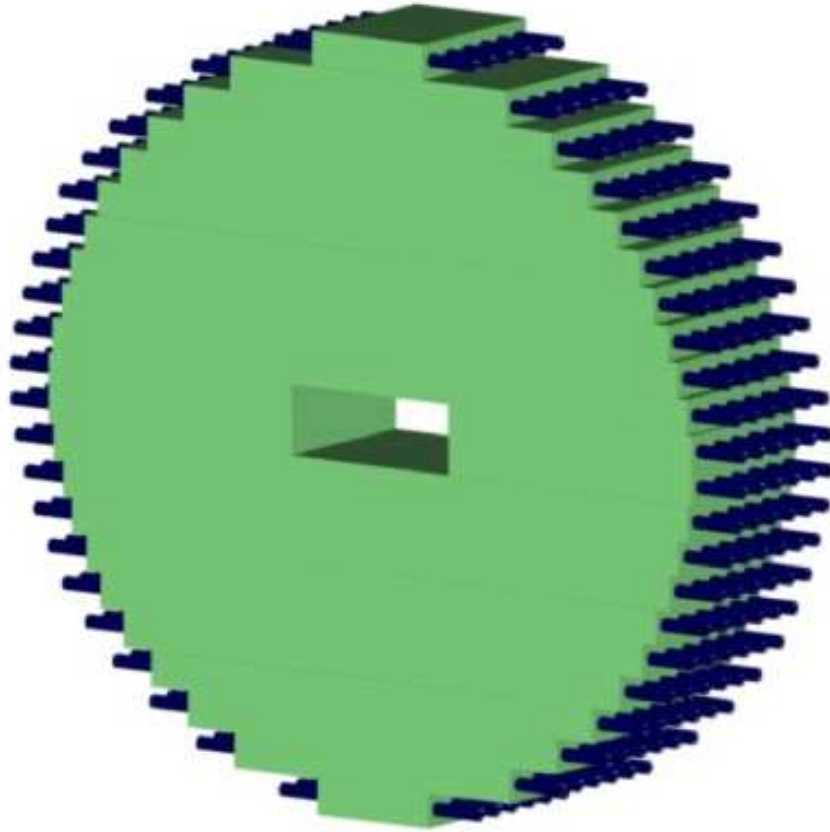


Fig. 6c.15. A view of the Upstream Veto wall made of 132 modules. Central modules are cut the for beam entrance.

the modules in the US detector. The first element is scintillator, to veto charged particles. This layer is in turn followed by alternating layers of lead and scintillator. In order to transport the light to phototubes in a field-free region, the WLS fibers are coupled to clear fibers at the scintillator layer ends. To get the fibers to the field-free region, a small gap between the side and the upper and lower modules is necessary. There is limited space in the magnet vacuum pipe, and so to get both spacial coverage and sufficient radiation lengths, there will be 20 layers of 2.5-mm lead sheets per module and 21 layers of scintillator. The scintillator layers above and below the beam will be 10-mm thick, while those on the side of the beam will be 5-mm thick. In the beam direction, the width of the layers is 155 mm. The modules above and below the beam are 2580-mm long, while those on the side are 620-mm long. Each scintillator layer has 19 grooves spaced about 7 mm apart for placement of Kuraray multiclاد Y11 fibers of 1 mm diameter. The backup for charged-particle conversion is about  $9.5 X_0$ , but is much larger for direct photons that make a small angle with the beam.

#### 6c.4 Readout and Electronics

The readout of the Photon Veto modules can be implemented with the photomultipliers 9903B (Electron Tubes Ltd.), which is under consideration for use in the KOPIO electromagnetic calorimeter. A large photocathode of 32 mm is well suited to readout a fiber bundle of about 500 fiber ends as in a BV Shashlyk module. Spectral sensitivity of a photocathode is extended in the green region to match the WLS fiber emission. One advantage of the 9903B is a power base developed to incorporate the high voltage inside the phototube unit. Several tubes were tested in a prototype Shashlyk array and show good performance in

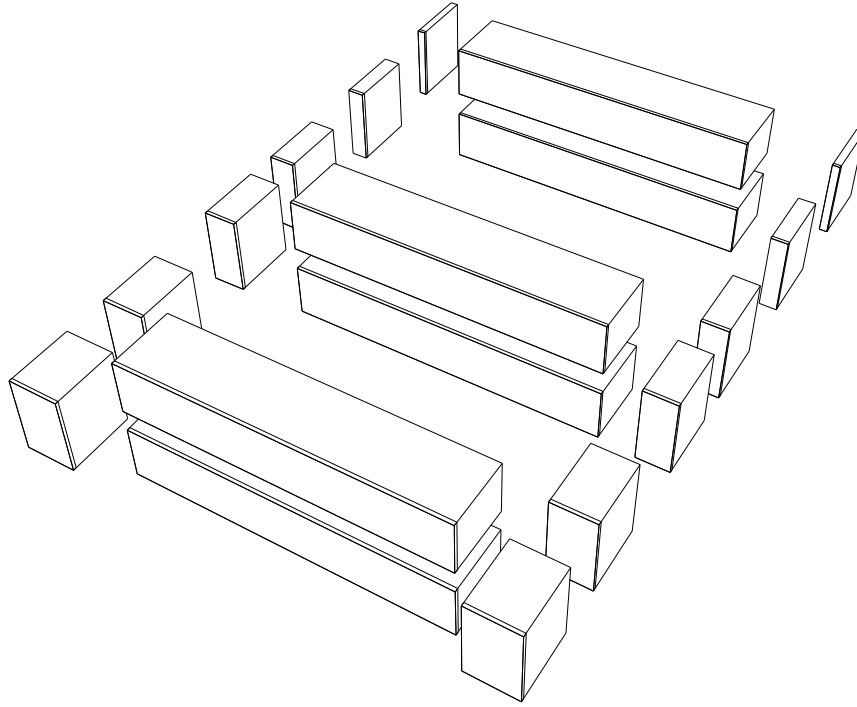


Fig. 6c.16. Location and segmentation of the Downstream Veto. Simulated volumes are shown.

energy resolution. Parameters for the 9903B Photomultiplier are given in Table 6c.3.

Table 6c.3. Specification for Electron Tubes 9903B photomultipliers.

Photocathode active diameter	32 mm
Number of stages	10
Quantum efficiency at 500 nm	15-18%
Gain at 1000 V	$2 \times 10^5$
Rise time	3 ns
Nonlinearity up to 150 mA peak current	<5%
Dark rate	300 Hz

Using the Barrel Veto as a calorimeter puts special requirements on the gain stability of a photomultiplier. One main source of gain fluctuations is the signal current through the dynode system. We plan to work with a low current and low gain, and employ a fast preamplifier at the output stage. Low current mode will enhance the life time. The reliability factor is crucial in the KOPIO experiment where even a single failed phototube will stop the data acquisition of the whole setup.

The front-end electronics is unified with that of the Calorimeter, and will have the same 10-bit, 250-MHz wave-form digitizers developed at Yale University. To check the required sampling rate, the real signal waveforms were collected in a cosmic test with a 5 GHz digital oscilloscope. Cosmic rays deposit about

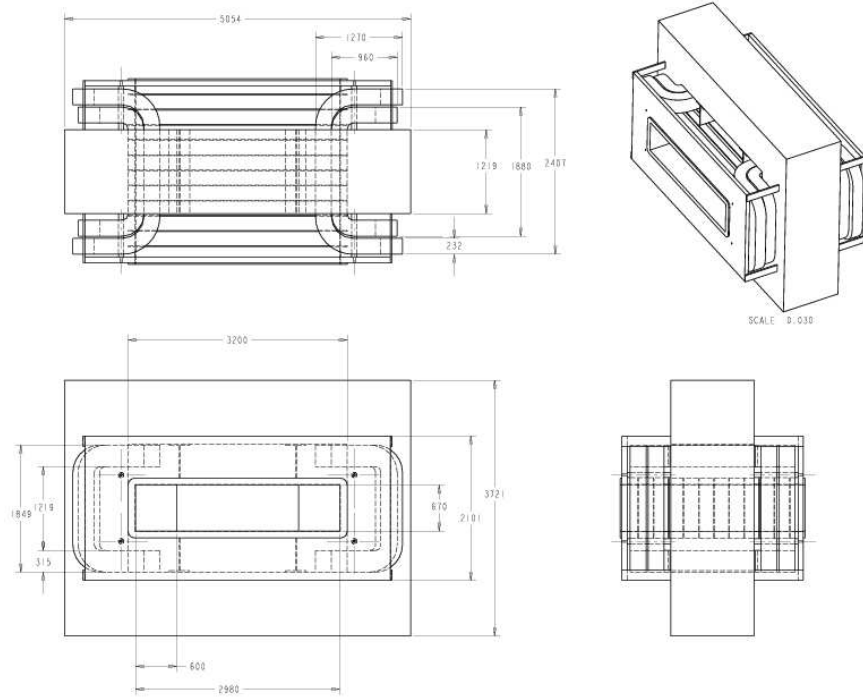


Fig. 6c.17. D4 magnet region, where the Magnet Photon Veto is located.

18 MeV in a prototype Shashlyk module readout with a 9903B tube. Fig. 6c.18 shows a typical signal. Then we reconstructed the signals with different sampling rates as low as 100 MHz and compared them with a reference signal recorded at 5 GHz rate. The  $\chi^2$  method was employed to study how well the reconstructed signal waveform fit the reference one. Results are presented in Fig. 6c.19 for two waveform reconstruction algorithms. In the linear fit, the sampling points are connected with straight lines. In the spline fit, the sampling points are connected with a smoothing method. As can be seen from the plot, the 250-MHz sampling rate provides a good reconstruction of the original waveform for both algorithms. For smaller rates the waveform distortion increases sharply.

## References

1. T. Yamanaka, talk at the *Kaon Decay Workshop for Young Physicists*, KEK, Japan, Feb.14-16, 2001.
2. A. Veyssiere *et al.*, Nucl. Phys. **A159**, 561 (1970).
3. M. Atiya *et al.*, Nucl. Instr. and Meth. A **321**, 129 (1992).
4. M. Antonelli *et al.*, Nucl. Instr. and Meth. A **379**, 511 (1996).
5. G. David *et al.*, IEEE Trans. Nucl. Science NS-43, 1491 (1996).
6. A. Bodek, P. Auchincloss, Nucl. Instr. and Meth. A **357**, 292 (1995).
7. Yu. Kudenko *et al.*, Nucl. Instr. and Meth. A **469**, 340 (2001).
8. R. Wojcik *et al.*, Nucl. Instr. and Meth. A **342**, 416 (1994).

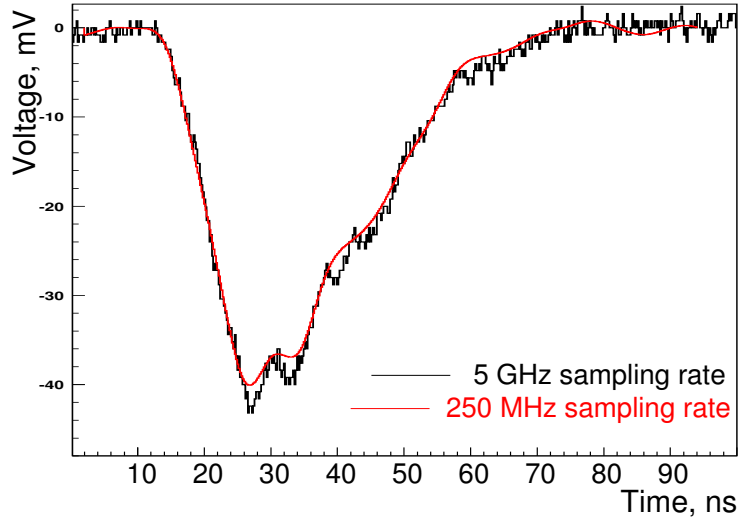


Fig. 6c.18. Waveform of a typical signal from a Shashlyk module recorded with a 5 GHz oscilloscope (black). Red color marks a signal reconstructed at 250 MHz sampling rate.

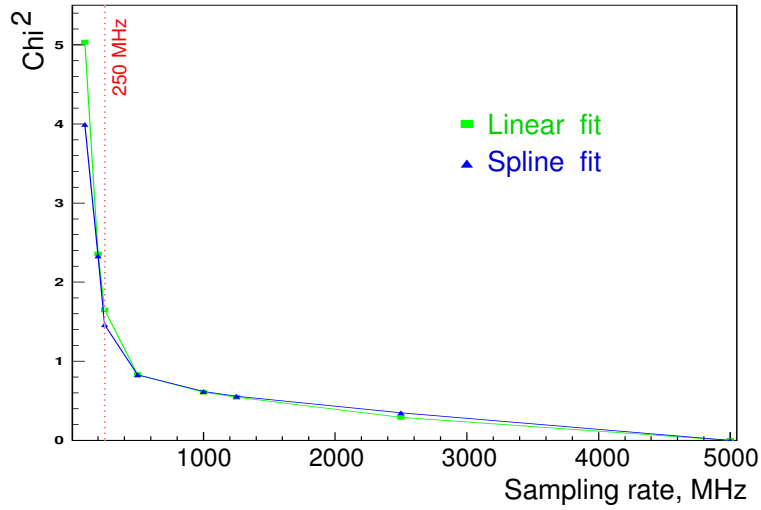


Fig. 6c.19.  $\chi^2$  versus the sampling rate.  $\chi^2$  was calculated as a fit of the reference signal with a signal waveform reconstructed at a smaller sampling rate. Reference signal was recorded at 5 GHz. Waveform was reconstructed by two algorithms, linear and spline fits.

## 6d Charged Particle Veto

### 6d.1 Purpose

The purpose of the Charged Particle Veto (CPV) is to provide an efficient identification of background processes in which an apparent  $\pi^0 \rightarrow 2\gamma$  decay inside the decay volume is accompanied by charged particle emission. Examples of such background processes are

- $K_L^0 \rightarrow \pi^+\pi^-\pi^0$ ,
- $K_L^0 \rightarrow \pi^0\pi^\pm e^\mp \nu$ ,
- $K_L^0 \rightarrow \pi^\pm e^\mp \nu \gamma$   
in which the  $e^\mp$  creates a second photon through Bremsstrahlung or  $e^+$  annihilation in flight, and
- $K_L^0 \rightarrow e^+\pi^-\nu$ ,  
again followed by  $e^+ \rightarrow \gamma$  whereas the  $\pi^-$  creates a photon through  $\pi^- p \rightarrow \pi^0 n$ .

In all cases, two particles with opposite electrical charge emerge. In all cases, the events may also produce signals in other detector elements, such as the Photon Veto (PV) system. For this reason, we discuss the performance of the combined CPV/PV systems below. Charged-particle detection efficiencies of 99.99% or better are required to keep these backgrounds below a few events in the final sample. The  $K_L^0 \rightarrow \pi^+\pi^-\pi^0$  decay would, however, still dominate the signal for low values of the center-of-mass energy  $E_{\pi^0}^*$  where about 10% of the signal events are expected.

### 6d.2 Requirements

The design of the CPV is based on the following requirements which result from extensive simulations of the various background processes mentioned above and our own tests of the momentum dependence of the detector response to various charged particles ( $\pi^\pm, \mu^\pm, e^\pm$ ):

- *intrinsic charged particle detection efficiency*  $> 99.99\%$   
Fundamental limitations to the detection efficiency of charged particles arise from processes in which a charged particle moves towards an active detector element but deposits no or insufficient visible energy. Examples are  $(\pi^-, xn)$  reactions, backscattering, or positron annihilation in flight. Our tests show that the efficiency requirement is met if the dead layer in front of the CPV is kept below  $\approx 20$  mg/cm<sup>2</sup> and the detection threshold is kept below  $\approx 50$  keV. The first requirement can only be met when the detectors are situated inside the decay tank and/or beam pipe.
- *solid angle*  $4\pi$  sr  
With the possible exception of the upstream beam hole, the detector has to extend to the full  $4\pi$  sr. This requirement in particular that particles moving downstream within the beam envelope have to be observed as well.
- *50-cm distance to the decay volume*  
In order to separate  $\pi^0$  decays from  $(n, \pi^0)$  reactions in the CPV from the events of interest on the basis of the different  $2\gamma$  vertex distributions, the detector elements have to be kept more than 50 cm from the fiducial decay volume (see Sec. 13.8.6).
- *time window*  $< 10$  ns.  
The spread in the time difference between the decay time as reconstructed from the  $\pi^0 \rightarrow 2\gamma$  decay kinematics and the signals observed in the CPV should be within  $\approx 10$  ns to avoid accidental vetoing by CPV signals from neighboring beam bunches. This requirement sets limits to the intrinsic time resolution and the granularity of the CPV. Still, very slow particles may be missed. As is discussed in Sec. 13.6.2,  $K_L^0 \rightarrow \pi^+\pi^-\pi^0$  decays with very slow charged particles can be removed by kinematic constraints.

- *veto blindness*

Depending on the algorithm used to analyze the digitized wave forms, veto signals may get lost when preceded by another signal in the same detector element. These losses are minimized by using fast detectors which are as thin as possible and by distributing the load over many channels. Minimizing the detector thickness reduces (i) the sensitivity to neutrons and low-energy photons, (ii) the dynamic range of the signals, which is beneficial for the double-pulse resolution, and (iii) the area required for the light sensors.

- *reliability*

Since access will be limited to less than a few times per year, the loss of a few readout channels must not result in substantial data loss. This requirement can be met by redundancy in the readout of each individual detector element.

### 6d.3 Description of the System to be Built

The Charged Particle Veto consists of three plastic scintillator systems:

- *the Barrel CPV (Fig. 6d.1)*

This subsystem consists of 2-mm-thick tiles of Bicron BC408 plastic scintillator covering the walls of the decay tank with the exception of the regions where the beam crosses. It consists of a central module situated inside the central part of the decay tank and two end-cap modules situated inside the tank domes. VM2000 wrapping foil on the inside of each module serves as a barrier between the high-quality beam vacuum and a moderate detector vacuum.

The central module consists of 16 identical arrays oriented parallel to the beam. Each array consists of 5 detector elements with 20-mm overlap, for a total of 80 identical elements. The arrays are viewed from one side by eleven photomultipliers, three per detector element but shared where they overlap. The two end-cap modules each consist of three concentric arrays of 16 detector elements, which results in 96 detector elements of 12 different shapes. These elements are viewed on the outside by using the same scheme of photomultipliers shared by overlapping neighbors. This arrangement results in  $16 \times 11 + 6 \times 32 = 368$  readout channels.

- *the Downstream CPV*

This subsystem lines the beam pipe that crosses the Preradiator and Calorimeter. This region is about 2 m long, 2 m wide and 20 cm high. Whereas the top and bottom layers are composed of  $20\text{-cm} \times 30\text{-cm} \times 2\text{-mm}$  scintillators, the side walls are covered with counters of dimensions  $20\text{ cm} \times 20\text{ cm} \times 2\text{ mm}$ . The resulting 198 scintillator elements are read out directly by 242 photomultipliers.

- *the D4 CPV*

This subsystem is integrated into the Photon Veto system lining the beam pipe where it crosses the D4 sweeping magnet. Scintillation light is collected with the help of embedded wave-length-shifting fibers and transported to photomultipliers situated outside the regions with high magnetic field.

### 6d.4 Fundamental Limitations to the Detection Efficiency of Charged Particles

Charged particles may disappear before depositing sufficient energy in an active detector element. The resulting inefficiency depends on the thickness of a possible dead layer in front of the sensitive medium as well as the threshold on detected energy, and varies for the different particles and momenta.

Extensive tests were performed at the Paul Scherrer Institute (PSI) to measure the inefficiencies for  $\pi^\pm$ ,  $\mu^\pm$ , and  $e^\pm$  at momenta between 185 and 360 MeV/c. The setup is shown in Fig. 6d.2. Figure 6d.3 shows, as an example, the distributions of detected energy in counter 4 for 290 MeV/c  $\pi^-$  and  $\pi^+$ . The broad distribution arises from pion-induced reactions in the scintillator. The prominent peaks near channel 200 are associated with events in which the pions pass through the scintillator with some energy loss. Events in the pedestal peaks are caused by interactions in the dead material between the scintillator and the preceding wire



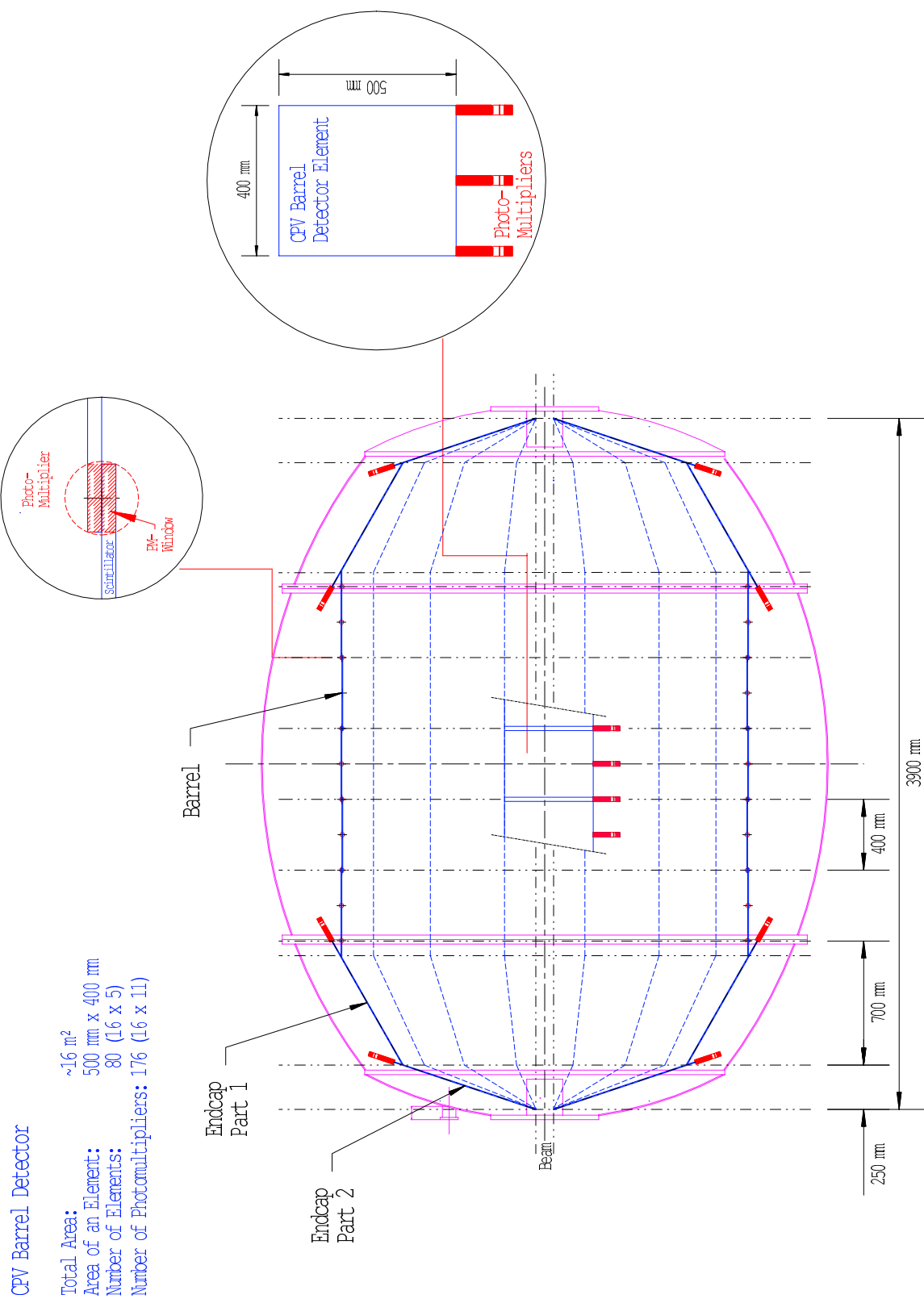


Fig. 6d.1. Longitudinal cross section of the barrel CPV. (The actual barrel will have three rings in each end-cap.)

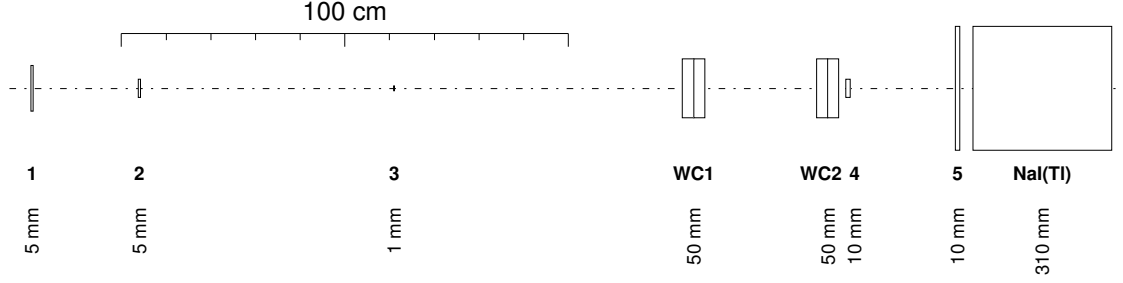


Fig. 6d.2. Scale drawing of the setup used to measure the response of a plastic scintillator to  $\pi^\pm$ ,  $\mu^\pm$  and  $e^\pm$ . Beam enters from the left. Counters 1-3 and wire chambers WC1-2 are used to identify an incoming beam particle and measure its trajectory. The dimensions indicate detector thicknesses in the beam direction.

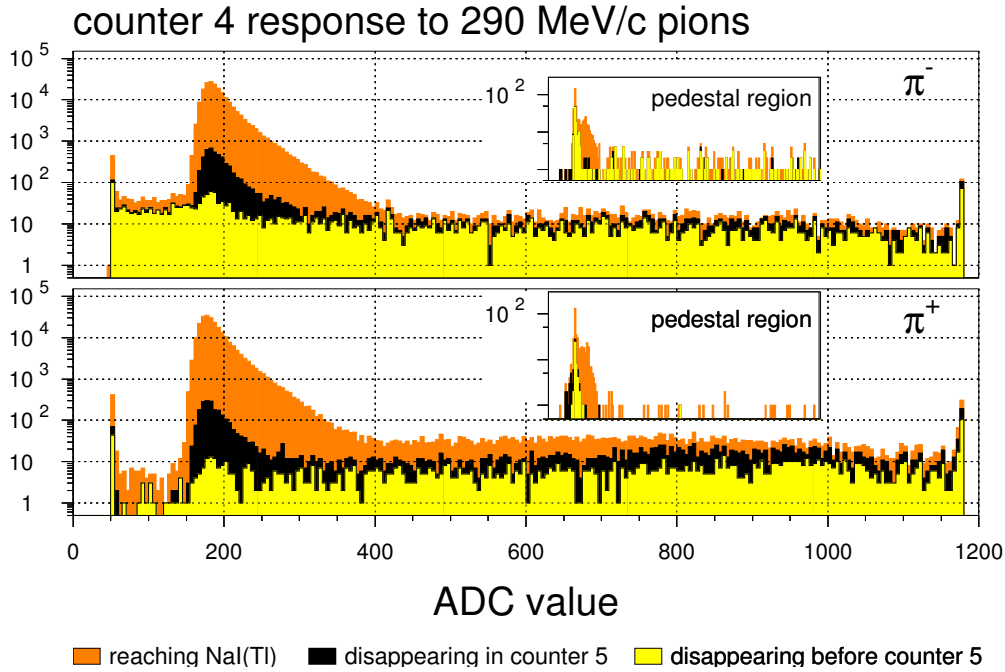


Fig. 6d.3. Response of plastic scintillator counter 4 to 290-MeV/c  $\pi^\pm$  for (i) all events with trajectories pointing at counter 4, (ii) the subset of (i) that are contained in the pedestal peak of the NaI(Tl) crystal, and (iii) the subset of (ii) contained in the pedestal peak of the second plastic scintillator, counter 5. Because the histograms are plotted on top of each other, the visible areas indicate the differences between two event samples, so orange corresponds to events of type (i) and not (ii), *i.e.* particles producing signals in the NaI(Tl) crystal. The insets give expanded views of the pedestal regions  $50 < \text{ADC} < 100$ .

chamber WC2. As can be seen, most of these events still produce a signal in the NaI(Tl) detector and would thus be observed by the PV. The continuum distribution is completely different for the two charges. In the case of  $\pi^-$ , the region between the pedestal peak and the main peak shows a flat distribution containing about 1% of the events. These events are explained by  $\pi^-$  reactions into all-neutral final states. For  $\pi^+$ , this region

is almost empty because neutral final states are very unlikely. The observed pion detection inefficiencies are plotted against beam momentum in Fig. 6d.4. All four distributions (no/small signal,  $\pi^+/\pi^-$ ) peak around 220 MeV/c. About 2/3 of the dead-layer losses are caused by the wrapping of the scintillator, which amounts to 55 mg/cm<sup>2</sup>. This effect means that the values plotted in Fig. 6d.4 correspond to a dead layer of  $\approx 80$  mg/cm<sup>2</sup>.

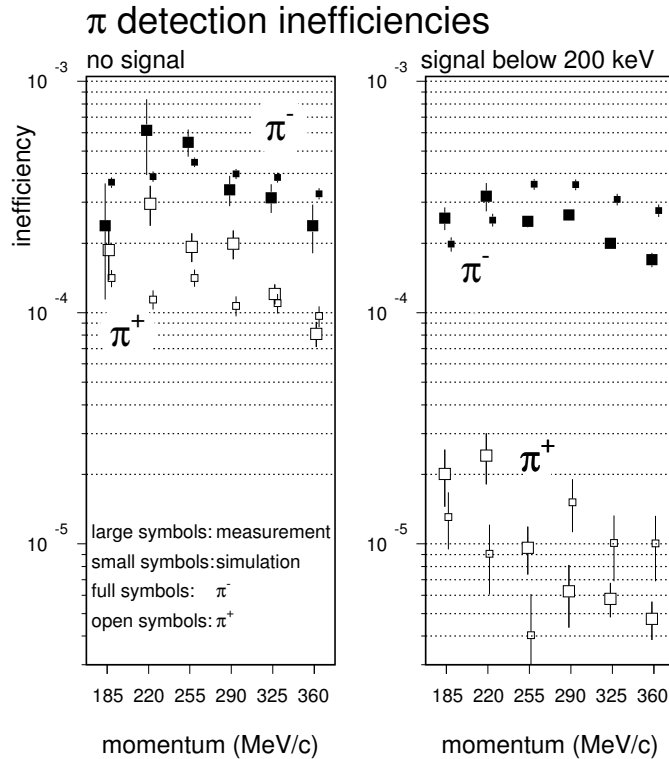


Fig. 6d.4. Pion detection inefficiencies caused by interactions in the 80-mg/cm<sup>2</sup> dead material between the scintillator and the preceding wire chamber (WC2), and by a 200-keV detection threshold. These results do not include an additional factor of two in rejection capability by the photon calorimeter behind the scintillator.

In order to keep the inefficiencies below 10<sup>-4</sup> at all momenta, a dead layer of  $< 20$  mg/cm<sup>2</sup> and a detection threshold below 50 keV should be achieved. As will be discussed below, it is our aim to stay significantly below these requirements.

The GEANT simulations reproduce the observed inefficiencies within a factor of two. We studied the nature of some of the simulated events in which no energy was deposited in the scintillator or where this energy was below 75 keV. In the case of  $\pi^-$ , losses were mainly caused by  $(\pi^-, xn)$  absorption. In the case of  $\pi^+$ , 60% of the inefficiency was caused by pion back scattering in the wrapping. Short-range protons and/or alpha particles were usually emitted. In about 40% of the cases, a  $\pi^0$  was produced. Those events would not escape detection in the  $4\pi$  sr PV.

### 6d.5 Detector R&D

Key features for the CPV are a minimal dead layer and low detection threshold. Additional concerns are the complications associated with operation in vacuum, *i.e.* out-gassing, electric sparking, vacuum feedthroughs, heat dissipation, and accessibility.

In the case of plastic scintillators, the detection threshold depends critically on the efficiency of light collection. For this reason, extensive studies were made of the light yield obtainable for various geometries and wrapping materials. Full-scale (400 mm  $\times$  500 mm) prototypes of the two light-collection schemes of interest were studied (see Fig. 6d.5). In addition, prototypes for the Downstream Charged Particle Veto system and for the scintillator planes of the Preradiator detector were tested. All measurements were done with 500-MeV/c  $\pi^-$ . Two  $X$ - $Y$  multi-wire proportional chambers (MWPC) were used to determine the impact position on the scintillator.

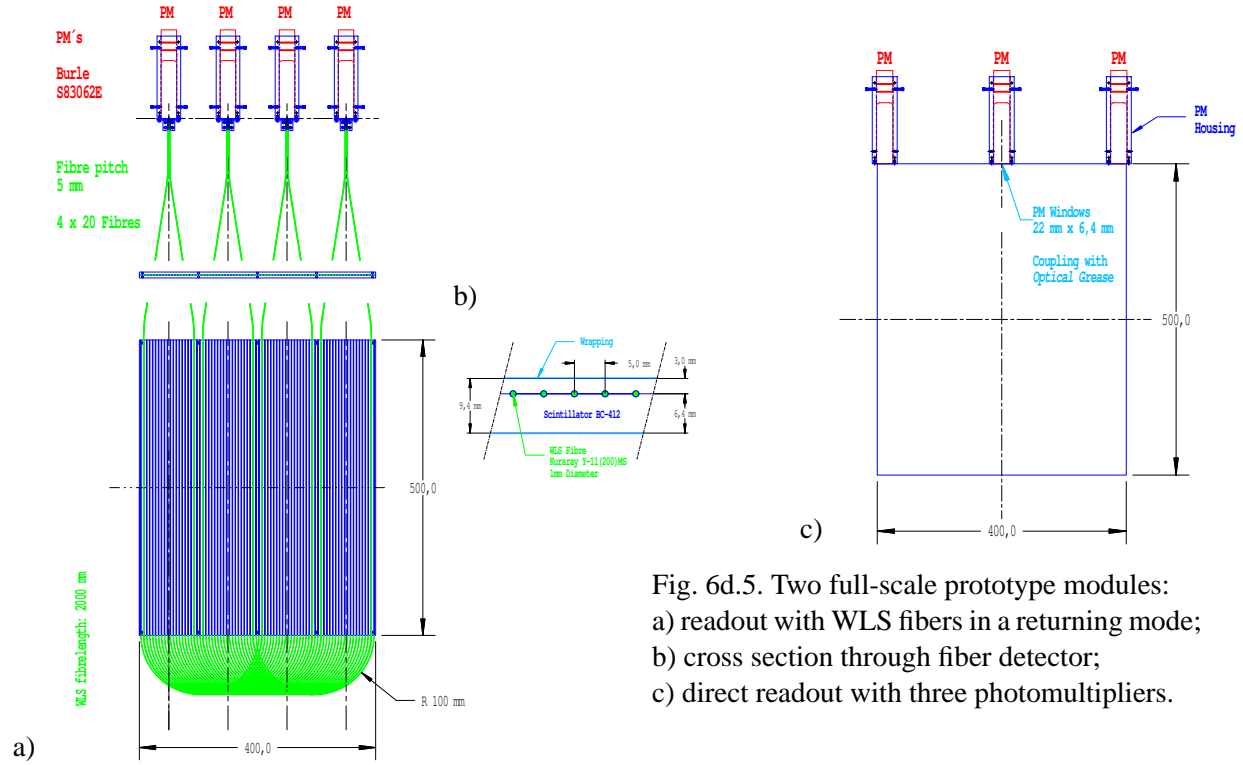


Fig. 6d.5. Two full-scale prototype modules:  
a) readout with WLS fibers in a returning mode;  
b) cross section through fiber detector;  
c) direct readout with three photomultipliers.

Table 6d.1. Photoelectron (p.e.) yields of various light collection schemes.  
Scintillator: BC-412 by BICRON; photomultipliers: Burle 83062E (Ø22 mm).

	Size [cm <sup>2</sup> ]	Thickness [mm]	Version		Wrapping	Nr. of PMT's	p.e.	p.e. in 10 mm
WLS fibers	20x25	2x6.4	Fiber	Geometry	Tyvek <sup>d</sup>	4	110	90
		⋮	Bicron <sup>a</sup>	straight <sup>c</sup>		⋮	130	110
	40x50	6.4+3.0	⋮	returning <sup>c</sup>	VM2000 <sup>e</sup>	⋮	115	125
Direct readout	20x25	6.4	Width of windows		black paper Tyvek <sup>d</sup>	4 <sup>f</sup>	130	200
			10 mm	no		⋮	260	400
	40x50	⋮	⋮	⋮	⋮	4 <sup>g</sup>	130	200
		⋮	22 mm	⋮	⋮	⋮	220	340
		⋮	⋮	yes	⋮	⋮	410	640
		⋮	⋮	⋮	VM2000 <sup>e</sup>	⋮	520	810
		3.0	⋮	⋮	⋮	⋮	200	670
		6.4	⋮	⋮	⋮	3 <sup>g</sup>	500	780
		⋮	⋮	⋮	⋮	2 <sup>g</sup>	330	520
		⋮	⋮	⋮	⋮	⋮	⋮	⋮

<sup>a</sup> BCF-92MC

<sup>b</sup> Y-11(200)MS

<sup>c</sup> read from both ends

<sup>d</sup> DuPont trademark

<sup>e</sup> radiant mirror film produced by 3M

<sup>f</sup> mounted at opposite sides

<sup>g</sup> mounted at one side

The results are shown in Table 6d.1. Light collection with Wavelength Shifting (WLS) fibers spaced by 5 mm was compared with a geometry in which photomultipliers were mounted directly onto the scintillator for detectors of two different sizes. As can be seen from the table, the light yield observed with direct coupling was significantly larger than for fiber readout. The best results were achieved with VM2000 radiant mirror film as a wrapping material. Not shown in the table are the light yields obtained with black paper and aluminized mylar (up to 50% less) and with teflon (similar to Tyvek but more thickness required).

## 6d.6 Detector Concepts

From the results presented in Table 6d.1 we conclude that a yield of  $\approx 250$  photoelectrons per MeV can be obtained for a 2-mm-thick detector, which is sufficient to reach a detection threshold as low as 20 keV. The use of VM2000 results in a dead layer of  $8 \text{ g/cm}^2$ . Alternatively, we are studying the option of a  $\text{MgF}_2$  coating which would reduce the dead layer to  $\approx 1 \text{ g/cm}^2$  at the cost of a factor-of-two loss in light collection efficiency. This option is of interest for the Downstream CPV where the effective thickness of the dead layer is boosted significantly because the particles move parallel to the detector surface.

APD's would give 2-3 times more quantum efficiency than photomultipliers but the required electronic amplification would introduce significant noise and a slower signal shape. The newly-developed Geiger-mode photodiodes then become an interesting alternative to photomultipliers. These devices are currently available with an area of  $3 \times 3 \text{ mm}^2$  and an effective efficiency (geometric times quantum efficiency) near 20%. Significant improvements can be expected in the near future. Some advantages include much smaller dimensions, lower price (so one can afford more of them), ease of operation, and immunity to magnetic fields. Compared to standard APD's, they do not require large electronic amplification, which makes them both faster and less noisy.

Figure 6d.6 shows as an example the pion inefficiencies of the combined CPV+PV system for a threshold of 50 keV on the detected energy and a dead layer of  $1 \text{ mg/cm}^2$ .

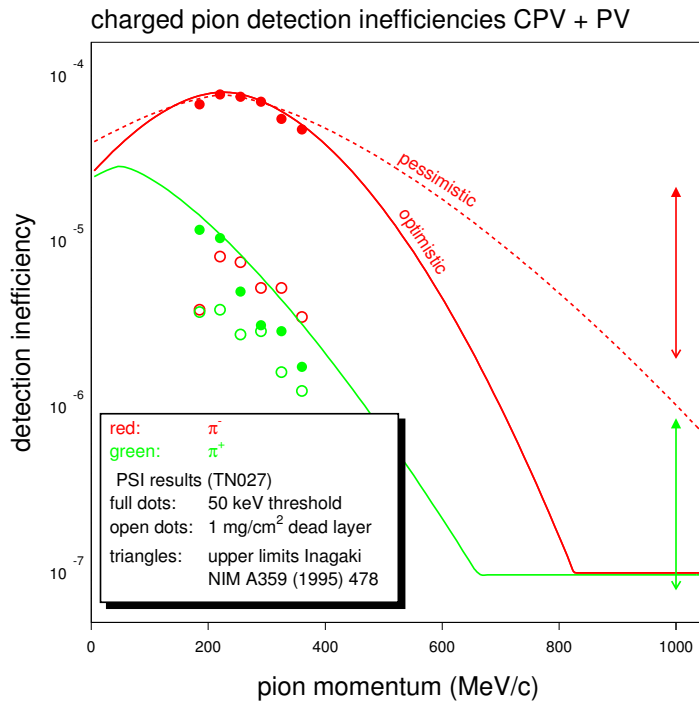


Fig. 6d.6. Pion detection inefficiencies for CPV+PV versus momentum. The PSI results are normalized to a 50-keV detection threshold and  $1 \text{ mg/cm}^2$  dead layer, corresponding to a coated scintillator.

### 6d.6.1 Barrel CPV

The Barrel CPV surrounds the decay region with the exception of the areas where the beam crosses. Simulations show that very few charged particles leave through the upstream hole, which may remain uncovered.

The design of the Barrel CPV (see Fig. 6d.1) closely matches the geometry of the decay tank. The detector consists of three modules corresponding to the central element of the tank and the two dome-shaped end-caps. Modules consist of arrays of detector elements (submodules) fixed on the outside to carbon-fiber support structures. Each module has a common wrapping foil (VM2000) on the inside separating the moderate detector vacuum from the high beam vacuum.

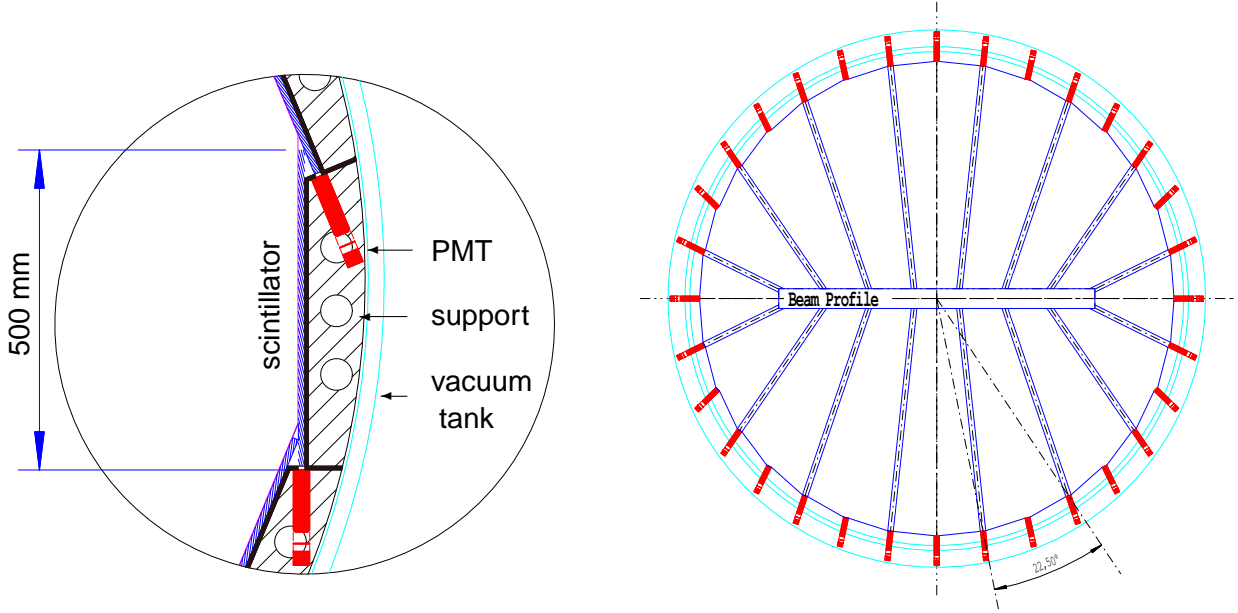


Fig. 6d.7. A design of the central charged-particle veto system.

Left: sector of a cross section perpendicular to the beam. Along the beam there would be  $\approx 10$  modules with overlap to avoid dead space. Right: end-cap detector. (The actual detector will have three rings.)

The central module of the Barrel CPV consists of 16 identical scintillator arrays arranged symmetrically about the beam axis (see Fig. 6d.7). Each array consists of five identical submodules arranged along the beam. Neighboring submodules overlap by  $\approx 20$  mm. Each submodule consists of a slab of  $400 \times 500 \times 2$  mm<sup>3</sup> BC408 plastic scintillator viewed from one side by three photomultipliers in close resemblance to some of the prototype detectors (see Fig. 6d.5). Because neighbors share a photomultiplier at the region of overlap, this arrangement results in 11 readout channels per module, or a total 176 channels for the central module. The use of submodules with three readout channels has the advantage that the loss of a few channels has little impact on the CPV efficiency.

The two end-caps of the Barrel CPV each consist of three scintillator arrays arranged concentric about the beam axis. Each array consists of 16 submodules. Mirror symmetry about the  $XY$ ,  $XZ$  and  $YZ$  planes leads to 12 different shapes for the 96 submodules. As for the central part, neighboring submodules overlap by  $\approx 20$  mm and the sharing of photomultipliers between neighbors results in 32 readout channels per module, or a total 192 for the end-caps of the Barrel CPV.

Figure 6d.8 shows distributions of light yields observed with the 6.4-mm prototype wrapped in VM2000. Apart from the regions just in front of the photomultipliers, the homogeneity of light collection is of the

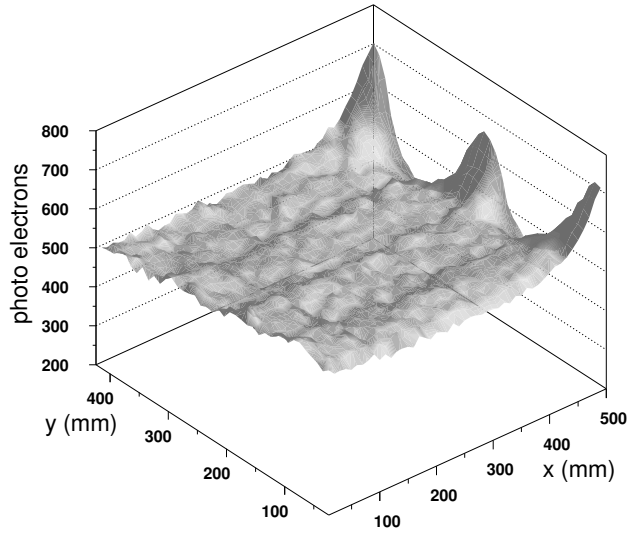


Fig. 6d.8. Position dependence of the light yield observed with three photomultipliers coupled directly to the scintillator, which has a thickness of 6.4 mm (see also Table 6d.1).

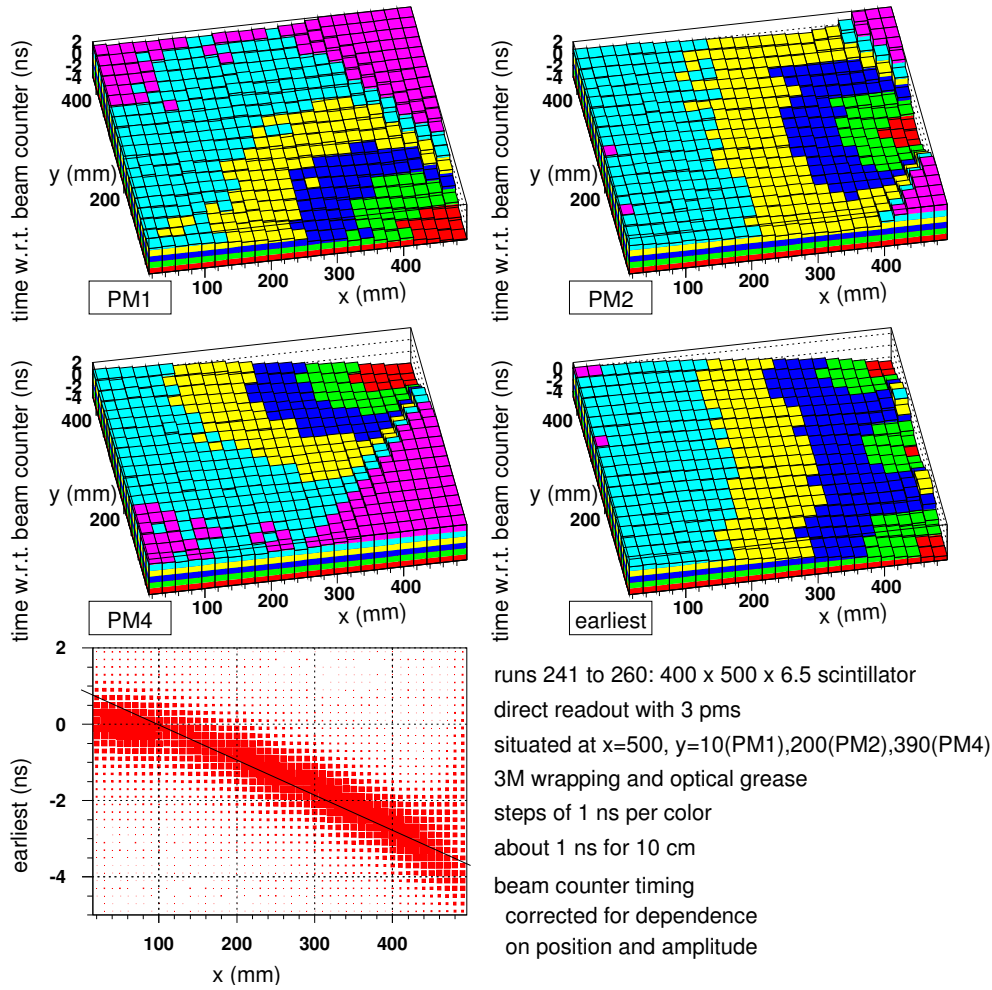


Fig. 6d.9. Position dependence of the leading-edge timing from the three photomultipliers, and their sum. Colors correspond to 1-ns intervals.



order of a few percent. Based on these results and those obtained with four readout channels for both 3-mm and 6.4-mm scintillator thickness, signals of at least 100 photoelectrons are expected for minimum ionizing particles crossing a 2-mm scintillator.

Figure 6d.9 shows the timing performance of the prototype detector. Without knowledge of the impact position, a timing uncertainty of  $\pm 2.5$  ns is observed, resulting from an effective velocity of light propagation of 12.5 cm/ns.

### 6d.6.2 Downstream CPV

The final portion of the CPV is located downstream of the Barrel CPV. It consists of plastic scintillators lining the beam pipe where it crosses the Preradiator and the Calorimeter. The region suffers from high rates and limited access, which render the design of counters a significant challenge. Fortunately, the region is already part of the detector vacuum, so outgassing of detector components is not a concern.

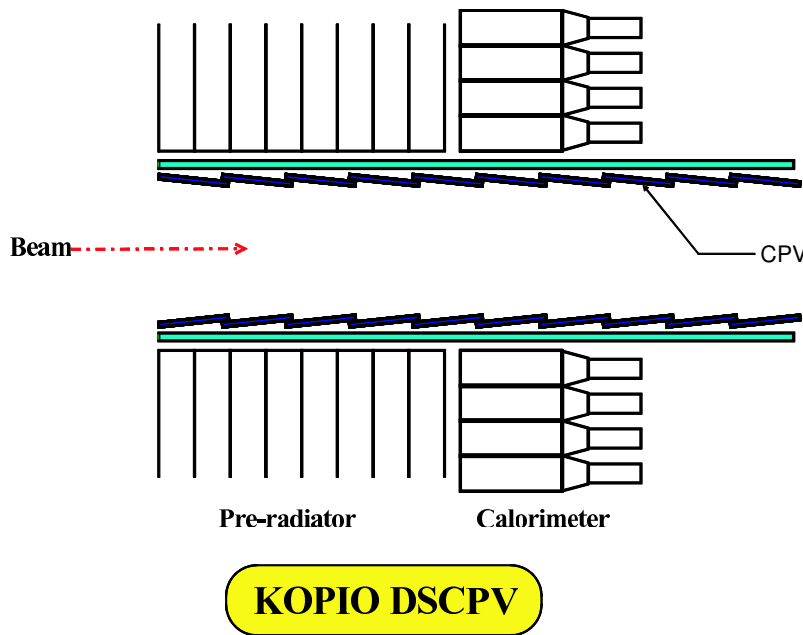


Fig. 6d.10. Vertical cross section through the Downstream CPV.

A schematic cross section is shown in Fig. 6d.10. The Downstream CPV covers an area of about 2-m long by 2-m wide by 20-cm high. The top and bottom layers are composed of 20-cm  $\times$  30-cm  $\times$  2-mm scintillators read out directly by PMTs in the vacuum. The side walls are covered with counters made of 20cm  $\times$  20-cm  $\times$  2-mm scintillators also read out directly by PMTs in the vacuum. The counters are tilted slightly so that successive counters shield the photomultipliers of the next downstream counter, which thus do not present dead material to the charged particles emanating from the fiducial region. The tilt ( $\sim 1:10$ ) also reduces the path lengths of these charged particles through the external wrapping or coating on the inner surfaces of the counters. This layer serves to complete the optical isolation of the counters (their other surfaces can be wrapped with Vikuiti film –VM2000, or perhaps aluminized Mylar). The counters covering the top and bottom of the beam pipe are overlapped transversely by approximately 1 cm in an alternating pattern. Altogether, there would be 198 modules and 242 photomultipliers. Each scintillator is read out by two PMTs, but the readout of adjacent scintillators mounted on the top and bottom overlap on the PMT face, so that these PMTs read out two scintillators. This arrangement prevents the loss of efficiency from cracks and allows some redundancy in the readout, while keeping the channel count as low as possible. The small counter size facilitates efficient readout and good timing properties.

The PMT proposed for the Downstream CPV is the Hamamatsu R7401P which has excellent response and gain. Its very small footprint is very attractive in this area of the detector, where the vertical space is quite limited. This PMT selection allows the active elements to be as close as possible to the walls of the vacuum tank.

Additional subsystems have also been considered, but are omitted from this CDR because we do not currently believe that they are needed to achieve the charged-particle rejection goals. These subsystems include a low-pressure MWPC in the beam located between the Barrel CPV and the Downstream CPV, and a second layer of counters surrounding the downstream modules. These devices can be retrofitted later, should experience show that additional rejection is desirable.

### **6d.6.3 Front-end Electronics**

Readout electronics, distribution of high-voltage to the photomultipliers, and LED monitoring and calibration will closely follow the general concepts described in Sec. 8. Photomultiplier gains will be limited to typically  $10^5$  to minimize power (heat) dissipation and count-rate instabilities. A 100-MHz preamplifier/driver in the base will match the signals to the 10-m transmission lines connecting the 500-MHz waveform digitizers.

## 6e Beam Catcher

### 6e.1 Overview

The main purpose of the Beam Catcher is to detect photons escaping through the beam hole. It is placed in and near the neutral beam about 12 m downstream from the main detector, 26 m from the production target. The beam size at the front face is 2.34 m (width) by 10.4 cm (height). The challenge in designing the Catcher system is to reduce the sensitivity to unwanted particles, such as neutrons and  $K_L$ s, while keeping high enough sensitivity to photons. Because the flux of the unwanted particles is very high, there would be a high probability of vetoing genuine signals if the Catcher were sensitive to these particles.

Considering these requirements, two types of detectors are employed; one is a lead/aerogel sandwich counter, and the other is a lead/lucite(acrylic) sandwich counter. The former (called “aerogel catcher”) is placed in the beam core region, while the latter (called “guard counter”) surrounds the Catcher. Both counters utilize Čerenkov radiation to detect electrons and positrons produced by an electromagnetic shower, and have low sensitivity to slow particles that are expected to be the main interaction products by hadrons. Of these two types, the aerogel catcher has lower neutron sensitivity, and thus is placed inside the beam.

Figure 6e.1 shows the energy spectrum of photons that the catcher and guard counter must detect, namely those photons that originate from the dominant  $K_L^0 \rightarrow \pi^0 \nu \bar{\nu}$  backgrounds,  $K_L^0 \rightarrow \pi^0 \pi^0$  after our standard kinematic cuts have been applied. The primary source of background photons entering the beam

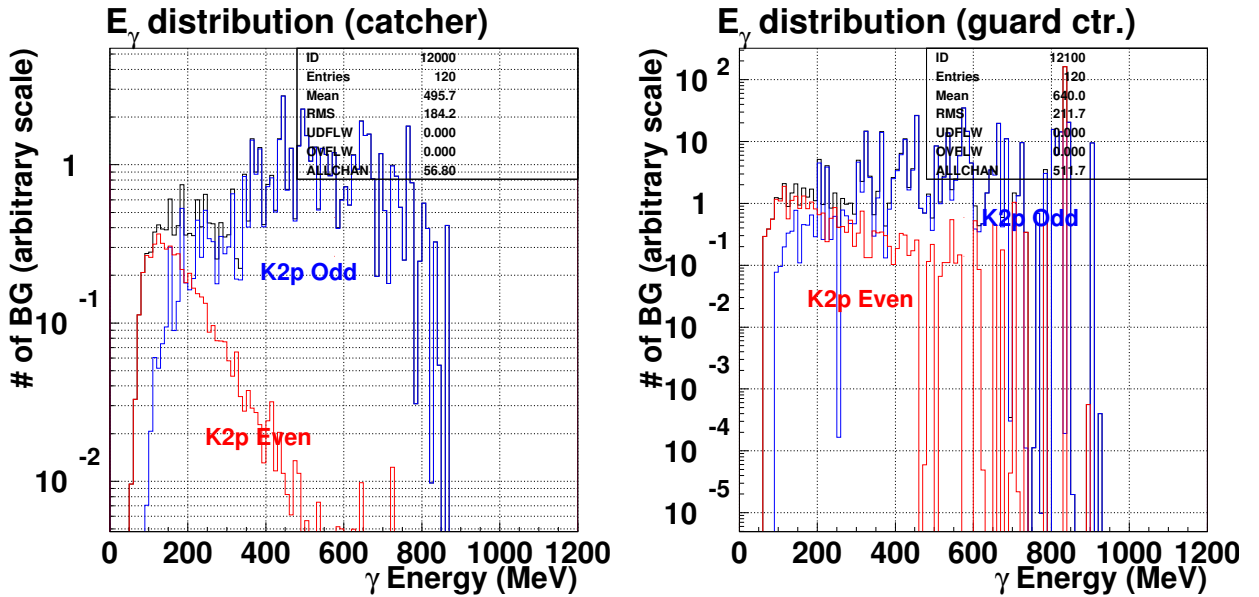


Fig. 6e.1. Energy distributions of photons in (left) and near (right) the neutral beam for  $K_{\pi 2 \text{ even}}$  (red) and  $K_{\pi 2 \text{ odd}}$  (blue) type events. Actually, the left (right) figure shows the energy spectrum of photons that hit the aerogel (guard) counter, described in the text. The vertical axis indicates the expected number of backgrounds after our standard cuts.

direction are due to the  $K_{\pi 2}$  “odd pairing” case in which one photon from each  $\pi^0$  has been detected and happens to reconstruct as a single  $\pi^0$ . These photons entering the beam direction generally have energy greater than 300 MeV. The  $K_{\pi 2}$  “even pairing” case in which both photons from a single  $\pi^0$  enter the beam direction are less prevalent. We demand that the Catcher system must have at least 99% efficiency for photons with energy greater than 300 MeV in order to suppress the  $K_L^0 \rightarrow \pi^0 \pi^0$  and other backgrounds, and to keep a good signal-to-noise ratio. At the same time, we demand that its sensitivity should be less

than 0.3% for neutrons with kinetic energies near 0.8 GeV, in order to reduce the false veto probability to an acceptable level (see below for a detailed discussions of the veto probability).

Similarly, the guard counter is required to have an efficiency of more than 99.5% for  $> 300$ -MeV photons. This counter covers the beam halo region, where the neutron yield will be two orders of magnitude lower than that in the beam core. Thus, the requirement for the neutron insensitivity is rather relaxed compared with that of the aerogel catcher, but it still should be suppressed to the level of a few percent.

## 6e.2 Aerogel Catcher

### 6e.2.1 Conceptual Design

The catcher inside the beam consists of a number of identical modules. Each module utilizes a lead sheet as a photon converter and an aerogel tile as a  $e^+/e^-$  detector. The principle is to use Čerenkov radiation so to avoid detection of heavy and slow charged particles produced by neutron interactions. Because the refractive index of aerogel we are planning to use is low ( $n = 1.05$ ), the Čerenkov threshold momentum is high. Another important feature of the catcher is its distributed arrangement. Photons come from far upstream, and thus their electromagnetic showers develop nearly along the beam direction. On the other hand, neutrons come into the catcher and interact with the lead sheets, and the secondary particles from the interactions tend to go isotropically. Therefore, neutron signals can be reduced further by requiring coincident hits along the beam direction, without losing photon efficiency. As mentioned above, the catcher consists of small modules arranged in an array that will provide information on a photon's direction.

### 6e.2.2 Base Design of the Aerogel Catcher

The aerogel catcher consists of 420 modules of the design shown in Fig. 6e.2. Each module is composed of 2-mm-thick lead, 50-mm-thick aerogel radiator ( $n = 1.05$ ), a light-collection system of a mirror and funnel, and a 5-inch photomultiplier tube. The aerogel cross section is 30 cm in height and 30 cm in

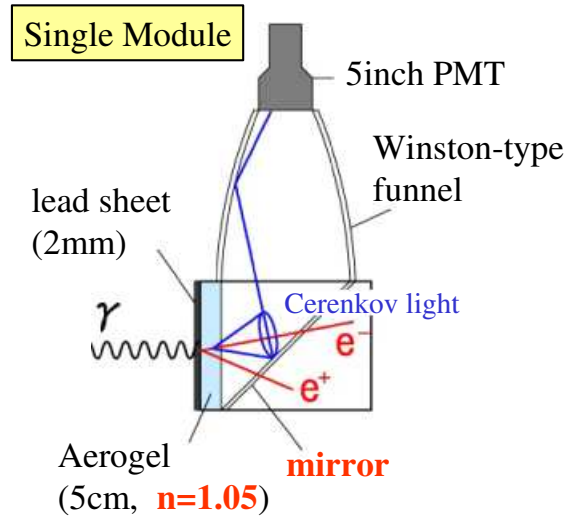


Fig. 6e.2. The design of the catcher module.

width. Figure 6e.3 schematically shows a top view of the catcher configuration. The modules are arrayed in 25 layers, which are spaced by 35 cm along the beam direction. There are 12 to 22 modules in each row, varying with the divergence of the beam. The modules in a row are staggered laterally by a half module from those in the following and preceding rows. There are 25 modules along the beam direction, making a total of 8.9 radiation lengths over a distance of 8.75 m. As indicated in the figure, 278 of 420 modules are placed

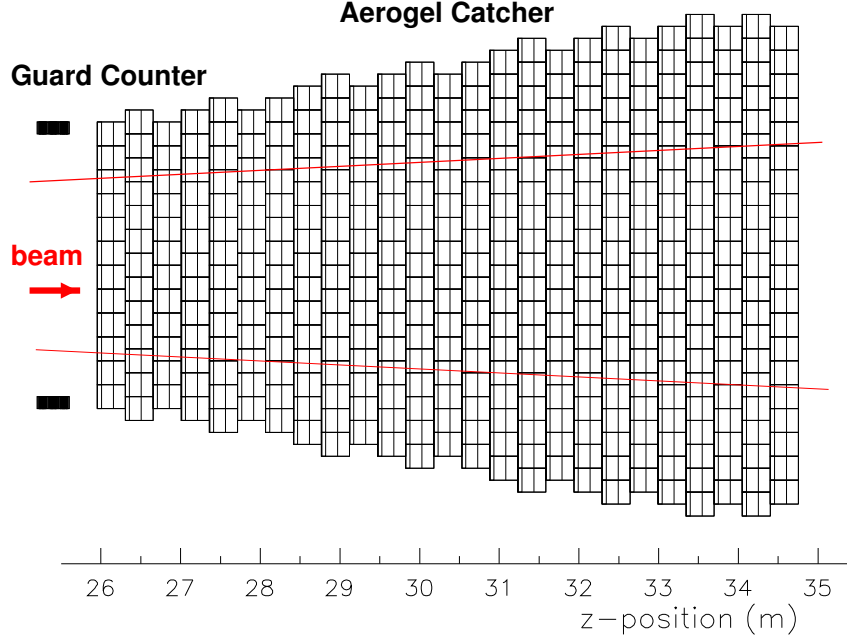


Fig. 6e.3. The design of the catcher configuration.

in the core beam region, and the rest (142 modules) cover the side region to catch photons with angles larger than the beam divergence.

**Choice of Radiator** In choosing an aerogel radiator, the points to be considered are its refractive index, transmittance, and ease for handling. The refractive index determines the yield of Čerenkov light, as well as the threshold momentum for radiation. It also changes the Čerenkov angle, and thus affects the light collection efficiency. The transmittance, dominated by the Rayleigh scattering in the case of an aerogel, is important because the emitted light passes through a few centimeters of aerogel tiles before reaching the light collecting optics. An aerogel with higher refractive index is less fragile and easier to handle, but tends to be less transparent. Recently, Matsushita Electric Works, Ltd., collaborating with the Belle group, has successfully developed transparent silica aerogels with a refractive index of about 1.05[2]. We plan to use this new type because it gives more light than other candidates with different indices, according to our simulation which took into account its actual optical properties.

**Design of the Optics** The light collecting system consists of a mirror and a Winston-type funnel. The mirror reflects Čerenkov light to the funnel input, and the funnel guides the light onto the photomultiplier's cathode. Each module is optically separated from adjacent ones by a very thin light-reflecting wall made with an aluminized mylar sheet. We plan to make the mirrors with a 2-mm-thick acrylic sheet. Their surfaces will be coated with Al and  $\text{MgF}_2$  by a vacuum evaporation method. The funnel will be made with a thin Al sheet pressed into the correct shape against a mold. Its inner surface will also be coated with Al and  $\text{MgF}_2$ .

Before settling on this design, four candidates for the optics were compared, as shown in Fig. 6e.4: a flat mirror with a Winston-type funnel (adopted); two flat mirrors and funnels with two photomultipliers; a flat mirror with a box-type funnel; and a concave mirror with a Winston cone (original design). On the basis of simulation results, which included ray-tracing and the effects of scattering and absorption in aerogel tiles, the first option was chosen. It is easier to mass produce, and gives a uniform light collection efficiency. The average light collection efficiency is 20% over the whole area of 30 cm by 30 cm, assuming the reflectivity of a mirror and funnel to be 80%.

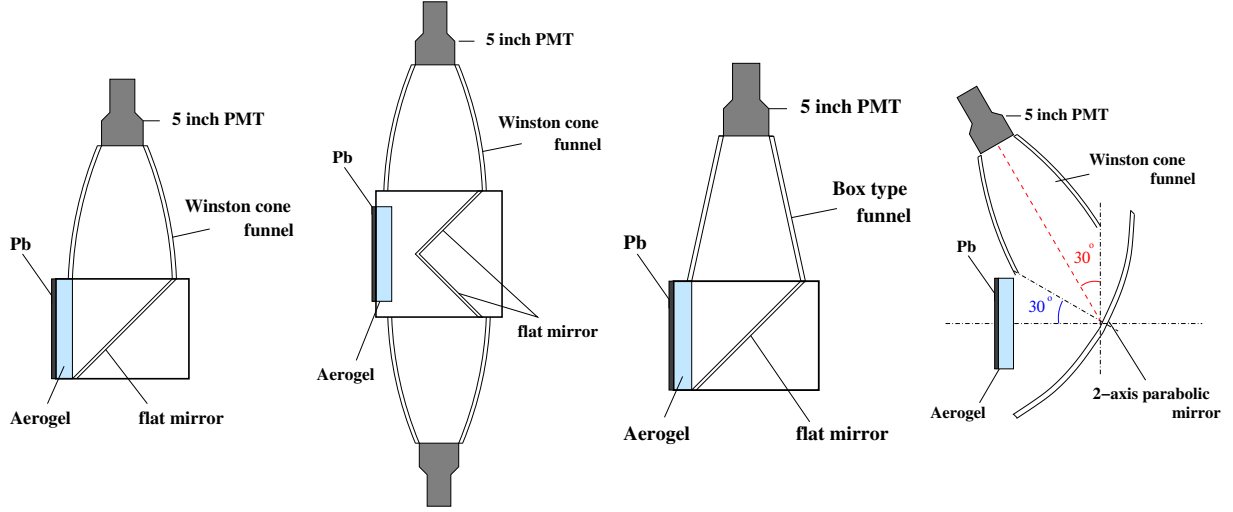


Fig. 6e.4. Side views of optical design candidates that were studied.

**Photoreadout** Each module is equipped with a 5-inch photomultiplier to detect Čerenkov light. We plan to use Hamamatsu R1250 PMTs, whose photocathode is a bialkali and the window is a borosilicate glass. The dynode structure is a linear-focus type and the timing property is expected to be good. Its quantum efficiency was evaluated during the beam tests described above, being folded into the spectrum of Čerenkov radiation, and is incorporated in the simulations. Operation voltage for the PMT will be supplied by the LV-HV scheme, common to the KOPIO photodetectors.

To maintain good performance under a high counting-rate environment, a stabilized base, *e.g.* by transistors, will be developed. The gain of the photomultiplier will be monitored by a LED flasher system. A waveform digitizing device will be used in the readout in order to identify a genuine signal with certainty even when it is smeared by accidental hits. To achieve a certain double pulse resolution, described later in the discussion of the efficiency loss by accidental activities, we use the 500 MHz waveform digitizer (WFD).\*

Detailed designs of the front-end electronics are described in Sec. 8).

**Summary of Baseline Parameters of the Aerogel Catcher** The parameters of the aerogel catcher are summarized in Table 6e.1.

### 6e.2.3 Experimental Study of Prototypes

To examine the design principle, we have constructed two generations of prototypes so far. The first one was used to evaluate the Čerenkov light yields from aerogel tiles. The results of the study, though not described here, were useful in the early design stage. The second prototype was built to test our design principle with charged beams. The main goal was to study the response to protons, which acted as substitutes for neutrons, and to check whether or not our simulation could reproduce the results. If so, we can then rely on neutron sensitivity simulations. As shown in Fig. 6e.5, the prototype module had a 5-cm-thick aerogel (a stack of 1-cm-thick aerogel tiles), a concave mirror, and a 5-inch photomultiplier. Two types of aerogel tiles with different refractive indexes,  $n = 1.05$  and  $n = 1.03$ , were tested in the measurement.

The layout of the test experiment is shown in Fig. 6e.6. First, the light yield from one module was measured. The results are shown in Fig. 6e.7, where the ordinate is the number of photoelectrons obtained for charged pions and the abscissa is  $1/\beta^2$ . The solid line is a fit to the data points and its slope gives the aerogel refractive index. The measured index was found to agree well with the catalogue value of the tile

\*There is a possibility to use the 1 GHz sampling WFD, in order to achieve the required resolution.

Table 6e.1. The base parameters of the aerogel catcher.

Items	Parameters
size of module	30 cm (H) by 30 cm (V)
Pb converter	2-mm thick
aerogel	refractive index=1.05
main mirror	30 cm (H) by 30 cm (V), 10-mm-thick×5 tiles
light funnel	flat, 45 degree inclined
photomultiplier	Winston cone ( $d_{in}=30$ cm, $d_{out}=12$ cm)
number of modules	420 (278 in the beam core, 142 in the side region)
number of layers	25
spacing between layers	35 cm
size in beam direction	875 cm (from $z=2596$ cm to $z=3471$ cm)
horizontal coverage	360 cm (12 modules) at the face 660 cm (22 modules) at the end

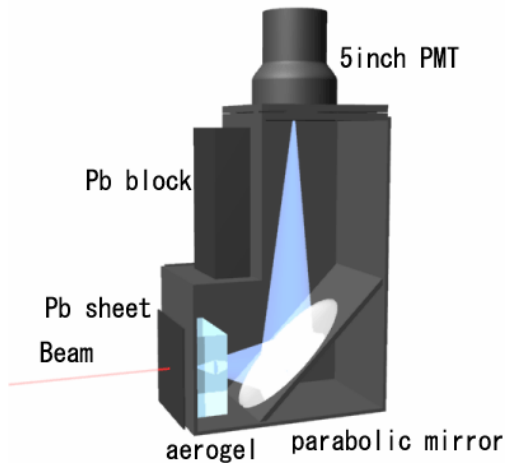


Fig. 6e.5. Sketch of the second prototype.

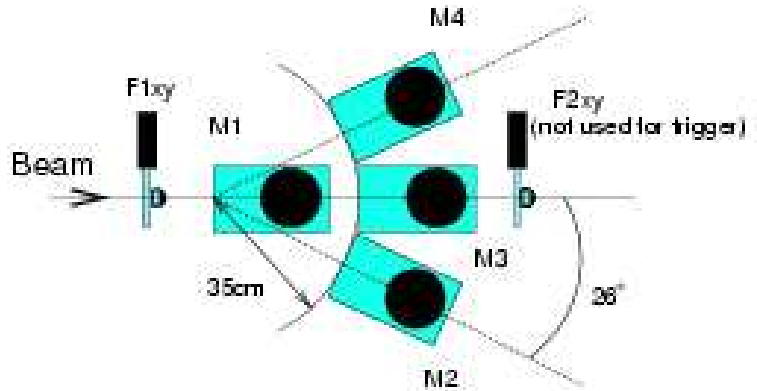


Fig. 6e.6. The experimental setup of the beam test for the second prototype.

used in this test ( $n = 1.03$ ). The light yield was also reproduced well by simulations that took into account measured optical parameters, such as transmittance of the aerogels and reflectivity of the mirror.

In the next stage, a proton beam was directed onto the upstream module (“M1”) to interact with the lead sheet. The coincidence probability of “M1” and one of the downstream modules (“M2” to “M4”) due to the produced secondaries was measured. A coincidence event was defined as that which had  $\geq 1$  photoelectrons (p.e.) both in “M1” and in “M2” to “M4”. As shown in Fig. 6e.8, the data and simulations agreed well each other. The single-module efficiency, *i.e.* the hit probability of “M1”, was also checked. The results are shown in Fig. 6e.9. The left (right) figure shows the efficiency with the threshold of 1-p.e. (2-p.e.). Good agreement was found for the case of 2-p.e. threshold, but there was relatively a large discrepancy in the case of 1 p.e. (see the open triangle in the left figure). Further investigation revealed that the discrepancy was caused by scintillation in nitrogen gas (air). Taking into account its emission yields as measured in a separate experiment[1], the results could then be reproduced well (see the open-square points). Nitrogen scintillation



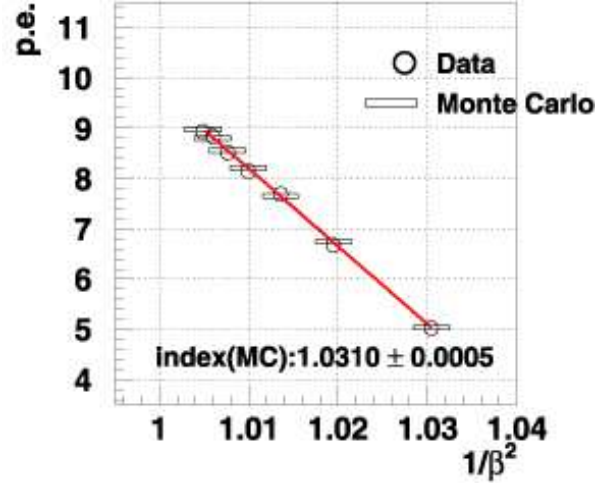


Fig. 6e.7. The measured number of photoelectrons of the second prototype as a function of  $1/\beta^2$ .

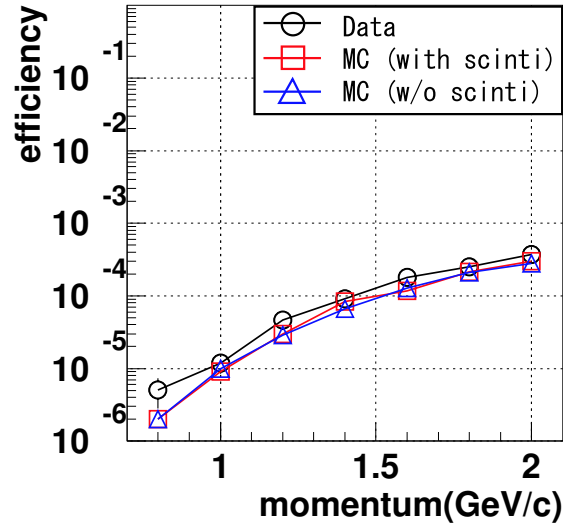


Fig. 6e.8. The measured efficiency for protons with the second prototype as a function of momentum. The efficiency here is the coincidence of two layers, as described in the text. The lines guide the eye.

might be annoying in the real experiment because protons knocked on by neutrons can make small signals with high rates. If it actually becomes a problem, we can suppress the effect by adding a quenching gas such as  $\text{CO}_2$ [1]. The study of the second prototype thus confirmed the design principle and provided various parameters needed to predict the catcher performance reliably.

### 6e.3 Guard Counter

The aerogel catcher detects photons traveling along the neutral beam. In addition, photons that travel toward the beam halo region must also be detected. The calculated beam profile at the face of the catcher is shown in Fig. 6e.10.

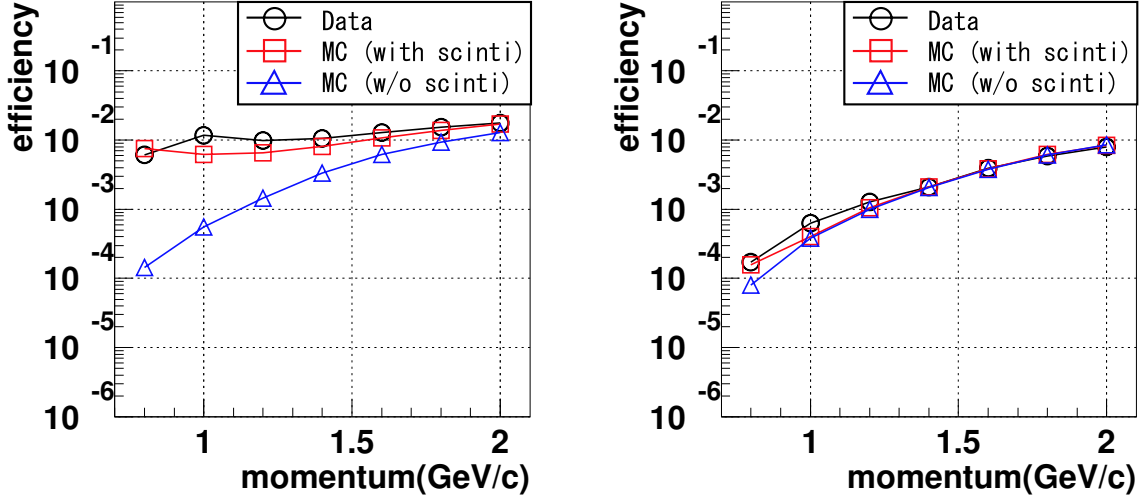


Fig. 6e.9. The measured efficiency for protons with the second prototype as a function of momentum. In the left (right) figure, the threshold was set to be 1 p.e. (2 p.e.). The lines guide the eye.

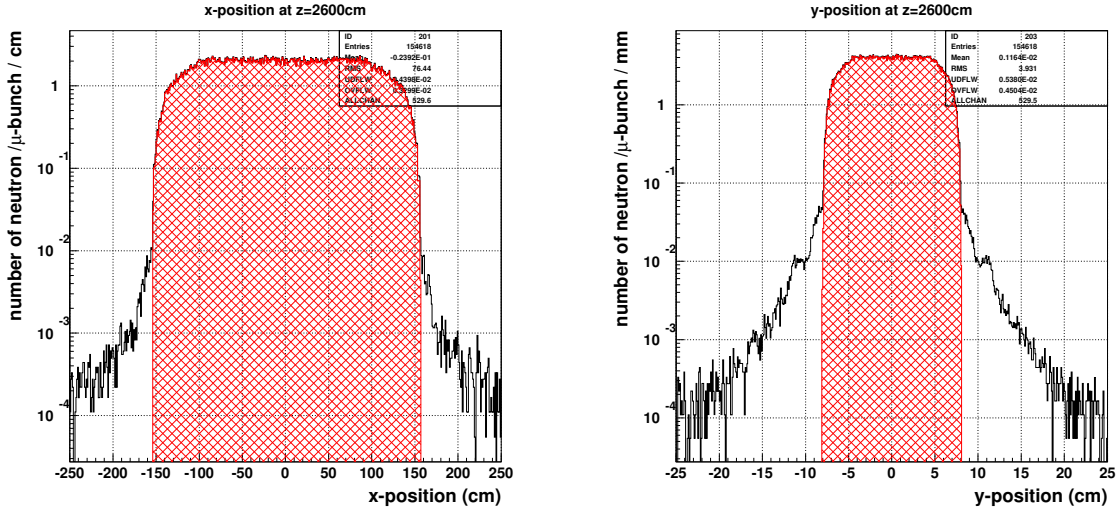


Fig. 6e.10. The profile of the neutrons at the face of the Catcher. Left (right) figure shows the horizontal (vertical) profile of the neutron beam. The vertical axis indicates the estimated number of neutrons in a microbunch. Note that these are the plots for wider (100 mrad in horizontal) aperture and thus the current horizontal beam profile (90 mrad) would be 10% narrower than in the figure.

At the upstream face of the Catcher system, the neutron flux from 8 to 15 cm (Or -8 to -15 cm) in the vertical direction is still high due to halos, although the rate is expected to be two orders of magnitude lower than in the beam core. To cover this region, we plan to install a series of lead/acrylic sandwich counters (“guard counters”) upstream of the Catcher. Conceptually, as with the aerogel catcher, it utilizes Čerenkov radiation in acrylic slabs. In addition, the total-reflection limit in the transport of Čerenkov light helps to reduce the sensitivity to low-energy secondary particles from neutron interactions, as drawn in Fig. 6e.11.

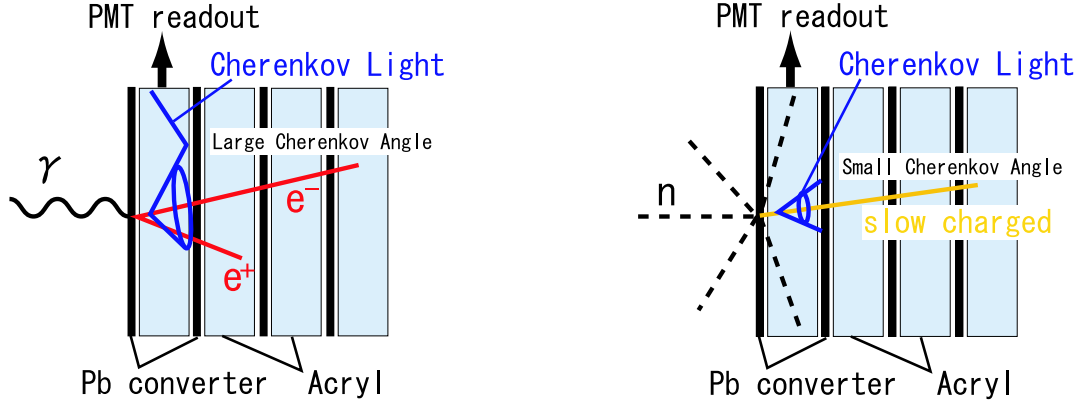


Fig. 6e.11. The schematic view of the concept of the guard counter. The left figure shows the mechanism to detect photons, while the right one indicates how the sensitivity to neutron-induced slow particles can be reduced.

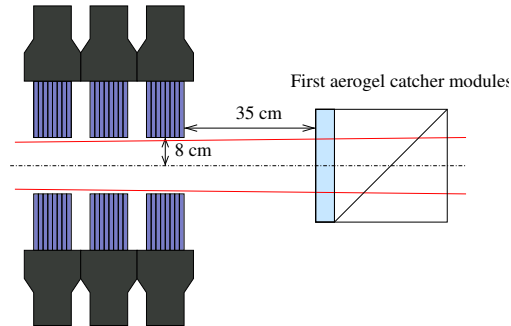
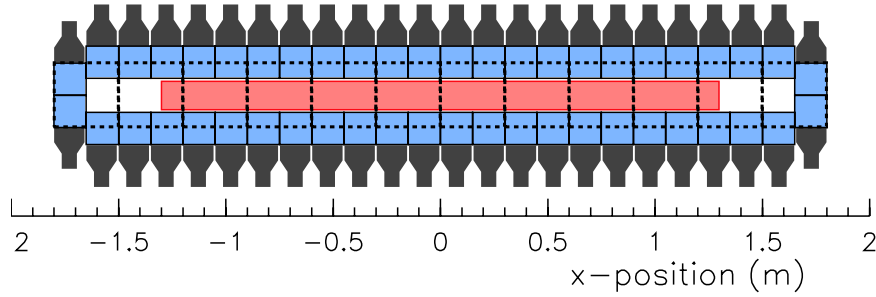


Fig. 6e.12. The schematic drawing of the guard counter. The upper (lower) figure shows the front (side) view of the counter. Each layer consists of 48 modules as in the left figure, and three modules are placed in sequence.

Figure 6e.12 shows a schematic view of the guard counter. The guard counter is composed of 144 modules, each of which consists of 8 layers of a 2-mm-thick lead sheet and a 10-mm-thick acrylic slab, whose cross section is 15 cm by 15 cm. Čerenkov light from the acrylic slabs are read by a 5-inch photomultiplier, the same one used in the catcher. Three modules are placed in sequence along the beam direction, which results in a total radiation length of  $9.3 X_0$ . This design was originally proposed in 1997 for the catcher and had been tested with the photon beam at KEK/INS in 1998. From the results, an efficiency of  $\geq 99.5\%$  can be obtained for  $\geq 300$ -MeV photons.

**Summary of Baseline Parameters of the Guard Counter** The parameters of the guard counter are summarized in Table 6e.2.

Table 6e.2. The base parameters of the guard counter.

Items	Parameters
size of module	15 cm (H) by 15 cm (V)
Pb converter	2-mm thick, 8 layers per module
acrylic slab	10-mm-thick, 8 layers per module
photomultiplier	5 inch in diameter, Hamamatsu R1250
number of modules	144 in total; 24 (H) $\times$ 2 (U/D) $\times$ 3 (Z)
aperture for the beam	330 cm (H) by 16 cm (V)
location in beam direction	end at z=2561 cm

#### 6e.4 Expected Performance

Monte Carlo simulations were performed to study the performance of the Catcher. The GEANT3 code was used, with the GCALE package for hadronic showers. All of the Čerenkov photons emitted by charged particles were traced by using our own subroutines. The simulations included the effects of the measured optical properties of aerogel tiles such as transmittance and Rayleigh scattering length, expected reflectivity of the mirror and Winston cone for the aerogel catcher, and total reflection in the acrylic slabs for the guard counters. In both cases, the quantum efficiency of the photomultiplier is taken as given in the Hamamatsu catalogue, with some correction factors obtained from our beam tests.

##### 6e.4.1 Efficiency for Photons

The photon detection efficiency as a function of its incident energy was calculated first. The incident angle of the photons in this calculation was fixed to be normal to the counter. The following photon identification procedure in this simulation was adopted. As for the aerogel catcher, the first module must yield  $\geq 4$  photoelectrons and the sum of the signals from two modules right behind it must have  $\geq 2$  photoelectrons. For the guard counter, the output of all modules was summed and required to be greater than 80 photoelectrons, which is equivalent to an incident energy of 50 MeV. Figures 6e.13 show the resultant photon detection efficiencies. In the calculation of the aerogel catcher efficiency, both the decay point in the fiducial region and the incident position at the catcher were randomly selected for each event, and thus the resultant efficiency is an average of those photons. Actually, the position at the catcher was chosen inside the coverage of the guard counters, i.e., 2.34 m in the horizontal and  $\pm 8$  cm in the vertical directions. In a similar way, the efficiency of the guard counter is an average over the whole active area. In the right figure, there are two lines for the efficiency of the guard counter, each of which indicates the efficiency for the guard counter alone and the combined efficiency with the aerogel catcher. The reason why the efficiency of the guard counter alone happens to be low, is that there are significant number of events with the shower leakage to the aerogel counter, which are covered by the combined efficiency with the aerogel catcher. As can be seen from the figures, the aerogel catcher and the guard counter give 99% efficiency for photons of 300 MeV and greater.

Next, the photon efficiency as a function of the incident position at the face of the Catcher was calculated. It was assumed that the photons come from the edge of the downstream end of the fiducial decay region, as shown in Fig. 6e.14. These photons have the largest angles for detection, and constitute the worst case for the Catcher. As can be seen in Fig. 6e.14, the Catcher has more than 99% efficiency within the region of  $\pm 20$  cm (vertical) by 3.4 m (horizontal).

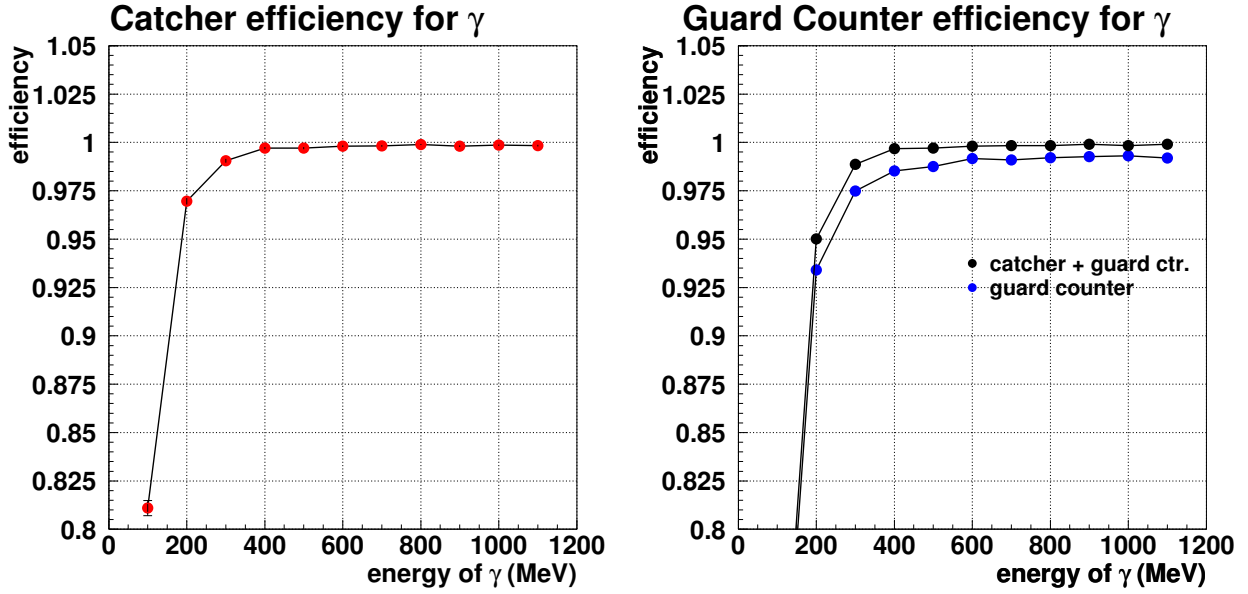


Fig. 6e.13. Efficiencies for photons as a function of incident energy. Each figure shows the efficiency of the aerogel catcher (left) and the guard counter (right). In the right figure, there are two lines indicating the efficiencies of the guard counter alone and the combined efficiency with the aerogel catcher.

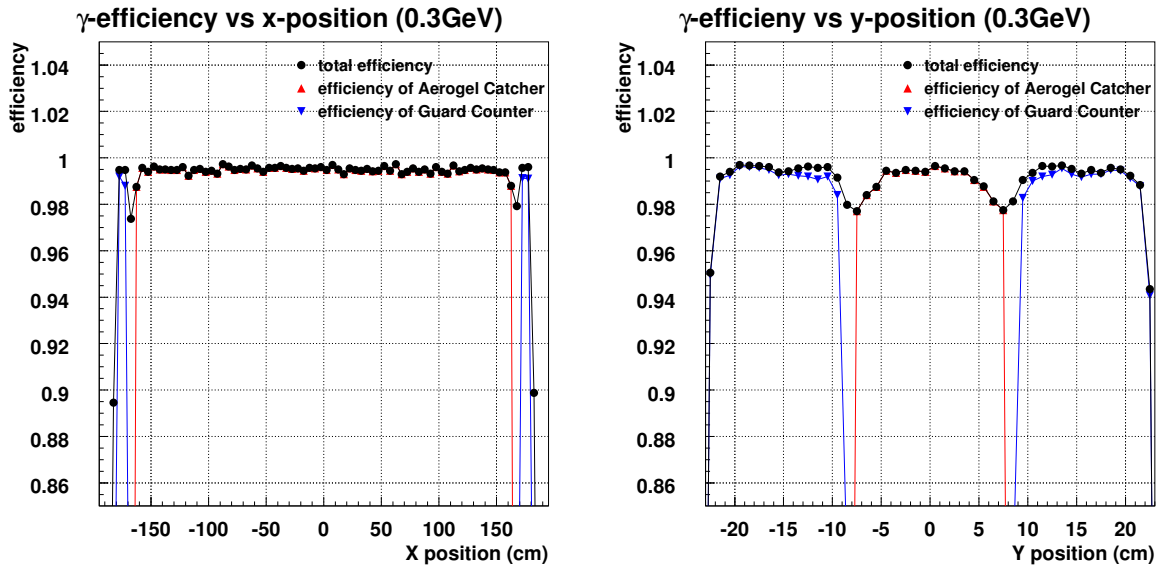


Fig. 6e.14. Efficiencies for photons as a function of the incident  $X$  (left) and  $Y$  (right) positions. The vertical (horizontal) position was fixed to be at the center in the left (right) figure.

### 6e.4.2 Response to Neutrons

Figure 6e.15 shows the hit probabilities for neutrons of the aerogel catcher and the guard counter. In the calculation, incident positions of neutrons were randomly set inside the core beam region, and thus the hit probability defined here is the average over the whole beam region. In addition, this means for the guard counter we only considered the effects of secondary particles from interactions in the beam region, i.e., interactions between the core beam and the aerogel catcher. Since we found that the influence from interactions directly between halo neutrons and the guard counter are relatively small compared with the in-beam interactions, we neglected it in our consideration for the guard counter. As can be seen in the left figure, the coincidence condition gives about 0.3% hit probability for 0.8-GeV neutrons, which are the main contributors to the false veto probability as described below, satisfying our requirement for the Catcher. The

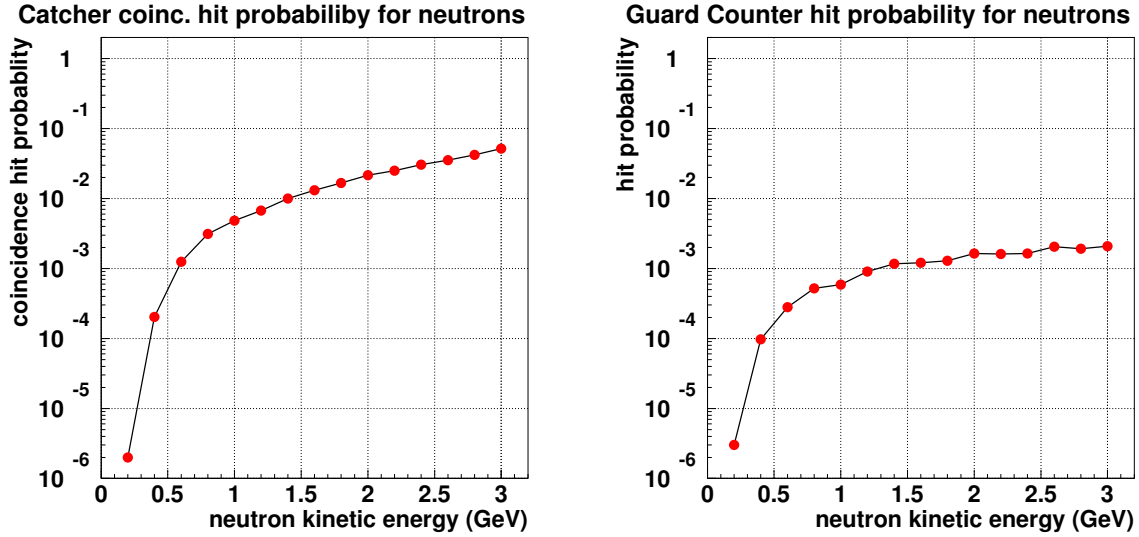


Fig. 6e.15. Hit probabilities for neutrons as a function of kinetic energy. Each figure shows the hit probability of the aerogel catcher (left) and the guard counter (right). The hit condition in each figure is same as the one described in previous section. Note that only the effects of secondary particles from interactions between the core beam and the aerogel catcher were considered in the right plot, because they are the main contributor to the count rate of the guard counter.

singles count rate of the photomultipliers is another concern because it can hinder their stable operation. This issue was checked, and Figure 6e.16 shows the estimated rates. In these figures, the top lines indicate the expected flux of neutrons as a function of the energy, with the beam intensity of 100 TP on the target and the production angle is 42.5 degree. The threshold level was assumed here to be set to 1 p.e. equivalent for the aerogel catcher and 50-MeV equivalent (80 p.e.) for the guard counter. The hit probability of a module when one neutron hit the counter was calculated first. It depends on the position of the module in the whole configuration. The maximum and averaged probabilities are indicated.

By multiplying the probabilities with the expected number of neutrons in a microbunch, the number of neutron-induced hits in a microbunch can be obtained, as shown in the figure. By integrating over the neutron energy (0.073 per a microbunch in the figure) and taking the microbunch frequency of 25 MHz, the maximum singles rate per module of the aerogel catcher was estimated to be 1.8 MHz. The count rate of the guard counter was estimated in the same manner and found to be safely low (105 kHz).

Another concern is that genuine signals could be vetoed and thus lost due to accidentals from neutrons. This false veto probability was estimated, and Figure 6e.17 shows the number of false coincident hits in a

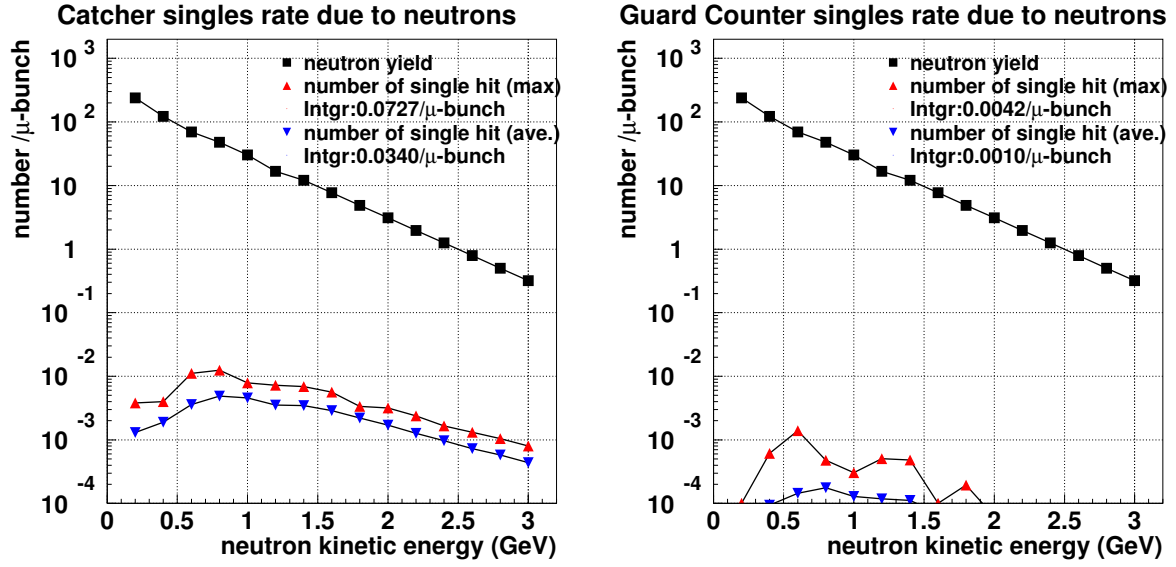


Fig. 6e.16. Estimated singles counting rate due to neutrons as a function of kinetic energy. Each figure shows the rate of the aerogel catcher (left) and the guard counter (right). As in Fig. 6e.15, only the effects of secondary particles from interactions between the core beam and the aerogel catcher were considered in the right plot.

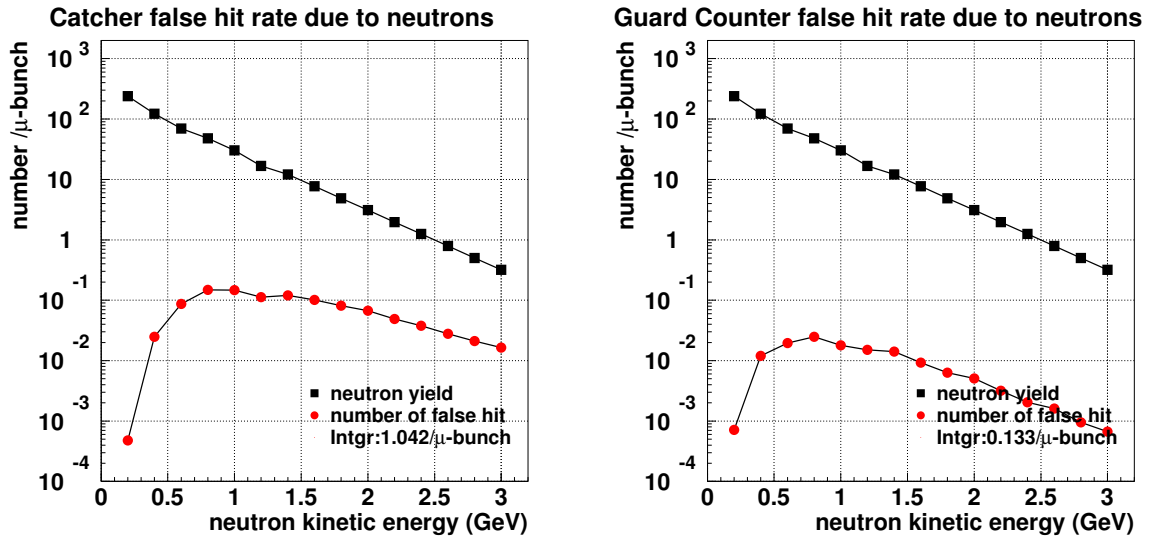


Fig. 6e.17. Estimated false veto probability due to neutrons. The upper line with square dots indicates the expected number of neutrons in a microbunch. Multiplying the coincidence hit probability shown in Fig. 6e.15, the false veto activity in a microbunch as a function of neutron kinetic energy could be obtained, shown as the lower line with closed circles. In the plots of the guard counter, only the effects of secondary particles from beam interactions were considered.



microbunch. Integrating the neutron contribution above 0.5 GeV where the neutrons come into the signal time window, 1.04 counts per microbunch was obtained. Assuming the timing resolution to be 0.5 nsec and a signal time window of 26.3 nsec,<sup>†</sup> the final false veto probability after  $\pm 3\sigma$  timing cuts is expected to be  $1.042 \times 3 \text{ ns} / 26.3 \text{ ns} = 11.9\%$ .

The real photon signal, which we want to catch and veto, might be smeared (and thus lost) by adjacent (early or late) particles. In particular, when unwanted signals are bigger than the real signal and arise just before it, they are likely to cause a loss in efficiency. Such loss due to neutrons was estimated by the simulations. It was simply assumed here that a module will be blind throughout the microbunch once a signal has been generated. The efficiency loss by accidentals, defined as the probability of destroying coincidences, was found to be 1.0%.

### 6e.4.3 Response to Neutral Kaons

The hit probability for  $K_L$ s that do not decay in the fiducial decay region but rather decay further downstream or interact directly with the Catcher was investigated. Figure 6e.18 shows the results. We considered both effects of the  $K_L$  decays upstream of and inside the Catcher and  $K_L$  interactions with the Catcher in this calculation. According to the simulation, the hit probability is 12% at 1 GeV/c, most of which is due to  $K_L$  decay in the Catcher.

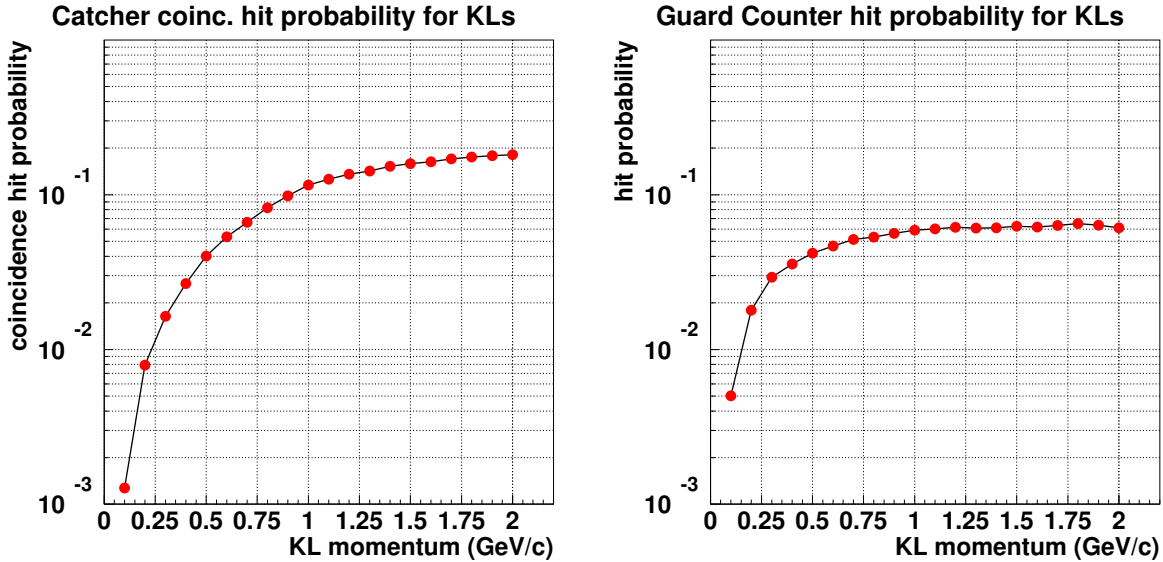


Fig. 6e.18. Hit probabilities for  $K_L$  as a function of momentum. Each figure shows the hit probability of the aerogel catcher (left) and the guard counter (right). The hit conditions in these figures are described in the section of "Efficiency for Photons".

Similar to the discussion about neutrons, the singles counting rate and false veto probability due to neutral kaons were also estimated, as shown in Figures 6e.19 and 6e.20. The upper lines with square dots indicate the expected number of  $K_L$ s in a microbunch which survived to the end of the fiducial decay region ( $z=14\text{m}$ ). Integrating over the whole momentum region, the maximum singles rates due to  $K_L$ s were estimated to be 325 and 175 kHz for the aerogel catcher and the guard counter, respectively. In a manner

<sup>†</sup>The time window was calculated with the  $K_L$  momentum range of  $0.4 < P_K < 1.3 \text{ GeV/c}$  and the full decay region length. It was defined as the arrival time difference at the upstream face of the catcher.

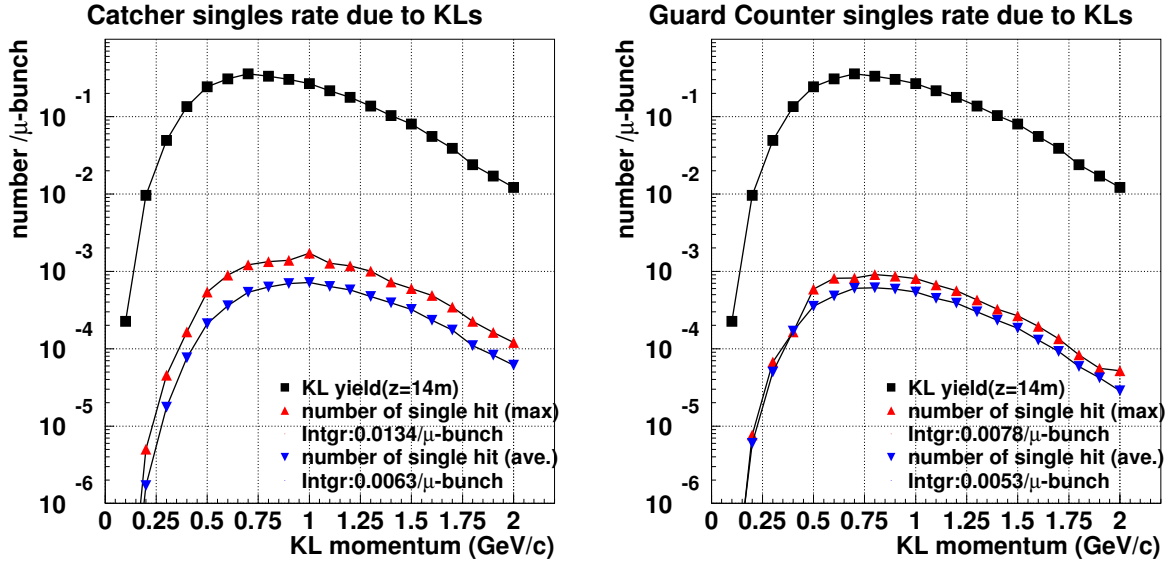


Fig. 6e.19. Estimated s counting rate due to neutral kaons as a function of kinetic energy. Each figure shows the rate for the aerogel catcher (left) and the guard counter (right).

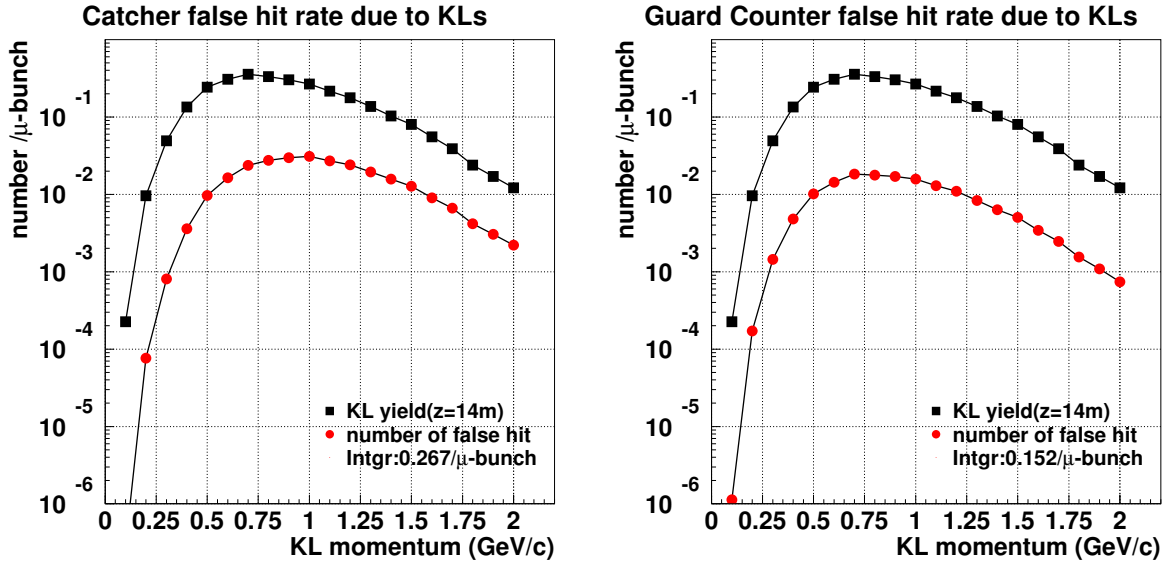


Fig. 6e.20. Estimated false veto probability due to neutral kaons. Multiplying the hit probability shown in Fig. 6e.18 with the false veto probability, the false veto activity in a microbunch as a function of  $K_L$  momentum was obtained, as the lower line with closed circles.

similar to that for neutrons, the false veto probability due to neutral kaons was found to be  $0.267(0.152) \times 3 \text{ ns} / 26.3 \text{ ns} = 3.0(1.7)\%$  for the aerogel catcher (the guard counter).

#### 6e.4.4 Responses to Beam Photons

In addition to the neutrons and  $K_L$ s, there exist photons that are produced directly in the production target. These photons (called “prompt photons”) may also contribute to the false veto probability.

From the expected energy spectrum and flux for the prompt photons, shown in Section 5, the coincidence count was calculated to be 0.06 per microbunch. However, there is no harm because they always arrive at the Catcher 2-ns faster than the fastest signal. Even in the case of the worse timing resolution, say 5 ns, the false veto probability can be safely neglected ( $<0.1\%$ ).

The singles rate by prompt photons is rather high and not negligible. The expected number of hits in a microbunch was found to be about 0.07, and thus the rate will be 1.8 MHz for a threshold of 1 photoelectron.

Another problem is the efficiency loss due to some modules being blind. The beam photons arrive at the Catcher more quickly than other particles. They always generate a signal before the real photon we want to catch and veto. Assuming the double-pulse resolution to be 3 ns, this loss was estimated to be 1.7%.

#### 6e.5 Summary

The design of the beam Catcher detector based on the combination of a distributed aerogel Čerenkov counter and a lucite sandwich counter has been examined. Their combined performance has been studied with Monte Carlo simulations based on measured and/or reliable parameters, and is found to meet the requirements for our experiment. The simulations yield 99% efficiency for 300-MeV photons, and 0.3% efficiency for 0.8-GeV neutrons. The relevant parameters are summarized in Table 6e.3.

Table 6e.3. The summary of the resultant parameters.

photon efficiency	$\geq 99\%$	above 300 MeV
neutron hit probability	0.3%	at 0.8 GeV
false veto probability	11.9%	due to neutrons
	3.0%	due to $K_L$ s in the aerogel catcher
	1.7%	due to $K_L$ s in the guard counter
singles rate (max.)	1.8 MHz	due to neutrons
	325 kHz	due to $K_L$ s in the aerogel catcher
	175 kHz	due to $K_L$ s in the guard counter
	1.8 MHz	due to beam photons
efficiency loss by blindness	1.0%	due to neutrons
	1.7%	due to beam photons

#### References

1. H. Morii *et al.*, “Quenching effects in nitrogen gas scintillation.”, Nucl. Instrum. Meth. A **526**, 399 (2004).
2. T. Matsumoto *et al.*, “Studies of proximity focusing RICH with an aerogel radiator using flat-panel multi-anode PMTs (Hamamatsu H8500).”, Nucl. Instrum. Meth. A **521**, 367 (2004).
3. E. Aschenauer *et al.*, “Optical characterization of  $n=1.03$  silica aerogel used as radiator in the RICH of HERMES.”, Nucl. Instrum. Meth. A **440**, 338 (2000).

## 6f Photon Detection Inefficiency

### 6f.1 Overview

The primary sources of photon detection inefficiency in KOPIO are:

- Sampling fluctuations (no visible energy detected in active material);
- Punch-through (escape of photons before conversion); and
- Photonuclear interactions (no electromagnetic shower).

Sampling fluctuations and punch-through, being purely electromagnetic processes, are well understood and well simulated by Monte Carlo tools. Photonuclear interactions are more problematic. Measurements of the interaction cross section as a function of photon energy are available for a large number of elements. In some cases, measurements are also available for the multiplicity, energies, and even angles of the outgoing particles following a photonuclear interaction. However, in most cases, a model must be used for the outgoing particles.

The strategy for predicting the photon detection inefficiency for KOPIO is as follows. First, the single photon detection inefficiency (SPI) for photon energies between 20 and 200 MeV was obtained from data for  $K^+ \rightarrow \pi^+ \pi^0$  decays in experiment E949. To project these results to the KOPIO photon veto situation, where a different arrangement of lead and scintillator is planned, the FLUKA Monte Carlo (FLUKA 2003.1b)[1] code was used; the validity of FLUKA was checked by simulating the E949 photon veto detectors and comparing them with the measurements. For photon energies where the agreement between FLUKA and E949 data was poor, the E949 measurements were simply carried over as the estimate of the KOPIO photon detection inefficiency. For photon energies below 20 MeV, we relied solely on FLUKA because sampling fluctuations are expected to dominate. For photon energies above 200 MeV, we relied primarily on measurements[2] of the inefficiency due to photonuclear reactions in lead-scintillator sandwich calorimeters. The E949 data were also used to estimate the effect on photon detection inefficiency of dead material (carbon) in front of the photon veto detectors.

Other potential sources of photon detection inefficiency include:

- Detector cracks;
- Photostatistics; and
- “Blindness” caused by overlap with previous activity in the counter.

Cracks (and/or WLS fiber holes) are dealt with by careful engineering design. The effects of photostatistics are expected to be negligible due to the high light output in the KOPIO photon detection systems. Blindness depends on the double-pulse resolution and on detector rates. In E949 scintillator-based systems, second pulses riding on the tail of another pulse were identifiable starting at around 6 ns. To cover smaller time separations (assuming the detector rates are high enough to warrant it), the veto window can be extended backwards in time by 6 ns. This shift would result in an acceptance loss, the effect of which is estimated in Sec. 13.

### 6f.2 Sources of photon detection inefficiency

#### 6f.2.1 Sampling fluctuations

Sampling fluctuations dominate the inefficiencies for low-energy photons. The effect comes from absorption of a photon’s charged products in the non-active material (lead). Therefore the thickness of a single lead layer is a parameter to be optimized. A high light output of the detector is another important factor for suppressing inefficiencies caused by low visible energy deposited in a scintillator. Sampling resolution and the visible fraction of deposited energy are shown in Fig. 6f.1 for 0.5- and 1-mm-thick lead layers.

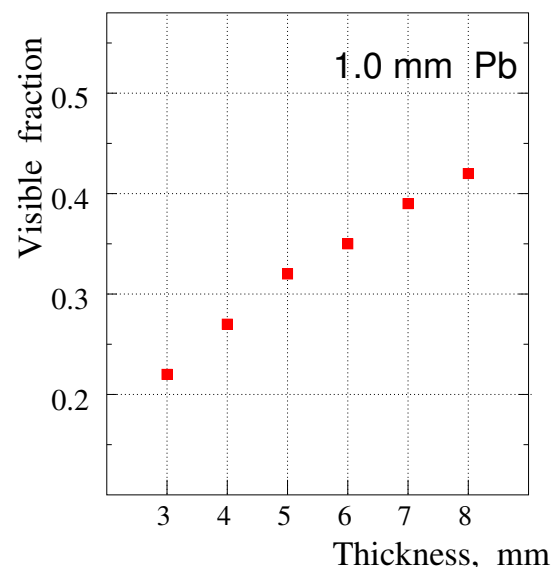
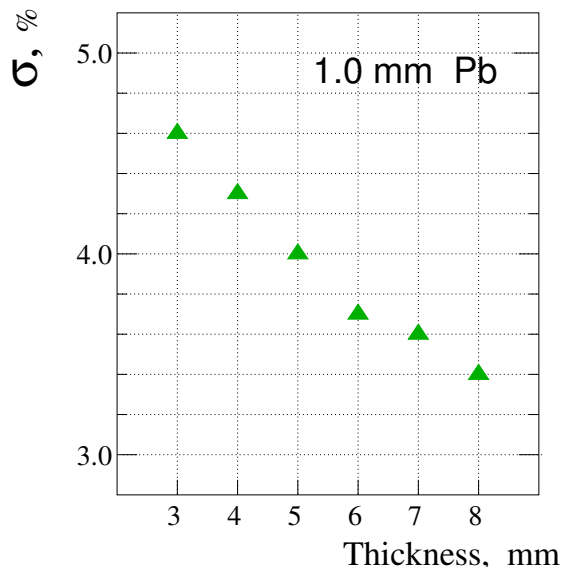
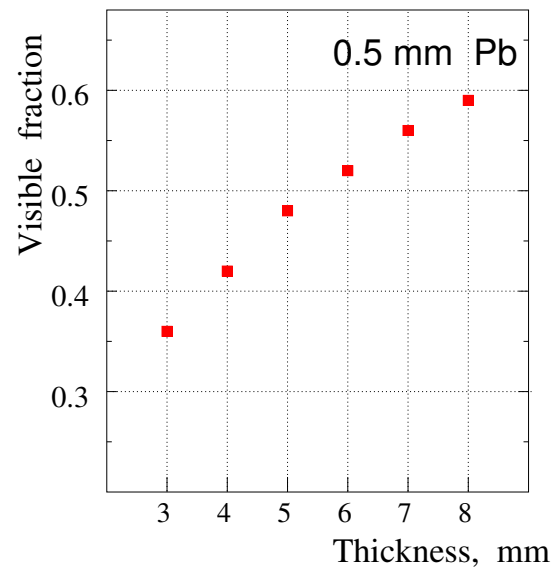
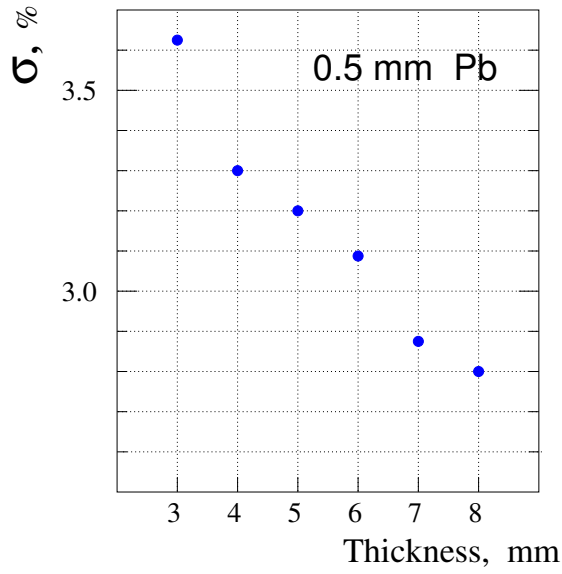


Fig. 6f.1. The energy resolution ( $\sigma/\sqrt{E}$ ) and visible fraction versus the thickness of a scintillator layer in the case of 0.5- and 1-mm lead. The resolution is determined from pure sampling and leakage fluctuations. The number of layers is 180 for 0.5-mm Pb, and 100 for 1-mm Pb.

A rough estimate of sampling inefficiencies can be obtained without detailed detector simulations. The sampling fluctuations cause a spread of the measured (visible) energy. The resulting inefficiency can be estimated by calculating the probability that the measured energy is below a specified detection threshold. For example, assuming a Gaussian distribution of the measured energy, an energy resolution  $\sigma_E / \sqrt{E_\gamma} [\text{GeV}] = 5\%$ , and a detection threshold of 1 MeV, the inefficiency is  $7 \times 10^{-5}$  for a 40-MeV photon, and goes up to  $6 \times 10^{-4}$  and even  $6 \times 10^{-3}$  for 30- and 20-MeV photons, respectively.

It is found in GEANT simulations that the first scintillator layer must provide the largest light output in order to detect the “back-going” charged particles emitted as a result of photon conversion in the first lead layer.

### 6f.2.2 Punch-through

The contribution of punch-through to the photon detection inefficiency can be calculated from the photon mass attenuation coefficients tabulated at NIST[3]. Good agreement was seen between such calculations and explicit Monte Carlo estimations.

### 6f.2.3 Photonuclear Interactions

Although the electromagnetic interactions are well understood and simulated, the photonuclear reactions are described by different nuclear models that are valuable for studying fundamental properties of nuclei. However, actual cross sections must be obtained through direct measurements. The energy range is commonly subdivided into three regions, reflecting the length scales on which the interaction occurs. In the energy range below approximately 30 MeV, typically called the Giant Dipole Resonance (GDR) region, the photon interacts with the nucleus as a whole, inducing dipole oscillations. Between 30 and approximately 200 MeV, known as the “quasi-deuteron” region, the photon can be described as interacting with “deuterons” in the nucleus. Photons above approximately 200 MeV are energetic enough to start producing pions. The photonuclear cross section typically has a GDR peak at around 20 MeV, then falls off in the quasi-deuteron region, rising slightly at the pion production threshold and staying roughly flat for photon energies of interest to KOPIO.

The photonuclear reaction threshold in lead is about 7.3 MeV. The absorption is peaked near 13.4 MeV and falls gradually above 25 MeV. Above 14 MeV (the threshold of  $2n$  or  $n+p$  production), there is in principle a chance that a proton will be emitted and detected. However, due to the large Coulomb barrier in heavy nuclei, the probability of this process is negligible compared with neutron production. In lead, a photon with typical energy of 80 MeV knocks out 5–7 neutrons with energies each around 2 MeV. Neutrons in this energy range travel outside the lead into the scintillator, where they lose their kinetic energy through collisions with hydrogen nuclei. Such neutrons can be detected when they kick out a proton that has energy above a detection threshold.

In lighter materials such as carbon, a photon knocks out neutrons and protons with roughly equal probability (in the GDR region, the proton to neutron ratio is roughly two to one). The photonuclear reaction threshold is around 15 MeV in carbon, and peaks near 23 MeV.

The photoneutron cross sections in the photon energy range of 25–130 MeV have been studied for lead in Ref.[4]. The results are shown in Fig. 6f.2 in comparison with the cross sections for electromagnetic interactions. The total photonuclear cross section in carbon (the base element of a plastic scintillator) was measured in Ref.[5]. The cross section was found to be about 1.5 mb in the photon energy range from 60 to 160 MeV. Below 60 MeV is the GDR region with a maximum cross section near 23 MeV. Total photonuclear absorption cross sections in lead and carbon (as the main component for scintillator) are shown in Fig. 6f.3. The data were compiled from Ref.[6].

## 6f.3 E949 Measurements of Photon Detection Inefficiency

The measurement of the E949 SPI was performed with  $K^+ \rightarrow \pi^+ \pi^0$  decays. The charged pion and one of the photons from the  $\pi^0$  were kinematically fit (assuming a  $K_{\pi 2}$  hypothesis) to obtain the direction and

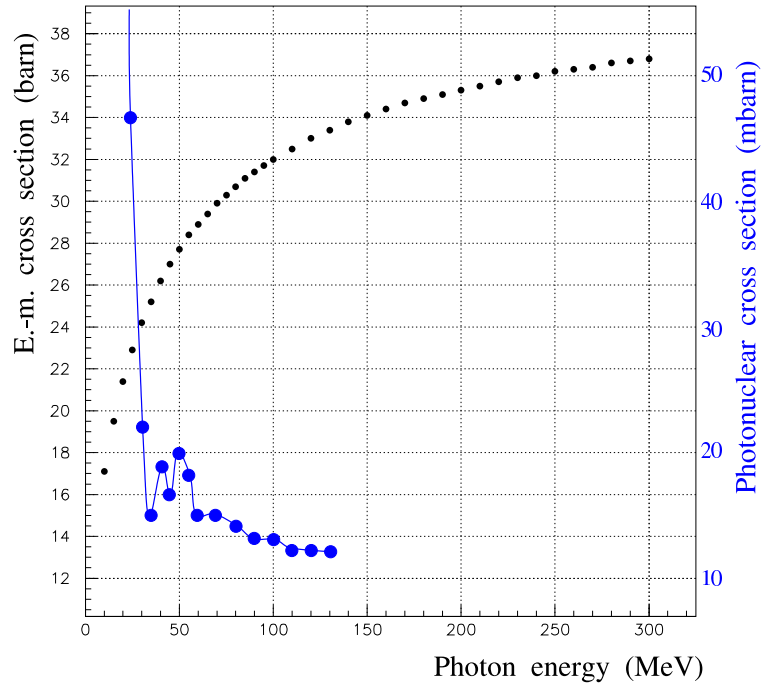


Fig. 6f.2. Total electromagnetic cross-section in lead vs. photon energy. Blue circles show the cross section of photonuclear absorption in Pb as measured in Ref.[4].

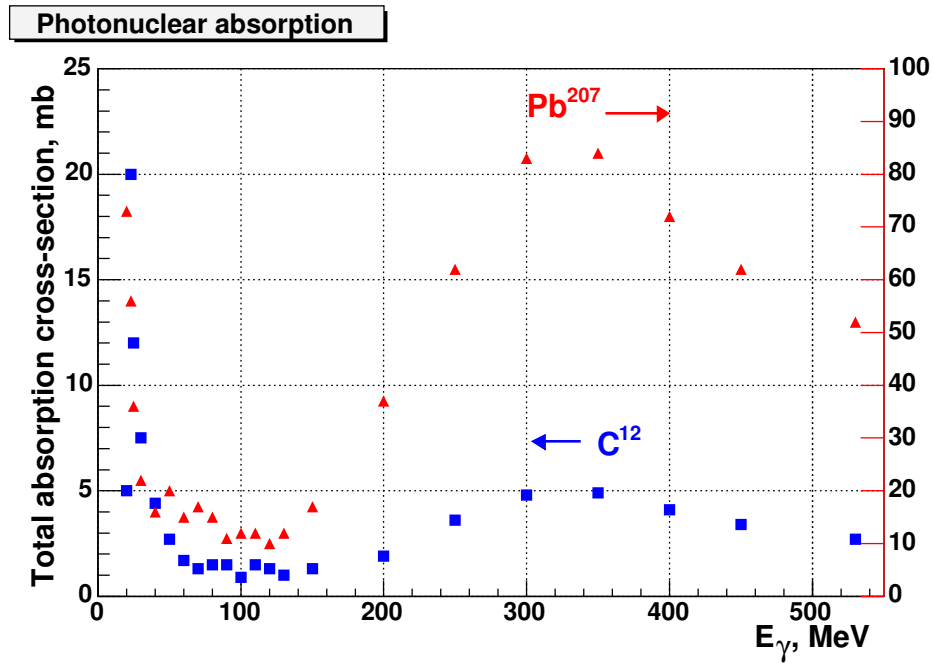


Fig. 6f.3. Total photonuclear cross-sections for lead and carbon versus the photon energy, and a compilation of experimental data.



energy of the second photon. The detection inefficiency for the second photon was measured for different visible energy thresholds as a function of photon energy and direction; veto time windows ranged from 6-10 ns (full-width). The result for normally incident photons is shown in Fig. 6f.4. Note that these results include the effect of veto blindness at the E949 counter rates. At normal incidence, the E949 photon veto system consists of 34.085 cm of scintillator (one layer 0.7cm thick followed by 17 layers, each 1.905cm thick, and then by one 1cm-thick layer; this is the so-called Range Stack), followed by 88 layers of 5mm-thick scintillator interleaved with 87 layers of 1mm-thick lead.

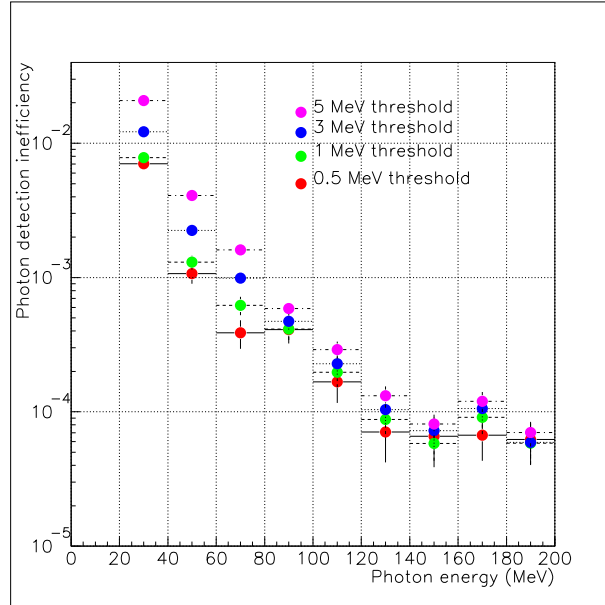


Fig. 6f.4. E949 photon detection inefficiency as a function of photon energy for normal incidence. Thresholds are for visible energy.

The E949 data were also used to estimate the effect of dead material (carbon) in front of the photon veto. The same SPI analysis as above was performed, but data from successive layers of the Range Stack were blanked out to simulate dead carbon of various thicknesses.

#### 6f.4 FLUKA Simulation of E949 Photon Veto

The E949 photon veto detectors were simulated in a planar geometry with the photons incident at the center. The energy deposited in the scintillator was summed (saturation effects were included) and the fraction of events with energy below a certain threshold was counted. The results for a 1-MeV visible energy threshold are shown in Fig. 6f.5 together with the E949 measurements.

Investigations of the discrepancy between FLUKA estimations and the E949 data have met with limited success, except perhaps for the 30-MeV bin where resolution effects in the photon angle reconstruction in E949 artificially increase the measured photon detection inefficiency. The significant discrepancy in the intermediate energy region (50-150 MeV) remains a mystery, especially since photonuclear effects are expected to be suppressed in this region. For photon energies of around 190 MeV, however, the agreement between FLUKA simulation and E949 data seems reasonable.

#### 6f.5 Estimation of KOPIO Photon Detection Inefficiency

The photon detection inefficiency for photon energies 20 MeV and below was estimated with FLUKA. The longitudinal segmentation was that of the KOPIO Barrel Veto: 0.5-mm lead and 1.5-mm scintillator.

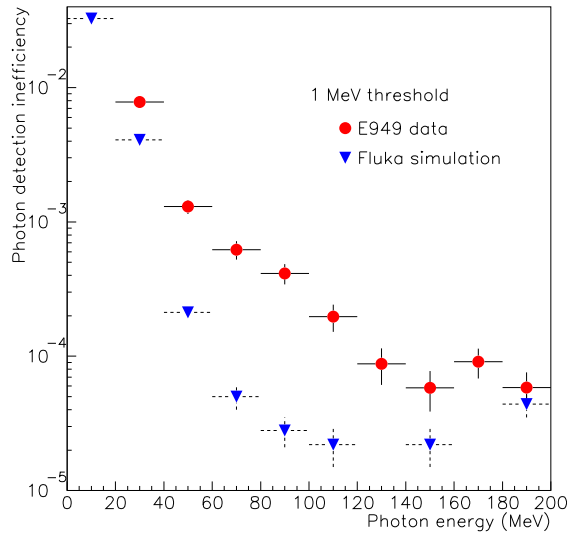


Fig. 6f.5. Dots: photon detection inefficiency as a function of photon energy, measured in E949 with 1-MeV (visible) threshold for normal incidence. Triangles: FLUKA simulation of E949. The horizontal error bars for the FLUKA points should be ignored.

The total thickness was  $17 X_0$ . The (small) punch-through contribution was calculated with the photon mass attenuation coefficients tabulated at NIST[3] and subtracted (to be added separately later after optimizing the total thickness of the photon veto).

For the 30-MeV bin, the inefficiency was estimated with FLUKA. The longitudinal segmentation was that of the KOPIO Calorimeter: 0.275-mm lead and 1.5-mm scintillator. The structure simulated was  $18 X_0$  thick although, as above, the punch-through contribution was accounted for separately. For 50-170 MeV, the E949 measurements were used because FLUKA could not be validated in this energy region. Again, the punch-through contribution was subtracted, for separate addition later. For 170-190 MeV, the inefficiency was estimated with FLUKA, again using the Calorimeter longitudinal segmentation. Above 190 MeV, the slope of the decrease in the inefficiency (due to photonuclear) as a function of photon energy was taken from[2], but normalized to the FLUKA photonuclear inefficiency at 190 MeV. The photonuclear inefficiency was not allowed to drop below  $1 \times 10^{-6}$ , to be consistent with the results in[2].

For all energies 20 MeV and above, a contribution to the inefficiency from the vacuum vessel was estimated from the E949 data and added (assuming 2 cm of carbon fiber). In all of the above estimations, normally incident photons and a 1-MeV visible energy threshold were assumed. (The treatment of angular dependence is described later.)

The resulting photon detection inefficiency for a structure with 0.275-mm lead and 1.5-mm scintillator with a total thickness of  $21.6 X_0$  is shown in Fig. 6f.6. The total thickness was chosen to make the contribution of punch-through negligible for all KOPIO photon energies, even for normal incidence. Monte Carlo studies showed that, in the region of the Preradiator/Calorimeter, the photon energies and angles were such that KOPIO would benefit from reducing punch-through. In the Barrel and Upstream veto regions where the photon spectra are softer and are frequently produced at larger angles, the required thickness was  $18 X_0$ .

The behavior of the photonuclear contribution in Fig. 6f.6 for photon energies below 30 MeV is a rough estimate based on the photonuclear cross section. The inefficiency due to photonuclear reactions is expected to drop as the photon energy falls below that of the Giant Dipole Resonance region. The exact shape of the

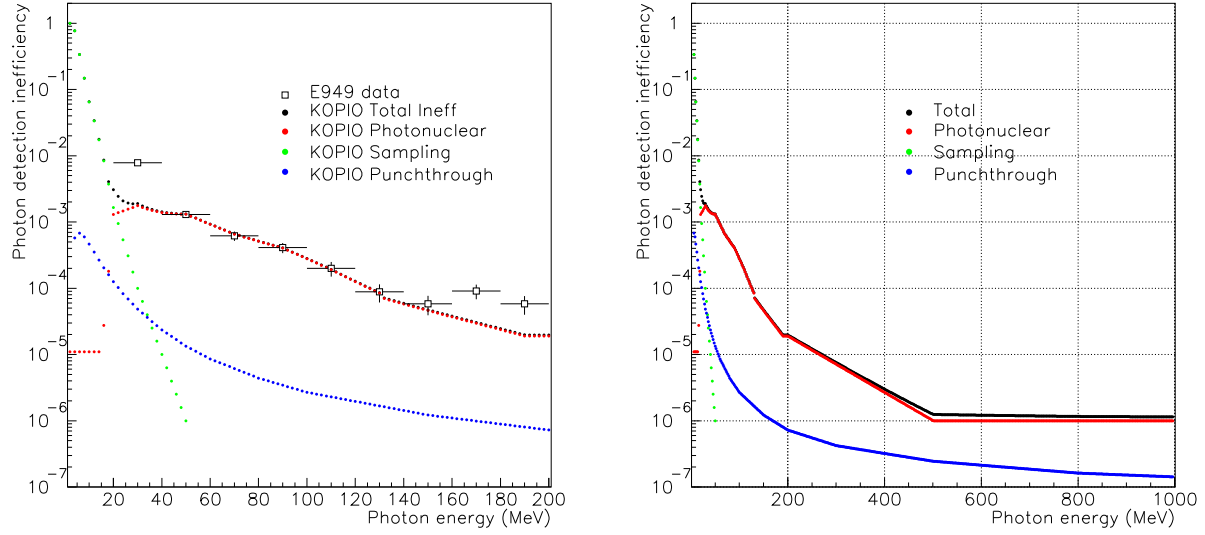


Fig. 6f.6. Left: Expected photon detection inefficiency in KOPIO, broken down by source, for a 1 MeV visible energy threshold and normally incident photons. Also shown is the photon detection inefficiency measured in E949. Right: the same plot on an expanded photon energy scale.

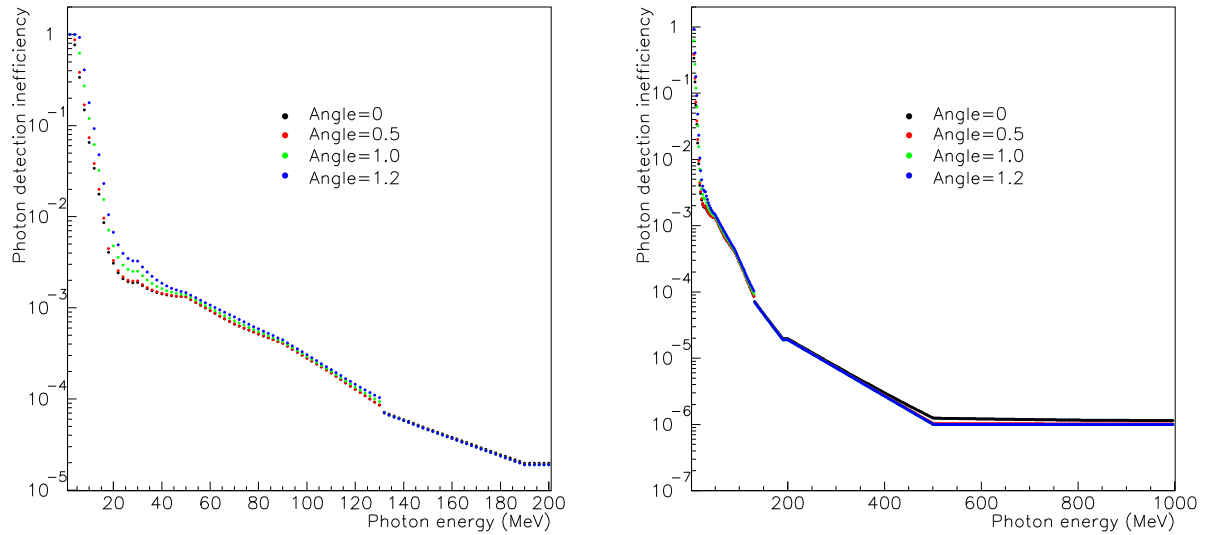


Fig. 6f.7. Left: Expected photon detection inefficiency in KOPIO as a function of photon energy and angle of incidence, for a 1-MeV visible energy threshold. Right: the same plot on an expanded photon energy scale.

photonuclear inefficiency in this region is not expected to affect the total inefficiency because the contribution from sampling fluctuations is rapidly rising.

The treatment of photons at non-normal incidence was as follows. The inefficiency due to sampling fluctuations was assumed to scale linearly with the lead thickness. The inefficiency due to the dead material was seen from the E949 studies to scale linearly with the thickness. The inefficiency due to punch-through was recalculated from the mass attenuation coefficients for each photon, based on its angle of incidence. The inefficiency due to photonuclear reactions appeared from the data in Ref.[2] to be independent of the lead thickness, at least up to a thickness of 1 mm; studies with FLUKA supported this picture. Given a thickness of 0.275 mm per lead layer, this insensitivity implied that the photonuclear contribution would be independent of incident angle up to  $\sim 70^\circ$ . The photon detection inefficiency as a function of energy and angle is shown in Fig. 6f.7.

### 6f.6 Future Work

Future work on this subject includes the following. The discrepancy between FLUKA simulations and E949 data will be investigated further. On the simulation side, studies have been started with GEANT4 which uses a different model for photonuclear effects. Timing and hermiticity effects in FLUKA for photonuclear reactions will be examined. Further studies of the systematics of the E949 SPI measurements are also planned. The parameterization of the expected KOPIO photon detection inefficiency for input to the KOPIO Fast Monte Carlo will be improved to take into account the different longitudinal sampling in the different detector systems; currently the Calorimeter sampling is used in both the Barrel and Upstream veto regions. The effects of the photon incidence angle on the inefficiency (in particular, sampling and photonuclear) will be studied further with Monte Carlo.

### References

1. <http://www.fluka.org>.
2. K. Kurebayashi, "Measurement of the photon detection inefficiency due to photonuclear reactions in lead/scintillator sampling calorimeters", Osaka University Masters Thesis (in Japanese, unpublished), Feb. 4, 1999.
3. <http://physics.nist.gov/PhysRefData/Xcom/Text/XCOM.html>.
4. A. Lepretre *et al.*, Nucl. Phys. **A367**, 237 (1981).
5. J. Ahrens *et al.*, Nucl. Phys. **A251**, 479 (1975).
6. <http://depni.npi.msu.ru/services/>.

## 7 The Vacuum

The challenge for the KOPIO vacuum system is to provide a high-quality vacuum in the beam path with a minimum amount of material between the decay region and the photon detectors. A vacuum of  $\sim 10^{-7}$  Torr is required in the beam path to suppress beam interactions with the residual gas. These interactions near the decay region can create neutral pions, which might be reconstructed as  $K_L^0$  decays. The motivation for this level of vacuum is described in Sec. 13 on sensitivity and backgrounds. The vacuum vessel for the decay region must be constructed from a minimum amount of material ( $< 7\% X_0$ ) to reduce photon conversion and photon generation from electrons and positrons. In addition, the decay region must have charged-particle veto counters located inside the vacuum vessel to provide sufficiently low thresholds for produced charged particles. These combined requirements make the KOPIO vacuum system a challenge.

Figure 7.1 displays the conceptual design of the vacuum system and the vacuum requirements in plan and elevation views. The good vacuum,  $\sim 10^{-7}$  Torr, extends from the upstream collimator system to past the Preradiator and Calorimeter. Downstream of the Calorimeter, the vacuum requirements are much less stringent. The vacuum pressure can be  $\sim 10^{-3}$  Torr in the downstream regions of the vacuum system. A thin membrane with a thickness of a few milligrams per  $\text{cm}^2$  will provide the transition between these two vacuum regions. Figure 7.1 shows that a region of poor vacuum exists between the decay volume and the vacuum tank wall. This region contains the charged-particle veto counters. Another thin membrane will isolate this region, with a pressure of  $\sim 10^{-3}$  Torr, from the fiducial decay volume where the high-quality vacuum is required. Pumping stations will be distributed along the vacuum system.

A senior vacuum engineer has examined the vacuum layout and requirements for KOPIO. He is confident that the goals of the experiment can be achieved. The pumping system will have a PLC-based controls system for regulation. The controls will provide for pump-down and bleed-up sequences, including protection for power failures. The high vacuum will be accomplished by mechanically-refrigerated cryosorption pumps. The rough vacuum will be provided by turbomolecular pumps.

The requirement for a thin ( $< 7\% X_0$ ) decay tank, entrance beam pipe, and exit beam pipe suggest the use of low-Z materials. Discussions with a Russian company experienced with composite structures are ongoing and may lead to a design based on carbon-fiber composite beam pipes and decay tank. However, the use of aluminum for the beam pipe and decay tank has been currently selected for the experiment. Figure 7.2 displays the layout of the decay tank with the beam pipes attached. Current engineering analysis has shown that the tank and beam pipes meet the necessary safety guidelines for vacuum vessels and nearly achieve the thickness goals of the experiment. The aluminum decay tank has a diameter of 2.5 meters and a wall thickness of 6 mm. The central portion of the tank is 4 meters long and is coupled to the end domes with flanges. The central body of the tanks has two flanges that will allow opening the tank for the charged-particle veto detectors. The flanges will also be used for mounting the feedthroughs for the charged-particle detectors inside. The section of beam pipe that goes through the Preradiator has transverse ribs appropriately spaced so that sections of the Preradiator fit between the ribs.

The vacuum required downstream of the Calorimeter is all poor-quality vacuum,  $\sim 10^{-3}$  Torr. The vacuum tank inside the D4 sweeper magnet, will be stainless steel and will contain the Magnet Photon Veto detector system. Figure 7.3 displays the conceptual design of the downstream tank that is connected to the magnet tank. This tank is constructed with steel in a rectangular geometry. The tank is reinforced with box beams to provide the necessary strength. The tank is 5 meters long but has been divided into two sections to allow for easier insertion of the photon veto and installation of the tank in the experiment. The end plates of the tank are reinforced as shown in the figure. The vacuum is terminated at the end of this tank with an aluminum window on the downstream end, which is 3-m wide and 20-cm high.

# KOPIO EXPERIMENTAL APPARATUS

## VACUUM SYSTEM

PRELIMINARY

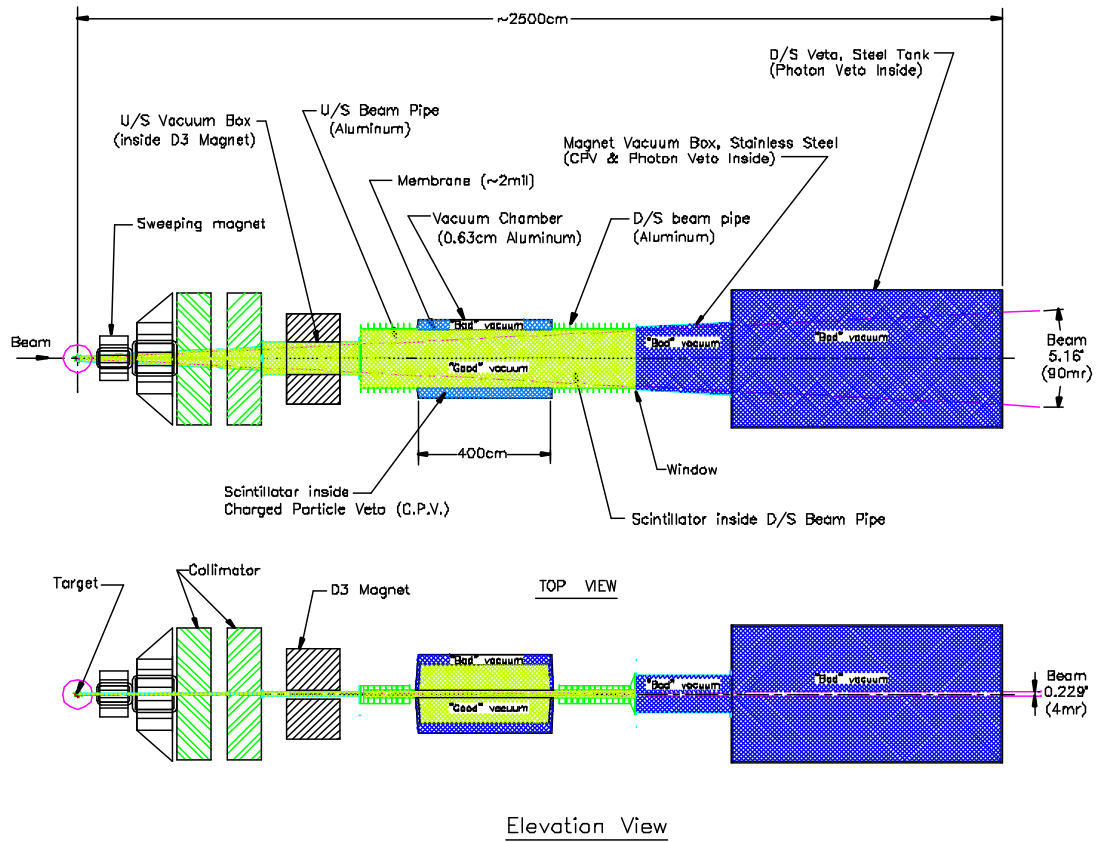


Fig. 7.1. Vacuum system design.

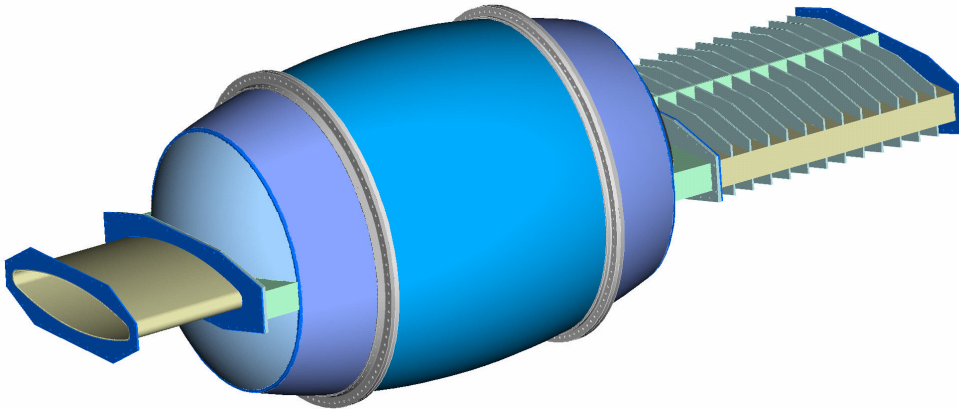


Fig. 7.2. Layout of the decay tank.

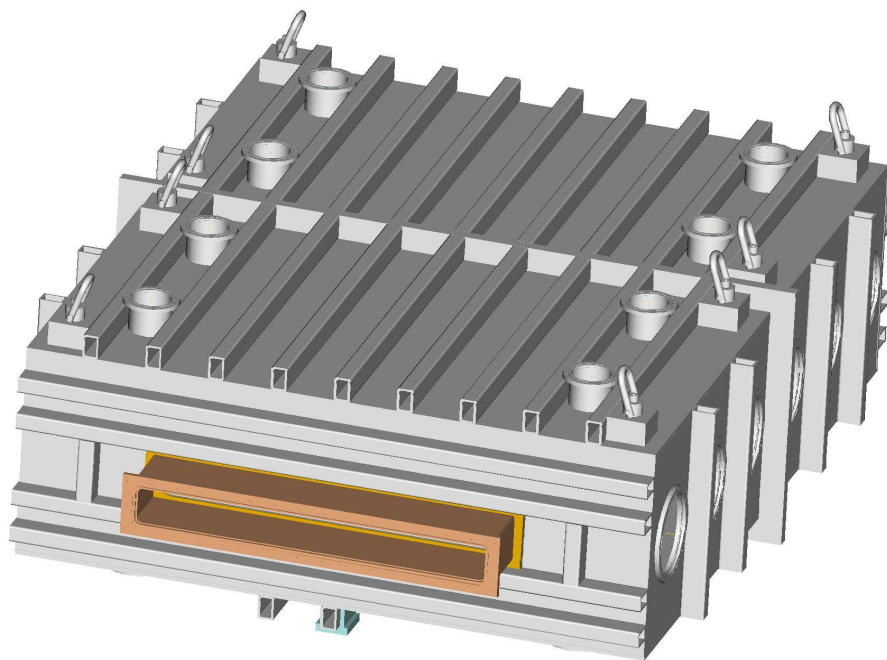


Fig. 7.3. Conceptual design of the downstream tank.



## 8 Photodetector Electronics

The front end electronics (FEE) for the KOPIO photosensor detectors are based on common designs as much as possible. These common FEE systems include everything from the output of the photosensor to the outputs to the DAQ and Trigger: high voltage (HV) and low voltage (LV) systems, preamplifiers, cabling, Waveform Digitizer (WFD) boards, and Crate Data Collection boards. The FEE also include a calibration/monitoring system. The FEE for the Preradiator chamber are discussed separately in Sec. 6a (Preradiator).

The common FEE include several components attached to the photosensor, including a preamplifier and a LV-HV converter. The associated power supplies are also common, whereas the cabling will be tailored somewhat differently for photosensors mounted in the vacuum to avoid excessive costs of vacuum penetrations.

The common design for the monitoring system will flash light into all photodetector systems through optical fibers. This triggerable system will allow for rapid detection of any failed channels and will provide a rapid calibration of photosensor gains with high precision. The details of the driving circuit and the distribution of the light sources and fiber optics may vary somewhat from system to system.

The common readout electronics includes WFDs with a standard layout of thirty-six 250 MHz, 10-bit flash analog-to-digital converters (FADCs). This board will allow for the readout of 36 channels of photosensors that require 250-MHz sampling frequency or 18 channels of photosensors that require 500 MHz. These boards will receive clock and trigger information from the Clock Receiver boards mounted on the Crate Data Collectors, in addition to the analog inputs. These boards will also provide output data to both the Trigger and data acquisition (DAQ) system.

### 8.1 Photosensor Mounted Systems

This section describes the common components located in the photosensor housing, but not including the photosensor itself. The photosensor, either an Avalanche Photo Diode (APD) or a Photomultiplier tube (PMT), is described in the respective section for each subsystem. The components in the ‘base’ of the photosensor, including the LV to HV converter, HV control, preamplifier, LV power, and cabling are described here. The standard cabling includes four cables: one signal, one LV power supply, one HV control, and one preamp power supply.

#### 8.1.1 HV System

The HV system is common for all photosensor systems and is based on an economic, compact, low-current individual HV-unit, mounted directly into each photosensor housing. This system eliminates expensive and bulky HV cables and connectors, lowers the power consumption per HV power supply, and reduces the electrical HV hazard associated with traditional HV supplies.

A picture of the photosensor housing for the Calorimeter, including the HV unit, is shown in Fig. 6b.18. A schematic diagram of one HV channel is shown in Fig. 8.1. One can see in this figure, and also in Fig. 6b.18, that the primary element of this scheme is a new commercial LV-HV converter: the C20 with analog control produced by EMCO Corporation[1]. This compact, regulated, and programmable HV power supply in a shielded package occupies only one cubic inch and, with a low-voltage input of 12 V, provides an output voltage up to 2,000 V with output currents up to 0.5 mA. This chip features low ripple ( $< 0.002\%$ ), high stability ( $< 50$  PPM/ $^{\circ}$ C), low noise generation (low EMI/RFI), and 0 to 100% programmable output via a 0–5-V control voltage that will be provided by a commercial 12-bit VME Digital to Analog converter (DAC) (XIP-TVME200/XIP-5220, produced by Xycom Automation Inc.). The expected cost of one HV channel is  $\sim$ \$140, which is almost half the cost of a ‘standard’ commercial HV-system. A sample of the new LV-HV converter was tested with a Calorimeter APD and its characteristics satisfy the APD HV-supply requirements.

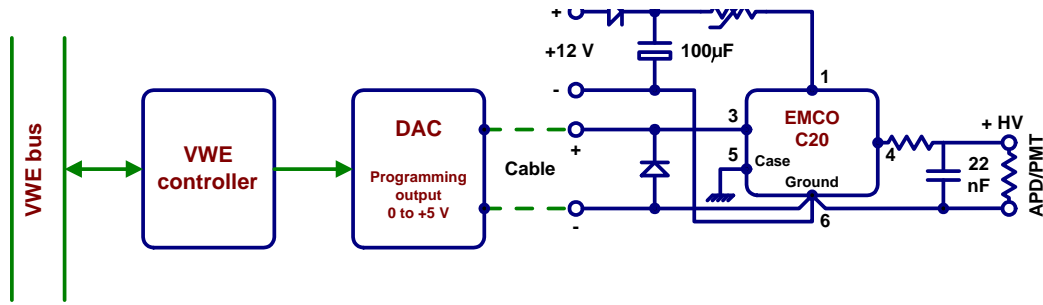


Fig. 8.1. Schematic diagram of one HV channel, with 12-V input power and 0–5-V control voltage from a VME based DAC.

### 8.1.2 LV System

The low voltage system consists of power and control for the LV-HV converter and power for the preamp. The low voltage power supplies sit in racks away from (but close to) the detector. The control for the LV-HV converter is provided by VME-based DACs. There are four daughter boards with 16 channels each per VME card. The LV power and control are brought to the photosensor housing by two cables, for systems outside of the vacuum. A reduction of the number of cables penetrating the vacuum for the remaining systems can be accomplished by splitting the LV power inside the vacuum.

### 8.1.3 Preamplifier

The preamplifier is based on a common design for all systems, but will require some tuning for each subsystem's requirements. The low voltage power will be provided via cables from the supplies near the detector along with the low voltage power for the LV-HV converters. The shaping times will be determined by the specifications of each detector. The Calorimeter APD system will have longer shaping times ( $\leq 20$ -ns peaking time), whereas the Charged Particle Veto (CPV) and Catcher systems, with fast PMT readout of scintillator or Cherenkov radiation, will have short shaping times. The Photon Veto (PV) and External Photon Veto (EPV) systems, with PMT readout of scintillator energy deposits read out through Wavelength Shifting (WLS) fibers, will have intermediate shaping times. A schematic of the preamplifier for the Calorimeter APD is shown in Fig. 6b.19. Some measurements of preamp noise are shown in Fig 6b.15. The scintillator-based photosensor systems are inherently fast, with good double pulse resolution that is ultimately limited by the ability to distinguish a second pulse close in time to an earlier pulse and the pulse width. To minimize pileup from earlier hits, the APD (or PMT) pulses may have to be shaped to reduce pulse tails. A second preamplifier design in which the pulse is shortened with a clipping line is under consideration and is shown in Fig. 8.2. The resistor-capacitor at the end of the line is adjusted to obtain a return to a zero-volt level after clipping, yielding a Calorimeter pulse of about 20 ns (FWHM) in duration. The exact values of the parameters of this arrangement depend on the fall time of the pulse. Similar shaping of other systems is planned. The shaped pulses are then sent by  $\sim 10$ -meter coaxial cables to the WFD boards located in crates near the detectors.

## 8.2 Calibration and Monitoring System

The ultimate calibration of the KOPIO detector will be done *in situ* with copious background  $K_L$  decays and specially triggered events acquired during the experiment. It is anticipated that events rejected by the Level 3 trigger (L3) will also be available for calibration purposes — the DAQ can store these events in condensed format (e.g. ntuples). The advantage of the *in situ* calibration is that it is carried out under the same conditions and with the same methods as those for the process being studied. This procedure also allows the Preradiator, Calorimeter, and Photon Veto systems to be calibrated both separately and as a single entity from the same data set. A drawback of this process is that it requires a relatively long period of

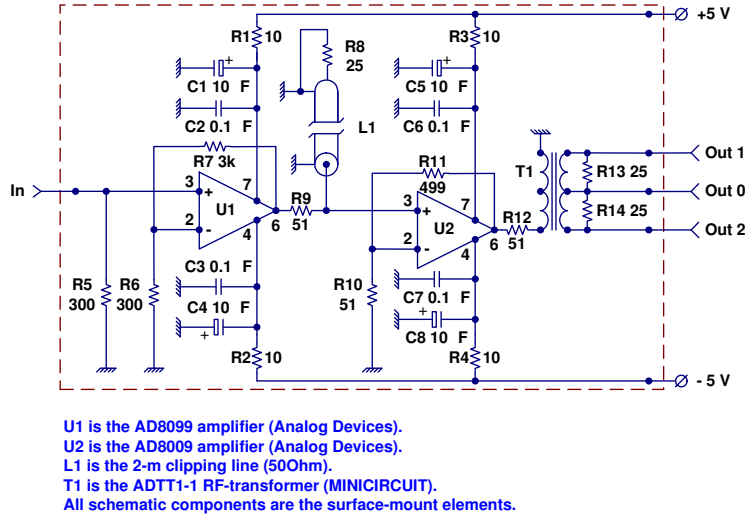


Fig. 8.2. Schematic diagram of a clipping preamplifier.

data accumulation to achieve a sufficient number of calibration events. Thus, two supplemental systems are required: one for pre-calibration with an accuracy of a few percent, and another to monitor its performance and restrict the variation of the photosensor gains to the order of 0.4%. The calibration system has two main functions:

- Rapid detection of failed channels, and
- Monitoring of gain changes between physics calibration samples.

To achieve sufficient veto hermiticity, the monitoring system should be able to detect a failed element within a few beam spills. To achieve the required KOPIO energy resolution, an appropriate calibration and monitoring system must be deployed.

### 8.2.1 Pre-calibration System

A pre-calibration will use cosmic-ray muons; this technique was successfully used by Experiment E865[2] with a calorimeter that had very similar characteristics to the KOPIO Calorimeter. This pre-calibration is based on the assumption that the mean value of signals from cosmic-ray muons passing vertically through Shashlyk modules is approximately the same for all modules. In E865, the 600 calorimeter modules were pre-calibrated with an accuracy of 4% in one hour, even from a ‘cold start’. Cosmic-ray muon calibration also provided long-term monitoring of the photosensor gains with an accuracy of 1–2%.

This technique simply requires a special trigger from the Level-1 trigger (L1) that recognizes cosmic muons vertically penetrating an entire detector system. In the Calorimeter, such a trigger can be formed from a coincidence between the top and bottom horizontal layers of modules, gated between AGS pulses; similar triggers can be created for all of the photodetectors that are used in the trigger, including the PR, PV, and CPV. Currently the only such systems not used in the trigger are the Catcher and External Photon Veto. These triggers will be generated for each subsystem with an appropriate prescale. The data will be read out through the standard DAQ stream.

### 8.2.2 Monitoring System

Every photodetector system will employ a monitoring system based on light sources and fiber optics to allow a rapid detection of any failed detector element and to monitor photosensor gains. The details of the design for those systems with photosensors in the vacuum will be somewhat different in order to minimize the number of vacuum penetrations. (None of the systems in vacuum are involved in  $\pi^0$  reconstruction or need a particularly high level of precision from the LED system). The monitoring system employs light flashers and must satisfy a number of specific requirements that vary somewhat for each detector subsystem:

- high long-term and short-term temperature stability — better than 0.1% is fairly straightforward to achieve;
- short light pulse duration —less than 50 ns, tailored to match each photosensor;
- small variation in the flash amplitude —less than 0.2% for the Calorimeter and other  $\pi^0$  detectors (less stringent for the CPV or Catcher);
- a large number of photons in the light pulse – more than 10,000 photons/channel for the  $\pi^0$  detectors (less for the CPV and Catcher);
- variable pulse repetition rate and intensity.

These requirements can be met with Light Emitting Diodes with a brightness of 5–10 Cd that have recently been developed (‘ultra bright LED lamps’), see Table 8.1. The preferred choice for KOPIO is currently the NSPB-500S which would be used to inject blue light into the scintillator of each detector. In turn, that light would be converted to green light by the those systems with WLS fibers (except for the Catcher system where the blue light would be injected directly into the PMT).

Table 8.1. Light intensity parameters of some commercial LED lamps.

LED		Photons/pulse( $10^6$ ) (8-ns driving pulse)	Photons/pulse( $10^6$ ) (60-ns driving pulse)
HP HLMP 8505	GREEN	2.8	28
NICHIA NSPB-500S	BLUE	45	500

The monitoring system is based on an electronic method of stabilization of the LED light output by means of an optical feedback provided by a PIN photodiode[3,4]. The PIN diode monitors the LED light output, and a feedback loop employs this signal to adjust the driving pulse amplitude of the LED. As shown in references[3] and[4], the PIN diode has a temperature coefficient  $\sim 4 \times 10^{-4}/^\circ\text{C}$ , with a long-term stability of better than  $10^{-4}$ . As a result, the monitoring system described in Ref.[3] shows a long-term stability of better than 0.1%.

A block diagram of the LED monitoring system is shown in Fig. 8.3. The input ‘start pulse triggers a stable pulse generator based on ECL elements and an external passive delay line (for stabilization of the pulse duration). The signal of specified duration is amplified in a linear mode and applied to a power transistor (pulse current  $\sim 2\text{ A}$ ), loaded on the LED. Part of the light (20–30%) from the LED is split off by a special optical beam splitter and sent through an optical collector to the input of the thermo-stabilized unit to provide an optical feedback. A Hamamatsu S3590-03 PIN diode will be use as the photoreceiver of the feedback channel. The signal from this diode will be amplified by a charge-sensitive amplifier and sent to a comparator for comparison with the reference  $U_{\text{REF}}$  level. The output signal from the comparator, which is proportional to the difference of the tested and reference level including the sign, is sent to a ‘LED current control block’. This block will correct the amplitude of the LED drive pulse to stabilize the PIN diode signals, *i.e.* the light signals on the photosensor. The signal from the PIN diode is also sent to a WFD for control measurements.

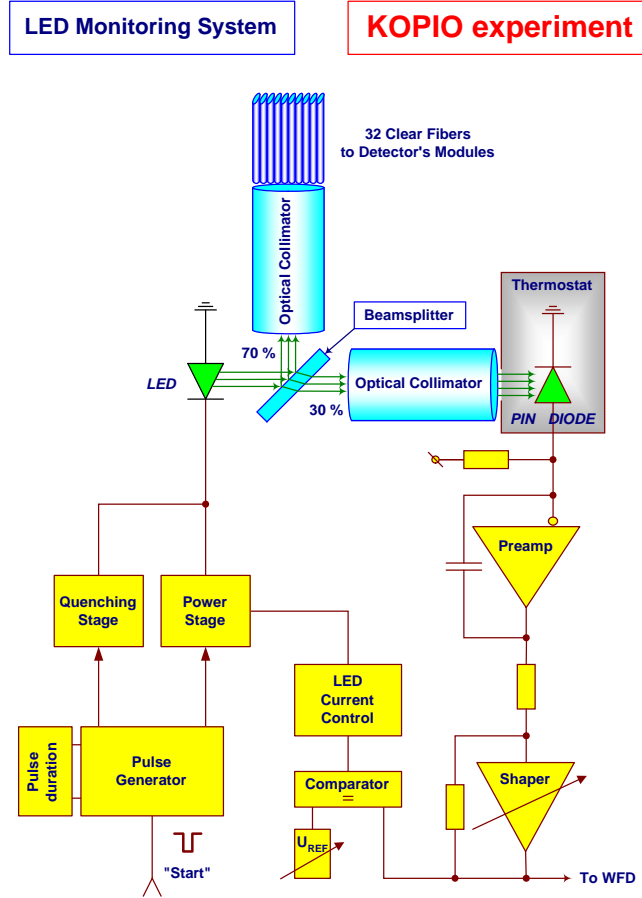


Fig. 8.3. Overview of the LED Monitoring System. This system is triggerable (Start) with feedback control from a PIN Diode, which is also readout into the standard DAQ system with a WFD.

The design of the driving and quenching units is well known[3,4]. We have tested the first prototypes of these units, and test measurements of the first 32-channel prototype of the monitoring system for the Calorimeter is planned for the Fall of 2005.

The monitoring system described above will service 32 front-end channels. The light monitoring signals will be delivered via 1.0-mm-diameter clear optical fibers to the front of each module.

From the analysis of existing monitoring systems and our preliminary test measurements of small prototypes, we conclude that the this type of monitoring system will have long-term and short-term stability that meets our most stringent requirement of 0.1%. The monitoring system will also serve as a pre-calibration of the module readout chain at the 10% level.

### 8.3 Readout System

The entire KOPIO readout system will be pipelined and deadtimeless. The WFD, Trigger, and DAQ are all designed with this idea in mind. The WFD is described below; the Trigger and DAQ are described in Sections 9 (Trigger) and 10 (DAQ). This design will be used for all photodetector systems in KOPIO (Preradiator, Calorimeter, Photon Vetoes, Charged Particle Veto, and Catcher scintillators). The chamber readout system is described in Section 6a (Preradiator). An overview of the readout architecture, with connections between WFDs, Trigger, and DAQ is shown in Fig. 8.4. The WFD data are synchronous with the 25-MHz

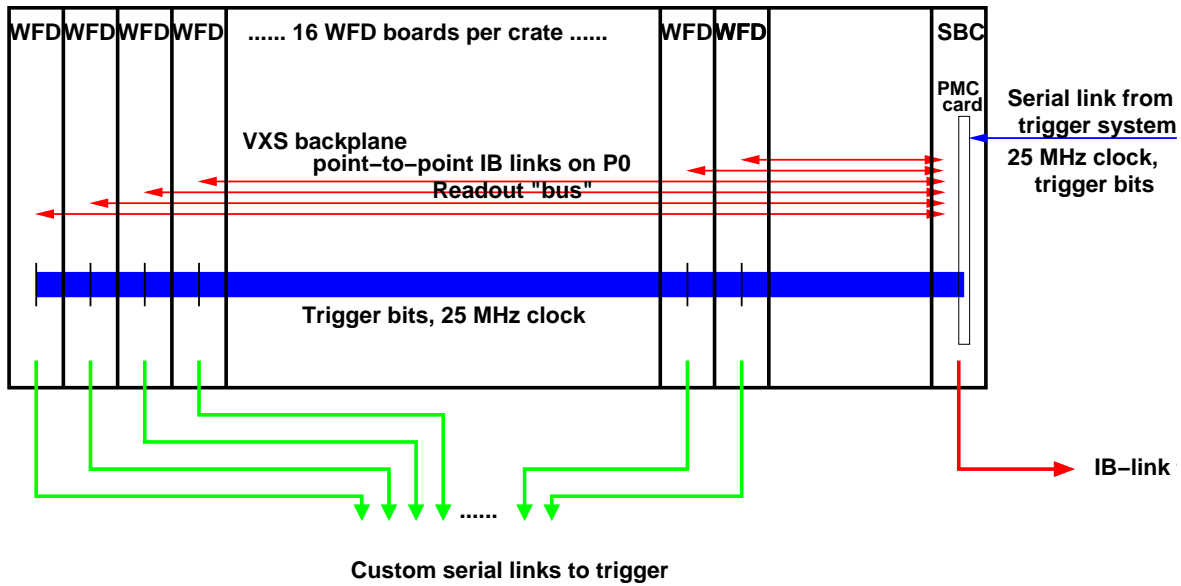


Fig. 8.4. Overview of the FEE/Trig/DAQ and their interconnections. This diagram shows a generic layout of one of the WFD VME crates. The Crate Data Collection module is labeled SBC and is connected via Infiniband links (IB) to the WFDs and to the DAQ. The crate data collector also hosts the Clock Receivers, which broadcast the clock and trigger information to each WFD. Data is transferred synchronously to the trigger from each WFD via custom serial links.

system clock, as is also the transfer of data to the Trigger Collector boards. The data transfer to the DAQ, through the Crate Data Collector boards (labeled by SBC in the figure) is driven by the the L1 trigger result. The FEE crates will be 9U VME crates in water-cooled racks near, but not on the detectors. The crates will in general contain 16 WFD cards and a Crate Data Collector card with a CPU/controller. For ease of triggering, the WFD crates for the Preradiator scintillators will be configured slightly differently, with only 8 WFD boards per crate, This arrangement will allow for an additional 3 Trigger Collector boards and 2 Trigger Routing boards in these crates (see Fig. 9.11) and keep a single view of one quadrant in each crate (eight such crates are needed).

### 8.3.1 Wave Form Digitizers (WFD)

The Wave Form Digitizers (WFD) will process photosensor signals and provide energy and timing information to the experiment's data-acquisition and trigger systems. The WFD is based on a 250-MHz, 10-bit flash analog-to-digital converter (FADC) and is designed to measure energies with an effective 12-bit dynamic range (0.5–1000 MeV for the Calorimeter) and the time of arrival with respect to the beam microbunch clock with an uncertainty of less than 100 ps. Operation of the WFD will be completely pipelined with no dead time.

The design of the FEE should satisfy the following conditions:

- peaking times of pulses  $\leq 20$  ns to optimize the energy/time resolution (the signal-to-noise ratio) and the double-pulse resolution in order to avoid pile-up effects;
- fast (250-MHz or 500-MHz sampling frequency) WFD based on 250-MHz FADC's with 10-bit dynamic range;
- data storage for the expected 10- $\mu$ s trigger latency; and



- transfer of zero-suppressed raw data, selected by L1 (3 microbunches will be readout for each trigger), to Crate Data Collection boards at 70 MByte/s per WFD board.

A schematic drawing of the WFD board is shown in Fig. 8.5. The expected density on the 9U VME boards is 18 channels at 500 MHz or 36 channels at 250 MHz. Nine channels at 1 GHz could be configured if needed for the Catcher. To achieve 500 MHz, two FADC's would be run on opposite phases of the 250 MHz clock.

Each WFD will receive the 25-MHz system clock from the Clock Receivers on the Crate Data Collector board (see below). This 25-MHz clock will be subdivided to 250 MHz to clock the FADC's. Both the 25-MHz and 250-MHz clocks will be fed into the front end FPGA's along with four FADC outputs. This scheme will allow each FPGA to process two ends of a PR scintillator, digitized at 500 MHz, to make a meantime and energy sum. The full waveform for each input channel will be buffered, either in the FPGA or external memory chips on the board, with the full 10 bits of FADC data plus some additional bits of control information until the trigger decision is returned in  $\sim 10 \mu\text{sec}$ . The trigger data words will also be decoded by the Clock Receiver and will be distributed to each WFD board.

Each WFD will provide up to 9 high-speed LVDS links to Trigger Collector boards. Data will be transferred to the trigger synchronously and will be received back by the WFD card from the Clock Receiver synchronously. The expected L1 latency is  $10 \mu\text{sec}$ .

For analog conversion, each WFD channel contains the following: a transformer-coupled analog input configuration with secondary-side termination, providing an excellent solution to convert a single-ended source signal to a fully differential signal and avoiding 'ground' problems; a monolithic 10-bit 250-MHz analog-to-digital converter optimized for outstanding dynamic performance at high frequencies; and a FIFO memory used as pipeline storage of raw digitized data.

All of the electronics will be constructed from commercial components: 10-bit 250-MHz ADCs (e.g. MAX1124), and large modern fast FPGA's (e.g. EP2C35C6/484). The latter will be used as processors, memories, and for the organization of the pipeline buffers, as well as for communications with the Trigger and Crate Data Collector boards.

### 8.3.2 Crate Data Collectors

Upon receipt of a L1 trigger, zero-suppressed data for that and the preceding and subsequent microbunches will be transferred from the WFD boards via high-speed Infiniband links on the VME crate backplane to the Crate Data Collection boards. The Data Collection boards are commercial boards (VXS1IB11100C from SBS Technologies). The data transfer is up to 20 Mbytes/sec. These Data Collection boards will also support Clock Receiver daughter cards that will distribute the 25-MHz system clock from the Clock Driver modules (Gigabit serial links) to each front-end card in its crate along the backplane. The Clock Receiver boards will also translate the serial Trigger Word that has been encoded as up to 40 bits into a parallel series of bits and transmitted to the front-end cards via the backplane. The data collection board will also serve as a crate controller for downloading and monitoring functions.

A channel count for FEE is provided in Table 8.2. There are 36 channels per WFD board for the Calorimeter and the Photon Veto systems. There are 18 channels per WFD board for the Preradiator, Charged Particle Veto and Catcher systems. There is one data collector board per WFD crate; each crate has 16 WFD boards, except for the Preradiator, where for triggering purposes there are only 8 WFD boards per crate (one view of one Preradiator quadrant per crate).

### References

1. <http://www.emcohighvoltage.com/>
2. R. Appel *et. al.*, Nucl. Instr. and Meth. A **479** 349 (2002).
3. W.L. Reiter *et. al.*, Nucl. Instr. and Meth. **173**, 275 (1980).
4. A. Fyodorov *et. al.*, Nucl. Instr. and Meth. A **413**, 352-356 (1998).



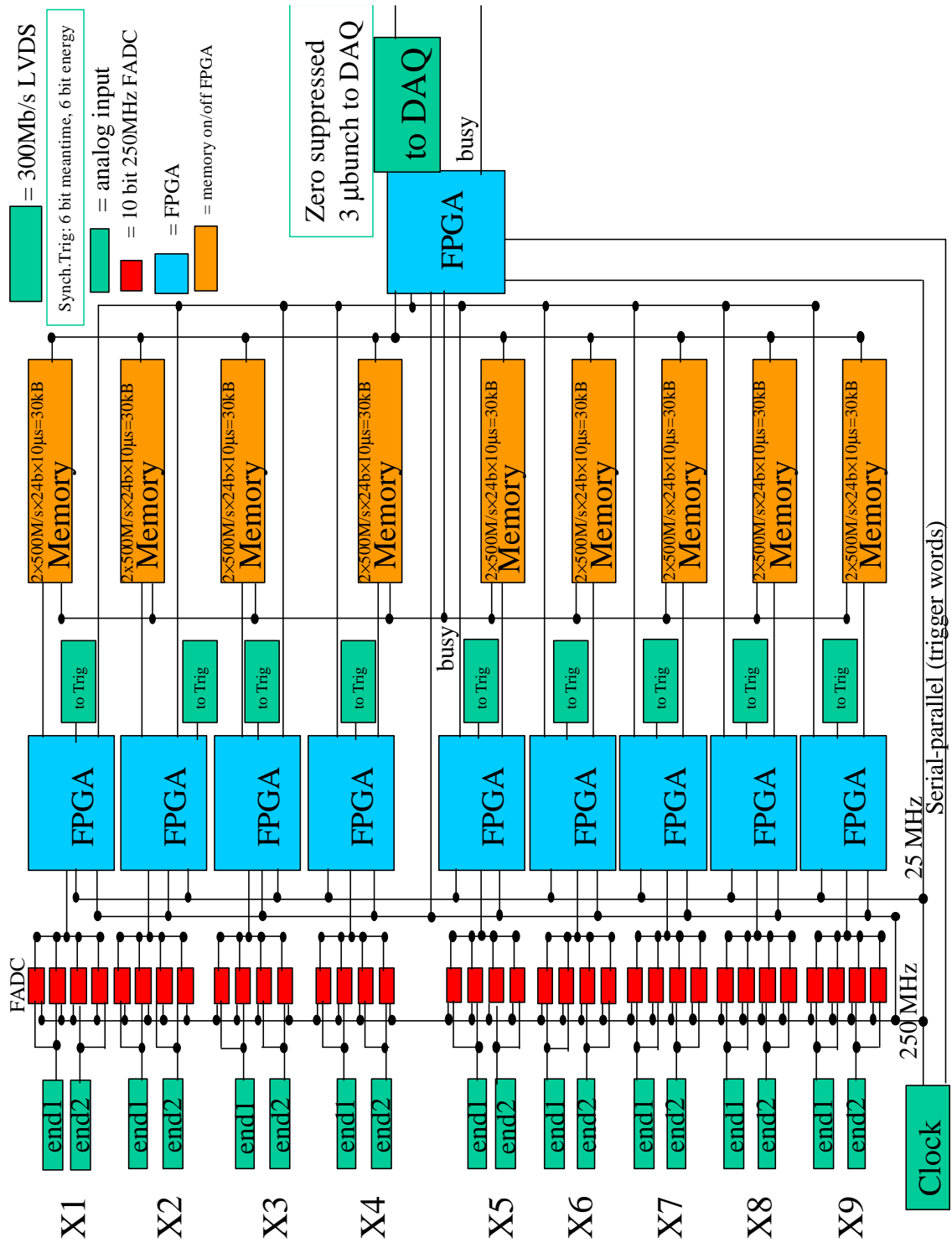


Fig. 8.5. Schematic diagram of WFD board.

Table 8.2. Channel count for photosensor based front-end electronics. The number of channels from the PMT/APD is listed along with the number of WFD boards and Crate Data Collector boards.

System	'PMT'	WFD	Collector
Calorimeter	1564	45	4
Cal-inner	36	1	-
<b>Cal Total</b>	<b>1600</b>	<b>46</b>	<b>4</b>
<b>Preradiator</b>	<b>1152</b>	<b>64</b>	<b>8</b>
EPV	1152	32	2
PV-us	264	8	-
PV-barrel	840	24	2
PV-magnet	160	5	-
PV-ds	280	8	-
<b>PV Total</b>	<b>2696</b>	<b>77</b>	<b>5</b>
CPV-barrel	368	21	2
CPV-magnet	160	9	-
CPV-ds	242	14	-
<b>CPV Total</b>	<b>770</b>	<b>44</b>	<b>3</b>
Catcher	420	24	2
Catcher-guard	144	8	-
<b>Catcher Total</b>	<b>564</b>	<b>32</b>	<b>2</b>
<b>Total</b>	<b>6782</b>	<b>263</b>	<b>22</b>

## 9 Trigger

### 9.1 Introduction and Requirements

The main goal of the trigger system is selection of  $\pi^0\nu\bar{\nu}$  events with an efficiency better than 95% for events that would be accepted in the data analysis. The system also has to provide the possibility to collect parallel triggers for calibrations and efficiency measurements and for other physics topics. Each trigger source will be individually selectable and prescalable in a programmable fashion.

The initial choices for the subdivision of trigger into levels and the targeted values for the rates at each level will be discussed with reference to the data-flow model shown schematically in Fig. 9.6.

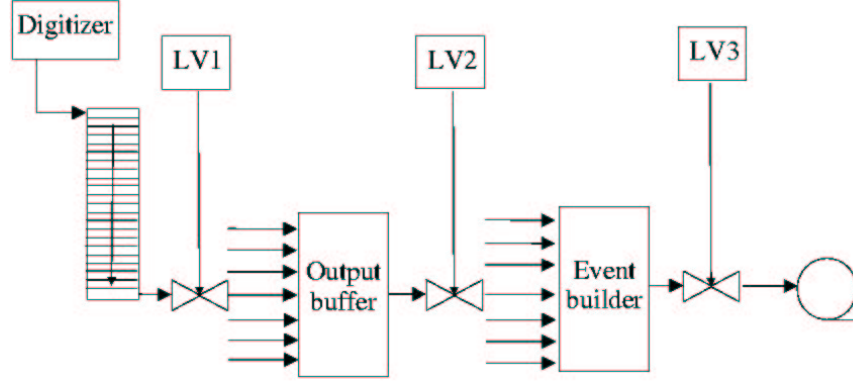


Fig. 9.6. Data-flow model.

Data produced by flash ADC's are stored in circular memories with sizes sufficient for latency times in the first level of trigger of the order of  $10\ \mu\text{s}$ . The first-level trigger (L1) controls the transfer of data from the circular memories to output buffers. Its maximum rate is thus determined by the bandwidth of the links connecting the circular memories to the output buffers and by the detector hit rates, because all front-end subsystems will perform zero suppression at this level. Preliminary estimates of the hit rates in the Preradiator wire chambers and in the different scintillator systems indicate that a L1 rate of 1 MHz could be sustained by all readout systems that are being designed.

A second-level L2 trigger would be needed only if there are rate limitations due to the bandwidth of the connection to the online data acquisition system (DAQ) or from the event building mechanism. The current design of the DAQ allows for the transfer of data at the maximum assumed L1 rate. Therefore the trigger design described in this report does not include a L2 trigger, and it will be assumed that all events in the output buffers will be transferred to the event builder. A possible L2 is still left as an option, however, and a final decision on this issue will be taken only after the results of a more complete simulation of the trigger system become available.

The final reduction of data to a level suitable for permanent storage and offline analysis will be performed by a software filter (L3) based on a simplified software event reconstruction that is carried out, after event building, in the data-acquisition online computers.

The design described in this report for the first-level trigger will use only information from scintillators and will make substantial use of veto conditions in selected regions of the detector. Strict requirements for the trigger come from the need to minimize accidental losses. Thus, there must be a flexible means to program the offsets and widths of veto coincidences down to the level of a few ns. This condition led us to the choice of a fully digital system based on the trigger outputs of the waveform digitizers described in section 8. In order to keep dead time negligible, the L1 trigger has to be fully pipelined.

This section concentrates on L1 trigger. The implementation of L3 and an analysis of the conditions that can be used at that level will be discussed in the data acquisition section.

## 9.2 Trigger Simulations

The simulation studies performed so far have concentrated on the selection of  $\pi^0\nu\bar{\nu}$  events with both photons crossing the volume of the Preradiator. A simulation program based on the GEANT3 package has been used to evaluate the discriminating power of a number of possible trigger conditions based on signals from scintillators and using in particular

- thresholds in regions of the Preradiator and Calorimeter;
- veto counters; and
- photon counting algorithms using Preradiator and Calorimeter elements.

Optimization of these conditions for the requirements presented in subsection 9.1 is still in progress. In this section, we present the results of a study where two different options have been analyzed. The first option yields rates in the ballpark of 100 kHz with inefficiencies around 20%. The second option represents an initial attempt to improve the efficiencies by using only a subset of the conditions, and it shows that the aforementioned requirements can be met. A better optimization will result from an adjustment of the parameters of the first option. Therefore, the full set of conditions used for the first option will be used to guide development of the baseline design of the trigger.

This section is organized as follows. The first subsection gives some details on the simulation program and on the definition of the samples for which the efficiencies are quoted. The second describes the trigger conditions that are used in the simulation and will form the basis for the L1 design presented later. Estimated rates and efficiencies for the two options mentioned above are presented in the last subsection.

### 9.2.1 Simulation programs

Although the trigger will be organized to use data in time slices of 40 ns, corresponding to the decays of interest produced by one microbunch of protons, a proper estimate of the rates and of the efficiency requires simulation of the activity in the detector associated with particles produced in a large number of microbunches.

The simulation program collects the energies deposited in the detector in 40-ns time slices associated with a microbunch. The association of the slice with a microbunch relies on the fact that photons from  $K_L^0$  decays in the accepted range of momentum and vertex position (“candidate” photons in short) produce, in the Preradiator and Calorimeter, signals contained in less than 30 ns. Thus the time window considered in any given detector is centered around the interval corresponding to photons in coincidence with candidate photons\*.

Sources of activity contributing to a given time slice are due with decays of multiple kaons and with interactions of neutrons produced within the microbunch of interest and in previous microbunches. All of these sources, including those coming from decays of long-lived particles such as stopping muons, are accounted for in the simulation.

Trigger conditions are applied to the signals of each time slice to determine the probability for accepting a time slice. The trigger rate is evaluated as the product of this probability times 25 MHz. For efficiency studies, the activity of one time slice is superimposed on a  $\pi^0\nu\bar{\nu}$  decay that satisfies setup cuts designed to reproduce the biases due to the offline selection.

Setup cuts include geometric and kinematic conditions as well as veto conditions. The list of the simplified geometric and kinematic conditions used for signal/background separation and for ensuring good quality measurements of the photons is presented in Table 9.3.

Veto conditions, as determined from all counters except the Downstream Photon Vetos and the Catcher, are included in the setup cuts in order to separate the specific losses, due to the trigger, from those due to

---

\*For veto counters, fluctuations in flight path, especially associated to backward photons and charged particles, and in velocity, for charged particles, would imply an extension of this window beyond 40 ns. However, restricting the windows to 40 ns is adequate for the trigger, where narrow veto windows are used.

Condition	Comment
$(z_{UV} + 75 \text{ cm}) < z < (z_{PR} - 50 \text{ cm})$	Longitudinal position of decay vertex away from upstream veto and Preradiator front face
$640 \text{ MeV} < E < 1490 \text{ MeV}$	Kaon energy
no $\pi^0$ Dalitz decay	
no $\gamma$ conversion before Preradiator	
both photon trajectories cross Preradiator volume	
$\geq 1\gamma$ conversion before module 8 of the Preradiator	
$E_1 > 10 \text{ MeV}; E_2 > 10 \text{ MeV}$	Photon energies
$ x_{fr}  < 150 \text{ cm};  y_{fr}  < 150 \text{ cm}$	Intersection of the photon trajectories with the front face of the Preradiator
$ x_{bk}  < 200 \text{ cm};  y_{bk}  < 200 \text{ cm}$	Intersection of the photon trajectories with the back face of the Preradiator
$188 \text{ MeV} < E_1^* + E_2^* < 234 \text{ MeV}$	Photon energies in the kaon rest frame
$0.33 (E_1^* - E_2^*) + 190 \text{ MeV} < E_1^* + E_2^*$	Photon energies in the kaon rest frame

Table 9.3. Conditions defining the sample of  $\pi^0 \nu \bar{\nu}$  events for which efficiency is quoted

unavoidable accidental coincidences already accounted for in the sensitivity estimates of Section 13. The offline treatment is applied, including flight path corrections and, for the Charged Particle Vetoes, offsets correlated with the event kinematics. Two separate values ( $\pm 3\text{ns}$  and  $\pm 10\text{ns}$  for the samples called SET1 and SET2 respectively in the following) for the width of the photon veto gates are used. The corresponding measured inefficiencies will probably bracket the actual values.

Trigger conditions are evaluated from the energies deposited in the active channels of the detector as simulated by GEANT3.<sup>†</sup> The information in a given channel is assigned a time corresponding to the time of the first energy deposit.<sup>‡</sup>

### 9.2.2 Trigger conditions

For the purpose of the trigger, the energy in the Preradiator is collected in “strip” sections, each section including the sum of the energies deposited in scintillators at the same transverse position in all layers of a given module. The energies deposited in the Shashlyk modules are also summed up in regions at transverse positions corresponding to the Preradiator strips, with one scintillator strip corresponding to two rows or columns of Shashlyk modules. These sums will be called “Calorimeter strips” in the following discussions.

Energies deposited in the  $X$  or  $Y$  Preradiator or Calorimeter strips are used to evaluate the number of photons by two different algorithms. In both algorithms, to avoid edge effects, strips with the same orientation in adjacent quadrants and touching along their short sides are summed to produce “superstrips” running across the entire detector.

In the first algorithm (*projection algorithm*), the energies are summed along the beam direction for superstrips at the same transverse position, and the number of clusters (groups of contiguous strips with  $E > 1 \text{ MeV}$ , separated by at least one strip below threshold) is counted.

<sup>†</sup>The GEANT3 simulation used for these trigger studies has not been updated to reflect recent evolution in the detector structure as described in the previous chapters of this report. In particular, a box geometry for the Barrel Photon Vetoes is assumed, and the geometry of some of the Charged Particle Veto counters is unrealistic.

<sup>‡</sup>The time evolution of the signals associated with optical photon emission and propagation or to the electronic processing is not simulated. The contribution of these effects is small because the time jitter at the trigger level is dominated by flight-path differences.

The second algorithm (*pattern algorithm*) uses only logical signals obtained by applying thresholds to the signals deposited in each superstrip; it counts patterns of hits consistent with “good” photons, *i.e.* photons originating from the fiducial decay region. First, a “shower seed” (*i.e.* a point close to the photon conversion point) is identified as the first superstrip with a hit, in a search order going from upstream to downstream and from the interior to the exterior edges of the Calorimeter. After the conversion point is identified, the algorithm goes on to associate hits in other planes which intersect an angle whose apex is at the seed and whose axis is chosen to maximize the number of hits intersected. The associated hits are erased and the algorithm is iterated to count the number of showers. Showers are counted as “good” photons only if the hits in the group of  $3 \times 3$  superstrips around the seed have a configuration that occurs with sufficiently high frequency in Monte-Carlo  $\pi^0 \nu \bar{\nu}$  events from the fiducial decay region. The trigger conditions studied use the number of photons evaluated by these algorithms in addition to energy sums in appropriate sections of the Preradiator and to the hits in selected veto counters.

Veto counters used in this trigger study are described in Table 9.4. Logical conditions are evaluated:

**for photon vetoes** by applying a 5-MeV threshold to a sum of the energies deposited in counters of the group. The sum is computed by including only channels with an energy deposit greater than 2 MeV which occur at times  $t$  within the window  $t_{\text{ev}} - t_{\text{offset}} - \Delta t < t < t_{\text{ev}} - t_{\text{offset}} + \Delta t$ , with  $t_{\text{offset}}$  and  $\Delta t$  given in the table and  $t_{\text{ev}}$  determined by the earliest hit in a module of the Preradiator.

**for charged particle vetoes** as the logical OR of hits above a threshold of 300 keV within time windows defined as above, in any counter of the group.

Group	$t_{\text{offset}}$	$\Delta t$	Description
CH <sub>1</sub>	15 ns	3 ns	Upstream end cap charged particle vetos
CH <sub>2</sub>	6 ns	6 ns	Barrel charged particle vetos
CH <sub>3</sub>	2 ns	3 ns	Downstream end cap charged particle vetos
CH <sub>4</sub>	0 ns	3 ns	Prerad beam pipe charged particle vetos
NE <sub>1</sub>	16 ns	3 ns	Upstream wall photon vetos
NE <sub>2</sub>	0 ns	6 ns	Barrel(left/right) photon vetos
NE <sub>3</sub>	0 ns	6 ns	Barrel(top/bottom) photon vetos
NE <sub>4</sub>	−6 ns	3 ns	Downstream (magnet) photon vetos

Table 9.4. Veto counters used for the trigger.

Information from the Preradiator and Calorimeter are summarized, for the purpose of this trigger study, in the following data:

**ETOT:** total energy deposited in the Preradiator and Calorimeter;

**MOD:** maximum energy deposited in any of the 32 modules of the Preradiator, with the energy in each module defined as the sum of the energies deposited in the  $X$  and  $Y$  scintillator strips of that module;

**NCL<sub>y</sub>:** number of clusters in horizontal superstrips found by the *projection algorithm*;

**NCL<sub>x</sub>:** number of clusters in vertical superstrips found by the *projection algorithm*;

**NSH<sub>y</sub>:** number of showers seeds in horizontal superstrips found by the *pattern algorithm*;

**NSH<sub>x</sub>:** number of showers seeds in vertical superstrips found by the *pattern algorithm*;

**NGPH<sub>y</sub>:** number of showers in horizontal superstrips classified as good photon by the *pattern algorithm*;

**NGPH<sub>x</sub>**: number of showers in vertical superstrips classified as good photons by the *pattern algorithm*;

**NSD7**: number of shower seeds in vertical or horizontal superstrips found by the *pattern algorithm* upstream of the 8<sup>th</sup> Preradiator module.

### 9.2.3 Efficiencies and rates

Table 9.5 shows results obtained by using the conditions described in the previous subsection. The contribution of each individual condition to the signal loss and to the rejection of background events is given, together with the values obtained when all conditions are applied. Efficiency losses are shown for two different assumptions for the width of the photon veto gates used in the setup cuts. As discussed in Subsec. 9.2.1, the widths used in defining SET1 and SET2 overestimate and underestimate these losses respectively.

Condition	Signal losses in %		Microbunch rej. fact.	Rate (kHz)
	SET 1	SET 2		
ETOT>120 MeV	—	—	$1.57 \pm 0.04$	
MOD>16 MeV	$0.2 \pm 0.1$	$0.2 \pm 0.1$	$1.01 \pm 0.01$	
$[(NCL_x = 2) \cap (1 \leq NCL_y \leq 3)] \cup$ $\cup [(NCL_y = 2) \cap (1 \leq NCL_x \leq 3)]$	$5.8 \pm 0.7$	$5.6 \pm 0.7$	$2.0 \pm 0.1$	*
$(1 \leq NSH_x \leq 3) \cap (1 \leq NSH_y \leq 2) \cap$ $\cap [(NGPH_x \geq 1) \cup (NGPH_y \geq 1)] \cap$ $\cap (NSD7 \geq 1)$	$5.5 \pm 0.7$	$5.0 \pm 0.7$	$2.0 \pm 0.1$	*
CH <sub>1</sub>	—	—	$1.01 \pm 0.01$	
CH <sub>2</sub>	$0.3 \pm 0.1$	$0.1 \pm 0.1$	$1.57 \pm 0.06$	
CH <sub>3</sub>	—	—	$5.2 \pm 0.3$	
CH <sub>4</sub>	$0.3 \pm 0.2$	$0.2 \pm 0.1$	$3.1 \pm 0.2$	*
NE <sub>1</sub>	$1.3 \pm 0.3$	$1.0 \pm 0.3$	$1.21 \pm 0.04$	
NE <sub>2</sub>	$0.5 \pm 0.2$	$0.1 \pm 0.1$	$1.39 \pm 0.06$	
NE <sub>3</sub>	$0.3 \pm 0.2$	—	$1.46 \pm 0.06$	
NE <sub>4</sub>	$0.5 \pm 0.2$	—	$1.28 \pm 0.04$	
“Low rate” option	$23 \pm 1$	$17 \pm 1$	$290 \pm 20$	$86 \pm 6$
“High rate” option	$10.1 \pm 0.8$	$4.5 \pm 0.6$	$29 \pm 1$	$876 \pm 33$

Table 9.5. Signal loss and rejection. Each line gives the effect of the individual conditions for microbunches satisfying all other conditions. The last two lines give the global results obtained applying all conditions (“Low rate” option) or all conditions except the ones marked with a \* in the Rate column (“High rate” option).

When all conditions are applied (“Low rate” option in Table 9.5), the expected rate is well below the maximum that can be accepted by the front-end systems, but with an efficiency that is still unsatisfactory. Further analysis will be performed in order to improve the discrimination by a reoptimization of the veto gates used in the trigger and of the pattern recognition algorithms.

A very crude test has been performed by removing from the trigger the conditions based on the photon counting algorithms and the Charged Particle Vetos inside the Preradiator beam pipe. The results of this test (“High rate” option in Table 9.5) give us confidence that the requirements stated in the introduction can be met after the optimization planned. Therefore the conditions listed in Table 9.5 are taken as reference for the baseline design of L1 trigger. The only addition included in this design is a subdivision of the veto counters



into three longitudinal and two azimuthal sections, in order to allow a finer tuning of the position of the veto gates.

### 9.3 Trigger Architecture Overview

The organization of the trigger systems and their communication with the front-end systems and the data acquisition is illustrated schematically in Fig. 9.7. The figure shows the currently favored model with a single level (L1) of trigger before the readout and a software level (L3), assumed to be part of the data acquisition system.

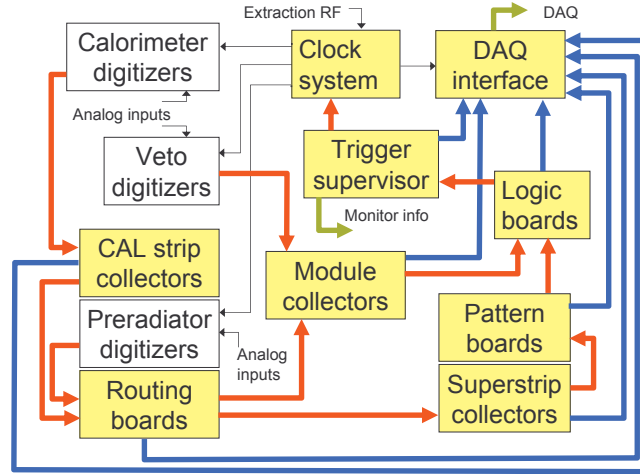


Fig. 9.7. Trigger functional scheme. Thick lines represent serial links carrying data used for trigger formation (red lines) or monitoring (blue lines). The clock system encodes the trigger decision received by the trigger supervisor over the clock signal (thin black lines) sent to the front end electronics.

The L1 system will be pipelined and regulated by a clock that is synchronous with the 25-MHz extraction RF. It is designed to produce a response for every microbunch (“time slot” in the following discussion), although internal operations can be clocked at multiples of this frequency. The input data consist of coded charge and time information from Preradiator, Calorimeter, and Photon Veto channels, produced at the microbunch frequency by digital processing of the outputs of 250-MHz flash ADC’s. This reduction will be performed in dedicated sections of the front-end modules, together with additional operations on the data such as computing mean times and sums of a small number of channels, as needed. The output data will be aligned in time, such that the information from the events of interests in a microbunch fit into a single time slot.<sup>§</sup>

The output of the digitizers will be sent, by means of serial links, to collector and routing modules, that perform different functions on data from more than one digitizer such as summing, applying thresholds, producing logical OR’s of discriminated signals, or redirecting the input data to outputs grouped according to the requirements of the subsequent logic processing.

Computation of the functions needed to evaluate the trigger conditions discussed in the simulation section, will require the development of two different logic modules. One of them will use data from the

<sup>§</sup>Hits from the particles of one microbunch can populate a time interval larger than 40 ns, but photons from  $K_L^0$  decays in the accepted range of momentum and vertex position produce, in the Preradiator and Calorimeter, signals contained in less than 30 ns. The window has to be extended for veto channels, but 40 ns is sufficient considering the narrow coincidence widths required to reduce accidental losses.

Preradiator and Calorimeter to implement the *projection algorithm* and the *pattern algorithm*. The second one is a general-purpose board that performs programmable logic combinations, with programmable time windows, of several serial inputs carrying the time information of logic signals.

The connection between the different stages of L1 will be made by serial links (red lines in Fig. 9.7) capable of carrying 300 Mb/s and of regenerating the 25-MHz clock, so that a direct connection to the clock system is not required. Data transferred between different stages are generally synchronous with the microbunch clock, except for the connection between routing boards and collector modules where this would require an unreasonably large number of serial connections. In this last case several channels will be multiplexed over a limited number of links, using zero suppression and sparsification. However, even in this case, synchronism at the output of every link will be restored, with sufficient buffering provided in order to avoid data losses or the introduction of dead time.

The operation of the L1 trigger will be coordinated by a trigger supervisor, which performs the tasks needed for trigger formation, control and distribution, handles dead times and other conditions of error, and provides monitoring data of the trigger operation. The trigger supervisor does not communicate directly with the front-end modules, but sends its commands to the clock system, which encodes them over the clock output.

For monitoring purpose, all modules in the trigger chain can send their output to the data acquisition through DAQ interface modules, which receive data by the serial L1 interconnection protocol (blue lines in Fig. 9.7) and interface to the trigger and to the DAQ for readout, with the same protocols used by all front-end modules. In addition to trigger-associated information, the trigger supervisor also provides, at the end of each accelerator cycle, summary data such as scaler outputs, which can be read out by the slow control system.

## 9.4 L1 Trigger

The scheme of the L1 trigger described in this section has been developed with reference to the trigger conditions summarized in Table 9.5. Evolutions of that scheme may still be expected as a result of the continuing simulation studies. The components of the trigger, which are only specified at a rather general level, will make wide use of programmable logic, so that their functionalities can be better specified when the simulation studies mature. Also, in order to ensure the required flexibility, particular attention has been given to identifying the interconnections needed and to specify a standard serial communication protocol.

For the following discussion it is convenient to subdivide the trigger components into the following groups:

1. collector modules;
2. logic modules; and
3. trigger supervisor.

The proposed communication protocols will be discussed first, distinguishing a *synchronous* and a *asynchronous* protocol.

In the *synchronous* protocol, 12-bit packets will be sent over each serial link for every microbunch. The content of the packet will have different meanings for different connections. For example, the WFD trigger outputs will code the information from a single detector channel in 6 + 6 bits, corresponding to the time within the microbunch and to the pulse height, respectively. The module collectors will code a logical output from the logical OR of several detector channels in 6 + 6 bits, corresponding to the times within the microbunch of the first and second hit, if any, in time order.

In the *asynchronous* protocol, zero-suppression and multiplexing is used to carry data from more than one channel on the same link. Data packets transmitted from one module to another will contain, in addition to the zero-suppressed data, a time slot field, identifying the microbunch,<sup>¶</sup> and a channel address field, as shown in Fig. 9.8. Because zero suppression and multiplexing introduce variable delays in the transmission,

<sup>¶</sup>Not to be confused with the fine time information which, when needed, is part of the data field.

Time slot	Channel address	Data (including time vernier)
-----------	-----------------	-------------------------------

Fig. 9.8. Format of the data packet for zero-suppressed multiplexed L1 communications.

synchronization is restored at the input of the receiving module by the mechanism illustrated schematically in Fig. 9.9, where the channel address is used to demultiplex the data from different channels and the time slot field is compared with the current clock counter to determine the write address in the memories used for time realignment.

The use of the *asynchronous* protocol will be limited as much as possible because it requires buffering to avoid data loss, and therefore increases the latency. The buffer sizes providing the best compromise between dead time and latency will be determined on the basis of realistic estimates of the data rates, produced by the program described in the simulation section, upgraded to reproduce all known sources of data.

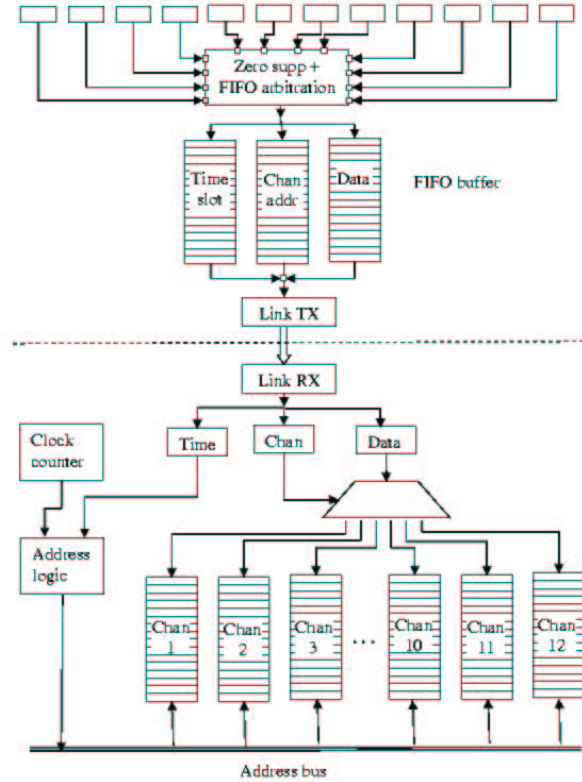


Fig. 9.9. Principle of the L1 asynchronous communication protocol. Data are zero-suppressed and multiplexed in output, demultiplexed and resynchronized in input.

#### 9.4.1 Trigger outputs of the photodetector digitizers (WFD)

Charge and time information for particle hits, at the level of granularity needed by the trigger algorithms, will be provided by special trigger outputs of the front-end modules of the photodetector Wave Form Digitizers (WFD) described in section 8.

The WFDs sample the input signals with 250- or 500-MHz FADC's, and the samples are used, after zero suppression, to compute charge and time hits. Basic processing involving information from a small number of contiguous detectors will also be performed inside the WFD. The particular type of combination will be determined by the firmware of a Field Programmable Gate Array (FPGA) controlling the trigger output stage.

For example, for scintillator strips in the Preradiator, which are read at both ends, the digitizers will compute the mean time and the sum of the charges from the signals at the two ends. In this case, one module handles the two PM outputs of nine strips and will produce one serial output for each of the strips. For the Calorimeter, each digitizer handles an array of  $6 \times 3$  Shashlik modules, and will produce 6 sums of 6 channels each according to the scheme illustrated in Fig. 9.10. As discussed later, these sums are further

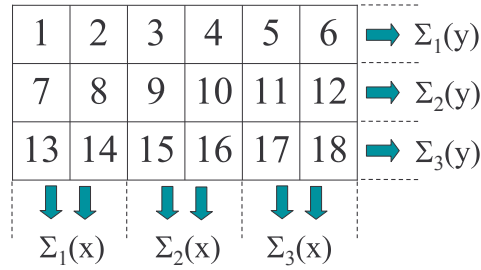


Fig. 9.10. Channel combinations for the trigger outputs of the Calorimeter digitizers.

combined in the Calorimeter strip collectors to produce a single output for each row (column) of  $18 \times 2$  ( $2 \times 18$ ) modules matching a Preradiator strip. Finally, for most veto systems a single output corresponding to a combination of up to 18 channels will be sufficient.

The result of the digital processing will be assigned to a specific time slot with offsets that will be programmable, channel by channel, at running time in such a way that the information of interest for kaon decays in the accepted momentum and vertex range is contained within a single time slot. This expedient will simplify the design of the trigger logic, which will only need to use information from a single time slot.

#### 9.4.2 Collector Boards

Data from more than one digitizer have to be combined to evaluate the trigger conditions listed in subsection 9.2. The combinations required are

- Calorimeter channels in rows or columns matching Preradiator strips (“Calorimeter strips”);
- scintillator strips in the two views of one module of the Preradiator or in one quadrant of the Calorimeter (“PR-CAL module”);
- groups of veto counters used in the trigger with the same time windows (“veto sectors”);
- opposing scintillator strips in two adjacent quadrants of the Preradiator or Calorimeter (“superstrips”); and
- superstrips at the same transverse position in the nine planes corresponding to the modules of the Preradiator and the Calorimeter (“projections”).

Two types of boards will be developed to perform these functions. The first type, the “routing board”, will be used in the crates housing the digitizers of the Preradiator so as to collect, via a specially designed backplane implementing 54 different point-to-point serial connections, the outputs of the nine strips with the same orientation (“view”) coming from each of six different modules. The routing board will have two types of serial outputs: 6 view outputs with the *synchronous* protocol which carry the sums of the strips of one view for each module, and 18 strip outputs with the *asynchronous* protocol, each carrying data from the three strips at the same transverse position in three different modules. A second strip routing board in the same crate will perform analogous functions for the strips of the two remaining Preradiator modules and for the Calorimeter strip outputs produced by the Calorimeter strip collectors (described later) sitting in the same crate. The second type of board, the “collector board”, is based on a single hardware layout that is designed to perform the functions of a PR-module collector and CAL strip collector or, with the use of different firmware, of a superstrip collector (see Fig. 9.7).

The “module collector” will be used to combine data from modules and veto sectors in which the channels grouped together have approximately the same timing features. It combines the data from serial inputs by using the *synchronous* protocol, to produce a global sum and a global OR based on thresholds applied to the inputs. Each module collector channel can combine up to six inputs. The number of inputs is chosen so that the board can be used as a Calorimeter strip collector, since one CAL strip is built by combining six different outputs of Calorimeter digitizers. When used as PR-module collectors, only two inputs, each corresponding to the sum of the scintillators in one view, will be used.

With different FPGA firmware, the board can be used as a superstrip collector to form superstrip outputs and projections. In this case, each serial input will carry data from three strips at the same transverse position in three modules of the Preradiator, by using the *asynchronous* protocol. Each group of six inputs can thus carry the data of all strips at the same transverse position in the nine modules of two adjacent quadrants, as needed to build a “projection.”

The arrangement of modules in the Preradiator WFD crates and their interconnections with PR-module collectors and strip collectors are sketched in Fig. 9.11. One crate will house the modules needed to process all strips with a single orientation ( $X$  or  $Y$ ) in a quadrant. This group includes the WFD modules (one per PR-module), the strip routing boards (labeled “Rout.” in the figure) and the Calorimeter strip collector boards (labeled “Coll.” in the figure). Each WFD is connected to the strip routing board with nine separate point-to-point links, represented as a single thick line in the figure. The strip outputs of the two strip routing boards of one view of one quadrant are used together with those of the boards serving the same view in an adjacent quadrant in nine strip-collector-module channels. Instead, the view outputs of the strip routing boards are combined two by two into eight module collectors<sup>||</sup> to compute the sum of the energies deposited in each Preradiator module.

The figure only shows the boards of one quadrant ( $A$  in the figure) and those of one of the adjacent quadrants ( $C$  in the figure) that are combined with it to make superstrip data.

### 9.4.3 Logic Modules

In order to implement the trigger conditions discussed in the simulation section, two separate circuits will be developed. The first one analyzes data from the scintillators of the Preradiator and from the Shashlyk modules with two different algorithms for photon counting. The second one will be a general purpose module that computes any logic function of several inputs.

**The pattern board** will implement the *projection algorithm* and the *pattern algorithm* described in the simulation section. The first algorithm utilizes the superstrip charges provided by six strip collectors, one for each group of 3 strips  $\times$  9 modules, computes sums of the superstrips at the same transverse position in different modules (projections), and counts clusters, *i.e.* groups of adjacent projections that have a total charge above a threshold (clusters). The horizontal and vertical view will be processed

---

<sup>||</sup>In the case of the Calorimeter, the  $X$ - $Y$  sum is not required, because the  $X$  and  $Y$  strips are different combinations of the same channels

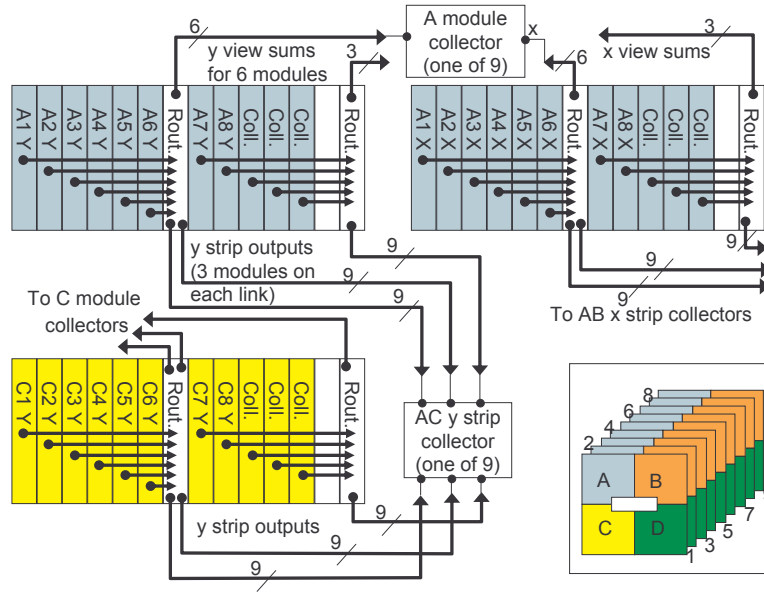


Fig. 9.11. Collector modules and their connections with Preradiator and Calorimeter digitizers. The figure shows the components needed to process signals from one of the quadrants (A, color code blue). For quadrant C only the components processed together with quadrant A are shown.

separately. The second algorithm, described in the simulation section, uses logical data ('hits') from each superstrip provided again by the strip collectors. In this case, the horizontal and vertical view will also be processed separately. The circuit will output the number of seeds, the number of "good" photons, and possibly the results of other logic conditions based on the seed positions, if further simulation studies prove them to be useful. We will also consider the possibility to output, over a separate link, data that characterize the photons found (*e.g.* the position of the seed and the coarse direction defined by the axis of the cancellation angle, *i.e.* the angle used to associate the hits to the seed, and the number of hits within the cancellation cone). We believe that the algorithm can be implemented in pipeline with high performance FPGA's and memory lookup tables, but no practical implementation studies have been performed yet.

**The boolean logic boards** are general purpose memory lookup units that compute any logical combination of ten 0 inputs. The inputs are supposed to be hits characterized by a fine time contained in the data field of the input packets. Each hit is internally extended backward and forward in time by a time window, which will be programmable separately for each input, so that the condition programmed in the lookup table can be evaluated at time intervals smaller than 1 ns to mimic the behavior of analog coincidence modules.

While the boolean logic board can separate hits at different times within the same time slot, the algorithms currently being studied for photon counting treat all signals within one time slot together and this will be the initial assumption for the circuits that implement them. However, if further trigger studies indicate the need to separate signals with different times, the design could be augmented by introducing a first stage that identifies the hits compatible in time and routes them to two (or more) parallel chains that perform the operations in parallel for the groups of hits that belong together.

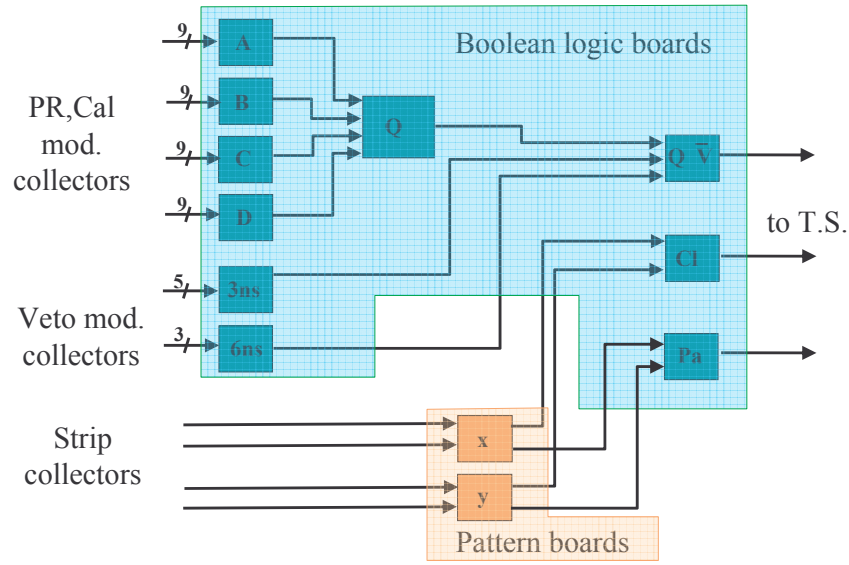


Fig. 9.12. Use of the logic modules to produce the trigger conditions of Table 9.5.

Figure 9.12 shows how the modules described could be interconnected to implement the conditions of Table 9.5. The different types of modules are identified by a color code. Data from the Preradiator and Calorimeter module collectors are processed in boolean logic boards to produce quadrant ( $A$ ,  $B$ ,  $C$ ,  $D$ ) OR's, and these OR's are combined to produce an event time in the boolean logic module labeled  $Q$ . For the Vetos, signals coming from different module collectors that group signals with the same timing are ORed together only when they can be used with the same coincidence windows in the final veto coincidence. This arrangement is shown in the figure by labeling the boolean logic board that performs the OR with the half-width of the coincidence window. Finally, the combination of the signal from the Calorimeter and the signals from the veto counters are performed in the boolean logic module labeled  $Q\bar{V}$ . It is also assumed in the figure that the outputs of the two ( $X$  and  $Y$ ) projection boards and the outputs of the two pattern boards are first processed through a "CI" and "Pa" boolean logic card, respectively, before being sent together with the output of the  $Q\bar{V}$  board to the trigger supervisor.

## 9.5 Trigger Supervisor

The trigger supervisor system will coordinate the tasks of trigger formation and control, handle the communication of the trigger with the front end systems, and will provide tools for monitoring the trigger operation.

Components of the trigger decision come from different systems. For example, the scheme of Fig. 9.12 shows three separate sources which provide results with different delays and with different amounts of associated information. In addition, there will be other sources of triggers based on pulsers or physical data such as for calibration systems. The first task of the trigger supervisor is the time realignment and the combination of data from different sources. In addition, parallel triggers will be formed by combining in different ways the information computed in the logic modules. Each parallel trigger will be individually selectable and prescalable. This flexibility will allow events to be collected concurrently from different decay channels that have different rates, or to relax some of the trigger conditions for studies of efficiencies or for calibrations.



To distribute the information necessary to identify a time slot selected by the trigger to the front-end system, the supervisor system will communicate with the clock system, sending it data to be encoded over the clock signal. In addition to a time slot identifier, these data may contain further information about the trigger, which can be used by the front-end systems to tailor the readout format to the trigger type, if needed. In order to preserve data integrity, the trigger distribution will be halted by the trigger supervisor when the front-end systems signal conditions of imminent filling of any of several buffers interposed in the data path. Such a centralized handling of the dead-time conditions allows for a cleaner safeguard against error conditions.\*\* Needless to say, the trigger and the front-end systems will be designed in a way to make the occurrence of these conditions extremely rare.

The trigger supervisor also provides monitoring information on the trigger operation. Two types of information can be made available. The first is information associated with triggers such as a record of the individual conditions that enter into forming a trigger, or the status of intermediate registers. The amount of information transmitted can be selected to allow several “debugging” options. If the information is to be transferred to the readout directly by the trigger supervisor modules, they would have to be equipped with all the interfaces used for front-end modules. A solution that we prefer is to develop a special interface module to the readout system, which could receive data through serial links under the L1 trigger protocol and be read out through the data acquisition. This procedure would allow the possibility to monitor, when needed, the behavior of other components of the trigger chain.

The second type of monitoring information is provided by scalers that could be read out at the end of each AGS cycle by the slow control system. The scalers could either be embedded in the design of the trigger modules or be commercial modules fed by signals output by the trigger supervisor modules or other modules in the trigger chain.

## 9.6 Clock System

The KOPIO clock is designed to synchronize all of the KOPIO front-end electronics at the AGS microbunching frequency of 25 MHz. The clock will provide the timing reference for all of the waveform digitizers as well as distribution of the L1 trigger decision to all front-end modules and the DAQ. The clock system consists of a single Master Clock, and a set of Clock Drivers that distribute the Master Clock signal to the Clock Receivers in each front-end crate. The Master Clock accepts the AGS microbunching RF signal and re-phases its own internal 25-MHz clock to that of the AGS RF signal; the Master Clock also receives the L1 trigger decision from the Trigger Supervisor. The Master Clock output is distributed, via the Clock Drivers, over optical links to ~55 Clock Receivers in each front-end crate.

---

\*\*Due to the zero suppression at early stages of the front-end modules, it may be difficult to design a handshake system that has total immunity to buffer overruns. A full analysis of the possibilities of such errors has not been performed yet. However, the front-end systems still have the responsibility to record the occurrence of these conditions.

## 10 Data Acquisition and High-Level Trigger

### 10.1 Overview

A full readout of the detector is initiated after a Level 1 (L1) trigger accept.\* The DAQ system has been designed to transfer data at a speed that would allow a L1 accept rate of around 1 MHz, allowing the possibility of running a relatively loose L1 trigger and thereby keeping the trigger acceptance high. A higher-level trigger (traditionally called Level 3) operates on complete events and performs additional filtering to reduce the event rate to permanent storage down to a level manageable by the offline analysis; this rate is currently envisioned at around a few kHz. The higher-level trigger will run selection algorithms similar (if not identical) to a subset of the offline analysis, thereby ensuring that the additional acceptance loss beyond the offline analysis would be kept low. A functional block diagram of the DAQ system is shown in Fig. 10.1.

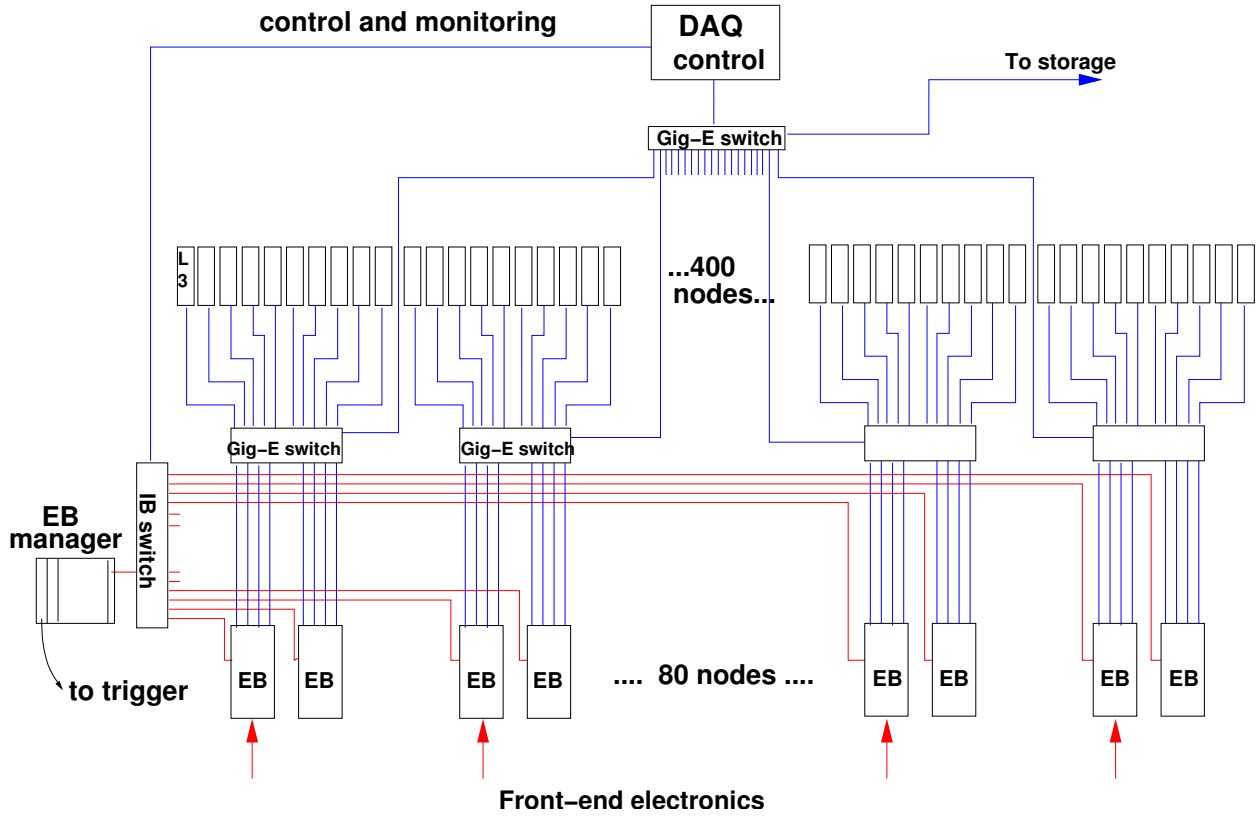


Fig. 10.1. Block diagram of the DAQ system. Red: Infiniband (or other multi-gigabit links). Blue: Gigabit ethernet

The design follows the “classical” distributed, networked readout paradigm, based on commercially available hardware, in which event fragments are read out through network links and combined into complete events through a network switch via a farm of Event Builder (EB) PCs. Complete events are sent over the network to another farm of Level 3 trigger (L3) PCs where they are subject to further filtering before being written to storage. The L3 farm would also be a natural place to perform detector calibrations on the fly with access to a larger dataset than would be available later from storage.

The DAQ system consists of 3 main components: event builder, Level 3 trigger, and online software. These subsystems are described in the following sections.

\*We retain the possibility of performing a partial readout for a Level 2 trigger.

## 10.2 Event Builder

The function of the Event Builder is to receive digitized data from the front-end electronics and combine the event fragments into complete events. It is based on a farm of computers communicating with the front end through a network switch.

From the Event Builder point of view, the front-end electronics appear as a collection of network links, each providing (serially) the digitized data from multiple detector channels. Data rates have been estimated by using the detector hit rates from the full KOPIO GEANT Monte Carlo. The following assumptions were used:

- 32 bits per Preradiator anode wire hit.
- 5 Preradiator cathode strips hit for each anode hit. 10 samples per cathode strip hit at 12 bits per sample.
- For the photodetectors, 20 samples per hit at 10 bits per sample.

For the “high rate” Level 1 trigger (1 MHz L1 accept rate), the data rate is estimated to be about 30 GB/s during the “beam on” part of the spill; this rate includes not only the data from the triggered microbunch but also from the one preceding and succeeding microbunch.<sup>†</sup>

We have started investigating Infiniband[1] technology as a potentially cost-effective way to move data at these rates. Infiniband is an emerging industry standard that is attracting widespread commercial support and much interest in the HPC (high-performance computing) community. The so-called “4X” standard specifies uni-directional data transfer rates of 10 Gbit(Gb)/s. We have acquired a small cluster consisting of six machines with “4X” Infiniband interfaces; four of the machines have a PCI-Express[2] internal bus and dual 3.2-GHz Xeon processors, and the remaining two have a 64-bit 133-MHz PCI-X bus and dual 1.5-GHz Itanium2 processors. The six machines are connected through an 8-port Mellanox Infiniband switch. Simple data transfer tests via UNIX sockets with home-grown software indicated a transfer rate of 0.7 GB/s. This rate might be expected to improve by perhaps 20-30%. We plan to implement 32 links for the Preradiator wire chamber readout and 22 links for the photodetector WFD readout, which should provide sufficient capacity to move data at the requisite 30 GB/s.

The requisite computing power was estimated by scaling up from our experience in E949 where four 200-MHz CPU’s were ample to handle event building at the rate of 30 MB/s. To reach 30 GB/s implies scaling up the capability by a factor of 1000. We assume that event building speed scales linearly with the CPU clock speed, and that 10-GHz CPUs will be readily available by the time KOPIO starts taking data; this enhancement gives a factor of 50. The remaining factor of 20 is obtained by increasing the number of CPUs from 4 to 80. We currently plan to implement 80 PCs with dual CPUs to give us a factor-of-2 safety margin.

Fifty-four of the EB computers will be connected to the read-out controllers of the front-end crates through a 4X optical Infiniband link. The front-end controllers will push their data into buffer memories residing in the EB computers. Complete events will be built by the 80 EB computers, pulling data from the buffer memories through a 96-port Infiniband switch. Such switches are already below state-of-the-art today and are available at less than \$1000/port. An EB manager process will run in a single-board computer (SBC), residing in a VME crate. The EB manager communicates with the EB machines through the Infiniband switch and can act as a “throttle” to slow down the data flow from the front-end controllers when the EB farm becomes overloaded. The SBC will send signals to the trigger system via I/O boards residing in the EB manager crate.

---

<sup>†</sup>This data rate was estimated for  $N_{K,bunch} = 3.57$  kaons per microbunch exiting the photon spoiler. In reality, the number of kaons per microbunch will be 2.14 (Sect. 13). It was further assumed that the L1 trigger rate was completely dominated by triggers designed for two photons converting in the Preradiator. In reality, there will be a non-negligible fraction of triggers designed for events with one photon each in the Preradiator and the Barrel Veto; such events presumably would contain less data, given the coarser readout segmentation in the Barrel Veto. There will also be calibration triggers and triggers for other physics modes; the data size for such events has not been estimated yet.

Although the baseline design is based on Infiniband, the intention is to keep to a technology-neutral design as far as possible. Commercial offerings in high-speed networking are evolving rapidly, with advances expected both in Infiniband as well as in competing technologies such as perhaps 10 Gigabit ethernet. We intend to keep abreast of the latest developments in the field and commit to a specific technology as late as possible.

### 10.3 Level 3 Trigger

The function of the L3 trigger is to receive complete events from the Event Builder, apply additional event filtering criteria, and send the surviving events to permanent storage. It is based on a farm of computers communicating with the Event Builder computers through Gigabit ethernet.

#### 10.3.1 Requirements

For a L1 accept rate of 1 MHz and a spill structure of 4.9-s beam on and 2.3-s beam off, L3 will have to process  $4.9 \times 10^6$  events every 7.2 seconds, implying an average processing time per event of  $1.4 \mu\text{s}$ . With a farm of 400 dual-CPU nodes, the average processing time per event per CPU would be 1.1 ms. To get some idea of the scale, the processing time to find and reconstruct tracks in the ATLAS Transition Radiation Tracker (TRT) Level 2 trigger has been estimated to be about 4.5 ms on a 2.4-GHz Xeon CPU.[3]. Assuming that the KOPIO tracking is of similar complexity, and further assuming that 10-GHz CPUs will be available for KOPIO with a linear scaling of the processing time, the processing time would be brought down to 1.1 ms. Because the track multiplicity in KOPIO will certainly be less than in the ATLAS TRT, and KOPIO tracking will have no magnetic field, the KOPIO goal for L3 processing time does not seem unreasonable. On the other hand, the reconstruction of EM showers in the KOPIO Preradiator would be different from the reconstruction of minimum-ionizing tracks in the ATLAS TRT; thus it remains to be seen whether or not the L3 processing time can be brought down to reach the KOPIO goal.

Assuming that the L3 output rate can be brought down to 5 kHz, the data rate to storage is estimated to be around 100 MB/s. For a run of  $10^7$  s, and assuming a duty cycle of 0.5, the total amount of data per run would amount to something on the order of 500 TB.

#### 10.3.2 Initial Look at Algorithms

Only been a cursory look has been made so far at Level 3 algorithms to get an initial idea of the type of cuts that might be effective. It was assumed that the “high-rate” option would be run at L1 (Sec. 9). So far, we have considered only triggers for two photons in the Preradiator. The following cuts were found to be effective at L3:

- Require two or more preradiator tracks to point back to the decay volume.
- Compute the invariant mass of all track pairs that point back to the decay volume. Select the pair closest to the  $\pi^0$  mass. Require consistency with the  $\pi^0$  mass within  $\pm 50$  MeV.
- Veto extra activity in the Preradiator and Calorimeter (not associated with the two tracks selected above). Sum over all hits within  $\pm 1$  ns of the  $K_L$  decay time (correcting for the  $Z$  position of  $K_L$  decay). Veto the event if the Preradiator prompt energy  $> 1$  MeV or the Calorimeter prompt energy  $> 1$  MeV.

The rejection and acceptance of these cuts is shown in Table 10.1. The rejection at L3 is about a factor of 200 (albeit with low statistics), which brings us close to our goal. After the first two L3 cuts, almost all of the remaining background comes from  $K_L \rightarrow \pi^0 \pi^0 \pi^0$  decays. As a result of the vetos from the Barrel and Upstream Photon Vetoes at L1, the remaining photons from these  $3\pi^0$  decays end up in either the Preradiator or Calorimeter, leading to the high rejection of the last L3 cut.

The distance (in units of Moliere radii,  $R_M$ ) between the extra photons in the Preradiator/Calorimeter for  $3\pi^0$  events and the “signal” photons is shown in Fig. 10.2. There is one entry per event. A loop is made

Table 10.1. Rejection and acceptance of the Level 3 cuts. Note that the offline photon vetoes were not applied as part of the setup cuts in this study; such cuts lower the apparent acceptance of the L1 trigger.

Cut	Background	Signal
Start	10000	10000
Offline setup cuts for signal		178
$E > 16$ MeV in PR module	4507	178
L1 vetoes	408	145
$\geq 2$ tracks pointing to decay volume	91	145
$\pi^0$ invariant mass	42	145
Preradiator/Calorimeter veto	2	141

over all extra photons that convert in the Preradiator or Calorimeter. The distance between each extra photon and the two signal photons is computed, and the minimum distance is taken as the separation for that extra photon. The maximum separation among all the extra photons is then plotted. Given that there is a high probability for an extra photon to be separated by  $5 R_M$  or more from the signal photons, there is some prospect that the extra activity can be identified at Level 3.

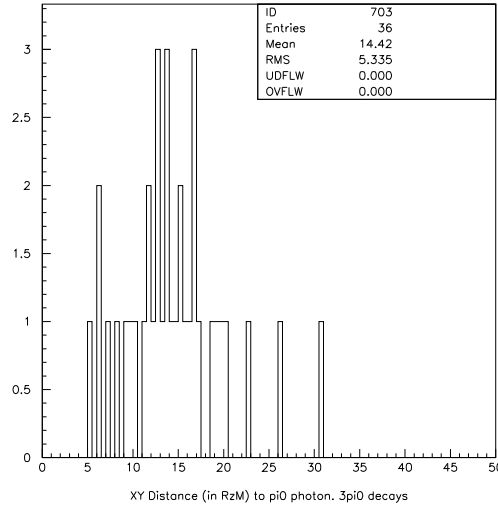


Fig. 10.2. Distance at Level 3 (in units of Moliere radii) between the “signal” photons and the extra photons in the Preradiator/Calorimeter.

#### 10.4 Level 2

Although a Level 2 (L2) trigger is not part of the baseline design, we intend to pursue an R&D program on L2 in parallel with the development of the L1 and L3 trigger systems and the Event Builder. Should the Event Builder turn out to be unable to build events at the required rate, a L2 system could reduce the trigger rate based on a decision made with a partial read-out of the detector. Should the L3 trigger turn out to be unable to filter events at the required rate, the L2 system could reduce the trigger rate based on a decision

made with fully built events.

It is understood that the distributed nature of the EB and L3 systems make them amenable to scaling up their power. Thus a shortfall by a factor of 2-4 in the processing power would probably most easily be made up by increasing the number of CPUs. On the other hand, a larger shortfall might be more effectively made up by the introduction of a L2 system. A L2 trigger could also ease the load on the L3 system, allowing L3 to perform more sophisticated filtering or monitoring algorithms. One possibility would be to have a software-based L2 trigger running in the EB nodes.

For a hardware-based L2 solution, it would be most natural to place the L2 hardware on the PCI-bus of the L3 PCs, taking advantage of the power/cooling infrastructure provided by the PC and at the same time obtaining direct access to the event data stored in memory.<sup>‡</sup> PCI cards hosting several high-performance FPGAs for data manipulation with custom firmware (so-called FPGA computing cards) have started to become available commercially[4] with sophisticated software tools for rapid firmware development. This approach has been studied, for example, by the ATLAS and ALICE collaborations.[5]

## 10.5 Online Software

The online software is the “glue” that holds the DAQ system together. It includes a run controller, a user interface, an event logger, along with interfaces to the Event Builder, to the L1/L3 trigger systems, to the slow control system, and to online monitoring/calibration tasks.

Historically, new experiments have tended to write their online software completely from scratch as opposed to the offline case where general tools such as PAW and ROOT are used worldwide. Adapting prior online software to a specific experiment has usually been more effort than that needed to write original code. However, recent trends in software development suggest that borrowing online code may now be a realistic, practical approach. This approach is made possible by the advent of general DAQ tools in which later decisions on configuration or hardware can be accommodated transparently.<sup>§</sup> Furthermore, the development efforts for these tools are increasingly organized as “open source” projects with many developers distributed worldwide, contributing a wide variety of test cases and rapid feedback, leading to a robust code base.

With these considerations in mind, we have started to explore the XDAQ suite of tools[6] that have been developed in the context of the CMS experiment at the LHC, but are designed to be adaptable to a wide variety of scenarios. The XDAQ framework for distributed event building and high-level triggering is a good match to our notions for the KOPIO architecture. With the recent addition of a run control component to the tool suite, there is the promise of drastically reducing the software development time for the three major pieces of the KOPIO DAQ system.

## 10.6 Open Issues and Near-term R&D

For the Event Builder, the outstanding issues include a more detailed estimate of the data rates, incorporating the latest information on the L1 trigger, readout multiplexing, neutron haloes, and the data generated by the digitizers for the Preradiator and photodetector systems. The implementation of the XDAQ suite and measurement of real-time performance of an Infiniband-based event builder are other near-term R&D goals.

For the L3 trigger, the most important point is the development of trigger algorithms and a coherent picture of the DAQ and all trigger levels. Measurements of the real-time performance (and optimization) of an “all software” L3 need to be made. This evaluation requires substantial development in the area of offline software. Tests of L2 with commercial FPGA processors and engineering studies of alternative designs need to be started.

For the online software, we plan to investigate the XDAQ framework in more detail. Implementation of the Event Builder on our small test cluster will provide a good test case of the feasibility of borrowing large portions of online code from other experiments.

---

<sup>‡</sup>If there is a bottleneck in the EB capabilities, the L2 hardware would naturally be placed in the EB PCs.

<sup>§</sup>The long lead times for mounting major experiments such as at the LHC, coupled to the fact that hardware choices for DAQ are best left as late as possible, naturally lead to the development of such DAQ tools.

## References

1. <http://www.infinibandta.org/home>.
2. <http://www.pcisig.com/specifications>.
3. ATLAS collaboration, private communication.
4. <http://www.sbs.com/products/fpga>.
5. C. Hinkelbein *et al.*, IEEE Trans. Nucl. Sci., **47**, 362 (2000).  
H. Tilsner *et al.*, Eur. Phys. J C **33**, 1041 (2004).
6. <http://sourceforge.net/projects/xdaq>.



## 11 Offline Computing

### 11.1 Overview

Offline Computing in KOPIO encompasses both hardware and software components. Significant computing resources are needed at the experimental site to analyze in real time a portion of the data collected, to monitor certain aspects of these data, to archive the raw data, and to process it for physics analysis. Several software packages also need to be developed, adapted, and integrated into a framework for use by all collaborators. This framework will make it possible to extract physics results in a timely fashion.

### 11.2 Offline Compute Farm

The KOPIO Online data acquisition system is designed to acquire events at a few kHz and to store these data on disk. The Offline compute farm must complement the Online system by providing a platform to monitor the performance of the detector, to calculate and monitor all calibration constants, and to archive the raw data. To accomplish these tasks, the farm must be powerful enough to reconstruct a significant portion of the events acquired, *i.e.* of the order of 1000 events/s. Full reconstruction algorithms that use simulated raw data as input do not yet exist, but it is possible to evaluate the CPU power needed by extrapolating the performance of current-day computers that are used by similar experiments.

For example, the GLAST (Gamma Ray Large Area Space Telescope)[1] detector is similar in concept to KOPIO. It has been designed for making observations of celestial gamma-ray sources in the energy band extending from 10 MeV to more than 100 GeV. This instrument consists of a precision tracker, a calorimeter, and an anticoincidence shield. The launch is anticipated in 2007 so the reconstruction software is already operational and is being tuned. The typical reconstruction rate for one-gamma events on a typical 2005 commodity Intel CPU is 5 events/s. Another benchmark is the full reconstruction of the E949 events where the photon veto analysis dominates the CPU time. This time is of the order of 100 ms. Adding twice the one-gamma reconstruction time to the photon veto analysis, one can safely extrapolate that approximately 1 to 2 KOPIO events could be reconstructed in one second on a 3-GHz Xeon processor. CPU power has been growing by a factor of two every 18 to 24 months while costs have remained flat. A 2009 vintage CPU should thus be able to reconstruct somewhere between 5 and 10 KOPIO events/s.

Compute farms can be built out of off-the-shelf white-box computers linked together by Ethernet connections or by “bladeCenter” solutions offered by several vendors such as IBM, HP, Fujitsu, *etc.* These blades allow for a more compact footprint and less power consumption to reduce operating costs.

These farms are built around a large network switch connecting several crates of blades with a global disk array, an archiving tape library, and a few dedicated nodes for user access and management. The blades consists of dual- or quad-CPU boards. Disk and tape capacities also grow at a fast pace although the cost of a given amount of disk space remains about three times higher than the equivalent tape media. For that reason, it is planned to have enough disk space to keep about one year’s worth of data on disk alongside a tape backup library. The current WBS costs are based on actual January 2005 costs for one rack of IBM blades (168 CPUs), a 25-TB disk array, and one tape silo housing 600 LTO2 tapes (capacity of 120 TB). A similar system is operational in Western Canada[2] and is already used for some of the current KOPIO simulation runs.

The Offline farm will also play an important role in the bulk processing of the data between each acquisition run. In this phase, all events must be fully reconstructed and output generated for the physics analysis phase. It is expected that the Online processors will be available to participate in this phase as well as significant resources at collaborator’s institutes. This scheme would quadruple the power of the proposed Offline compute farm. Currently, the bulk of the simulations are conducted on the TRIUMF Kdecay cluster (40 CPUs) and the shared UBC/TRIUMF Westgrid cluster (1672 CPUs)[2], and at the Arizona State University local cluster.

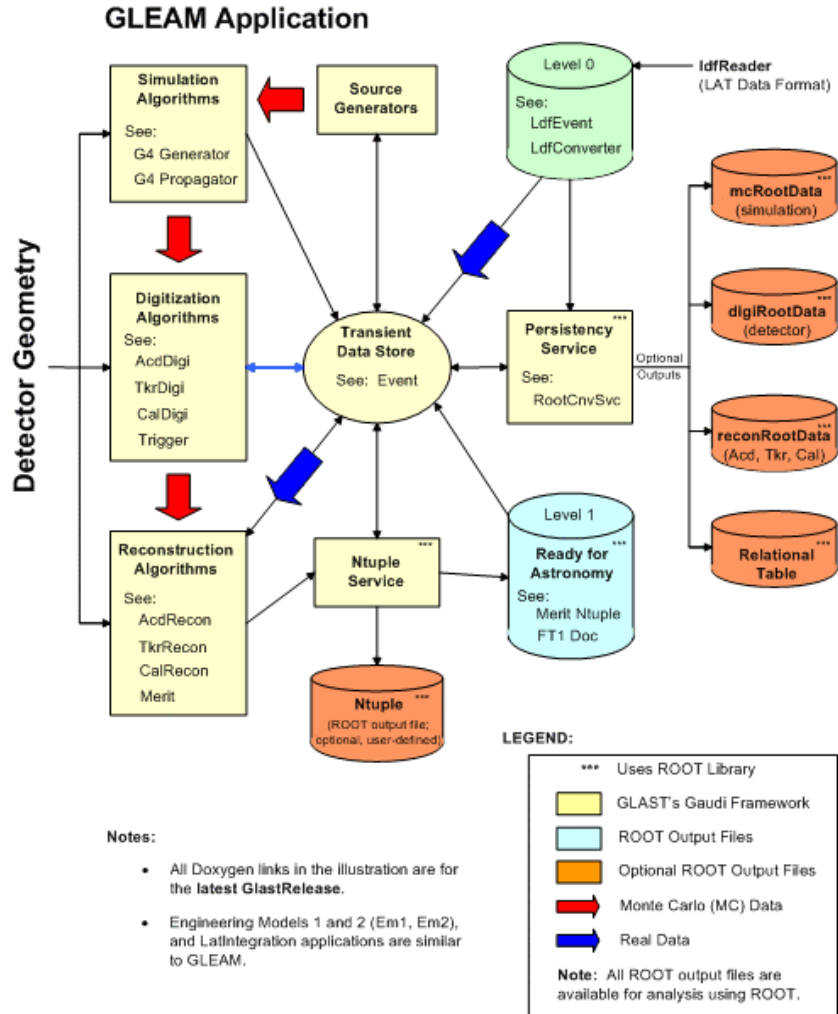


Fig. 11.1. Dataflow of GLEAM, the top-level GLAST package.

### 11.3 Offline Software

The software for KOPIO has to be designed and developed to last for fifteen to twenty years until final results are published. It should use modern compilers and share in the use of active HEP packages as much as possible. At the moment, support is planned only for Linux operating systems. Support for Windows could be added if enough collaborators request it and personnel to support both operating systems are available.

#### 11.3.1 Software Framework and Components

Several elements are needed to put together a comprehensive and efficient software environment. First, one must develop a software framework that ties together the various components. This task is a huge one, so we have investigated frameworks already in use by other HEP groups. At present, we intend to adapt as a starting point the GLAST framework[3] based on GAUDI[4], a software package developed by the CERN LHCb group and adopted by the GLAST collaboration. Figure 11.1 shows an overview of GLEAM, the GLast Event Analysis Machine.

Some of the software tools that will need substantial customization by a dedicated computer professional include the following:

**Detector description language.** A scheme must be developed to describe all of the detector dimensions and parameters that can be used as a common input for simulations, event reconstruction, analysis, and web applications. The candidate of choice at the moment is the XML language.

**Data format.** A data format and related input/output libraries must be chosen to efficiently store and retrieve the event-by-event information produced by the detector. This software becomes the interface between Online and Offline software.

**Data management system.** With the large amount of data expected, and in order to incorporate seamlessly diverse computing resources on-site and remotely, we need to implement a modern data management scheme, probably grid-based.

**Calibration databases.** Databases will be used to store several categories of information related to the detector: calibration results, conditions of runs, *etc.* Having only one database system that could be used for all needs of the collaboration would be desirable. User-friendly, web-based interfaces will be developed.

**Documentation.** A significant effort is necessary to document all aspects of the software components from simple recipes for collaborators wanting to visualize events and histograms to full algorithm descriptions needed by the code developers. All documentation should be accessible on the web. For documenting the source code and algorithms, we will use Doxygen. All code will be included in CVS repositories and will be visible through a CVS-web application.

Software workshops for collaborators must be held periodically. These meetings are essential to help everyone be educated in efficiently using the tools provided, and to ensure that we have a common approach to software development.

### 11.3.2 Simulations

The KOPIO collaboration has been using various simulations programs from the conception of the experiment. Special Monte Carlo codes have been used to study beam characteristics (see Section 4 and Section 5, while several variants of GEANT3 and FLUKA have been used to determine the parameters of the main detector components in Section 6. The most important studies have been the signal and background estimates reported in Section 13. A ‘fast’ Monte Carlo simulation (FastMC) technique 13.1 is being used for the most important studies of signal and background estimates. The next step is to develop a full Monte Carlo based on GEANT4 with the current detector geometry. This work is just beginning. In parallel, an effort to parameterize the detector responses has started to provide input for digitization algorithms.

### 11.3.3 Event Reconstruction

Event reconstruction is a central software component. The input consists of raw data events collected by the Online system or simulated by Geant4. After decoding the raw data and accessing the databases for calibration information, it prepares hit lists to pass to the photon tracking algorithms and the veto counters analysis routines. ROOT trees (ntuples)[5] are filled and output to files for further analysis. Some event rejection based on loose criteria can be implemented at this stage. Event visualization is also an important component of this software component.

The problem of reconstructing the showers produced by photons in a multi-layer converter/tracker such as the Preradiator has been the subject of considerable study and effort in connection with a series of such trackers that have been launched into orbit since the 1970’s to detect photons of extra-terrestrial origin. The current state of the art is embodied in the set of three competing tracking algorithms that have been developed for GLAST[6]. Only one of these algorithms currently performs sufficiently well for use by GLAST. KOPIO

is beginning to study this body of work to learn what elements might be adapted and incorporated. Of course the requirements for KOPIO differ significantly from those for satellite observatories. For example, the photon energy range is smaller by orders of magnitude (but included in the satellite range). However, the limits on inefficiency for distinguishing an additional photon in the vicinity of a shower of interest are much more severe. Furthermore, the characteristics of the GLAST tracking elements (silicon strip detectors) are quite different from those of the cathode-strip drift chambers of KOPIO. Current efforts by others to apply the GLAST shower reconstruction to data from the now-defunct satellite EGRET[7] are motivated by the improved performance that is expected from the advances in the algorithm that have been made in the past decade. Some symbiosis is likely because this tracker is based on spark chambers that bear a closer resemblance to our Preradiator. Nevertheless, it is clear that a substantial effort will be required to develop the shower reconstruction algorithm needed for KOPIO. The comprehensive diagnostic and display tools developed by GLAST to expedite this task will greatly assist this effort.

### References

1. <http://www-glast.slac.stanford.edu/index.html>.
2. <http://guide.westgrid.ca/>.
3. <http://www-glast.slac.stanford.edu/software/CHEP03/Talks/GLAST-Overview.pdf>.
4. <http://lhcb-comp.web.cern.ch/lhcb-comp/Frameworks/Gaudi/>.
5. <http://root.cern.ch>.
6. [http://www-glast.slac.stanford.edu/IntegrationTest/SVAC/Instrument\\_Analysis/Workshop-3/Talks/Leon\\_Tracker\\_talk.pdf](http://www-glast.slac.stanford.edu/IntegrationTest/SVAC/Instrument_Analysis/Workshop-3/Talks/Leon_Tracker_talk.pdf).
7. <http://www.gae.ucm.es/emma/tesina/node12.html>.

## 12 Conventional Systems and Integration

Systems integration will provide four important functions for integrating the detector subsystems into a unified experiment. The KOPIO system integration will include subsystem installation, subsystem integration, conventional utilities, and testing and commissioning of the neutral beam and the detectors. These functions are common in large experiments and do not represent a technical challenge. A brief description of these function for KOPIO will be given below.

### 12.1 Installation and Integration

Subsystem integration will be a dominant task for systems integration early in the construction phase of KOPIO. The detector subsystems provide an almost hermetic detector surrounding the neutral beam. The potential interference between detector systems or their support utilities and structures must be examined carefully to avoid problems. CAD solid modeling will be used to define geometries in an unambiguous manner. The solid models will be used to examine service and assembly scenarios for the detectors in the experimental area.

Figures 12.1 to 12.11 illustrate the overall assembly of the detector systems. A pit (Fig. 12.1) will be located below the main floor of the laboratory building to provide space for some of the large components and access to them. The D3 sweeping magnet (see Sec. 5.2.2) is placed at the first opening of the pit as shown in Fig. 12.2. The six layers of log modules, illustrated in Fig. 12.3, are assembled into the Upstream Veto Wall (see Sec. 6c.3.3 and Fig. 6c.15) which is located just beyond the regions of the D3 magnet. The Barrel Veto Detector is composed of sections of rings as shown in Fig. 12.4, which are then moved together. The Preradiator and Calorimeter are shown separated and joined together in Figs. 12.5 and 12.6. The locations of these detector components above the pit are shown in Figs. 12.7 and 12.8, respectively. Next, after the D4 sweeping magnet with its Magnet Photon Veto system (see Sec. 6c.3.3), comes the tank assembly which houses the Downstream Charged Particle Veto (Sec. 6d.6.2), and Downstream Photon Veto (Sec. 6c.3.3), and Catcher (Sec. 6e) systems. Solid-model drawings of the subassemblies and the full tank assembly are shown in Figs. 12.9 and 12.10. The full detector is illustrated in Fig. 12.11.

The installation of detector subsystems into the experimental area will be part of the services provided by systems integration. The activities to support detector installation are substantially different from detector assembly and are managed by systems integration. Such activities will include items such as the survey of the area for the experimental equipment, installing the support structures, installing electronics racks, *etc.* Installation of detector components will accommodate the restrictions of the overhead crane, limited working space in the experimental area, and changes in detector subsystem schedules. The installation of all utilities and specialized access platforms will be included in this effort.

### 12.2 Conventional Utilities

Conventional utilities will be engineered, designed, and procured to meet the requirements of the detector systems. Mechanical systems will include chilled water for heat removal from electronics racks, and air conditioning for stable air temperature and humidity control. Electrical systems will be designed for low-noise AC power distribution for electronics (clean power) and “dirty” power for support functions such as motors and compressors. Uninterrupted power supplies will be provided where controlled shutdown is required on the loss of AC power. Ground fault monitoring will be provided for the clean power distribution to detect any ground loops that might be inadvertently created.

### 12.3 Protection and Safety

Equipment protection will be provided by a system of global interlocks and alarms. The detector systems will be reviewed by the C-A Department Experimental Safety Committee. An approved system of smoke, heat, and water-leak detectors will be distributed throughout the experiment to protect equipment from damage due to fire or water leaks. The system will provide alarms and, when appropriate, interlock off

the power or water to an affected area to reduce the potential for equipment damage. The operation, maintenance, and certification of the equipment protection system will be the responsibility of the C-A Department. The interlock and alarm system will be similar in design to those in operation for the STAR experiment at RHIC. The C-A Department will provide any systems necessary for personnel protection.

The availability of neutral beam and commissioning is expected to start in FY2009. The initial commissioning effort will focus on verifying the primary beam design, proton targeting, and the neutral beam design. Prototype detectors will be used to measure the characteristics of the neutral beam with measurements of the  $K_L^0$  production, neutron beam, and halo rates. The magnet vacuum tank with installed photon vetos is expected to be available for these measurements as well as a  $10 \times 10$  Calorimeter array, a Preradiator quadrant, and the Catcher and Guard Counters. Tests will be conducted on the wave-form digitizer, trigger, and DAQ designs. If the 25-Mhz cavity is available, the first measurements of the microbunch width and interbunch extinction will be conducted. In FY2010, a substantial portion of the detector system will be available for beam tests. The beam tests will shift from characterizing the neutral beam to characterizing the detector, trigger, and DAQ performance.

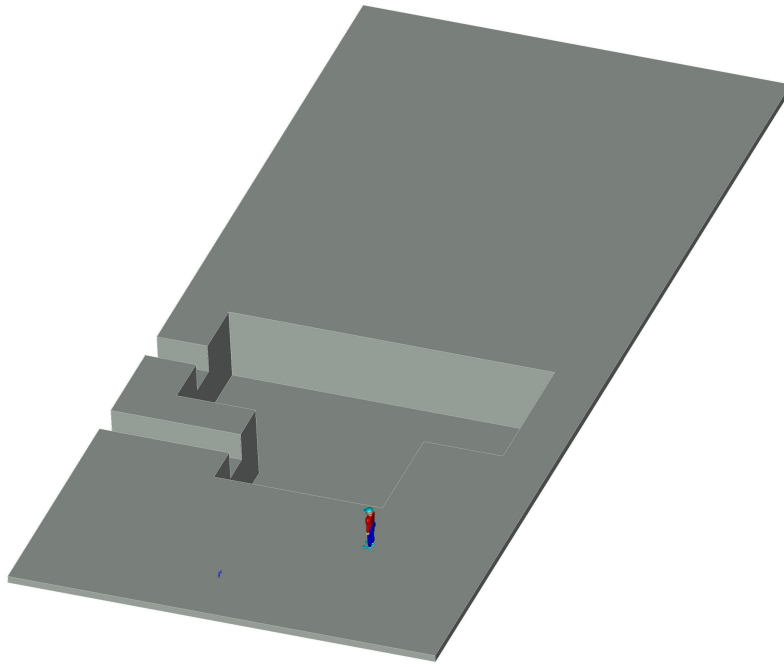


Fig. 12.1. The pit for the KOPIO detector.

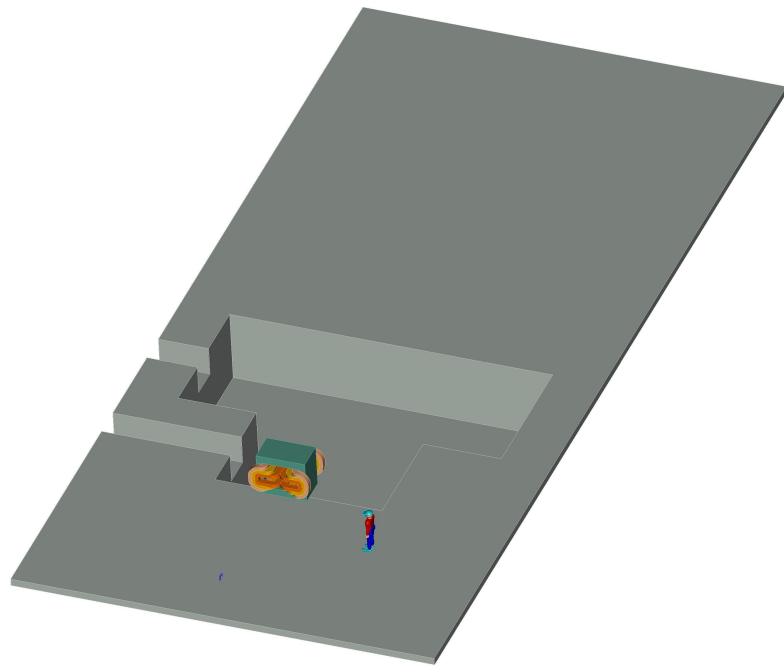


Fig. 12.2. The pit with the D3 magnet



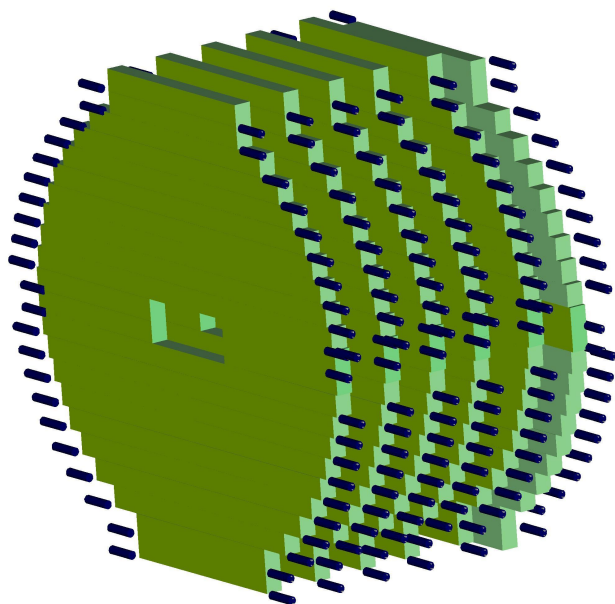


Fig. 12.3. The Upstream Photon Veto assembly.

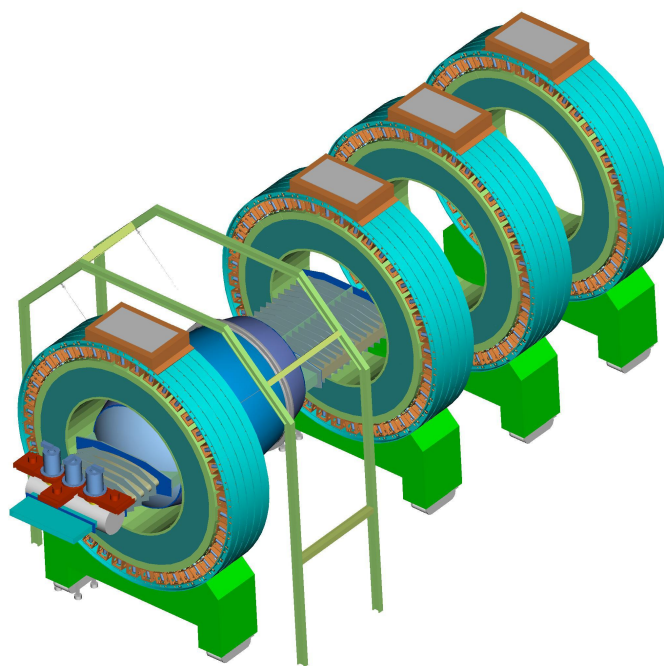


Fig. 12.4. The Barrel Photon Veto assembly.

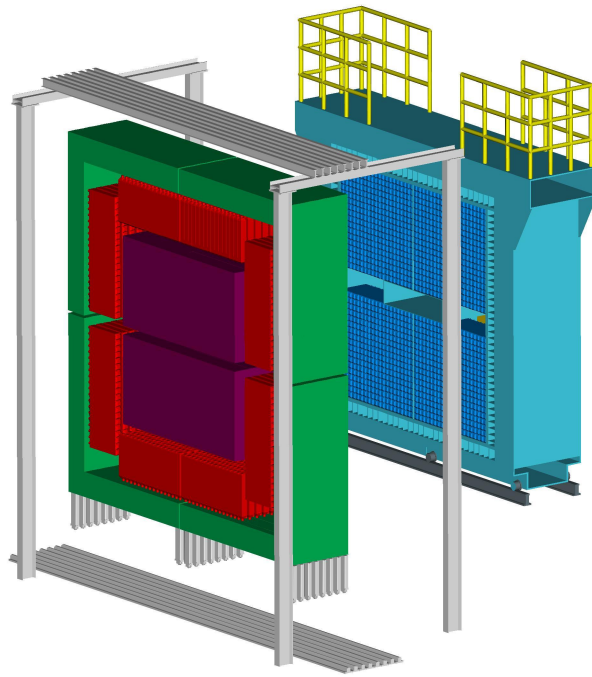


Fig. 12.5. The Preradiator and Calorimeter components.

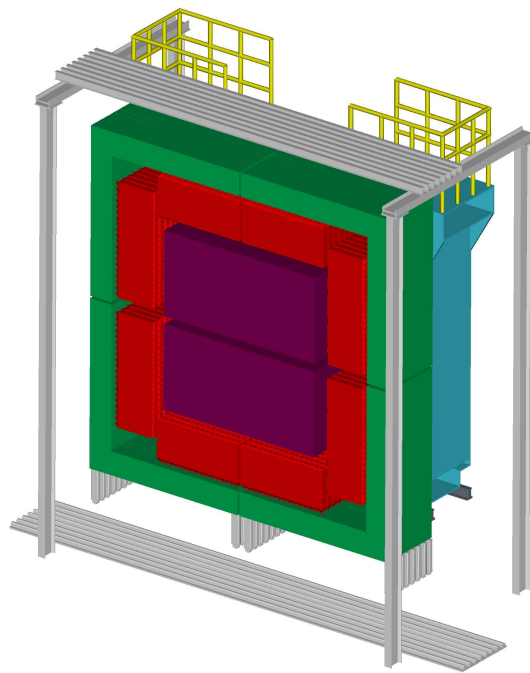


Fig. 12.6. The Preradiator and Calorimeter joined together.

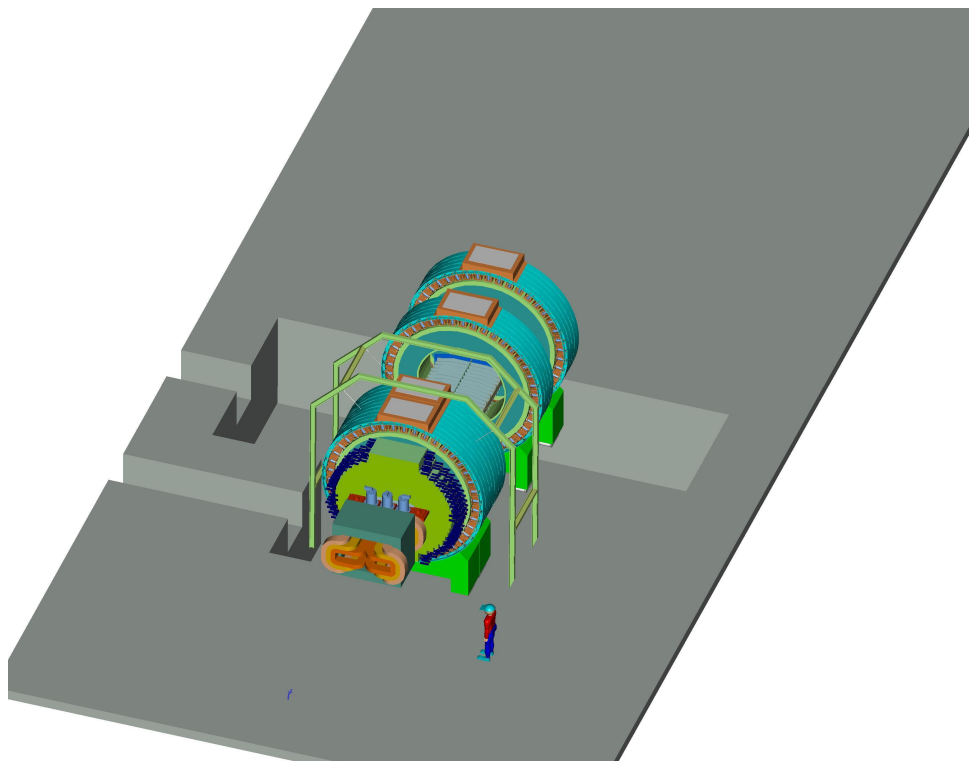


Fig. 12.7. The KOPIO assembly through the Barrel Veto.

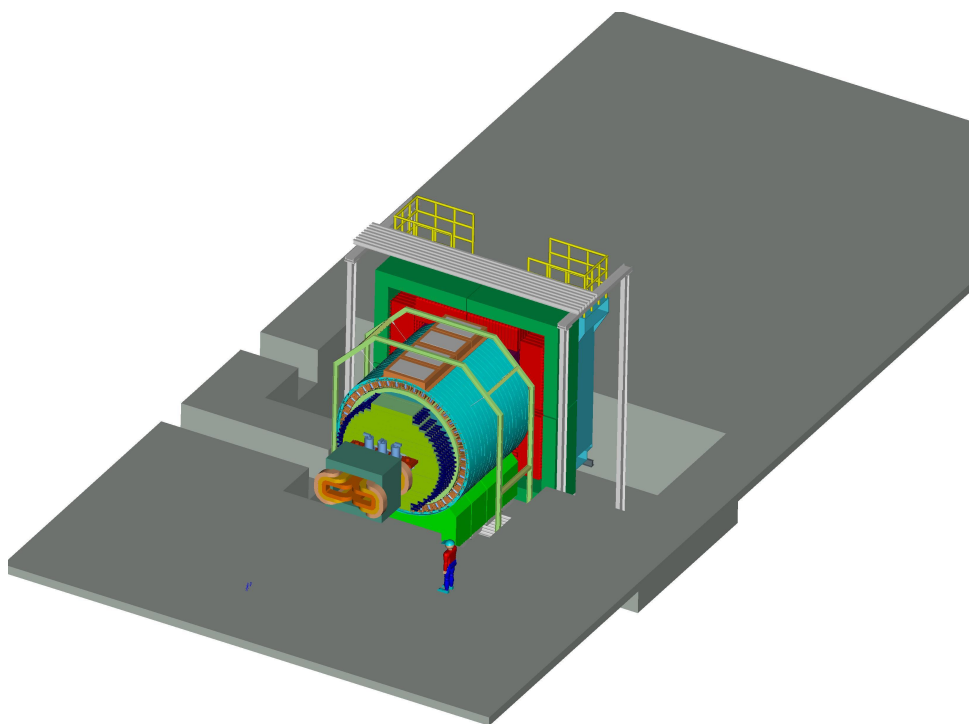


Fig. 12.8. The KOPIO assembly through the Preradiator/Calorimeter.

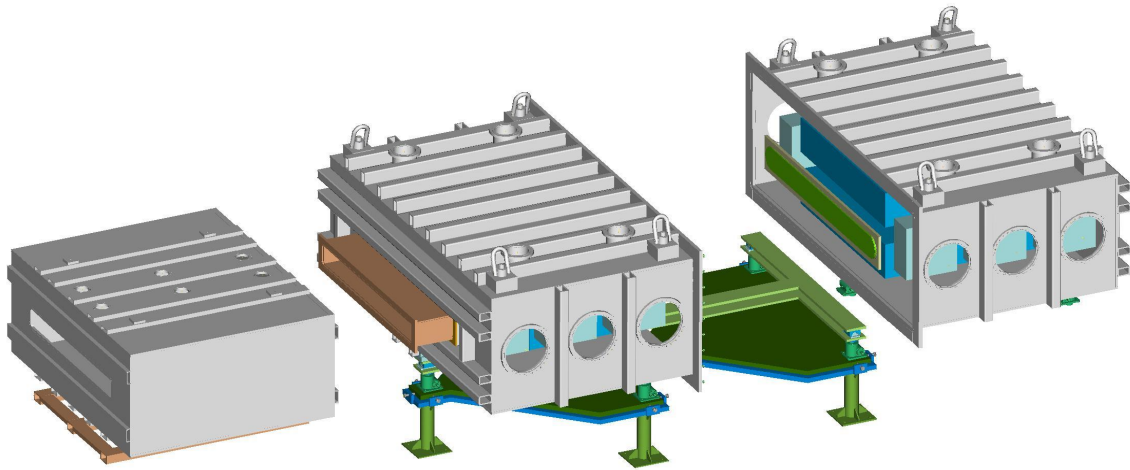


Fig. 12.9. The downstream tank assembly.

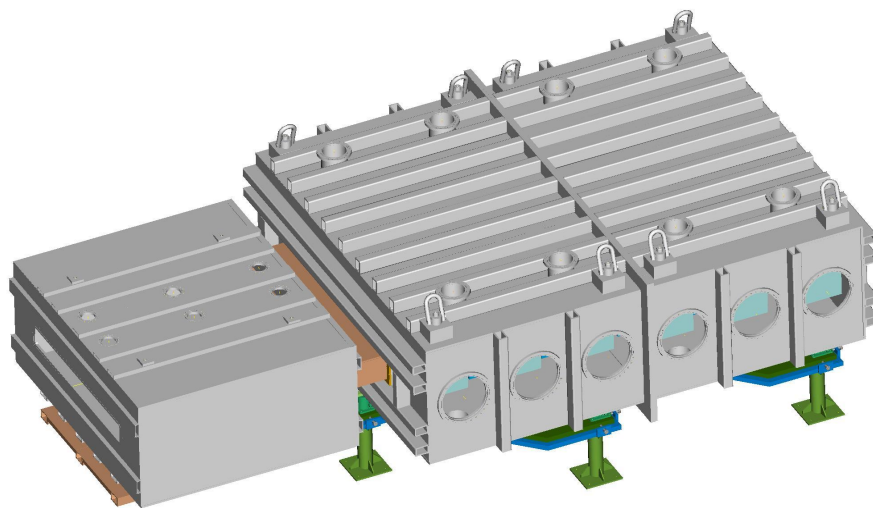


Fig. 12.10. The downstream tank components joined together.

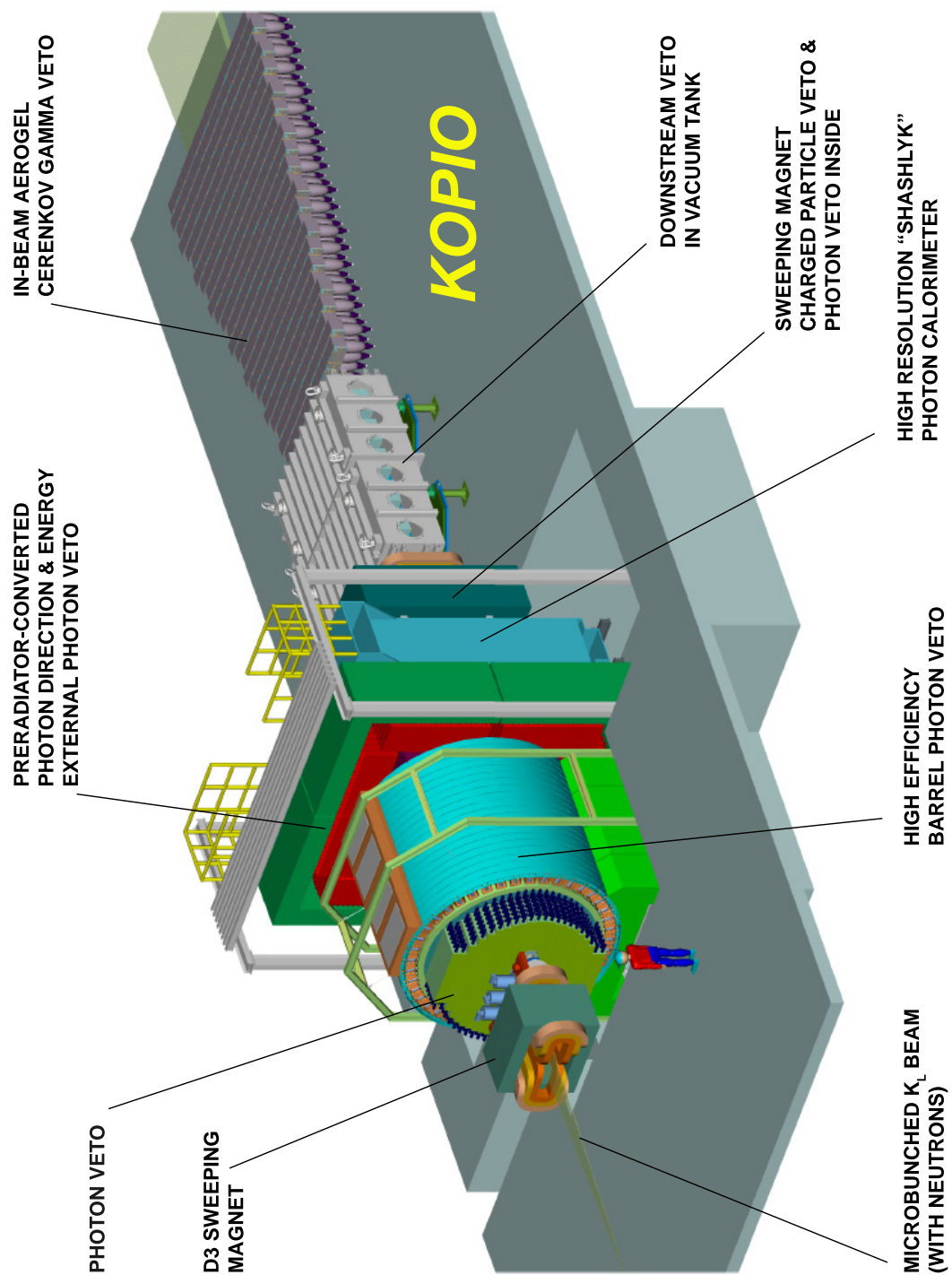


Fig. 12.11. The assembled KOPIO detector.

## 13 Signal and Background Estimates

A measurement of  $K_L^0 \rightarrow \pi^0 \nu \bar{\nu}$  requires suppression of backgrounds by a factor of  $10^{11}$  or more. In order to reach a sensitivity at the level of the Standard Model (SM) with a precision of 10% on the measurement of the branching ratio  $\mathcal{B}(K_L^0 \rightarrow \pi^0 \nu \bar{\nu})$ , KOPIO employs both kinematic constraints and charged-particle or photon vetoing to suppress the backgrounds. The techniques and assumptions used to make reliable estimates as well as the methods of signal detection and background suppression are described in this section.

The organization of this section is as follows. Section 13.1 describes the simulation tools used to make these estimates. Sections 13.2 and 13.3 describe the assumptions concerning the  $K_L^0$  flux, the veto inefficiency, and the resolution. The signal detection methods are described in Sec. 13.4, and the background mechanisms and expected rates are described in Sects. 13.5–13.8.3. Signal losses aside from analysis cuts are described in Sec. 13.9.

### 13.1 Tools

The signal and background estimates in this section are currently based primarily on a ‘fast’ Monte Carlo simulation (FastMC) that uses parameterization of the detection response and event weighting. These calculations are supplemented by a GEANT3.21-based simulation to assess potential signal loss due to trigger and reconstruction algorithms, and vetoing due to accidentals.

The FastMC approximates the KOPIO detector with a simplified geometry consisting of rectangular parallelepipeds with no magnetic fields. The  $K_L^0$  are generated from the production target in accordance with the expected time structure of the incident proton beam (Sec. 4) and target dimensions. The angular and momentum dependence of the  $K_L^0$  beam are taken from extrapolation of measurements from proton-nucleus reactions at 14.6 GeV/c (Sec. 5). All known  $K_L^0$ ,  $\pi^\pm$ ,  $\pi^0$ , and  $\mu^\pm$  decay modes and their matrix elements with branching fractions from Ref.[1], as well as all decays in flight, are included in the simulation.

The impact position, angle, energy, and time of photon trajectories which project to the photon detectors are ‘smeared’ according to the expected resolution of the Preradiator (PR), Calorimeter (CAL), External Photon Veto (EPV), and Barrel Veto (BV) system as described in Section 13.3.3.

Two sequential kinematic fits are attempted for each pair of signal candidate photons. The first fit does not impose the  $\pi^0$  mass constraint, and the second fit imposes the mass constraint. Additional constraints placed on both fits include a common vertex in space and time as well as a vertex located within the vertical beam envelope. The vertex of the second fit is used to construct a  $K_L^0$  candidate, assuming production from the target center at the central time of the microbunch. Physically valid ( $\beta(K_L^0) < 1$ ) candidates are accepted for further scrutiny. Physically invalid solutions can result from backgrounds due to  $K_L^0$  from outside the microbunch and from non- $K_L^0$  sources of  $\pi^0$  candidates as discussed in Sections 13.5 and 13.8.6.

### 13.2 Flux Assumptions

The total useful  $K_L^0$  flux is determined as follows. We expect  $N_{K,\text{prod}} = 6.64 \times 10^8 K_L^0\text{s}$  for  $100 \times 10^{12}$  protons per spill on a 10.6cm Pt target into 360  $\mu\text{sr}$  centered at  $42.5^\circ$  (Sec. 5), as obtained from a thin-target approximation. Taking into account the effects of target length and secondary production, the flux is reduced by a factor of  $a_{\text{tgt}} = 0.75$ . The photon spoiler (Sec. 5) reduces the flux by an additional factor of  $a_{\text{spoil}} = 0.527$ . Combining all these factors gives

$$N_{K,\text{prod}} \times a_{\text{tgt}} \times a_{\text{spoil}} = N_{K,\text{exit}} \quad (7)$$

$$6.64 \times 10^8 \times 0.75 \times 0.527 = 2.625 \times 10^8 \quad (8)$$

$K_L^0$  exiting the spoiler per spill. The relative uncertainty on the  $K_L^0$  flux is estimated to be  $\pm 20\%$  by taking into account uncertainties in the production and attenuation of the  $K_L^0$  beam.

The length of the spill is set to maximize the sensitivity while taking all sources of rate-dependent vetos into account (Sec. 13.9). Sources of rate-dependent vetos are  $K_L^0$  decays in the same and neighboring microbunches, stopped muons, and neutrons. In addition, there are two significant rate-independent losses. The

first is the “self-veto” loss and is due to loss of signal when part of the shower from a signal photon deposits enough energy far from the main shower to veto the candidate. The second is due to photon absorption in the decay vessel or beam pipe. The signal survival rate is  $\mathcal{S}_{\text{self}} = 0.88$  for “self-veto” and  $\mathcal{S}_{\text{abs}} = 0.86$  for photon absorption. When all of these factors are taken into account, a survival factor of  $\mathcal{S}_{\text{tot}} = 0.383$  is expected with a spill length of  $t_{\text{spill}} = 4.90$  s (Fig. 13.1), where we also assume a  $t_{\text{inter}} = 2.3$ -s interspill (Sec. 4). Combining these factors yields

$$(N_{K,\text{exit}} \times \mathcal{S}_{\text{tot}})/(t_{\text{spill}} + t_{\text{inter}}) = N_{K,\text{useful}} \quad (9)$$

$$(2.625 \times 10^8 \times 0.383)/(4.90 \text{ s} + 2.3 \text{ s}) = 1.40 \times 10^7 \quad (10)$$

“useful”  $K_L^0$ s exiting the spoiler per calendar second. This rate corresponds to a total of  $0.60 \times 10^{15}$  useful  $K_L^0$ s exiting the spoiler for a 12,000-hour run. At the optimum spill length, the number of  $K_L^0$ s exiting the spoiler per microbunch for a  $f = 25$  MHz microbunch frequency is

$$N_{K,\text{exit}}/(t_{\text{spill}} \times f) = N_{K,\text{bunch}} \quad (11)$$

$$2.625 \times 10^8/(4.90 \text{ s} \times 25 \times 10^6 \text{ s}^{-1}) = 2.14 . \quad (12)$$

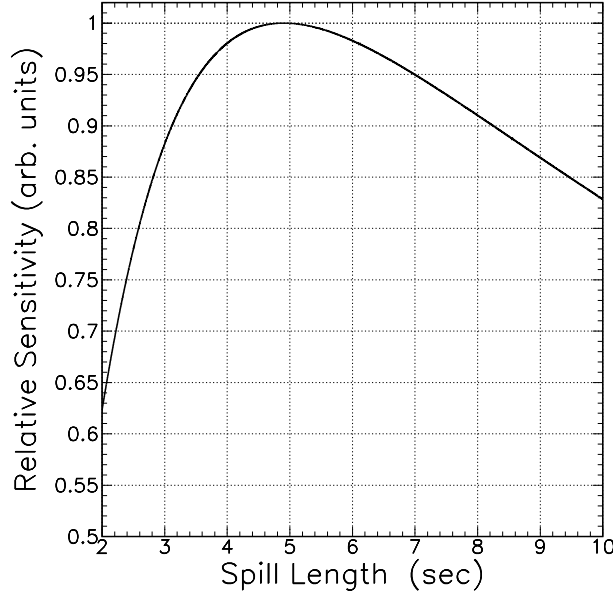


Fig. 13.1. The relative KOPIO sensitivity as a function of spill length. The optimum spill length is 4.90 seconds; however, spill lengths from  $\sim 3.5$  to  $\sim 7$  seconds would entail a loss of only  $\sim 5\%$  in sensitivity.

### 13.3 Veto Inefficiency and Resolution

Highly efficient photon and charged particle vetoing as well as good angular, position, time, and energy resolution are essential to the successful observation and measurement of  $K_L^0 \rightarrow \pi^0 \nu \bar{\nu}$ . The assumptions about the veto inefficiencies and detector resolutions used to estimate the signal and background are based on measurements and supplemented with results from simulation. Details of the photon veto efficiencies assumed in the current estimates are given in Section 6f.



### 13.3.1 Photon Veto Inefficiency

Photon vetoing (PV) is accomplished with two types of detectors in KOPIO. Lead-scintillator ‘sandwich’-style detectors occupy the regions outside the beam (Section 6c). A novel ‘beam Catcher’ based on observation of Cherenkov radiation produced by  $e^+e^-$  pairs from photons converting in lead and radiating in aerogel is used within the beam envelope. The Catcher design minimizes sensitivity to neutrons while maintaining high veto efficiency for photons. A lead-lucite sandwich-style detector, dubbed the ‘Guard Counter’, occupies the near-beam region (Section 6e). The photon veto efficiency for the Catcher used in the FastMC is parameterized as a function of photon energy. The photon veto efficiency for the Catcher is based on prototype measurements and simulations as described in Sec. 6e and shown in Fig. 13.2.

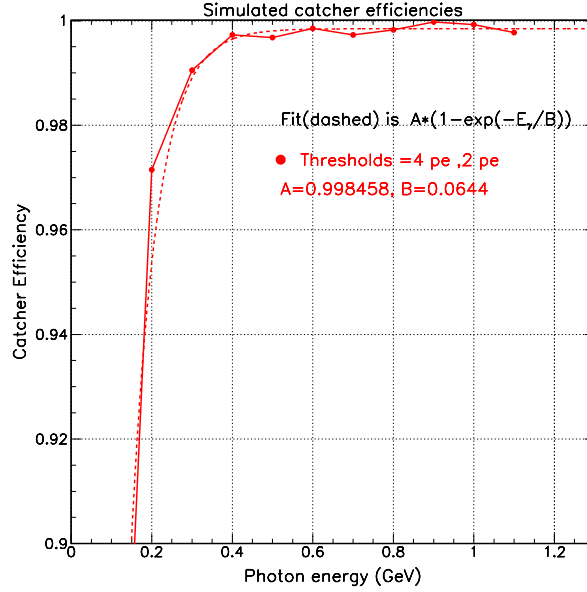


Fig. 13.2. The dashed line represents the parameterized photon veto efficiency for the beam Catcher. The points are taken from simulation and the solid line is drawn to guide the eye. “Threshold = 4pe, 2pe” refers to the photon identification procedure described in Sec. 6e.

The photon veto inefficiency of the lead-scintillator ‘sandwich’-style detector is based on measurements supplemented by simulation as described in Sec. 6f. In the FastMC, the photon veto inefficiency is parameterized as a function of incident photon angle and energy and is shown in Figs. 6f.6 and 6f.7. The geometry of the photon Barrel Veto detector is approximated in the FastMC as a cylinder with a radius equal to the inner radius of the Barrel Veto and ends coincident with the Upstream Veto and Preradiator. The lead and scintillator sheets of the photon veto are assumed to be parallel to the ends of the cylinders. For photons that strike the Barrel Veto, the lead and scintillator sheets are assumed to be parallel to the tangent to the cylinder at the point of photon impact. The incident angle is defined as the angle with respect to normal incidence on the lead and scintillator sheets.

To calculate the veto inefficiency for a given photon, the photon trajectory is projected to the cylinder described in the previous paragraph. Photon trajectories that would exit the detector through the hole for the incoming beam are assumed to escape detection. Photon trajectories that would strike the catcher/guard counter are given an energy-dependent photon veto inefficiency as shown in Fig. 13.2. Remaining photons are assigned an energy- and angle-dependent photon veto inefficiency. Implicit in the assumption of an assigned photon veto inefficiency is the hermiticity of the photon veto detectors.

### 13.3.2 Charged Particle Veto Inefficiency

The Charged Particle Veto (CPV) detectors in KOPIO and the fundamental limits to charged particle detection are described in Sec. 6d. The primary means of detection is scintillation light produced by the traversal of the charged particle. As described in Sec. 6d, in cases where the incident particle interacts before producing sufficient scintillation light for detection, the particles produced in the interaction may be detectable by the CPV or PV detectors. Thus it is appropriate to assume the performance of the combined CPV/PV system when evaluating the charged particle veto inefficiency.

Figures 13.3 and 13.4 shows the charged particle veto inefficiency as a function of incident momentum as assumed in the FastMC. Additional possible sources of charged particle detection inefficiency are discussed in Section 6d, and the effects of such sources on specific backgrounds are discussed in Sects. 13.6.2 and 13.6.3.

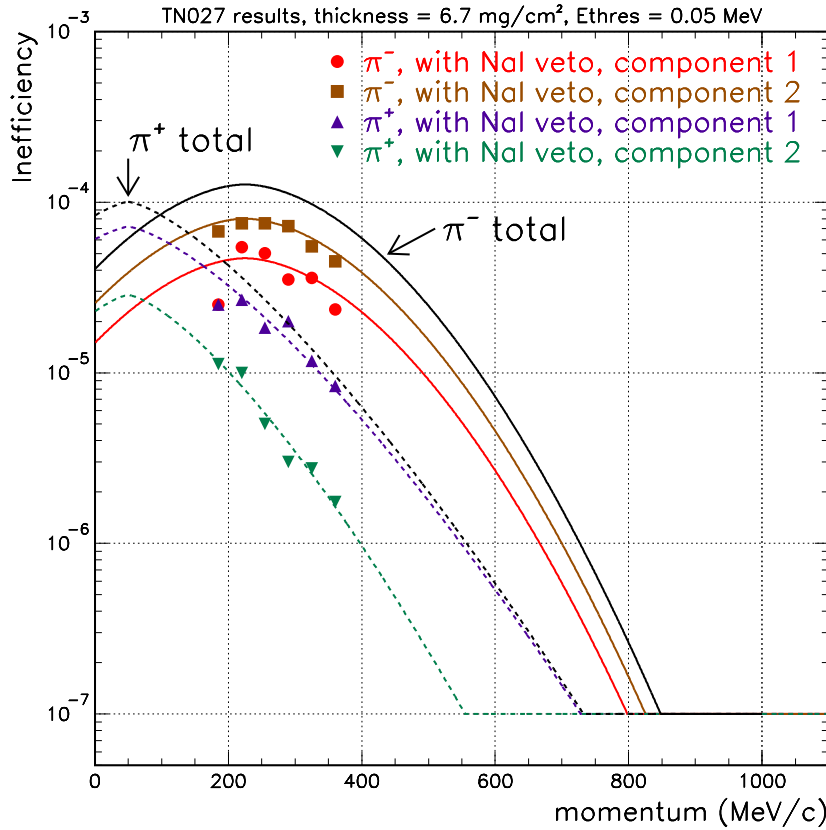


Fig. 13.3. The charged pion veto inefficiency as a function of the pion momentum. The charged pion inefficiencies are taken from fits to PSI measurements (Sec. 6d) and extrapolated for a dead material thickness of 6.7 mg/cm<sup>2</sup> and a 50-keV energy threshold. Component 1(2) corresponds to the effect of dead material (threshold). The “NaI veto” in the legend corresponds to measurements made with a NaI detector behind the CPV to take into account the effect of the PV in KOPIO.

As described in Sec. 13.1, decay-in-flight is taken into account in the FastMC, although the effects of fringe magnetic fields in the decay region from the D3 and D4 magnets (Sec. 5) are neglected. The effects of D4 on charged particles that exit the decay region via the downstream beam pipe are approximated by truncating the flight path of charged particles 200 cm from the downstream end of the decay region.

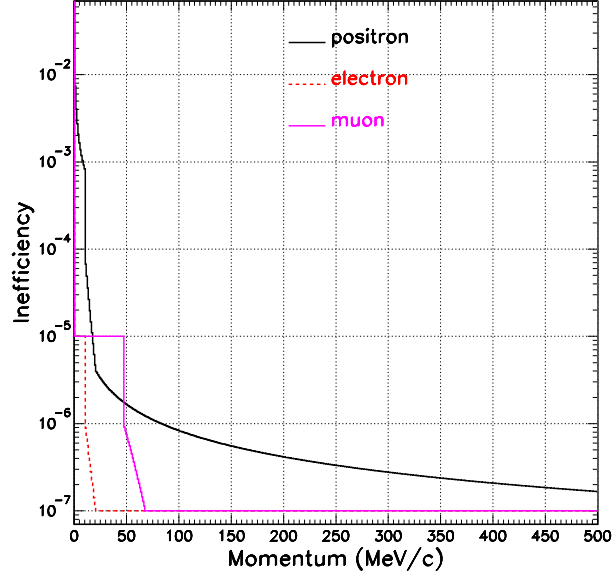


Fig. 13.4. The charged lepton veto inefficiencies as a function of momentum. The momentum-dependence of the positron inefficiency is an approximation to annihilation cross-section. The discontinuity in the curves corresponds to the assumption that the inefficiency is reduced by up to  $\times 0.01$  due to detection by PV behind all CPV elements for kinetic energy above 10 MeV.

### 13.3.3 Detector Resolutions

The relevant detection resolutions for the different detection methods are listed in Table 13.1 and are based on results given in Sects. 6a and 6b, and in Table 6c.2. The angular resolution is taken from simulations described in Sec. 6a and shown in Fig. 6a.1.

Table 13.1. The assumed detector resolutions ( $\sigma$  of a Gaussian) used for estimates of signal and background yields by the FastMC simulation. All energies are in GeV. PR/(CAL&EPV) corresponds to the primary detection method where both photons convert in the PR and the energy is accumulated in the PR, CAL and EPV (Sections 6a and 6b). CAL corresponds to the detection method that requires a single photon conversion in the PR and the other photon conversion in the CAL (Sec. 6b). BV corresponds to the detection method that requires a single photon conversion in the PR and the other photon conversion in the BV (Sec. 6c.2). Detection methods are described in Sec. 13.4.

Detector System	Energy Resolution (%)	Time Resolution (ns)	Transverse Position Resolution (cm)	Longitudinal position Resolution (cm)
PR/(CAL&EPV)	$2.7\%/\sqrt{E}$	0.2	0.02	—
CAL	$2.7\%/\sqrt{E}$	$0.09/\sqrt{E}$	3.17	1.5
BV	$4.0\%/\sqrt{E}$	$0.09/\sqrt{E}$	6.34	1.5

### 13.4 Detection Methods

The primary signal detection method (PR/CAL) involves both photons converting in the PR with the energy accumulated in the PR and CAL and has the best overall position, angle, and energy resolution. The second method ( $2\gamma$ PR/CAL&EPV) also requires that both photons convert in the PR with the energy accumulated in the PR, CAL and EPV and is expected to have comparable position and angular resolution and slightly degraded energy resolution. This method is referred to as  $2\gamma$ PR in the following.

The next three methods only require a single photon conversion in the PR with the other photon converted in the CAL, EPV, or BV and are labeled PR/CAL, PR/EPV, and PR/BV, respectively. In practice the anticipated signal yield from PR/EPV combinations is very small and is neglected in the evaluation of the total possible signal yield. The methods PR/CAL and PR/BV are referred to collectively as  $1\gamma$ PR.

Taken together, these methods result in twice the number of signal events compared to using  $2\gamma$ PR events alone. However, the  $1\gamma$ PR events have a lower signal-to-background ratio due to poorer resolution.

### 13.5 Background Mechanisms

Five potential background mechanisms were identified and studied. Three are distinguished by the production time of  $K_L^0$  relative to the center of the microbunch. The other two mechanisms are related to mis-identification of accidental activity in the detector as photon activity, or merging of nearby photon showers. The expected rates of these backgrounds will be discussed in detail in the following sections. A brief description of each mechanism is given here.

Microbunch timing of the neutral beam is defined with respect to the time that the center of the proton beam crosses the midpoint of the production target. This time is taken as  $t = 0$  ns. The  $K_L^0$  produced at this time are referred to as “in-bunch” and are by far the largest component of the background. The “in-bunch” background is described in detail in the next Section.

The  $K_L^0$  produced in the previous microbunch at  $t = -40$  ns are a potential source of “wrap-around” background. This background occurs when a slow  $K_L^0$  produced at  $t = -40$  ns is reconstructed and mistakenly assumed to be from the microbunch at  $t = 0$  ns. The third mechanism is due to  $K_L^0$  production during the 40-ns interval between “in-bunch” production. This process is referred to as “interbunch” background.

Wrap-around and interbunch backgrounds arise because the assumed production time assigned to a  $K_L^0$  candidate can be incorrect. KOPIO’s time-of-flight technique would thus calculate an incorrect velocity for the candidate. If the calculated velocity is physically valid ( $0 < \beta(K_L^0) < 1$ ), then both the quantities calculated in the  $K_L^0$  rest frame and the missing energy will be incorrect and the kinematic background suppression (discussed in Sec. 13.6) will be reduced. As discussed in the next Section, wrap-around background is small ( $< 10\%$ ) compared to the in-bunch background and interbunch backgrounds are negligible.

Another background mechanism comes from additional activity in the photon detectors due to stopped muon decays or neutron-induced showers that are mistakenly identified as a photon-induced shower. The rate of these backgrounds was estimated by including the properties of such showers, as determined from the GEANT3 simulation, in the FastMC. Backgrounds due to this mechanism can be suppressed to a negligible level by requirements on timing, shower energy, and the  $\chi^2$  of the two-photon fit. The final background mechanism is due to incorrect reconstruction of two-photon showers as a single shower and is discussed in more detail below.

### 13.6 Backgrounds due to $K_L^0$ Decays

The main source of background to  $K_L^0 \rightarrow \pi^0 \nu \bar{\nu}$  is due to other  $K_L^0$  decays. The branching fractions of all  $K_L^0$  decays are listed in Table 13.2. Backgrounds from other sources can be suppressed to negligible rates. In this section, the mechanism for each  $K_L^0$  decay mode that contributes to the background will be described as well as the means available to KOPIO to suppress each background. The section concludes with quantitative estimates of the signal and background yields for selection criteria of decreasing severity.

Table 13.2. The name, final state, branching fraction[1] and branching fraction relative to signal for  $K_L^0$  decay modes assuming the standard model rate for signal.

Name	Final state	Branching fraction	$\mathcal{B}/\mathcal{B}(K_L^0 \rightarrow \pi^0 \nu \bar{\nu})$
Kpnn	$\pi^0 \nu \bar{\nu}$	$0.3000 \times 10^{-10}$	1.000
Kp2	$\pi^0 \pi^0$	$0.9320 \times 10^{-3}$	$0.31 \times 10^8$
Kcp2	$\pi^+ \pi^-$	$0.2090 \times 10^{-2}$	$0.70 \times 10^8$
Kgg	$\gamma \gamma$	$0.5900 \times 10^{-3}$	$0.20 \times 10^8$
Kp3	$\pi^0 \pi^0 \pi^0$	0.2105	$0.70 \times 10^{10}$
Kcp3	$\pi^+ \pi^- \pi^0$	0.1259	$0.42 \times 10^{10}$
Ke3	$\pi^\pm e^\mp \nu$	0.3881	$0.13 \times 10^{11}$
Km3	$\pi^\pm \mu^\mp \nu$	0.2719	$0.91 \times 10^{10}$
Ke3g	$\pi^\pm e^\mp \nu \gamma$	$0.3530 \times 10^{-2}$	$0.12 \times 10^9$
Km3g	$\pi^\pm \mu^\mp \nu \gamma$	$0.5700 \times 10^{-3}$	$0.19 \times 10^8$
Kpgg	$\pi^0 \gamma \gamma$	$0.1410 \times 10^{-5}$	$0.47 \times 10^5$
Ke4	$\pi^0 \pi^\pm e^\mp \nu$	$0.5180 \times 10^{-4}$	$0.17 \times 10^7$
Km4	$\pi^0 \pi^\pm \mu^\mp \nu$	$0.1400 \times 10^{-4}$	$0.47 \times 10^6$
Ke2g	$e^+ e^- \gamma$	$0.1000 \times 10^{-4}$	$0.33 \times 10^6$
Km2g	$\mu^+ \mu^- \gamma$	$0.3590 \times 10^{-6}$	$0.12 \times 10^5$

### 13.6.1 $K_L^0 \rightarrow \pi^0 \pi^0$ Background

The largest single source of background is due to  $K_L^0 \rightarrow \pi^0 \pi^0$  ( $K_{\pi 2}$ ), branching fraction  $(9.32 \pm 0.12) \times 10^{-4}$ , when two of the photons are undetected and the detected photons mimic the kinematics of  $K_L^0 \rightarrow \pi^0 \nu \bar{\nu}$ .

KOPIO suppresses the  $K_L^0 \rightarrow \pi^0 \pi^0$  background with the Photon Veto and with kinematics. Background from  $K_L^0 \rightarrow \pi^0 \pi^0$  manifests itself as “ $K_{\pi 2}$ -even” and “ $K_{\pi 2}$ -odd” when the reconstructed  $\pi^0$  candidate contains photons from the same or different  $\pi^0$ , respectively. The  $K_{\pi 2}$ -even background is characterized by a monochromatic peak in  $T_{\pi^0}^*$  equal to the kinetic energy of the  $\pi^0$  in the  $K_L^0$  rest frame (Fig. 13.5) and a reconstructed two-photon mass  $M_{\gamma\gamma}$  centered on the  $\pi^0$  mass (Fig. 13.6). In contrast, the  $K_{\pi 2}$ -odd background is characterized by a two-photon mass distribution that is relatively constant in the region of the  $\pi^0$  mass (Fig. 13.6) and a  $T_{\pi^0}^*$  spectrum that decreases as  $T_{\pi^0}^*$  increases (Fig. 13.5). These characteristics can be used to distinguish the  $K_{\pi 2}$  background from the  $K_L^0 \rightarrow \pi^0 \nu \bar{\nu}$  signal spectrum which increases monotonically with increasing  $T_{\pi^0}^*$  (Fig. 13.5) and has a reconstructed two-photon mass centered on the  $\pi^0$  mass.

The  $K_{\pi 2}$  background can be further suppressed by application of the Photon Veto on the two non-candidate photons. From the energy dependence of the Photon Veto inefficiency (Fig. 13.2), it is clear that the maximum  $K_{\pi 2}$  suppression is possible for higher photon energies. The reconstructed kinematics of the  $K_L^0$  and  $\pi^0$  candidates permits the measurement of the missing energy  $E_{\text{miss}}$  of the  $K_L^0$ , which should be equal to sum of the energy of the two non-candidate photons. Thus candidate events with high  $E_{\text{miss}}$  have, on average, lower photon veto inefficiency. The effect of the suppression of the  $K_{\pi 2}$  background by the Photon Veto is seen by contrasting the spectra in Figs. 13.7 and 13.8.

The  $K_{\pi 2}$  background can be exacerbated if photons hide in the showers of other detected photons, but we expect that the consequent inefficiency to be small based on the following discussion as well as on simulations of shower overlaps in the FastMC. These overlapping photons occur less than a few percent of the time in  $K_L^0 \rightarrow \pi^0 \pi^0$  events for distances between the two photons at the Calorimeter of less than 50 cm (about 8 Molière radii). For separation distances  $\leq 20$  cm, the probability is  $< 1\%$  for  $K_L^0 \rightarrow \pi^0 \pi^0$  decays. When the distance between two photons is between 20 and 50 cm, we identify the overlapping photons by

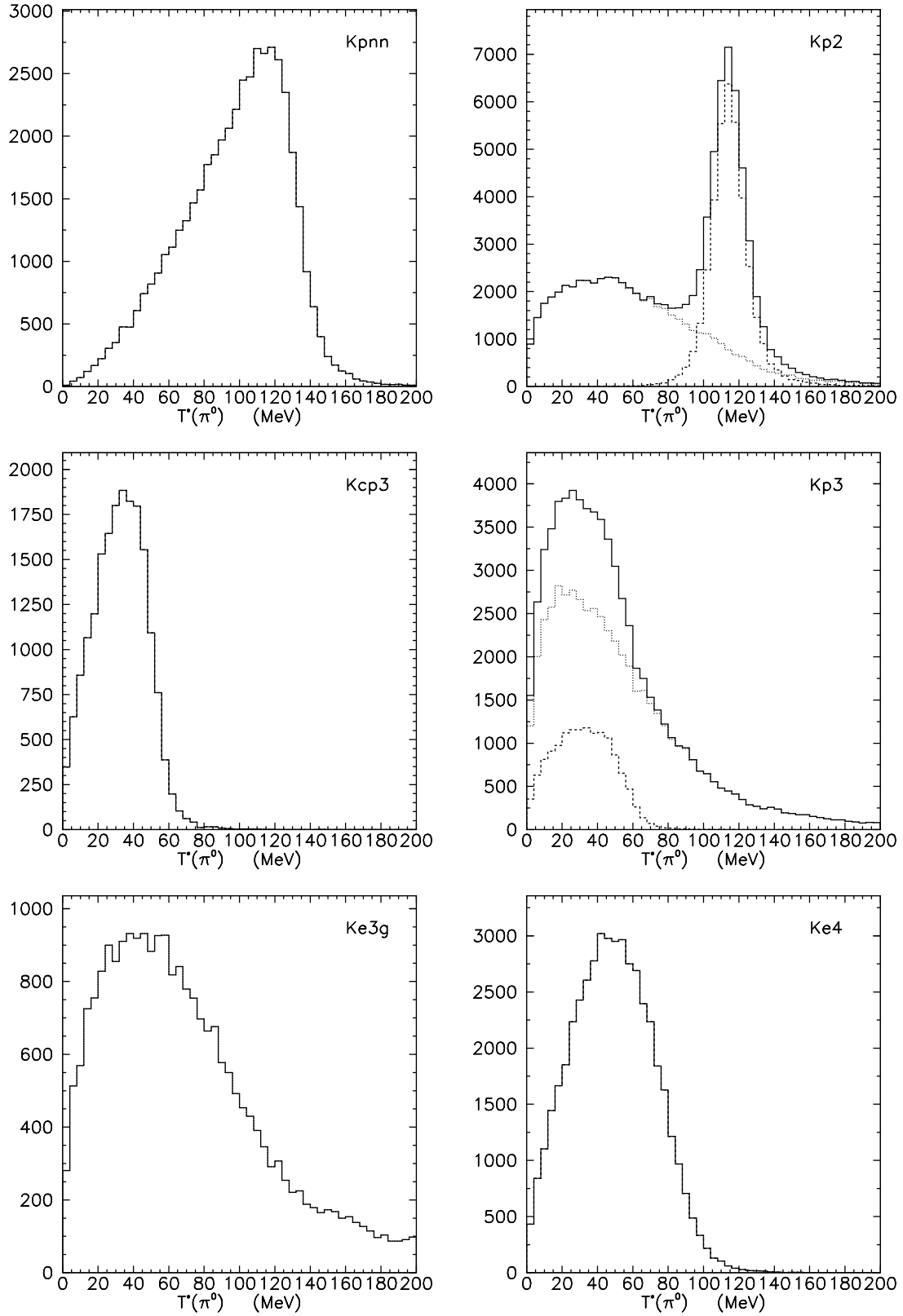


Fig. 13.5. The reconstructed kinetic energy distributions of the  $\pi^0$  in the  $K_L^0$  rest frame for signal and backgrounds. The dashed (dotted) lines in the histograms show the spectrum for “even” and “odd” combinations.

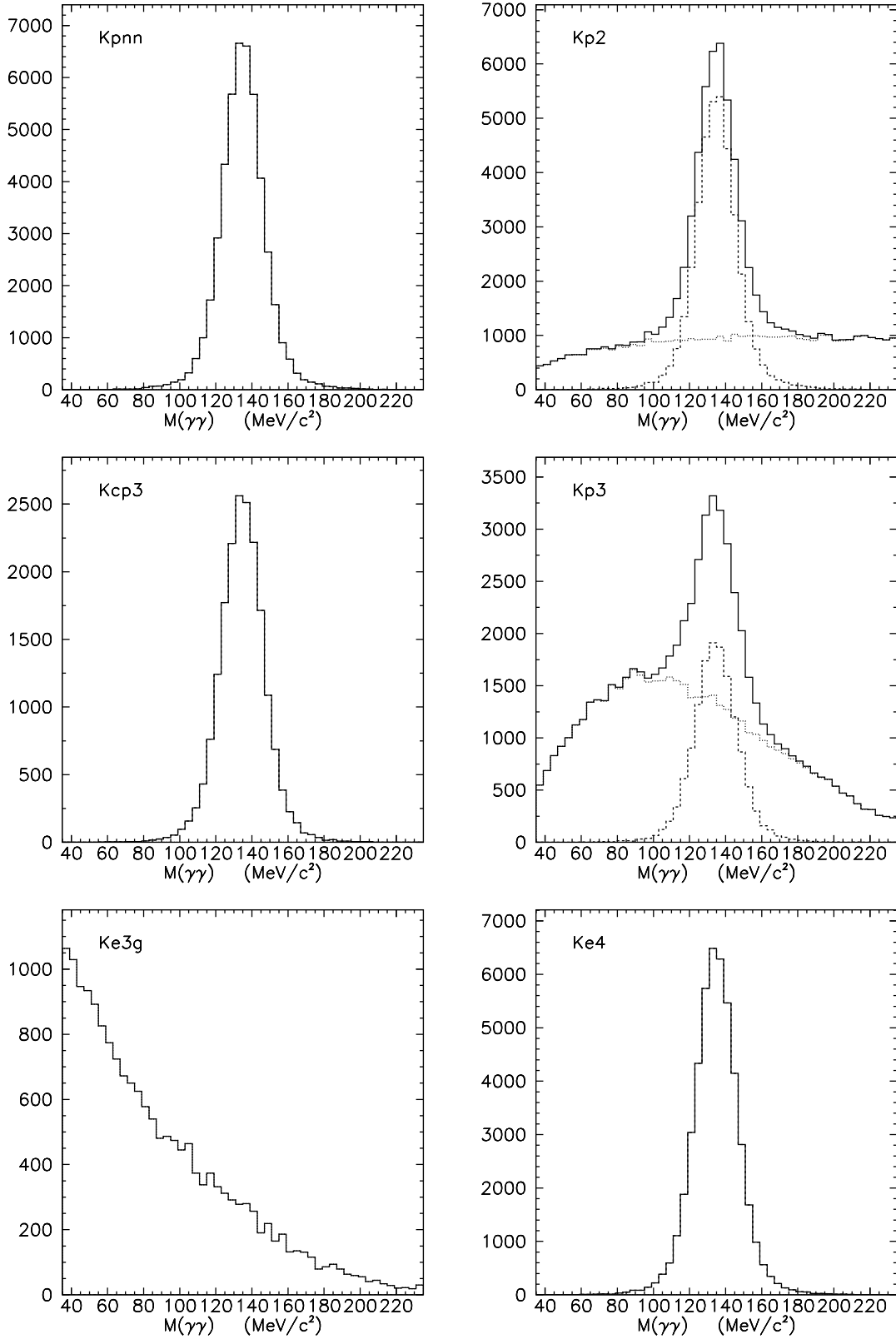


Fig. 13.6. The reconstructed two photon mass spectrum for signal and backgrounds. The dashed (dotted) lines in the histograms show the spectrum for “even” and “odd” combinations.



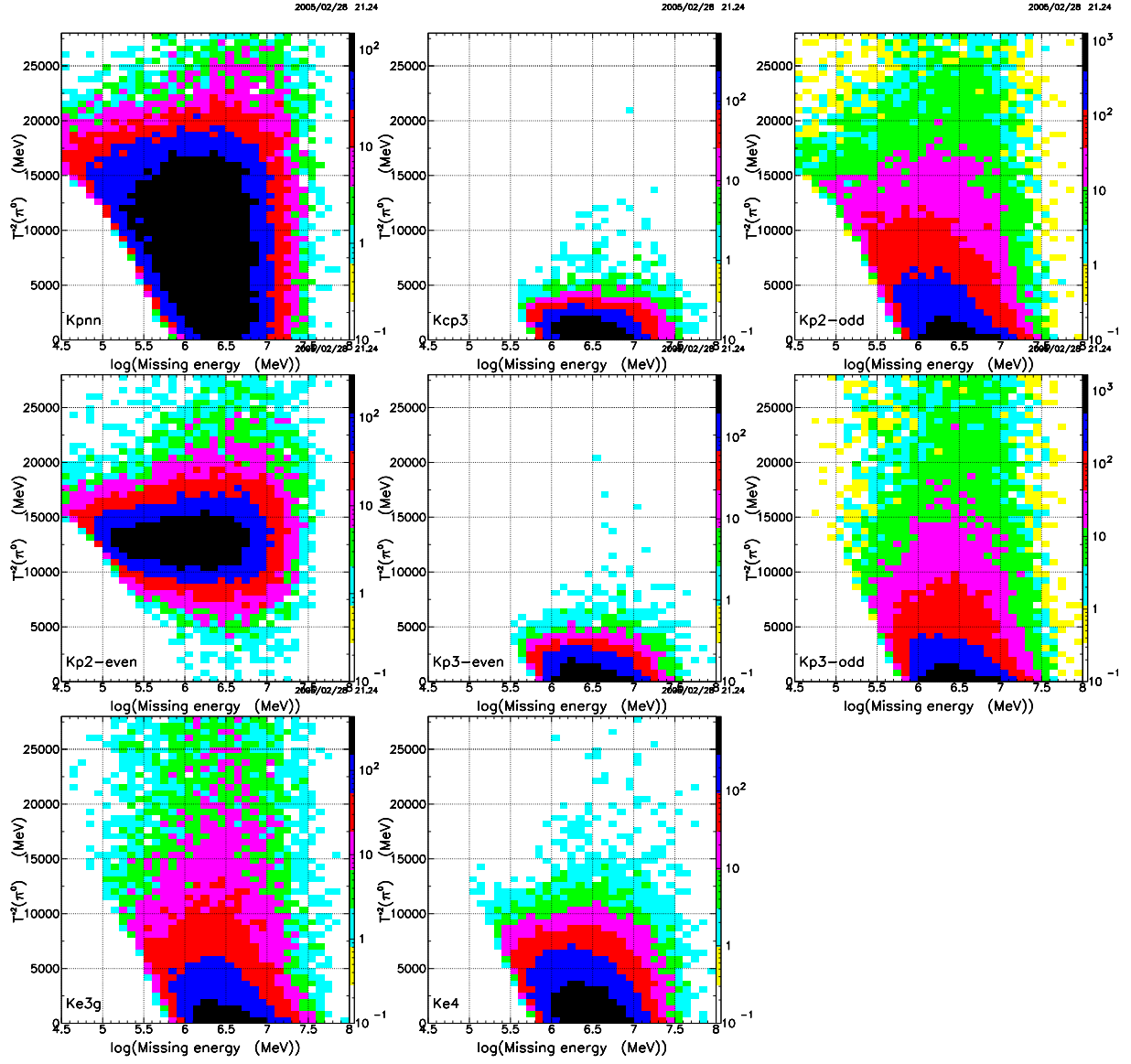


Fig. 13.7. The  $T_{\pi^0}^{*2}$  vs  $\ln(E_{\text{miss}}(\text{MeV}))$  distributions for signal and backgrounds.

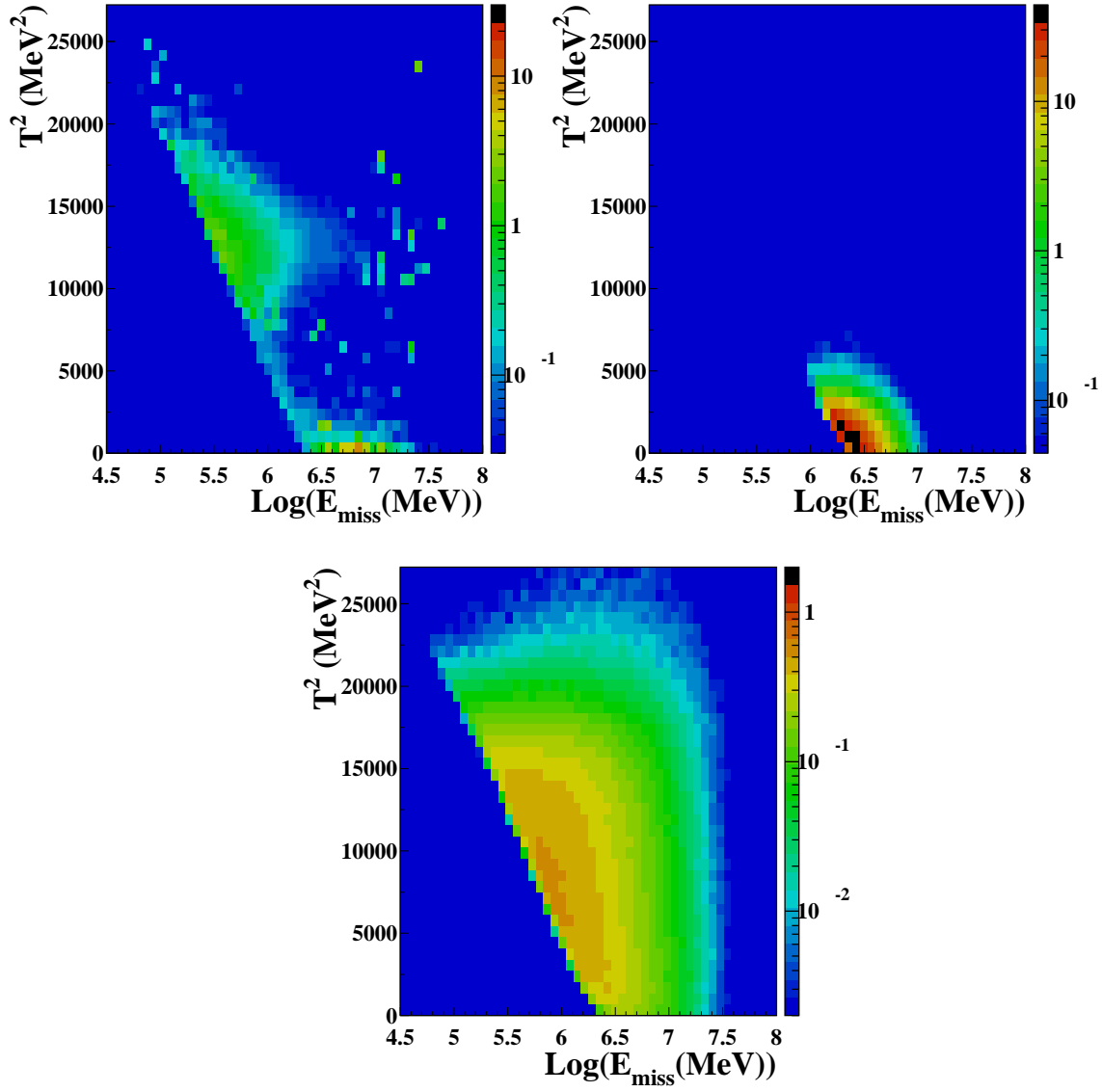


Fig. 13.8. The  $T_{\pi^0}^{*2}$  vs  $\ln(E_{\text{miss}} \text{ (MeV)})$  distribution for  $K_{\pi^2}$  background (top,left), Kcp3 background (top,right) and signal (bottom) weighted by the photon veto inefficiency.

comparing the shower center of gravity in the Calorimeter (position resolution  $\sigma \sim 3$  cm) to the expected position from the Preradiator. With an estimated inefficiency of  $10^{-3}$  for the center-of-gravity method, and including the probability of the conversion of the extra photon in the Preradiator, the inefficiency due to overlapping photons is  $10^{-5}$ . When the separation is less than 20 cm and the overlapping photons merge, the invariant mass of the photons becomes much larger than the  $\pi^0$  mass, and the missing energy and mass are small. The inefficiency of this invariant mass cut is limited by the photonuclear reaction probability (a few times  $10^{-3}$ ) of the overlapped photon. Again, taking into account the photon non-conversion probability, the photon detection inefficiency due to overlap in the region of separation  $< 20$  cm is also estimated to be  $10^{-5}$ . We have also found that the loss of acceptance due to cuts aimed at eliminating overlapping photons is only a few percent.

### 13.6.2 $K_L^0 \rightarrow \pi^0 \pi^+ \pi^-$ Background

The three-body decay  $K_L^0 \rightarrow \pi^0 \pi^+ \pi^-$  (Kcp3) is a potential source of background if the two charged pions escape detection and the kinetic energy of the  $\pi^0$  in the  $K_L^0$  rest frame is near the kinematic limit of 54 MeV. The reconstructed  $T_{\pi^0}^*$  spectrum for Kcp3 is contrasted with signal in Fig. 13.5 and shows that Kcp3 background can be kinematically suppressed by excluding low  $T_{\pi^0}^*$ .

Additional suppression can be achieved by detection of the two charged pions. As for photons, the veto inefficiency for charged pions decreases as the pion energy increases as shown in Fig. 13.3, thus a requirement of large  $E_{\text{miss}}$  reduces the overall charged particle veto inefficiency as demonstrated in Fig. 13.8.

The  $K_L^0$  decay modes with charged particles in the final state can be difficult to reject if the charged particles are slow and/or decay in flight. Such events can be kinematically suppressed with a requirement on  $M_\nu^2$  where  $M_\nu^2 \equiv (P(K_L^0) - P(\pi^0) - P(\pi))^2$  with the assumption that  $P(\pi) = M(\pi)$ . This variable is effective in suppressing backgrounds with slow charged particles and was originally conceived to suppress  $K_L^0 \rightarrow \pi^- e^+ \nu \gamma$  background (as described in Sec. 13.6.3) when one photon from  $e^+$  annihilation is paired with the radiative photon to produce the  $\pi^0$  candidate and the  $\pi^-$  is slow. Note that  $M_\nu^2 = M_K^2 + M_{\pi^0}^2 + M_\pi^2 - 2M_K E_{\pi^0}^* - 2M_\pi E_{\text{miss}}$  where  $E_{\pi^0}^* = T_{\pi^0}^* + M_{\pi^0}$ , so a cut on  $M_\nu^2$  is a straight line [curve] in the  $E_{\pi^0}^*, E_{\text{miss}}$  [ $T_{\pi^0}^*, \ln(E_{\text{miss}})$ ] plane. The effect of slow charged particles can be seen in Fig. 13.9 which shows the  $\Delta$  vs.  $M_\nu^2$  distributions for the Kcp3, Ke3g, and Ke4 backgrounds, where  $\Delta \equiv t_{\text{hit}} - t_{K_L^0} - |\vec{x}_{\text{hit}} - \vec{x}_{K_L^0}|/c$ . In this expression,  $t_{\text{hit}}$  and  $\vec{x}_{\text{hit}}$  are the time and position of the veto hit, and  $t_{K_L^0}$  and  $\vec{x}_{K_L^0}$  are the reconstructed time and position of the  $K_L^0$  decay. With no bias in  $t_{K_L^0}$  and  $\vec{x}_{K_L^0}$ , the  $\Delta$  distribution is expected to be symmetric about zero for photons and have a tail at positive  $\Delta$  due to slow charged tracks and decay-in-flight. As shown in Fig. 13.9, a requirement of  $M_\nu^2 < -30000$  (MeV/c<sup>2</sup>)<sup>2</sup> suppresses candidates with slow charged tracks and permits a reasonable veto timing window to be set.

### 13.6.3 $K_L^0 \rightarrow \pi^\pm e^\mp \nu \gamma$ Background

Radiative decays  $K_L^0 \rightarrow \pi^\pm e^\mp \nu \gamma$  (Ke3g) can be a source of background for the final state  $K_L^0 \rightarrow \pi^- e^+ \nu \gamma$  when the positron annihilates before detection and an annihilation photon is paired with the radiative photon to form a  $\pi^0$  candidate as sketched in Fig. 13.10. The positron and radiative photon ( $\gamma_2$ ) have a small opening angle and, to a good approximation in the  $e^+ e^- \rightarrow \gamma_0 \gamma_1$  annihilation process,  $p(\gamma_1) \approx p(e^+)$  and  $p(\gamma_0) \approx p(e^-)$ , so that the  $\gamma_1, \gamma_2$  mass spectrum is peaked at low mass for this background (Fig. 13.6). In addition, the reconstructed  $T_{\pi^0}^*$  is also peaked at low values (Fig. 13.7).

### 13.6.4 $K_L^0 \rightarrow \pi^0 \pi^\pm e^\mp \nu$ Background

The decay  $K_L^0 \rightarrow \pi^0 \pi^\pm e^\mp \nu$  (Ke4) is a potential background when both the charged pion and  $e^\pm$  have low energies. It can be suppressed kinematically by rejecting events with low  $T_{\pi^0}^*$  and can be suppressed by the Charged Particle Veto.

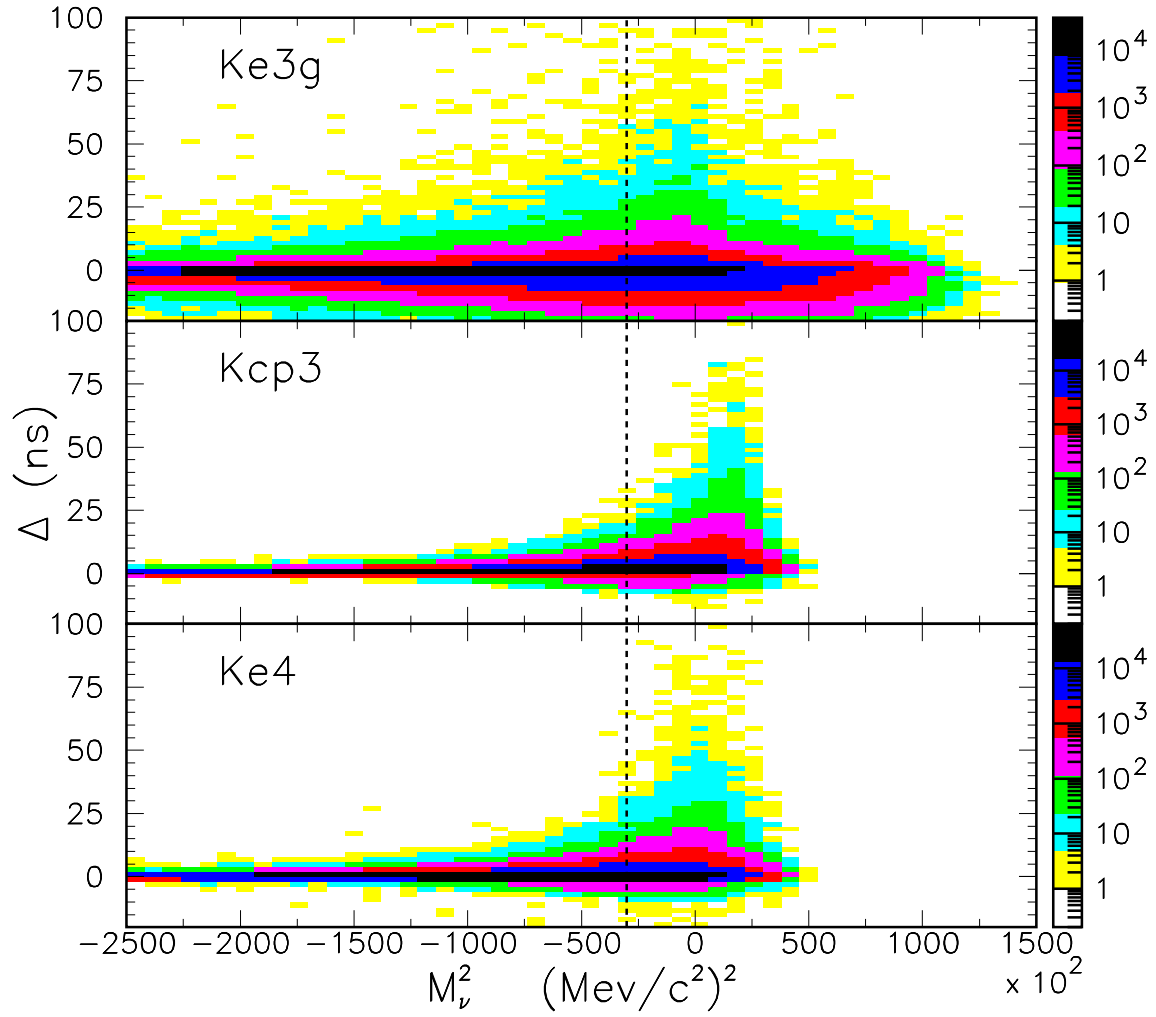


Fig. 13.9. The  $\Delta$  vs.  $M_\nu^2$  distributions of Ke3g, Kcp3, and Ke4 before setup cuts. The vertical dashed line shows the setup cut that suppresses background with slow tracks and/or decay-in-flight.

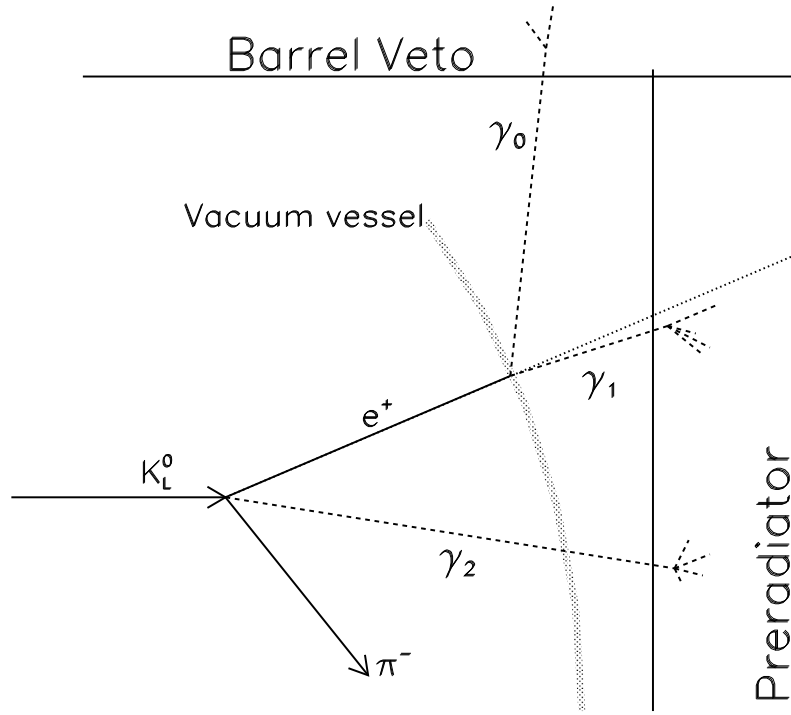


Fig. 13.10. Cartoon showing the mechanism for  $K_L^0 \rightarrow \pi^- e^+ \nu \gamma$  background. The positron annihilates before detection in the CPV that lines the vacuum vessel and produces  $\gamma_0$  and  $\gamma_1$ . The neutral pion candidate is formed from the radiative photon  $\gamma_2$  and one of the annihilations photons  $\gamma_1$  whilst  $\gamma_0$  is undetected. The negative pion from  $K_L^0$  decay must also escape detection for this decay to form a background.

### 13.6.5 $K_L^0 \rightarrow \gamma\gamma$ , $K_L^0 \rightarrow \pi^0\pi^0\pi^0$ , and $K_L^0 \rightarrow \pi^0\gamma\gamma$ Backgrounds

The  $K_L^0 \rightarrow \gamma\gamma$  decay is very tightly constrained by kinematics. Cuts on the invariant mass and the total energy of the two photons in the  $K_L^0$  rest frame brings this process under control. A negligible contribution from this background source is expected.

Despite the large branching fraction of 21%,  $K_L^0 \rightarrow \pi^0\pi^0\pi^0$  is not a significant background due to the veto possibilities for the high multiplicity of additional photons in the decay. Some kinematic suppression is also available for both the Kp3-even and Kp3-odd components as shown in Fig. 13.7 where “even” and “odd” denote candidates formed from photons from the same and different neutral pions, respectively. A negligible contribution from this background source is expected.

Although the kinematics of the  $\pi^0$  in  $K_L^0 \rightarrow \pi^0\gamma\gamma$  decays are similar to that in  $K_L^0 \rightarrow \pi^0\nu\bar{\nu}$  decays, the rate of  $K_L^0 \rightarrow \pi^0\gamma\gamma$  is only  $5 \times 10^4$  times that of the signal and the photon veto provides abundant suppression. A negligible contribution from this background source is expected.

## 13.7 Candidate Event Selection

To select  $K_L^0 \rightarrow \pi^0\nu\bar{\nu}$  candidates, we adopt a procedure to take advantage of the correlations between the kinematic variables  $T_{\pi^0}^*$ ,  $M_{\gamma\gamma}$ , and  $E_{\text{miss}}$  along with the veto rejection as described in the previous Sec. 13.6. We apply “setup” cuts (Table 13.3), ideally with high signal acceptance, that are designed to suppress non- $K_L^0$  background and  $K_L^0$  background due to veto timing considerations.

Table 13.3. Description of the “setup” cuts. DOCA is the distance of closest approach of the two candidate  $\gamma$ ,  $z(K_L^0)$  is the reconstructed  $z$  of a  $K_L^0$  candidate,  $z_1$  is 75cm (100cm) from the upstream end of the decay volume for the 2 $\gamma$ PR (1 $\gamma$ PR) detection method, and  $z_2$  is 50cm (100cm) from the downstream end of the decay volume for the 2 $\gamma$ PR (1 $\gamma$ PR) detection method.  $DK12 \equiv \sqrt{(\text{DOCA1} + \text{DOCA2} - 5.)^2 + (z_1(K_L^0) - z_2(K_L^0))^2}$  where  $\text{DOCA}i$  is the distance of closest approach of the  $i^{\text{th}}$  measured photon to  $\vec{X}_2(K_L^0)$ , the fitted  $K_L^0$  vertex from the fit 2, and  $z_i(K_L^0)$  is the reconstructed  $z_{K_L^0}$  from the  $i^{\text{th}}$  fit. Fit 1(2) fits the two photons to a common vertex without (with) a  $\pi^0$  mass constraint. The performance of these cuts on signal and backgrounds is shown in Table 13.4.

Cut	Explanation
$\chi^2 < 100$	Reasonable kinematic fit
$\text{DOCA} < 60 \text{ cm}$	Suppress non- $K_L^0$ backgrounds
$z_1 < z(K_L^0) < z_2$	Suppress neutron-induced background
$P(K_L^0) > 400 \text{ MeV}/c$	Suppress $K_L^0$ background from next microbunch
$M_\nu^2 < -30000 \text{ (MeV}/c^2)^2$	Suppress background involving slow charged tracks
$DK12 < 30 \text{ cm}$	Suppress background involving mis-reconstructed $z(K_L^0)$
$-30 < M_{\gamma\gamma} - M_{\pi^0} < 40 \text{ MeV}$	Suppress background when photons are not from a single $\pi^0$
$E_{\pi^0}^* < 300 \text{ MeV}$	Suppress non- $K_L^0$ backgrounds

The motivation for the setup cuts is briefly explained in Table 13.3. The motivation for the use of  $M_\nu^2$  was described in Section 13.6.2. The motivation for the  $z(K)$  cuts is described in Section 13.8.6.

The motivation for the DK12 cut is suppression of candidates with mis-reconstructed  $z(K)$  when the photon candidate pairs do not originate from a neutral pion. Examples are Kp2 and Ke3g. The effect of a mis-reconstructed  $z(K)$  on the relative timing  $\Delta$  of a potential veto hit (Sec. 13.6.2) is shown in Fig. 13.11. The mis-reconstruction is caused by large scattering in the  $Y$  direction on one photon coupled with energy mis-measurement of one or both photons. In particular, it occurs when one photon has a relatively small angle with respect to the horizontal plane. When the photons are not from a  $\pi^0$  and the energy is mis-measured, imposing the  $\pi^0$  mass constraint can shift the reconstructed  $z(K)$ . Note that the KOPIO time-of-flight technique to reconstruct the  $K_L^0$  momentum preferentially accepts  $z(K, \text{recon}) > z(K, \text{true})$ , because the inequality implies  $P(K, \text{recon}) > P(K, \text{true})$  and thus increases the apparent missing energy of the candidate. There is also a correlated effect that makes  $\Delta$  more negative for Kp2. The relation  $z(K, \text{recon}) > z(K, \text{true})$  sometimes implies  $d(\text{recon}) > d(\text{true})$  for  $K_{\pi^2\text{-odd}}$  with backward-going photons, where  $d$  is the distance from the kaon decay vertex to the veto hit position. To suppress candidates with mis-reconstructed  $z(K)$ , the variable DK12 (Table 13.3) combines quantities that are correlated with  $z(K, \text{recon}) - z(K, \text{true})$ . These quantities are the difference in  $z$  of the reconstructed kaon decay vertex from the two fits  $z_2(K) - z_1(K)$  and the distance of closest approach of each of the measured photon candidates to the reconstructed  $z_2(K)$ .

We use these three variables,

1.  $M(\gamma\gamma) - M(\pi^0)$ ,
2.  $T^{*2}$ , and
3.  $\ln(E_{\text{miss}})$  ( $E_{\text{miss}}$  in MeV),

and utilize a three-dimensional binned ‘likelihood’ method to maximize the signal-to-background ratio (S/B) for a given signal rate. The procedure is:

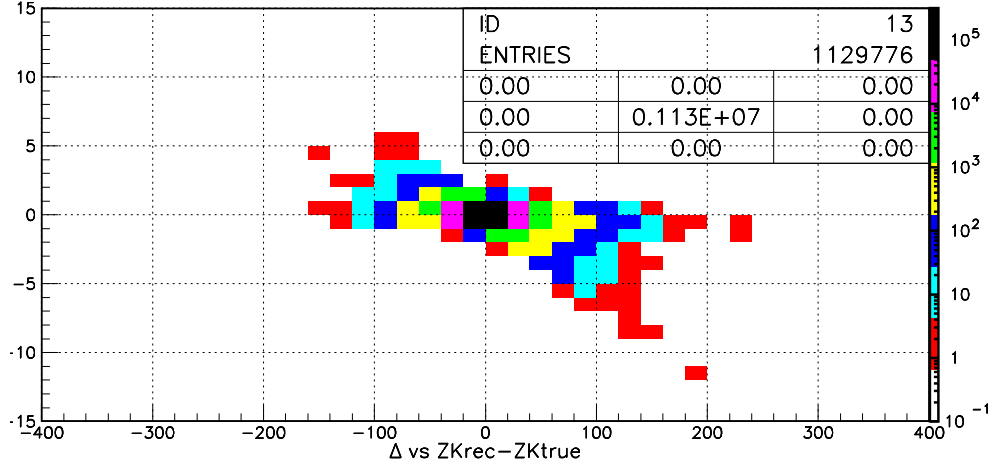


Fig. 13.11. The  $\Delta$  (ns) vs  $z(K, \text{recon}) - z(K, \text{true})$  (cm) after setup cuts on  $\chi^2$ , DOCA and  $z(K)$  (Table 13.3). An additional cut  $|M_{\gamma\gamma} - M(\pi^0)| < 20$  MeV has also been applied.

1. For each bin defined by the above three variables:
  - (a) Add up all backgrounds.
  - (b) Add up the signal.
  - (c) Calculate S/B.
2. Sort bins by decreasing S/B and integrate S & B according to the sort order.
3. Define specific realizations of the general cut by noting when the integrated S crosses various arbitrary thresholds.

Inclusion of additional variables in the method did not give a significant improvement in the signal purity. The results of the optimization for the  $2\gamma\text{PR}$  mode for the three quantities listed above is shown in Figs. 13.12 and 13.13 for tight and loose cuts, respectively.

Table 13.4 shows the expected  $2\gamma\text{PR}$  rates for “in-bunch” background after veto suppression, the setup cuts, and six specific realizations of cuts of increasing severity based on the likelihood method described above. The results are shown graphically in Fig. 13.14. As shown in the table and the figure, the highest signal-to-background rates are achieved for the tightest cut.

Tables 13.5 and 13.6 show the expected  $1\gamma\text{PR}/\text{BV}$  and  $1\gamma\text{PR}/\text{CAL}$  rates “in-bunch” background, respectively, after veto suppression, setup cuts and cuts of increasing severity based on the likelihood method described above.

Figure 13.15 shows the fractional rate of wrap-around background as a function of the signal yield. The fractional rate of the wrap-around background decreases from 10% for the tightest cut to 1.5% for the loosest cut. The largest component of the wrap-around background is  $K_{\pi^2}$ .

The distribution and composition of interbunch background are shown in Fig. 13.16. The expected yield of the interbunch background, taking into account the extinction measurements of Sec. 5, is negligible as shown in Fig. 13.17. Figure 13.18 shows the total background with the in-bunch, wrap-around, and interbunch components as a function of the signal yield.

Similar distributions are seen for the  $1\gamma\text{PR}$  detection methods. The signal-to-background ratio as a function of the total signal is shown in Fig. 13.19 for the three detection methods,  $2\gamma\text{PR}$ ,  $\text{PR}/\text{CAL}$ , and  $\text{PR}/\text{BV}$ .



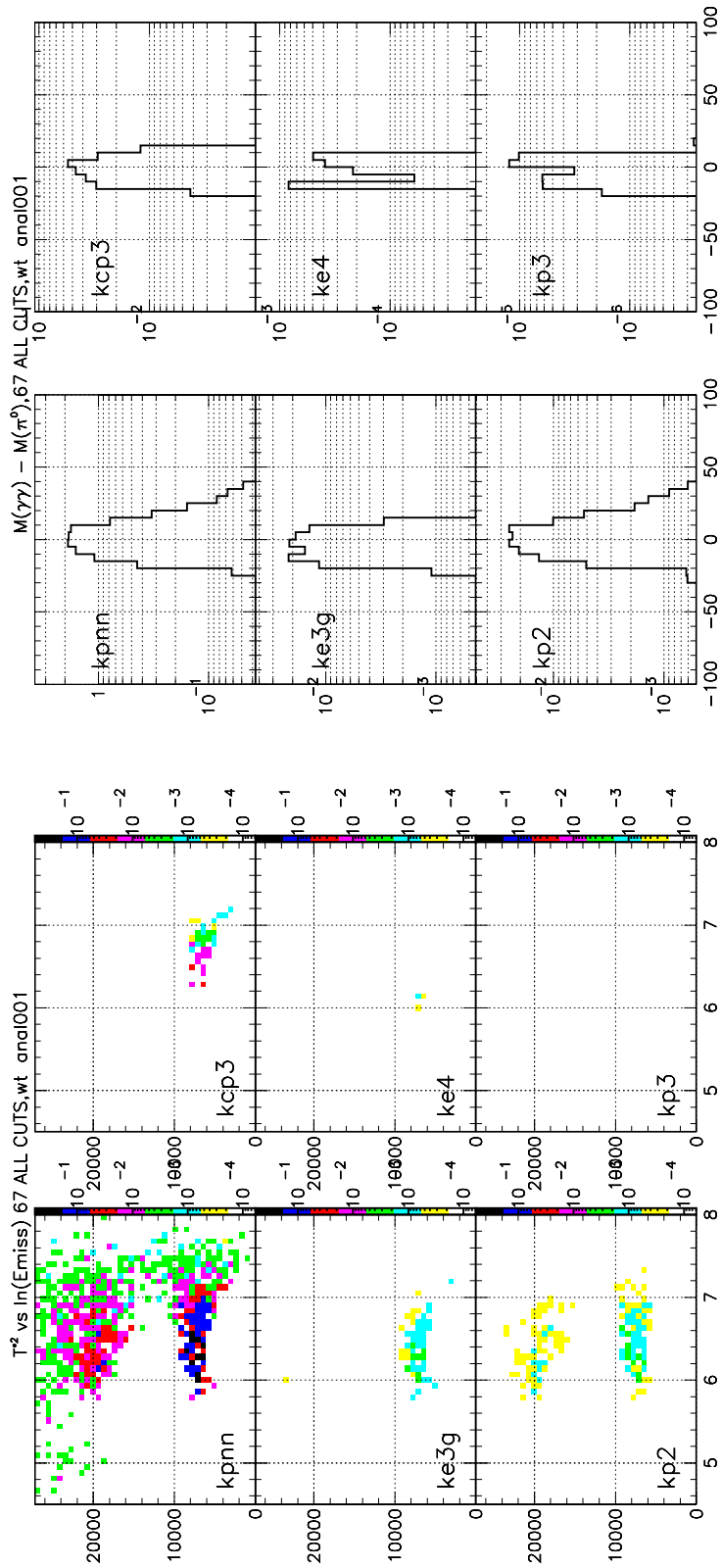


Fig. 13.12. Left columns:  $T^{*2}$  vs  $\ln(E_{\text{miss}})$  and Right columns:  $M(\gamma, \gamma) - M(\pi^0)$  for the  $2\gamma$ PR detection method for signal and backgrounds after tight cuts. These distributions are weighted such that total number of entries in each distribution is the total number of expected events.

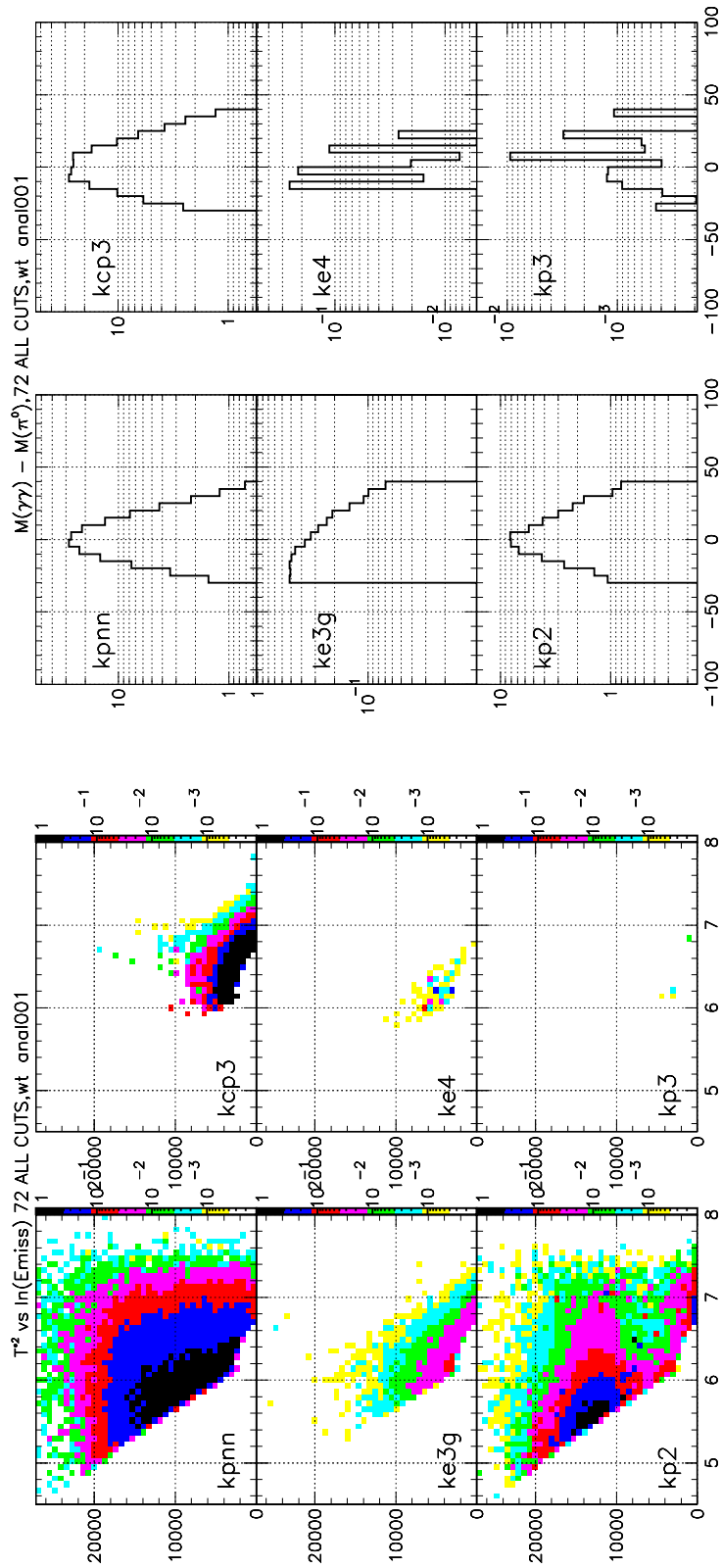


Fig. 13.13. Left columns:  $T^{*2}$  vs  $\ln(E_{\text{miss}})$  and Right columns:  $M(\gamma, \gamma) - M(\pi^0)$  for the  $2\gamma$ PR detection method for signal and backgrounds after loose cuts. These distributions are weighted such that total number of entries in each distribution is the total number of expected events.

Table 13.4. The total number of decays in the decay volume and candidates for the  $2\gamma$ PR detection method for each decay mode surviving the listed cut. Only in-bunch candidates are considered; that is, “wrap-around” backgrounds are not included. The cuts are applied sequentially from top to bottom. There can be more than one candidate per generated decay due to combinations of the available photons.  $\mathcal{A}(\text{Geom})$  is the geometric acceptance,  $\mathcal{P}(\text{decay})$  is the  $K_L^0$  decay probability,  $\mathcal{P}(\text{conv.})$  is the two photon conversion probability in the PR, and  $\bar{\epsilon}$  is the veto inefficiency. The results between the double horizontal lines show the suppression due to the setup cuts. The “likelihood” cuts at the bottom of the table are cuts of increasing severity resulting from the optimization procedure.

<b><math>2\gamma</math>PR detection method</b>						
Kpnn	Kp2	Kcp3	Kp3	Ke3g	Ke4	Cut
19546.	$6.0723 \cdot 10^{11}$	$8.2029 \cdot 10^{13}$	$1.3715 \cdot 10^{14}$	$2.2999 \cdot 10^{12}$	$3.3750 \cdot 10^{10}$	Total decays
18510.	$2.8810 \cdot 10^{12}$	$7.7812 \cdot 10^{13}$	$1.9520 \cdot 10^{15}$	$1.5672 \cdot 10^{12}$	$3.2008 \cdot 10^{10}$	Total candidates
364.14	33850.19	3201.57	15.04	167.04	10.89	$\mathcal{A}(\text{Geom}) \cdot \mathcal{P}(\text{decay}) \cdot \mathcal{P}(\text{conv.}) \cdot \bar{\epsilon}$
362.53	33412.98	3191.73	14.54	150.04	10.89	$\chi^2 < 100$ , DOCA $< 60$ cm
251.90	19555.02	2059.74	8.54	99.23	8.26	$z(K)$ in fiducial
247.31	17935.38	2022.82	8.02	73.94	8.01	$P(K) > 400 \text{ MeV}/c$
236.61	7276.02	1956.22	1.93	7.77	7.45	$-30 < M_{\gamma\gamma} - M_{\pi^0} < 40 \text{ MeV}$
235.97	7247.02	1956.22	1.93	7.77	7.45	$E_{\pi^0}^* < 300 \text{ MeV}$
153.34	280.31	655.00	0.41	2.64	0.92	DK12 $< 30$ , $M_\nu^2 < -30000 (\text{MeV}/c^2)^2$
147.62	178.19	173.82	0.26	1.65	0.63	Likelihood loosest
98.07	46.85	8.13	0.05	0.65	0.35	Likelihood looser
73.44	22.80	3.88	0.04	0.44	0.32	Likelihood loose
48.91	9.62	2.03	0.02	0.28	0.12	Likelihood tight
24.33	2.64	0.56	0.00	0.12	0.01	Likelihood tighter
9.65	0.55	0.20	0.00	0.04	0.00	Likelihood tightest

Table 13.5. The total number of decays in the decay volume and candidates for the  $1\gamma\text{PR/BV}$  detection method for each decay mode surviving the listed cut. Only in-bunch candidates are considered; that is, “wrap-around” backgrounds are not included. The cuts are applied sequentially from top to bottom. There can be more than one candidate per generated decay due to combinations of the available photons.  $\mathcal{A}(\text{Geom})$  is the geometric acceptance,  $\mathcal{P}(\text{decay})$  is the  $K_L^0$  decay probability,  $\mathcal{P}(\text{conv.})$  is the photon conversion probability in the PR, and  $\bar{\epsilon}$  is the veto inefficiency. The results between the double horizontal lines show the suppression due to the setup cuts. The “likelihood” cuts at the bottom of the table are cuts of increasing severity resulting from the optimization procedure.

<b><math>1\gamma\text{PR/BV}</math> detection method</b>						
Kpnn	Kp2	Kp3	Ke3g	Ke4	Cut	
19546.	$6.0723 \cdot 10^{11}$	$1.3715 \cdot 10^{14}$	$2.2999 \cdot 10^{12}$	$3.3750 \cdot 10^{10}$	Total decays	
18351.	$2.8768 \cdot 10^{12}$	$1.9407 \cdot 10^{15}$	$1.5635 \cdot 10^{12}$	$3.1843 \cdot 10^{10}$	Total candidates	
566.84	246109.94	7385.03	246.35	39.13	$\mathcal{A}(\text{Geom}) \cdot \mathcal{P}(\text{decay}) \cdot \mathcal{P}(\text{conv.}) \cdot \bar{\epsilon}$	
548.76	239826.59	7051.99	204.65	37.75	$\chi^2 < 100$	
316.99	48197.59	4584.58	149.51	13.75	z(K) in fiducial	
300.77	28095.60	4263.84	86.08	10.74	$P(K) > 400 \text{ MeV}/c$	
247.36	11967.65	3781.52	21.96	8.83	$-30 < M_{\gamma\gamma} - M_{\pi^0} < 40 \text{ MeV}$	
244.28	11780.47	3779.88	21.74	8.83	$E_{\pi^0}^* < 300 \text{ MeV}$	
203.28	3086.50	1129.04	10.00	1.99	$M_{\nu}^2 < -30000 (\text{MeV}/c^2)^2$	
147.08	249.94	80.27	3.81	0.32	Likelihood looser	
97.24	87.10	25.03	2.07	0.05	Likelihood loose	
73.25	50.27	14.20	1.40	0.02	Likelihood tight	
48.91	25.10	7.47	0.83	0.01	Likelihood tighter	
24.66	8.99	2.48	0.36	0.00	Likelihood tightest	

Table 13.6. The total number of decays in the decay volume and candidates for the  $1\gamma\text{PR}/\text{CAL}$  detection method for each decay mode surviving the listed cut. Only in-bunch candidates are considered; that is, “wrap-around” backgrounds are not included. The cuts are applied sequentially from top to bottom. There can be more than one candidate per generated decay due to combinations of the available photons.  $\mathcal{A}(\text{Geom})$  is the geometric acceptance,  $\mathcal{P}(\text{decay})$  is the  $K_L^0$  decay probability,  $\mathcal{P}(\text{conv.})$  is the photon conversion probability in the PR, and  $\bar{\epsilon}$  is the veto inefficiency. The results between the double horizontal lines show the suppression due to the setup cuts. The “likelihood” cuts at the bottom of the table are cuts of increasing severity resulting from the optimization procedure.

<b><math>1\gamma\text{PR}/\text{CAL}</math> detection method</b>						
Kpnn	Kp2	Kp3	Kp3	Ke3g	Ke4	Cut
19546.	$6.0723 \cdot 10^{11}$	$8.2029 \cdot 10^{13}$	$1.3715 \cdot 10^{14}$	$2.2999 \cdot 10^{12}$	$3.3750 \cdot 10^{10}$	Total decays
18351.	$2.8768 \cdot 10^{12}$	$7.7488 \cdot 10^{13}$	$1.9407 \cdot 10^{15}$	$1.5635 \cdot 10^{12}$	$3.1843 \cdot 10^{10}$	Total candidates
95.24	9247.55	719.31	4.31	41.06	2.35	$\mathcal{A}(\text{Geom}) \cdot \mathcal{P}(\text{decay}) \cdot \mathcal{P}(\text{conv.}) \cdot \bar{\epsilon}$
94.16	8321.21	710.78	4.04	36.43	2.35	$\chi^2 < 100$
38.31	3869.14	223.61	1.06	14.36	1.02	$z(K)$ in fiducial
37.95	3656.45	222.63	1.02	11.42	1.02	$P(K) > 400 \text{ MeV}/c$
34.13	1683.57	207.04	0.36	1.20	0.99	$-30 < M_{\gamma\gamma} - M_{\pi^0} < 40 \text{ MeV}$
33.89	1675.61	207.04	0.36	1.20	0.99	$E_{\pi^0}^* < 300 \text{ MeV}$
21.78	57.88	85.51	0.09	0.35	0.20	$M_\nu^2 < -30000 (\text{MeV}/c^2)^2$
19.74	30.56	8.40	0.04	0.17	0.14	Likelihood tighter
9.88	3.28	0.90	0.01	0.06	0.02	Likelihood tightest

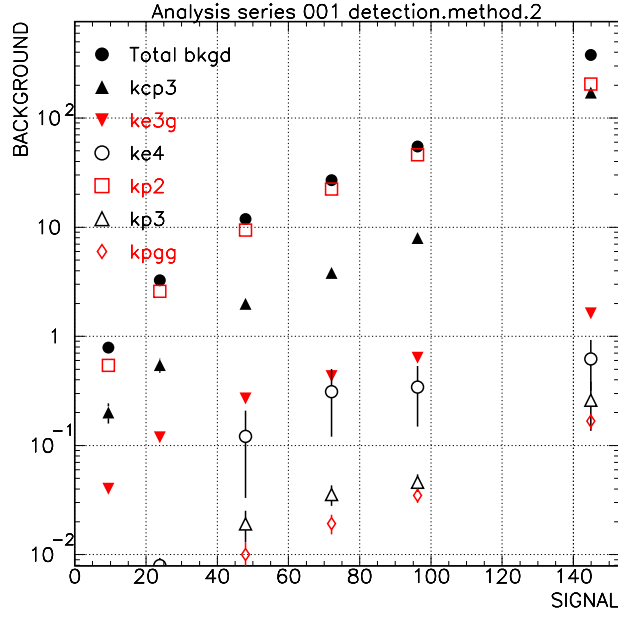


Fig. 13.14. For the  $2\gamma$ PR detection method, the total in-bunch background and the components of the in-bunch background by  $K_L^0$  decay mode vs. the expected number of signal events as the likelihood cut severity is decreased.

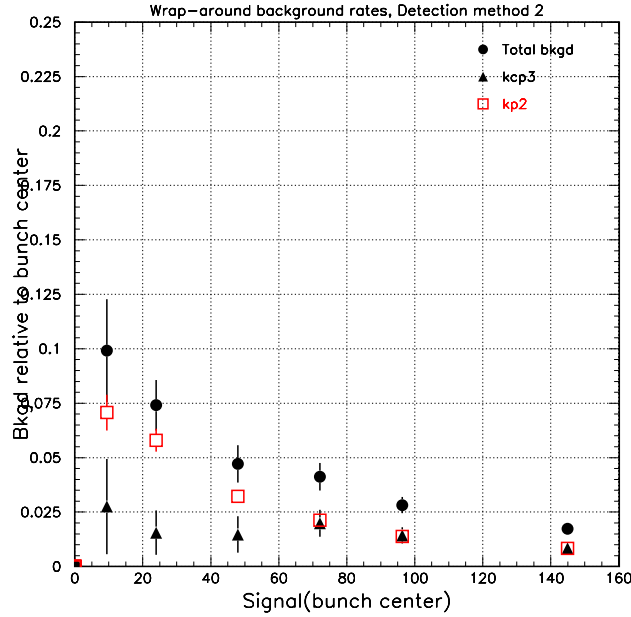


Fig. 13.15. For the  $2\gamma$ PR detection method, the relative rate of the total wrap-around background to the total in-bunch background and the relative rate of the components of the wrap-around background by the  $K_L^0$  decay mode vs. the expected number of signal events as the likelihood cut severity is decreased.

Cut set 7 Contour.DM3.1,  $S(0)=144.9\pm0.7$ ,  $S/B=0.384\pm0.006$ , Detection method 2

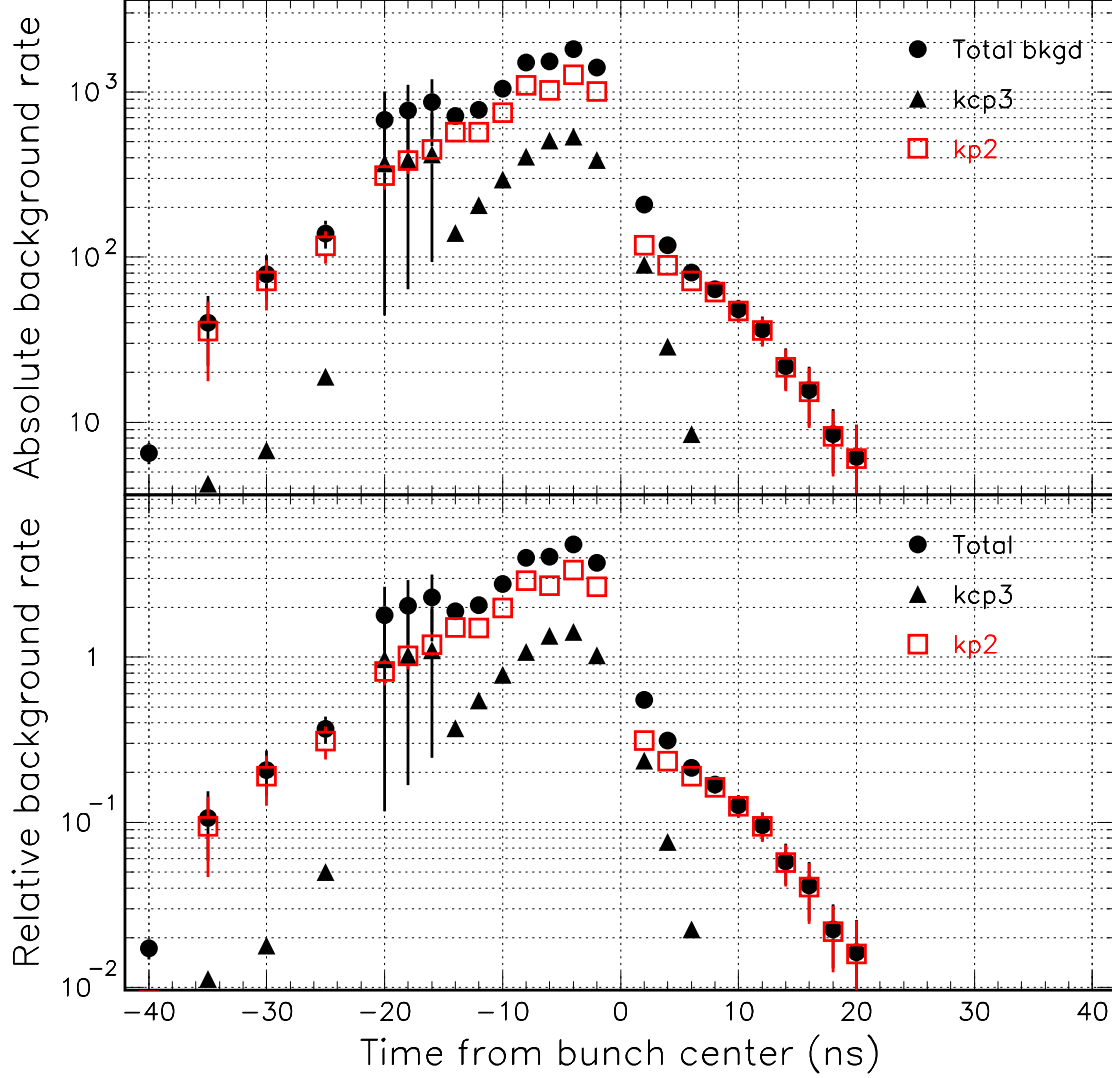


Fig. 13.16. For the  $2\gamma$ PR detection method, absolute rate (upper) and rate relative to in-bunch (lower) background of the interbunch background *before applying the interbunch extinction rate* and the rates of the significant components of the interbunch background as a function of the time from the central time of the “in-bunch” bunch for the loosest of the likelihood cuts for the  $2\gamma$  PR detection method. The  $K_{\pi 2}$  background dominates the interbunch rate. For negative times, the reconstructed kaon momentum is less than the actual kaon momentum so that the reconstructed  $T_{\pi 0}^*$  is less than the true  $T_{\pi 0}^*$  and moves the  $K_{\pi 2}$ -even peak into the low background region.



Cut set 7 Contour.DM3.1,  $S(0)=144.9\pm0.7$ ,  $S/B=0.384\pm0.006$ , Detection method 2

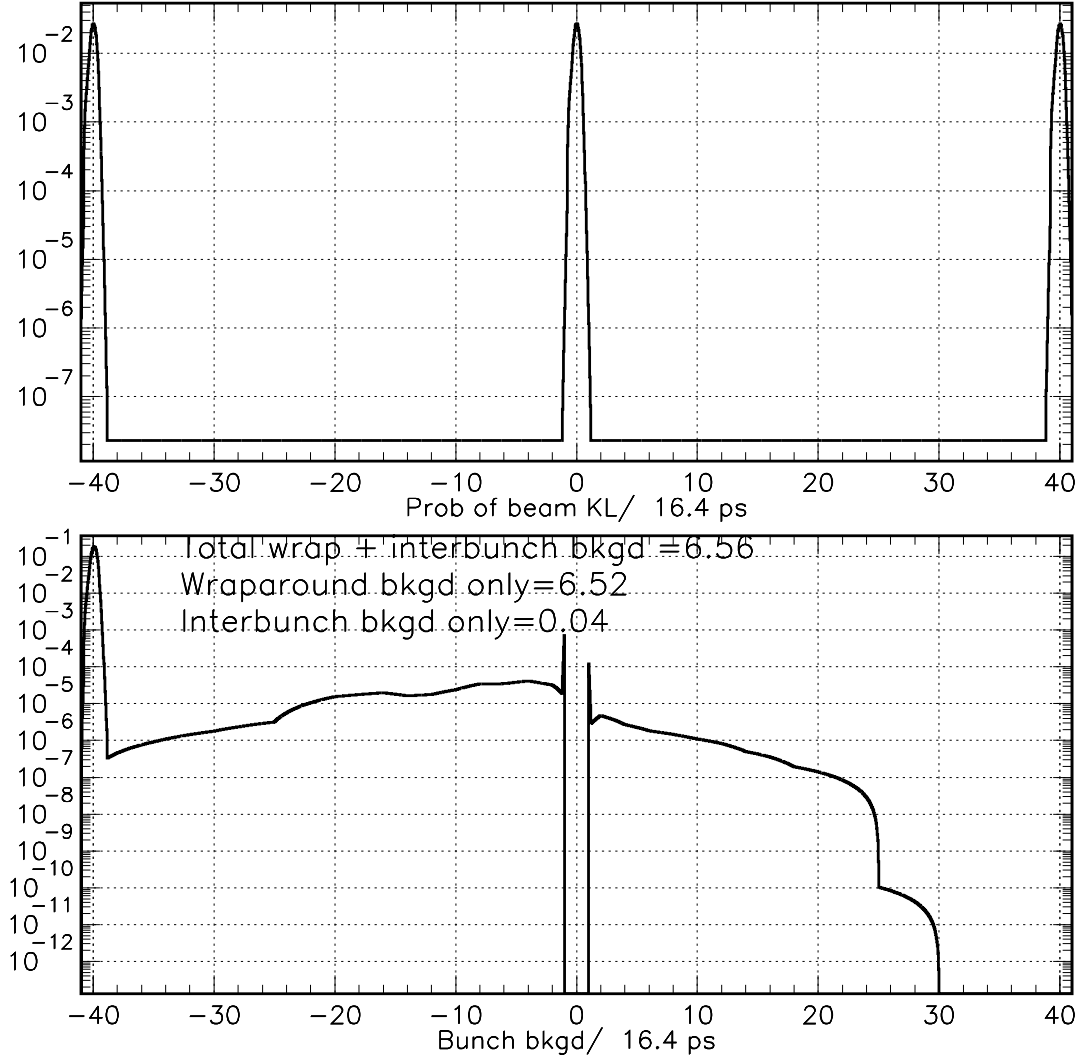


Fig. 13.17. The upper distribution shows the probability of of beam  $K_L^0$  per 16.4 ps determined from the interbunch rate measurements of Section 5 where we assume that the interbunch background is constant between the bunches. The lower distribution shows the calculated total background rate as function of the time from the central time of the “in-bunch” bunch for the loosest of the likelihood cuts for the  $2\gamma$  PR detection method using the rates shown in Fig. 13.16. The  $\pm 1$ -ns region is classified as the “in-bunch” background and is removed from this calculation. The total background rate from the wrap-around mechanism is 6.5 events for these cuts. The interbunch background makes a negligible contribution to the total background rate.

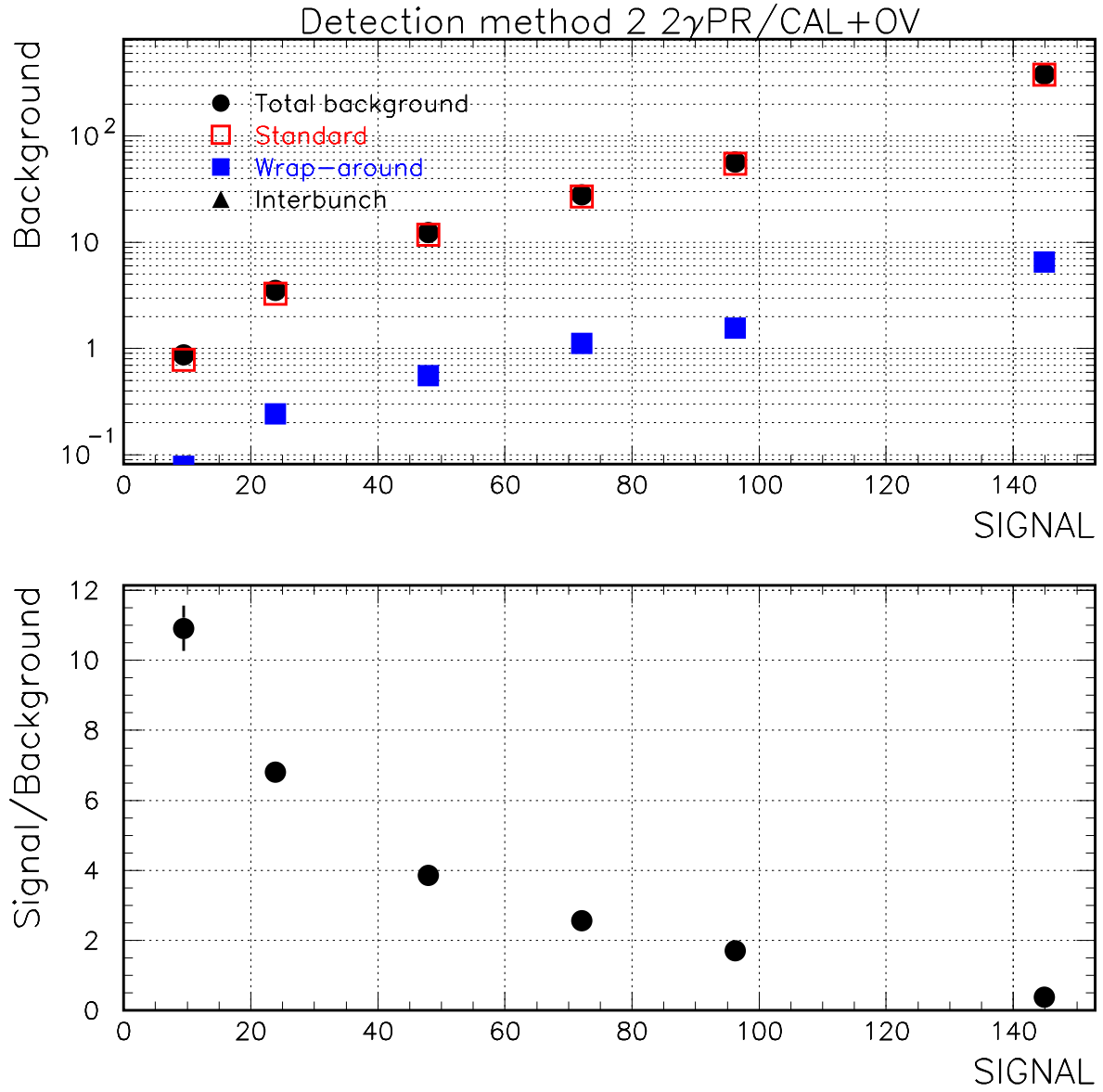


Fig. 13.18. Top: The total background and the components as a function of the signal yield for the  $2\gamma$ PR detection method. The “standard” background is the in-bunch background. The lower figure shows the signal over the total background as a function of the signal yield.

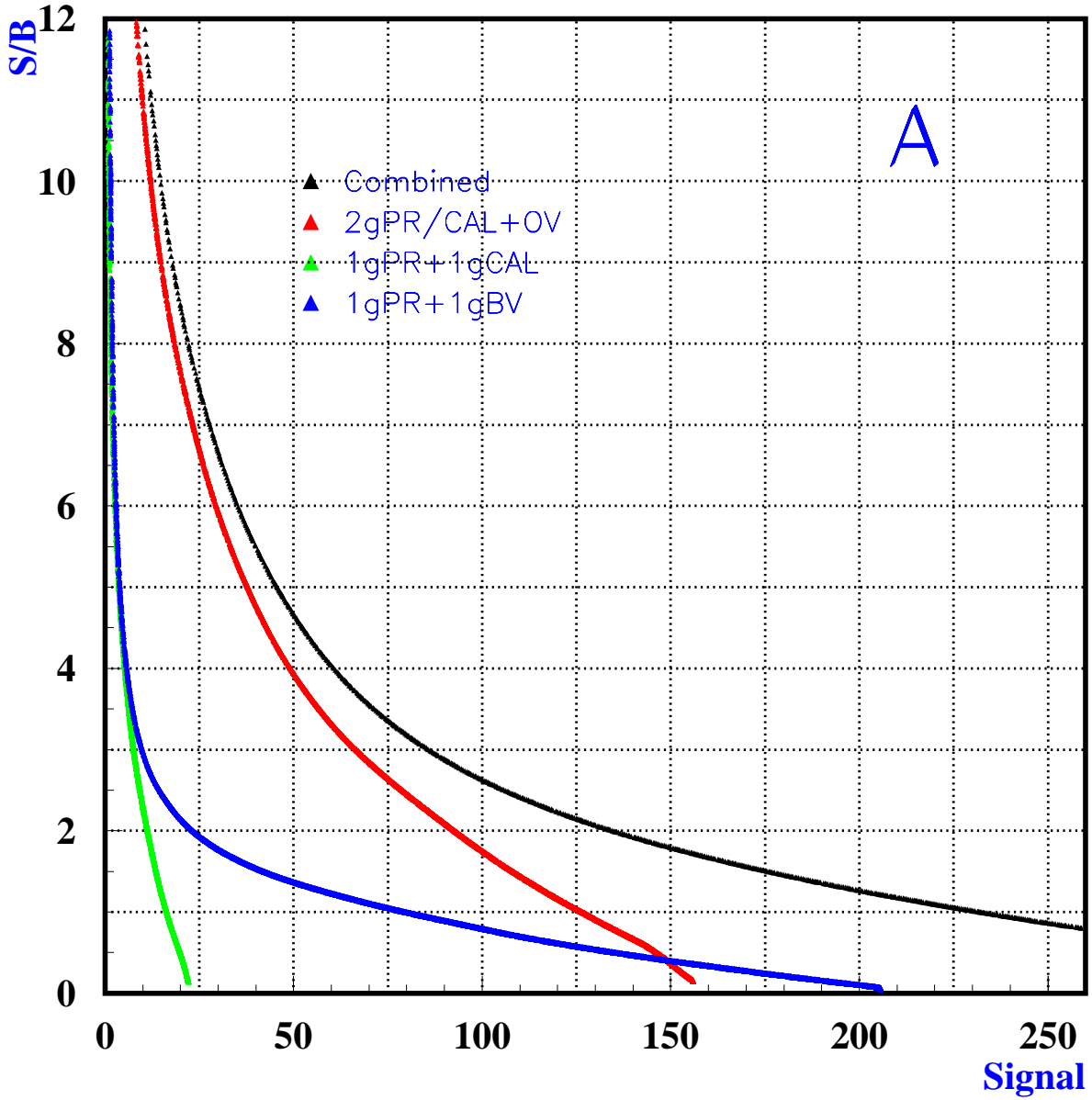


Fig. 13.19. The signal-to-background ratio (S/B) as a function of signal for all detection methods (black line) and for each of the three detection methods. The  $2\gamma$ PR method is shown in red, the  $1\gamma$ PR/CAL method is shown in green and the  $1\gamma$ PR/BV method is shown in blue.

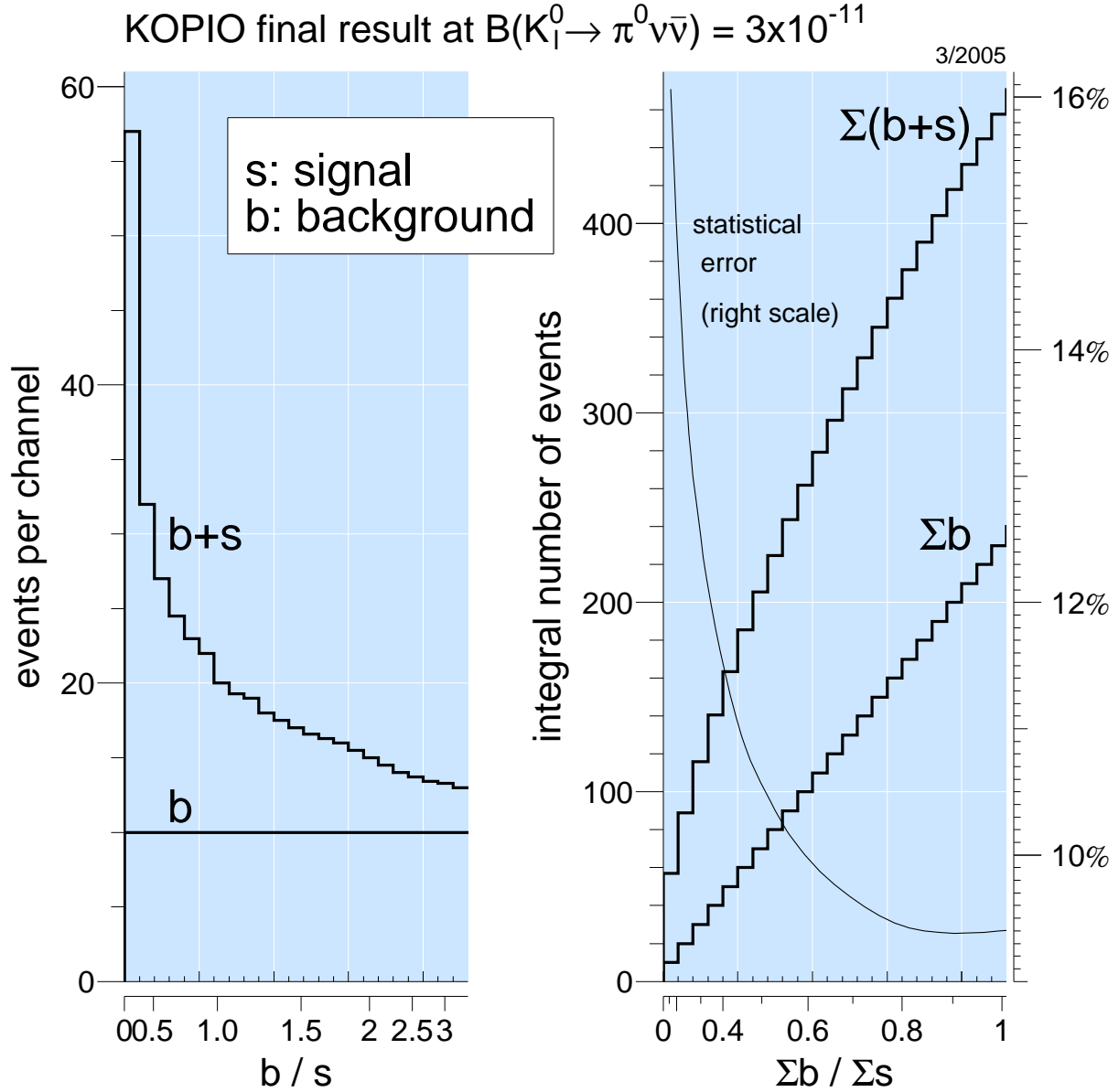


Fig. 13.20. Left: Events per channel where events are sorted into channels by  $b/s$  until a channel contains ten background events. The upper curve shows the total number of events expected in each channel. Right: The integrated number of events as a function of the total background to total signal ratio in each channel. The “statistical error” (right scale) shown is the square root of the integrated number of events divided by the total signal yield at each channel. This would be the relative uncertainty on a  $K_L^0 \rightarrow \pi^0 \nu \bar{\nu}$  branching fraction measurement if there were no uncertainty in the background yield and if the full power of the likelihood method were not employed.

## 13.8 Other Potential Backgrounds

### 13.8.1 Background from $\Lambda \rightarrow \pi^0 n$

Decays of  $\Lambda$  to  $\pi^0 n$  ( $\mathcal{B}(\Lambda \rightarrow n\pi^0) = 35.8\%$ ), if they occurred in the fiducial region, would be a potential source of background. Due to the soft production spectrum  $P(\Lambda) \leq 3.5 \text{ GeV}/c$ ,  $\Lambda$ s that are produced in the target or spoiler are suppressed by  $\sim 10^{-17}$  by the short  $\Lambda$  lifetime ( $c\tau = 7.89 \text{ cm}$ ).

The effect of  $\Lambda$  production at the upstream end of the decay region is estimated below. The  $K_L^0 p \rightarrow \Lambda \pi^+$  cross-section peaks at 3.5 mb[2] in the energy range of the  $K_L^0$  beam. Assuming that all  $K_L^0$  striking the last 5 cm of a stainless steel beam pipe interact with the peak cross-section, the interaction rate per is  $K_L^0$ .

$$3.5 \times 10^{-27} \text{ cm}^2 \times 5 \text{ cm} \times 7.87 \text{ g/cm}^3 \times 6 \times 10^{23} = 0.083 .$$

The relative number of incident  $K_L^0$  is estimated by assuming that the ratio of the  $K_L^0$  halo to the beam is  $10^{-4}$ , approximately the same as the neutron halo-to-beam ratio (Sec. 5), and that 1/10 of the  $K_L^0$  halo interacts in the 5 cm of beam pipe. Finally, if the  $\Lambda$  momentum spectrum is assumed to be the same as that of the  $K_L^0$  beam, then  $\sim 10^{-10}$  of the  $\Lambda$  produced at the upstream end of the decay volume will survive 75 cm to reach the fiducial volume. The rate of  $\Lambda$  decays to  $\pi^0 n$  in the fiducial region to the  $K_L^0$  beam rate is

$$0.083 \times 10^{-4} \times 10^{-1} \times 10^{-10} \times 3.6 \times 10^{-1} \approx 3 \times 10^{-17}$$

which is negligible relative to the SM rate of  $K_L^0 \rightarrow \pi^0 \nu \bar{\nu}$  decays.

### 13.8.2 Background from $K_S^0$ Decays

The decay  $K_S^0 \rightarrow \pi^0 \pi^0$  ( $\mathcal{B}(K_S^0 \rightarrow \pi^0 \pi^0) = 31\%$ ) occurring in the fiducial region would pose the same background problems as  $K_L^0 \rightarrow \pi^0 \pi^0$  as potential sources of in-bunch and interbunch background if the relative rate of  $K_S^0$  decays is significant compared to  $K_L^0$  decays.

From the arguments in section 13.8.1,  $K_S^0$  produced in the target or spoiler are suppressed by  $\sim 10^{-20}$  due to the  $K_S^0$  lifetime ( $c\tau = 2.68 \text{ cm}$ ). Following the discussion of section 13.8.1, and using the peak  $\sigma(K_L^0 p \rightarrow K_S^0 p)$  at 5.1 mb[2], there are  $\sim 1.2 \times 10^{-8}$   $K_S^0$  per beam  $K_L^0$  so the effective branching fraction relative to the  $K_L^0 \rightarrow \pi^0 \pi^0$  rate is

$$1.2 \times 10^{-8} \times \mathcal{B}(K_S^0 \rightarrow \pi^0 \pi^0) / \mathcal{B}(K_L^0 \rightarrow \pi^0 \pi^0) = 1.2 \times 10^{-8} \times 0.31 / (9.32 \times 10^{-4}) \approx 4 \times 10^{-4} ,$$

which is negligible if the  $K_S^0$  have the same momentum spectrum as the  $K_L^0$  beam. If the  $K_S^0$  have a different momentum spectrum, then  $K_S^0 \rightarrow \pi^0 \pi^0$  would have similar temporal properties as interbunch  $K_L^0 \rightarrow \pi^0 \pi^0$  decays and  $4 \times 10^{-4}$  is smaller than the requisite interbunch extinction of  $10^{-3}$ .

### 13.8.3 Background from Charged Kaons in the Beam

The D3 magnet bends charged particles away from the decay volume and suppresses interaction products produced in the upstream beam pipe and collimators from reaching the decay volume. A relative rate of  $K^\pm / K_L^0 = (2 \pm 1) \times 10^{-7}$  has been determined from GEANT3 simulation of the collimation system and magnets (Sec. 5). In addition, the D3 magnet deflects the charged kaons outside the neutral beam envelope (Fig. 5.7) which provides an additional suppression of  $\sim 1/20$  or more (limited by the statistics of the simulation, Sec. 5). The charged kaon decay modes most likely to be troublesome are decay modes to a single charged track and a  $\pi^0$ , or  $K^\pm \rightarrow \pi^0 \pi^\pm$ ,  $K^\pm \rightarrow \pi^0 \mu^\pm \nu$ , and  $K^\pm \rightarrow \pi^0 e^\pm \nu$  with branching fractions of 21.13%, 3.27%, and 4.87%, respectively. Other  $K^\pm$  decay modes with additional charged tracks or  $\pi^0$ s would provide additional veto suppression. The average single charged-track veto inefficiency can be conservatively estimated as  $\sqrt{\langle \bar{\epsilon}_{\pi^+} \times \bar{\epsilon}_{\pi^-} \rangle} = \sqrt{6.9 \times 10^{-11}} = 8.3 \times 10^{-6}$ , evaluated for  $K_L^0 \rightarrow \pi^+ \pi^- \pi^0$  decays where  $\bar{\epsilon}_{\pi^\pm}$  is the veto inefficiency for  $\pi^\pm$ . This estimate is conservative because the majority of the charged kaons are positively charged and  $\bar{\epsilon}_{\pi^+} < \bar{\epsilon}_{\pi^-}$ . In addition, the veto inefficiency of leptons is much better than that for charged pions. Combining all these factors and dividing by the SM

$\mathcal{B}(K_L^0 \rightarrow \pi^0 \nu \bar{\nu}) = 3 \times 10^{-11}$  yields an upper limit on the relative rate of background from charged kaon decays of

$$2 \times 10^{-7} \times 0.05 \times 0.29 \times 8.3 \times 10^{-6} / 3 \times 10^{-11} \approx 8 \times 10^{-4}.$$

#### 13.8.4 Background from $K_L^0 \rightarrow K^\pm e^\mp \nu$

Background from  $K_L^0$  beta decay is similar to background from charged kaons in the beam as described in section 13.8.3. The expected rate relative to the signal is

$$\mathcal{B}(K_L^0 \rightarrow K^\pm e^\mp \nu) \times \mathcal{B}(K^\pm \rightarrow \pi^\pm X) \times \bar{\epsilon}_X / \mathcal{B}(K_L^0 \rightarrow \pi^0 \nu \bar{\nu}) \approx 1. \times 10^{-8} \times 0.29 \times 8.3 \times 10^{-6} / 3 \times 10^{-11} = 8 \times 10^{-4}$$

where  $K^\pm \rightarrow \pi^\pm X$  is the sum of the three charged kaon decays listed in Sec. 13.8.3 with a total branching fraction of 29%,  $\bar{\epsilon}_X$  is the estimated veto inefficiency for the charged track, and the SM values of  $K_L^0 \rightarrow K^\pm e^\mp \nu$  and signal are used.

#### 13.8.5 Background from $\pi^\pm \rightarrow \pi^0 e^\pm \nu$

Charged pion beta decay ( $\mathcal{B}(\pi^\pm \rightarrow \pi^0 e^\pm \nu) = 1.025 \times 10^{-8}$ ) is a potential source of background when the charged pion is the result of  $K_L^0$  decay. Since the  $\pi^0$  from the pion beta decay has essentially the same four-momentum as the charged pion, the decay chain  $K_L^0 \rightarrow \pi^\pm e^\mp \nu$ ,  $\pi^\pm \rightarrow \pi^0 e^\pm \nu$  (Ke3) is potentially the most dangerous of this type of background because the dynamics and kinematics of the pion from  $K_L^0$  decay are very similar to that of the  $\pi^0$  from  $K_L^0 \rightarrow \pi^0 \nu \bar{\nu}$ . The other three-body semileptonic decay  $K_L^0 \rightarrow \pi^\pm \mu^\mp \nu$  (Km3) is less dangerous because the kinematics differs from that of the signal.

Table 13.7. FastMC estimate of  $K_L^0 \rightarrow \pi^\pm \ell^\mp \nu$ ,  $\pi^\pm \rightarrow \pi^0 e^\pm \nu$  background. In the table  $\mathcal{B}(K) = \mathcal{B}(K_L^0 \rightarrow \pi^\pm \ell^\mp \nu)$ ,  $\mathcal{B}(\pi) = \mathcal{B}(\pi^\pm \rightarrow \pi^0 e^\pm \nu)$ , and  $\mathcal{B}(s) = \mathcal{B}(K_L^0 \rightarrow \pi^0 \nu \bar{\nu})$ . The upper portion of the table gives the number of surviving candidates after the listed cuts. The lower portion of the table has the background rate relative to the signal after successive cuts.

Cut	$K_L^0 \rightarrow \pi^\pm e^\mp \nu$	$K_L^0 \rightarrow \pi^\pm \mu^\mp \nu$
None	300000	200000
Fiducial	1871	1445
$E(e_\pi) < 2$ MeV	204	158
$\Delta > -5$ ns	24	4
$\mathcal{B}(K)$	0.3881	0.2719
Rate relative to signal		
$\mathcal{B}(K)\mathcal{B}(\pi)/\mathcal{B}(s)$	129.4	90.6
$\times \epsilon(\text{Fiducial})$	0.802	0.652
$\times \epsilon(\Delta)$	$0.010 \pm 0.002$	$0.002 \pm 0.001$

These two decays were studied with the FastMC and the results are listed in Table 13.7. The “Fiducial” cuts require the reconstructed  $\pi^0$  vertex to lie within the envelope of the beam in the fiducial region, and suppress the background with no significant signal loss. These cuts take advantage of the fact that the charged pion frequently leaves the beam envelope before decaying. The “ $\Delta > -5$  ns” cut requires that the time and position of the impact of the lepton from the  $K_L^0$  decay at the charge veto be consistent with a  $\beta = 1$  particle propagating from the  $\pi^0$  decay vertex. The effect of this cut is to select pion beta decays that are significantly displaced from the  $K_L^0$  decay vertex. It is more effective on the semi-muonic decay mode because the pion has lower momentum and the slow ( $\beta < 1$ ) muon compensates for the displacement between the  $K_L^0$  and  $\pi^\pm$  decay vertices.

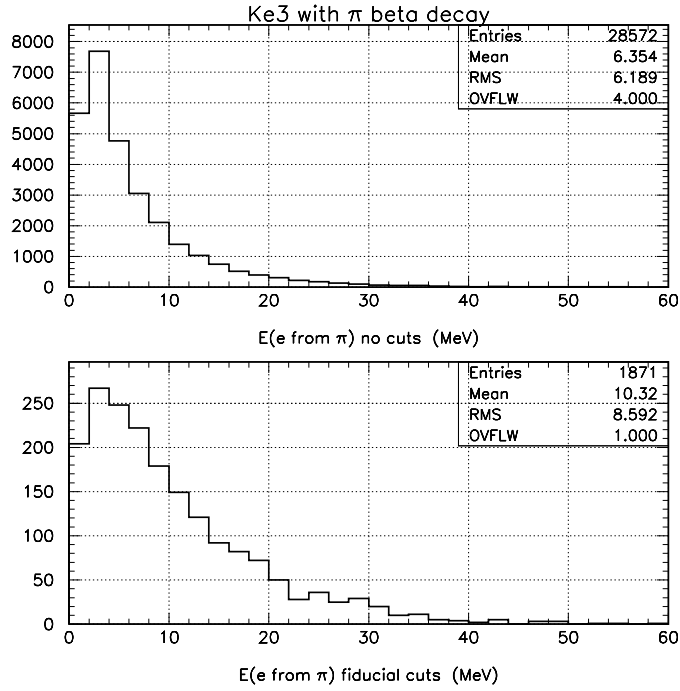


Fig. 13.21. The energy spectrum of the  $e^\pm$  from pion beta decay for pions from Ke3. The upper (lower) plot shows the distributions with no (fiducial) cuts.

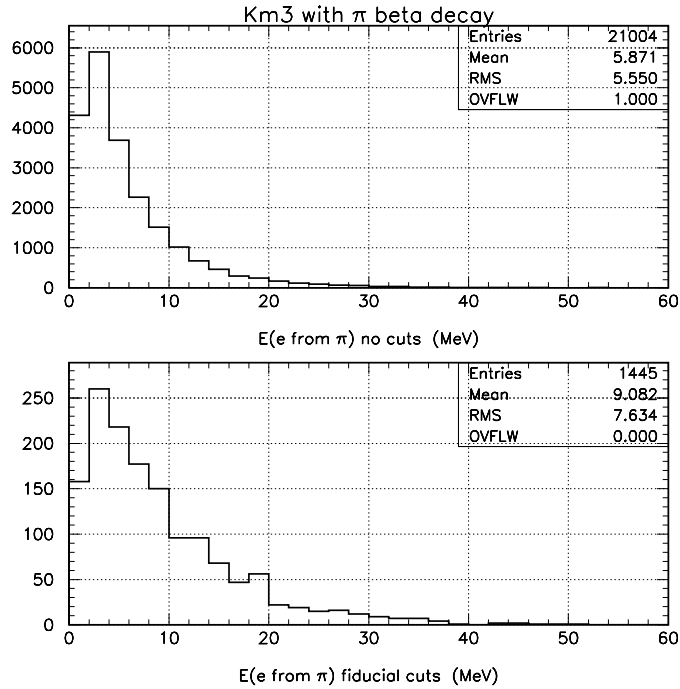


Fig. 13.22. The energy spectrum of the  $e^\pm$  from pion beta decay for pions from Km3. The upper (lower) plot shows the distributions with no (fiducial) cuts.



The main veto suppression comes from the lepton from the  $K_L^0$  decay. Additional suppression is possible by detecting the  $e^\pm$  ( $e_\pi$ ) from the pion beta decay. The energy spectra of the  $e_\pi$  for Ke3 and Km3 decays are shown in Figs. 13.21 and 13.22, respectively. The fiducial cuts select a harder  $e_\pi$  energy spectrum because the charged pion is required to be more forward in the lab. Conservatively assuming that  $e_\pi$  with energy above 2 MeV can be vetoed provides an additional background rejection of  $\sim 10$  times.

Assuming that the contribution to this background from  $K_L^0 \rightarrow \pi^+\pi^-\pi^0$  is negligible due to the reduced phase space and the veto opportunities from the  $\pi^0$ , the contribution to the background from  $K_L^0 \rightarrow \pi^\pm \ell^\mp \nu$ ,  $\pi^\pm \rightarrow \pi^0 e^\pm \nu$  is estimated to be  $\sim 0.012$  of the signal rate. This background would be suppressed by an additional factor of  $\sim 6$  if the  $\Delta < -5ns$  requirement is increased to  $\Delta < -11ns$  to avoid loss of veto inefficiency due to veto blindness (Sect. 13.9), with only a 2% loss of signal acceptance.

### 13.8.6 Background from Neutrons

There are two potential sources of background due to neutron interactions  $nN \rightarrow \pi^0 X$  where X is invisible. The first source is due to interactions of the neutron beam with the residual gas in the decay region. The second source is due to interactions of the neutron halo with the beam pipe or detector at the upstream or downstream end of the decay region.

The estimates of these potential sources were performed with a different version of the FastMC by generating  $nN \rightarrow \pi^0 X$  interactions according to phase space and baryon number conservation and with a neutron beam spectrum parameterization of the measured momentum spectrum at a  $46.5^\circ$  production angle[3]. The momentum spectrum of the neutron halo was conservatively assumed to be identical to the neutron beam spectrum. The neutron halo was assumed to be  $10^{-4}$  of the neutron beam, and the neutron beam was taken to be 1000 times the  $K_L^0$  production rate. Neutron interactions were generated at the center of the decay region to estimate the background from the first source. The residual gas in the decay region was approximated as 500 cm of air at  $10^{-7}$  Torr. Neutron interactions were generated at the upstream and downstream ends of the decay region to estimate the backgrounds from the second source. The active region of the upstream wall was taken to be one radiation length of lead (0.56cm) and the active region at the downstream end of the decay region was taken to be 15 cm ( $\sim 5$  times the  $\pi^0$  vertex resolution in  $z$ ), of polystyrene (1.032 g/cm<sup>3</sup>). The possibility that the neutron interactions in the detector material generated additional particles that could serve to veto the event was ignored.

The entire neutron-nucleon cross-section above the  $\pi^0$  production threshold was conservatively assumed to be due to the reaction  $nN \rightarrow \pi^0 X$ . The neutron-nucleon cross-section was assumed to be 35 mb, which is approximately the maximum  $np$  total cross-section above 1 GeV/c[1]. The actual  $\sigma(nN \rightarrow \pi^0 X)$  is at least 3 times smaller (Fig. 13.23).

The rates from neutrons were estimated based on loose cuts on kinematic quantities optimized for suppression of background from  $K_L^0$  decays. Potential neutron backgrounds from interaction at the upstream and downstream ends of the decay region are sufficiently suppressed by a fiducial cut on  $z(K)$ , the reconstructed  $z$  position of the  $K_L^0$  candidate vertex. For the  $2\gamma$ PR ( $1\gamma$ PR) detection modes,  $z(K)$  is required to be 75 cm (100 cm) and 50 cm (100 cm) from the upstream and downstream ends of the decay region, respectively. For the  $2\gamma$ PR detection mode, the  $z(K)$  resolution varies from approximately 15 cm at the upstream end of the decay region to 3 cm at the downstream end of the decay region. The  $z(K)$  resolution for the  $1\gamma$ PR detection modes is constant at approximately 20 cm over the length of the decay region. These cuts reduced the relative neutron background to signal rate to  $\sim 1\%$ . The dominant component of this background would be from the upstream end of the decay region. Additional suppression would be possible by utilizing the  $\chi^2$  of the kinematic fit as shown in Fig. 13.24.

There is also additional rejection due the relative timing of neutron-induced events. The reconstructed kaon decay time vs. momentum is shown in Fig. 13.25 for signal and neutron halo interactions generated at the upstream end of the decay region. The FastMC simulation used for these results neglected any dispersion in neutron interaction time due to interactions in the collimators, the distribution of neutron interactions over the US wall, or the neutron and kaon production times. Nonetheless, it appears that substantial additional neutron halo rejection can be achieved with only a slight acceptance loss based on the reconstructed time

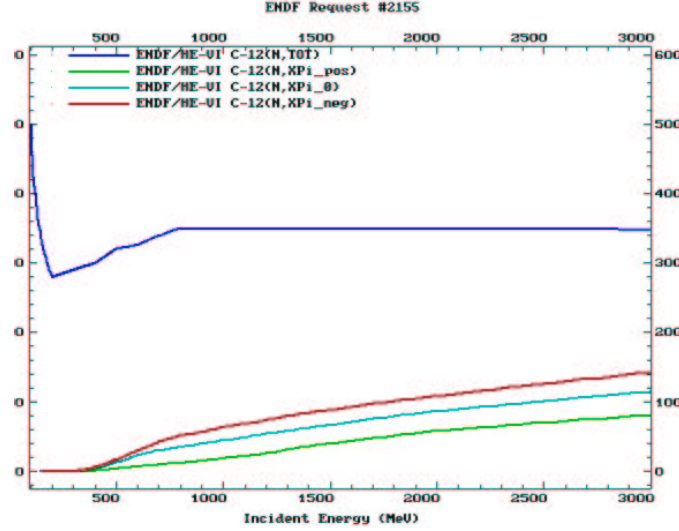


Fig. 13.23. Neutron carbon-12 cross-sections for neutron energies from 200 to 3000 MeV from the ENDF compilation[4]. The dark blue line is the total cross-section, the turquoise line is the cross-section into one or more neutral pions.

and momentum.

The total rate of neutron background from interactions from the residual gas is estimated to be  $< 1\%$  of the signal with the loose kinematic cuts, indicating that a vacuum of  $10^{-6}$  Torr would be tolerable from the point of view of neutron interactions.

### 13.8.7 Background from Antineutrons

The  $42.5^\circ$  production angle suppresses  $\bar{n}$  flux in the KOPIO beam line; nonetheless they are present and are a potential source of background via interactions with the residual gas in the decay volume. The rate of  $\bar{n}$  production from the KOPIO target was determined from a GEANT3 simulation to be  $3.9 \times 10^{-3}$  times the rate of neutron production for neutrons above 775 MeV/c (the approximate  $\pi^0$  production threshold). The relative  $\pi^0$  production rate for  $\bar{n}$  and  $n(p > 775 \text{ MeV}/c)$  interactions in the residual gas of the decay volume (approximated as water vapor) was determined from GEANT3 simulation to be  $\sim 2.5$ . Thus the rate of potential  $\pi^0$  candidates from  $\bar{n}$  interactions to that from  $n$  interactions in the residual gas is  $(3.9 \times 10^{-3}) \times 2.5 \approx 0.01$ . Since neutrons interactions in the residual gas were determined to be  $< 1\%$  of the signal rate, antineutron background is negligible.

## 13.9 Signal Losses

The spill length optimization used in Section 13.2 takes into account accidental coincidence losses due to the following items:

1. additional  $K_L^0$  decays in the microbunch,
2.  $K_L^0$  decays in other microbunches,
3. stopped muon decays,
4. halo neutron interactions, and
5. neutron interactions in the beam catcher.

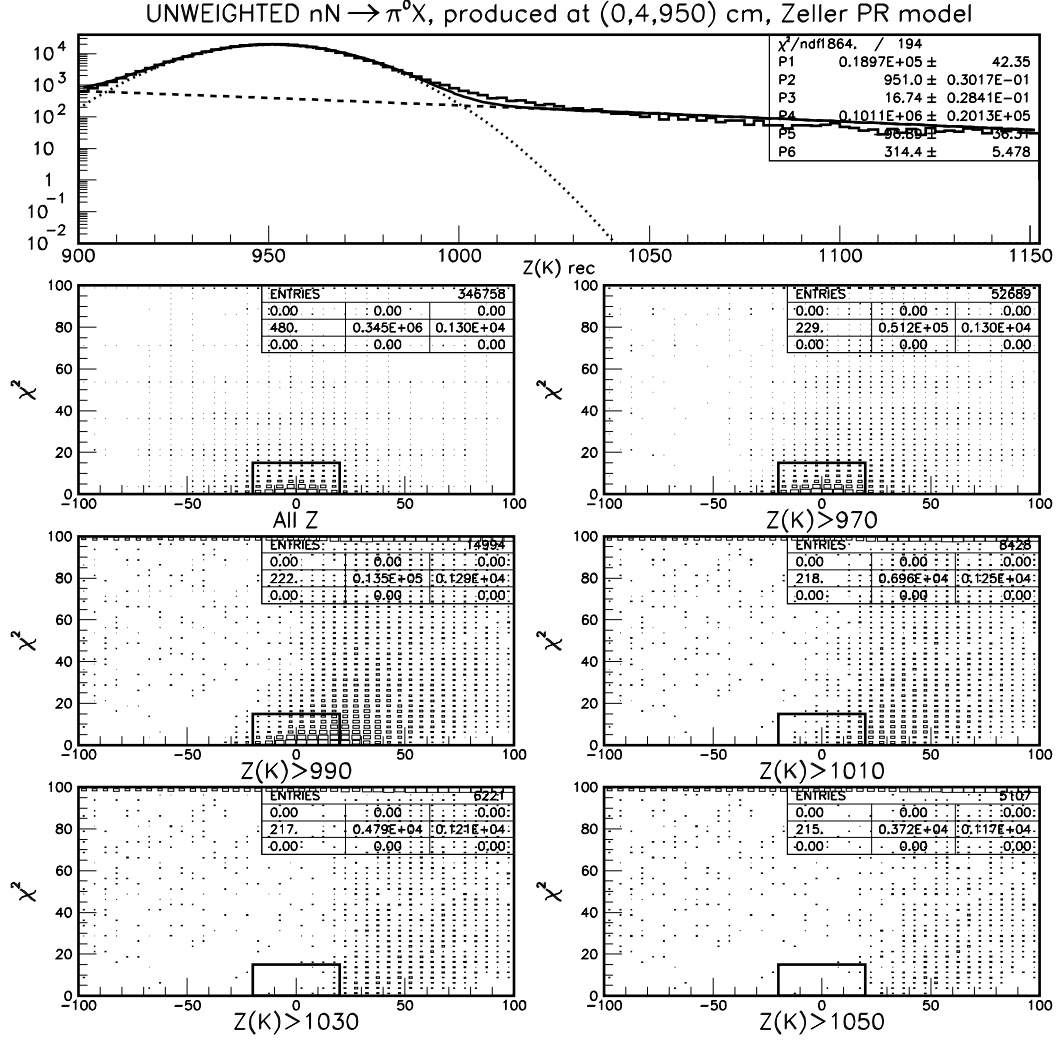


Fig. 13.24. Upper: The reconstructed  $z(K)$  distribution for  $nN \rightarrow \pi^0 X$  production at (0,4,950) cm fitted with a double Gaussian. P2 and P5(P3 and P6) are the fitted means (sigmas). (For this study, the decay region extended from 950 to 1350 cm.) The other plots from top to bottom and left to right show the distributions of  $\chi^2$  vs  $M_{\gamma\gamma} - M_{\pi^0}$  in MeV for increasingly harder cuts on  $z(K)$ . The box in these plots corresponds to  $\chi^2 < 15$  and  $|M_{\gamma\gamma} - M_{\pi^0}| < 20$  MeV. These plots correspond to the  $2\gamma$ PR detection mode and used an early, more pessimistic model of the PR.

$399.3 < p(K) < 1400.2 \text{ MeV}/c$ ,  $|M(\pi^0) - M(\gamma\gamma)| < 20 \text{ MeV}$ ,  $\chi^2 < 15$

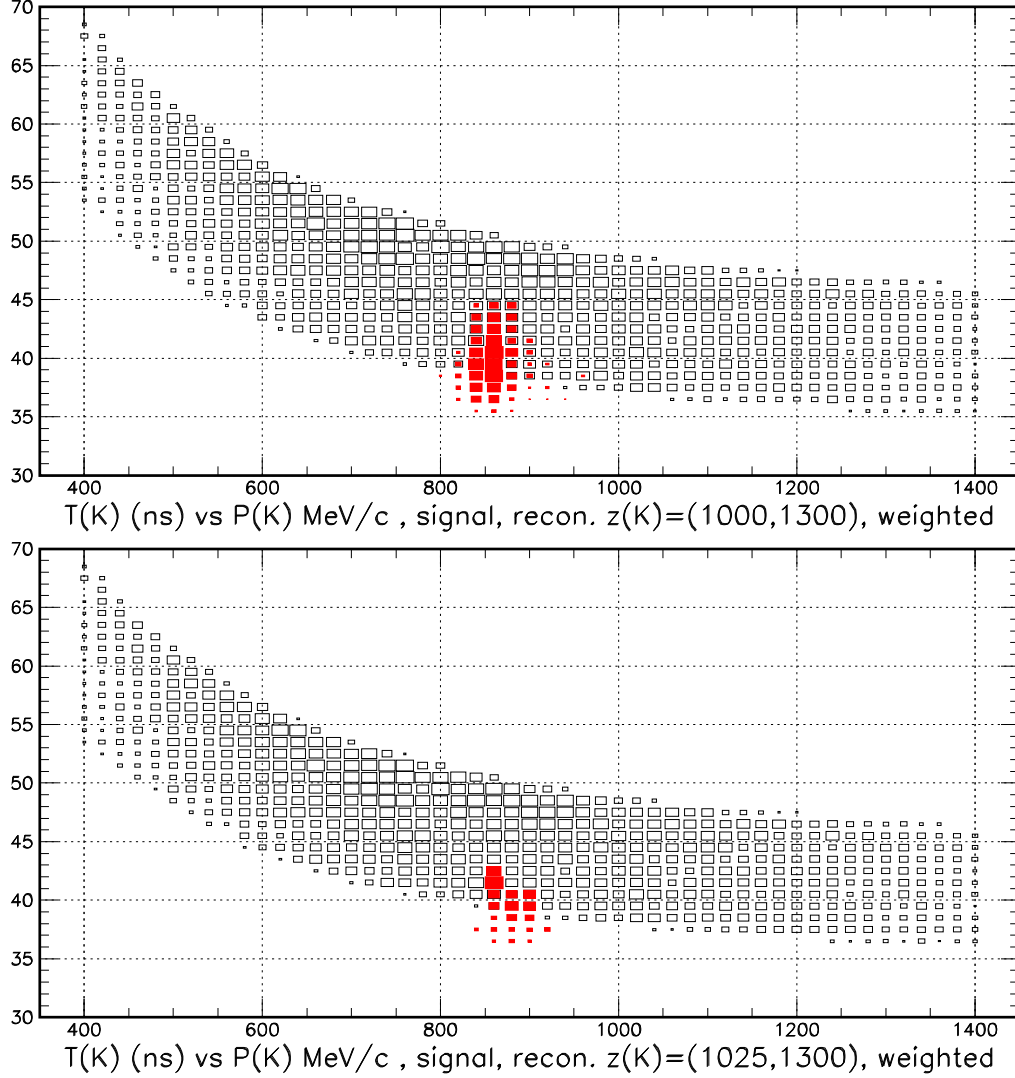


Fig. 13.25. Comparison of the reconstructed kaon decay time vs reconstructed kaon momentum for signal(open boxes) and neutron halo(red shaded boxes) events from the upstream end of the decay region. Only basic reconstruction cuts are applied and are listed in the figure. The lower plot has the current nominal cut on  $z(K)$ ; the upper plot has a looser  $z(K)$  cut to increase statistics. Each reconstructed event is weighted by the production weight (decay probability) for neutrons (kaons).

The relative sensitivity  $\Sigma$  corresponds to the number of useful  $K_L^0$  decays per calendar second and is defined by

$$\Sigma = N v e^{-kv} \left( \frac{1}{v\Delta + 1} \right), \quad (13)$$

where  $N$  is the number of decays in the fiducial volume per spill,  $v$  is the reciprocal of the spill length in seconds,  $\Delta$  is the interspill time (2.3 s, Section 4),  $k \equiv (1+r)N/f$ ;  $f$  is the microbunch frequency (25 MHz) and  $r$  is an adjustable parameter representing the relative fraction of  $K_L^0$  decays outside the fiducial region that can veto a decay in the fiducial region. The parameter  $r$  can be determined from the measurement of the survival factor  $\mathcal{S}$  of 0.435 measured at a rate of  $N_K = 3.57 K_L^0$  per microbunch exiting the spoiler with a spill length of  $1/v = 2.4$  s and  $N = 1.63 \times 10^7$  decays in the fiducial region per spill in a GEANT3 simulation of the KOPIO detector. The survival factor  $\mathcal{S}$  is the number of decays in the fiducial volume per calendar second

$$\mathcal{S} = e^{-kv} = e^{-(1+r)Nv/f}. \quad (14)$$

Solving for  $r$  gives

$$r = \frac{-f \ln \mathcal{S}_{3.57}}{Nv} - 1 = 2.06, \quad (15)$$

which indicates that, on average,  $K_L^0$  can veto an otherwise good event over a region three times as large as the fiducial region.

The survival factor due to item 2 in the list has been evaluated with a GEANT3 simulation to be 0.9621 at  $N_K = 3.57$ . This loss is proportional to the instantaneous rate or  $\mathcal{S}_{\text{otherK}} = e^{-0.0386 N_K / 3.57}$ , where  $-0.0386 = \ln(0.9621)$ .

The survival factor due to item 3 has been evaluated with the GEANT3 simulation to be 1.38% and 0.24% per nanosecond of the PV and CPV gate, respectively, at  $N_K = 3.57$ . For 12 ns PV and CPV gates, this evaluation corresponds to a survival factor of 0.8056. In general  $\mathcal{S}_{\text{stopped}\mu} = e^{\ln(1-0.0138\delta^\gamma-0.0024\delta^+)N_K/3.57}$  where  $\delta^\gamma$  and  $\delta^+$  are the PV and CPV gates in ns, respectively.

The rates in the CPV and PV (excluding the beam Catcher) due to halo neutron interactions have been estimated with a GEANT3 simulation of the KOPIO neutral beam to be 1 MHz and 1.5 MHz, respectively, at  $N_K = 4.32$ . This result gives a survival factor due to item 4 of  $\mathcal{S}_{\text{halo}} = e^{\ln(1-0.001\delta^\gamma-0.0015\delta^+)N_K/4.32}$ .

The random losses in the beam Catcher due to neutron interactions (item 5) is estimated from a GEANT3 simulation to be 2.8% at  $N_K = 4.32$  for a survival factor of  $\mathcal{S}_{\text{catcher}} = e^{-0.0284 N_K / 4.32}$ .

Taking all the survival factors into account, one has the overall sensitivity  $\Sigma'$

$$\Sigma' \equiv N v e^{-kv} \left( \frac{1}{v\Delta + 1} \right) \times \mathcal{S}_{\text{otherK}} \times \mathcal{S}_{\text{stopped}\mu} \times \mathcal{S}_{\text{halo}} \times \mathcal{S}_{\text{catcher}}, \quad (16)$$

where one makes the replacement  $N_K = Nv/fF_D$  in the survival factors  $\mathcal{S}$  in order to maximize  $\Sigma'$  as a function of spill length  $1/v$ , and  $F_D = 7.6\%$  is the fraction of  $K_L^0$  exiting the spoiler that decay in the fiducial volume. Taking into account the rate-independent survival factors of  $\mathcal{S}_{\text{self}} = 0.88$  for signal “self-veto” and  $\mathcal{S}_{\text{abs}} = 0.86$ , the total survival factor is

$$\mathcal{S}_{\text{tot}} \equiv e^{-kv} \times \mathcal{S}_{\text{otherK}} \times \mathcal{S}_{\text{stopped}\mu} \times \mathcal{S}_{\text{halo}} \times \mathcal{S}_{\text{catcher}} \times \mathcal{S}_{\text{self}} \times \mathcal{S}_{\text{abs}}. \quad (17)$$

and  $\mathcal{S}_{\text{tot}} = 0.383$  at maximum sensitivity.

To avoid loss of veto inefficiency due to previous detector activity (veto “blindness”, Section 6f), it may be necessary to extend the 12-ns width of the veto gates. Assuming a double-pulse resolution of 6 ns based on the E949 experience with waveform digitizers would increase the veto gate to 18 ns. Re-optimizing by using Eq. 16 with  $\delta^\gamma = \delta^+ = 18$ -ns gates would give a 2% loss of overall sensitivity  $\Sigma'$  at an optimal spill length of 5.36 s.

### 13.10 Summary of Signal and Backgrounds

Taking into account a signal at the SM level and including the backgrounds and acceptance losses indicated above, the anticipated signal-to-background ratio for events to be acquired in the full KOPIO running period is shown as a function of the observed signal level in Fig. 13.19. Including events up to a signal to background ratio of 0.5 there will be a total of 303 signal events. The data will be analyzed with a maximum likelihood method[5] in which candidate events are sorted into 'cells' corresponding to the relative signal-to-background of each event for each detection method. Each cell is defined such that it would contain ten background events for the full running time of KOPIO. The contribution of the resulting cells to the precision on the branching fraction is evaluated by using the maximum likelihood method and taking into account the average signal-to-background of each cell and the estimated number of observed events per cell. A presentation of the total background and signal yield showing the division into cells is shown in Fig. 13.20.

Figure 1.1 shows the exclusion limits that KOPIO will be able to achieve as a function of the fraction of the total run. Clearly, many of the models with predictions in the region between the Grossman-Nir limit[6] and the SM branching fraction would be excluded in the early part of the KOPIO program. The latter stages of the KOPIO run would achieve a relative statistical precision on the  $K_L^0 \rightarrow \pi^0 \nu \bar{\nu}$  branching fraction of 9%, in the absence of new physics, if the SM prediction were correct. The precision on a higher rate signal of non-Standard Model origin would be greater both because the signal yield would be higher and because the background would be relatively lower.

### 13.11 Parameter variations

We investigated the change in sensitivity when parameters and assumptions governing the expected signal yields were varied. Table 13.8 lists the parameters and variations. The results of the parameter variations on the sensitivity were described by three figures of merit (FOM):

1. The signal (S) yield for  $S/B = 2$  for the sum of all detection methods,
2. The signal yield for  $S/B = 8$  for the sum of all detection methods, and
3. The signal yield for  $S/B = 8$  for the  $2\gamma PR$  detection method alone.

The first FOM is a measure of the total signal yield that would be used for a precision measurement of the branching fraction. The second and third FOM are measures of the signal yield that would be used for the establishing the existence of the signal decay.

In each of the Figures 13.26, 13.27, 13.28, 13.29, 13.30, 13.31, 13.32 and 13.33, we plot the relative variation in the 3 FOMs as a function of the parameter variations. In all cases, the variations are compared to the FOM for the standard or 'baseline' parameters.

### References

1. S. Eidelman *et al.* (Particle Data Group), Phys. Lett. **B592**, 1 (2004) (URL:<http://pdg.lbl.gov>)
2. M.J. Corden *et al.*, Nucl.Phys. **B155**, 13 (1979).
3. Figure 18 of "KOPIO: Measurement of the decay  $K_L^0 \rightarrow \pi^0 \nu \bar{\nu}$ , Technical Design Report for the National Science Foundation, 8 June 2001.
4. Data from <http://www.nndc.bnl.gov/ndf/>.
5. T. Junk, Nucl. Instrum. Meth. A **434**, 435 (1999) [arXiv:hep-ex/9902006].
6. Y. Grossman and Y. Nir, Phys. Lett. **B398**, 163 (1997); V. Anisimovsky *et al.* [E949 Collaboration], Phys. Rev. Lett. **93**, 031801 (2004).

Table 13.8. Parameter variations. Parameters in bold list the baseline assumptions. A variation of the resolution by  $\pm 20\%$  indicates that the resolutions used to smear the appropriate quantities are modified as  $\sigma(\text{new}) = \pm 1.20 \times \sigma(\text{baseline})$ . “50% worse” PV inefficiency means that the inefficiency is globally increased by a factor of 1.50, or  $\bar{\epsilon}(\text{new}) = 1.50 \times \bar{\epsilon}$ .

Parameter	Variation	Figure
BV inner radius	$\pm 10\%$	13.26
X0 assumption for PV	16, 18, <b>21.6</b> , 26	13.27
Energy resolution	$\pm 20\%$	13.28
PR angular resolution	$\pm 20\%$	13.29
Position resolution	$\pm 20\%$	13.30
PV inefficiency	50% worse	13.31
X0/layer for PR	3.4%, <b>4.0%</b> , 5.0%	13.32
Time resolution	$\pm 20\%$	13.33

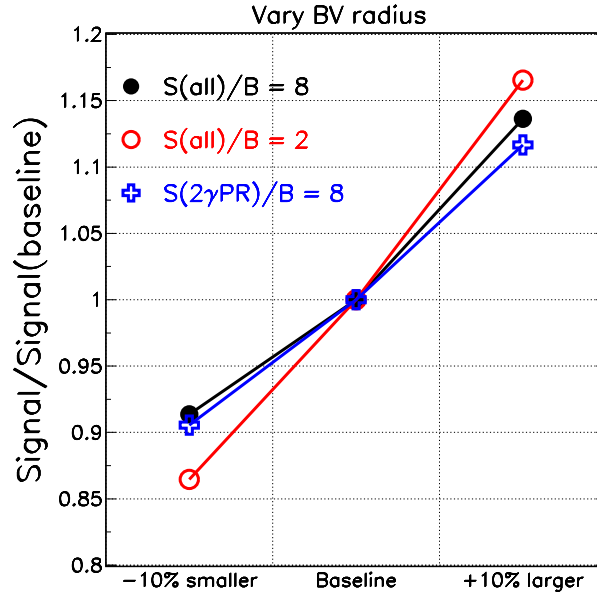


Fig. 13.26. Variation of the three FOMs as the BV radius is changed. The FOM variation is approximately  $\pm 12\%$  as the BV radius is changed by  $\pm 10\%$ , as expected qualitatively because the area of the PR increases as the radius increases.



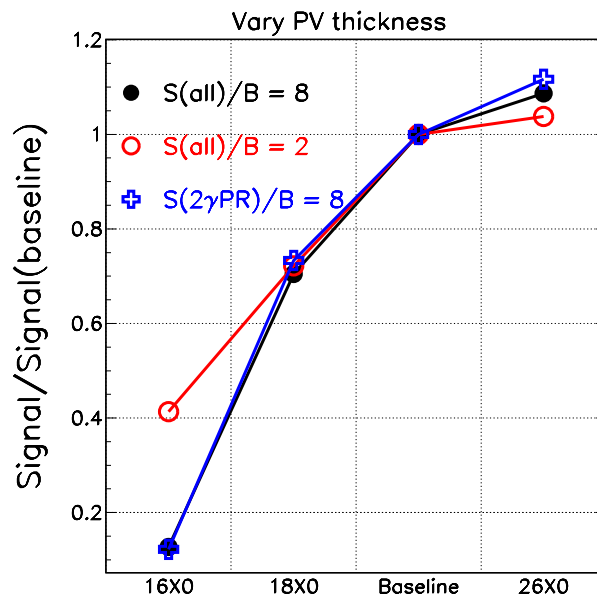


Fig. 13.27. Variation of the three FOMs as the global PV thickness in radiation lengths is changed. There is little improvement in the FOM with a thicker PV.

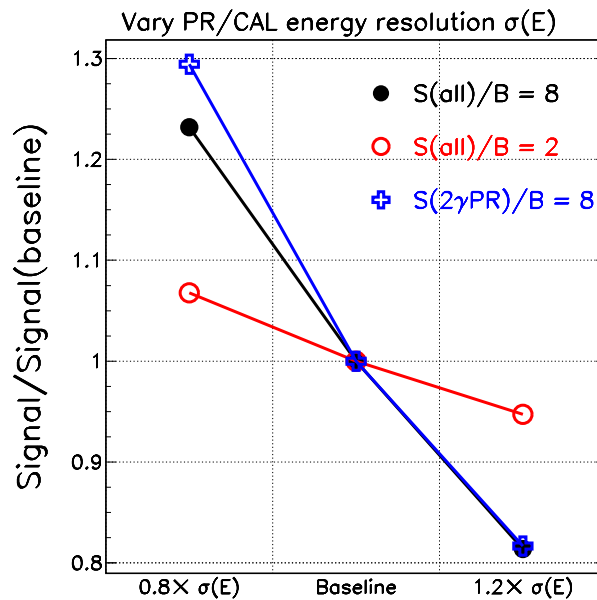


Fig. 13.28. Variation of the three FOMs as a function of the energy resolution. The FOMs for  $S/B=8$  has changes by  $\approx 20\%$  as the energy resolution changes by  $20\%$ . The signal yield for  $S/B=2$  is less sensitive to the energy resolution.

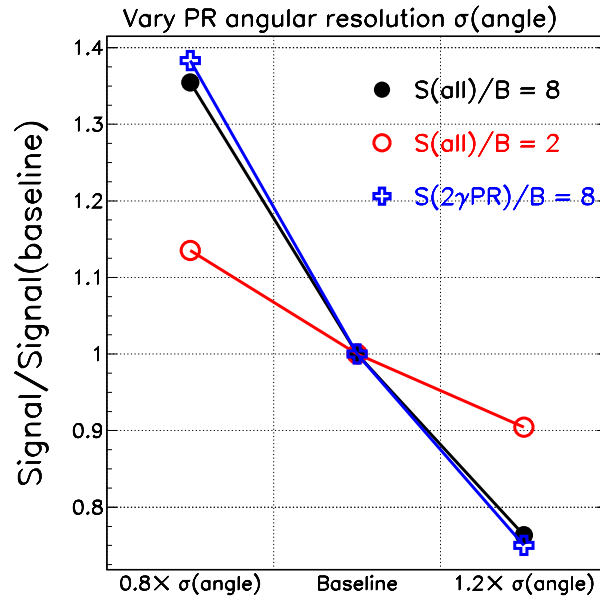


Fig. 13.29. Variation as a function of the PR angular resolution. As for the energy resolution, the high purity signal yield has the most dramatic dependence on the angular resolution of the PR.

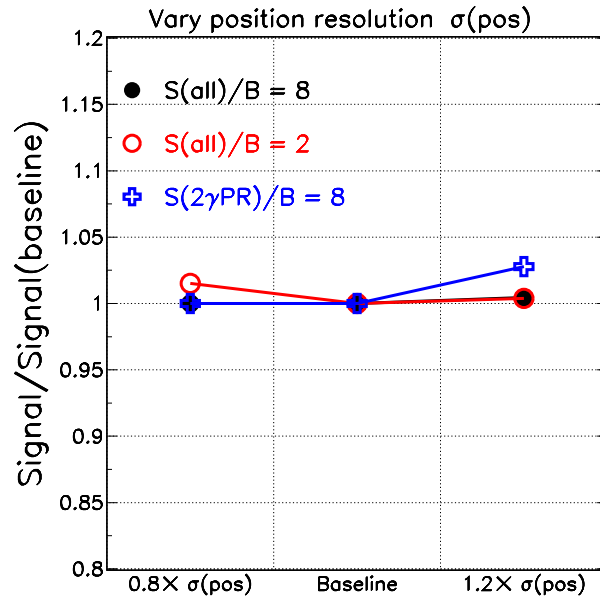


Fig. 13.30. Variation of the three FOMs as a function of the position resolution.

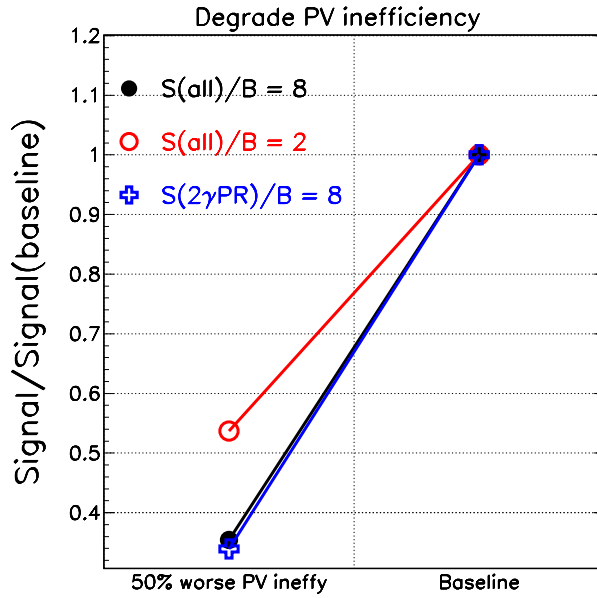


Fig. 13.31. Variation of the three FOMs as the PV inefficiency is globally degraded. Globally increasing the PV inefficiency by a factor of 1.5 decreases the signal yield by factors of 0.35 ( $S/B=8$ ) to 0.54 ( $S/B=2$ ). Roughly speaking, an increase of the inefficiency by a factor of 1.5 should increase the  $K_{\pi 2}$  background by  $1.5^2 = 2.25$ .

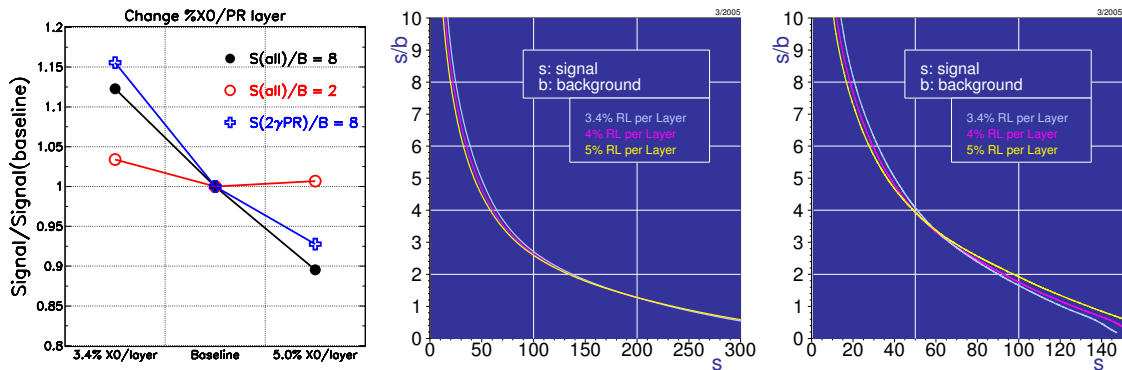


Fig. 13.32. Left: Variation of the three FOMs as the thickness in radiation lengths of each layer of the PR is changed. The dimensions of the PR are fixed so the total thickness of the PR in radiation lengths changes in proportion to the change in thickness of each layer. Center: The  $S/B$  vs  $S$  for the sum of all detection methods. Right: The  $S/B$  vs  $S$  for the  $2\gamma\text{PR}$  detection method only. In general, increasing the thickness per layer increases the conversion probability but decreases the resolution due to the increase in multiple scattering.

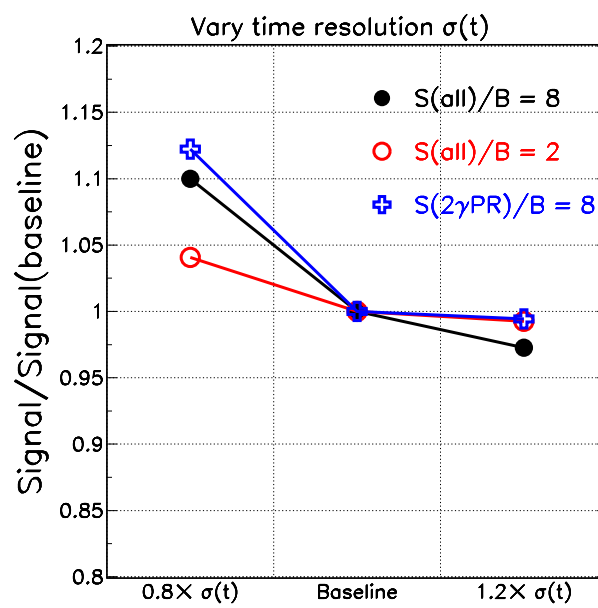


Fig. 13.33. Variation of the three FOMs as the time resolution is changed. The signal yield is only slightly degraded if the time resolution worsens.

## 14 Additional Physics Goals

### 14.1 Introduction

The KOPIO apparatus is designed on the basis of the requirements for the decay  $K_L^0 \rightarrow \pi^0 \nu \bar{\nu}$ . It has a list of remarkable properties, which can be summarized as follows:

- sensitivity corresponding to  $\sim 10^{14}$   $K_L^0$  decays;
- hermetic veto coverage;
- measurement of energy and direction of photons and electrons;
- measurement of the  $K_L^0$  momentum.

These characteristics make it an ideal tool for the measurement of rare  $K_L^0$  decays with photons and electrons in the final state. Because the KOPIO sensitivity is optimized for  $K_L^0 \rightarrow \pi^0 \nu \bar{\nu}$ , we will also have sensitivity to any decays  $K_L^0 \rightarrow \pi^0 X$  where  $X$  is unobserved.

### 14.2 $K_L^0 \rightarrow \pi^0 X$ and $K_L^0 \rightarrow \pi^0 \pi^0 X$

In models with spontaneous supersymmetry breaking, the superpartners of a Goldstone fermion, pseudoscalar  $P$  and scalar  $S$  goldstinos, should exist. In some versions of gravity-mediated and gauge-mediated theories[1] one or both of these weakly interacting bosons (sgoldstinos) are light enough to be observed in kaon decays.

If the scalar sgoldstino is lighter than the pseudoscalar, then the decay  $K_L^0 \rightarrow \pi^0 S$  is favored. Such a decay could be signaled by the highly constrained two-body kinematics of the  $\pi^0$  in the kaon rest frame. A search for the charged version[2]  $K^+ \rightarrow \pi^+ S$  placed a limit on the branching ratio of  $5.9 \times 10^{-11}$  for a massless long-lived  $S$ . KOPIO could expect to place a similar limit on the neutral analog. If the  $S$  is not long-lived, it is expected to decay via  $\gamma\gamma$  or  $e^+e^-$ . KOPIO would have good sensitivity to either of these decay modes as well.

If  $P$  is lighter than  $S$ , sgoldstinos may be observed in the decay  $K_L^0 \rightarrow \pi^0 \pi^0 P$ , rather than in the much better constrained  $K_L^0 \rightarrow \pi^0 S$ . The phenomenology of light sgoldstinos in this scenario is considered in detail in Ref.[3].

Under the assumption that sgoldstino interactions with quarks and gluons violate quark flavor and conserve parity, low-energy interactions of pseudoscalar sgoldstino  $P$  with quarks are described by the Lagrangian:

$$L = -P \cdot (h_{ij}^D \cdot \bar{d}_i i \gamma^5 d_j + h_{ij}^U \cdot \bar{u}_i i \gamma^5 u_j) , \quad (18)$$

where

$$d_i = (d, s, b) , \quad u_i = (u, c, t) ,$$

and with coupling constants  $h_{ij}$  proportional to the left-right soft terms in the mass matrix of squarks:

$$h_{ij}^D = \frac{\tilde{m}_{D,ij}^{(LR)2}}{\sqrt{2}F} , \quad h_{ij}^U = \frac{\tilde{m}_{U,ij}^{(LR)2}}{\sqrt{2}F} , \quad (19)$$

where the scale of supersymmetry breaking is denoted as  $\sqrt{F}$ .

The 90% confidence level (CL) constraints on the flavor-violating coupling of sgoldstinos to quarks, evaluated by using the  $K_L^0 - K_S^0$  mass difference and  $CP$  violating parameter  $\epsilon$  in the neutral kaon system, are:

$$|h_{12}^D| \leq 7 \cdot 10^{-8}; \quad |\text{Re}(h_{12}^D) \text{Im}(h_{12}^D)| < 1.5 \cdot 10^{-17}. \quad (20)$$

A search[4] for  $P$  in the charged kaon decay  $K^- \rightarrow \pi^- \pi^0 P$  by the ISTRA<sup>+</sup> collaboration obtained a 90% confidence level upper limit for the branching ratio  $\mathcal{B}(K^- \rightarrow \pi^- \pi^0 P)$  of  $\sim 9 \cdot 10^{-6}$  in the effective

mass range  $0 < m_P < 200 \text{ MeV}/c^2$ , excluding the region near  $m_{\pi^0}$  where it degrades to  $\sim 3.5 \cdot 10^{-5}$ . An independent measurement by KOPIO should have sensitivity for the  $\mathcal{B}(K_L^0 \rightarrow \pi^0 \pi^0 P)$  of better than  $10^{-10} - 10^{-11}$ . Thus it will be possible to increase the sensitivity for the supersymmetry-breaking parameter  $\sqrt{F}$  very significantly.

The main decay channels for light sgoldstino are  $P \rightarrow 2\gamma$  or  $P \rightarrow e^+e^-$ . The two-photon decay dominates almost everywhere in the parameter space. Depending on the parameter  $g_\gamma = \frac{1}{2\sqrt{2}} \frac{M_{\gamma\gamma}}{F}$ , where  $M_{\gamma\gamma}$  is the photino mass, sgoldstinos will have a very different lifetime. In particular, if the sgoldstino is sufficiently long lived to decay outside the detector, it is “invisible”. The estimates from Ref.[3] show that, at  $M_{\gamma\gamma} \sim 100 \text{ GeV}$  and  $\sqrt{F} > 1 \text{ TeV}$ , sgoldstinos fly away from the detector if  $m_P \leq 10 \text{ MeV}$ ; for  $\sqrt{F} > 10 \text{ TeV}$ , the borderline is  $m_P \sim 200 \text{ MeV}$ . For KOPIO measurements, the best sensitivity will obtain for an invisible  $P$ , but it will be possible to search for  $P \rightarrow 2\gamma$  inside the detector.

### 14.3 Radiative Decays: $K_L^0 \rightarrow \gamma\gamma$ , $K_L^0 \rightarrow \gamma\gamma^*$ , $K_L^0 \rightarrow \gamma^*\gamma^*$ , $K_L^0 \rightarrow \gamma\gamma\gamma$

The study of radiative decays has received continued interest in the past decade[5]. On one hand, they provide phenomenological information needed to interpret the measurement of other rare decays in terms of fundamental parameters of the SM. On the other hand, they are a testing ground for theoretical approaches to the calculation of non-perturbative effects of strong interactions in weak decays.

In this context, chiral perturbation theory[6] ( $\chi PT$ ) has grown to be one of the most fruitful tools. This low-energy effective theory, in which the fundamental fields are those associated with the octet of pseudoscalar mesons, is based on a power-series derivative expansion of a Lagrangian, the form of which is fixed by the ansatz of the chiral symmetry of the QCD Lagrangian in the limit of massless quarks. Within this framework, amplitudes for physical processes can be expressed as a perturbative expansion in terms of a few free parameters. Relations among different processes can be established and precision measurements serve the dual purpose of verifying the assumptions on which the theory is based and fixing its parameters.

Interest in these channels arises mainly in connection with the theoretical description of the decay  $K_L^0 \rightarrow \mu^+\mu^-$ , whose branching ratio has been measured with  $\sim 6200$  events by the E871 collaboration[7]  $\mathcal{B}(K_L \rightarrow \mu^+\mu^-) = (7.27 \pm 0.14) \times 10^{-9}$ . The short-distance contribution to this decay proceeds through internal quark loops, dominated by the top quark. Thus it can provide information on the  $\rho$  parameter of the Wolfenstein parameterization of the CKM matrix. However, the description of the decay includes the absorptive contribution, dominated by the  $K_L^0 \rightarrow \gamma\gamma$  contribution, and a long-distance dispersive contribution dominated by virtual photon exchange. These contributions can be constrained with precision measurements of the branching ratio of the two photon decay, as well as by accurate information on the branching ratios and form factors for channels involving virtual photon exchange such as  $K_L^0 \rightarrow \gamma e^+e^-$ ,  $K_L^0 \rightarrow \gamma \mu^+\mu^-$ ,  $K_L^0 \rightarrow e^+e^-e^+e^-$ ,  $K_L^0 \rightarrow e^+e^-\mu^+\mu^-$ , and  $K_L^0 \rightarrow \mu^+\mu^-\mu^+\mu^-$ .

A summary of the current knowledge on these decays is provided in the Table 14.1.

Although detailed calculations of acceptances and background separation have yet to be performed, a rough comparison of the number of kaon decays with the  $\sim 10^{14}$  expected in KOPIO indicates the possibility of studies with high statistics also for the rarest channels. Muon identification and measurement, for muons ranging in the Calorimeter, will also be considered. This possibility, which relies on the low average density of the Preradiator, the favorable sampling fraction of the Calorimeter and the use of kinematic fits to improve resolution, will be studied in due course.

Valuable information will thus be provided by KOPIO on the following items:

- precision measurements of the branching ratios; these will probably be limited by the knowledge of the branching ratios for the normalization channels (for which, however, an improved situation is expected after completion of the KLOE program);
- study of the form factors for the decay  $K_L^0 \rightarrow \gamma e^+e^-$ , with good sensitivity in the region of high  $e^+e^-$  effective mass. The results will allow a more stringent comparison with different models[14,15] and clarify the discrepancy between the  $\alpha_{K^*}$  parameter of the BMS[14] parameterization measured in  $\gamma e^+e^-$  and in  $\gamma \mu^+\mu^-$ , which is more sensitive to the form factor;

Table 14.1. Current status of radiative decay branching ratios of the  $K_L^0$  and the experiments that defined them.

Decay	Experiment	Kaon decays	Events	Background	PDG Value
$\gamma\gamma$	NA31[8]	$4.7 \times 10^8$	110000	700	$\mathcal{B} = (5.90 \pm 0.07) \times 10^{-4}$
$\gamma e^+ e^-$	NA48[9]	$4.1 \times 10^9$	6864	10	$\mathcal{B} = (1.00 \pm 0.05) \times 10^{-5}$
	KTEV[11]	$6.4 \times 10^{11}$	93400	476	$\alpha_{K^*} = -0.186 \pm 0.011 \pm 0.009$
$\gamma \mu^+ \mu^-$	KTEV[10]	$6.4 \times 10^{11}$	9327	222	$\mathcal{B} = (3.62 \pm 0.04 \pm 0.08) \times 10^{-7}$ $\alpha_{K^*} = -0.160^{+0.026}_{-0.028}$
$e^+ e^- e^+ e^-$	KTEV[11]	$6.4 \times 10^{11}$	1056	7.9	$\mathcal{B} = (4.16 \pm 0.13 \pm 0.13) \times 10^{-8}$ $\alpha_{K^*} = (-0.03 \pm 0.13 \pm 0.04)$
$e^+ e^- \mu^+ \mu^-$	KTEV[13]	$6.4 \times 10^{11}$	132	0.8	$(2.69 \pm 0.24 \pm 0.12) \times 10^{-9}$

- c) measurement of the form factor for  $K_L^0 \rightarrow \gamma^* \gamma^*$ , by a study of the decay to two lepton pairs, especially in the high mass region; this study will be best performed in the  $K_L^0 \rightarrow e^+ e^- \mu^+ \mu^-$  channel because the decay  $K_L^0 \rightarrow e^+ e^- e^+ e^-$  would suffer from ambiguity in the charge assignment.

The decay  $K_L^0 \rightarrow \gamma\gamma\gamma$  is allowed, but suppressed by gauge invariance and boson statistics. Estimates for the branching ratio are on the order of  $10^{-19}$ [16]. Observation would indicate new physics. The best limit, from NA31[17] is  $\mathcal{B} < 2.4 \times 10^{-7}$ . Because this channel is very well constrained in KOPIO, it is reasonable to expect that the limit can be pushed to the  $10^{-11}$  -  $10^{-12}$  range.

#### 14.4 $K_L^0 \rightarrow \pi^0 \gamma \gamma$ and $K_L^0 \rightarrow \pi^0 \pi^0 \gamma$

The measurement of the decay  $K_L^0 \rightarrow \pi^0 \gamma \gamma$  provides information on a possible CP-conserving contribution to the decay  $K_L^0 \rightarrow \pi^0 e^+ e^-$ , a channel that could exhibit large effects of direct CP violation[18] (although its measurement could be hindered by an overwhelming physics background from the decay  $K_L^0 \rightarrow \gamma \gamma e^+ e^-$ ). The CP-conserving contribution to  $K_L^0 \rightarrow \pi^0 e^+ e^-$  is associated with two-photon exchange and its estimate can be constrained by the measurement of  $K_L^0 \rightarrow \pi^0 \gamma \gamma$ .

In terms of the invariant variables

$$y = \frac{p_K \cdot (q_1 - q_2)}{m_K^2} \quad \text{and} \quad z = \frac{(q_1 + q_2)^2}{m_K^2} = \frac{m_{\gamma\gamma}^2}{m_K^2}$$

and in the approximation of CP conservation, the double differential rate for unpolarized photons is given by an expression involving two amplitudes ( $A$  and  $B$ ) corresponding to two different total angular momentum states for the two gammas ( $J = 0$  and  $J = 2$ , respectively).

$$\frac{d^2\Gamma}{dydz} = \frac{m_K}{2^9 \pi^3} \left\{ z^2 |A + B|^2 + \left[ y^2 - \frac{1}{4} \lambda \left( 1, z, \frac{m_\pi^2}{m_K^2} \right) \right] |B|^2 \right\}$$

with

$$\lambda(x, y, z) = x^2 + y^2 + z^2 - 2(xy + xz + yz) .$$

The existing experimental information[19] gives a  $\mathcal{B} \sim 1 \times 10^{-7}$  and shows a  $z$  distribution concentrated at high values ( $z > 0.3$ ), indicating a dominance of the  $A$  amplitude. This value would lead to a small contribution of two-photon exchange to  $\pi^0 e^+ e^-$  because, in the coupling to two electrons, the  $J = 0$  amplitude ( $A$ ) is subject to helicity suppression. This conclusion is not without problems for the  $\chi_{PT}$  description of this decay[20]. The calculation at  $O(p^4)$  would indeed predict a vanishing  $B$  amplitude, but it underestimates the rate ( $K_L^0 \rightarrow \pi^0 \gamma \gamma$ ) by a factor of 3. This situation has led theorists to consider contributions that



go beyond  $\mathcal{O}(p^4)$ . The processes include vector meson contributions for which phenomenological models have been formulated. Experimental information on this rather complicated situation requires a study of the  $z$  distribution in the low  $z$  region, where current data are insufficient. In KOPIO this will require adequate suppression of the  $2\pi^0$  background, which is important in this  $z$  region.

The  $K_L^0 \rightarrow \pi^0\pi^0\gamma$  decay proceeds through  $\mathcal{O}(p^6)$  terms in  $\chi PT$ . There is a conflict in the prediction of the rate with Heiliger and Sehgal[21] predicting  $\sim 1 \times 10^{-8}$ , while Ecker, Neufeld and Pich[22], predict  $\sim 7 \times 10^{-11}$ . KOPIO should be able to reach below the existing limit of NA31[23]; ( $\mathcal{B}(K_L \rightarrow \pi^0\pi^0\gamma < 5.6 \times 10^{-6}$ ).

### 14.5 $K_L^0$ beta decay, $K_L^0$ Lifetime, and Tagged $\pi^0$ Decays

The sample of  $\sim 10^{14}$  kaon decays that KOPIO expects to accumulate will allow for many precision measurements.

KOPIO has the potential to measure the beta decay of the  $K_L^0$ ,  $K_L^0 \rightarrow K e \nu$ . The highly constrained kinematics of this low- $Q^2$  decay may make it possible for KOPIO to measure its branching ratio. Current estimates predict a branching ratio near  $10^{-8}$ . We would look for the decay  $K^+ \rightarrow \pi^+\pi^0$  with a displaced vertex. The  $\pi^0$  would be reconstructed as in  $K_L^0 \rightarrow \pi^0\nu\bar{\nu}$ . Because the  $K^+$  has nearly the same momentum as the  $K_L^0$ , the energy  $E^*(\pi^0)$  of the  $\pi^0$  in the kaon rest frame will have a peak characteristic of two-body decay. The electron comes away with very low energy. Another handle to suppress the major background,  $K_L^0 \rightarrow \pi^+\pi^0 e \nu$ , is the angle between the two pions. They are nearly back-to-back in the kaon beta decay, but are produced at small angles in the background decay. In addition to the measurement of this rare decay mode, the beta decay measurement holds the potential to yield the  $K_L^0 - K^+$  mass difference to a precision of  $\sim 10$  keV.

The current value for the  $K_L^0$  lifetime is measured to  $\sim 1\%$ . The large sample of  $2\pi^0$  and  $3\pi^0$  decays will give us the opportunity to do much better. It also allows for tagging of  $\pi^0$  decays by using either the  $2\pi^0$  or  $3\pi^0$  decay mode. From this sample, we may well be able to improve on the measurement of  $\pi^0 \rightarrow e^+e^-$  which has a branching ratio of  $6.2 \times 10^{-8}$ , or improve on the 90% C.L. upper limit for  $\pi^0 \rightarrow \nu\bar{\nu}$ , which is currently  $1.7 \times 10^{-6}$ .

### References

1. G. Giudice and R. Rattazzi, Phys. Rep. **322** (1999) 419; S. Dubrovsky, D. Gorbunov and S. Troitsky, Usp. Fiz. Nauk **169** (1999) 705, English translation in Phys. Usp. **42** (1999) 623 (hep-ph/9905466).
2. S. Adler et al., Phys. Rev. Lett. **88**, 041803 (2002).
3. D.S. Gorbunov and V.A. Rubakov, Phys. Rev. D **64**, 054008 (2001).
4. O.G. Tchikilev et al., Phys. Lett. B **602** (2004) 149-156.
5. For a recent review, see A.R. Barker and S.H. Kettell, Ann. Rev. Nucl. Part. Sci. **50**, 249 (2000).
6. J. Gasser and H. Leutwyler, Ann. Phys. **B158**, 142 (1984);  
J. Gasser and H. Leutwyler, Nucl. Phys. **B250**, 465 (1985).
7. D. Ambrose et al., Phys. Rev. Lett. **84**, 1389 (2000).
8. H. Burkhardt et al., Phys. Lett. **B199**, 139 (1987).
9. V. Fanti et al., Phys. Lett. **B458**, 553 (1999).
10. KTeV Collaboration, A. Alavi-Harati et al., Phys. Rev. Lett. **87**, 071801 (2001).
11. Jason LaDue, University of Colorado - Boulder Thesis, May 2003.
12. A. Alavi-Harati et al., Phys. Rev. Lett. **86**, 5425 (2001).
13. A. Alavi-Harati et al., Phys. Rev. Lett. **90**, 141801 (2003).
14. L. Bergström, E. Massó and P. Singer, Phys. Lett. **B131**, 229 (1983).
15. G. D'Ambrosio, G. Isidori and J. Portols, Phys. Lett. **B423**, 385 (1998).
16. P. Heiliger et al., Phys. Lett. **B327**, 145 (1994).
17. G.D. Barr et al., Phys. Lett. **B358**, 399 (1995).
18. See, e.g. J.F. Donoghue et al., Phys. Rev. D **51**, 2187 (1995).
19. KTeV Collaboration, A. Alavi-Harati et al., Phys. Rev. Lett. **83**, 917 (1999);  
NA48 Collaboration, M. Contalbrigo, in J. Tran Thanh Van, Ed., Proc. XXXV Rencontres de Moriond, Les Arcs, France, March 2000 (Paris, Ed. Frontieres, 2000).

- 20. G. D'Ambrosio *et al.*, Nucl. Phys. **B492**, 417 (1997).
- 21. P. Heiliger and L.M. Sehgal, Phys. Lett. **B307**, 182 (1993).
- 22. G. Ecker, H. Neufeld and A. Pich, Nucl. Phys. **B413**, 321 (1994).
- 23. G.D. Barr *et al.*, Phys. Lett. **B328**, 528 (1994).

## 15 Operations Plan

The first KOPIO operations are currently scheduled for the third and fourth years of the construction project with a total of 840 hours at low duty factor for beam tests (as presented at the November 4–5, 2004 RSVP AGS Review). The goals of these beam tests are to verify the performance of the neutral beam ( $K_L$  production, neutron halo, ambient rates), the microbunching system (beam bunch width, interbunch extinction), and prototype detectors for each subsystem (rates, thresholds, efficiencies, double-pulse resolutions).

An engineering run of 800 hours is scheduled during the last year of the construction project. The primary purpose of this run is to verify the performance of the entire detector system, smoke out any problem channels, and calibrate the entire detector. During this run for 200 hours, assuming that the detector is essentially fully debugged, KOPIO should reach a world record sensitivity of better than  $1 \times 10^{-10}$  (eclipsing the expected limit from E391a at KEK).

To achieve the full sensitivity discussed in previous chapters, KOPIO requires 12,000 hours of physics operation with a proton intensity of 100 Tp/spill. The KOPIO experiment has been optimized from Monte Carlo studies of rates and detector performance to run with 100 Tp/spill of 25.5-GeV/c protons, an AGS cycle of 5.3s/7.6s, and an expected  $K_L$  flux of  $2.9 \times 10^8$ /spill through the spoiler. After actual  $K_L$  production, rates, and detector performance have been measured, the experiment can be re-optimized, if necessary, by adjusting the spill length. Based on calculations by the Collider Accelerator Division (CAD), the AGS should be able to run with spill lengths of up to 6–7 seconds at the nominal AGS momentum of 25.5 GeV/c. Should KOPIO find an optimum spill length greater than such values, then the AGS momentum can be lowered commensurately at the cost of a small reduction in the  $K_L$  flux. We assume an interspill time of 2.3 seconds with 6 Booster transfers to the AGS per cycle, as has been successfully operated in 1998 and 2001–02. With the current simulation of operating conditions, a sensitivity per hour of  $1.8 \times 10^{-9}$  is achieved. The dependence on spill length is shown in Figure 13.1.

The physics program of KOPIO has two phases: 1) the first year of operations (2500 hours) will give KOPIO a five sigma discovery potential of any new physics to the level of  $B(K_L^0 \rightarrow \pi^0 \nu \bar{\nu}) \geq 1 \times 10^{-10}$ , and 2) the remainder of the running will yield a sensitivity 200 times below the SM prediction and give a precise measurement of  $\eta$  or a five sigma discovery of new physics at  $B(K_L^0 \rightarrow \pi^0 \nu \bar{\nu}) \geq 5 \times 10^{-11}$ .

Given the substantial CAD fixed labor cost of operating a high intensity program at the AGS, the most cost-effective plan for running RSVP will be one that maximizes the number of weeks run in each year. The CAD plan, based on an assumption of 27 weeks per year of RHIC operations, allows a minimum (maximum) of 15 (19) weeks per year of RSVP operations along with RHIC and 10 weeks per year outside of RHIC operations. The available running time per week with RHIC is currently estimated as 80 hours, and without RHIC it is 120 hours. Following the RSVP AGS Review of November 4–5, 2004, we assume an average of 27 weeks per year (17 weeks with RHIC and 10 weeks without RHIC). The total running time per year would be 2560 hours (1360 + 1200). If we assume 2 weeks per year for tune-up, we are left with 2400 hours/year. The KOPIO exposure could therefore be completed with five years of running.

## 16 Summary

In this Conceptual Design Report, the scientific motivations, techniques, and instrumentation associated with the KOPIO measurement of  $K_L^0 \rightarrow \pi^0 \nu \bar{\nu}$  have been described. Many promising approaches to physics beyond the Standard Model (SM) will be tested by this high sensitivity measurement, and the results will be complementary to measurements at the high energy frontier. For instance, if supersymmetry or other new physics were to be discovered at the LHC, the results from KOPIO would be critical for unraveling whether the flavor structure of this new physics is governed by the SM Yukawa couplings (e.g. Minimal Flavor Violation) or whether there are new sources of CP violation with a new flavor structure.

The goal of KOPIO is to uncover new physics processes, if they are present, in  $K_L^0$  decays that have experimental signatures similar to that of  $K_L^0 \rightarrow \pi^0 \nu \bar{\nu}$ . KOPIO's sensitivity will extend below the SM prediction for the  $K_L^0 \rightarrow \pi^0 \nu \bar{\nu}$  branching ratio. In the absence of a non-SM result, KOPIO will obtain a precision of 10% or better on the  $K_L^0 \rightarrow \pi^0 \nu \bar{\nu}$  branching ratio at the SM level resulting in the single most precise measurement of the parameter governing CP violation in the SM. The KOPIO approach results in an experiment that under all assumptions explores the most fundamental aspects of particle physics.

The basic features of the measurement involve an intense microbunched beam of  $100 \times 10^{12}$  protons on target during each spill of the AGS used to produce an intense carefully collimated neutral kaon beam. The detection system employing a unique high efficiency, high resolution pointing calorimeter is used to identify the single  $\pi^0$  signal in the decaying kaon's center-of-mass system while highly efficient photon veto and charged particle vetos ensure that no other particles were present in coincidence.

The techniques to be used in KOPIO to achieve unprecedented levels of sensitivity involve advances to aspects of accelerator and detector technology including 25-MHz microbunching at full intensity, photon and charged particle detection efficiency, and pointing and sampling calorimeter resolution. However, all important principles of the technique have been tested experimentally with prototypes and/or studied with extensive simulations. The maximal levels of information obtained on the characteristics of each event, including measurements of kaon time-of-flight, energy, position, and angle of photons, and the absence of additional coincident detected particles, allow suppression of backgrounds to the required level and foster the robustness of the approach.